Characterisation of sedimentary structure and hydraulic behaviour within the unsaturated zone of the Triassic Sherwood Sandstone aquifer in North East England

Steven William Truss

Submitted in accordance with the requirements for the degree of

Doctor of Philosophy

University of Leeds

School of Earth Sciences

June 2004

The candidate confirms that the work submitted is his own and that appropriate credit has been given where reference has been made to the work of others.

To the memory of William Frederick Truss.

Acknowlegements

Firstly I would like to express my sincere thanks to Dr Jared West and Professor Jim Best for their help, supervision and continual encouragement throughout this project. Their support, advice and friendship helped me through the times when I believed that I was never going to see light at the end of the tunnel. I also need to thank Jared for the days spent accompanying me in the field, and for all the pub lunches.

On a personal note, my thanks also must go to Katie Truss, for believing in me throughout both my Open University and Leeds degrees, and for the thousand and one ways in which she has helped over the years. To Pam, for being my special friend, for always being there and for accepting the fact that sometimes my work would take priority. To Norma Rothwell who convinced me that I could succeed at PhD level and helped with references and applications.

To the members of my transfer group, my examiners and other people who supported me at various times. In no particular order I would like to thank Graham Stuart, Noelle Odling, Tavi Murray, Charlie Bristow, Martin Shepley and Andy Binley for their willing and helpful advice and encouragement. I am very grateful to several people for invaluable assistance in field and laboratory data collection. Silke Hartmann and Pamella Vose, Graham, Pete and Mark at the various quarries for putting up with us, to Nicholas Leinart for the grain size analysis, Kirk Handley for probe construction and help in the labs, Lesley Neve for the XRD work, Pete Winship for starting the ball rolling, Yi Huang and Mansor Nakhkash at Liverpool, and Matt Kilner for too many days spent walking around quarries to the beat of a beeping radar.

A special mention is reserved for those with whom I shared an office, Matt and Silke (again) Emma, Trish, Egerton, Sergio and Dave for putting up with me, without you my time at Leeds would have been the poorer. I would also like to thank everybody else at Leeds who has contributed help, food, advice, coffee, sympathy or beer.

Finally I would like to thank the people who made it all possible, NERC through CONNECT grant NER/D/S/1999/0079, the Environment Agency and University of Leeds for their financial support.

Abstract

A study of the sedimentological framework and permeability characteristics of the Sherwood Sandstone has been undertaken together with a detailed investigation of moisture migration in the vadose zone at a single field site. Sedimentary structure and likely permeability variations were studied by use of laboratory grainsize analysis, logging of nearby outcrops, borehole geophysics and Ground Penetrating Radar (GPR). GPR is ideal for vadose zone hydrogeological applications as the majority of the features imaged are visible to radar as a result of variations in capillary held moisture, and the amount of capillary retention is controlled by the size of the pore throats in the sediments, which directly influences their permeability properties. Combined use of GPR, reconstruction of sedimentary facies and quantification of permeability characteristics has provided detailed 3D models of the sedimentary subsurface.

Time Domain Reflectometry (TDR) was used to monitor water movement within the Sherwood Sandstone at a site near Selby in Yorkshire, creating a vertical and lateral profile of groundwater movement within the unsaturated zone. Moisture content has also been monitored using a neutron probe, and a commercially-available portable packer system, which have provided verification of the accuracy of the custom-made TDR system. The TDR installations consisted of automated arrays of TDR probes, permanently installed upon borehole packers at varying depths, and these have provided moisture content data of a high temporal resolution. The TDR system has allowed monitoring of seasonal moisture variation under natural rainfall loading, and the results have been interpreted in order to gain a better understanding of groundwater migration at a different scale to data previously available.

The bulk of the rock in the Sherwood Sandstone aquifer study area consists of relatively permeable medium-grained sandstones. However, results suggest that vertical flow in the unsaturated zone may be impeded by the presence of relatively impermeable fine sandstone units, which correspond to bar top and slack water environments, and occasional mudstone layers representing overbank deposits. This restriction to vertical flow may cause localized perched aquifer conditions, which provide sufficient hydrostatic head to initiate horizontal migration in the overlying rock. Modelling of real rainfall events suggests that 25% of the water present in the perched aquifer layers undergoes lateral or bypass flow (i.e. it drains laterally rather than through the fine-grained layers). In the saturated zone, the horizontal flow of groundwater in the Sherwood Sandstone aquifer is likely to be dominantly via the relatively coarse, trough-stratifed sandstone layers, so that a low proportion of the total aquifer porosity may provide a route for rapid contaminant transport.

Table of Contents

CHAPTER 4

GROUND PENETRATING RADAR

CHAPTER 5

MOISTURE CONTENT PROFILING USING THE GRAVIMETRIC, NEUTRON PROBE AND TRIME METHODS

List of figures

List of Tables

List of abbreviations.

Ch.	Full Name	Abbv.	Pp.
1.1	Dense non-aqueous polar liquid	DNAPL	1
1.1	Light non-aqueous polar liquid	LNAPL	1
1.1	Environment Agency	EA	2
1.1	Source protection zone	SPZ	2
1.2	Time Domain Reflectometry	TDR	3
1.3	TDR with intelligent micromodules	TRIME	4
2.2	London-Brabant Massif	LBM	9
2.4	Scanning Electron Microscope	SEM	16
2.4	Redox potential	Eh	17
2.5	Non-aqueous phase liquid	NAPL	24
3.2	Electronic distance meter	EDM	41
3.3	X-ray diffraction	XRD	61
4.1	Ground Penetrating Radar	GPR	68
4.1	Electromagnetic	EM	68
4.3	Automatic gain control	AGC	82
4.3	Spreading and exponential gain	SEC	82
4.3	Automatic gain control	AGC	82
4.3	Two way travel time	TWT	83
4.3	Common Mid Point	CMP	83
5.1	Meteorological Office Rainfall and Evaporation Calculation System	MORECS	112
5.1	British Atmospheric Data Centre	BADC	113
6.2	Finite Difference Time Domain	FDTD	157

CHAPTER 1
INTRODUCTION.

1.1 Background.

Water is an essential requirement for life, and clean uncontaminated drinking water is a prerequisite for keeping human populations healthy. Contaminated water kills an estimated 2.2 million people per year worldwide (United Nations, 2003) and so protecting clean water resources from contamination is essential for the future. Groundwater is an essential source of water in many areas and may be defined as 'all the water contained in the void space within fully saturated rocks' (Allaby and Allaby, 1990, Freeze and Cherry, 1979). The term 'groundwater' excludes water migrating through the unsaturated (or vadose) zone, toward the water table. The vadose zone however, often acts as an important buffer, where pollutant degradation can occur, and is typically a three-phase environment, where air, water and rock are all in free contact with each other. Naturally filtered by soils and rocks, aquifer-derived groundwater is therefore generally more resistant to contamination than surface waters, and often occurs in areas where surface water supplies are rare.

Although groundwater is generally less vulnerable than surface waters, contamination may still occur. Furthermore, contamination of groundwater is less obvious than surface water, since pollutants often remain unseen until they are abstracted and enter the public water supply, and once contaminated, remediation of polluted groundwater is very difficult. Natural attenuation processes that take place in a few days or weeks in surface waters may take decades in groundwater (Environment Agency, 1998). Sandstone aquifers are generally efficient at filtering out impurities, with the vadose zone acting as a buffer, reducing contaminant levels by filtration and chemical/biological breakdown of pollutants. Pathogens with a smaller diameter than the sandstone pore throats may however, still pass through to the saturated (phreatic) zone (Bloomfield *et. al.*, 2001). DNAPLS (Dense Non-Aqueous Polar Liquid) from industrial processes, LNAPLS (Light Non-Aqueous Polar Liquid) such as petrol, and dissolved ionic pollutants such as nitrates from fertilisers may also pass through the vadose zone. Biological, chemical and physical processes within the vadose zone all act to degrade such pollutants into less harmful substances but these attenuation processes take time, and so the ability of the vadose zone to remediate polluted water is related to residence time. Residence time depends upon the velocity and path of substances migrating through it, as well as vadose zone thickness and composition. Clays, organic content, temperature, free water abundance and oxygen levels all influence the chemical filtering process.

In England and Wales, the Environment Agency (EA) is responsible for protecting groundwater, and employs various methods, grouped under the general title of Groundwater Resource Protection, to assess the vulnerability of subsurface water resources to both diffuse and point sources. A primary method of predicting groundwater vulnerability used by the EA is the concept of groundwater vulnerability assessment and mapping. The nature of the overlying soil, drift-deposits, geological stratification and the thickness of the unsaturated zone are all taken into account and combined to predict travel times to the water table (Environment Agency, 1998). These data are used to predict and map groundwater vulnerability at a regional scale.

However, the groundwater vulnerability mapping approach may cause difficulties when applied at a smaller scale. The accuracy of groundwater vulnerability maps depends upon data density. Local permeability variations may allow pollutants to break through into the aquifer, particularly if combined with a concentrated point source of pollution. To address the issue of local permeability variation, the EA define Source Protection Zones (SPZs), which are areas in unconfined aquifers around water abstraction locations, where restrictions are placed upon potentially damaging activities. The aim of SPZs is to provide sufficient time for pollutants to degrade within the aquifer before they are abstracted along with the groundwater. However, if travel times prove higher than anticipated by current models of groundwater behaviour, then contamination may occur.

Current models of moisture migration though the vadose zone generally tend to be over-simplistic, considering vertical migration to be the only means of transmission, which in a homogeneous rock medium, would be perfectly adequate. However, many aquifers are far from homogeneous, possessing a richly detailed sedimentary structure, which is strongly suspected of diverting flow away from the vertical and focussing/directing it through high permeability zones. This type of non-vertical flow mechanism could have serious effects on the transit time of fluids through the vadose zone, and may have implications for assessment of groundwater vulnerability.

The work presented in this thesis looks at the sedimentary structure of the Triassic Sherwood Sandstone aquifer in Northeast England, the seasonal variation in moisture in the vadose zone, responses of the rock:water:air system to periods of natural drought and flood, and seeks to increase understanding concerning the mechanisms of moisture, and therefore pollutant, migration through the vadose zone of the aquifer.

1.2 Research objectives.

The research presented in this thesis aims to determine the pathways taken by moisture migrating through the vadose zone of the Sherwood Sandstone aquifer. It is anticipated that the heterogeneous nature of the aquifer may be deflecting water from the vertical pathway assumed by most models that are used to assess groundwater vulnerability. The possibility of non-vertical flow has implications for water management, as lateral flow may allow high-velocity, indirect travel that may reduce travel times to the water table, causing increased risk of contamination of groundwater supplies.

The physical and geological properties of the sandstone in the Selby-Doncaster study area are examined in detail by outcrop, core and gamma logging, together with investigations using ground-penetrating radar. Results from these investigations are used to create linked sedimentary and radar facies schemes which characterise the Sherwood Sandstone structure in this area. Data from the literature is then used to suggest likely permeability characteristics for a test site at Great Heck in West Yorkshire that contains a typical sedimentary sequence.

Further investigation using borehole moisture monitoring techniques is conducted which provides detail on the hydraulic behaviour of the facies units encountered at the test site. Data from monitoring changes in moisture distribution within the vadose zone, resulting from natural rainfall events, are combined with the sedimentary and radar facies schemes derived in earlier chapters, and used to construct two opposing conceptual models of moisture migration. The models assume either that water flows in a predominantly vertical direction or travels laterally, following high permeability zones in coarser grained facies units. The models also predict the response of high-density time-series moisture content measurements for either scenario.

A fully automated, packer mounted, Time Domain Reflectometry (TDR) system is designed and installed at Great Heck Quarry, and moisture contents are obtained daily for approximately fifty separate TDR probes, giving an unparalleled time-series dataset over a time period of one year. This dataset is used to determine which model best fits the response of the natural system to rainfall events and provides an accurate estimate of field-scale travel times to the water table.

Hence, the aims of this research are to determine the primary mechanism of moisture transmission through the vadose zone. To determine accurate travel times for moisture migration between the surface and the phreatic zone and to design, install and field-test a method of applying the TDR system within a rock environment.

1.3 Outline of thesis

Chapter 2 provides a comprehensive literature review of the Sherwood Sandstone and its behaviour, discussing its physical properties, mode of formation and hydrogeology.

Chapters 3 and 4 all concern the distribution of sedimentary and radar facies within the Sherwood Sandstone, the derived facies scheme is then used in Chapter 5, as a framework for two alternative conceptual models of moisture flux through the vadose zone.

Chapter 3 concerns test site information, sedimentary logging, grainsize analysis, borehole coring and other methods of directly measuring rock properties, leading to the construction of a sedimentary facies model.

Chapter 4 contains an introduction to dielectric permittivity, discusses the use of ground penetrating radar as a tool for characterisation of sites and leads to a radar log / radar facies model.

Chapter 5 concerns the measurement of moisture content using gravimetric, TDR with intelligent micromodule elements (TRIME) and neutron probe methods and provides detailed information of the hydrological behaviour of each facies unit in the vadose zone.

Chapter 6 develops and applies a model that describes the packer-based behaviour of the vadose zone of the Sherwood Sandstone. The thesis then concludes in Chapter 7, where implications for groundwater vulnerability and vadose zone moisture movement, environmental impacts and potential for future work are discussed.

CHAPTER 2

SEDIMENTARY STRUCTURE, PALAEOGEOGRAPHY, DIAGENESIS AND HYDROGEOLOGY OF THE SHERWOOD SANDSTONE: A REVIEW.

2.1 Introduction.

The Sherwood Sandstone Formation is a fluvially-deposited sandstone, occurring in a discontinuous north-east to south-west trending belt that runs from North Yorkshire to the Dorset coast and also occurs extensively in the north west of England (Figure 2.1). The formation, formerly known as the Bunter and Keuper Sandstones, Bunter Pebble Beds and Waterstones, is an extremely important aquifer, providing 25% of the groundwater abstracted in England (approximately 600 million m^3/year, Downing, 1998).

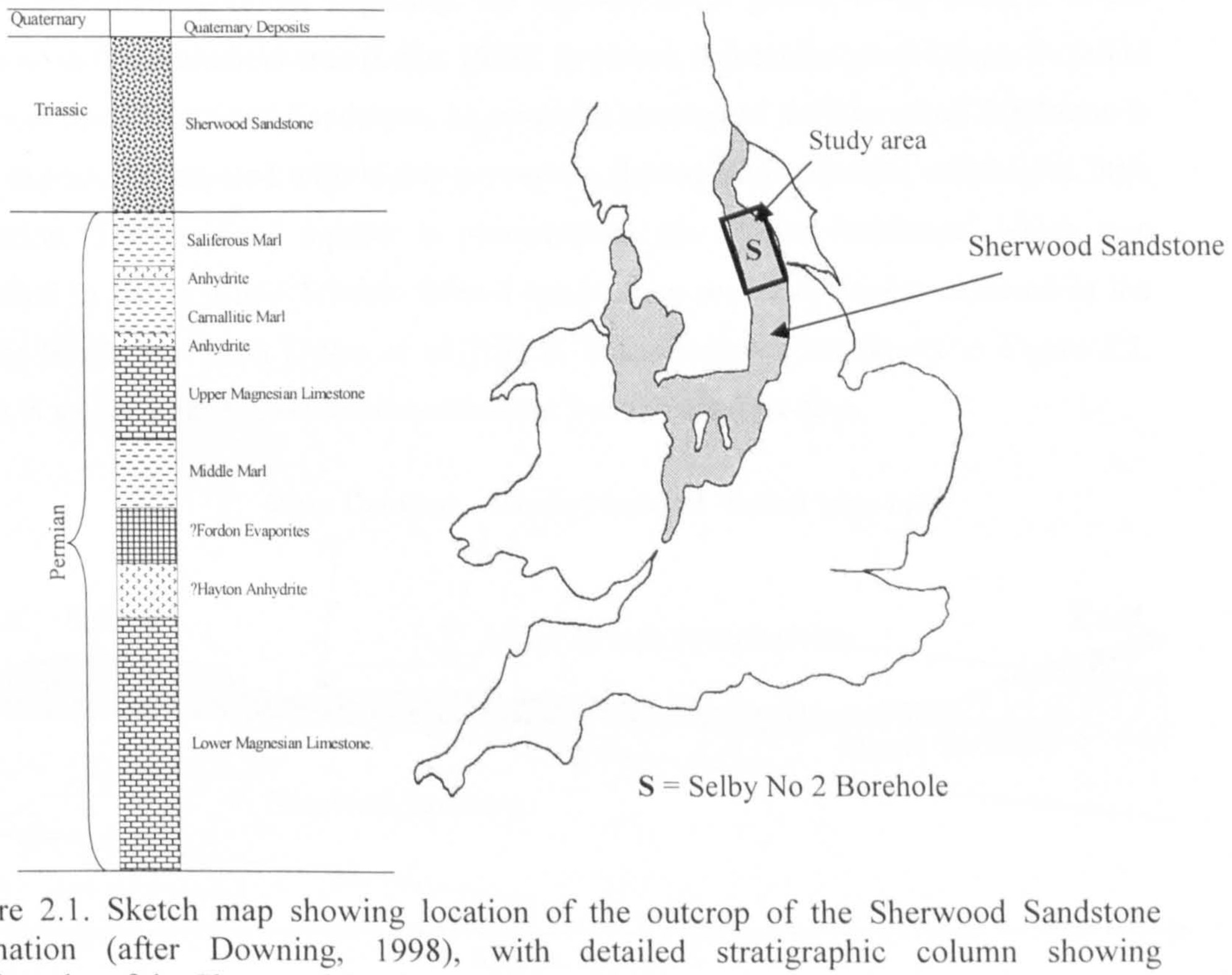

Figure 2.1. Sketch map showing location of the outcrop of the Sherwood Sandstone Formation (after Downing, 1998), with detailed stratigraphic column showing stratigraphy of the Sherwood Sandstone in the Selby No.2 Borehole. (Gaunt, 1994).

A large proportion of the sediment in the Sherwood Sandstone Formation was sourced from landmasses far to the south (London Brabant Massif, Armorican Platform) and has been transported over long distances (Burley, 1984; Nirex, 1997; Ruffell and Shelton,

1999; Allen *et al.*, 1997). At the time of deposition in the Lower Triassic (approximately 220Ma ago), the climate was hot and arid and the depositional environment varied laterally according to proximity to the basin margin. The various outcrops of Sherwood Sandstone were formed in sedimentary basins lying between topographic highs, which periodically provided a local sediment source (Allen *et al.*, 1997). The Sherwood Sandstone in the Leeds/Wakefield area was deposited near the western margin of a large intracontinental basin centred in the general area now occupied by the North Sea (Bryant and Burley, 1989). For the Selby-Bawtry area, it is likely that there was a secondary sediment source to the west-northwest (Bryant and Burley, 1989).

The Yorkshire/Nottinghamshire outcrop of the Sherwood Sandstone wedges out to the west, onlapping upon the older rocks and increases in thickness to the east. This is possibly a result of a prograding fluvial system rather than tectonic control of the sedimentary environment, as evidenced by seismic sections that show little variation in the thickness of the Sherwood Sandstone into faults (Jackson and Mulholland, 1993, Ruffell and Shelton, 1999). Typically, the regional dip is gentle, being some 2^0 to the northeast in the Wakefield area (Lake, 1999). In places, substantial glacial deposits shield the unconfined Sherwood Sandstone, however the outcrop of the Sherwood Sandstone is often exposed or covered with highly permeable fluvioglacial deposits, which give little protection. The confined aquifer is protected by the Mercia Mudstone, which was deposited in the mid-late Triassic from a hypersaline sea environment centered in the present North Sea basin (Allen *et al.*, 1997). These features are shown in Figure 2.2, which is a generalized cross-section across the South Yorkshire area.

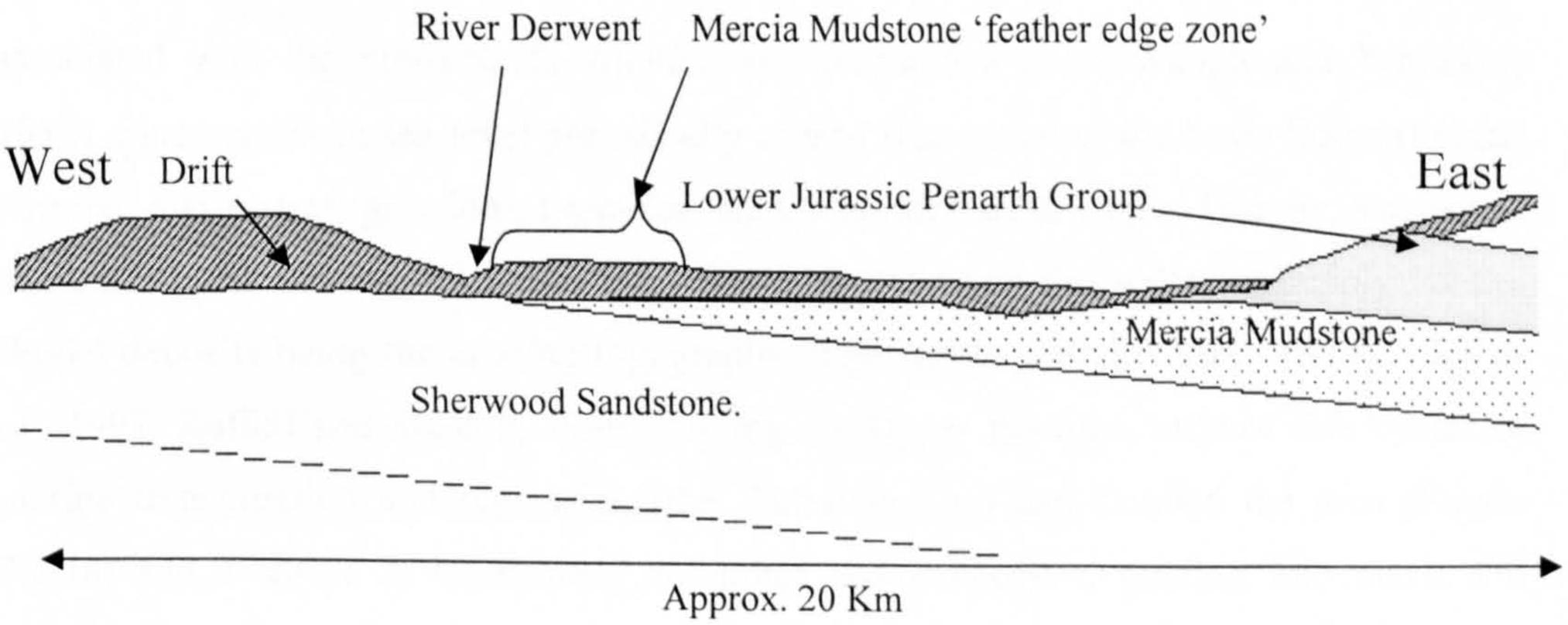

Figure 2.2 Sketch geological cross-section across the Vale of York (Hawkins and Chadha, 1990). Vertical scale exaggerated.

The Sherwood Sandstone aquifer of Yorkshire is generally a poorly cemented, friable and permeable rock. In the South Yorkshire area, following shallow burial, the Tertiary inversion of the North Sea Basin (a result of the Alpine Orogeny) uplifted the sediments and allowed leaching of carbonate cements in the exposed outcrops by meteoric water (Bryant and Burley 1989). This leaching increased the porosity of the rock, thereby improving its potential as an aquifer.

2.2 Basin evolution and palaeonvironment

In order to place the Sherwood Sandstone in the correct depositional environment, it is worth reviewing the depositional and tectonic history of the UK, as the framework for deposition is dependent on the geological history of the area.

During the late Carboniferous, the Variscan Orogeny caused uplift to many areas of modern Britain (Allen *et al.*, 1997), and these uplifted areas were then eroded in desert conditions. At the same time, as a result of a regional tensional regime, downwarping of some areas occurred, often along pre-existing fault lines, creating sedimentary basins. These basins included the East Yorkshire/Lincolnshire, Wessex, Cheshire/West Lancashire, Carlisle and Worcester Basins. Development of these Mesozoic basinal areas continued throughout the Permian and Triassic (Allen *et al.*, 1997).

During the Triassic, the palaeolatitude of the U.K. was about 15^0 north of the equator, at a latitude similar to that of the present day Sahara. Great Britain was toward the middle of the 'supercontinent' Pangaea and consisted of high ground surrounded by basins associated with the proto-North Atlantic and North Sea rifts (Waugh and Whitaker, 1982). Fluctuations in sea-level periodically caused inundation of the basin floors (i.e. the Permian marine transgression). From the late Carboniferous to Upper Triassic, a series of aeolian, fluvial and marine sediments were deposited, with the sediment supply for the fluvial deposits being the eroding topographic highs (Bryant and Burley, 1989; Allen *et al.*, 1997; Ruffell and Shelton, 1999). During the Upper Permian, at least five cycles of marine transgression and regression (the Zechstein Sea) had flooded the area (Figure 2.2.1a) and a series of limestones, dolomites and evaporites, grading into marls and sandstones, were deposited (Allen *et al.*, 1997). These salt rich Zechstein deposits often form the lower aquitard of the Sherwood Sandstone aquifer.

By the Lower Triassic, semi-arid continental conditions had returned (Yates, 1992; Figure 2.3b), as a result of evaporation of the Zechstein sea. Continuing erosion of the high

ground fed a series of major braided river systems that transported sufficient sediment to allow deposition of extensive fan deposits around the perimeters of the basins (Allen *et al.,* 1997). The Sherwood Sandstone was deposited by fluvial systems but sediments outside major river channels were periodically left exposed to subaerial conditions (Nirex, 1997; Ruffell and Shelton, 1999). This subaerial exposure allowed haematite staining to occur by precipitation of iron from solution as a result of degradation of some unstable minerals such as augite and hornblende (Walker *et al.*, 1978).

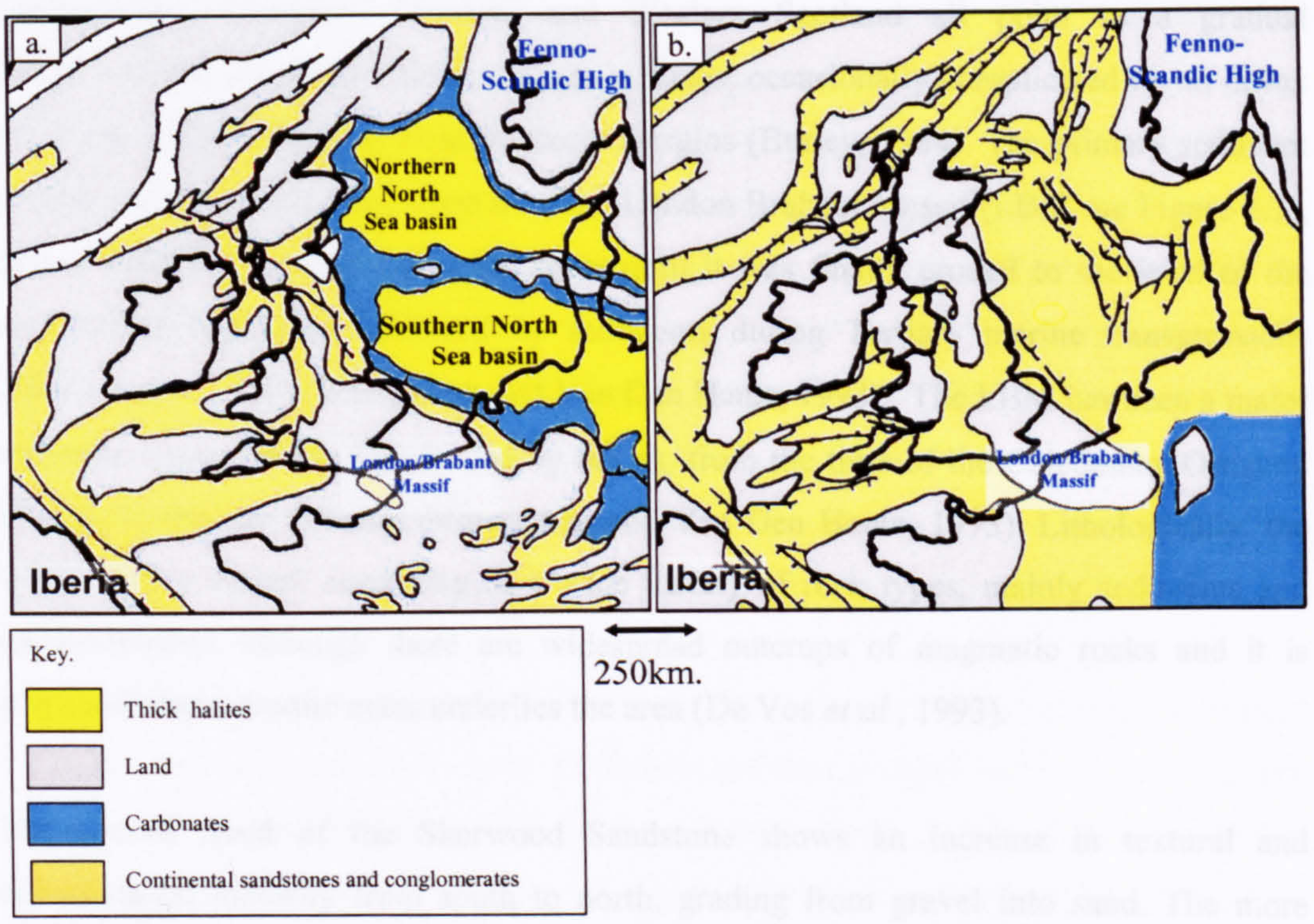

Figure 2.3. Rock distribution sketch map of a). the upper Permian and b). lower Triassic, (Open University, 1995).

By the mid-Triassic, a marine transgression had flooded all the areas shown on Figure 2.3b except for those areas shaded grey. This transgression allowed limestones to form in Central Europe and flooded much of the Lower Triassic sandstone, allowing deposition of marine muds and clays (the Mercia Mudstone Group). The lower beds of the Mercia Mudstone have been attributed to low sinuosity, meandering, sandy rivers, gradually giving way to inland and coastal playa lakes (Allen *et al.,* 1997; Ruffell and Shelton, 1999). However, these lakes must have had an open connection to the sea at some times in order to account for the extensive evaporite deposits, as repeated marine incursions were required to supply sufficient quantities of salts (Ruffell and Shelton, 1999). Interbeds of halite, gypsum and anhydrite are common, and in places sand and siltstone horizons occur and often form the upper aquitard of the deeper sections of the Sherwood Sandstone, although erosion has removed them in many areas.

The Lower Triassic Sherwood Sandstone is therefore predominantly fluvial, compared with the largely marine units that lie above and below in the stratigraphic record (Gaunt, 1994; Allen *et al.*, 1997). Palaeogeographic reconstruction of the lower Triassic sedimentation patterns in Britain suggest that the Sherwood Sandstone was deposited by a series of major rivers, flowing from the south, transporting vast quantities of alluvium on a northerly inclined palaeoslope (Waugh and Whitaker, 1982; Burley, 1984; Yates, 1992). Detailed studies of the sedimentary structure of the sandstone undertaken in Devon, Staffordshire, Cheshire, Cumbria and Western Scotland all point to a gradual South→North, proximal→distal, change in facies, occasionally complicated by an influx of coarse grained material from the basin margins (Burley, 1984). The primary sediment source was the roughly east-west trending London Brabant Massif (LBM see Figure 2.3), which existed from mid-Devonian times until it was finally eroded to the level of the surrounding basins and covered by sediments during Tertiary marine transgressions (Pharaoh *et al.*, 1993; Vercoutere and Van Den Haute, 1993). The LBM has been a major sediment source, being surrounded by basins, from the time of the Caledonian Orogeny through to the late Jurassic (Vercoutere and Van Den Haute, 1993). Lithologically, the LBM is very varied, consisting of a wide variety of rock types, mainly sediments and metasediments, although there are widespread outcrops of magmatic rocks and it is suspected that a granite mass underlies the area (De Vos *et al.*, 1993).

The overall trend of the Sherwood Sandstone shows an increase in textural and mineralogical maturity from south to north, grading from gravel into sand. The more northerly areas, such as the Irish Sea and the Central North Sea Basin experienced continuous deposition by fine-grained, sandy, braided rivers (Allen *et al.*, 1997), as did the sand-dominated Yorkshire area. Large-scale aeolian deposition did occur, but was rare and restricted to specific areas i.e., Northern Cheshire and Cumbria (Nirex, 1997; Evans *et al.*, 1993). The base of the Sherwood Sandstone in northeast England is markedly diachronous as a result of the progradation of the braided river system, and finer-grained sediments were deposited towards the top of the Sherwood Sandstone Group as a whole, as the source area topography was gradually eroded (Burley, 1984; Allen *et al.*, 1997).

The South→North transport model does not fully describe the origins of all the sediments deposited. In some areas there are local variations in sediment source and many of the lithic fragments have a different provenance than the normal London-Brabant Massif source that is usually quoted for the Sherwood Sandstone (Allen *et al*, 1997; Nirex, 1997; Ruffell and Shelton, 1999.). For example, fragments of the Ordovician Borrowdale

Volcanic Group have been identified in the St Bees Sandstone and may form up to 40% of the rock locally (Nirex, 1997). Similarly, the Marchwood Borehole in the Wessex Basin has encountered locally derived pebble beds comprising 40 to 60% of the whole rock, contrasting markedly with the overlying feldspathic sandstones (Burley, 1984).

Feldspar is easily broken down by weathering, and one criteria for compositional maturity of a sedimentary rock is its quartz:feldspar ratio (higher ratios indicate more mature sediments). However, detrital feldspar is a common constituent of the Sherwood Sandstone as a whole (Burley, 1984), and not just the areas dominated by locally-derived sediment. One possible means of conserving feldspar is that preservation of unstable minerals in the rock record is a function of topographic relief (Pettijohn, 1957). High relief encourages rapid erosion and transportation, with sediment generation and transport rates outstripping chemical dissolution, which may make it possible for feldspar to have survived as a significant detrital constituent of the Sherwood Sandstone (Arche and Gomez-Lopez, 1999). The presence of feldspars in the Sherwood Sandstone is important to its properties as an aquifer, since diagenetic processes may alter these feldspars into clay minerals, which have a large influence upon the hydraulic properties of the rock.

The depositional environment of the Sherwood Sandstone has therefore been suggested from previous work to be a series of fluvial sediments deposited by braided rivers, occurring along the western margin of the Southern North Sea Basin (Gaunt, 1994). South of the study area, in Nottinghamshire and as far North as the East Retford District, pebble beds are common, often appearing some way up the sequence. These pebble beds (the Nottingham Castle Formation, formerly known as the Bunter Pebble Beds) imply higher rainfall and steeper gradients at the sediment source and have been interpreted as evidence for continuing, albeit spasmodic, uplift of the London Brabant Massif (Ruffell and Shelton, 1999).

Tectonic and thermal effects on sedimentation

During the development of sedimentary basins, faulting is often associated with syn-sedimentary deposition. Downwarping at the basin margin creates accommodation space that may then be infilled with sediment depending on sediment supply (Brown *et al* 1996). As accommodation space is a prerequisite for sediment preservation, tectonic activity often exerts considerable control upon the degree of sedimentation. The Sherwood Sandstone has long been suspected as having been deposited in a syn-rift phase of fluvial deposition which occurred over much of Europe (Chadwick 1985; Evans *et al.*, 1993; Jackson and Mulholland 1993). The available literature cites the major sediment

source as the London-Brabant Massif (Allen *et al.*, 1997; Nirex, 1997; Ruffell and Shelton, 1999), the sediments in South Yorkshire are therefore distal, which accounts for the sand sized nature of the grains. The Mercia Mudstone Group has been interpreted as being deposited in a hypersaline sea situated in an area lowered by post-rift thermal subsidence (Burley, 1984; Whittaker, 1985).

It is possible that the basins within which the Sherwood Sandstone was deposited were thermal relaxation basins, caused by thermal contraction of the crust following the early Permian extension phase that affected the North Sea area (Ruffell and Shelton, 1999). In the northern, distal regions (such as the study area), the base of the Sherwood Sandstone is fine grained, and much of the sequence consists of fine sand-sized subarkosic sandstone. This may be as a result of fluvial deposition in an arid environment in a gently subsiding basin (thermal subsidence caused by earlier (Permian) rifting) with gentle tectonic uplifting of the sediment source regions (Ruffell and Shelton, 1999).

2.3 Braided river sedimentology

The literature contains many studies of braided river morphology, evolution, characterisation and preservation. The overall geometry of a braided river comprises multiple anabranch channels that migrate over the braidplain, separated by bars and islands (see Figure 2.4; Dade, 2000). Braided rivers are characterized by the presence of multiple intertwined channels, which are normally wide and shallow, and in sandy braided rivers are normally floored by dune bedforms (Tucker, 1991). Channels may be classified into a variety of scales, ranging from (1) first order channels (whole braidplain), through second order channels (2) which are individual anabranches of the first order channel and onto third order channels (3) into which the individual anabranches are split (Bristow, 1987; Thorne et al, 1993). These minor third order channels are very variable in direction and are topographically higher than major channels and so are greatly affected by river stage (Cant & Walker, 1978). Bar top and minor chute channels (4) often cut across braid-bars and are present within the preserved Sherwood Sandstone in the Selby area (Bryant and Burley, 1989).

The braid bars that divide the river into smaller channels are complex structures, formed by a variety of accretion processes around a low stage emergent nucleus (Cant, 1978; Cant and Walker, 1978; Walker, 1992; Bridge, 1993; Bristow, 1987; 1993; Ashworth *et al.*, 2000; Best *et al.*, 2003; Bridge and Lunt, *pressim.*). Accretion processes acting on braid bars have been described by many researchers and consist of downstream,

upstream, oblique cross-channel, vertical and lateral accretion (Cant and Walker 1978; Bridge, 1993; Bristow, 1993; Best *et al.,* 2003). Accretion on bars often occurs during falling stage following flood events (Best *et al.,* 2003), and typically bar deposits consist of large bar-margin slipfaces, medium to small scale dune cross-stratification and mud drapes (Best *et al.,* 2003).

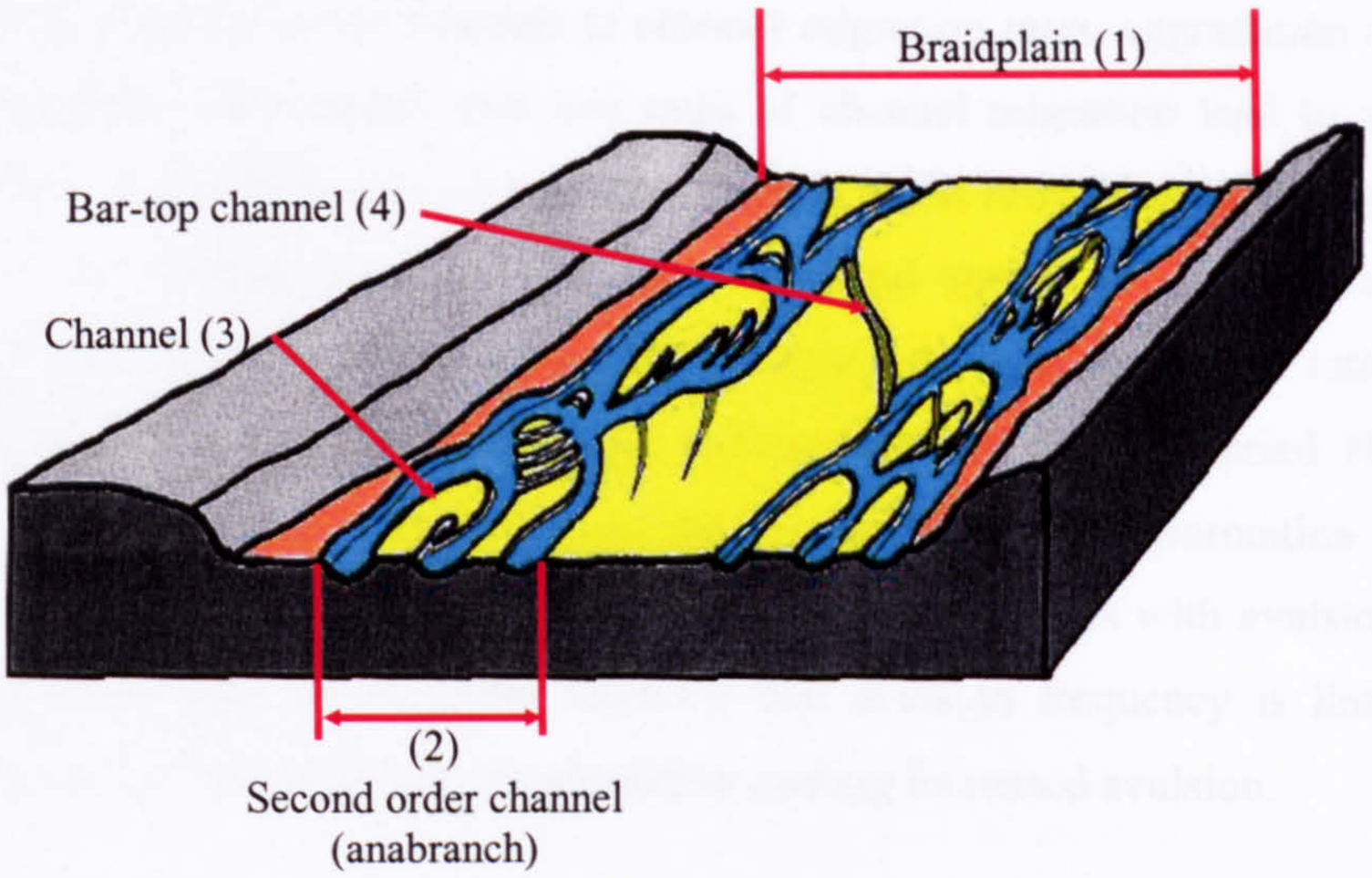

Figure 2.4. Generalized view of a sandy braided river showing different channel scales.

Upper-stage planar beds are generally restricted to bar tops (Bristow, 1993; Best *et al.,* 2003), and are deposited as a result of upstream accretion during high stage flow (Bristow, 1993). On waning flow detrital clays may be infiltrated into the upper-stage, planar bedforms by 'washing in' (Pay *et al.,* 2000) as flow returns to the dune-floored active channels and relatively slow moving water, carrying suspended clay particles, drains through the bar fabric. Bristow (1993) also reports significant quantities of ripple laminated units overtopping braid bars, particularly on the downstream margins of medial, lateral and point bars.

Aeolian processes at low stage flow (Allen *et al.,* 1997) may alter bar-top sediments although the preservation potential of aeolian bedforms is low, and in the ancient sandstones from the northeast of England, only frosted sand grains suggesting aeolian conditions have been found (Bryant and Burley, 1989). Evidence of significant aoelian deposition within the Sherwood Sandstone Formation has been reported, in areas such as the Cheshire basin and west Cumbria, but significant evidence of aeolian processes is generally scarce (Evans *et al.,* 1993; Nirex, 1997).

The morphological features of braided rivers are transient and perpetually being reworked by current action. Hence, many of the forms created by the river in falling stages will be

eroded by the next flood event, such a dynamic system is characterized by frequent erosive surfaces and a constantly shifting series of cycles of feature growth, evolution and destruction. Large braided rivers may form levees alongside the channel area, and may experience avulsion events (Leddy *et al.*, 1993, Morozova and Smith, 2000, Bristow *et al.*, 1999). Bristow and Best (1993) and Skelly *et al.* (2003), relate the amount of sediment reworking by active channels to channel migration rates, aggradation rates and avulsion frequency and suggest that low rates of channel migration lead to vertically stacked channels and high rates of migration lead to much reworking of the braidplain. High levels of avulsion result in an increased lateral spread of channels and high aggradation rates allow preservation of more braidplain deposits than lower rates, as the channels only have a limited time to rework sediments before they are buried. Hence the distribution of channel sequences can potentially provide much information on river morphology. Bristow *et al.*, (1999) also compare aggradation rates with avulsion events for the Niobrara River in Nebraska, showing that avulsion frequency is linked with aggradation rate, with high levels of aggradation causing increased avulsion.

Hence a typical large sandy-braided river (Figure 2.4) will contain channels of varying size and direction, normally floored with sand dunes. Such a river will also contain braid-bars, which may be predominantly trough cross-stratified but with some zones of upper-stage planar-beds on their tops and ripples at the downstream bar margins, with some mud drapes. The relative abundance of in-channel deposits is related to avulsion frequency, which is influenced by aggradation rates.

The permeability of preserved braided river deposits is greatly influenced by the relative proportions of planar-laminated, trough cross-stratified, ripple-laminated and mud drape facies. Generally, within the Sherwood Sandstone in the Selby area, coarser grained units are more permeable than the finer facies (Pokar, 2002). Trough cross-stratified facies are typically coarser grained and therefore more permeable than the planar-laminated facies, and the fine-grained mud drapes are largely impermeable. Scale modelling studies of the braided Ashburton river in New Zealand conducted by Moreton *et al.*, (2002) show that channel fills may be highly permeable, and finer, floodplain sediments are less permeable.

2.4 Diagenesis and mineralogy

As a result of the maturation of Sherwood Sandstone sediments as they were transported northwards, there is a gradual decrease in grain size within the Sherwood Sandstone from south to north, and an associated increase in textural and mineralogical maturity. Burley

(1984) defined the sediments within the Sherwood Sandstone Group as being of lithic-arkose / sub-arkosic-litharenite composition to the south, grading into quartz-arenite / sub-arkose / sub-litharenite composition to the north. These data may be plotted (Figure 2.5) to show lithological variation and the increasing maturation of sediments with more northerly deposition.

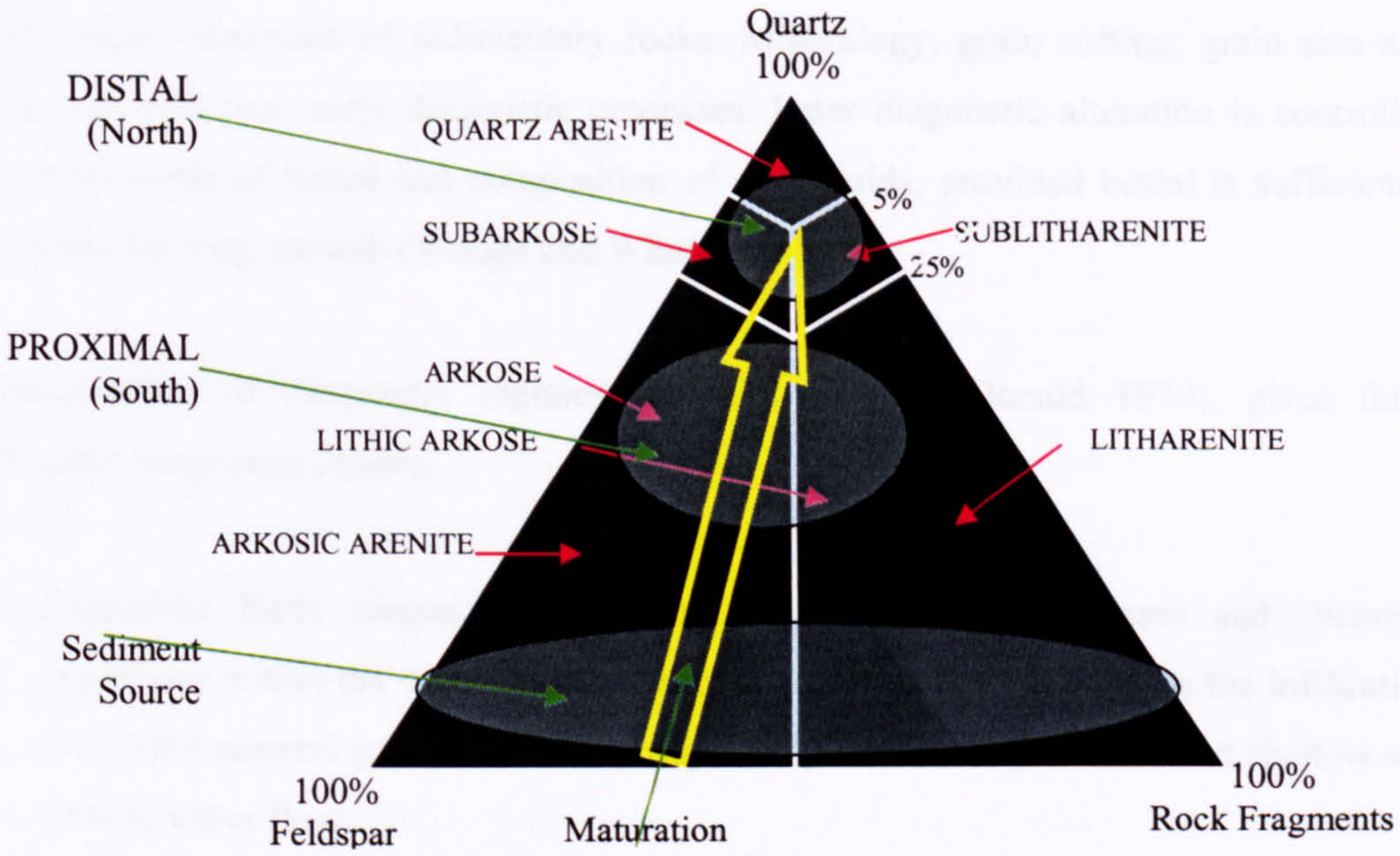

Figure 2.5 Composition of the Sherwood Sandstone; data from Burley (1984).

The terms proximal and distal are defined as '*applied to a sediment or sedimentary environment close to the source or origin of the deposit'* and '*applied to a depositional environment sited at the furthest position from the source area, and generally characterised by fine grained sediments*' respectively (Allaby and Allaby, 1990). The more proximal (southerly) sediments of the Sherwood Sandstone Group contain a mixture of rock clasts set in a matrix that is primarily quartz, with a high proportion of potassium feldspar (Burley, 1984). Other minerals present include mica, heavy minerals and opaques, but these only make up a minor component of the rock (Burley, 1984.). The proximal deposits are characterised as being rich in feldspar and are generally lithic-arkoses or sub-arkosic litharenites, having feldspar contents of up to 30% and the more lithic units containing up to 50% rock fragments, with sedimentary, igneous and metamorphic origins (Burley, 1984). The more distal sediments show a greater degree of compositional maturity, consisting primarily of simple quartz grains. Quartz typically accounts for more than 65% of the rock. Feldspars (again dominantly potassium feldspar) account for 10-15% and lithic fragments for a further 10-15%. Rock fragments (where present) consist of the more resistant metamorphic and igneous rock types (Burley, 1984). Distal deposits are finer grained than proximal, and may be classified as sub-arkoses, sub-

litharenites and quartz arenites (Burley, 1984.). However, mud rip up clasts are common in the more northerly areas from the erosion of floodplain muds.

Diagenesis

The sedimentary fabric and chemical content of the original deposits largely controls the early stage diagenesis of sedimentary rocks. Mineralogy, grain sorting, grain size and shape all influence early diagenetic processes. Later diagenetic alteration is controlled more by depth of burial and composition of pore fluids, provided burial is sufficiently deep and for long enough (Waugh and Whitaker, 1982).

Classification of diagenetic regimes (Schmidt and MacDonald 1979), gives three principal diagenetic phases:

- Eogenetic: Early diagenesis that is related to physical processes and chemical conditions within the depositional environment. An example of this is the infiltration of detrital mineral grains into newly deposited sediments by surface and shallow sub surface water flow.
- Mesogenetic: The intermediate phase of diagenesis, including burial is related to deeper subsurface conditions and chemical processes occurring during burial, such as dissolution and replacement of fabric by supersaturated saline porewaters at elevated pressures and temperatures.
- Telogenetic: Late phase diagenesis related to exhumation and the re-introduction of surface waters where near surface processes again become dominant. An example of a telogenetic process is leaching of mesogenetic fabric by comparatively fresh groundwater.

Unlike the various reservoir sands that line the grabens of the North Sea, the Triassic sandstones of Yorkshire have never experienced deep burial (>1km) or any great degrees of heat (>70°C) or pressure (Burley, 1984). In other areas of the country, burial depths of up to 5km have been determined for the Sherwood Sandstone (Burley, 1984). Hence the burial history of the Sherwood Sandstone is not straightforward, different basins have been buried to different depths and there are lateral depth variations between the edges and the centres within individual basins. Many of the basins have also experienced Tertiary basin inversion and the Sherwood Sandstone has been exhumed to near or actual surface conditions in many areas.

The Sherwood Sandstone is an important aquifer and evidence presented below shows that diagenesis has augmented primary porosity with secondary porosity. The fact that the Sherwood Sandstone in the Yorkshire area contains mixed illite –smectite clays that have not undergone illitisation at depth, points to only a moderate degree of burial. Further evidence of this is provided by the lack of quartz cement (Burley, *op. cit.*). Quartz cement is an important diagnostic feature of sediments that have experienced deeper burial, often being formed from pressure solution at grain interfaces. Quartz is resistant to dissolution by meteoric water, and so poorly cemented silica rich sandstones are unlikely to have been subjected to significant mesogenetic alteration.

In general, the processes of diagenesis tend to reduce textural maturity and increase the mineralogical maturity of sediments (Walker *et al.*, 1978). Eogenetic processes may include infiltration of detrital clay, possibly very soon after deposition of the original sediment. Stream flow is extremely efficient at carrying clay sized particles in suspension, and falling stage rivers may infiltrate fine sediments through coarser sands and gravels, provided the clays and silts are fine enough to pass through the pore throats of the grain-supported original sedimentary fabric.

In arid environments, such as northeast England in the Triassic water tables are often low (Waugh & Whitaker; 1982). Interstitial voids are often dry and are much larger than any clay particles that may carried in suspension (Pay *et al.*, 2000; Bloomfield *et al.*, 2001). Runoff water from periodic flooding events may infiltrate into the sediment via the network of interstitial voids. Because these voids are so much larger than the clay particles little filtering of clay minerals will occur. Hence clays will be carried into the matrix of the sediment and may be 'unloaded' to contribute to a secondary matrix fabric. This type of clay deposition is common directly above low permeability areas and may be detected in SEM (scanning electron microscope) images as mixed sizes of clay platelets orientated parallel to the grain fabric of the surrounding sediment (Waugh and Whitaker; 1982, Pay *et al.*, 2000). Further eogenetic diagenesis of the Sherwood Sandstone is related to the surface interstitial porewater redox potential (Eh) which controls the activity of dissolved materials. Grain dissolution has intensively leached lithic fragments, heavy minerals and feldspars from the rock matrix, thereby increasing porosity. Evidence of this is provided by the presence of large pores and relic haematite rims, indicating grain removal are common (Burley, 1984).

Eogenetic processes often dissolve heavy minerals from the rock, leaving only those most resistant to dissolution behind. Within the Sherwood Sandstone, heavy minerals, although rare, consist almost entirely of highly stable minerals such as zircon, rutile, tourmaline and staurolite, which are largely insoluble at moderate temperatures and pressures (Burley, 1984.). This indicates that a significant amount of dissolution has taken place as moderately resistant minerals such as hornblende, plagioclase and augite have been completely removed from the rock, leaving voids, hollow grains or clay coatings where the grain once was (Burley, 1984). The secondary porosity resulting from grain dissolution may be reduced by precipitation of replacement minerals, or by compaction processes collapsing the void, but sometimes this secondary porosity may be preserved (Walker *et al.*, 1978). The Sherwood Sandstone typically contains leached grains that have been partially or entirely replaced by authigenic minerals such as clays, haematite and carbonates (Burley, 1984).

Authigenic clays found in the Sherwood Sandstone tend to be either potassium-rich illite, derived from feldspars or have a chloritic/smectite composition, related to its derivation from basic ferromagnesian grains (Burley, 1984). The formation of illite-smectite and chloritic clays may occur with only moderate burial depths and so can be found in sediments that have only experienced the early stages of diagenetic alteration (Waugh and Whitaker, 1982). Randomly stratified illite-montmorillonite clays have also been cited as being the result of authigenic replacement of unstable silicate minerals. Replacement clays are rarely preserved as intact pseudomorphs of the parent grains, and overburden pressure normally causes the soft clays to deform between more rigid framework grains (Walker *et al.*, 1978).

Authigenic haematite staining is widespread and gives the Sherwood Sandstone its typical red colouration. For much of the exposed Yorkshire Sherwood Sandstone, the degree of cementation is low, resulting in weak, friable sandstones (Burley, 1984). This lack of cement fabric is a result of telogenetic leaching of carbonate cement by meteoric waters rather than a lack of eogenic cement. For South Yorkshire/Nottinghamshire in the confined aquifer to the east, where the Mercia Mudstone acts as a seal preventing the ingress of meteoric waters, the Sherwood Sandstone is well cemented, with poikiloptic calcite and non-ferroan dolomite comprising up to 20% of the rock (Burley, 1984). In contrast, at outcrop and where meteoric water has gained access to the rock fabric, carbonate cement content is less than 10%, typically less than 5%, and the rock is friable and weak (Burley, 1984). It is probable that the aquifer in the Yorkshire area was once uniformly cemented, as the shallow 5^0 regional dip would have resulted in a similar

pressure and temperature regime for the whole area. The variation in cementation between confined and exposed parts of the aquifer suggests that telogenetic processes in the unconfined aquifer and at outcrop have leached much of the carbonate cement away (Burley, 1984).

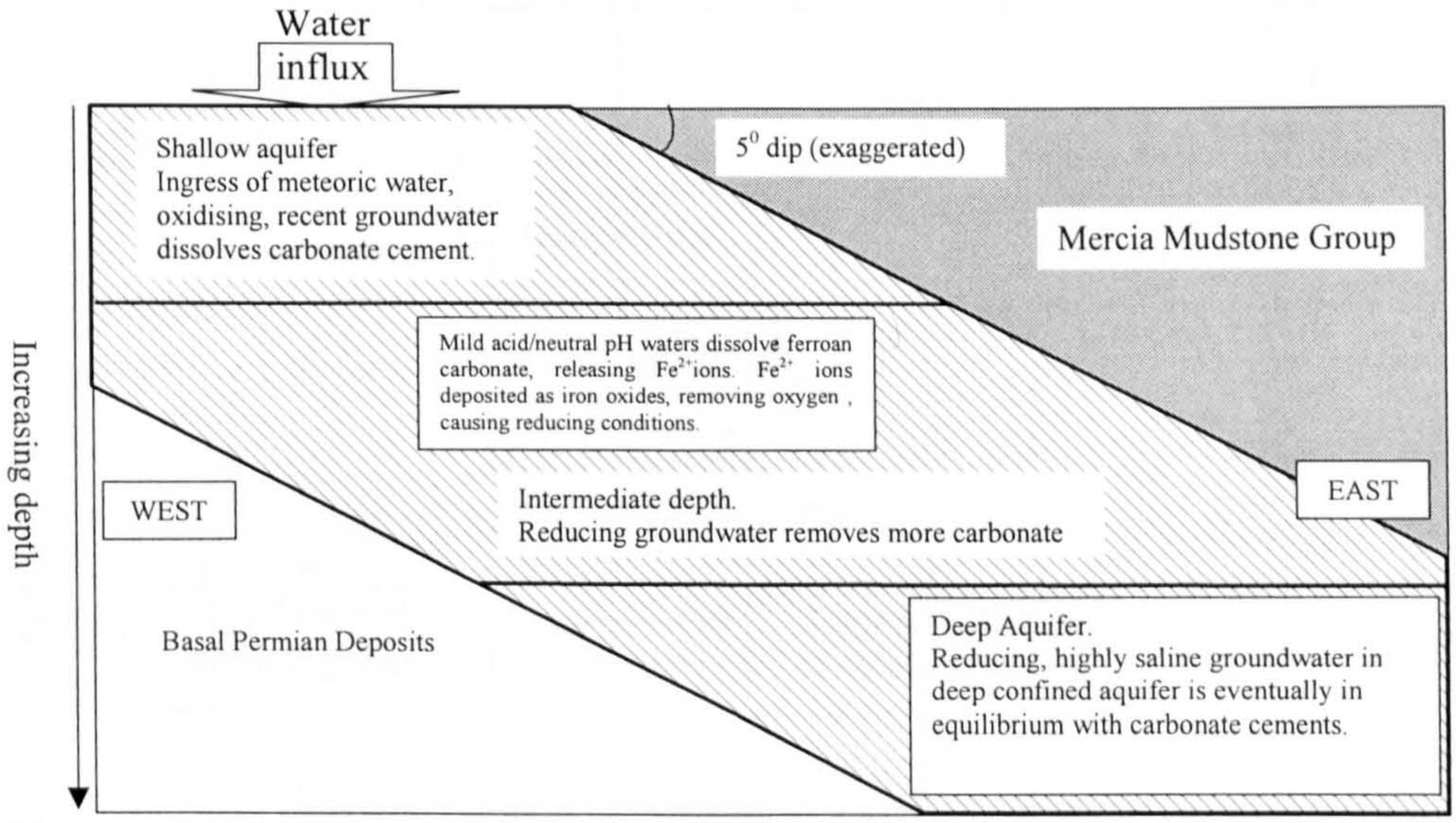

Figure 2.6. Telogenetic processes in the Sherwood Sandstone (data from Burley, 1984).

Figure 2.6 suggests one explanation for the pattern of telogenetic carbonate dissolution in the Sherwood Sandstone and also helps to explain some of the haematite staining typical of the Sherwood Sandstone. Ferroan carbonates are dissolved by meteoric water giving Fe^{2+} ions, which then combine with available oxygen to precipitate in-situ as red haematite (Fe_2O_3) deposits (Burley 1984). As diagenetic processes tend to dissolve grain fragments and replace them with different sized ones (fine clay minerals or poikiloptic calcite for example), the overall effect is to decrease textural maturity, as a variety of grain sizes not present in the original sediment are introduced. Unstable silicate minerals are replaced with stable clays. This process increases the Quartz : Feldspar ratio, thereby diagnetically increasing the mineralogical maturity of the sediment and reducing its permeability. The various diagenetic processes that have the potential to affect the Yorkshire Sherwood Sandstone at the edge of the basin are summarised in figure 2.7

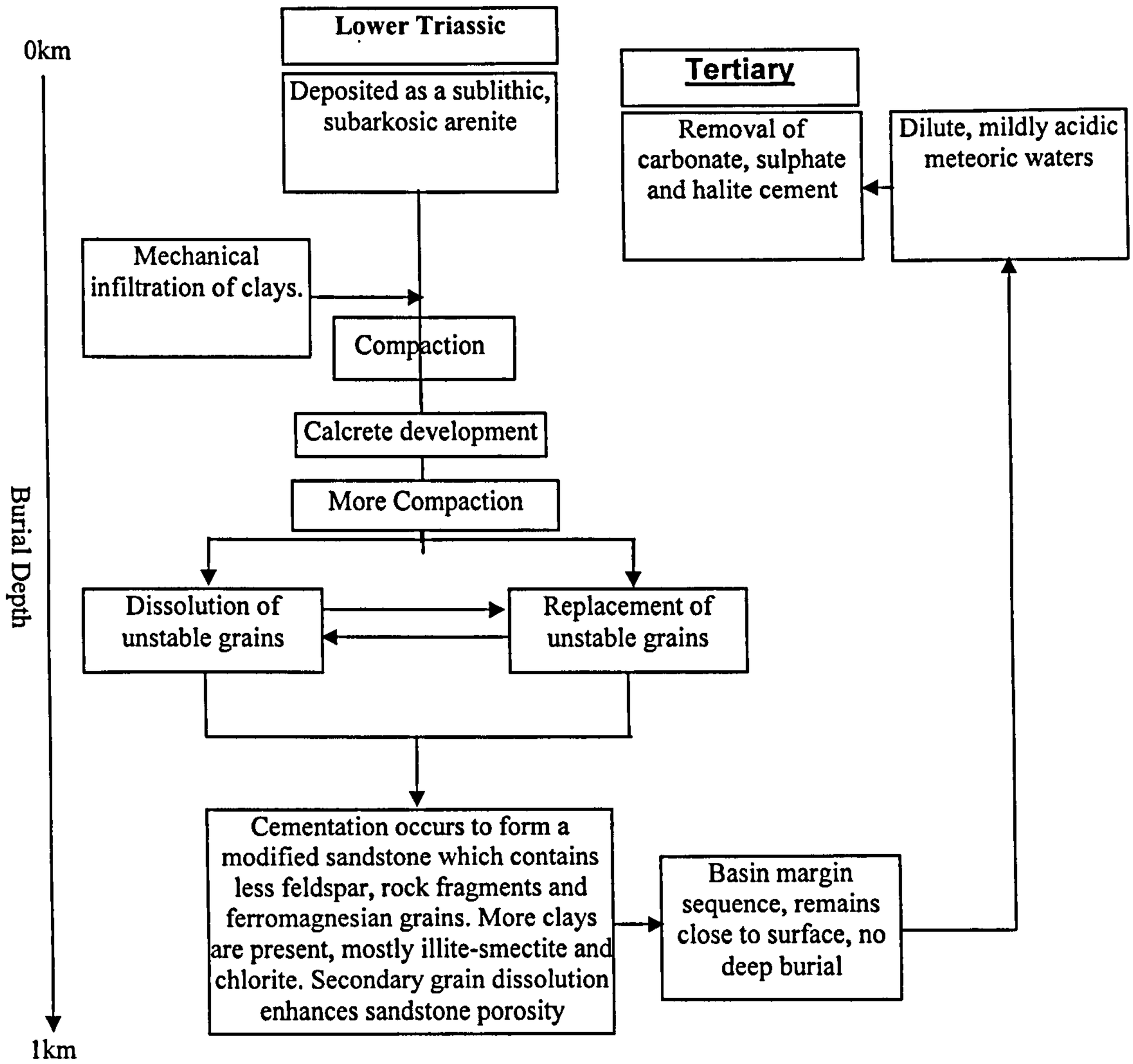

Figure 2.7. Probable diagenetic processes for the Yorkshire Sherwood Sandstone (after Burley, 1984).

The net result of the various diagenetic processes that have affected the Sherwood Sandstone in northeast England is that the rock is often highly porous, highly permeable and very weakly cemented. The sandstones will have had significant primary porosity, which has been increased by secondary dissolution of grains (Waugh and Whitaker, 1982). Carbonate cements were present and would have reduced the porosity but telogenetic leaching has counteracted this and increased porosity above its original value. Porosities of over 30% have been measured in the Yorkshire area (West *et al.*, 2003, Pokar, 2002; Pokar *et al.*, 2003). However, the Sherwood Sandstone in the study area is not homogenous, fine-grained layers and clays are interspersed with coarser sandstones. This means that the shallow aquifer is anisotropic as regards grainsize, mineralogy, and the hydrogeological properties of the aquifer. The in-situ preservation of the original quartz grains of various grainsize, and the variable proportions of clay minerals leads to a

wide variation of pore throat sizes, and these ultimately control capillary moisture retention and moisture movement within the rock.

2.5 Hydrogeology and heterogeneity

The hydrogeology of aquifers is heavily influenced by the degree of heterogeneity that they exhibit. Both aquifers and hydrocarbon reservoirs possess a wide range of heterogeneities, which dictate their potential usefulness as a resource. Of particular importance with regard to shallow aquifers is their ability to prevent contaminants from reaching the water table. The contaminants may originate from a variety of locations, from point sources such as industrial sites, landfill sites or other localised inputs, or more diffuse sources such as agrochemicals and faecal matter from grazing animals. Generally, sedimentologists have regarded heterogeneity as a source of information on depositional environment and processes. Hydrogeologists have tended to underestimate subsurface heterogeneity and engineers have normally ignored it (Huggenberger and Aigner, 1999).

Although aquifers such as the Sherwood Sandstone are often considered to be homogeneous for groundwater modelling purposes, investigations at outcrop scale quickly reveal the presence of significant sedimentary heterogeneity, which will greatly influence their local permeability characteristics. One factor to be taken into account in hydrogeological investigations is the difference between laboratory and field measurement of permeability. Field measurements normally give data on the bulk properties of the rock mass, including fracture zones, discontinuities and sand lenses and generally give higher permeability readings than laboratory testing of cored samples. Barker and Worthington (1973) show this effect clearly from a comparison of falling head permeameter tests and pumping tests on abstraction boreholes in the Fylde area of northwest England. Laboratory based tests can only show intergranular permeability of recovered and unfractured core and provide little data regarding bulk permeability since they are carried out on entire rock samples, where only microfractures normally occur.

The situation regarding cored samples is further complicated by the effects of the coring process on the rock, the removal of the in-situ rock stress field and the necessity of choosing homogenous and relatively unfractured samples to test. Yet further complications are caused by the presence of authigenic clay minerals, which are present in the Sherwood Sandstone in significant quantities. If cores are preserved so that they retain their original moisture content, then they often exhibit lower permeabilities than cores that have been dried prior to measurement: varying the treatment of cored samples

is likely to affect the results (Brereton *et al.*, 1998). In areas with low core recovery or fissures, flow may be dominated by factors that cannot readily be tested in laboratory conditions, and laboratory-derived permeabilities should be considered as minimum potential permeabilities (Barker and Worthington, 1973). However, laboratory testing may provide important information on the intergranular permeability of unfractured rock, and may be used to estimate hydraulic anisotropy where fractures are not present.

On a laboratory sample scale, the permeability 'signature' of the Sherwood Sandstone shows a wide range of permeabilities, showing significant heterogeneity at both the bed and facies scale and hydraulic anisotropy within bedforms (Bloomfield *et al.*, 2001). For example, Ramingwong (1974) showed that the matrix permeability of the Sherwood Sandstone in Worcestershire, UK, was five hundred times lower in fine-grained units than in interbedded coarser units. Previous laboratory tests on the Sherwood Sandstone aquifer in north-eastern England (Koukis, 1974; Pokar, 2002) have also shown that the matrix permeability varies over several orders of magnitude as a result of variations in grainsize and porosity. For example, Koukis (1974) reports hydraulic conductivity values for horizontally oriented samples from the Vale of York, UK, ranging from ~0.001 to ~3 $m.day^{-1}$, the lower values being for clay-rich units. Lithology also influences the contrast between laboratory scale horizontal and vertical permeability. For two sandstone cores drilled from sites between Selby and Doncaster, Pokar (2002) reports that vertical permeability can be up to a 35 times less than horizontal permeability in finer grained sandstone facies units, owing to millimetre-scale horizontal silt/clay laminations.

Hence, the hydraulic properties of the Sherwood Sandstone and similar sandstone aquifers can be shown to be a result of variations in degree of cementation, clay content, grain size, sorting, diagenetic fabric and original sedimentary features. Of these, the degree of cementation, grain dissolution and the proportion of clays are the most important as regards pathogen transport (Bloomfield *et al.*, 2001), as these factors tend to control the size of the larger pore throats. The median pore throat size with the highest frequency of occurrence in the Sherwood Sandstone has been quoted as approximately 17μm (Bloomfield *et al.*, 2001), and ranges between 10.8 and 63.8μm (Pokar, 2002). This means they are sufficiently large to allow the uninterrupted passage of many pathogens including faecal *enterococci, E coli, Salmonella, Clostridia* and *Cryptosporidium.* Only 30% of the pore throats in the Sherwood Sandstone are able to filter *Cryptosporidium*, and only 3.5% are able to filter faecal *enterococci* (Bloomfield *et al.*, 2001).

Field scale hydraulic testing yields a range of transmissivity values for the Sherwood Sandstone ranging from $50m^2\ day^{-1}$ to $700m^2\ day^{-1}$ (Allen *et al.*, 1997). Plots of effective aquifer thickness versus transmissivity indicate average hydraulic conductivity is around $2m\ day^{-1}$, which agrees with values from regional scale groundwater flow modelling in the area of $1\text{-}3m\ day^{-1}$ (Allen *et al.*, 1997; Yoshida, 2003). However, conductivity values from both pumping tests and regional flow modelling are significantly higher than most values measured in laboratory tests 0.001 to $2m\ day^{-1}$ (Koukis, 1974; Allen *et al.*, 1997; Pokar 2002). This difference is not likely to be the result of fracture flow, since fracture flow in the Sherwood Sandstone outside the study area (around Middlesborough and Nottingham) has been reported to produce very high transmissivity values of several thousand $m^2\ day^{-1}$ (Allen *et al.*, 1997). Hence, the discrepancy between field and laboratory values must lie in the spatial distribution of the various sedimentary facies comprising the aquifer, e.g. the interaction between high and low permeability zones. In order to determine the permeability behaviour at outcrop scale from laboratory scale measurements, it is necessary to understand and quantify the spatial distribution and geometry of the individual facies units.

Vadose zone of the Sherwood Sandstone

In unconfined sandstone aquifers such as the Sherwood Sandstone, the water table may be many metres below ground, particularly close to active water abstraction wells. Generally, in the quarries visited as part of the preliminary survey of the study area the thickness of the unsaturated (or vadose) zone was between 10 and 20 metres.

In a homogeneous sandstone aquifer there are three main hydrological divisions within the vadose zone:

1) **The soil zone.** This is bound together with plant roots and contains an organic (humic) fraction that may be greater than the mineral fraction of the soil. This zone is the site of evapotranspiration and is extremely important in limiting recharge through the vadose zone. As the aim of this thesis is to characterise flow within the Sherwood Sandstone, all the test sites chosen had minimal soil and vegetation cover.

2) **The free drained zone.** This is the area of the vadose zone between the soil zone and the capillary fringe. Here, moisture flux is determined by the lithological framework of the aquifer, and may travel vertically to sub-horizontally depending upon the detailed sedimentary architecture of the aquifer.

3) **The capillary fringe.** This is the area directly above the water table and represents the retention and 'pulling up' of moisture into the fabric of the rock by capillary action. This region acts as a transition zone between the vadose and phreatic (saturated) parts of the

aquifer, with moisture content increasing rapidly as the water table is approached. The thickness of the capillary fringe is related to the pore sizes of the rock matrix.

As a general rule, water recharge moves downward towards the water table under gravity but is acted upon by capillary forces and may be held by capillary suction in rock pores. Hence water retention (θ_r) within the rock is a product of hydraulic gradient (i) and pore size distribution (ϕ_p) according to the formula:

$$\theta_r = i \times \phi_p \qquad \text{Equation 2.1}$$

Hence a mixture of gravity and capillary suction controls moisture movement through the vadose zone. The Sherwood Sandstone has a wide range of preserved sedimentary and diagenetic fabrics which may provide a range of impediments to water flow, as well as preferential pathways and discrete zones of increased seepage velocity. Pokar (2002) demonstrates that the Sherwood Sandstone in the Hatfield/Eggborough area is highly anisotropic with regard to moisture flow, and may possess differing permeabilities depending on flow direction. Thus the vadose zone may exhibit wide ranges in porosity, permeability and capillary suction which will affect moisture migration patterns and have serious consequences for the vulnerability of the underlying aquifer to contamination. In soils and rocks where preferential flow occurs there is a serious risk of aquifer contamination as pollutant migration velocity may be greatly increased (Nissen *et al.*, 1999).

Regional groundwater flow

Groundwater flow in the South Yorkshire region is generally down-dip, in an eastward direction, from the feather-edge towards the confined aquifer (see Figure 2.1.2) (Edmunds and Smedley, 1992; Pokar, 2002). The low angle of dip probably results in a low natural hydraulic gradient, but the flow is at present dominated by high abstraction rates (Edmunds and Smedley, 1992).

Pollutant migration

The migration of water and dissolved or entrained pollutants through rock is dependent on the permeability, porosity and attenuating properties of the rock, and occurs within intergranular pore spaces or fractures. The ability to permit water movement is a function of the connectivity of the pore spaces, pore diameter and fracture width. Only interconnected pore spaces and fractures that provide an unbroken path allowing water

flow will contribute to the bulk permeability of the rock. However, blind pores and 'dead ends' contribute to the porosity of the rock, increasing the storage capacity of the aquifer and allowing more accommodation space for dissolved materials to dissipate (Brereton *et al.*, 1998). Clays decrease permeability in sandstones by restricting pore throat size, which increases the amount of water held by capillary retention and drastically reduces seepage velocity. If clay content is sufficient for clays to bridge or fill pores then the permeability of the sandstone is further reduced (Pay *et al.*, 2000) and may present barriers to local vertical groundwater migration. In places, 'double aquifer conditions' may occur, where an interlayered marl horizon separates the aquifer into two layers. This has occurred at Bridgenorth, Wolverhampton and Stourbridge in the Midlands (Allen *et al.*, 1997). Tests on water quality have shown that the upper and lower layers of the aquifer are not in hydraulic continuity. Where this occurs, the effective thickness of the aquifer is reduced, and since this controls the hydrological behaviour of the aquifer, then laterally extensive barriers to vertical water migration become very important.

Faults: effects on hydrogeology

Fracture zones may act as preferential flow paths and recharge boundaries, or seals that inhibit water flow. An example of a fracture inhibiting water movement within the Sherwood Sandstone is the Roaring Meg Fault in Merseyside, which prevents water flow across the fault plane. Evidence of the lack of aquifer lateral continuity across this fault is that hydrochemical changes and potentiometric head differences may be detected across the fault plane (Allen *et al.*, 1997). Another example in Triassic Sherwood Sandstone sediments is provided by a fault near to the Eggborough No. 3 borehole (SK 482 390), which appears to be acting as a recharge boundary as it does not allow cones of depression to extend across the fault plane (Allen *et al.*, 1997). Sediment filled fractures have been reported in the Cheshire Basin (Wealthall *et al.*, 2001) but these were considered not to be a major problem with regard to moisture movement within the vadose zone unless the fracture angle was high and cut through low permeability layers such as mudstones. Open fractures were considered a potential pathway for vapours, but not liquid water, except for during extreme hydraulic surcharge events. Infilled fractures were cited by Wealthall *et al.*, (2001) as possessing lower permeabilities than open ones, and would be unlikely to permit water passage at a higher rate than the surrounding rock. Open fractures were however cited by Wealthall *et al.*, (2001) as being highly significant pathways for non-aqueous phase liquid (NAPL) pollution, and in the phreatic zone as highly significant with regard to groundwater and NAPL alike.

Effects of layering in the vadose zone

Lower permeability layers, such as laterally extensive clay horizons, may act as funnels, channeling recharge into specific zones. Boreholes, or the attendant borehole annuli themselves, are also a likely pathway, allowing a bypass route through the vadose zone, and feeding directly into the phreatic layer of the aquifer (Ford and Tellam, 1994). The anisotropic nature of sedimentary deposits makes it likely that water may migrate laterally for a considerable distance in order to exploit high velocity pathways to the water table. Hence, even thick clay layers may not prevent vertical water movement in the vadose zone, but may simply divert the flow elsewhere, affecting recharge rates much less than might be expected by observation of laterally restricted borehole lithology alone.

Previous studies of groundwater vulnerability in the Sherwood Sandstone

Tests conducted on borehole groundwater response to industrial pollutants released over many decades by Ford and Tellam (1994), at a variety of sites in the Birmingham area suggest that the Sherwood Sandstone aquifer is vulnerable to surface pollution in the long term and that a deep unsaturated zone, coupled with thick layers of Quaternary cover and Mercia Mudstone may not be sufficient to provide adequate protection. In west Birmingham, where there is some 20-40m of cover and unsaturated aquifer, and the aquifer has a significant clay fraction, water quality within the aquifer has still been severely compromised by anthropogenic pollution (Ford and Tellam, 1994).

Lewin *et al.*, (1996) investigated the behaviour of fluids within the unsaturated zone of the Sherwood Sandstone on behalf of the Department of the Environment. The leachate plume from two uncontained landfill sites was monitored as it penetrated the Sherwood Sandstone and the results from this monitoring were used to infer vertical pollution penetration rates through the unsaturated zone. Initially, the rates of penetration were low, 0.7 $m.year^{-1}$ between 1978 and 1981. Water balance calculation involves many assumptions as to runoff rates and projected rainfall, and usually water balance calculations carried out on landfill sites show that it takes several years for landfills to begin producing leachate. Subsequent years showed the progress of the leachate front as having accelerated to 1.7 m $year^{-1}$ as leachate generation rose. The position of the leachate front was then inferred from the relative positions of the chloride fronts in cored samples taken in different areas on different dates. However, no account appears to have been made as to the probability that the leachate front had migrated laterally in order to find preferential pathways through the unsaturated zone. It has been established in previous sections of this chapter that the Sherwood Sandstone is highly anisotropic and so the presence of even a thin laterally extensive mudstone, fine-grained sandstone, or other

low permeability layer may easily alter the direction of flow from vertical to horizontal. Hence there is a possibility that the leachate has been moving faster than the results of Lewin *et al.*, (1996) suggest, especially as the position of the leachate front was inferred rather than actually measured. Harris and Lowe (1984), commenting upon the same sites, conclude that there was little evidence of attenuation of pollutants from the landfill sites, and these findings suggest the aquifer may be more vulnerable than previously expected.

Vulnerability modelling

Modelling transport mechanisms through the vadose zone has generally not been conducted with regard to complex lithology. Studies have been conducted where detailed sedimentological information has been used to model and predict oil movement through complex reservoirs (Willis and White, 2000). Generally, the complexity of heterogeneous media means that the tendency among most researchers has been to develop transport theory based on simple conceptual models (Persson and Berndtsson, 1998). Thus more data, such as that presented in this thesis are required to improve modelling parameters.

The current standard technique for predicting the time taken by pollutants to travel through the vadose zone, utilized by the LandSim modelling program and widely applied by the Environment Agency in the UK, is known as the 'plug-flow' model:

$$t = \frac{dan_e}{Q} \qquad \text{Equation 2.2}$$

where:

t = travel time to water table.

Q = infiltation rate.

d = thickness of the unsaturated zone.

n_e = effective porosity (moisture content is used here).

a = cross sectional area of infiltration zone

However, this equation takes no account of the lithology through which the water is passing. Recent work (Binley *et al.*, 2002) using cross-borehole radar appears to show that the travel time to the saturated zone within the Sherwood Sandstone at the two test sites is much faster than predicted by the 'plug flow' model, showing that groundwater vulnerability is possibly being underestimated. Binley *et al.*, (2001a, b) also show that, at least for the Hatfield site, water flow appears to be in a predominantly vertical direction, particularly for tracer injection tests. However, Sandberg *et al.*, (2002) demonstrated that flow in anisotropic aquifers may be strongly influenced by the sedimentary structure.

Hence it may be conjectured that preferential pathways and barriers to flow may exist in the heterogeneous Sherwood Sandstone and that water may migrate laterally for some distance in order to find high permeability features. These effects have not yet been directly observed because data at the relevant scale are lacking. Measurements of regional water table response to rainfall and responses of single boreholes are available but there is little detailed information at scales between these two extremes for this aquifer. One of the primary aims of this thesis is to quantify the response of the unsaturated zone of the Sherwood Sandstone aquifer in the Selby-Doncaster area to seasonal rainfall variations, at a scale of tens of metres. Data on likely vadose zone response at this scale are important to help improve current groundwater models and ultimately will assist in estimating the vulnerability of the Sherwood Sandstone aquifer to surface pollution.

CHAPTER 3
FIELD DESCRIPTION AND LABORATORY CHARACTERISATION OF THE SHERWOOD SANDSTONE IN THE STUDY AREA.

3.1 Introduction

Outcrop and borehole observations reported in this chapter show that a wide range of sedimentary structures are present in the Sherwood Sandstone in the Selby/Mansfield area. These outcrop observations are used to assist interpretation of GPR images (see Chapter 4). A comprehensive suite of grain size analyses were conducted, and the results used to identify the source of the radar reflections within the sandstone, as well as providing information to assist in estimating permeability distribution within the aquifer.

The literature survey (Chapter 2) reviewed past work on the depositional environment of the Sherwood Sandstone in the study area (between Selby and Mansfield in North-East England) and suggests the sediments were deposited by a series of sandy braided rivers transporting large amounts of sediment from the south. The distal nature of the deposits in the Doncaster/Selby area therefore means that gravels are relatively infrequent compared with the more proximal sediments found to the south. Hence, in the Doncaster/Selby area, the sediments are typically medium to fine-grained sands.

Borehole data provides a snapshot of the lithology and stratigraphy directly beneath the drilling point. Essentially boreholes provide a highly detailed one-dimensional view of the rock. The lack of detail regarding the lateral extent of features encountered limits the usefulness of boreholes for sedimentary logging (Bridge and Tye, 2000). As an example, a thin shale layer may only appear a minor feature in a cored or logged borehole, even if it is laterally extensive and presents a major obstacle to vertical migration. Alternatively, the borehole may intersect a thick mud lens that may appear to be an extremely effective seal, but may have only a limited lateral extent and have little effect on the vertical movement of water within the bulk rock. Hence, this chapter endeavors to draw together field evidence on the composition and hydrology of the Sherwood Sandstone from outcrop, cut faces and borehole logs. This evidence is used to suggest palaeoenvironment, facies distribution and permeability distribution for the study area.

3.1.1 Test site locations and description

Field and site investigation work was conducted on a range of sites situated in the northeastern limb of the Sherwood Sandstone outcrop area following extensive outcrop and quarry visits. Six sites were chosen as representative of the Sherwood Sandstone in the study area and detailed observations have been made at these locations (Fig. 3.1). The various operations conducted at each site are summarised in Table 3.1.

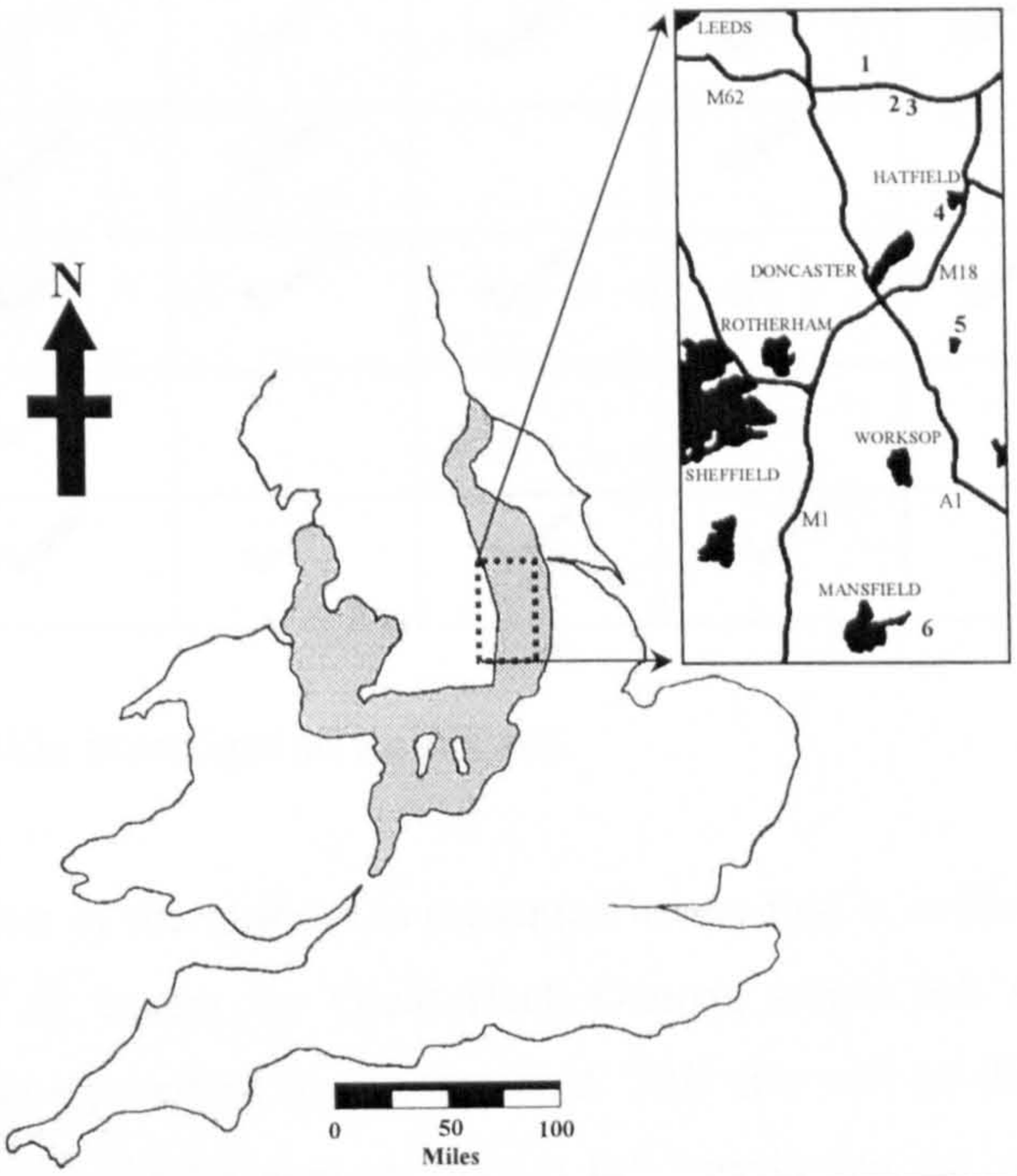

Quarry name	Number on Figure 3.1	Grid Reference
Eggborough	1	SE 573 228
Great Heck	2	SE 588 213
Pollington	3	SE 612 201
Hatfield	4	SE 653 075
Austerfield	5	SK 672 953
Rufford	6	SK 596 608

Figure 3.1. Outcrop of the Sherwood Sandstone and the sites investigated. The shaded area represents the main outcrop of the Sherwood Sandstone with the inset detail showing major towns/cities and motorways and quarry locations according to the numbering scheme shown in the inset table.

Quarry	Field sketches and photographs	Detailed sedimentary logging	Grainsize analysis, thin section or X-ray Diffraction tests	Radar imaging of specific sedimentary features	Radar lines	Permanent borehole installations (TDR, TRIME, NP etc).
Eggborough	✓		✓			
Great Heck	✓	✓	✓	✓	✓	✓
Pollington	✓	✓		✓		
Hatfield	✓	✓	✓	✓	✓	✓
Austerfield	✓					
Rufford	✓	✓	✓	✓		

Table 3.1. Site specific investigation techniques.

A general description of the quarries is presented herein that is sufficient to describe the salient features of all except for Great Heck Quarry, where full site installations of moisture monitoring equipment were completed. This site will be discussed in detail in section 3.1.2. Hatfield Quarry also received a full installation for moisture monitoring some 12-18 months prior to Great Heck Quarry. However this installation is not described fully as the deep instrumentation was not fully functional.

All of the quarries, except Hatfield had thick (>10m) vadose zones as they were all situated adjacent to active water abstraction boreholes and so were within the drawdown cone. The drawdown from abstraction increases the thickness of the vadose zone, making the quarries more economically viable. Hatfield is a slightly different case, in that it is situated near an abstraction borehole, and used to have a thicker vadose zone. However, pumping has (for the present) been suspended at Hatfield and so the water table has risen, flooding the quarry bottom and forming an extensive lake, reducing the unsaturated zone thickness to approximately 10m.

At the start of this research all of the quarries were actively being worked except for Pollington Quarry which has been landscaped and turned into a nature park, but Eggborough Quarry has since been 'mothballed' by its owners. This is an important

point as far as sedimentary logging is concerned, since it was found that little sedimentary structure was visible on freshly worked quarry faces. Time was thus needed for the face to weather (1-2 years) and the structure become more visible. Beyond 3-4 years vegetation would become firmly established, faces would collapse into talus slopes and again sedimentary logging becomes problematic. Hence, the quarries chosen were either active or recently active, but large enough for faces to weather naturally while other areas of the quarry were being worked.

The advantage of radar imaging in quarries (Chapter 4) is that often the overburden has been removed. Pebbles and conductive materials in the fluvoglacial drift deposits that overly much of Sherwood Sandstone in the study area cause scattering and attenuation of radar signals and often prevent accurate imaging of the subsurface. Radar surveys were conducted at Heck, Hatfield, Rufford and Pollington Quarries. Drift deposits had been removed for all the radar lines collected at these sites.

3.1.2 Great Heck

The Great Heck test site has been the main centre of activity during this research. Located close to Eggborough, near Selby this active sand quarry has been subjected to a wide range of geophysical and sedimentological investigation techniques. The site comprises two main areas, the main quarry where much of the sedimentary logging was conducted and the quarry bench area where the overburden was stripped off many years ago and used to landscape around Drax power station. This bench area has had time for vegetation to become re-established and proved to be the ideal site for borehole installation and radar data acquisition due to its easy access, combined with a sheltered and secure location, lack of overburden and most importantly enthusiastic and co-operative quarry personnel.

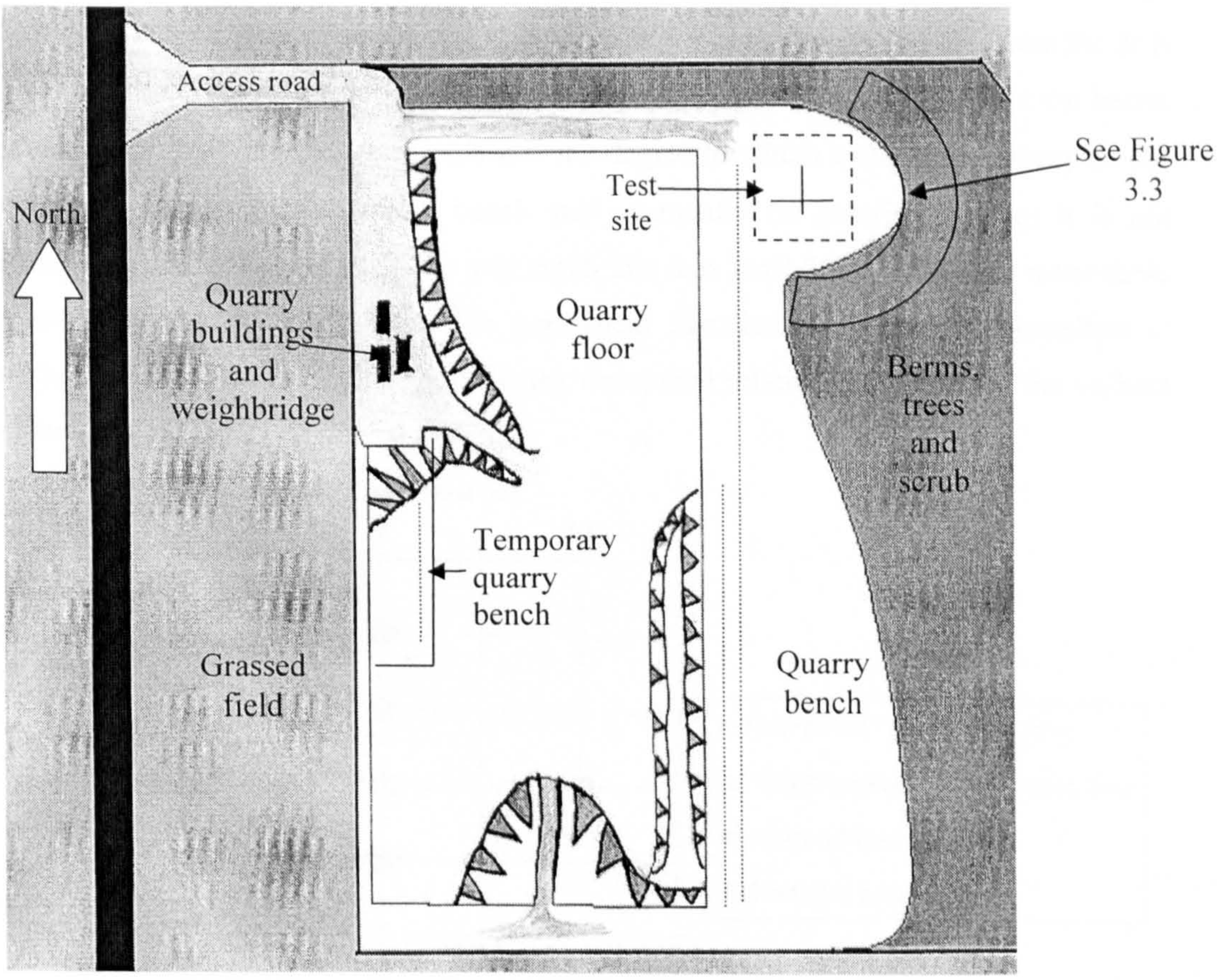

Figure 3.2. Sketch plan of Great Heck Quarry (not to scale), however quarry is approximately 250m from north to south.

The permanent site instrumentation was installed within the test site area shown above, and details of these installations are given in the relevant chapters. An automatic logging rain-gauge was installed on top of one of the quarry huts, near the weighbridge.

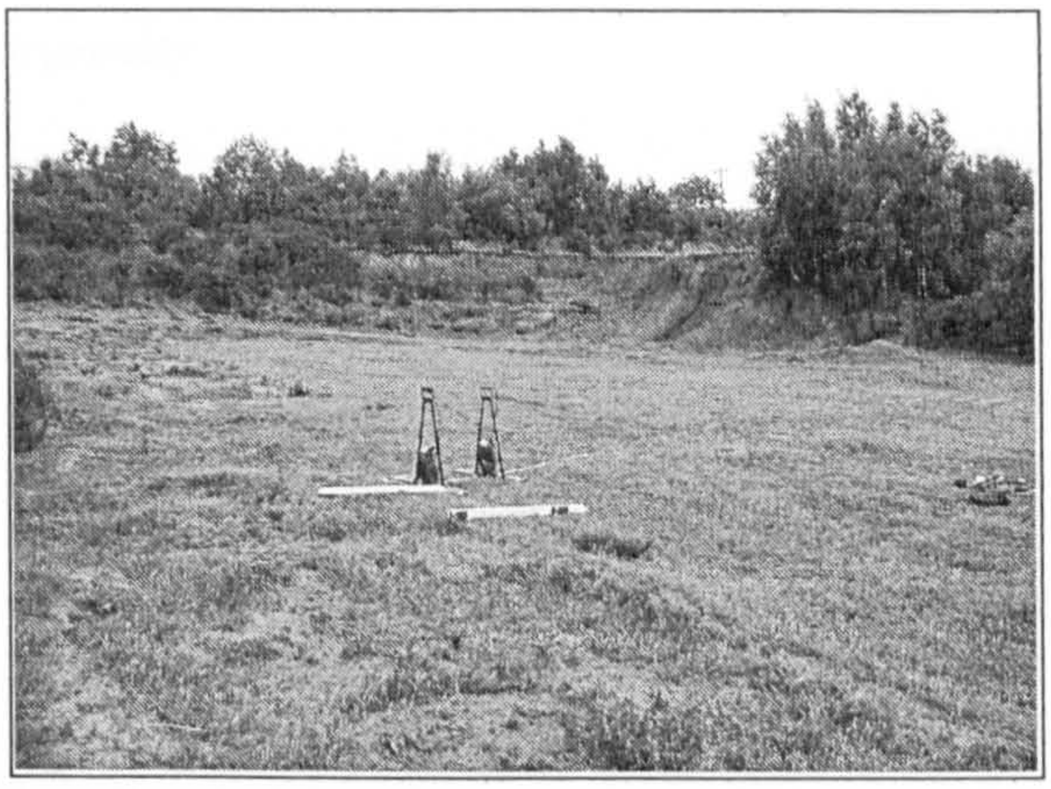

Figure 3.3. Pulse EKKO 100 radar equipment at Great Heck test site. Looking east into area marked 'test site' on Figure 3.2.

Figure 3.3 shows the test site where the borehole instrumentation was installed. Taken during the radar characterisation phase, prior to drilling, the image shows where the drift cover has been removed prior to re-colonisation by vegetation. Also shown are the berms (earth banks) that line the quarry site and the degree to which trees have reoccupied the area. This section of the quarry bench will eventually be quarried out but it is not anticipated that quarrying activities will reach this area until 2007-2008. The water table is generally below depth 14m. The permanent installation of borehole geophysical hardware is detailed in Figure 3.4, showing the spatial relationships between the various boreholes.

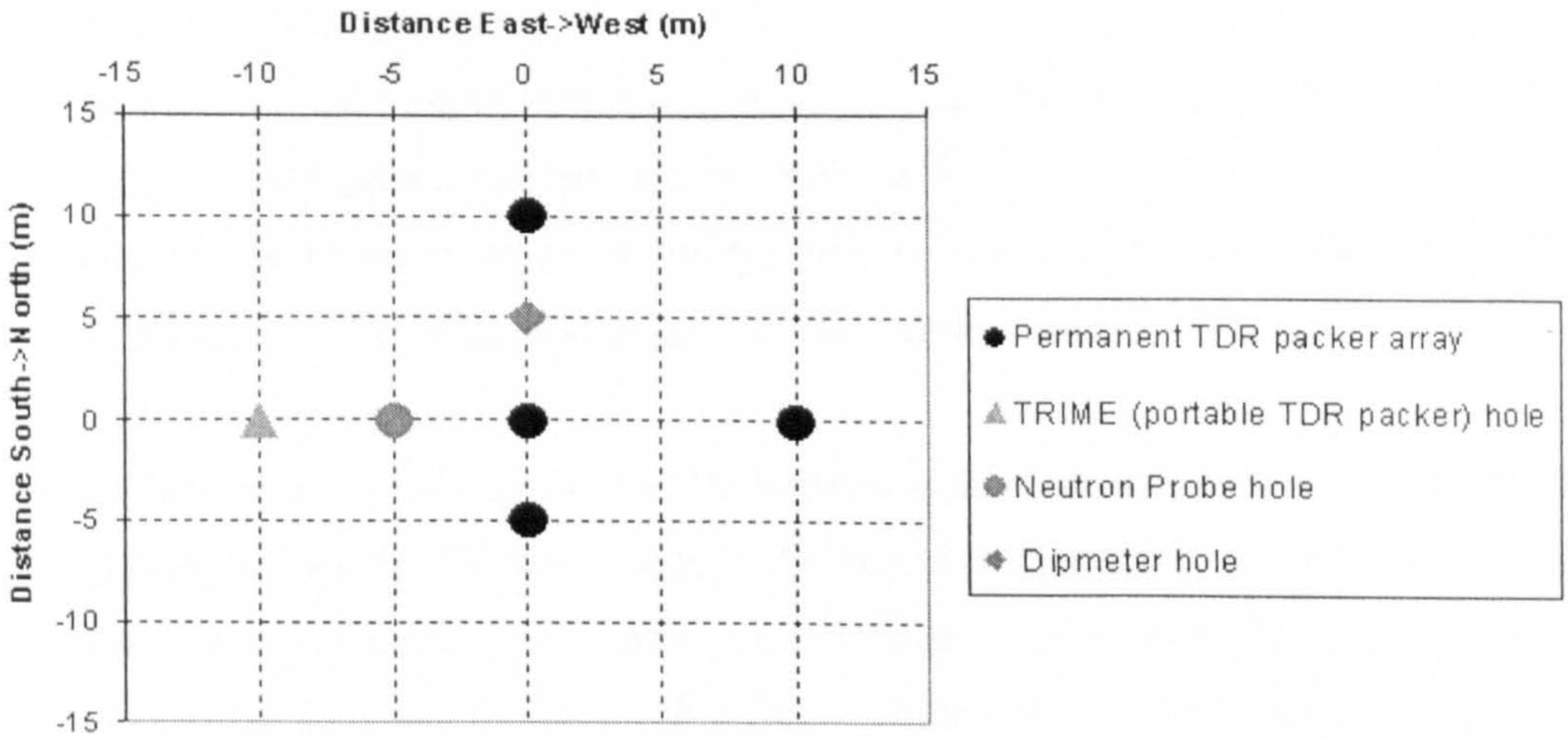

Figure 3.4. Plan map of borehole installation, Great Heck quarry.

The quarry faces at Heck Quarry provided an excellent opportunity to examine the sedimentary structure of the Sherwood Sandstone. Many faces were cut 2-4 years ago, providing optimum face conditions for logging, and many faces, particularly in the south-east corner of the quarry, and the temporary bench shown in Figure 3.2, were readily accessible and were used for detailed logging and sampling for grainsize analysis.

3.1.3 Scales of heterogeneity

When considering the fabric of reservoir rocks, a common approach is to model the bulk properties of the aquifer as a whole. Hence the effects of localised fracturing, preferential pathways or aquicludes and aquitards within the bulk rock may be averaged out and effectively ignored. This approach fails when applied to more restricted areas, and the smaller the area of interest, then the more likely a whole-aquifer model will be significantly in error. This error may be of real significance when considering contaminants, local variation in rock mass properties can greatly increase or decrease the potential of these contaminants to reach the water table.

Huggenberger and Aigner (1999) examined the hierarchy of heterogeneities with regard to aquifer sedimentology, and discuss a five level scale, linking size of heterogeneity with sedimentary process. This hierarchy may be summarised as,

1) Giga-scale hydrostratigraphy of an entire basin, related to sequence stratigraphy and basin tectonics.
2) Mega-scale facies associations, related to depositional system, i.e. braided vs. meandering fluvial systems.
3) Macro-scale architectural elements, related to facies dynamics at the coset level, where 'cosets' are defined as 'a number of cross beds preserved in a single bed' (Allaby and Allaby, 1990).
4) Meso-scale sedimentary structures, related to sedimentary dynamics, i.e. trough vs tabular stratification, laminar vs cross-stratified sands.
5) Micro-scale variation in permeability, porosity and mineralogy, related to original grain sorting, diagenesis and original mineral composition.

Hence heterogeneity is important and a large proportion of this dissertation is aimed at quantifying the levels of heterogeneity in the Sherwood Sandstone in the study area. This section briefly summarises the heterogeneities in one section of rock, from Eggborough Quarry (≈2km from Great Heck, ≈5km from Pollington). This examination is conducted at a range of scales, from the macro-scale to the micro-scale, to link with 1-5 above.

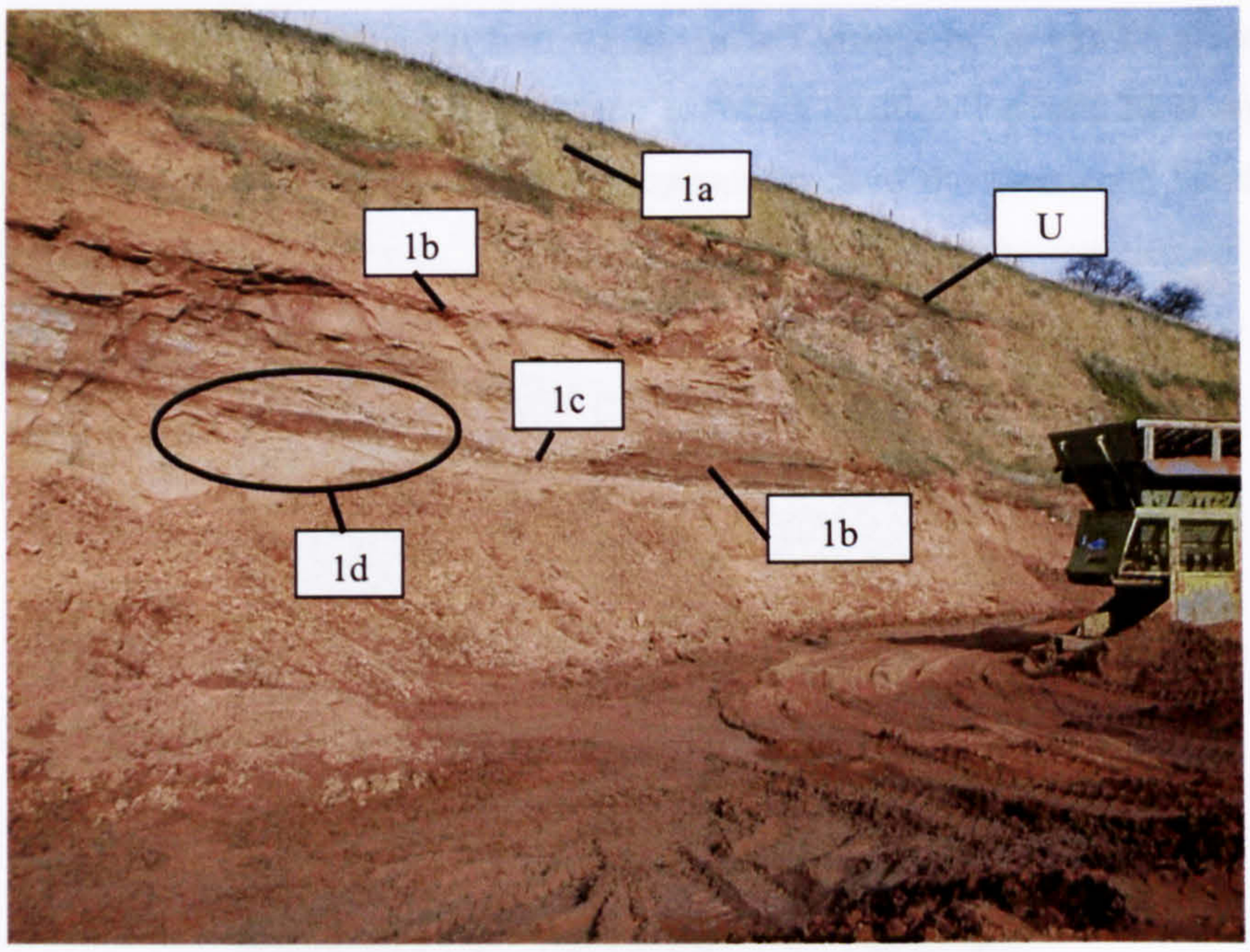

Figure 3.5. Scale 1, Tens of metres (Macro-scale). Rock face at Eggborough Quarry.

At the outcrop (macro) scale (Figure 3.5) the rock shows only relatively minor heterogeneity. Feature 1a is the overlying fluvoglacial drift deposits, which are separated from the underlying Sherwood Sandstone by a major unconformity (U). Feature 1b shows relatively darker layers in the rock, which are horizontally or sub horizontally laminated, with a scour feature visible (1c). The area 1d shows the location of the larger scale images presented below.

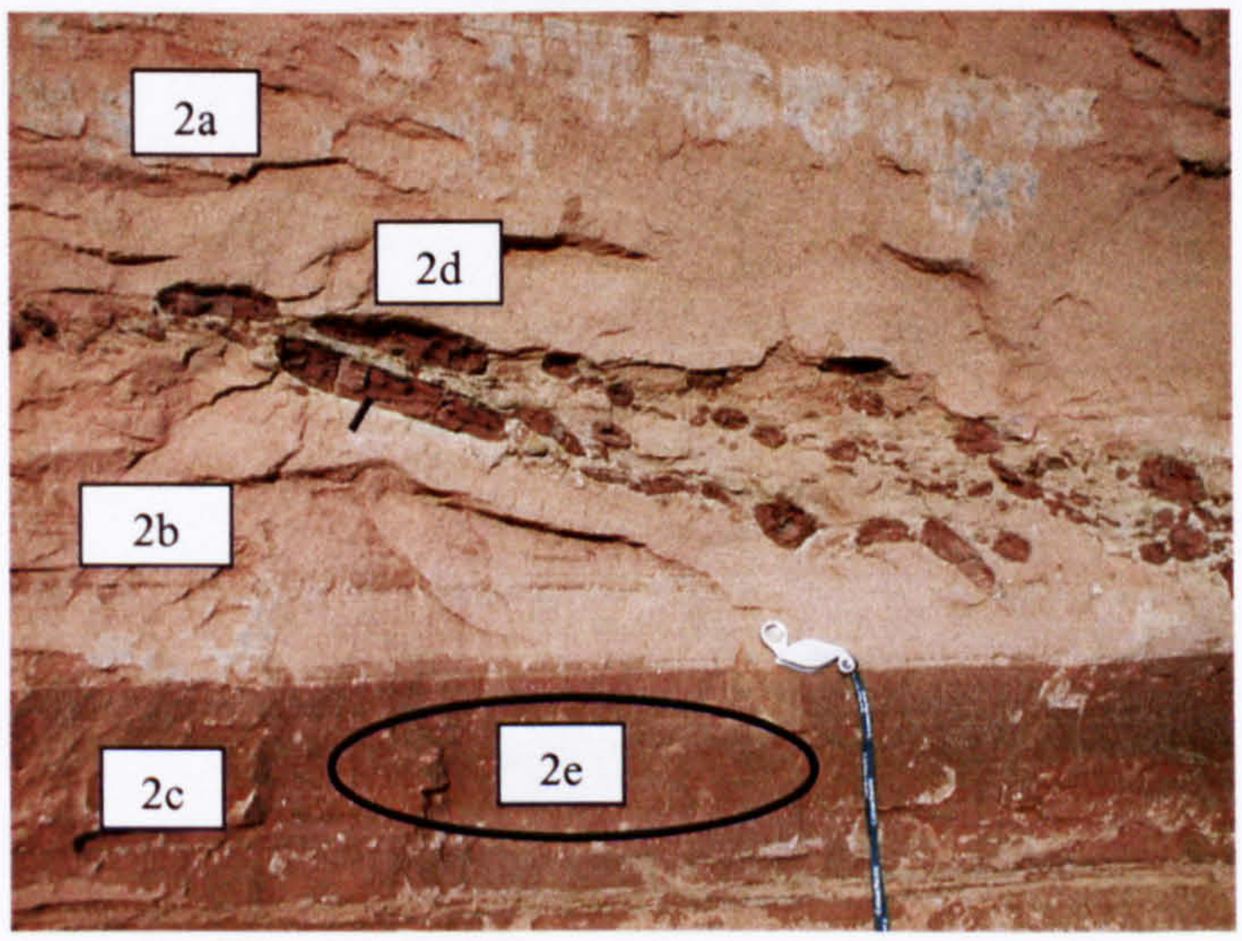

Figure 3.6. Scale 2, Metres (Meso-scale). Same rock face, field-of-view now 1metre across (approx.).

At the meso-scale, more levels of heterogeneity can be observed. Feature 2a is cross-bedded, 2b and 2c are planar laminated, but the darker colour of 2c can be clearly seen. Feature 2c is an argillaceous layers described later this chapter. Feature 2d is one of the prolific mud intraclasts which are visible throughout much of the Sherwood Sandstone in the Selby-Doncaster-Rufford area. The circled area (2e) shows the location of the thin section presented below.

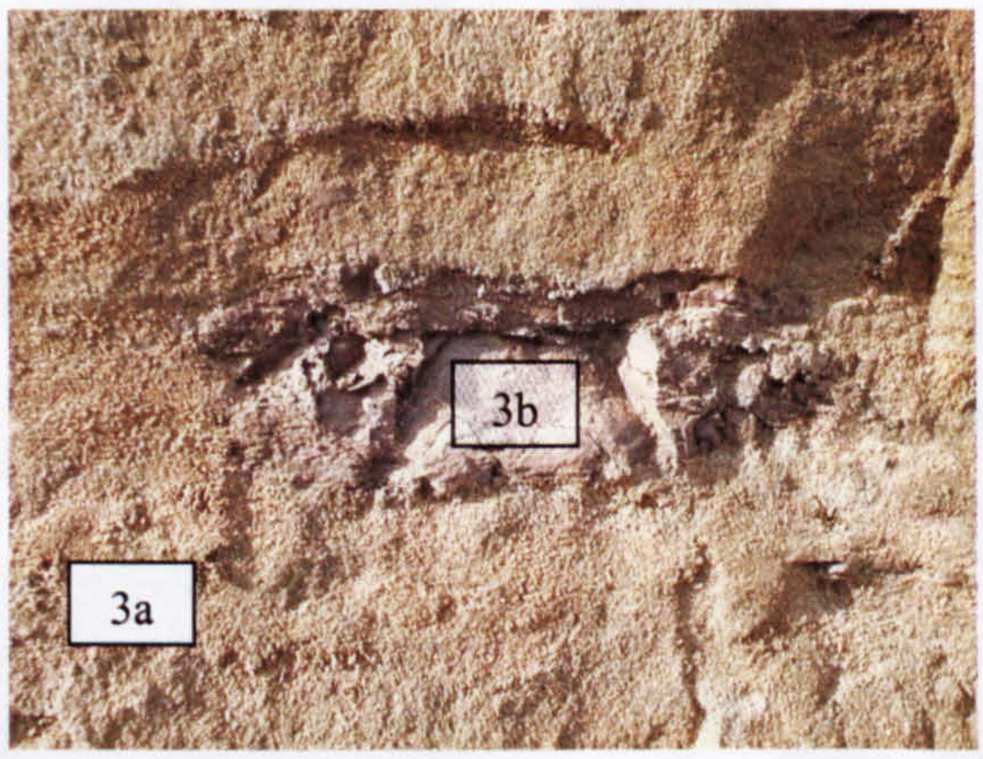

Figure 3.7. Scale 3. Centimetres (Meso-scale). Mud intraclast. Field of view approx. 10cm across.

Feature 3a highlights the horizontally laminated nature of the fine-grained sandstone rock, and shows horizontal laminae within the mud intraclast (3b).

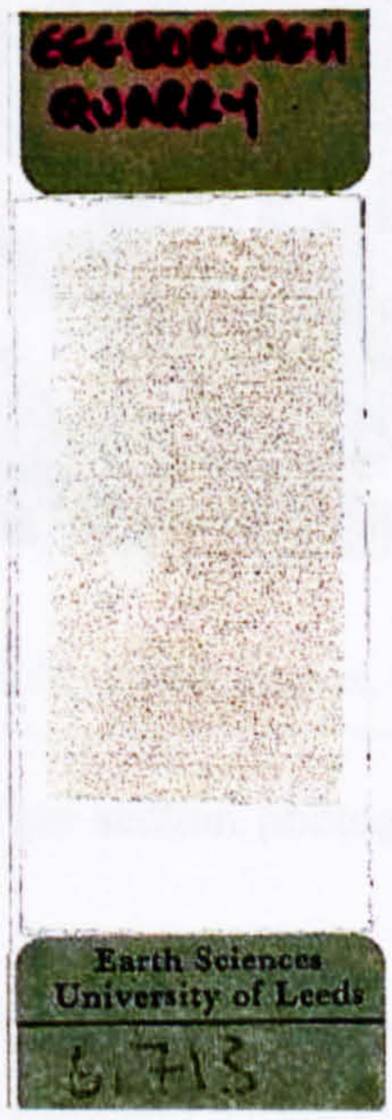

Figure 3.8. Scale 4. Millimetre (meso-micro-scale). Slide is 7.5x2.5mm across. Taken from ringed area on figure 3.6.

This slide shows the rock in its correct orientation (i.e. up on the slide is up at outcrop). Here the fine millimetre scale laminae present in the fine-grained units are readily apparent. Rocks with this degree of lamination are highly likely to exhibit high degrees of hydraulic anisotropy.

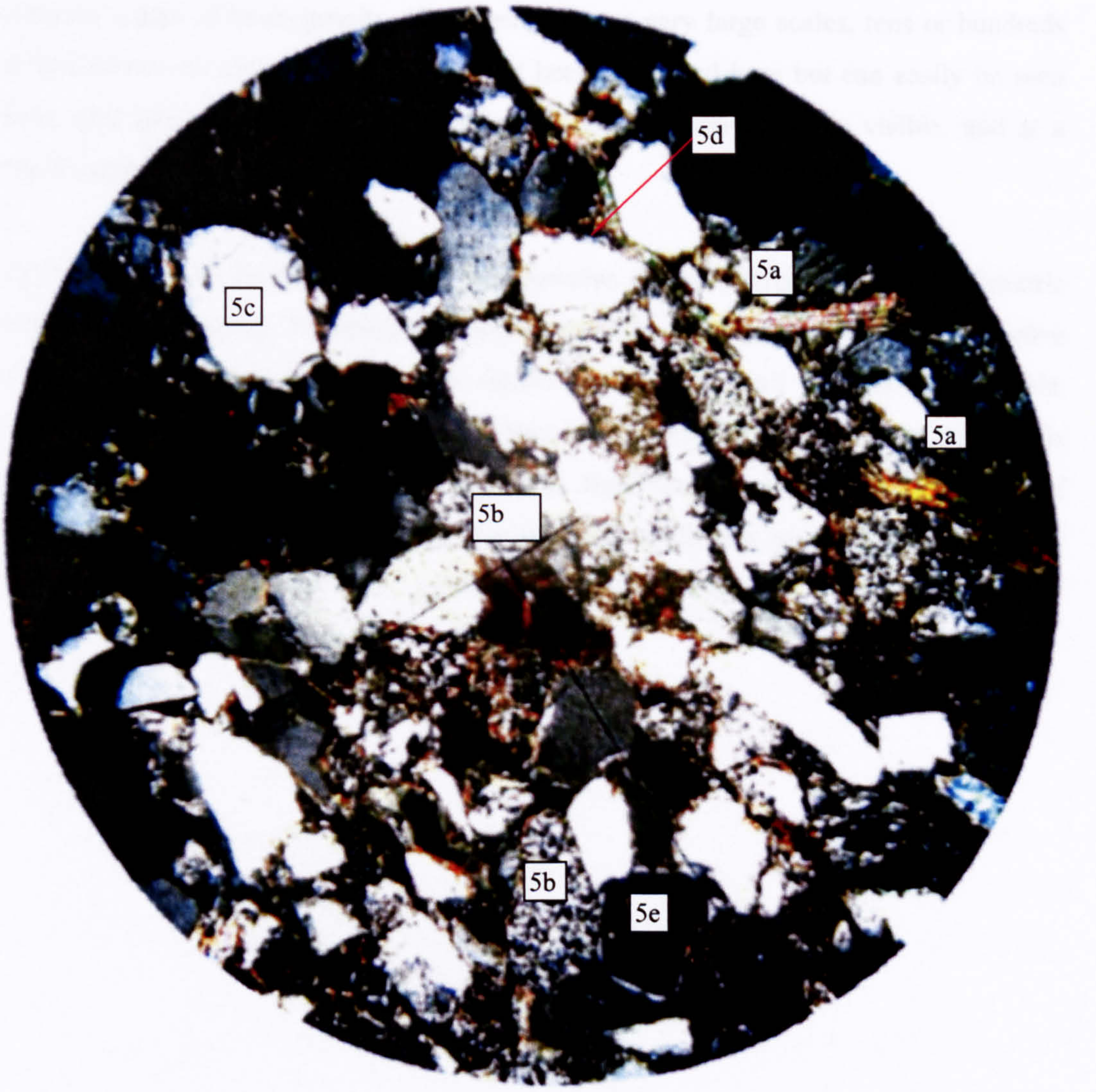

Figure 3.9. Scale 5. Micro-scale. Thin section photograph of the Eggborough Sherwood Sandstone.

Taken under crossed polarized light, Figure 3.9. shows grain orientation and lamination at a microscopic scale. Biotite micas orientated parallel to bedding may be seen, particularly to the top and right of the image (5a), and evidence of grain dissolution and replacement with clays (5b) may also be seen. At (5c) an intact quartz grain is seen. Little pressure solution of quartz has occurred, suggesting this rock has been subjected to low-pressure environments only. At (5d) fine intergranular pores are filled with detrital clays. Some of

the black areas such as 5e are probably grain dissolution voids, although it is possible that some voids may have been introduced by 'grain plucking' during thin section manufacture.

Hence it is relatively easy to demonstrate that the Sherwood Sandstone exhibits several different scales of heterogeneity. Heterogeneity over very large scales, tens or hundreds of kilometres, or kilometre scales have not been illustrated here but can easily be seen from geological maps. At the bedform scale, heterogeneity is easily visible, and at a microscopic scale the rock is highly anisotropic.

Laboratory testing helps define the characteristics of the microscopic and millimetric scales of heterogeneity. Pumping tests may characterize the scales of hundreds of metres to the kilometre scale, and large-scale aquifer models cope well with the largest scale, where the aquifer is essentially homogeneous. The research presented in this thesis attempts to provide data at the missing scale, from tens of centimetres up to tens of metres, is an attempt to provide data that may help to further reconcile the dichotomy between laboratory and field scale permeability measurements.

3.2 Methods.

A variety of methods, both qualitative and quantitative were employed to investigate the structure and properties of the Sherwood Sandstone in the study area. Each technique will be described here, together with details of where the various methods were used.

Face inspection and photography. This was the most basic and subjective site characterisation method used, and was generally only employed as a reconnaissance tool to enable efficient identification of targets for more rigorous methods. Requiring only a notebook, compass clinometer, camera and pencil it was very easy to visit many outcrops in a very short time and so this technique was invaluable in deciding which quarries and faces were worthy of repeat visits. This method was used at all sites, including several other sites visited as part of the reconnaissance of the field area that are not reported here as no data from them is presented.

It was soon discovered that the face inspection and photography technique had severe limitations. Photographs only show gross features, any subtlety is lost and so photographic logging of quarry faces proved to be useful only for characterising large or exceptionally well-defined sedimentary features. Nevertheless, some features were more photogenic than others, and some good data were recorded using this method, but a better method was needed to examine detailed structure. One advantage of face photography is that, provided care is taken to keep the camera axis perpendicular to the face as much as possible, the relative size of features are preserved with less distortion than free sketching, allowing photographic images to be used to constrain notebook field sketches.

Field sketching and detailed logging. To investigate detailed structure more fully, it was decided to sketch quarry faces. Initially this appears to be a retrograde step, potentially introducing more errors than face photography but a methodology was devised to constrain scaling errors and it proved possible to record useful data, together with detailed descriptions of the rock faces using this method. The methodology employed involved two people working together, one 10-20m away, the other standing right next to the face. The person at a distance conducted the sketching, with length along the face and face height being constrained by tape measurements. Once the basic outline of the face, with obvious features was sketched the person adjacent to the rock called out grain size data, foreset angles and other detailed information and pointed out the contacts between different units. By this method it was possible to sketch highly accurate representations of the quarry walls. Although this technique was highly effective it was slow. However,

comparison of radar images with the field sketches showed a high degree of correlation. This technique was used at Hatfield, Rufford, Heck and Pollington Quarries. Digital manipulation of the field sketches was used to correct any scaling or perspective problems using the distances measured by tape. As a check on the accuracy of the sketching method a face at Rufford Quarry was surveyed using a total station EDM theodolite and the discrepancies between the sketch and surveyed face proved minimal.

There are significant advantages resulting from the use of sketches rather than photographic results. Sketches may contain more relevant detail, and contain a degree of interpretation as well as providing a record of the rock. Sketches are also a two-dimensional record, allowing visualisation of relationships between several different sedimentary units at once, whilst providing a qualitative or quantitative (see next section) estimation of the relative abundance of sedimentary features.

Core logging. A single core was taken from the Great Heck Quarry test site. The coring method used an air flush rather than a liquid or mud flush, to prevent alteration of the hydraulic properties of the borehole, and a double tube coring system was employed to maximise core recovery. The friable nature of the Sherwood Sandstone at Heck prevented complete recovery, with the air flush tending to 'blow out' fine-grained and argillaceous layers. The core was visually inspected in the laboratory and described according to BS5930 (1999). Grain sizes were estimated using a GEO grain size comparison chart, and the results presented in graphic log format for easy comparison with other methods (see section 1.2). BS5930 (1999) provides detailed information on how to describe the properties of cored rocks as well as various parameters that deal with fracture state such as total core recovery and solid core recovery. This method provided data that could be input to one of the standard rock mass classification schemes and estimates of the load-bearing capacity, tunnel stand-up time and other engineering properties of the bulk rock mass may be determined. The Sherwood Sandstone in the study area is very weak and friable, and while it will be capable of resisting compressive forces when undisturbed, it possesses very poor properties as a tunnel or construction stone. Furthermore, inspection of the quarry walls shows that the core contained many more fractures than the in-situ rock, and hence tended to fracture during extraction. Hence the core was used to provide supplementary evidence on the distribution of the various architectural elements directly beneath the site rather than being the primary characterisation method.

Particle size analysis. To further improve the quality of the face logged data, samples were taken from some sedimentary units and particle size distribution curves obtained at

Leeds University by Nicholas Leinart using a Coulter Counter series LS230. This system uses the diffraction of laser light by particles of different size passing through a sample cell. The amount of scattering of the light by diffraction is detected and used to provide an accurate grainsize profile. This technique is well established and is known to yield good results in Sherwood Sandstone (Pokar, 2002) provided the samples are thoroughly disaggregated by hand in a pestle and mortar, and then treated with Calgon (sodium hexametaphosphate) solution.

Gamma logs. Gamma ray measurements were taken from two boreholes at Heck Quarry to further constrain the subsurface geology. This method relies on the lowering of a portable gamma scintillation counter into the borehole. These scintillation counters are normally of a sodium iodide or a caesium iodide type (Geological Survey of Canada, 2003). Different rocks produce differing amounts of gamma radiation, normally by the decay of potassium, thorium and uranium compounds. Of the constituents of the Sherwood Sandstone, clays contain the greatest amounts of radioactive minerals, and so gamma logs were used to locate clay and clay rich horizons.

Rock sequences are logged by measuring the gamma radiation every 0.1m or so over a selected time integration. Measured times and counts are stored electronically and a plot of probe depth against counts/second is the normal method of viewing results. Plots of the gamma curve placed next to the lithological column provide an excellent calibration for both the gamma logs and other geophysical methods (Aigner *et al.*, 1995).

Fracture mapping. The Hatfield test site is immediately adjacent to the intersection of two quite major faults. Face logging at Hatfield Quarry revealed the presence of abundant, clay-filled, sub-vertical cracks and minor faults associated with this larger scale faulting (see later). These vertical features posed a potential barrier to horizontal flow and so an EDM total station theodolite was used to accurately map the location of these features across the quarry floor to determine their lateral extent, degree of continuity and whether there were any preferred orientations. This process was only carried out at Hatfield as similar faults and tension cracks were not found in any significant numbers elsewhere. Samples were taken from the linings of these faults and were analysed by Lesley Neve at Leeds University, using quantitative X-ray diffraction techniques, to determine the likely origin of the clays.

3.3 Results

Detailed logging at a range of quarries in the Sherwood Sandstone using the methods described in the previous section allowed a five-fold facies association to be devised for the study area. This section describes the different facies identified and provides evidence for each, before presenting evidence regarding the relationships between facies and the relative facies abundance. The facies identified were;

1) Metre-scale trough cross-stratified sandstone;
1b) Reworked mudstone intraclasts situated within facies 1
2) Low-angle or planar-laminated sandstone;
3) Claystone, sandy claystone or clayey sandstone lenses and drapes.
4) Ripple cross-laminated sandstone
5) 5-10m scale channel and scour features infilled with Facies 1-4 above.

Facies 1. Trough cross-stratified sandstone. (Figures 3.10, 3.11.). This is the most common facies (see Table 3.2) and consists of trough cross-stratified sandstones that have been produced by deposition from migrating sand dunes or sinuous crested bars. Facies 1 is interpreted to represent deposits of dunes within the active braided channels, where trough cross-stratified units are deposited throughout the rising, peak flow and falling stages of flooding events and forms the bulk of the Sherwood Sandstone in the quarries visited. These trough cross-stratified sandstones often incorporate stringers of mudstone intraclasts, Facies 1b (presumably rip-up clasts from facies 3, see below), along erosion surfaces at the bases of the individual dunes or lying on the foreset avalanche surfaces.

Generally the trough cross-stratified sandstones were very fine to medium grained and free draining, and it was anticipated that this unit would not present a serious barrier to moisture migration in the vadose zone. Grainsize analysis (Figures 3.3.20, 3.3.21) shows an upwards fining trend within the trough cross-stratified units. This trend is consistent with an upwards fining within the dune foresets, and the possible accumulation of fine material infiltrating into the tops of each bedform in the lee of the next advancing dune. This change in grain size between dune cross-sets has important implications for permeability and the generation of GPR reflections. The thickness of the cross-sets tends to reduce upwards within individual sequences (see Figure 3.10), consistent with dune height reducing as channel depth shallows (see Bridge, 1993, 2003; Ashworth *et al.*, 2000 for examples within braided rivers).

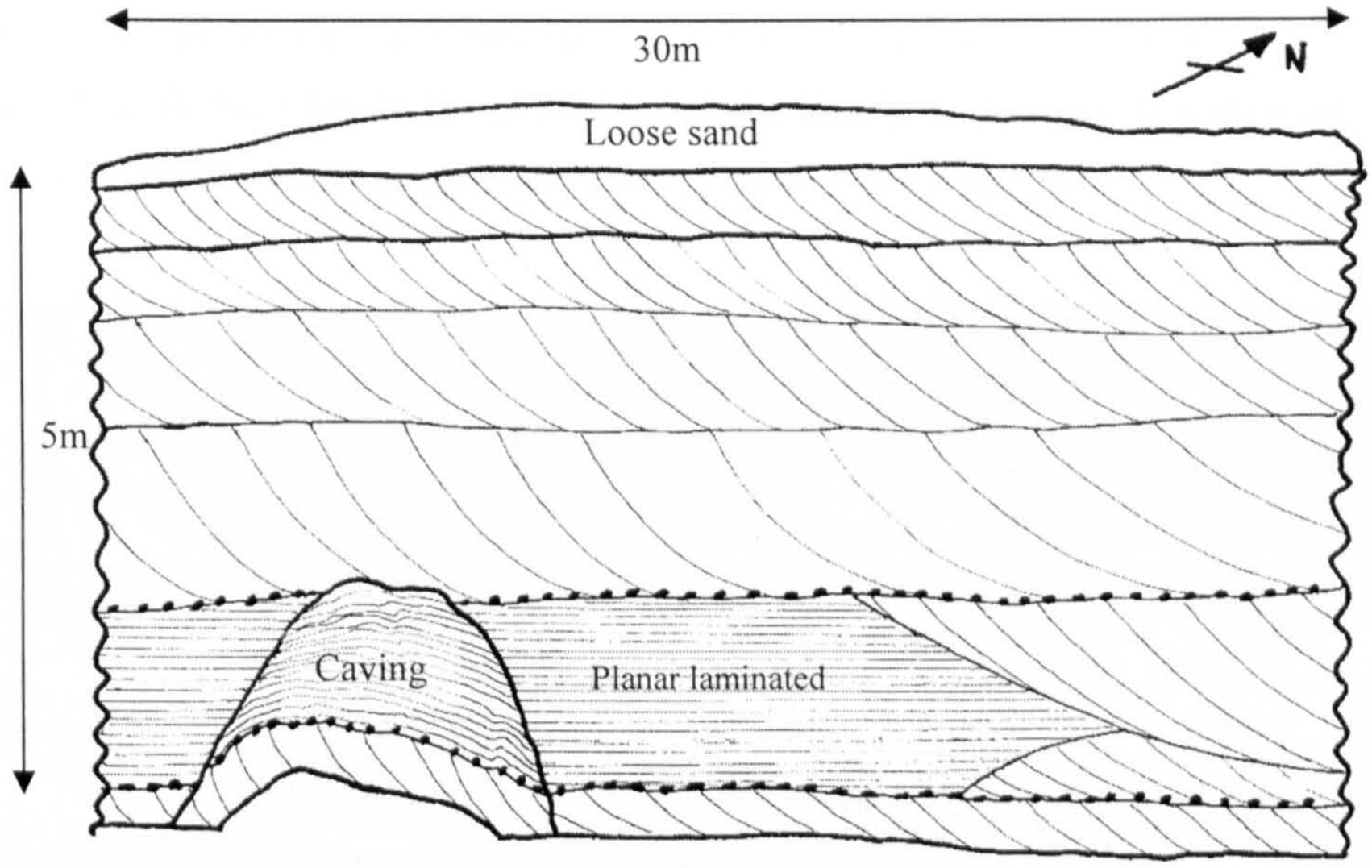

Figure 3.10. Planar and cross-stratified units at Austerfield RMC Quarry (SK 672953), showing decreasing thickness of beds of trough cross-stratified sandstone with height in the quarry face.

Visible in Figure 3.10. is an area where the trough cross-beds of facies 1 have cut down into the planar-laminated facies 2 layer below. This represents a potential change in palaeocurrent, from East→West at the top 3m of the sequence, to roughly South→North where the trough units cut into the laminated units, and then back to East→West again for the basal half-metre of the section.

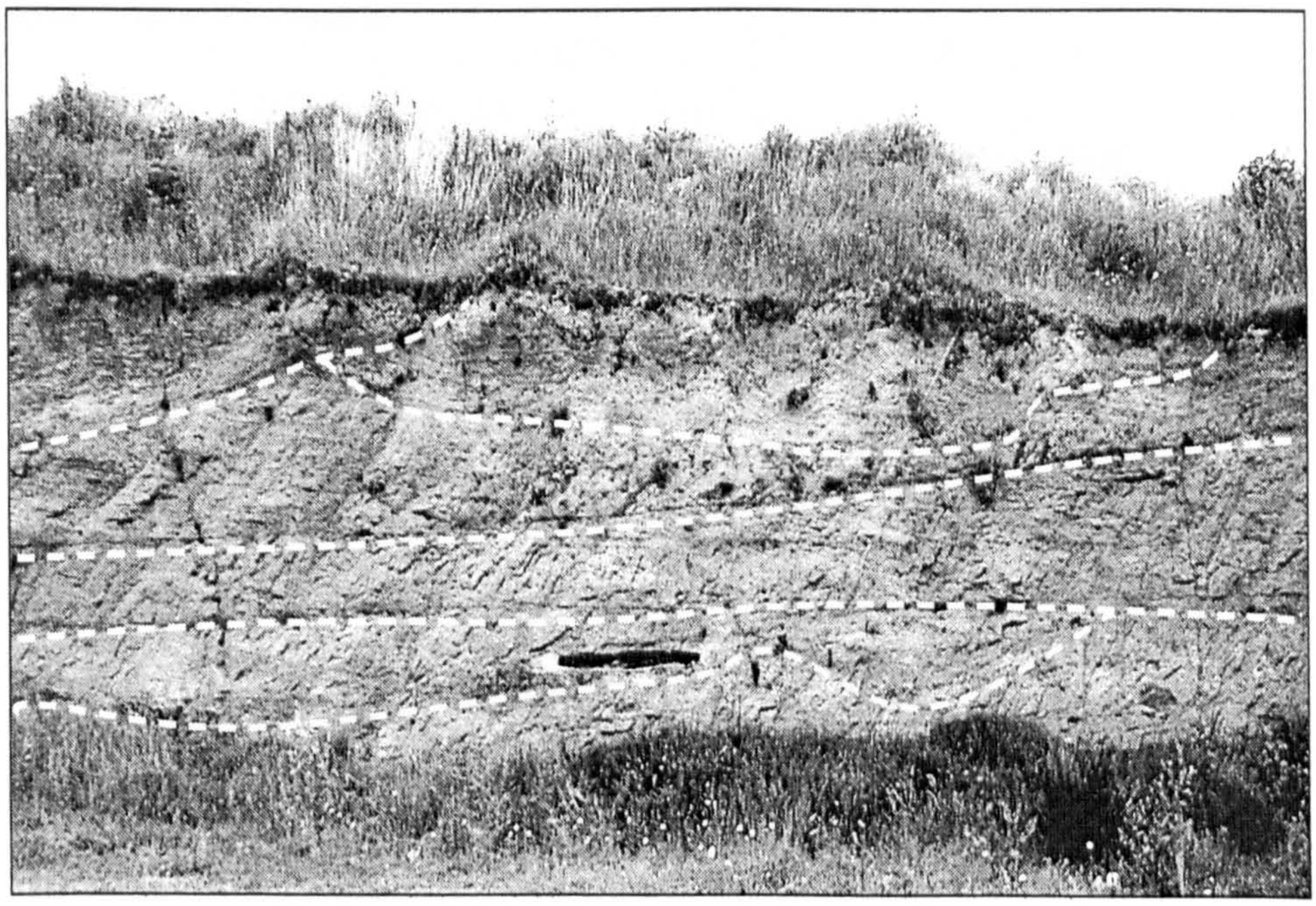

Figure 3.11. Stacked trough cross-stratified units at Rufford Quarry (SK 596608). The quarry face is orientated east-west, is 5m high and 15m long and the set boundaries (interfaces between each migrating dune) are highlighted with white dashed lines.

Figure 3.12 shows Facies 2 and 1b in one image. The darker colouration of the upper layer (d) in facies 2 below the scour (c) may be clearly seen, together with a lag layer of clay clasts (b) above the scour feature that is cutting down into (d).

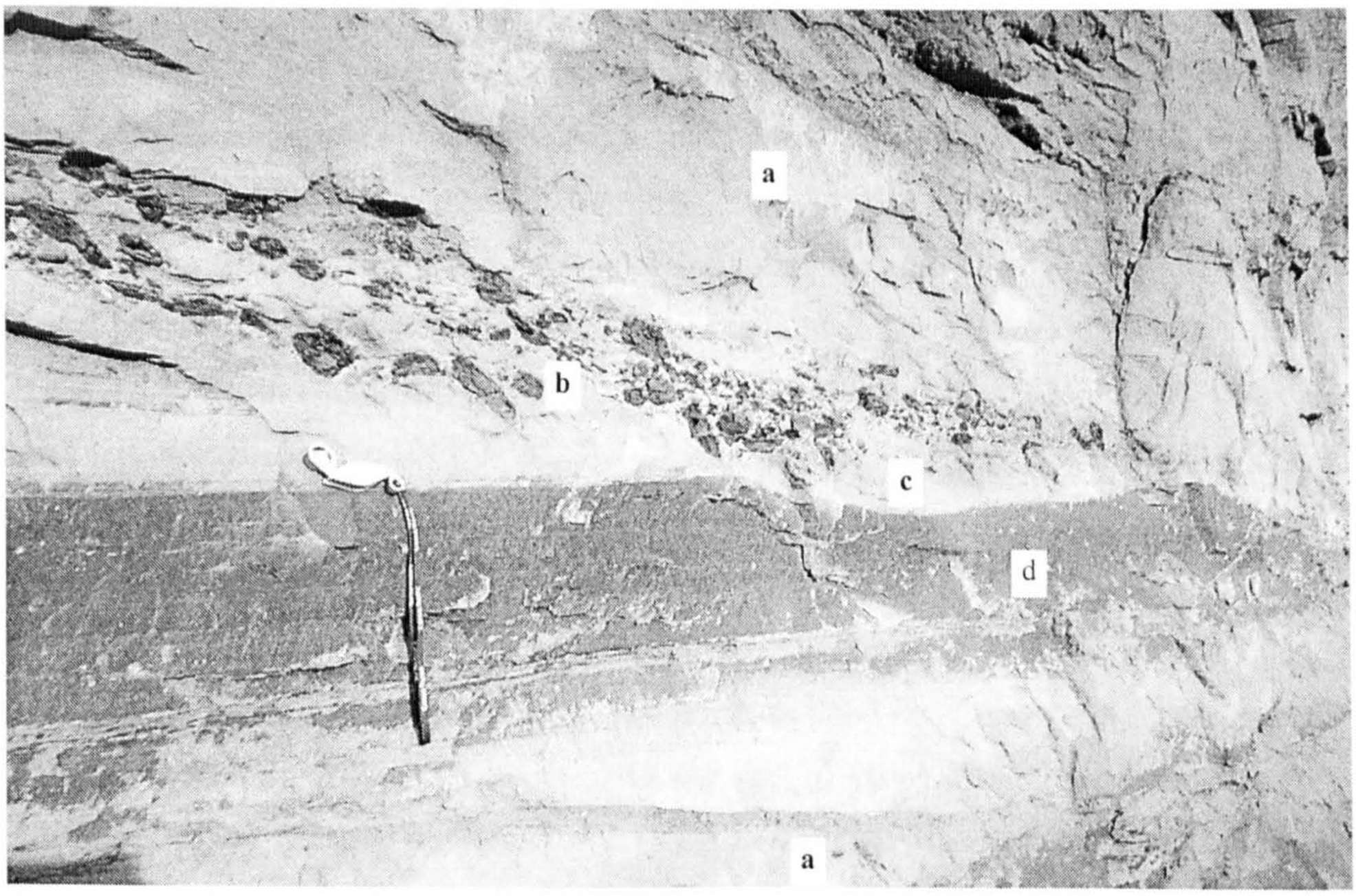

Figure 3.12. Photograph from Eggborough Quarry (SE 573228). Hand lens approx. 10cm long a) trough cross stratified sandstone (facies 1). b) Mud intraclasts (facies 1b). c) Scour eroding underlying top of d. d) Dark (high moisture content) argillaceous top of planar laminated sandstone facies 2.

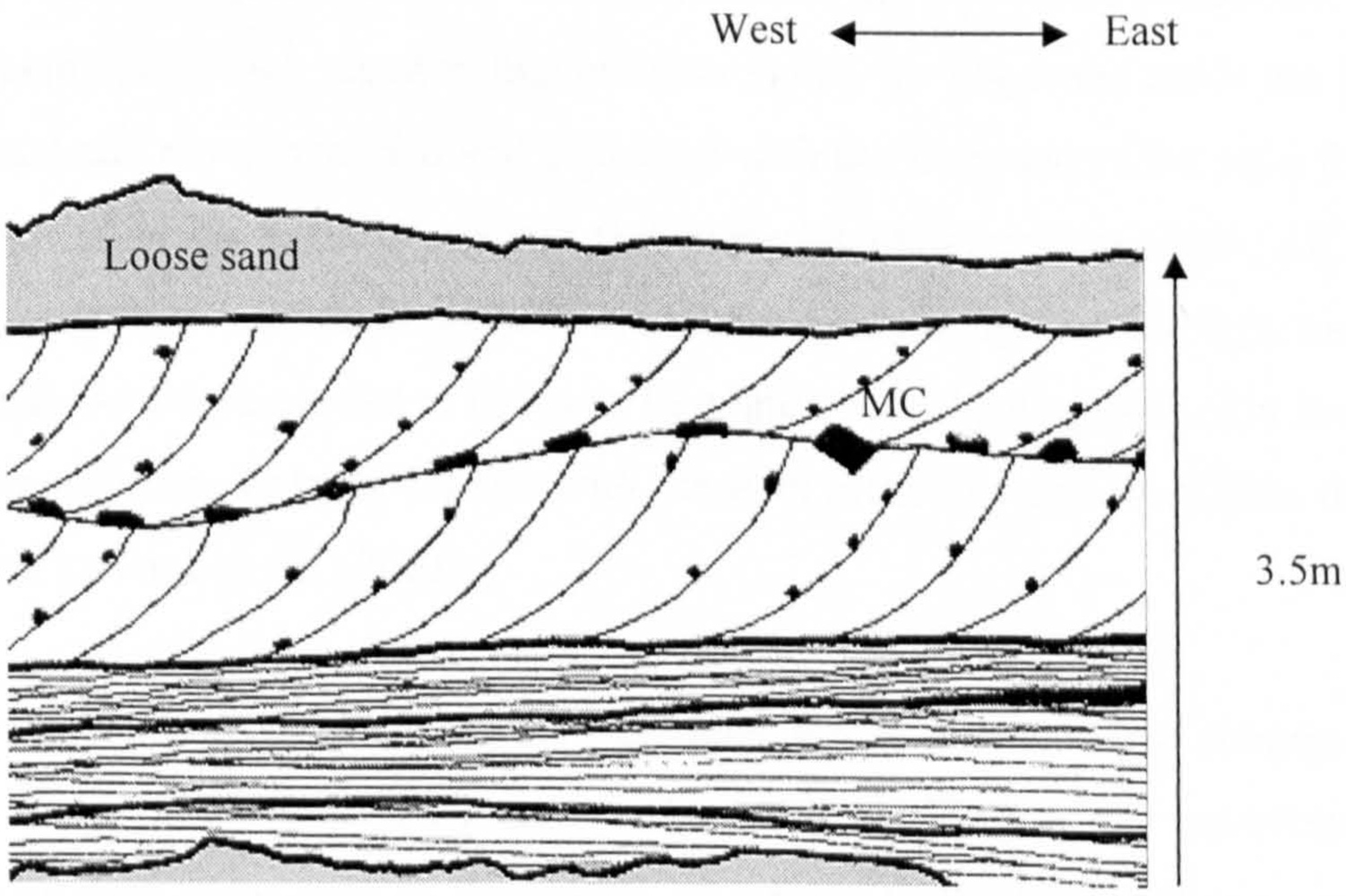

Figure 3.13. Sketch log showing planar laminated and cross-stratified units at Eggborough (SE 573228). MC denotes large mud clast.

Palaeocurrent data may be inferred from outcrop observations. Figure 3.13 shows trough cross-stratified facies 1 overlying planar laminated facies 2. abundant mud clasts (facies

1b) are present, some large, showing preferred orientation that suggests palaeocurrent was flowing East→West (right→left).

Facies 2. Low-angle or planar-laminated sandstone. This facies consists of fine-grained clay/silt-rich low-angle or horizontally laminated sandstones, which often lie directly above facies 1 with trough cross-sets grading into low-angle laminae. This facies is interpreted to represent either lower angle washed-out dunes, or upper-stage plane beds. At periods of overbank flow, river flow extends beyond the active channels, giving rise to large areas of rapidly-flowing, shallow water. This allows the deposition of upper-stage facies 2 across the braidplain and large areas of planar sheet flood facies may thus be deposited, which in cross-section, parallel to palaeocurrent, may appear to be similar to facies 1. In the Sherwood Sandstone the top layers of facies 2 (10cm > 0.5m) were frequently rich in infiltrated silts and clays (hence its darker appearance when damp). Two possible models for this clay infiltration are: **1)** Clay and silt sized particles may infiltrate through the tops of the sands as near static or pond conditions temporarily return to the braidplain on falling water levels. This model of clay infiltration agrees with the results of Pay *et al.*, (2000), who were able to relate clay content with depositional environment for the Devonian-Carboniferous sandstones of the Clair oilfield. Their sedimentological interpretation was that the principal method of clay introduction was infiltration by clay-laden surface waters or adhesion of clay minerals on damp sand grains either during or shortly after deposition. However, this model does not fully account for the scarcity of further waning-flow clay-rich bedforms in the Sherwood Sandstone. **2)** An alternative explanation which resolves this problem is that the clays and muds are part of the river bedload and are transported and deposited with the finer end of the sand fraction as fine mud pellets which break down into their constituents after deposition. All of the subsequent waning flow braidplain deposits could then contain significant clays, but most of these deposits would be eroded at the next flooding event, leaving only thin layers of clay/silt rich sandstones. This model fits with the data presented for Australian dryland rivers presented by Page *et al.*, (2003).

Facies 2 was frequently encountered in the field area, although it was less abundant than facies 1 (see Table 3.2.). Individual units were often highly laterally persistent, and although usually they were only in the region of 0.5-1m thick it was often possible to trace them laterally for hundreds of metres (see Figure 3.14). Facies 2 was significantly more fine-grained than facies 1(see grainsize analysis below – this section), and was often argillaceous, which allowed it to retain more moisture by capillary retention..Often appearing darker in the field than the trough cross-stratified sandstone, samples taken

from facies 2 would dry to a similar colour if left in a warm environment. This suggested that facies 2 had retained moisture due to significantly increased capillary action than facies 1.

Figure 3.14. Photograph from Austerfield Quarry (SK 672953). The quarry face, orientated east - west, is approximately 12-15m high and over 50m long. The feature marked by the arrow is a laterally continuous (>50m) fine-grained, argillaceous, planar-laminated sandstone (facies 2).

Figure 3.15. Perched water tables at Eggborough Quarry (SE 573228).

Field photographs provide evidence that the fine-grained facies 2 does cause perched water tables and horizontal flow in the vadose zone in the overlying facies 1 during periods of heavy rainfall (Figure 3.15). The cliff face shown (approximately 5-7m high) consists primarily of trough cross-stratified facies 1 with some layers of sub-horizontal fine-grained facies 2. The cliff face was generally dry but water was seen to be running

out of the face (circled areas) along the tops of the finest grained units following heavy rainfall in February 2001. Vadose zone water migration such as this is strong evidence of bypass flow occurring due to hydrostatic heads, caused by permeability variations, which themselves are a result of sedimentary heterogeneity.

Facies 3. Mudstones and claystones. This facies is the least extensive in terms of area (see Table 3.2.) and consists of occasional detrital claystone, sandy claystone, or clayey sandstones, which may be up to 0.5m thick and tens of metres in length. Facies 3 is interpreted to represent sedimentation in low-velocity regions, probably in slack water, in abandoned channels, or overbank areas, which are preserved as rare intact layers or lenses, which form the source material for the abundant mud intraclasts (facies 1b). Quantitative X-ray diffraction analysis of the clay mineralogy (reported below) reveals a dominant mixed illite/smectite composition and supports the argument that Facies 3 provides the source material for the prolific mudstone intraclasts. A low resistance to sediment reworking reduces the preservation potential of Facies 3.

Facies 3 occurs as intact clay horizons. In all the quarries investigated only two intact clay layers were found, one at Hatfield, one at Rufford. Figure 3.16. shows a clay layer at Hatfield Quarry. Intact clay layers would represent serious barriers to moisture flow. However, they are rare and only of limited lateral extent.

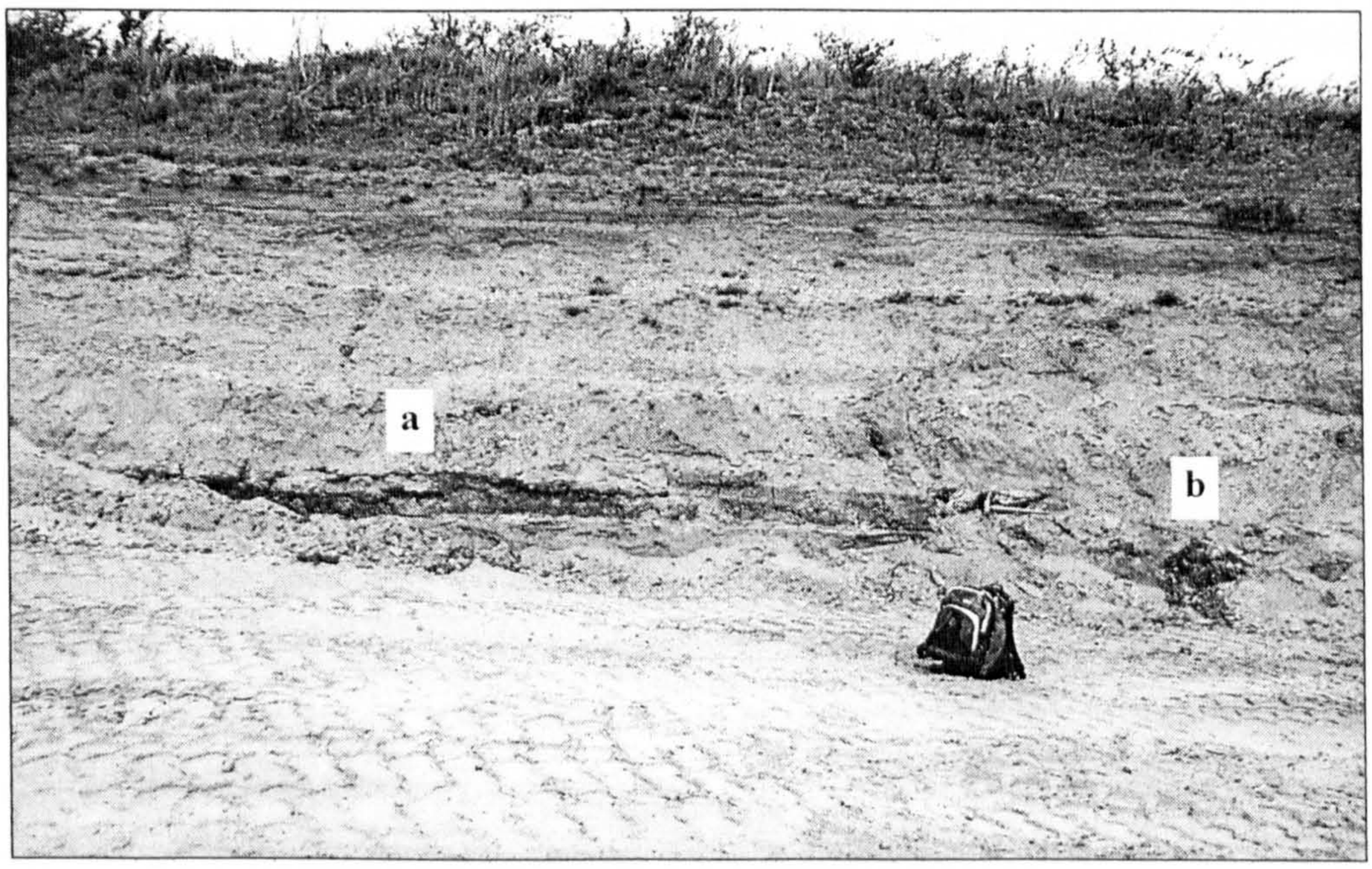

Figure 3.16. Photograph from Hatfield quarry (SE 653075) showing large clay layer and intraclast. Rucksack for scale. a) Large (9.5m long 0.45m thick) clay layer. b) Large intraclast detached from (a).

Facies 4. Ripple laminated sandstone.. This facies consists of centimetre-scale cross-lamination produced by asymmetric ripples, which are sometimes climbing, and occasionally are found overlying facies 1 trough cross-stratified sandstones. Facies 4 was interpreted as deposits left by low, current ripples in shallow water pools or shallow channels on bar tops (Figure 3.17).

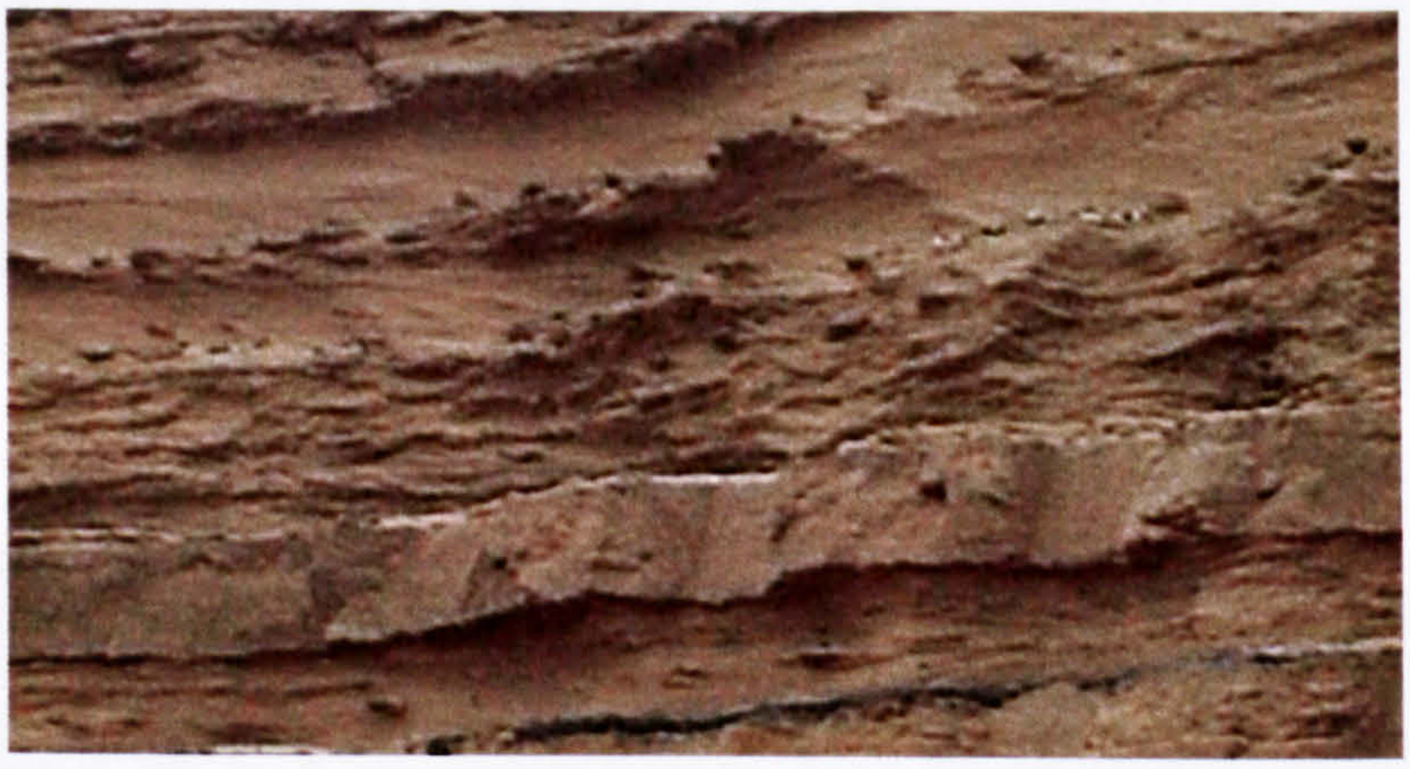

Figure 3.17. Ripple cross-laminae from Darrington Quarry (SE 610209). Field of view approximately 1.5m across.

Facies 5. Minor infilled scours and channels. This facies consists of small-scale (up to 10m wide) scour or channel features that may be infilled with any of Facies 1-4. These features are too small to represent the major first or second-order channels and either represent minor bar top and chute channels or infilled minor scours. Figure 3.18 shows two such features, one at Rufford Quarry infilled with facies 2 and one at Pollington Quarry infilled with facies 1. There is also an abandoned channel feature at Pollington infilled with clay/silt rich deposits and this is examined below. The Rufford channel and Pollington abandoned channel have been shown using GPR to persist tens of metres behind the cliff face, and are therefore confirmed as channels, however similar features seen at Heck and Pollington may not be laterally persistent into the rock and therefore may represent infilled scour features. Hence facies 5 includes both channels and infilled scours, and normally consists of reasonably prolific, small features, commonly <10m across and have been seen at Hatfield, Heck, Eggborough, Pollington and Rufford Quarries. However, Facies 5 is nowhere near as common as facies 1 and 2 (see Table 3.2). Facies 5 may restrict water migration in the vadose zone where low permeability infills are present (as shown by the vegetation that is able to thrive on them on the quarry faces). Thus, infilled scours may represent a significant local barrier to moisture flow, although it is not anticipated that they would have any significant effects over the aquifer as a whole because of their limited lateral extent.

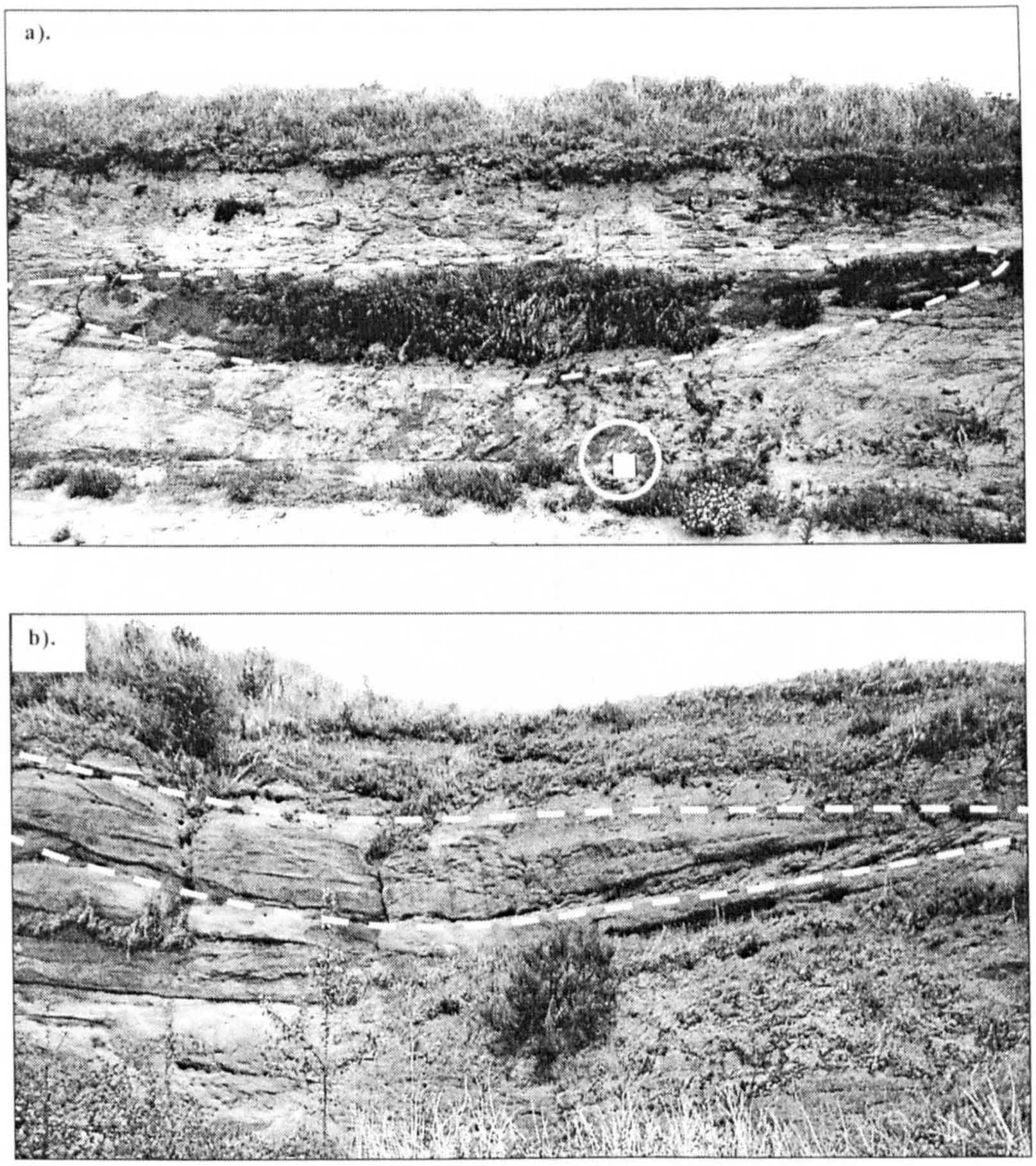

Figure 3.18. Photographs of infilled channels a) Channel at Rufford Quarry (SK 596608), infilled with fine sand/silt (facies 2). A4 clipboard for scale (circled). b) Channel at Pollington Quarry (SE 612201), infilled with medium sand (facies 1). Field of view approximately 5 x 10m.

A sketch log taken from the abandoned quarry at Pollington is shown in Figure 3.19 The main feature is an abandoned minor channel that has been infilled with fine sand and silt. Trough cross-bedding is again the dominant unit in the sketched face, although there is a planar laminated unit visible to the top of the exposure.

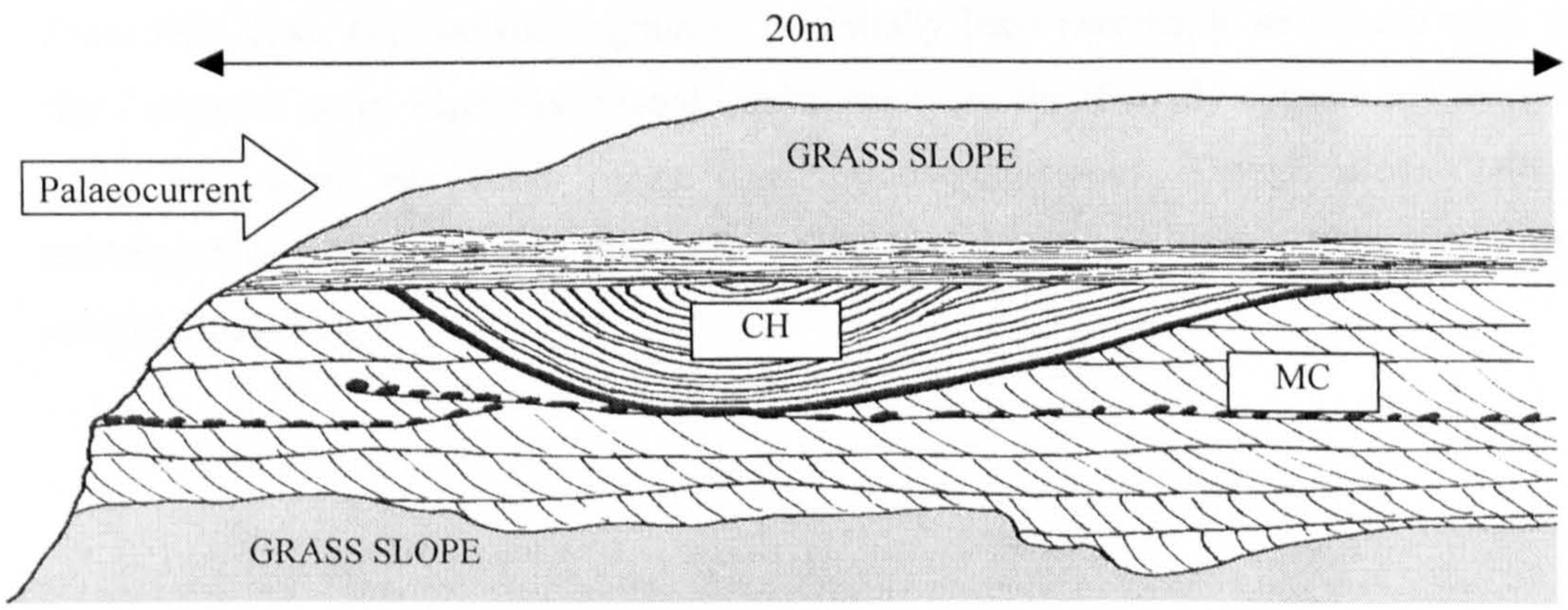

Figure 3.19. Sketch log of abandoned channel (CH) at Pollington (SE 612201). MC denotes mud intraclasts.

Further characterisation of the sedimentary facies scheme was provided by a particle size analysis that was conducted upon a range of samples from several sites and subjected to Coulter-Counter grainsize analysis. Samples were taken from the tops and bases of several trough cross-beds (facies 1) and low angle / planar laminated horizons (facies 2) so that typical grain sizes could be obtained. The results of this are shown in Figure 3.20 below.

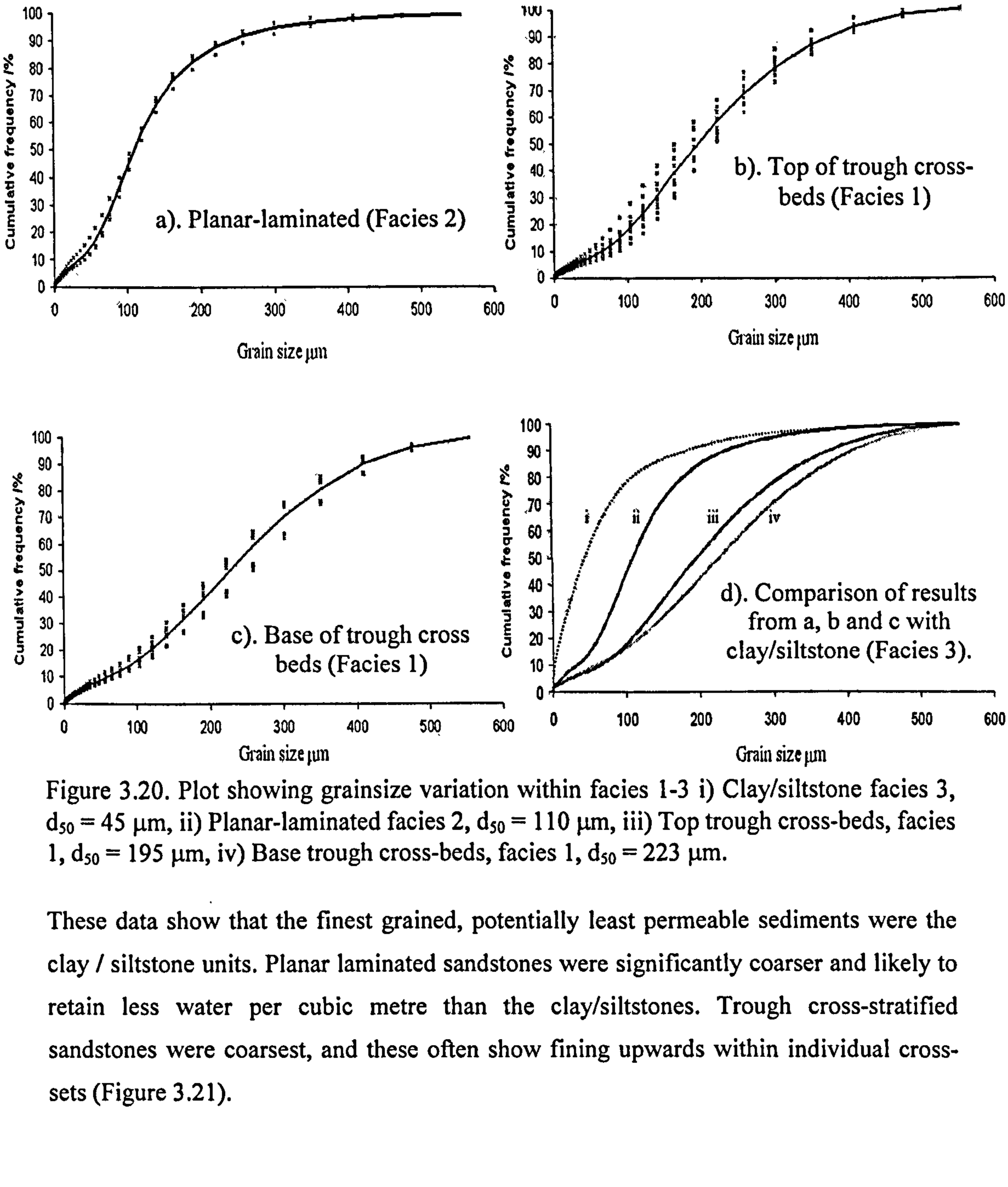

Figure 3.20. Plot showing grainsize variation within facies 1-3 i) Clay/siltstone facies 3, d_{50} = 45 µm, ii) Planar-laminated facies 2, d_{50} = 110 µm, iii) Top trough cross-beds, facies 1, d_{50} = 195 µm, iv) Base trough cross-beds, facies 1, d_{50} = 223 µm.

These data show that the finest grained, potentially least permeable sediments were the clay / siltstone units. Planar laminated sandstones were significantly coarser and likely to retain less water per cubic metre than the clay/siltstones. Trough cross-stratified sandstones were coarsest, and these often show fining upwards within individual cross-sets (Figure 3.21).

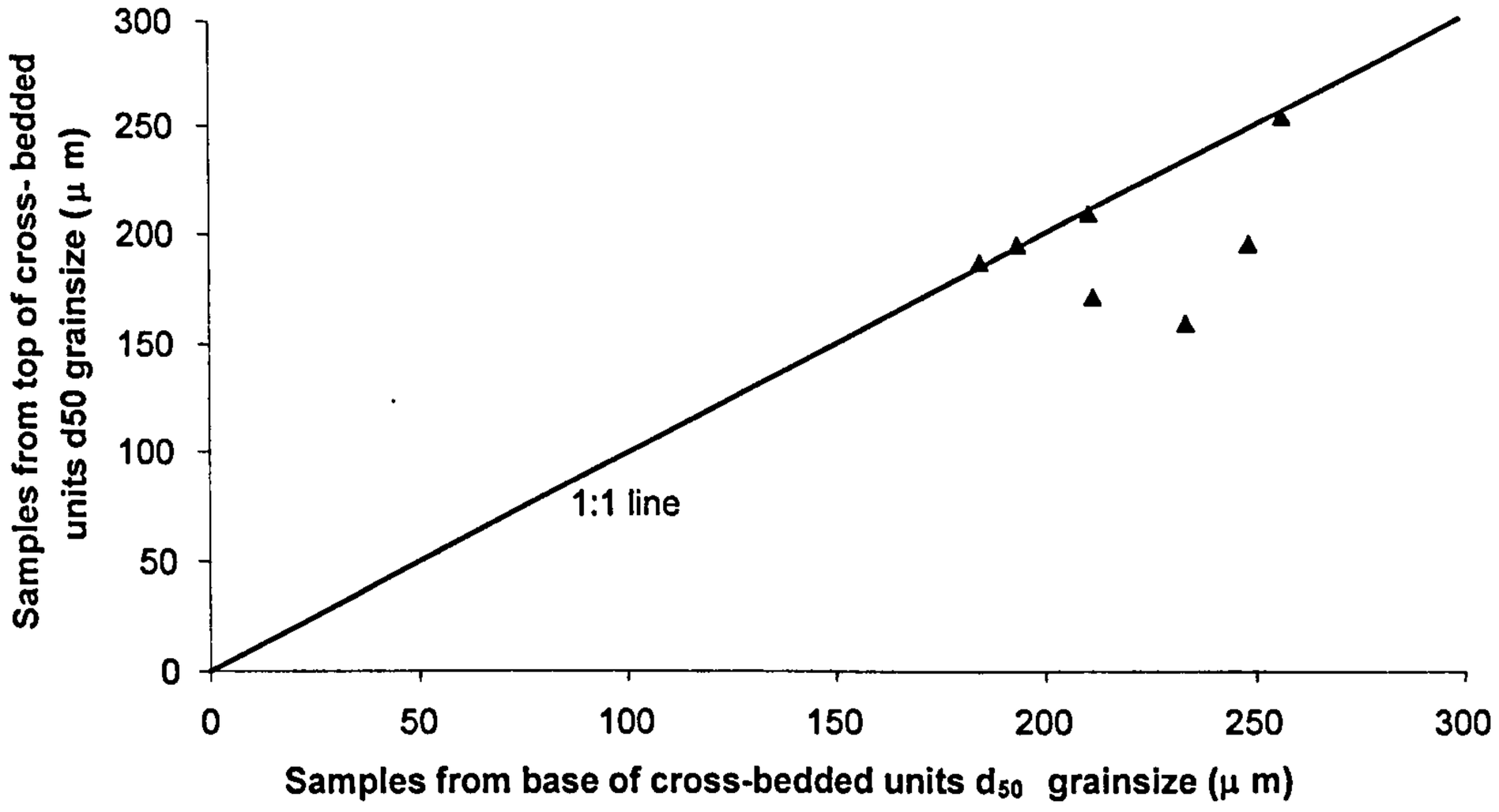

Figure 3.21. Plot of top / basal grainsize for individual trough stratified units.

The relative abundance and relationships between the various facies was investigated using sketch logs. Figure 3.22 is a sketch log representing the Southeast corner of Great Heck Quarry (palaeocurrent right→left). Several facies are present, trough cross-stratified and planar-laminated facies 1 and 2 (see Figure key) are abundant and there are several small facies 5 channel features (CH) and areas containing facies 1b mud intraclasts (MC) shown.

Figure 3.23 from Rufford Quarry (palaeocurrent left→right) shows trough cross-stratified units as more abundant and planar laminated units less abundant than Figure 3.22. Also visible are facies 3 'muddy sandstone' layers, mudstone lenses (ML) and a significant quantity of facies 4 ripple cross-beds (see figure key). This level of preservation of these facies is unusual within the study area, at other quarries visited they were extremely rare (see Table 3.2).

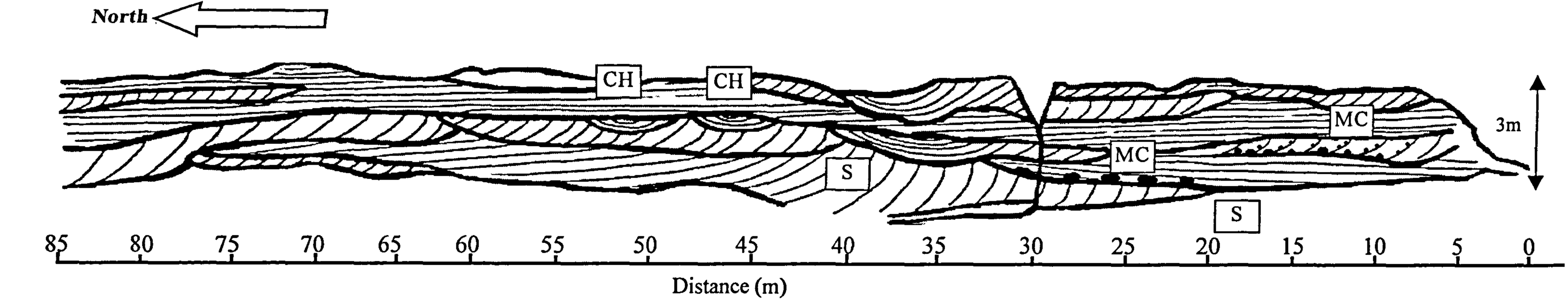

Figure 3.22. Sketch log from South East corner, Great Heck Quarry (SE 588213)

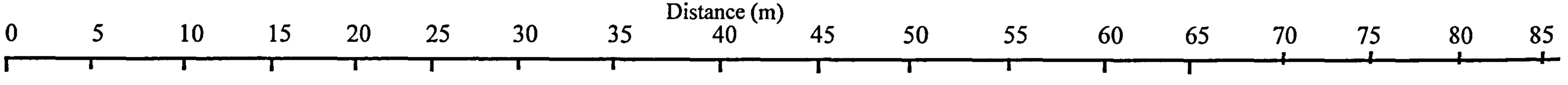

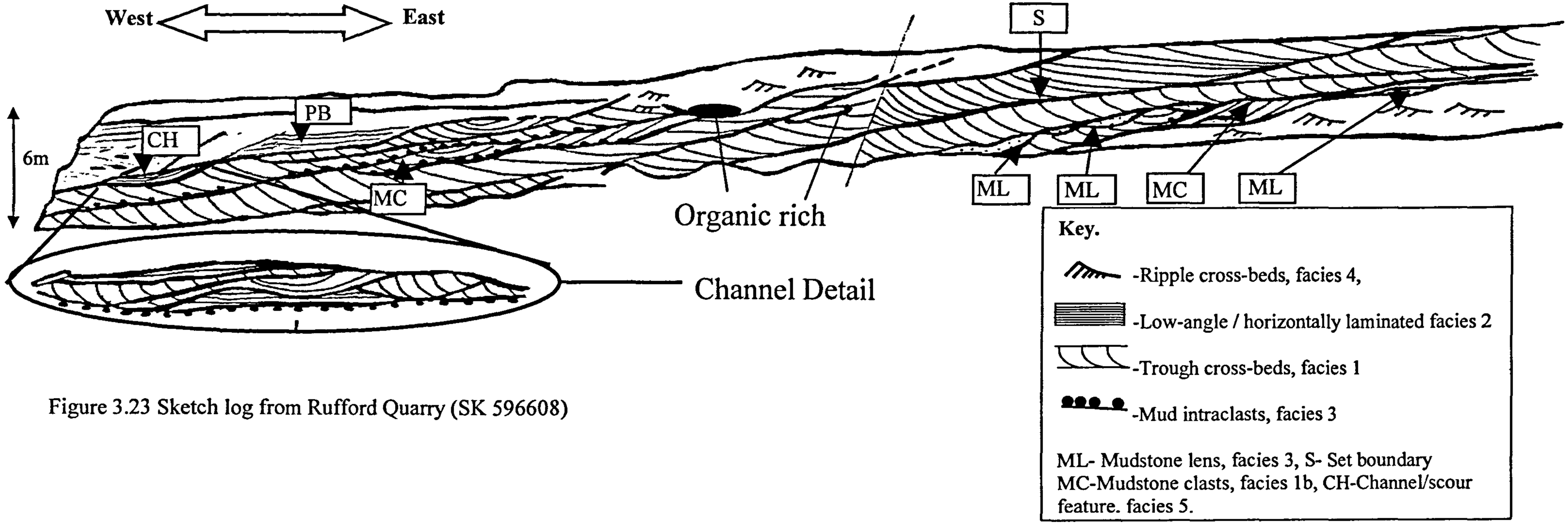

Figure 3.23 Sketch log from Rufford Quarry (SK 596608)

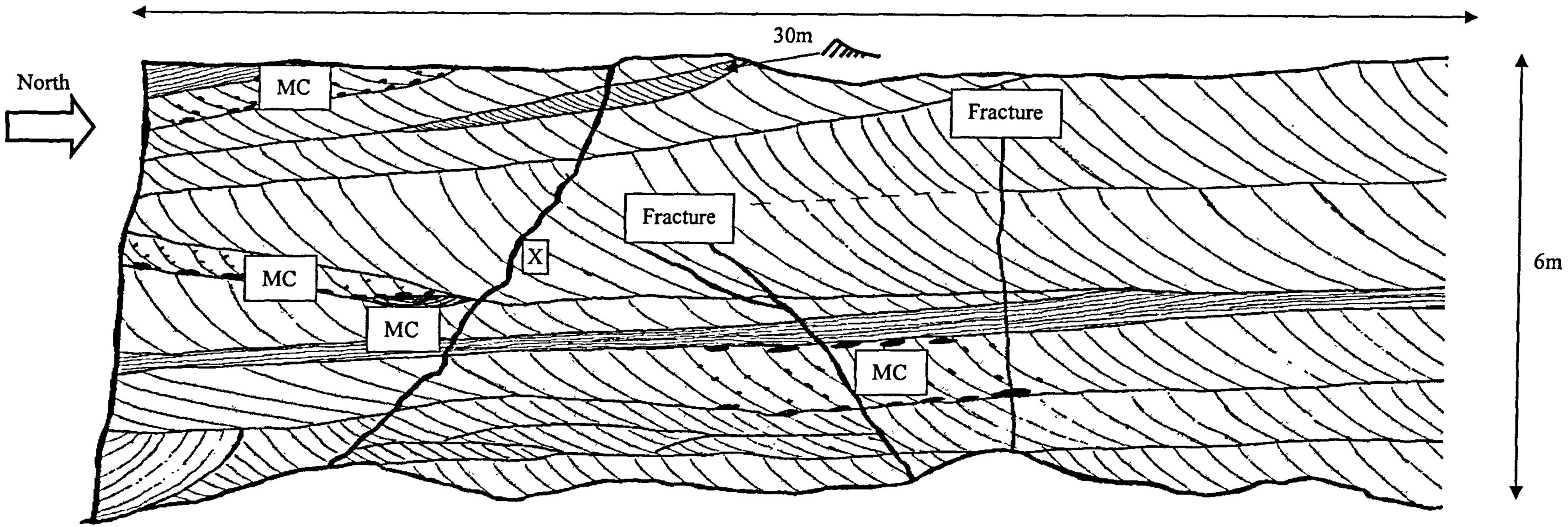

Key.

-Ripple cross-beds, facies 4,

-Low-angle / horizontally laminated facies 2

-Trough cross-beds, facies 1

-Mud intraclasts, facies 1b

ML- Mudstone lens, facies 3, S- Set boundary
MC-Mudstone clasts, facies 3.

Figure 3.24 Sketch log of temporary bench, Heck Quarry. (SE 588213)

The edge of a quarry bench at Great Heck Quarry (palaeocurrent left→right) is shown in Figure 3.24. The bench was situated on the eastern wall of the quarry. This sketch has a large proportion of facies 1, with a small channel infill (facies 5) and only limited quantities of facies 2, although the bed of facies 2 extends across the entire bench face. There are some limited areas of very fine cross bedding visible at the top of the exposed sequence, and these were interpreted as ripple-bedded units, although this is the only location at Heck Quarry where this facies were observed. Some small-scale, sand infilled fractures were also observed, although these were not continuous throughout the face. The feature marked (X) on figure 3.24 is not a fracture, but simply represents a line of limited face collapse as a result of quarrying activity.

The sketched faces from all localities were logged at 10m intervals and the percentage of each facies unit within each log was calculated and the Great Heck Quarry face logs (Figure 3.25) are given as an example. The total height of each unit from all the logs is presented as a percentage of the sum total height of all logs to give an estimate of the overall facies distribution for the Sherwood Sandstone in the Selby-Mansfield area (see Table 3.1).

Facies No.	Description	Relative abundance
1	<1.5m thick trough cross stratified sandstones with mud intraclasts (Facies 1b)	71%
2	Fine grained low angle / horizontally laminated sandstones.	25%
3	Claystone, sandy claystone or clayey sandstone lenses and mud drapes	1%
4	Ripple cross-stratified sandstones	1%
5	Channel features that may be infilled with any of units 1-4.	2%

Table 3.2. Revised facies scheme for the Sherwood Sandstone n the study area.

The values for Great Heck Quarry were calculated as; trough cross-stratified sandstones – 71 percent, channel units – 2 percent, horizontally laminated units – 27 percent and ripples – 1 percent. These values strongly suggest that Great Heck is largely representative of the Sherwood Sandstone within the Selby-Mansfield area as a whole.

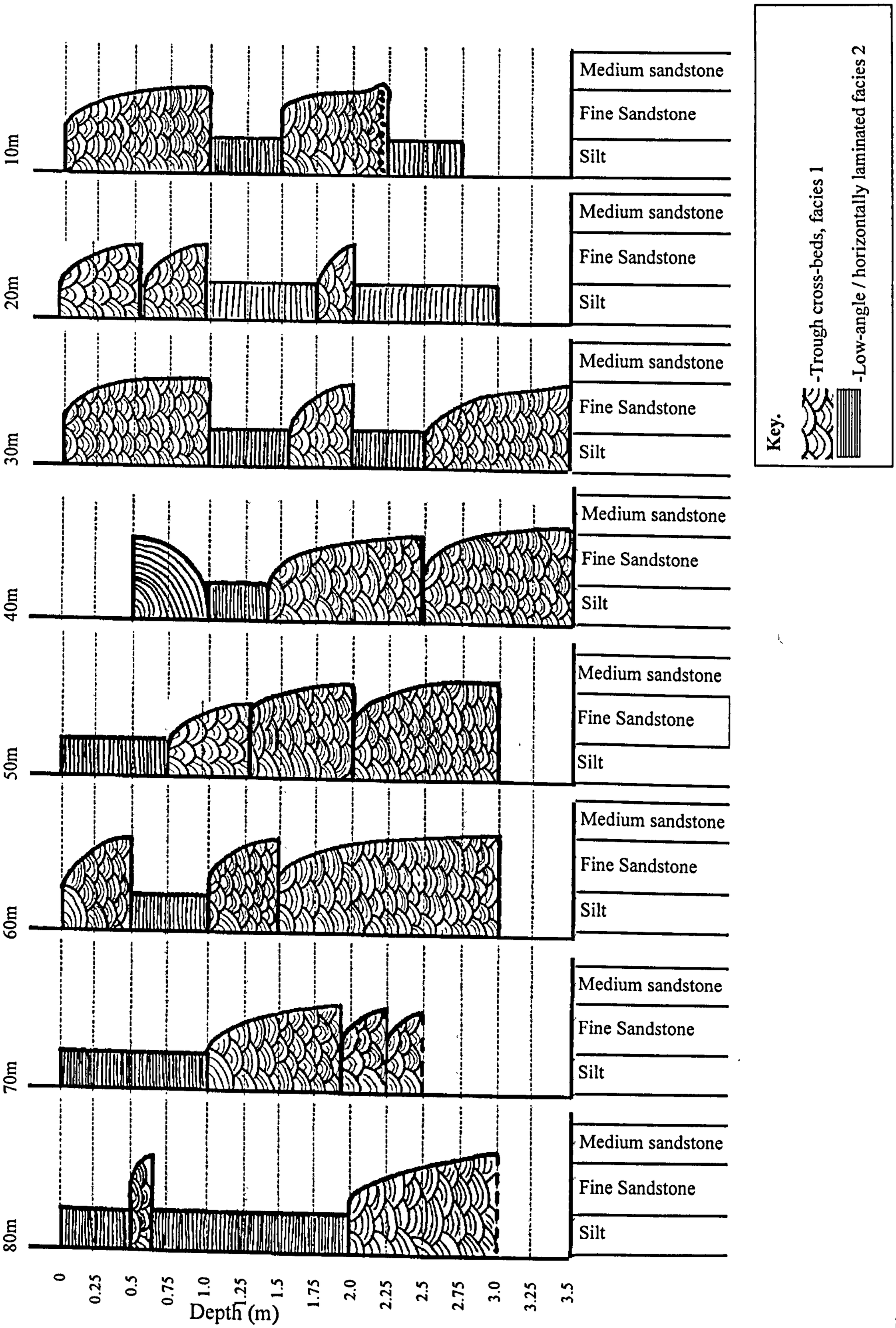

Figure 3.25. Face Logs with sylised fill at Great Heck Quarry (SE 588213). Distances show log position on scale

Core and gamma logging. Having described a facies scheme for the Sherwood Sandstone (above-this section) it was necessary to provide some verification that the facies scheme was directly applicable to the Great Heck test site. Hence a core and a gamma log were taken to provide a record of the subsurface lithology directly beneath the Great Heck test site. The results of the core logging are summarised in Figure 3.26. Note the sections where no recovery occurred. The log lists these units as fine-grained, as fine-grained layers are generally the most likely to be lost by this type of coring in the Sherwood Sandstone. The log shows interbedded facies 1 and 2 for the top 1.5 metres, followed by thick facies 2 to 5 metres, with a narrow layer of facies 3 at just under 4.5 metres. Between 5 and 7 metres depth, again interbedded facies 1 and 2 may be seen, although there is not full core recovery. The 7-9 metre band is missing, and below 8 metres facies 1 is dominant. Despite being incomplete, this core is extremely useful, and is referred to several times in this thesis, as it does provide unambiguous baseline data for ground-truthing the geophysical methods described in Chapters 4 and 5.

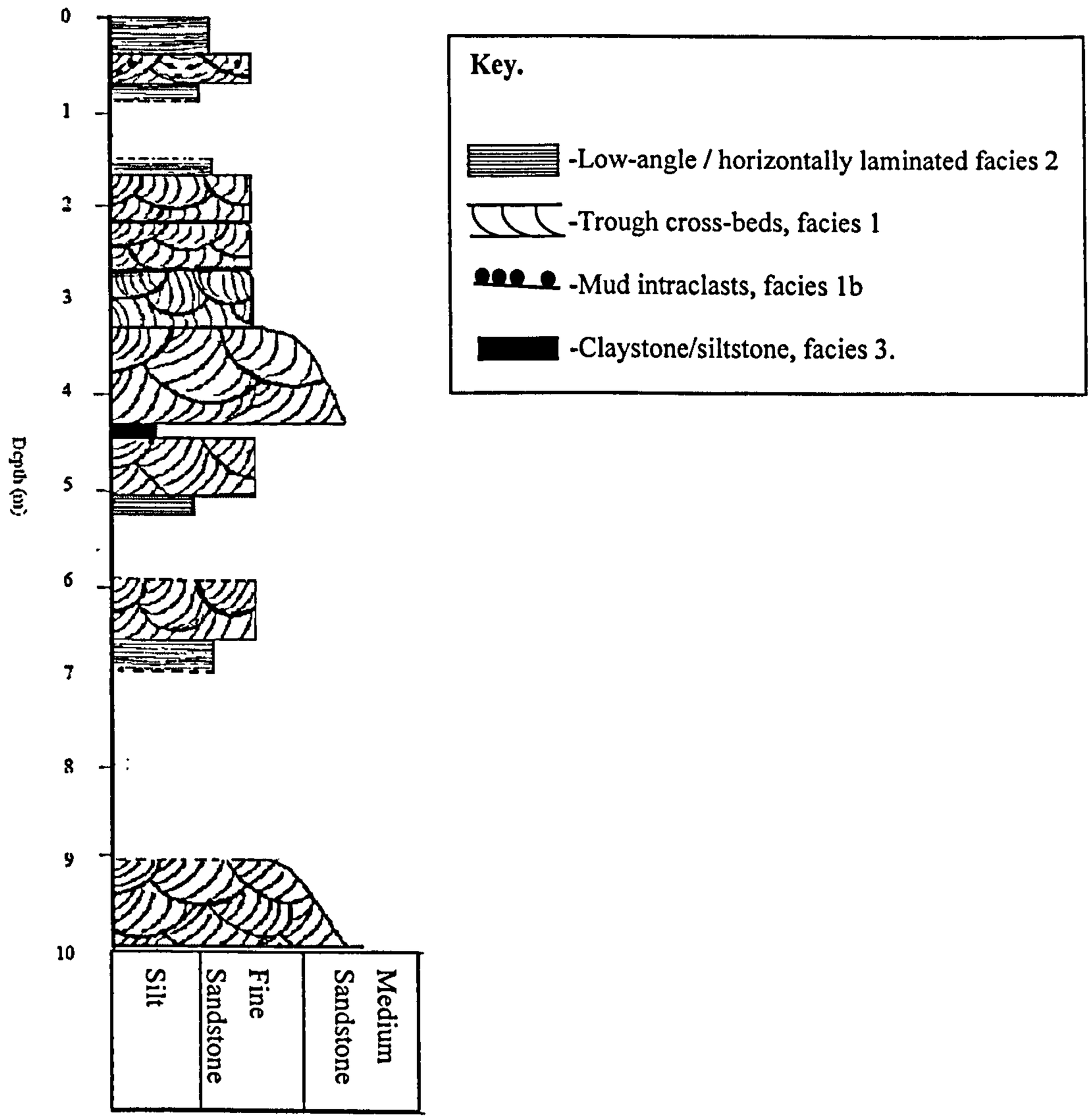

Figure 3.26. Core log with stylised fill from Great Heck Quarry (SE 588213).

Gamma logging.

Results of the gamma logging using the Mount Sopris gamma logger at the Great Heck test site are shown below. Results were corrected into true depth below ground by the subtraction of the length of casing showing above ground, and the addition of the distance down the gamma probe to the scintillation counter. The zero counts per second baseline for each run was moved right by 10 counts per second (cps) between successive runs to avoid superimposition of traces. This movement of baseline was accounted for when the data were subsequently digitised.

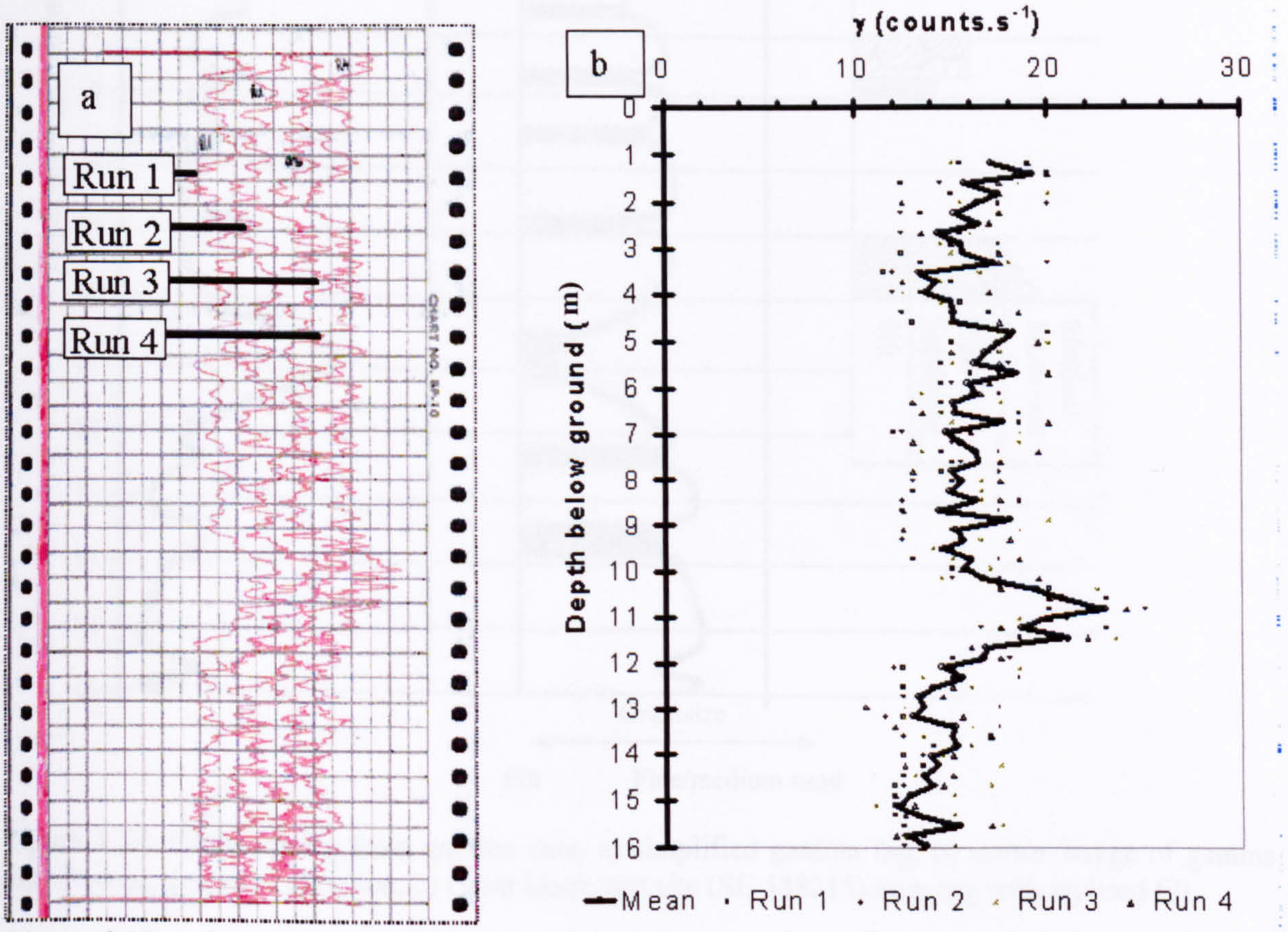

Figure 3.27. γ logging results. a) raw results, vertical depth of all runs = 51.3 feet, each major division in x – direction = 5 counts per second. b) Plot of digitised data showing data range and mean at true depth below ground.

The results from the gamma log were digitised by hand picking to an accuracy of 0.5cps over 72 regularly spaced depth intervals. The resulting plot showing degree of data scatter and mean gamma values is shown in Figure 3.27b. The mean gamma plot shows some variation in γ returns with depth, between 9 and 11m, there is a major γ peak, evidence of clay-rich lithology, and at 3-4 and 12-15m depth the γ values are low, indicating 'clean' sandstone. There is a continuum of γ values between these extremes, and a simplified tracing of the mean gamma plot is shown below in Figure 3.28a. If γ peaks are assumed to be fine-grained units, and the low γ values coarse sandstones, a synthetic grainsize log may be constructed from these data. Such a log is shown in Figure 3.28b, alongside the core log from the Great Heck Test Site (Figure 3.28c).

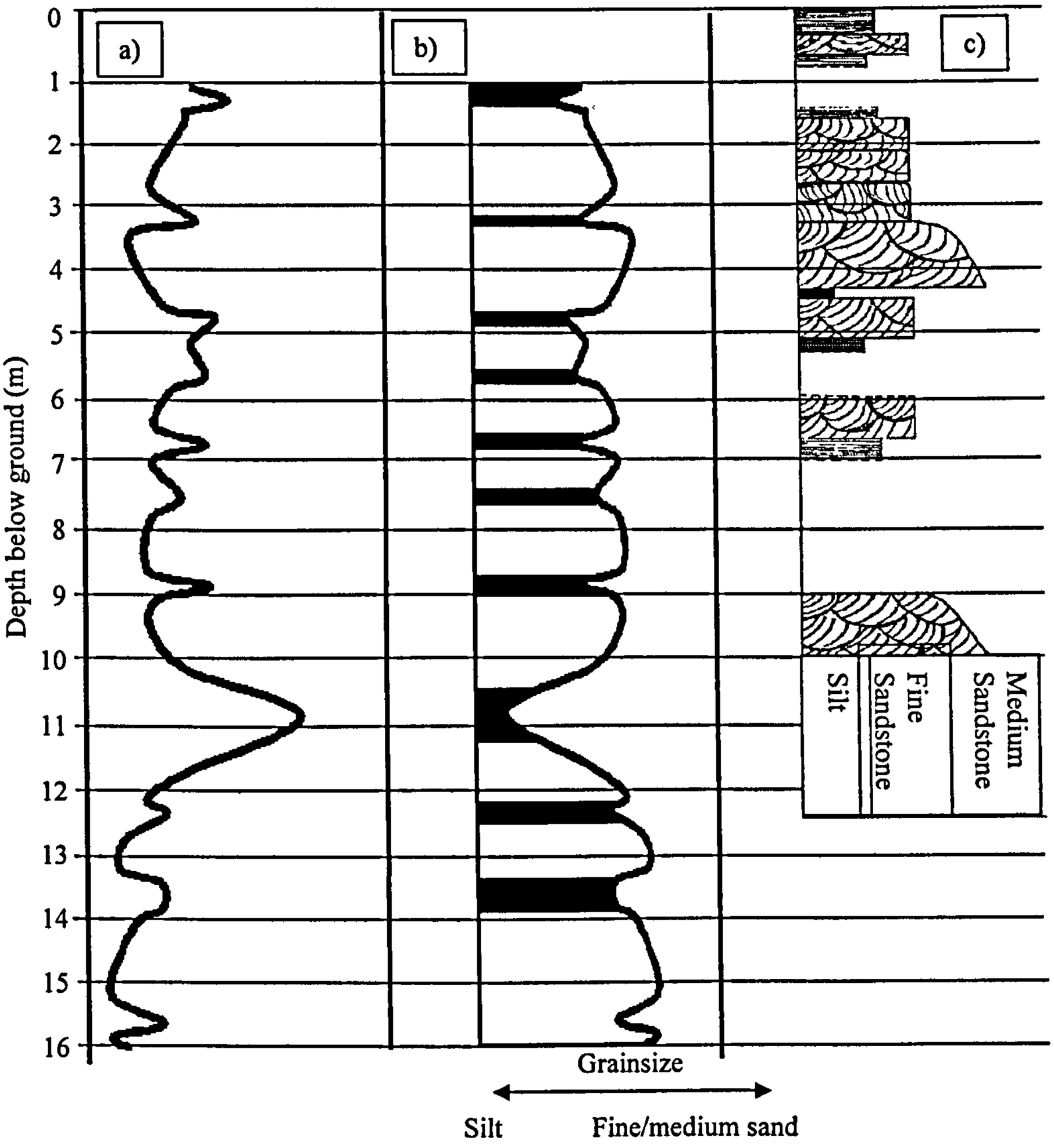

Figure 3.28. Grainsize log from gamma data. a) simplified gamma log, b) mirror image of gamma log showing grainsize variation, c) Great Heck test site (SE 588213) core log with stylised fill.

The grainsize log derived from gamma data shows a lithology that is predominantly sand dominated, with a significant clay/fine-grained horizon at 10-11m. Comparison between the Great Heck core log and gamma-grainsize log shows some similarities. The core log is not deep enough to reflect the fine-grained layer at 10-11m. A pattern of coarse sandstone units being broken up by finer grained layers at 3, 4.5, 6.5 and 8.5m may be seen in the gamma log, and the core log shows variation at approximately the same depths. However, the fact that the core is incomplete, and was extracted 14m from the TRIME hole precludes too close a comparison.

Fracture mapping.

An exposed quarry bench at Hatfield Quarry contained significant numbers of sub-vertical fractures. Most of the fractures were infilled with sandy clay or clayey sand (Figure 3.29) and thus a sub-vertical network of fractures such as this could potentially compartmentalise the vadose zone into discrete cells and effectively prevent lateral migration of meteoric water.

Figure 3.29. Typical clay lined sub-vertical fractures from Hatfield (SE 653075).; same scale for both images

Wealthall *et al.* (2001) studied a similar network of fractures in the Sherwood Sandstone in Cheshire, with the main difference being that the Cheshire fractures were infilled with sand, which is much more permeable than the clays found at Hatfield. Wealthall *et al.* (2001) concluded that even the sand filled fractures were not considered a major pollutant pathway unless they crossed low-permeability layers at high angles. The fact that the Hatfield fractures were clay lined should ensure that they are not preferential flow paths even where they intersect low permeability units. In fact, they may act to reduce preferential flow by reducing lateral migration in the vadose zone. The main implication of fracture networks such as this is probably with regard to the phreatic zone, where they are likely to act as no-flow boundaries.

Mapping at the Hatfield Quarry aimed to quantify the spatial distribution of fractures (Figure 3.30). This type of high-frequency fracturing was only seen at Hatfield Quarry, which is located at the intersection of two major faults. The fracture networks do occur in the eastern side of the quarry bench, however this section of the bench generally has loose material scattered on the quarry floor so fractures were hard to see. Where fractures could be seen but not positively be identified because of loose material on quarry floor, they are denoted by dotted lines. The sub vertical network of fractures

surveyed fall into two groups, north-south and southeast-northwest, and are laterally extensive over 50 to 100m or more.

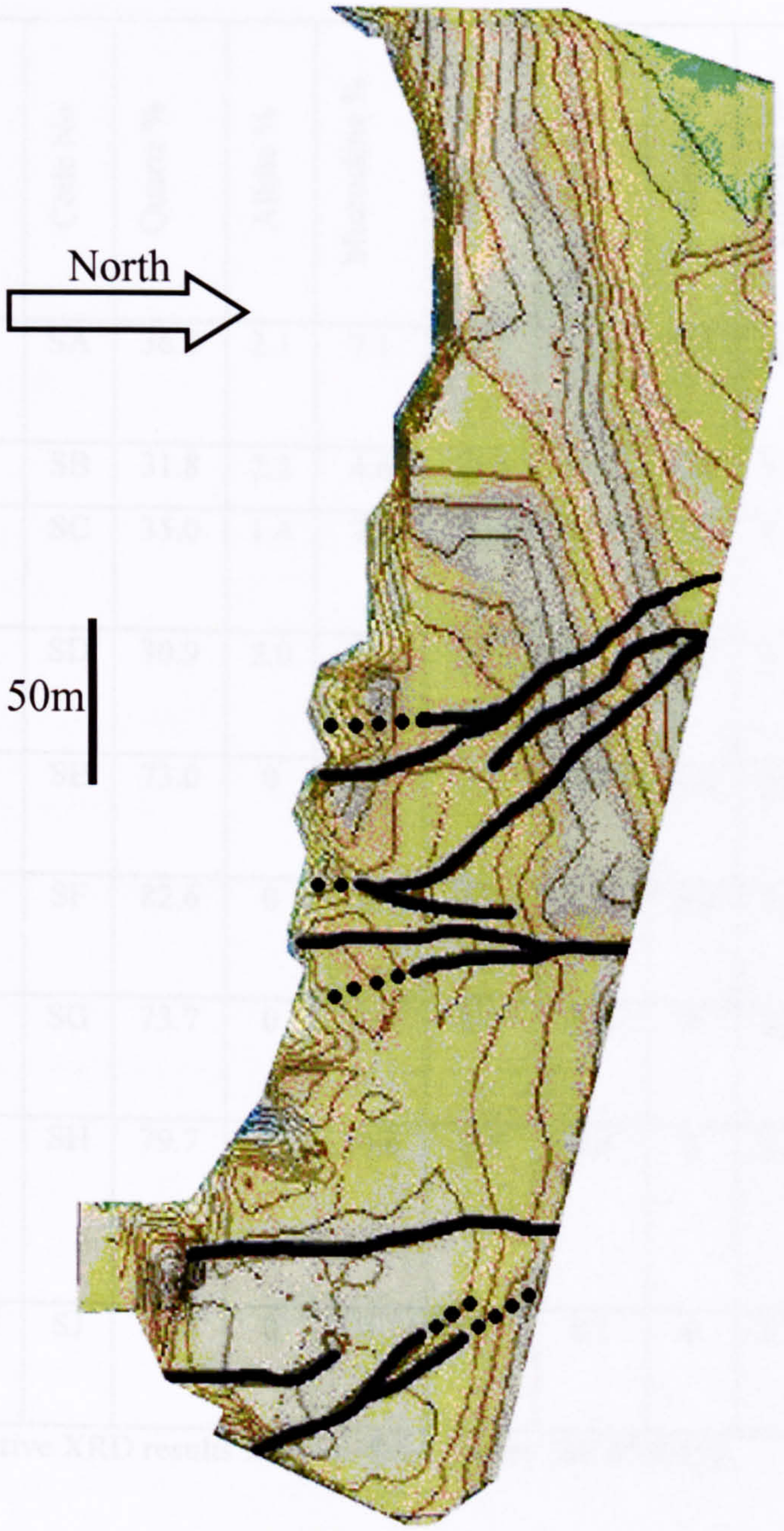

Figure 3.30. Fractures observed on exposed quarry bench at Hatfield Quarry (SE 653075).. Contours at 0.25m intervals- See appendix 4.

Some fractures were also visible at other sites, Eggborough and Heck Quarries both have fractures noted on some of the faces, but these fractures are (a) not clay lined and (b) are rare. Hence sub-vertical fracture networks were not considered to be typical of the Sherwood Sandstone in the study area.

Quantitative X-ray diffraction (XRD) techniques were applied to samples taken from various fractures at Hatfield Quarry to attempt to pinpoint the origins of some of the clays.

Sample location	Code No	Quartz %	Albite %	Microcline %	Mica %	Illite -Smectite %	Kaolinite %	Chlorite %	Haematite %	Total %
Brown claystone layer (unit 3)	SA	36.5	2.1	7.1	13.7	31.5	3.0	3.0	3.2	100.1
Mud intraclast	SB	31.8	2.2	4.6	21.9	31.2	1.5	2.9	2.8	98.9
Brown clay fracture infill	SC	35.0	1.4	7.8	15.3	33.7	0	5.1	2.3	100.6
Green (weathered) mud intraclast	SD	30.9	2.0	7.7	20.5	32.0	3.1	5.1	0.5	101.8
White (altered?) clay fracture infill	SE	73.0	0	12.1	5.1	10.0	1.0	2.0	0.3	103.5
Light brown sandy clay fracture infill	SF	82.6	0	10.4	3.4	3.9	0.7	1.2	0.2	102.4
Brown sandy clay fracture infill	SG	73.7	0	9.9	5.2	9.6	0	2.8	0.5	101.7
Broken sandstone from fracture shear zone	SH	79.7	0	10.6	2.2	4.4	0	2.3	0.3	99.2
Brown clayey sand from fracture zone	SJ	81.8	0	10.1	0	8.1	0	1.9	0.3	102.2

Table 3.3. Quantitative XRD results from Hatfield Quarry (SE 653075)..

The main focus of interest was the origins of the clay minerals, particularly illite – smectite and chlorite. In order to normalise the results, to remove varying quartz and other mineral contents, the percentage of illite – smectite and percentage of chlorite were divided by the sum of the percentages of the other minerals (quartz, albite, microcline, mica, kaolinite and haematite) and then plotted against each other (Figure 3.31). This showed that there were three main populations of clay minerals present.

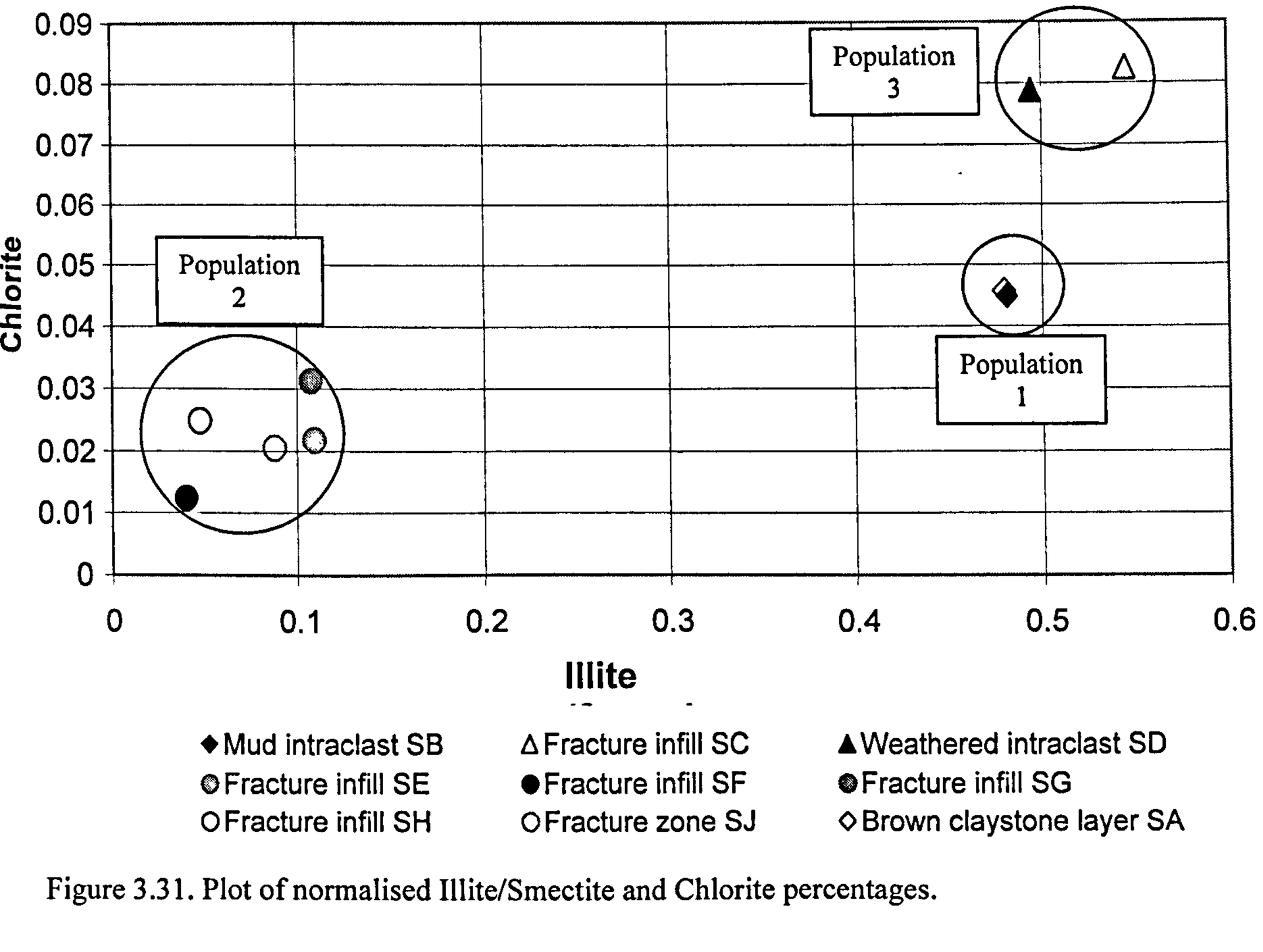

Figure 3.31. Plot of normalised Illite/Smectite and Chlorite percentages.

Population 1, the claystone layer (SA) and mud intraclast (SB) share an almost identical ratio of clay minerals (10:1 illite-smectite : chlorite), strongly suggesting that the clay lenses and drapes are the source of material for the abundant mud intraclasts found in the Sherwood Sandstone. The second population has an illite-smectite : chlorite ratio of around 3:1, suggesting a different source to the first population. The fact that the fracture clays have high quartz contents, and the detrital mud intraclast / drape clays do not, is strong evidence for the fracture clays having a diagenetic origin. A possible mode of formation is that diagenetic clays were pervasively deposited in dilated, sand-filled fractures. Burley (1984), states that diagenetic clays in the Sherwood Sandstone are preferentially deposited along planes of weakness such as fractures, and form a mixture of relic grain (in this case quartz) and clay infills. This interpretation is consistent with the results from Hatfield Quarry. The high levels of illite-smectite, and the fact that these clays have not been altered to highly crystalline, K-rich illites, is further evidence for a lack of mesogenetic diagenesis of the Sherwood Sandstone in this area (see Chapter 2.3). It is likely that the third population (SC and SD) is derived from population 1 or 2 by weathering or leaching, especially as SD is known to be a highly weathered clay clast, with a distinctive green colour indicative of increased chlorite concentration.

3.4 Interpretation

Sedimentary facies

Study of outcrops and cut faces of the Sherwood Sandstone at the three quarries indicates the presence of five main sedimentary facies. The geometrical and grainsize characteristics of these facies and their genesis are discussed in this section, whereas implications for the generation of radar reflections and permeability distribution are discussed in subsequent sections. Similar sedimentary facies have been reported elsewhere. For example, Buist and Thompson (1982), describe similar sand facies in their scheme for the Sherwood Sandstone in North Staffordshire. Marshall (2000), describes how the deposition of facies 1 and 2 is dictated by river flow stage, and describes the transition from trough cross-bedding to upper stage plane beds for the braidplain of the Devonian Skrinkle Sandstones in Dyfed. The most direct comparison with the facies scheme described herein is the work of Bryant and Burley (1989) who produced a facies scheme based on observations at four quarries in the Selby/Doncaster area; of these four locations, two quarries (at Great Heck and Pollington) were also investigated in this study. However, Bryant and Burley (1989) did not report features such as the abandoned channel unit at Pollington Quarry, and it is probable that worked face locations and conditions in the quarries will have changed significantly since the late 1980's. However, the difference between the Bryant and Burley (op. cit.) facies scheme and the one reported here is that they report a lower proportion of trough cross-bedded units to large-scale planar-laminated units.

A summary graphic log, constructed from the various outcrop observations is presented below, which draws upon all the sedimentary data provided from the various logging methods. This log will be used in subsequent chapters as a basis upon which a hydrological model will be developed.

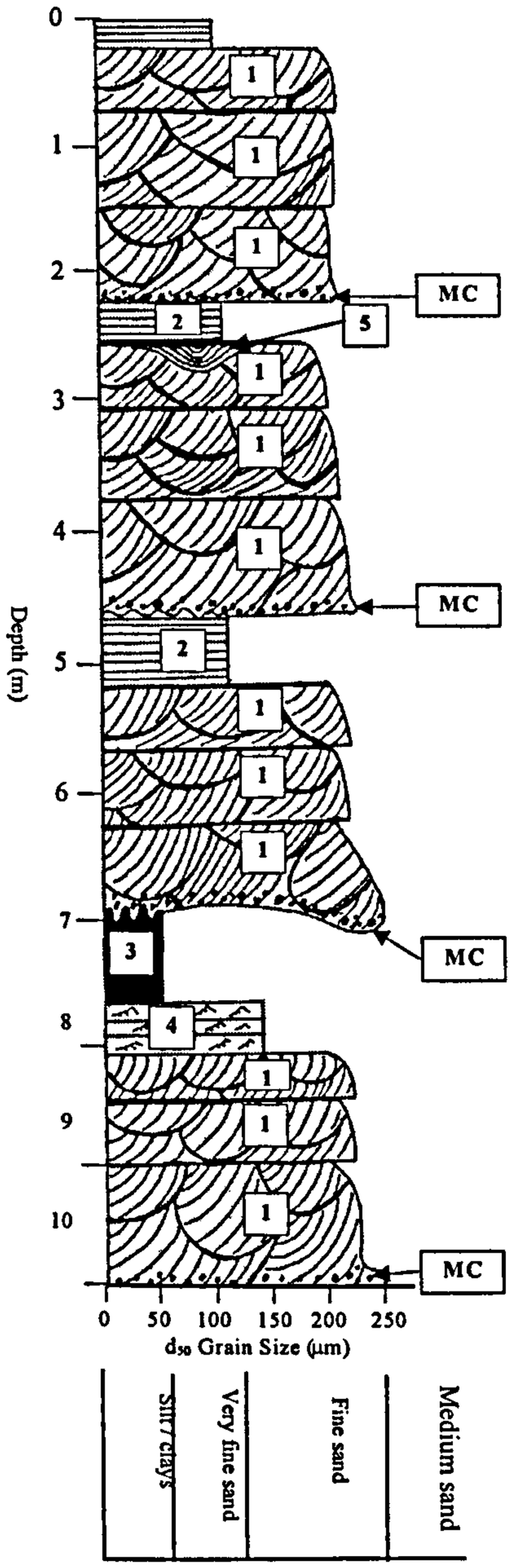

KEY.

Numbers in boxes indicate sedimentary facies.

1) Stacked trough cross-bedding (facies 1)
2) Fine-grained planar unit (facies 2)
3) Clay layers (facies 3)
4) Ripple bedding (facies 4
5) Infilled minor channel (facies 5)

MC denotes abundant mud intraclasts.

Fining upward sequences shown between 0.5-2.25, 2.5-4.6, 5.25-7 and 7-10.5m represent channel fills.

Figure 3.32. Summary graphic log with stylised fill for the Great Heck Sherwood Sandstone showing d_{50} grain sizes and thickness of typical units.

Mud intraclasts were particularly common in basal lag deposits. These are often significantly coarser than is usual for Unit 1, and may have implications for fluid migration. This is discussed further in Chapters 5, 6 and 7.

A summary graphic log (Figure 3.32) shows the typical relationships between the sedimentary facies based on outcrop observations and consists of distinct cyclic sequences of trough cross-bedded sandstones, decreasing in thickness in an upward direction, with erosive bases. These cross-stratified sandstones may grade up into laminated sands (facies 2), but more commonly are topped by erosive surfaces overlain

by further cyclic sequences of trough cross-bedded sediments. The top of each cycle may also be terminated by facies 4 (ripples) or facies 3 (claystones), which represent slack water and bar-top deposits. These sequences are interpreted as channel fills that are dominated by dunes, the decreasing set size within each sequence probably representing shallowing flow towards the bar-tops. These major channels and associated bar and dune deposits are larger than the scales of many outcrops (some individual sets and cosets are over 100m in length along palaeocurrent) and thus the complete channels and channel edges are not usually seen.

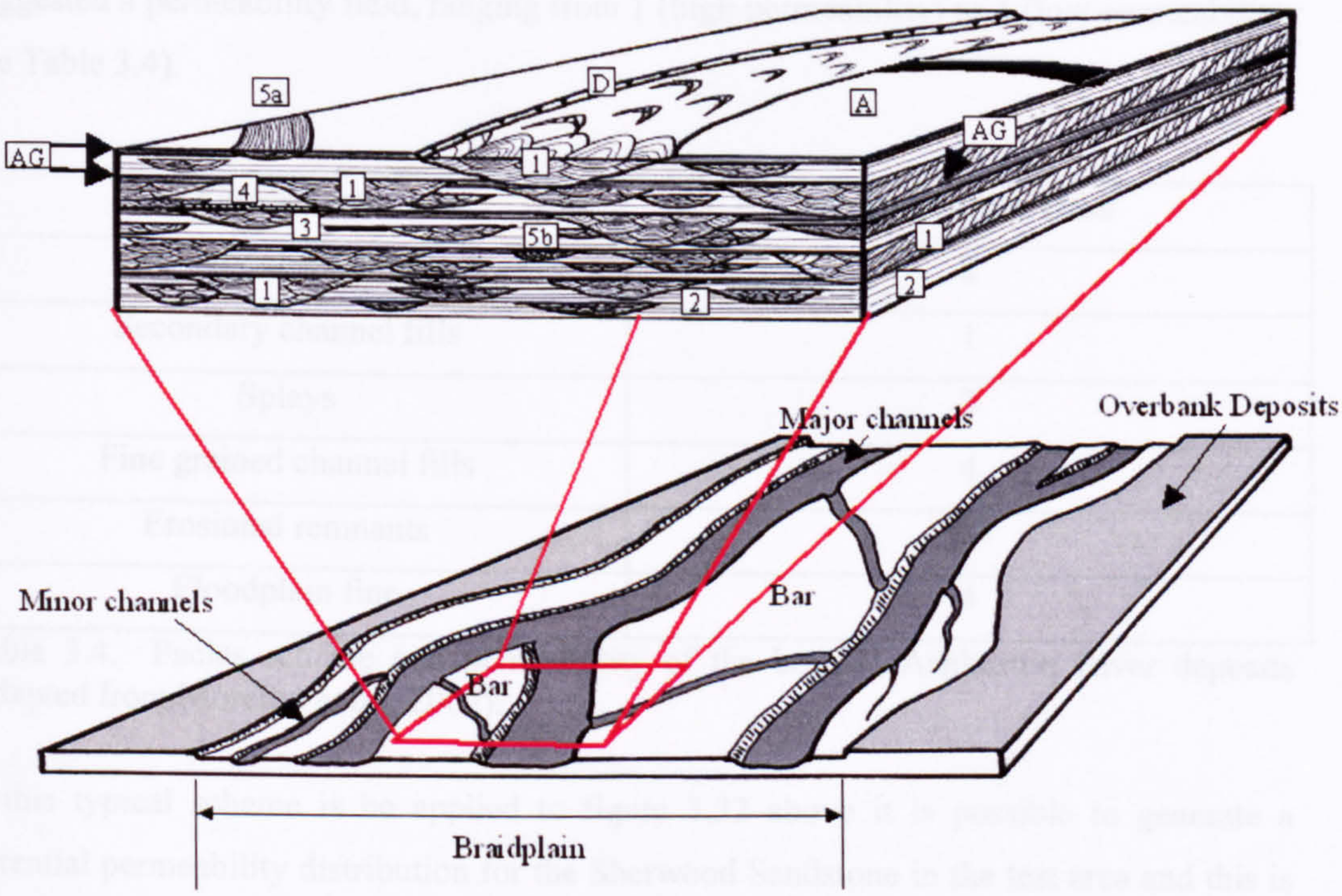

Figure 3.33. Distribution of facies. D shows dune migration in active channel, A shows aeolian environment during low stage flow.

These facies may be combined to form a block model of the depositional environment (Figure 3.33) where, (1) denotes trough cross bedded channel fills, with cross-set thickness often decreasing as channels become infilled with sediment and become shallower. These trough cross-bedded units are occasionally topped with current ripples (4). (2) denotes upper stage planar beds which are often topped with argillaceous layer (AG). (3) represents muds and clays which are rare as in-situ deposits, but very common as rip up clasts, and (4) denotes current ripples, again rarely observed at outcrop. facies (5) shows bar-top channel fills, (5a) is abandoned and filled with fine muds (Unit 3), (5b) is filled with sands. Some limited aeolian deposition also may occur (A), with the surface being scoured clear on subsequent rising stage.

The paucity of ripples and overbank sediments suggests a low preservation potential for higher level facies units, and suggests that active channel deposits may be preferentially preserved. This suggests either low aggradation rates or high levels of channel migration and avulsion during deposition (Bristow and Best, 1993).

Moreton *et al.* (2002) conducted a series of flume experiments modelled on the braided Ashburton River in New Zealand which resulted in a sixfold facies scheme, dominated by channel fill deposits. They also linked their facies scheme with permeability and suggested a permeability field, ranging from 1 (high permeability) to 4 (low permeability, see Table 3.4).

Facies Type	Permeability class
Primary channel fills	2
Secondary channel fills	1
Splays	3
Fine grained channel fills	4
Erosional remnants	3
Floodplain fine	4

Table 3.4. Facies scheme and permeability of the braided Ashburton River deposits (adapted from Moreton *et al.*, 2002).

If this typical scheme is be applied to figure 3.32 above it is possible to generate a potential permeability distribution for the Sherwood Sandstone in the test area and this is summarised below.

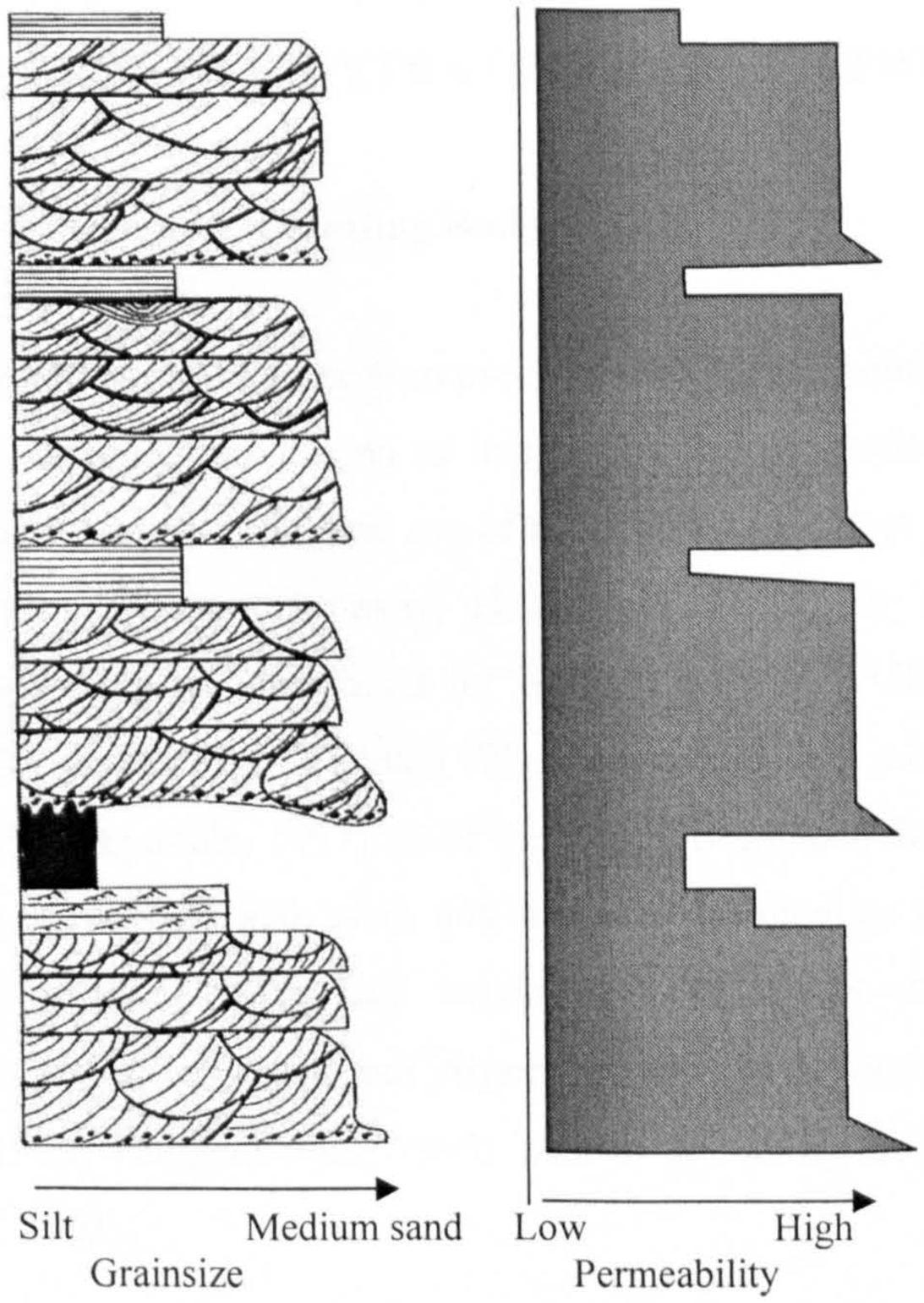

Figure 3.34. Permeability distribution based on Figure 3.32 and Moreton *et al.* (2002).

It can be seen from Figure 3.34, which is an initial approximation of the permeability of the Sherwood Sandstone in the test area, that the rock appears to be divided into high and low permeability areas in a fairly regular manner, with high permeability horizons being separated by narrow zones of lower permeability. This initial permeability profile will be examined and refined in subsequent chapters, where geophysical methods are employed to provide more detail on the ground structure and hydraulic behaviour within the Great Heck test site.

CHAPTER 4
GROUND PENETRATING RADAR (GPR).

4.1 Introduction to Ground Penetrating Radar

Ground Penetrating Radar (GPR) has been used for many years, being an electromagnetic (EM) geophysical technique employed to image physical properties of the subsurface. The first publication demonstrating the use of radar pulses to detect buried objects is the patent awarded to a German company, Hülsenbeck & Co. in 1926. Subsequently, although GPR systems were developed for military purposes, GPR was not publicly available until the end of the Vietnam War, when the first civilian systems were developed by GSSI (Reynolds, 1997). Over the past two decades the GPR technique has been successfully developed and used, and has now become an accepted method for investigating the shallow subsurface structure of relatively non-conductive soils, sediments and rock (e.g.. Aspiron and Aigner, 1999; van Overmeeren, 1998; Bridge, 1993; Bristow, 1993; Huggenberger, 1993; Best *et al.*, 2003; Bridge and Lunt, 2003; Woodward *et al.*, 2003).

GPR provides a rapid and reliable method of imaging variations in subsurface dielectric properties, and in the unsaturated zone normally provides images of sedimentary structures to decimetric resolution whilst penetrating to several metres in depth (Jol, 1995). Under ideal conditions, GPR surveys provide rapid and high-resolution data over a large area, and can be used to detect stratigraphy, archaeological features or any sudden change in subsurface dielectric properties. Major advantages of GPR over other EM based methods such as resistivity surveying, are that GPR is relatively insensitive to variations in pore water chemistry, and produces high resolution images that allow less ambiguity in interpretation of results (Binley *et al.*, 2001b).

Radar surveys may consist of single lines, showing underground features (by imaging of subsurface dielectric variations) in 2D or they may be combined to form closely spaced grids, which may be interpolated to give 3D images of the subsurface (Anderson *et al.*, 1999; Aspiron and Aigner, 1999; Gloaguen *et al.*, 2001; Corbeanu *et al.*, 2001, 2002, Szerbiak *et al.*, 2001; Hammon *et al.*, 2002; Jol *et al.*, 2002). The radar system records time taken for EM waves to be reflected back to the surface from underground features. These returning waves may be plotted as amplitude traces for adjacent locations using a time axis, and the time axis can be converted to depth if an electromagnetic wave velocity for the medium under investigation is known.

Combining many traces on one plot thus enables a profile or radargram to be constructed, and this is usually done in real time so that the radar profile can be observed as it is being generated.

It is tempting to consider GPR surveys as analogous to seismic reflection surveys as the returned images are similar, both methods rely on velocity contrasts in the subsurface, and some of the data processing techniques may be shared between the two methods (Cardimona *et al.*, 1998). However, there are important differences. Radar waves, being EM waves, have a vector nature and this often results in incorrect assumptions when seismic processing techniques are applied. EM waves also behave differently to pressure waves, and some of the processing steps designed for analysis of seismic data (such as f-k filters and deconvolution (Conyers and Goodman, 1997)) may not perform correctly when applied to GPR data, even though most radar processing packages allow these steps to be used. However, some seismic processing methods yield good results, with radar waves acting in a manner similar to seismic shear (S) waves (Reynolds, 1997).

At subsurface boundaries, the reactions of the EM and acoustic waves are dependent upon different rock properties, these being acoustic impedance for seismic waves and dielectric impedance for the radar, both of which control the velocity of the propagating wave through the rock. A further complication in the relationship between GPR and seismic reflection surveying is the trend of the wave velocity with depth. As a general rule seismic velocities increase with depth as the degree of compaction and density of the material increase. However, electromagnetic wave propagation velocity increases as the dielectric constant of the surrounding material decreases. This has the effect of effectively decreasing the wave velocity as saturation increases, leading to a decrease in wave velocity toward the water table.

However, the major operational difference between seismic reflection and GPR is the balance between penetration and resolution, which is dependent on the wavelength of the propagating wave. Seismic methods (long wavelengths) offer great penetration into the rock, but at low resolution, and sedimentary structures at the individual bedform level are far too subtle to be resolved by this method. GPR however, only allows penetration of metres to tens of metres, but with much greater resolution than seismic reflection, that allows individual bedforms to be imaged. This inverse relationship between penetration and resolution persists at GPR frequencies with higher frequencies producing higher resolution images with lower depths.

According to Van Dam & Schlager (2000) and Reynolds (1997) the theoretical resolution is given by:

Resolution = $\lambda/4$ Equation 4.1

i.e. where λ is the wavelength, for a velocity of 0.1m ns^{-1} and frequency of 200MHz, the resolution is 0.125m, whereas at 100MHz it is 0.25m and at 50MHz it is 0.5m. In practice however, reflections from features smaller than $\lambda/4$ in thickness are often visible in radargrams. Nevertheless, $\lambda/4$ provides an indication of the minimum expected resolution.

From equation 4.1, it follows that if the velocity of an electromagnetic wave in a particular environment is known, then the resolution may be calculated for each of the 3 radar frequencies used here, 50, 100 and 200MHz. Jol (1995) conducted a field investigation into the penetration and resolution of GPR at differing frequencies using an identical system to the one used in the present study by analysing the return spectra for each of the radar frequencies, and using equation 4.1 to calculate resolution. The lithology studied by Jol (1995) was clean, but saturated, sand with mean EM wave velocity of 0.07m ns^{-1}.The results are shown in Table 4.1 below.

Frequency (MHz)	Max. Penetration (m)	Field Resolution (m)
25	28	0.76
50	22	0.37
100	19	0.21
200	14	0.15

Table 4.1. A comparison between GPR penetration and resolution at differing frequencies in saturated sands, after Jol (1995).

The plan area of the reflector is also important, and GPR is unable to resolve features that are smaller than the first Freznel zone (see Figure 4.1, Reynolds, 1997), the radius (r) of which is given by equation 4.2, where z is the depth to the reflected interface.

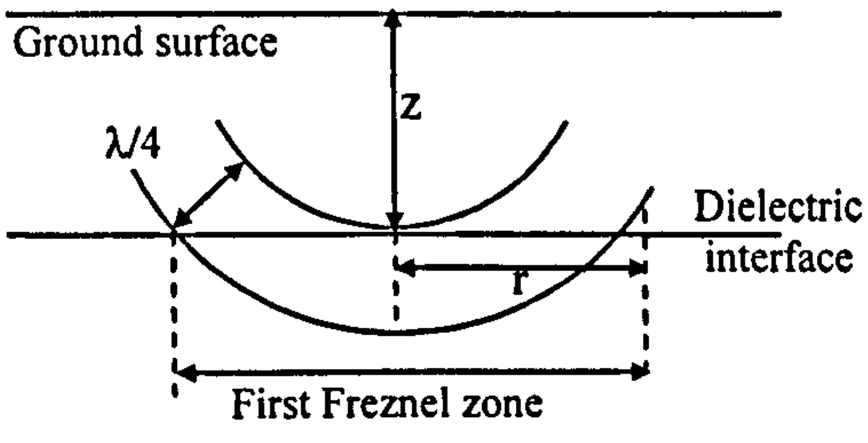

$$r = \left(\frac{\lambda^2}{16} + \frac{\lambda z}{2} \right)^{\frac{1}{2}}$$ Equation 4.2.

Figure 4.1. Definition of first Freznel zone (Reynolds, 1997).

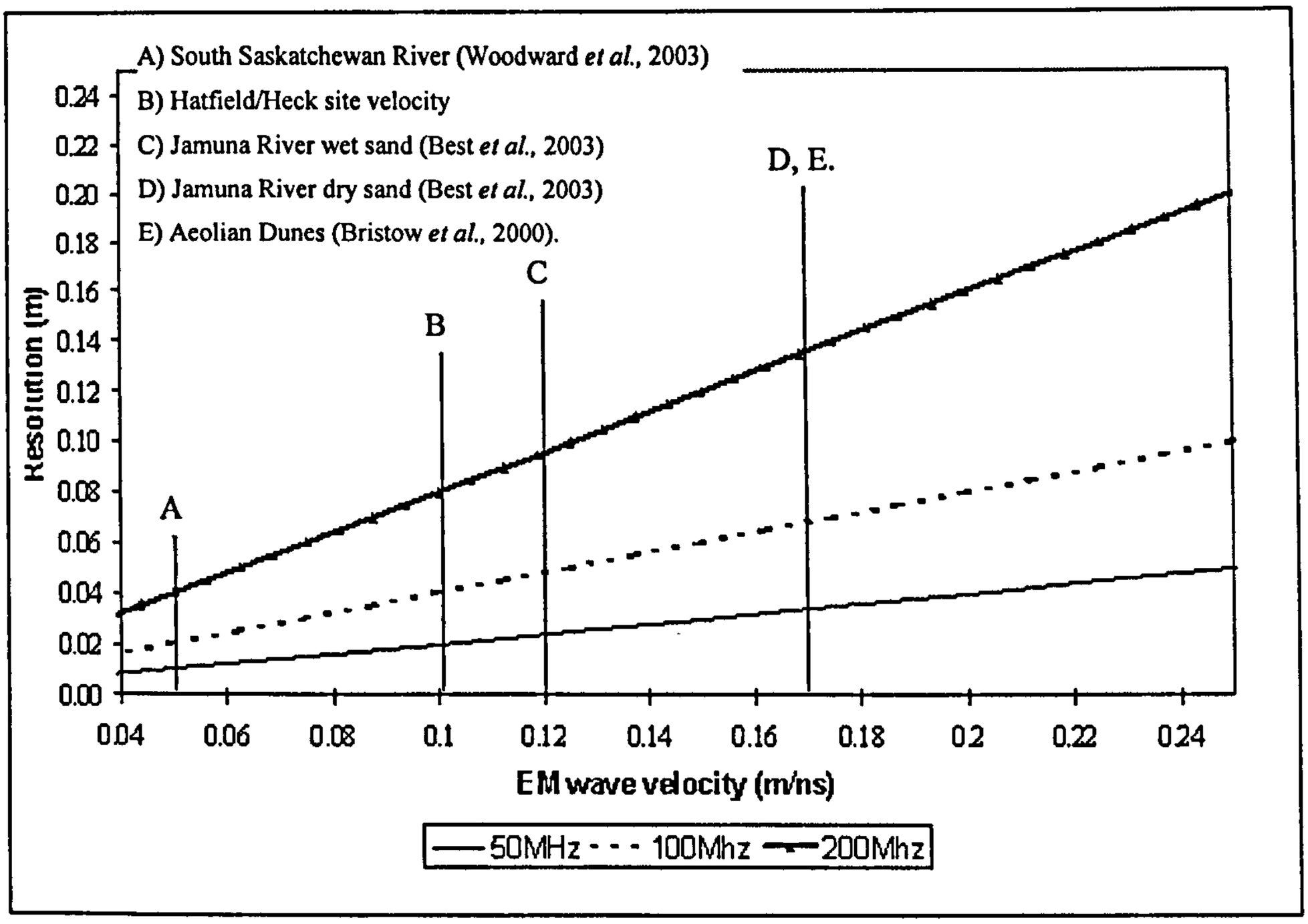

Figure 4.2. Resolution versus velocity for commonly used radar frequencies.

The radar wave velocity (V_m) in a medium is given by equation 4.3. (Reynolds, 1997),

$$V_m = \frac{c}{\left\{\left(\varepsilon_r \mu_r / 2\right)\left[\left(1+P^2\right)+1\right]\right\}^{\frac{1}{2}}} \qquad \text{Equation 4.3.}$$

where c is the velocity of light in a vacuum, ε_r is the relative dielectric permittivity in Farad.m^{-1}/Farad.m^{-1} and μ_r is the relative magnetic permittivity (Henry.m^{-1}/ Henry.m^{-1}), P is the dielectric loss factor, given by the equation $P=\sigma/\omega\varepsilon$, where ω is the angular frequency in Hertz (equal to the frequency multiplied by 2π) and σ is the electrical conductivity (S.m^{-1}). For most materials, the relative magnetic permeability, μ_r is approximately unity, so μ_r is normally a constant and variations in μ_r have little effect on radar wave propagation. However, where significant traces of iron and iron compounds are present, μ_r may be significantly increased, increasing potential losses.

In low-loss and non-magnetic materials, P is negligible, and equation 4.3. may be simplified as;

$$V_m = \frac{c}{\sqrt{\varepsilon_r}} \qquad \text{Equation 4.4.}$$

Hence the velocity of EM waves in the subsurface is controlled by relative permittivity (ε_r). Thus, water has the greatest influence on rock dielectric behaviour (ε_r~80 approx., see Table 4.2), so radar wave velocity is usually at its greatest when ε_r is low, i.e. where little free water is present. The TDR system, the ground penetrating radar and the TRIME unit described in subsequent chapters all rely on this fundamental property of the rock/water/air system.

Material	Relative Permittivity (ε_r)	Velocity (mm/ns)
Air	1	300
Water (fresh)	81	33
Water (sea)	81	33
Sand (dry)	3-6	120-170
Sand (wet)	25-30	55-60
Clay (wet)*	8-15	86-110
Sandstone (wet)	6	112
Shale (wet)	7	113
Average 'soil'	16	75

Table 4.2. Dielectric constants of some common bulk rock materials. (Reynolds, 1997) *West *et al.* (2003) suggest that swelling clays such as montmorillonite can have much higher dielectric constants at radar frequencies.

Table 4.2 shows that dielectric constants for dry rock-forming materials are normally low (<15), and that water is the primary cause of higher dielectric permittivities. However, some rock forming minerals such as 'swelling' clays may also increase permittivity values for the rock (West *et al.*, 2003) so mineralogically-induced errors in moisture content determination are possible. For 'clean' sandstone, such as the Sherwood Sandstone Formation, clays, where present, only form a relatively small proportion of the rock mass and so should not cause significant errors.

The fundamentals of dielectric constants with regard to electromagnetic wave propagation have been discussed by Larossa-Rodriguez *et al.*, (1999). The basic definition and properties of permittivity are discussed here, to avoid repetition in later chapters.

Permittivity is a proportionality constant between the intensity of an electric field and electric displacement. In a vacuum, this constant is approximately 8.85×10^{-12} farad per

metre and is known as the permittivity of free space ε_o. In other materials permittivity is often much higher than this and permittivity is usually expressed as a ratio relative to ε_o, rather than an absolute permittivity. Relative permittivity is a measure of the polarizability of a substance, or its ability to absorb charge in the presence of an electric field (West *et al.*, 2001). For example, liquid water, a highly polar substance has a relative permittivity of around 80, and air, which is non-polar, has a relative permittivity of 1.

Other terms for relative permittivity are apparent dielectric constant, permittivity or dielectric constant. Most rock forming minerals have relative permittivities of less than 5 and only very few have permittivities over 15 (see Table 4.1.2). Hence the biggest influence upon permittivity is the presence of water. The TDR and TRIME systems work by measuring the permittivity of the rock/air/water system and then use this value to calculate moisture content. GPR, by way of contrast, works by reflection and refraction of electromagnetic waves, which are also controlled by propagation velocity and hence, the rock permittivity.

Radar rays transmitted into the ground may be refracted or reflected at interfaces in the subsurface according to Snell's Law, where the degree of refraction and/or the amount of energy reflected is controlled by the variation in relative permittivity across the interface. According to Snell's Law, the reflection or refraction of electromagnetic waves at the boundary between two layers with differing dielectric properties is controlled by the dielectric contrast across the boundary. For an electromagnetic wave approaching a permittivity contrast at right angles, the reflection coefficient (Γ) is given by

$$\Gamma = \frac{\sqrt{\varepsilon_2} - \sqrt{\varepsilon_1}}{\sqrt{\varepsilon_2} + \sqrt{\varepsilon_1}} \qquad \text{Equation 4.5a,} \qquad \Gamma = \frac{(V_1 - V_2)}{(V_1 + V_2)} \qquad \text{Equation 4.5b.}$$

where ε_2 and ε_1 are the relative dielectric constants for the sequential layers encountered and V_1 and V_2 are the radar wave velocities (Reynolds, 1997). As the permittivity of the air/rock/water system has been shown to be controlled by the water content of the rock (see above), it follows that GPR tends to detect layers with significant differences in water content. In sedimentary rocks, variations in water content are often linked with grain size and variation in porosity (Topp *et al.*, 1980; Roth *et al.*, 1990; Huggenberger, 1993). As water content controls permittivity, which controls EM wave velocity, GPR may be used to examine variations in lithology caused by varying sedimentary structure.

Radar systems vary in style, degree of shielding and construction, but all share similar features, consisting of a transmitter and a receiver (although these may be combined in a monostatic system, see below). The system shown in Figure 4.3. is based on the Pulse Ekko unit, which is connected by fibre optic cables to a control box, which in turn is connected to a laptop computer. Other systems may rely on in-built computers, or may produce output on paper rather than via laptop, but their principle of operation is the same.

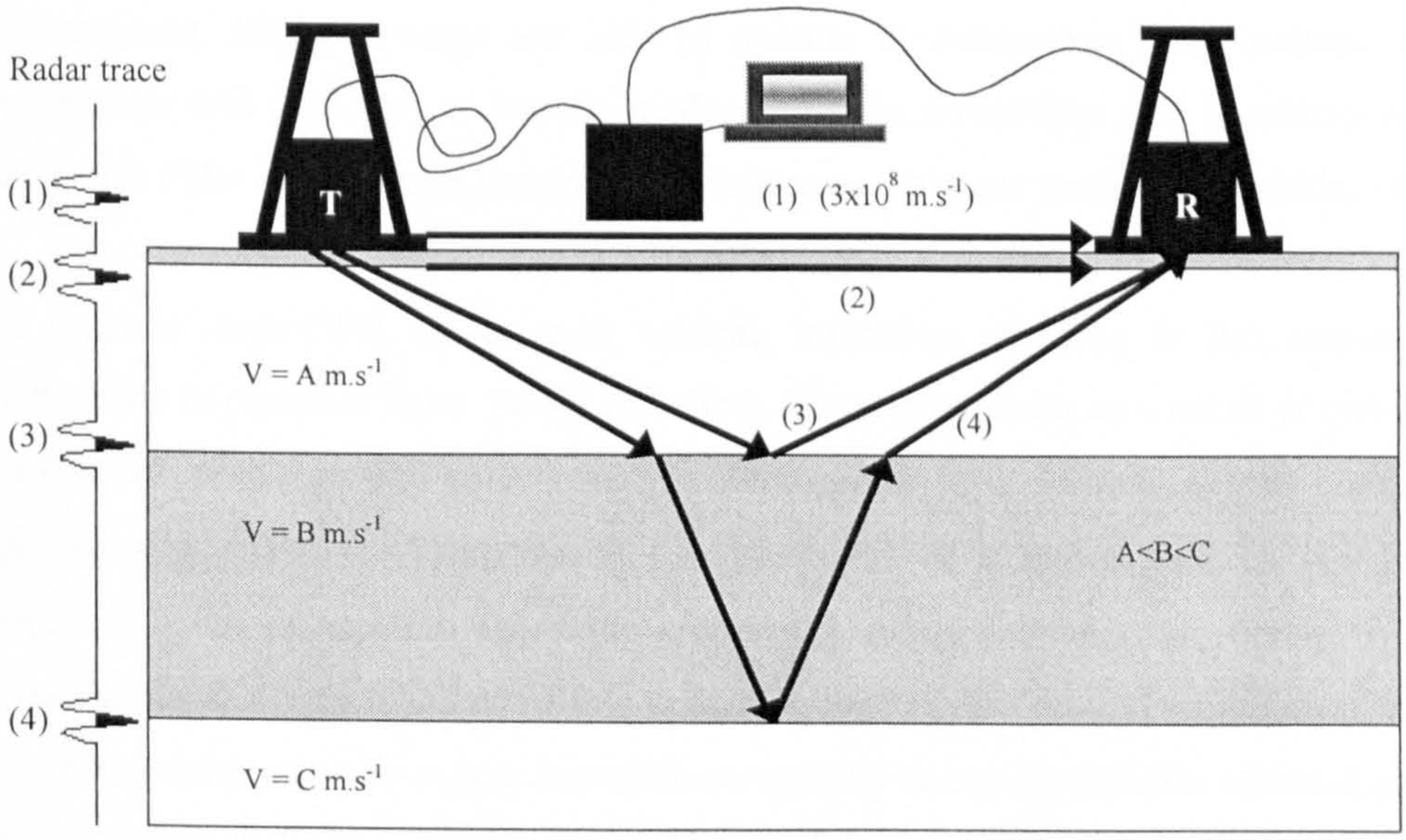

Figure 4.3. GPR system and associated radar trace (after Van Dam and Schlager, 2000).

The GPR system sends a signal through the fibre optic cable to the transmitter, which causes it to transmit a pulse of electromagnetic energy, via an antenna, into the ground. This pulse then radiates out in all directions, and may be intercepted by the receiver. The radar wave travels some 3 times faster in air than in the ground and so the first signal to reach the receiver is the air wave (1) which travels above ground, directly from transmitter to receiver. The second arrival (2) is the ground wave, which is also a direct wave, this time travelling through the ground surface. Later arrivals have travelled into the ground and have been reflected from dielectric boundaries in the ground (3&4).

The control box records the arrival time and strength of the arriving radar pulses and is able to plot traces of the results in real time on the attached laptop. The system is moved along the ground surface in a series of steps, with a trace (as shown in figure 4.3 above) taken at each step, and a 2D picture of the subsurface is built up incrementally. It is possible to collect data in continuous or step modes. In continuous mode the radar antennae are drawn along the ground surface at a continuous rate and radar returns collected at preset time intervals. This method can reduce the quality of data collected and

may make some processing steps less reliable (Woodward *et al.*, 2003). A more controlled and reliable approach is the step method, where the radar transmitter and receiver are moved along the ground in discrete steps, pausing between each for a reading to be taken. The radar equipment is also usually set to work on a timer, with longer timings being necessary on difficult or rough terrain. This technique also has the advantage that the antennae are stationary when radar readings are taken, with the antennae in good contact with the ground, and so more reliable and repeatable data may be obtained. Many systems are able to operate in monostatic (one antenna used as transmitter and receiver) or bistatic modes (separate transmitter and receiver), although the Pulse Ekko system used herein only operates as a bistatic system (Reynolds, 1997).

A property that GPR shares with seismic reflection profiling is the occurrence of diffraction hyperbolae from 'point' reflectors. These may occur as a result of out-of-plane reflections, above ground objects such as electricity pylons, discrete objects buried in the ground (e.g. pipes, services), trenches or boreholes, or scattered pebbles. As shown in Figure 4.4, the radar wave enters the ground (1) and is diffracted (scattered) by, in this case the vertical step (2). Part of this scattering reaches the ground surface and is picked up by the radar receiver as it is moved incrementally along the traverse (from A to B). As the receiver moves from A to B, the wavepath of the scattered radar pulse gets longer, and thus it has a longer travel time. This is deciphered by the plotting software as a line reflection, which gets deeper in the form of a hyperbola as a result of the system geometry. Above ground hyperbolae can usually be distinguished by calculating the velocities of the hyperbola 'limbs' using the 'hyperbola fitting' method (see section 4.3.). The velocities calculated from above-ground hyperbola may be distinguished from those derived from below-ground hyperbolae by their high velocities ($3x10^8 m.s^{-1}$). If required, hyperbolae may be removed at the processing stage by migration to identify the location of the point reflector, and reveal features obscured by the hyperbola limbs.

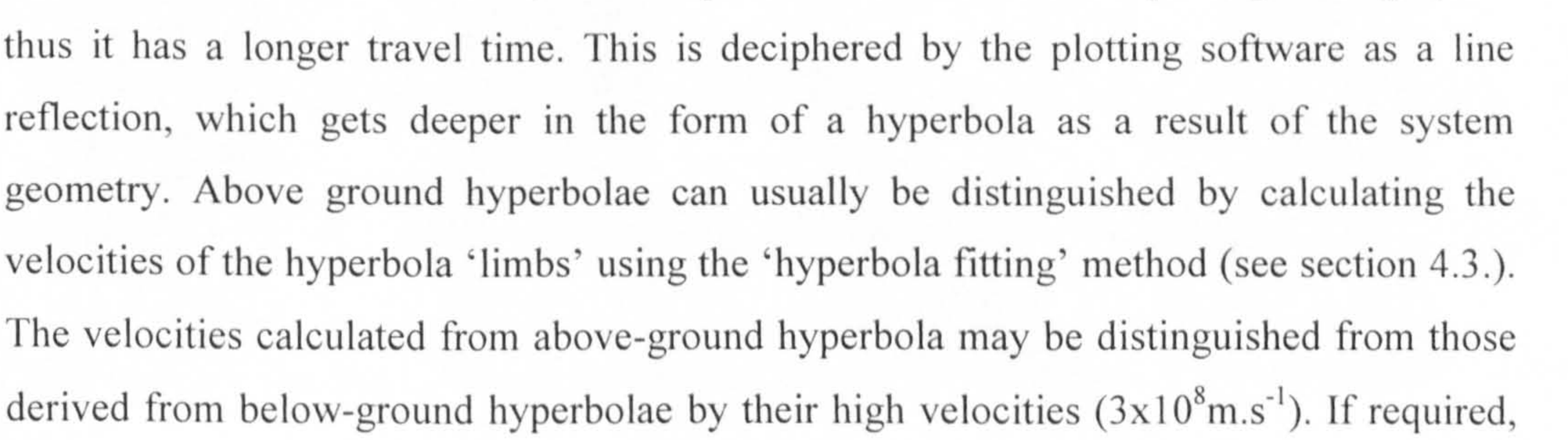

Figure 4.4. Diffraction hyperbolae.

GPR reflections may also exhibit a different phase (polarity) than the transmitted pulse. Phase changes occur when the radar wave moves across a velocity boundary, according to whether the reflection coefficient changes from negative to positive or *vice-versa* (see Equation 4.5. and Figure 4.5.). Polarity changes are obvious when imaging large subterranean air-filled voids, within rock however, phase changes may be subtler. Phase changes have been observed in GPR modelling, and in GPR surveys may be observed at the bases of some fine-grained units where the radar wave passes from wet to dry rock (see Sections 4.4. and 4.5.).

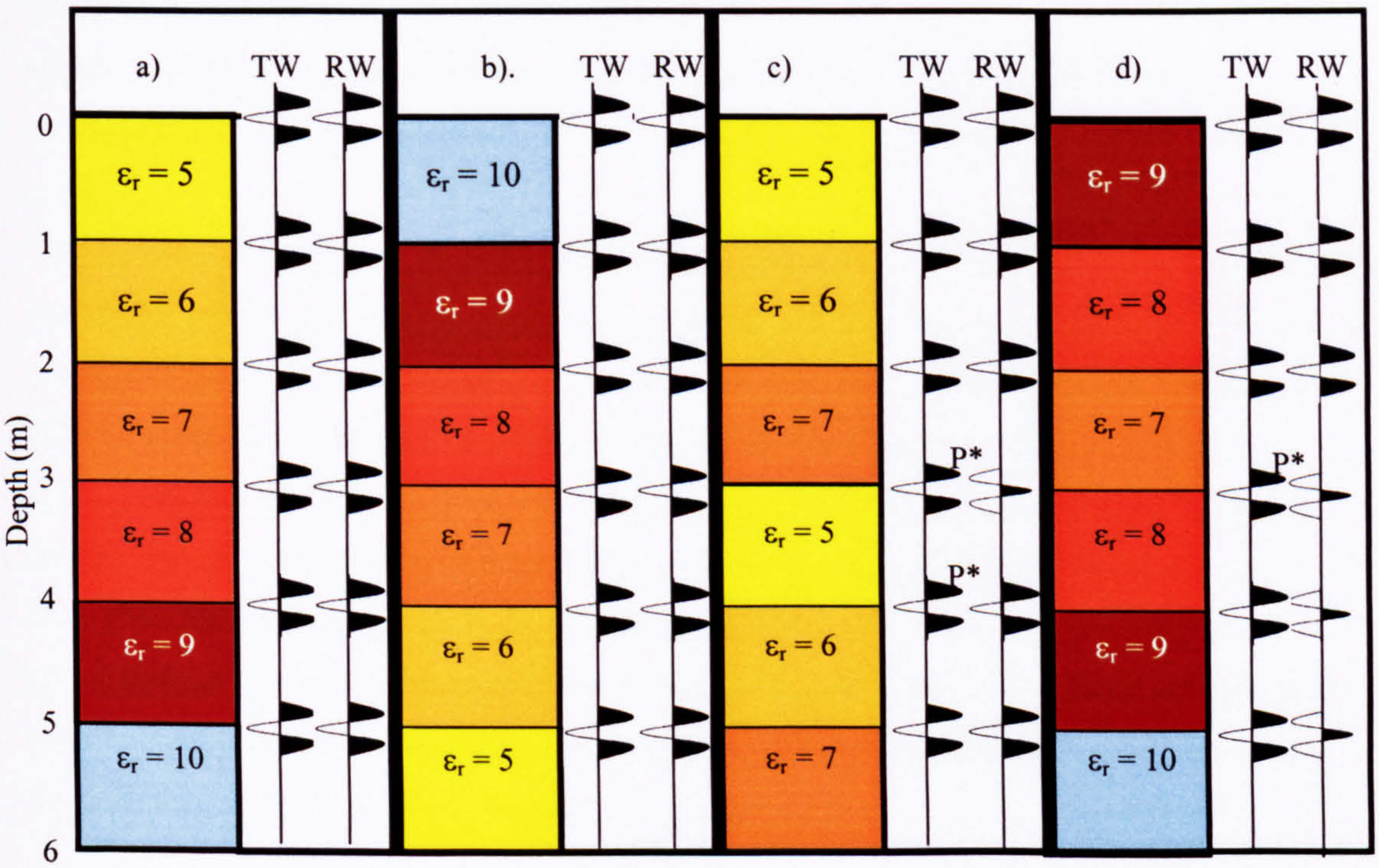

Figure 4.5. Occurrence of radar wave polarity changes at permittivity boundaries. TW represents transmitted waveforms and RW represents reflected waveforms, P* denotes polarity reversal.

Figure 4.5. shows where polarity reversals would be seen in radar images. Figure 4.1.5a. shows that as ε_r increases with depth, the reflection coefficient (R) calculated from Equation 4.5a. is always positive, so no polarity changes can occur. Figure 4.5b. shows that when ε_r decreases with depth, R is always negative, so again no polarity changes can occur. Figure 4.5c. shows polarity changes at 3 and 4 metres depth. From 1 to just under 3 metres depth, all the reflection coefficients are positive as dielectric permittivity increases with depth. However, at 3m depth there is a change to a negative reflection coefficient, where ε_r decreases across the dielectric boundary, therefore according to Equation 4.5a. a

polarity reversal must occur. At 4m, the dielectric boundary is from lower permittivity to higher permittivity, R is therefore positive again, so another polarity reversal occurs. Deeper than 4m, R remains positive, so no further reversals are shown. Figure 4.5d. shows only one polarity reversal, at 3m, where the reflection coefficient changes from negative to positive. Below 3m R remains positive, so no further polarity reversals occur.

4.2 GPR methods.

The permeability characteristics of poorly cemented braided river deposits, such as the Triassic Sherwood Sandstone in northeast England, are strongly influenced by the distribution of sedimentary facies, which can be observed in outcrop, or inferred from geophysical data provided adequate linkage between sedimentary and geophysical characteristics can be established. GPR survey locations were selected where it was possible to obtain data that may be 'ground truthed' by comparison with adjacent cut faces. A variety of radar images, taken from three sites on the Sherwood Sandstone aquifer over a distance of 70 km between Mansfield and Selby, UK, are presented and interpreted, and these results are linked together with field observations from previous chapters. Additionally, a modelling study is reported that uses ray tracing to assist in survey design and interpretation.

The Sherwood Sandstone is relatively well sorted, salt free with an overall low clay content (1.1-4.4% by weight, West *et al.*, 2003), factors which combine to give ideal conditions for GPR. GPR velocities were obtained for the sites by Common Mid Point (CMP) analysis, by cliff face profiling and by hyperbola fitting. Velocities of $0.17m.ns^{-1}$ for dry sand and $0.12m.ns^{-1}$ for wet sand were achieved by Best *et al.* (2003) on the modern Jamuna river sands in Bangladesh. A velocity of $0.05m.ns^{-1}$ was also calculated from the (depositionally analogous) South Saskatchewan River (Woodward *et al.*, 2003), and $0.17m.ns^{-1}$ for aeolian dune sands were reported by Bristow *et al.* (2000). The values reported here, for the vadose zones at the test sites at Heck and Hatfield lie somewhere in the middle, at between $0.098\text{-}0.108m.ns^{-1}$ (see Figure 4.2).

Results show that interpreting sedimentary structure in the Sherwood Sandstone using GPR is feasible. Other researchers (Best *et al.*, 2003; Bridge and Lunt, 2003; Bristow, 2002; Bristow *et al.*, 2000; Cardimona *et al.*, 1998; Corbaneau *et al.*, 2002; Davis and Annan, 1989; Hammon *et al.*, 2002; Jol, 1995; Van Dam and Schlager, 2000; van Overmeeren, 1988; Woodward *et al.*, 2003) have shown good results in similar sandy environments. GPR is ideal for hydrogeological applications as the majority of the features imaged are visible to radar as a result of variations in capillary held moisture, and the amount of capillary retention is controlled by the size of the pore throats in the sediments, which directly influences their permeability properties. Provided appropriate relationships are available linking the pore size distribution with the permeability characteristics of each sedimentary facies, GPR data can form the basis of stochastic outcrop and regional scale flow modelling and many researchers have used GPR surveys

to create permeability fields for various reservoirs and aquifers (Szerbiak *et al.*, 2001; Hammon *et al.*, 2002; Sandberg *et al.*, 2002; Corbeanu *et al.*, 2002; Aspiron and Aigner, 1997, 1999; Gloaguen *et al.*, 2001).

All the radar work was conducted using a Sensors & Software Pulse-EKKO 100 GPR, made by Sensors and Software Inc. of Mississauga, Ontario, Canada. This system has been upgraded to operate at 1000V giving greater penetration into the rock. Three antennae were used, 50MHz, 100MHz and 200MHz allowing imaging at differing resolution when necessary. The Sensors and Software antennae are resistively loaded dipole antennae (Murray *et al.*, 1997), which are directional, and the bulk of the energy transmitted into the ground is concentrated in an ellipse perpendicular to the long axis of the antenna (Annan *et al.*, 1975). Hence, the surveys undertaken were conducted with the antennae perpendicular to the radar line so that off-line reflections were kept to a minimum.

Generally, radar images presented in this thesis were collected at a central frequency of 200MHz, although some radar lines were taken at lower frequencies. All radar images presented here were taken using the step method. The vast majority of the data were obtained using the same configuration as Bristow *et al,* (2000), i.e. 100MHz antennae were used with a separation of 1.0m and 0.5m step, 200MHz antennae were used with a separation of 0.5→1.0m and step of 0.2m. Information on step size, frequency and line spacing for each line presented is shown in Appendix 1, and the location of each line within the quarries is given in Appendix 4. At a frequency of 50MHz, the penetration is excellent, certainly for the purpose of investigating the vadose zone of the Sherwood Sandstone, but the resolution only allows the larger features to be imaged, whereas at 200MHz, the resolution is excellent, but the depth of penetration suffers (see Figure 4.2). This is known as the 'range-resolution trade off' (Davies and Annan, 1989). Thus, the frequency of all the radar lines collected as part of this investigation were individually chosen as a result of trial radar lines, at various frequencies, and vary according to the location and the nature of the feature under investigation. Surface soils are known to cause scattering of the radar signal, resulting in large areas of overlapping hyperbolae that often mask underlying features (van Overmeeren *et al.*, 1997). Preliminary radar lines collected at the Hatfield test site, adjacent to Hatfield Quarry at Lings Farm smallholding (National Grid Reference SE 653 078), where soil layers and glacial sands and pebbles overlie the Sherwood Sandstone, are greatly scattered and were unusable (see Appendix 1). As a result of this, further radar lines were collected in quarries where the glacial overburden had been removed, and there was minimal soil cover. At these sites the radar

waves were therefore able to pass directly into the Sherwood Sandstone with no scattering from soil cover and the results were greatly improved.

Two types of radar profiling have been used in the present study: i) constant offset profiling and ii) common mid-point profiling. The five groups of radar line listed below all fall into categories i) and ii). Constant offset profiling is used to provide a radargram of the subsurface structure whereas common mid-point (CMP) surveys provide an estimate of the electromagnetic wave velocity, and enable the radargram time axis to be converted to depth. In a constant offset survey, the spacing between transmitter and receiver is kept constant and the antennae are moved together along the line of the radar traverse. With common mid-point surveys, both transmitter and receiver are moved apart in steps. For a detailed explanation of CMP and constant offset profiling see Reynolds (1997, pp. 709-711).

The radar lines undertaken for the work presented here may be classified into five groups:

1). **Single lines**. These were taken to provide long profiles for radar characterisation, to determine the best frequency and/or system set-up information or to provide a quick view of the subsurface. These were collected mainly at Hatfield quarry and Great Heck Quarry to assist in deciding where to situate boreholes and site test equipment. Some long lines (over 300m) were also collected at Hatfield and Heck Quarries.

2). **Face lines**. These were single lines collected directly behind logged faces to provide a direct comparison between sedimentary structure visible in outcrop and visible by radar. A potential problem was the reflection of radar energy back to the receiver from the cliff face itself, producing a strong reflection across the radar image. Corbeanu *et al.*, (2001) state that cliff face reflections are less of a problem with GPR data than in seismic data, provided the antennae are orientated correctly. Trial face lines conducted at Great Heck quarry validated this view, and face reflections were not a problem in practice, provided the antennae were oriented perpendicular to the face. Face lines presented herein were taken from the Rufford, Hatfield, Heck, and Pollington quarries.

3). **Grids.** These were multiple parallel lines, taken closely together for interpolation into 3-D block images of the subsurface. Sometimes all of the lines were collected in the same direction, but usually two series of lines perpendicular to each other were collected over the same area to reduce potential anomalies caused by the directional nature of the antennae (Annan *et al.*, 1975). Grids were collected at Hatfield and Great Heck quarries.

4). **CMP surveys.** They were used to provide velocity data for depth conversions and were collected at all sites where the radar was used. These will be considered more fully in section 4.3.

5). **Cliff-face profiles.** These surveys are described and discussed in section 4.3. This type of radar image was only collected at Great Heck quarry, in order to estimate radar wave velocity.

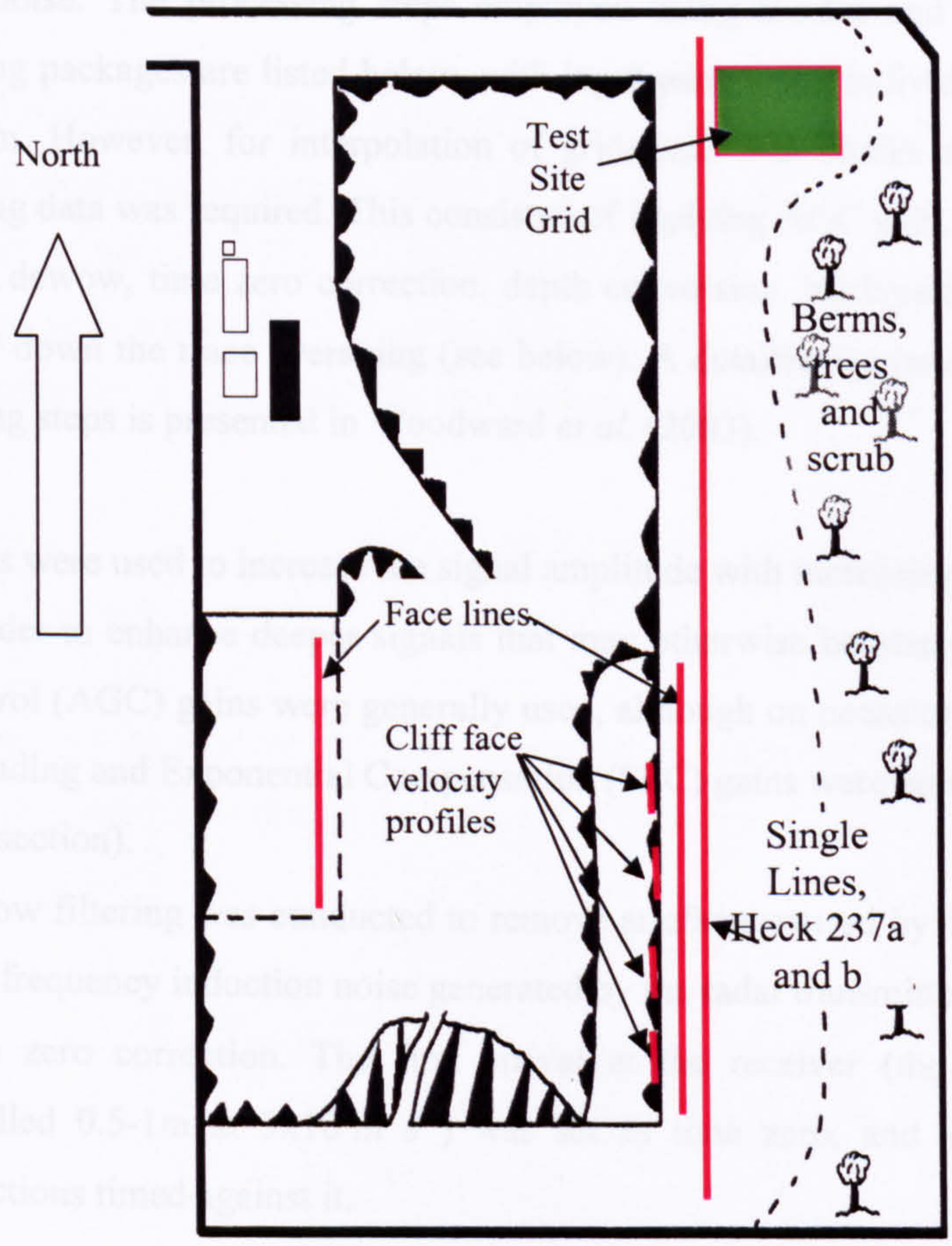

Figure 4.6. Location of main radar lines, profiles and grids, Great Heck Quarry (SE 588213). (Not to scale, however quarry is approximately 250m North to South).

As a general rule, radar images were either collected parallel to palaeocurrent (usually North→ South) or perpendicular (usually East→ West). Palaeocurrent direction was normally obtained by examination of cut faces, and considering the imbrication of pebbles and intraclasts or by viewing larger scale sedimentary structure. Radar images were corrected for topographical variation where necessary, but normally radar lines were collected over even, clear ground as it was considered important to acquire 'clean' radar traces that required a minimum number of processing steps.

4.3 Data Processing

Some radar processing is always necessary, with the aim of improving the signal:noise ratio (Reynolds, 1997; Overmeeren, 1998; Woodward *et al.*, 2003). Domain filtering methods may be employed to enhance the radar images (Young and Sun, 1999) but these methods have not been used herein as the radar images obtained tended to be relatively free of noise. The processing steps employed using Gradix and Sensors & Software processing packages are listed below, with input parameters individually tailored to each radargram. However, for interpolation of grids into 3-D blocks a standard method of processing data was required. This consisted of applying AGC gain, with a one trace time window, dewow, time zero correction, depth conversion, background removal and trace to trace / down the trace averaging (see below). A detailed explanation of the individual processing steps is presented in Woodward *et al.* (2003).

- Gains were used to increase the signal amplitude with increasing two-way travel time, in order to enhance deeper signals that may otherwise be obscured. Automatic Gain Control (AGC) gains were generally used, although on occasion Linear (Constant) or Spreading and Exponential Compensation (SEC) gains were applied as necessary (see next section).
- Dewow filtering was conducted to remove artefacts caused by the radar system itself (low frequency induction noise generated by the radar transmitter).
- Time zero correction. The first arrival at the receiver (the airwave, which has travelled 0.5-1m at $3x10^8 m\ s^{-1}$) was set as time zero, and all of the subsequent reflections timed against it.
- Conversion of two-way travel times into true depth using results from velocity analysis techniques detailed below.
- Background removal was used to eliminate repetitive noise signals caused by ringing in the antennae, which produces horizontal banding parallel with the airwave.
- Trace to trace (spatial filter) and down the trace (time filter) averaging was used to smooth the radar traces (see next section).

The aim of processing was to convert field data into an accurate picture of subsurface structure and wherever possible, processing was kept to a minimum. The results were then available for comparison with sedimentary architecture data obtained from photographic surveys and field logging at outcrop.

4.3.1. Velocity analysis

Two-way travel times (TWT) were converted to depth using the average velocity of the radar wave within the sediment for each site. Radar velocities were determined using three methods: common mid-point surveying (CMP), cliff face profiling and hyperbolae fitting. These methods are described below and the resultant estimates of velocity discussed.

Method 1: Common Mid Point (CMP, Fig. 4.7). This method is one of the most common ways of determining velocity, in which the transmitter and receiver are moved away from each other at each step. The first arrival (a) is the air wave (0.3m ns^{-1}), the second (b) is the ground body wave which gives the velocity just below the ground surface (0.1m ns^{-1}) and the third (c) is caused by the first reflector, for which a velocity may be obtained using.

$$t^2 = t_0^2 x^2/v^2 \qquad \text{Equation 4.6.}$$

where v is velocity, x is the antennae separation, t is two-way travel time at separation x, and t_0 is two-way travel time at the apex of the hyperbola (Keary and Brooks, 1991).

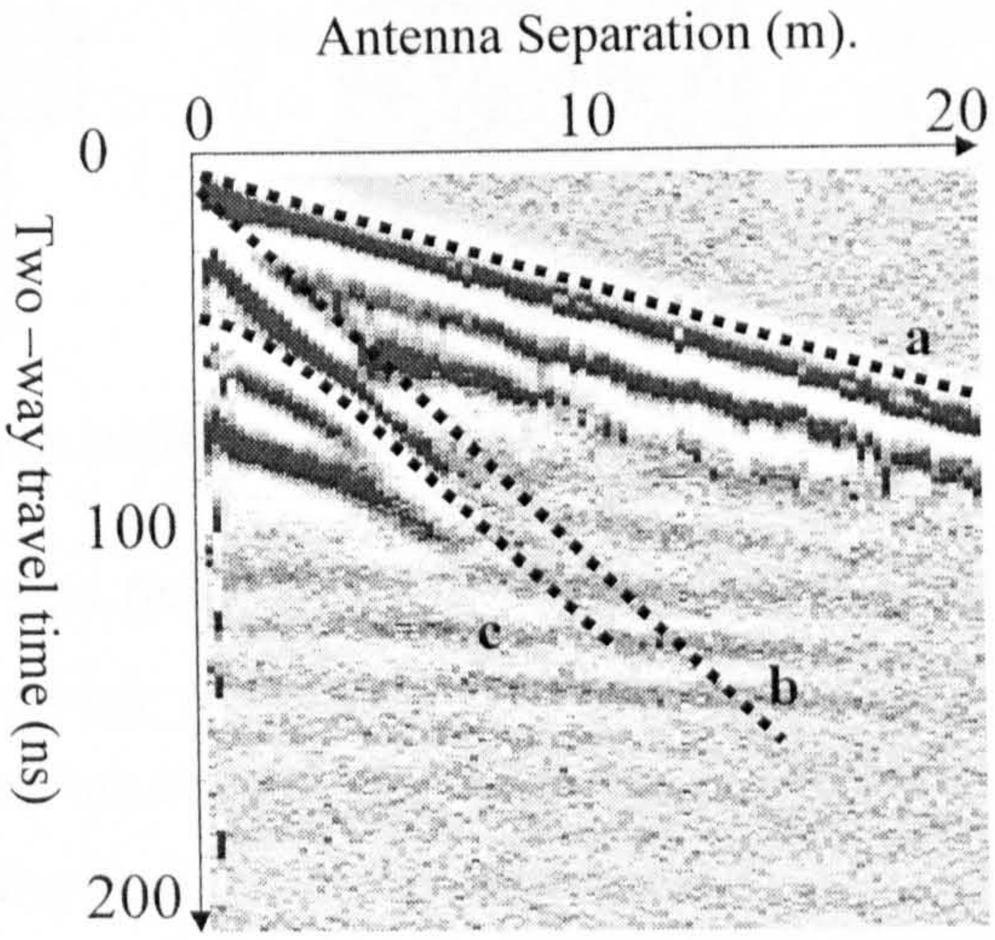

Figure 4.7, Radargram of CMP profile at 100 MHz from Great Heck Quarry (SE 588213). a) Air-wave (velocity 0.3m ns^{-1}), b) Ground body wave (velocity 0.1m ns^{-1}), c) Returned wave from the first reflector (velocity 0.087m ns^{-1}).

The CMP technique provides a reasonable approximation of the subsurface radar velocity, with the accepted error margin being 20% (Reynolds, 1997). CMP velocities within the test sites ranged from 0.080 to 0.105m ns^{-1}.

Method 2: cliff face profiling (Fig. 4.8). In this method, the transmitter was situated 1m back from the cliff face and the receiver moved down the face in 0.1m steps (Fig. 4.8a). The prominent 'reflection' that represented the direct wave arrival through the sediment, was determined (Fig. 4.8b) and a series of gradients from successive points for this 'reflection' were determined. These gradients were converted to an average velocity through the rock for each direct ray-path using true transmitter to receiver distances. Velocities for the different raypaths within the sediment were also used to give a velocity profile (Fig. 4.8c). Finally the EM velocities were found for four profiles – the mean overall velocity was 0.089m ns^{-1} and velocities ranged from 0.085 to 0.095m ns^{-1}, Figure 4.8c shows the resulting velocity profile for the line Heck V3.

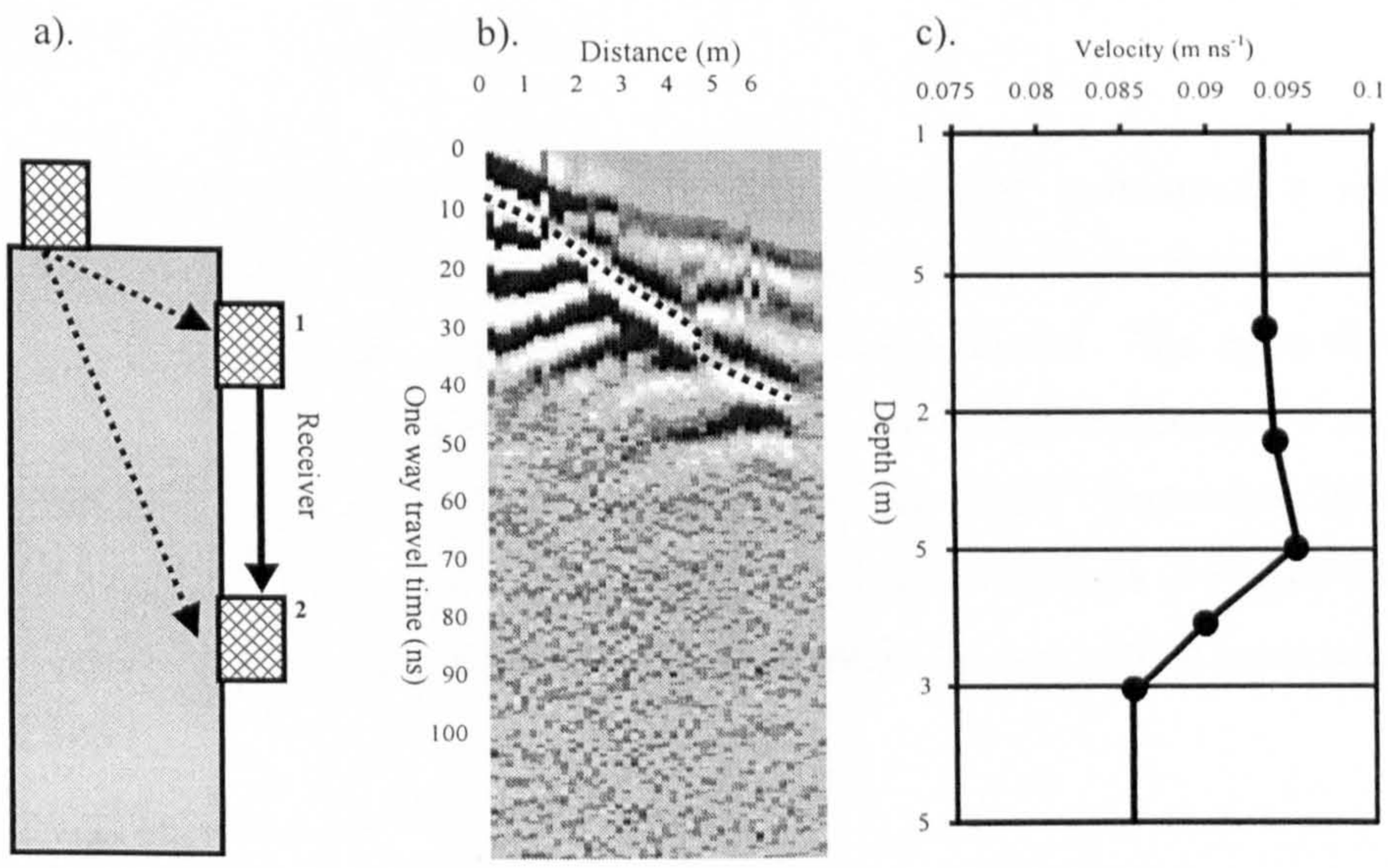

Figure 4.8, Cliff face profiling, method and results from Great Heck Quarry (SE 588213).

Method 3: Hyperbola fitting (Fig 4.9). Point reflectors, such as large mud clasts, often give rise to hyperbolae whose shape is related to the depth of the point reflector, its diameter and the velocity of the radar wave (Interpex, 1997). By assuming that hyperbolae arise from point reflectors, it is possible to use the steepness of their limbs to estimate subsurface velocity at a range of depths. This was accomplished using Gradix software (Interpex Ltd), and the subsurface velocity computed for a range of hyperbolae.

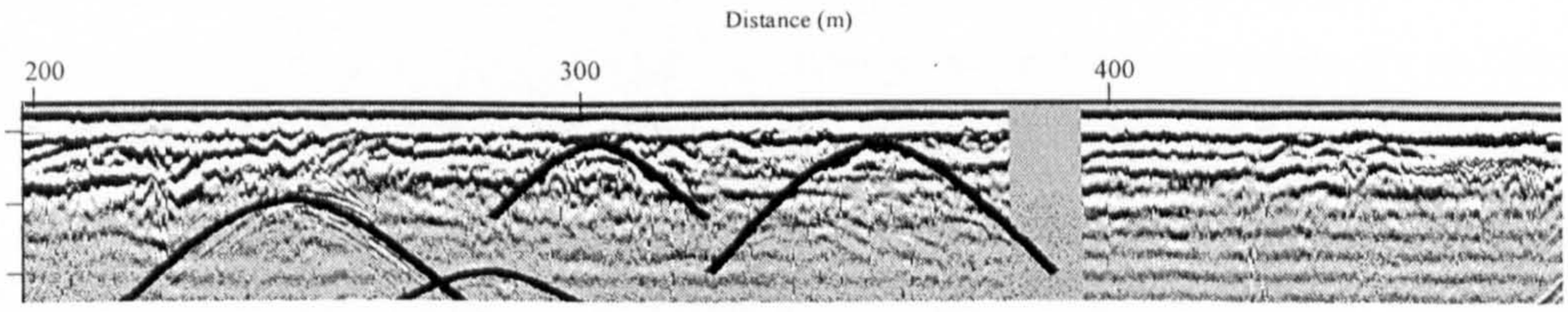

Figure 4.9. Hyperbola fitting at Great Heck quarry (SE 588213). (Line at 100MHz)

Typical values using the hyperbola fitting technique ranged from 0.095-0.13m ns^{-1} with a mean value of 0.105m ns^{-1}.

The range of velocity values in the unsaturated Sherwood Sandstone for all techniques was between 0.085 and 0.11m ns^{-1}, with a mean 0.95m ns^{-1}. This value is consistent with velocities expected from measured vadose zone moisture contents in the Sherwood Sandstone and those obtained using the relationship between laboratory-derived radar frequency dielectric constant and moisture content derived by West *et al.* (2003). The range of methods applied indicate that a velocity value of 0.1m ns^{-1} will probably be within 15% of true velocity for sedimentary units within the sites investigated, and so this velocity has thus been used for depth-scaling of the radar data.

4.3.2 Processing: An example line.

To demonstrate the use of the various data processing techniques, a radar line, HEKGD_AA, taken from Great Heck Quarry is processed in stages below using Sensors and Software Pulse Ekko and Interpex Gradix 1.0 software. The radar line was a North→South line, taken parallel to palaeocurrent with 200MHz antennae, a step size of 0.2m and antenna separation of 1m. The line was run on 23rd September 2002, and is directly over the line where boreholes TDR 1, 2, 3 and 4 were later drilled, it is therefore an important line for radar characterisation of the Heck site and will be considered later in this chapter.

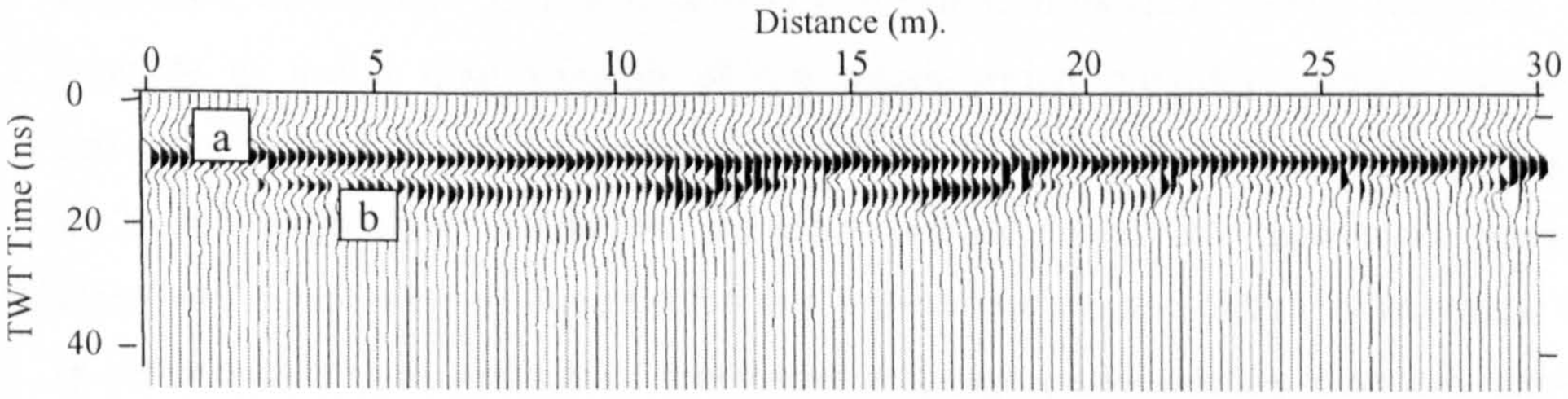

Figure 4.10. Unprocessed radar image HEKGD_AA. (Sensors & Software Pulse Ekko software used to generate image).

Figure 4.10 shows that even at 200MHz, little useful sedimentary structure can be seen. The first arrival (a) is visible as a solid horizontal black line, and there are (b) other features below this, above 20ns, but these are indistinct.

Gains. Figure 4.11 shows application of an SEC (Spreading and Exponential Compensation) gain, which attempts to compensate for the spherical spreading losses that

occur as the radar wave passes through the ground. This method allows the preservation of relative amplitude variations, and is best at imaging strong reflectors at the expense of weaker ones (van Overmeeren, 1998).

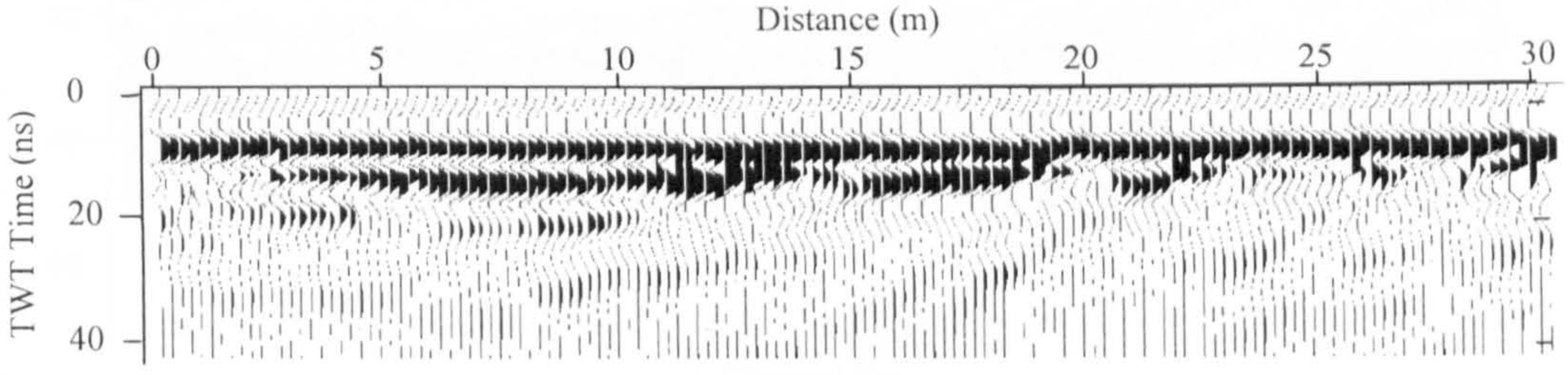

Figure 4.11. SEC gain with attenuation factor of 0.3dB.m^{-1} using Sensors & Software Pulse Ekko software.

An attenuation of 0.3dBm^{-1} was applied, which is the maximum value quoted for sands in the Pulse Ekko program. Figure 4.11 (SEC gain), shows more detail than Figure 4.10 and strong upper reflectors are better delineated, and there is some evidence of deeper, more subtle features, down to 40ns. The image obtained from applying SEC gain is not adequate for characterisation of weaker reflections such as those related to sedimentary structure.

Figure 4.12 shows the application of an AGC (Automatic Gain Control) gain. This method of applying gains attempts to equalise all signals by applying a gain that is inversely proportional to the return signal strength. This method is good at imaging weaker signals, especially if applied over a time window of one trace, but signal amplitude information is lost (Figure 4.12a van Overmeeren, 1998). However, it is possible to use a time window of 4-6 traces which provides imaging of weaker reflections, whilst preserving some of the amplitude information (Figure 4.12b). Figures 4.12a and 4.12b show details that are vastly improved over any figures yet presented. However, examination of Figure 4.12a and b show that a time window of one radar trace is better than a time window of four traces at imaging sedimentary structure, allowing structures down to a two-way travel time of 40ns to be imaged in greater detail. Hence, although a longer window length preserves more amplitude data than a shorter length, it does not provide sufficient resolution of weaker traces for the Sherwood Sandstone at Great Heck Quarry.

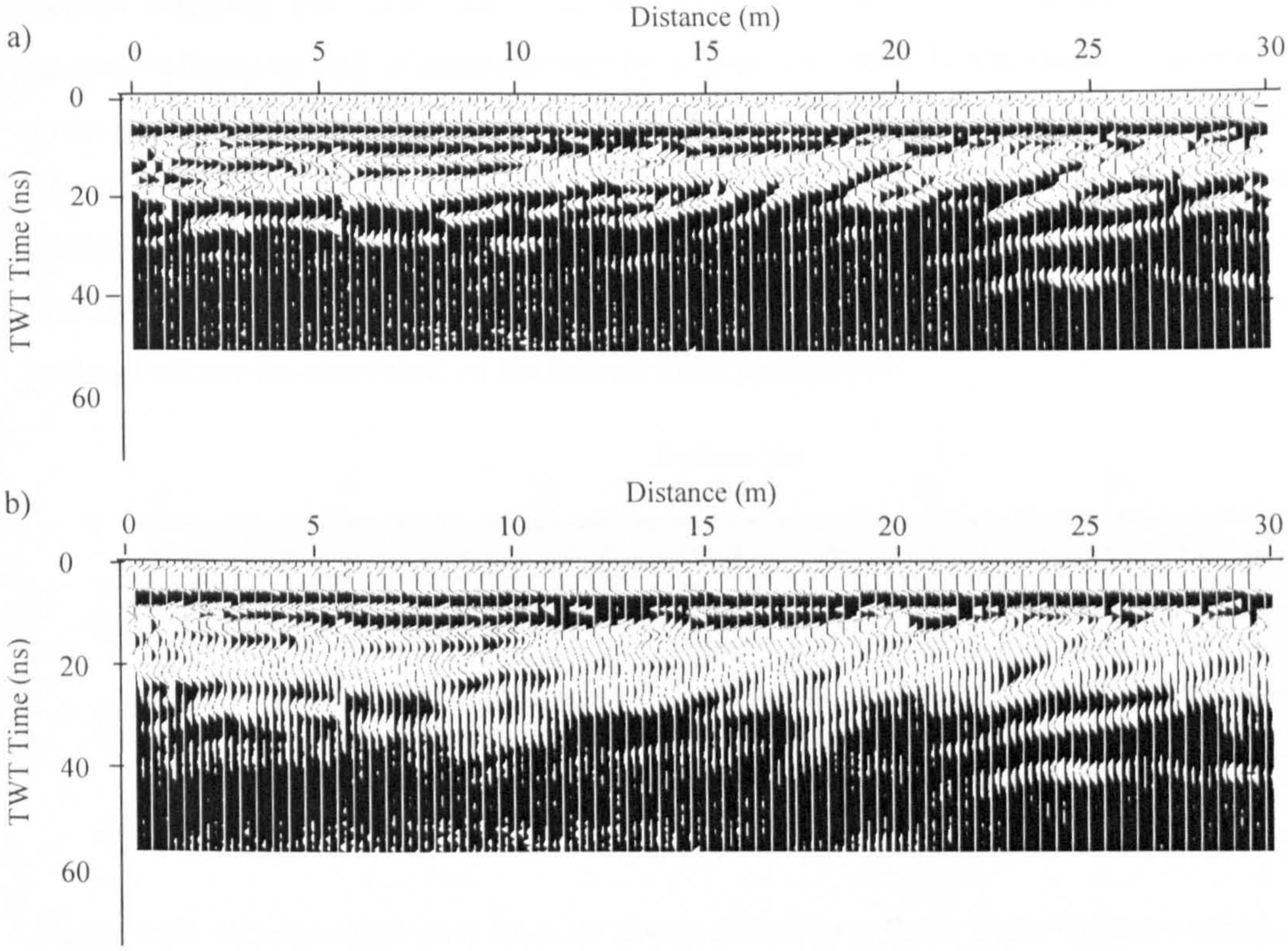

Figure 4.12. AGC gains. a). time window of 1 trace, b). time window of 4 traces using Sensors & Software Pulse Ekko software.

The final gain type, Figure 4.13, shows the application of a linear (or constant) gain, where a modifier is applied to the returned signal. The gain applied here used a constant multiplier of 50.

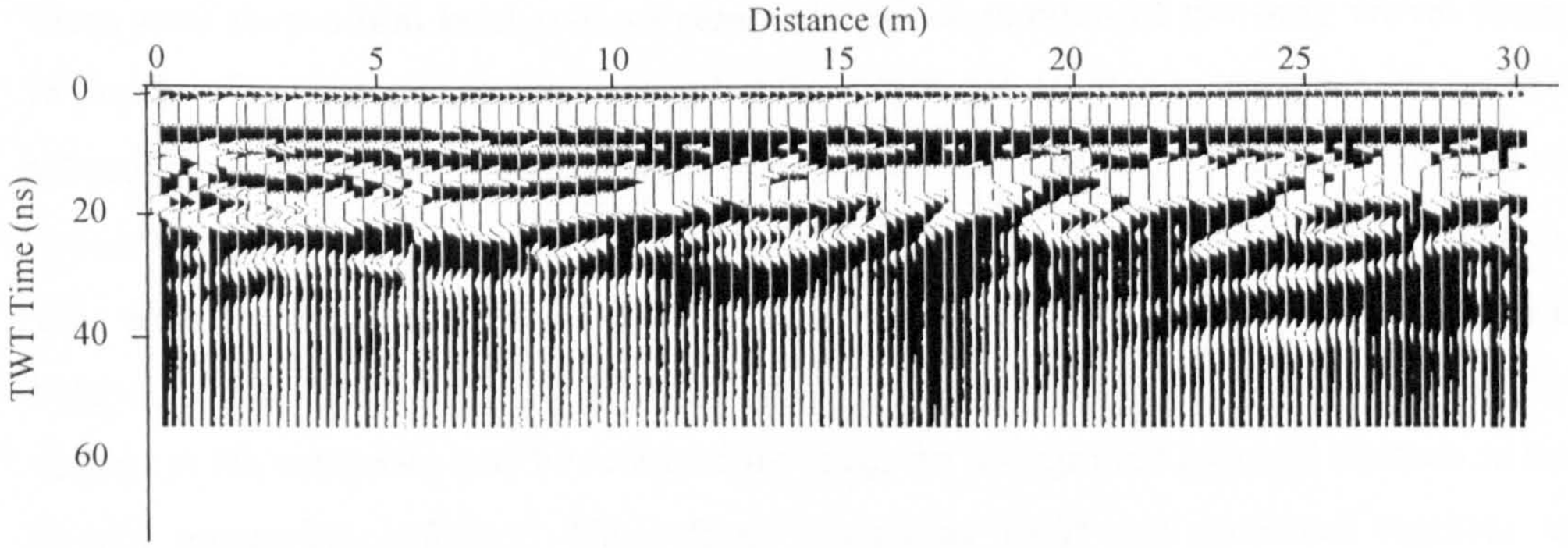

Figure 4.13. Linear gain, multiplier of 50. (Sensors & Software Pulse Ekko software used).

Figure 4.13 shows good resolution of sedimentary features at depth. However, some of the more subtle features are less well resolved than in Figure 4.12, and the whole image appears to have less 'texture'. Hence the gain applied to this radargram throughout this section is an AGC gain with a time window of 1 trace, as this shows the best detail of the sedimentary features of interest.

Dewow filtering. The radar transmitter often emits low frequency noise that may obscure genuine reflections and is characterised by a large DC shift in the results, but may be removed by applying a high-pass filter to the data (Interpex, 1997). Gradix software allows the plotting of the frequencies of returned radar signals, and the operator may choose the cut-off frequency below which frequencies are removed, as well as three methods of removing these frequencies. The Sensors and Software Pulse Ekko processing package allows no user input on the dewow filter parameters.

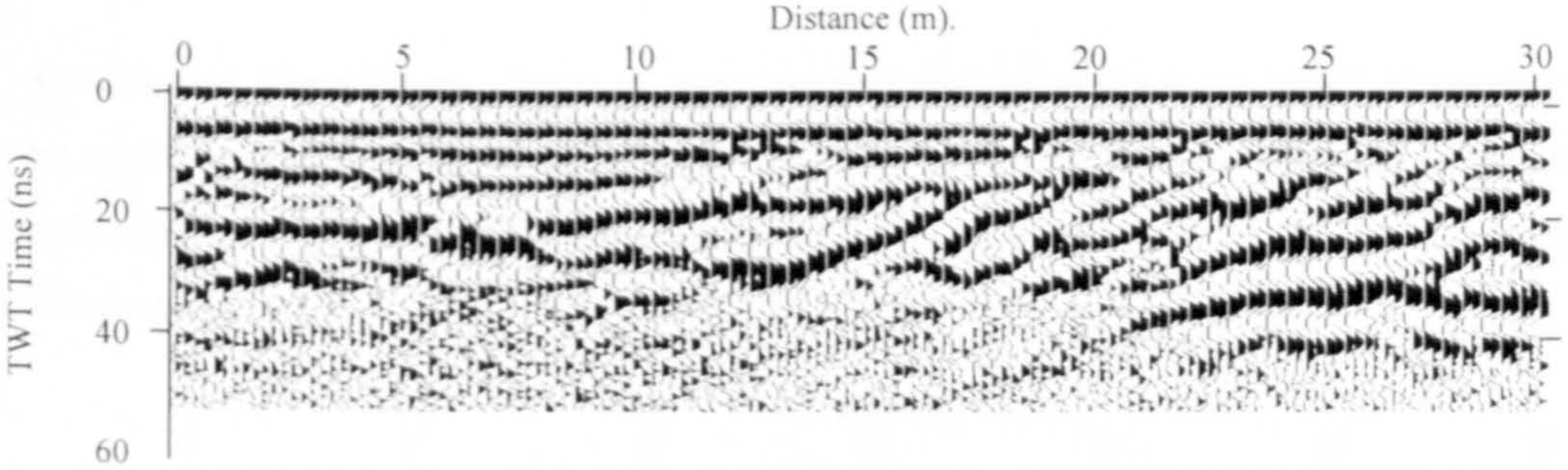

Figure 4.14. Effects of Dewow filter. (Sensors & Software Pulse Ekko software used).

Sedimentary structure may now be clearly seen down to a two-way travel time of over 40ns, with some detail at about 50ns. Removal of the low frequency noise that was obscuring useful data has allowed a much-improved radargram to be produced.

Time zero correction, background removal and conversion of two-way travel times to depth. The first ground-wave arrival at the receiver is set at zero nanoseconds, and all subsequent arrivals are timed after it. This allows the EM wave velocity determined earlier this section to be applied to the radar image, allowing a depth scale to be used. This enables direct comparison of radar images with other data such as cut faces and borehole logs. Additionally, horizontal banding, parallel to the airwave and caused by ringing in the antennae, may be removed by using the background removal routines in the Gradix processing software. These three processing steps are presented together as individually they do not greatly alter the radar image.

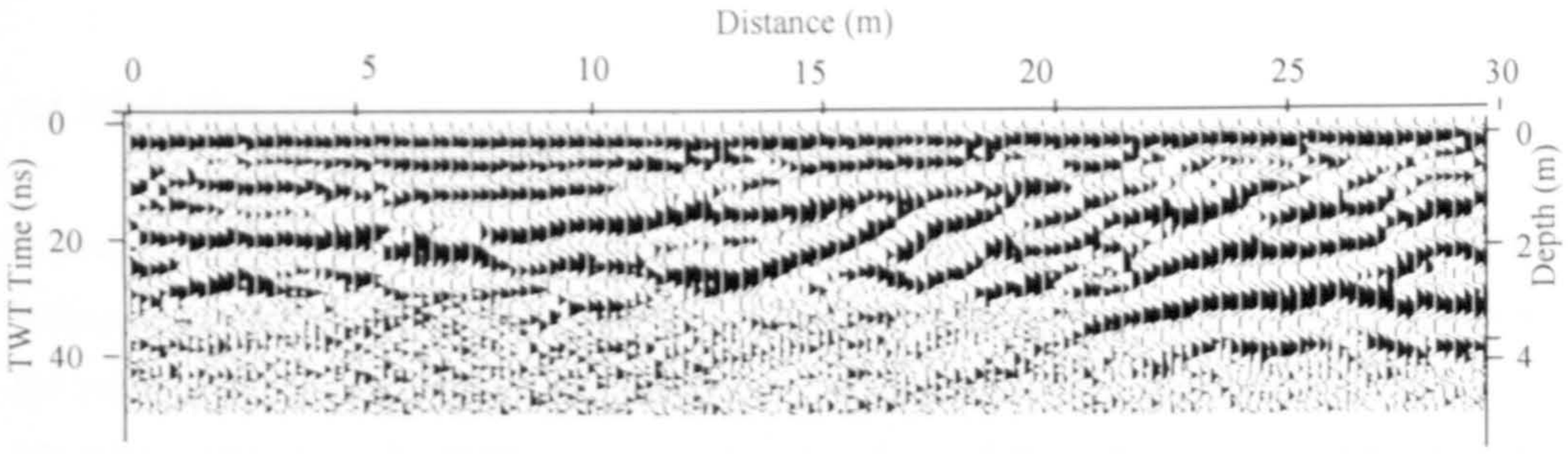

Figure 4.15. Application of Time zero correction and Depth conversion, using Interpex Gradix software.

Spatial and Time filters. Trace to trace (spatial) and down the trace (time) filters may be applied to average across and down the radar image to smooth variation between individual pulses by averaging between adjacent pulses. Figure 4.16 shows the effects of this process.

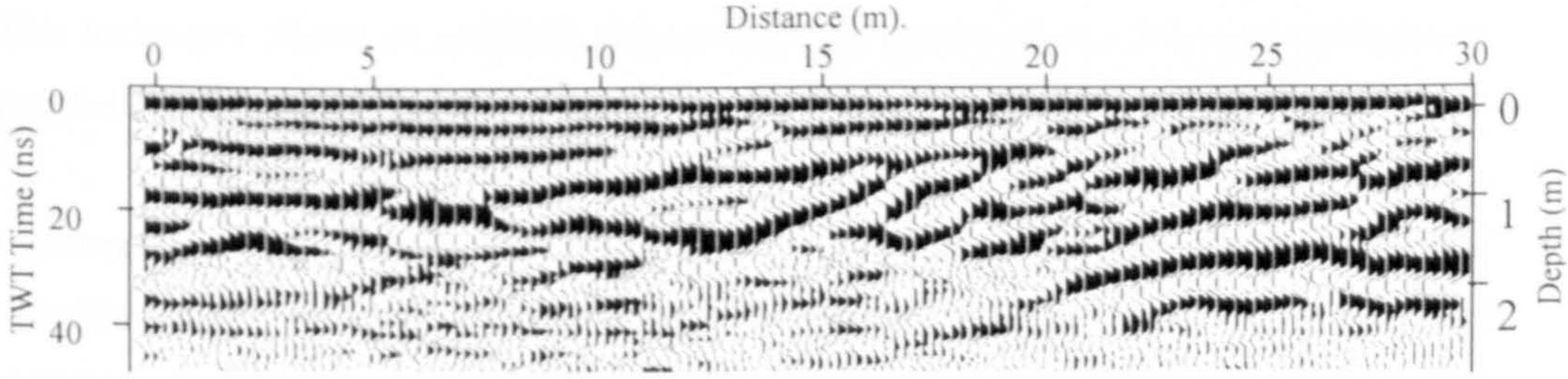

Figure 4.16. Trace to trace and down the trace filters applied using a trace window of 3 traces in Sensors & Software Pulse Ekko software.

The processed result, (Figure 4.16) bears little resemblance to the highly attenuated initial radargram. Sedimentary structure is clearly visible down to a depth of almost three metres, enough for comparison with face logs. This level of processing was applied to all radar images collected, and further processing such as migration and more restrictive filtering of data was rarely done. The traces were sufficiently 'clean' not to require such methods, and in practice the additional methods tended to reduce the resolution of the radar images. This minimal processing approach was successful, and has been utilised by many researchers working in similar environments (Woodward *et al.*, 2003., van Overmeeren, 1998).

4.4 Modelling GPR

In order to better understand the origin of radar reflections in the Sherwood Sandstone, information on the sedimentary structures gained from outcrop observations, plus values for relative permittivity and conductivity at various saturation levels measured in the laboratory (West *et al.*, 2003), were used as input parameters for radar modelling using GPRSIM software (Goodman, 1994). This radar modelling software uses the ray-tracing method, where radar waves are simulated by individual 'rays' projected into the ground at various angles. Refractions and reflections are calculated for each ray at permittivity boundaries according to Snell's Law. The amplitude and frequency for any rays reflected or refracted back to the receiver are logged, the angle of the incident ray is then altered incrementally and the process repeated until all possible raypaths have been used. The transmitter and receiver are then moved to their next location and the process is repeated. This technique allows an artificial radargram to be generated in a manner analogous to real field radar results.

Goodman (1994) provides an explanation of the full theory behind the GPRSIM modelling package but the essential features are presented below. The modelling package simulates the reflection, attenuation and refraction of radar waves in the subsurface. The power reflected from a radar target in a dissipative (lossy) soil (P_r) may be calculated using Equation 4.7; (Goodman, 1994).

$$P_r = \frac{G_t P_t A_e C}{(4\pi)^2 R_t^2 R_r^2} \exp[-2a(R_t + R_r)], \qquad \text{Equation 4.7}$$

where, G_t is transmitter gain, P_t the transmitted power (Watts), R_t the transmitter-target distance (m), R_r the receiver-target distance (m), A_e the effective area of receiving antenna (m^2) and C the target radar cross-section (m^2). A loss coefficient to account for attenuation (a) is also included (see below).

From Equation 4.7, losses due to spherical spreading of the waveform are accounted for by the $(4\pi)^2.R_t^2.R_r^2$ factor. The modelling software also takes account of factors such as the shape and orientation of target reflectors (for detailed description see Goodman, 1994), as well as the relative permittivity (ε), angular frequency (ω), conductivity (σ) and magnetic permeability (μ) of the rock (see section 4.1.). These factors are combined to calculate the loss coefficient (a) using conductive-dissipative wave theory (Goodman, *op.*

cit.) and both real (DC losses) and imaginary (AC polarisation) losses are taken into account. The real part of the attenuation losses are given by Equation 4.8, where ε' is the real part of the dielectric permittivity and tan δ is a loss tangent used to account for frequency-dependant dispersion and DC conduction, and is defined by Equation 4.9, where ε" is the imaginary part of the dielectric permittivity.

$$a = \omega\left(\frac{1}{2}\mu\varepsilon'\left[\left(1+\tan^2\delta\right)^{\frac{1}{2}}-1\right]\right)^{\frac{1}{2}}, \qquad \text{Equation 4.8.}$$

$$\tan\delta = \left[\frac{\left(\sigma+\omega\varepsilon''\right)}{\omega\varepsilon'}\right], \qquad \text{Equation 4.9.}$$

Reflection (Γ) and transmission (T) at interfaces (1 and 2) are calculated using equations 4.10 and 4.11, where Z is the electromagnetic impedance and θ is the incident angle, (equations 4.10. and 4.11. also form the basis for the TDR equations 6.3. and 6.4 see Chapter 6.2.). Equation 4.10, is a more general version of equation 4.5a, accounting for incident angles other than 90^0 and including conductancy effects.

$$\Gamma = \frac{Z_2\cos\theta_1 - Z_1\cos\theta_2}{Z_2\cos\theta_1 + Z_1\cos\theta_2} \qquad \text{Equation 4.10.}$$

$$T = \frac{2Z_2\cos\theta_1}{Z_2\cos\theta_1 + Z_1\cos\theta_2} \qquad \text{Equation 4.11.}$$

Refraction of raypaths at interfaces between two different materials is calculated using Snell's Law. Hence, the GPRSIM software, although using conceptually simple ray-tracing techniques, accounts for many of the factors that affect real radar images. The software models radar target shape, dielectric losses, spherical spreading and attenuation, as well as further factors such as the directional responses of antennae. The main simplifications of the software are that out of plane reflections are not considered (Conyers and Goodman, 1997), dielectric boundaries are assumed to be larger than the radar signal wavelength and the effects of interference between radar rays are ignored (Goodman, 1994). This type of modelling is a simplified version of the real propagation of radar waves, but proved adequate for outcrop-scale modelling of the sedimentary features found in the study area.

In order to select suitable starting models to generate synthetic radar images it was necessary to understand the likely causes of dielectric contrasts in the Sherwood Sandstone. Referring to Chapter 3, clay layers and mudstone clasts (sedimentary facies 3) have a mean d_{50} grainsize of ~75μm, and remain essentially fully saturated in the vadose zone due to capillary held water, which leads to a high dielectric constant. Additionally, swelling clay minerals are present and enhance the dielectric constant further owing to Maxwell-Wagner relaxation effects (West *et al.*, 2001; 2003). This combination of high water content and swelling clays is likely to give these clays very high dielectric constant values, and a value of 50 was assigned for modelling purposes. The laminated fine sandstones (sedimentary facies 2) have a mean d_{50} of ~110μm and contain more fine grained sediments at their tops due to clay and silt infiltration on waning flow. In-situ moisture content measurement at the Great Heck site, using the TRIME TDR packer (see Stacheder *et al.*, 1994 and Chapter 5 for details of this instrument), indicates that this facies is sufficiently fine grained to remain fully saturated in the vadose zone, which is likely to result in dielectric constant values of around 15-30. The trough cross bedded sediments (sedimentary facies 1), which have a mean d_{50} of ~210μm, are sufficiently coarse grained to drain to their residual moisture content of around 10-15% by volume in the vadose zone, which is likely to result in dielectric constant values of around 8 (measured using the TRIME system). The grainsize data also indicates that the tops of the trough units are finer grained than their bases, probably resulting from upwards fining due to leeside avalanching and the possible infiltration of finer particles into the top of the exposed underlying unit in the lee of the next advancing dune. The presence of fine particles in the tops of the cross-sets will greatly reduce pore throat size leading to an increase in capillary moisture retention, producing a dielectric contrast between sets and cosets within sedimentary facies 1.

A series of model geometries were devised in order to investigate the radar signatures produced by the dielectric variations described above (Fig. 4.17, left hand column). A layer of wet fine sand was positioned at the base of each model, representing the dielectric variation across a boundary between two trough cross-bedded units. A variety of sedimentary structures were modelled at a shallower depth, including claystone clasts of varying sizes (both singly and in groups), sandstone and fine sandstone/claystone infilled channels and claystone layers. The electrical properties used for each lithology were as follows:

1) Clean sandstone (free drained), relative permittivity 8, conductivity 0.0067mho m^{-1} (sedimentary facies 1).

2) Fine sandstone (saturated), relative permittivity 16, conductivity 0.017 mho m^{-1} (sedimentary facies 2).

3) Claystone (saturated) relative permittivity 50, conductivity 0.1 mho m^{-1} (sedimentary facies 3).

The relative permittivity and saturation values for free drained clean sandstone and saturated fine sandstone are based on those measured in boreholes at the Heck and Hatfield sites, using a portable Time Domain Reflectometry (TDR) device (manufactured by IMKO, Germany). Conductivity values used are estimates based on laboratory measurements conducted by Jared West at the University of Leeds, on sandstone cores using a four-electrode measurement system.

Figure 4.17 shows the input models, an amplitude vs. two-way travel time GPR simulation, and also the return waves arriving at the receiver from each dielectric interface. The first input model (Figure 4.17a.), shows three different objects, a small clay clast, a larger clay clast and a group of clay clasts all set within a free-drained sandstone matrix. The GPR simulation returns two very similar, strong, reflections for the two single clasts, which would be expected as the GPRSIM software model assumes that the dielectric boundaries are of sufficient size to cause reflections. The returns column shows two very clear hyperbolae (H) from the two clasts, with the hyperbola from the larger clast being better formed as a result of its larger upper surface area. The final object, the group of clasts, produces a mass of overlapping hyperbolae both on the GPR amplitude simulation and the returns plot. The truncation of some of the hyperbolae and GPR returns is likely to be an artefact caused by the inability of the ray-tracing method to image diffractional spreading.

The second input model (Figure 4.17b.), shows a fine-grained, wet sandstone channel set within a free-drained sandstone matrix. The GPR simulation images the channel clearly, although some evidence of hyperbolae (H) may be seen from the channel margins. A slight 'push-down' of the underlying dielectric boundary (P) may also be seen as a result of the decreased radar wave velocity in the wet sandstone. Also visible is a phase change (PC) associated with the transition from wet to dry sand, with the associated change in ε_e. The returns column shows the individual reflections which were combined to form the radar image. The GPR image consists of reflections from the channel top (T), the channel base (B), with a multiple reflection caused by signal reverberation within the channel (M) and two hyperbolae (H) from the margins of the channels.

The third input model (Figure 4.17c.), shows a fine-grained, clay or siltstone filled sandstone channel set within a free-drained sandstone matrix. Again, the GPR image shows this feature clearly, but not as clearly as Figure 4.17b. The reason for this is apparent in the returns column. The GPR image results from reflections from the top of the channel and a truncated reflection from the base, but is complicated by the presence of several strong hyperbolae from the channel margins and a multiple reflection from within the channel. A more pronounced push-down may be seen in the reflection from the surface of the underlying wet sandstone layer. The reason for this push-down being greater than in Figure 4.17b, above is that the radar wave velocity will be slower in the clay/silt than in the sandstone. Unless data regarding the velocity variation described above are input into a site velocity profile, the plotting software will assume too high a velocity for waves travelling through the low-velocity horizons. Hence, reflections from beneath a clay or silt layer will tend to be plotted deeper than they truly are, unless the variation of radar velocity in different sediments is accounted for. The returns from the underlying wet sandstone layer are also attenuated (A), plotting as weak reflectors because of signal attenuation in the clay/siltstone lens. The phase change associated with the change in polarity of the reflection coefficient (R) is also apparent as the sediments move from dry→wet to wet→dry interfaces between units.

Figure 4.17d. shows two thick horizontal layers, one of clay/siltstone and one of wet sandstone set within a free-drained sandstone matrix. Again, the GPR simulation is a composite of radar reflections from the top of the layers, their bases, one hyperbola and very strong multiple reflections, with the phase change (PC) associated with polarity variation in R. The velocity push-down from these thicker layers is so pronounced that the reflection from the underlying wet sandstone layer cannot be seen.

This ray-trace modelling has identified three key features that have been observed in both simulated and real radar images (Table 4.17.):

1. Claystone clasts produce hyperbolae at depth and groups of claystone clasts give rise to 'noisy' areas of many overlapping hyperbolae (Fig. 4.17a).
2. Channels are visible whether they are infilled by fine wet sandstone or claystone; (Figures 4.17b. and 4.17c). Such channels may, however, obscure features that lie beneath them or cause apparent depths to the underlying features to increase, particularly where the channels are infilled by claystone.
3. Claystone layers are highly attenuative and cause significant multiple reflections whilst obscuring the underlying structure (Fig. 4.17d).

A summary of the radar modelling results is given in Table 4.5.

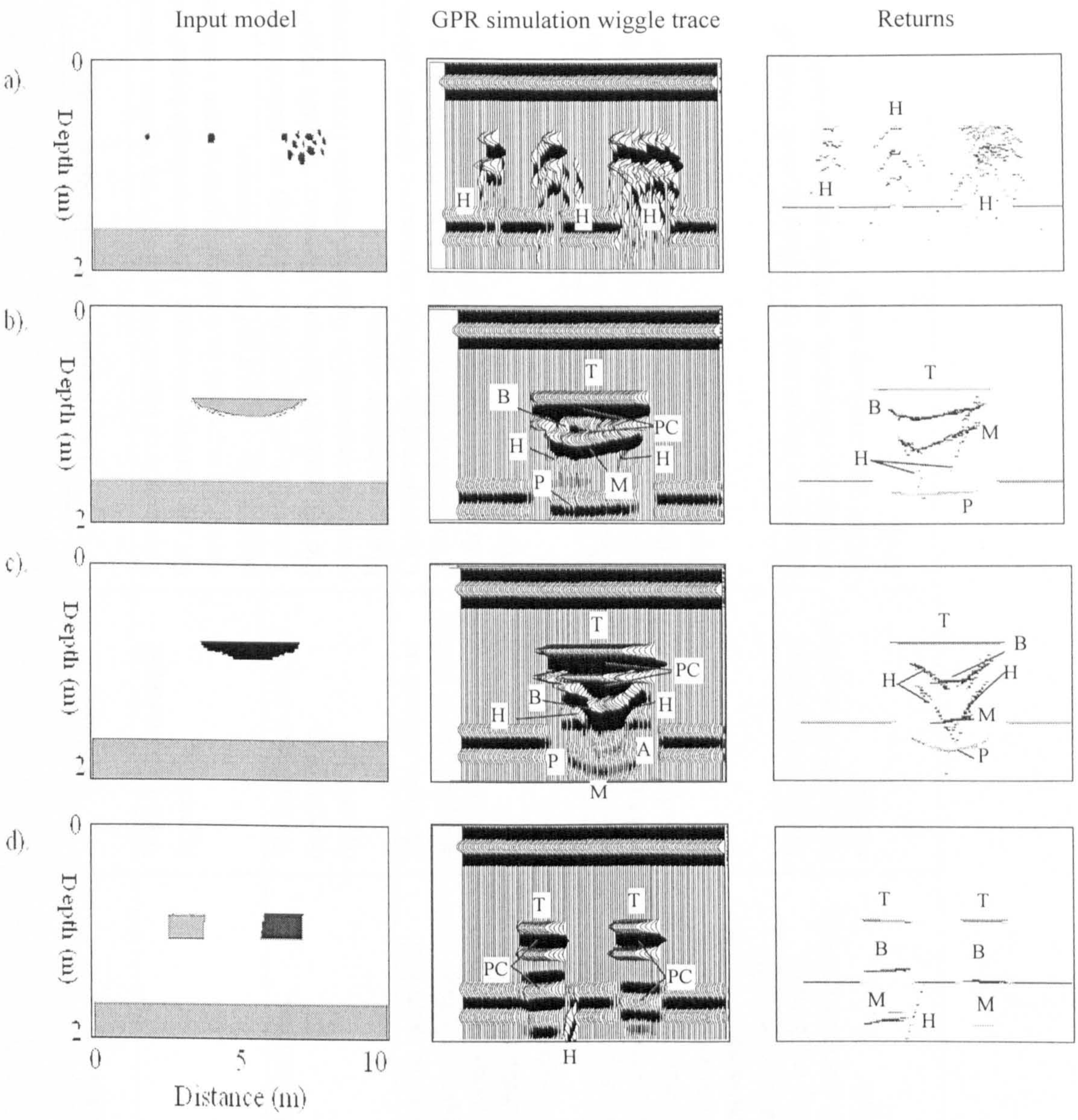

Unit 1	Free drained sandstone,	Relative permittivity 8,	Conductivity 0.00667mho m^{-1}
Unit 2	Fine/wet sandstone,	Relative permittivity 16,	Conductivity 0.017mho m^{-1}
Unit 3	Clay/siltstone,	Relative permittivity 50,	Conductivity 0.1mho m^{-1}

Figure 4.17, Modelling results using GPRSIM.
The sedimentary features that were modelled are shown in the first column of Fig. 4.1.1. a) Claystone clasts and groups of clasts in free-drained sandstone. b) Wet sandstone channel in free-drained sandstone. c) Clay/siltstone infilled channel in free-drained sandstone. d) Clay/siltstone and fine sandstone layers in free-drained sandstone. The dielectric and conductive properties of the modelled units are shown in the key.

Figure	Input Model Description	GPR Simulation	Returns	Implications for field radar images
4.4.1.a	Single Claystone clast (sedimentary facies 1b)	Single truncated hyperbola	Well-formed single hyperbola	Truncation of hyperbola probably an artefact caused by the ray tracing technique. However single hyperbolae would be expected in field radargrams from a single high permittivity clast of sufficient diameter.
4.4.1.a	Multiple Claystone clasts (sedimentary facies 1b)	'Rough zone' of overlapping hyperbolae, somewhat truncated.	Well-formed zone of overlapping hyperbolae.	Truncation of hyperbolae probably an artefact caused by the ray tracing technique. However multiple hyperbolae would be expected in field radargrams from a group of high permittivity clasts.
4.4.1.b	Fine wet sandstone filled channel (sedimentary facies 2)	Channel reflectors tend to be strong, with high amplitudes. Well-defined channel showing multiple reflections caused by radar 'rays' being internally reflected within the channel. Noticeable 'push down' and attenuation of signal returned from underlying reflectors.	Multiple reflections and push down clearly visible.	Channels may be visible as concave upward reflectors, with internal structure. Push down of underlying reflectors and multiple reflections would also be expected.
4.4.1.c	Claystone filled channel (sedimentary facies 4)	Channel reflectors tend to be strong, with high amplitudes. Well-defined channel showing many multiple reflections caused by radar 'rays' being internally reflected within the channel (as 13b). Stronger 'push down' and attenuation of signal returned from underlying reflectors than 13b	Multiple reflections and strong push down clearly visible.	Channels may be visible as concave upward reflectors, with internal structure. Push down of underlying reflectors and multiple reflections would also be expected.
4.4.1.d	Claystone and fine wet sandstone layers (sedimentary facies 2 and 3)	Hyperbolae visible at ends of layers. Strong multiple reflections. Reflectors tend to be strong, high-amplitude and well defined.	Multiple reflections and push down clearly visible	Claystone layers may be visible by push down of underlying reflectors, multiple reflections and hyperbolae marking their ends.

Table 4.3. Summary of radar modelling results.

4.5. Results of GPR surveying in the Sherwood Sandstone

Van Overmeeren (1998) defines radar facies as 'the sum of all characteristics of a reflection pattern produced by a specific rock formation or by a sedimentary sequence. The term radar facies thus refers to visible differences in the reflection pattern of a GPR section.' This definition is applicable to the Sherwood Sandstone, and production of a radar facies formed a central part of the radar work reported here.

This section presents a range of radar images, from Great Heck, Hatfield, Pollington and Rufford quarries, and interprets them in light of known sedimentary structure, before defining GPR facies and presenting images showing the linking of these facies in the radargrams. By comparing radar images with known features in outcrop and cliff faces it has been possible to,

a) Define a radar facies scheme for the study area.

b) Produce a detailed radar log of the subsurface at the Great Heck test site.

c) Produce interpolated images showing 3-D sedimentary structure from closely spaced radar lines.

These results may then be combined with borehole logs and complimentary geophysical data from previous chapters to produce a comprehensive summary of the hydraulic properties and sedimentary structure of the Sherwood Sandstone (see Chapter 5).

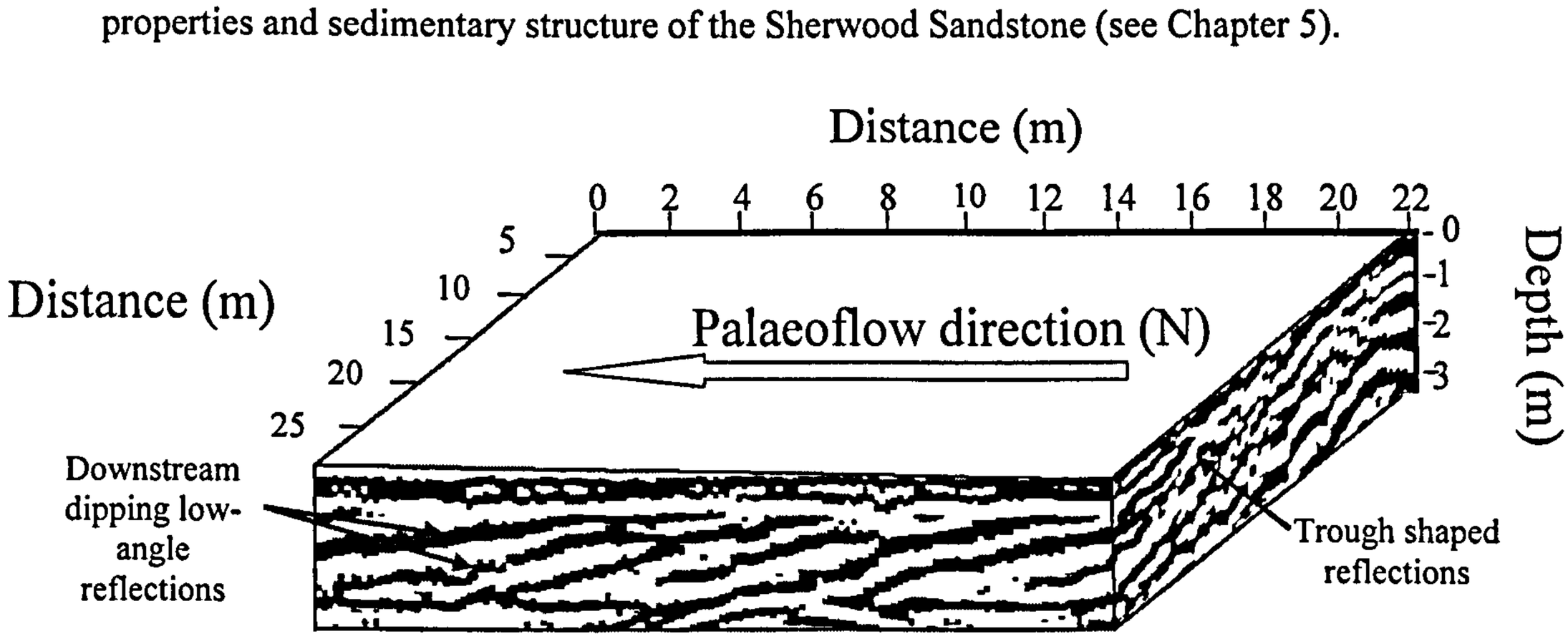

Figure 4.18. 3D radar view of trough cross beds from Heck Quarry Grid (SE 588213) at 200MHz, 0.5m spacing between lines, standard processing (see section 4.3).

Figure 4.18 shows a typical 3-D block through a series of trough cross bedded units, interpolated perpendicular to palaeoflow using (Pixotec LLC.) Slicer-Dicer software. The GPR reflections are interpreted as low angle cosets, parallel to palaeocurrent, with trough cross-stratification being visible perpendicular to palaeocurrent.

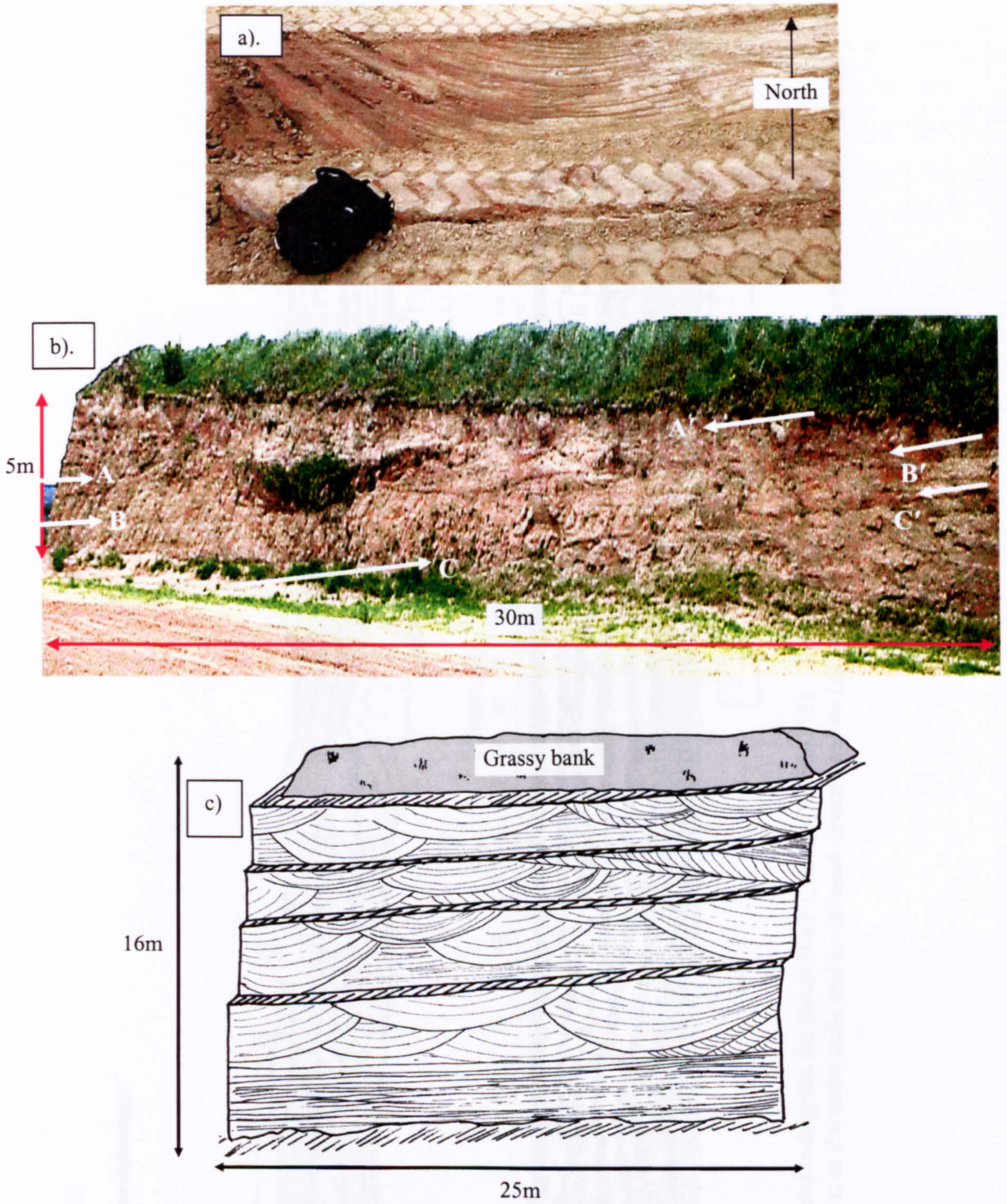

Figure 4.19. Sedimentary structure of trough cross stratified units. a) Plan view photograph from Hatfield quarry (SE 653075), showing trough crossbeds with curved upper surface pattern; rucksack for scale. b) Laterally continuous dipping cosets (A-A′, B-B′ and C-C′ at Rufford quarry (SK 596608), palaeoflow from right to left. c) Trough cross-stratification from north wall, Great Heck quarry (SE 588213).

The same features as those seen in Figure 4.18. are visible in Figure 4.19. A plan view of a trough cross-stratified quarry floor is shown in a), showing a characteristic semi-circular foreset pattern. Trough cross-stratified units are visible in c), with b) showing low angle cosets. By comparison between the features shown Figures 4.18 and 4.19, it is apparent that the radar image is depicting features that may be directly observed at outcrop.

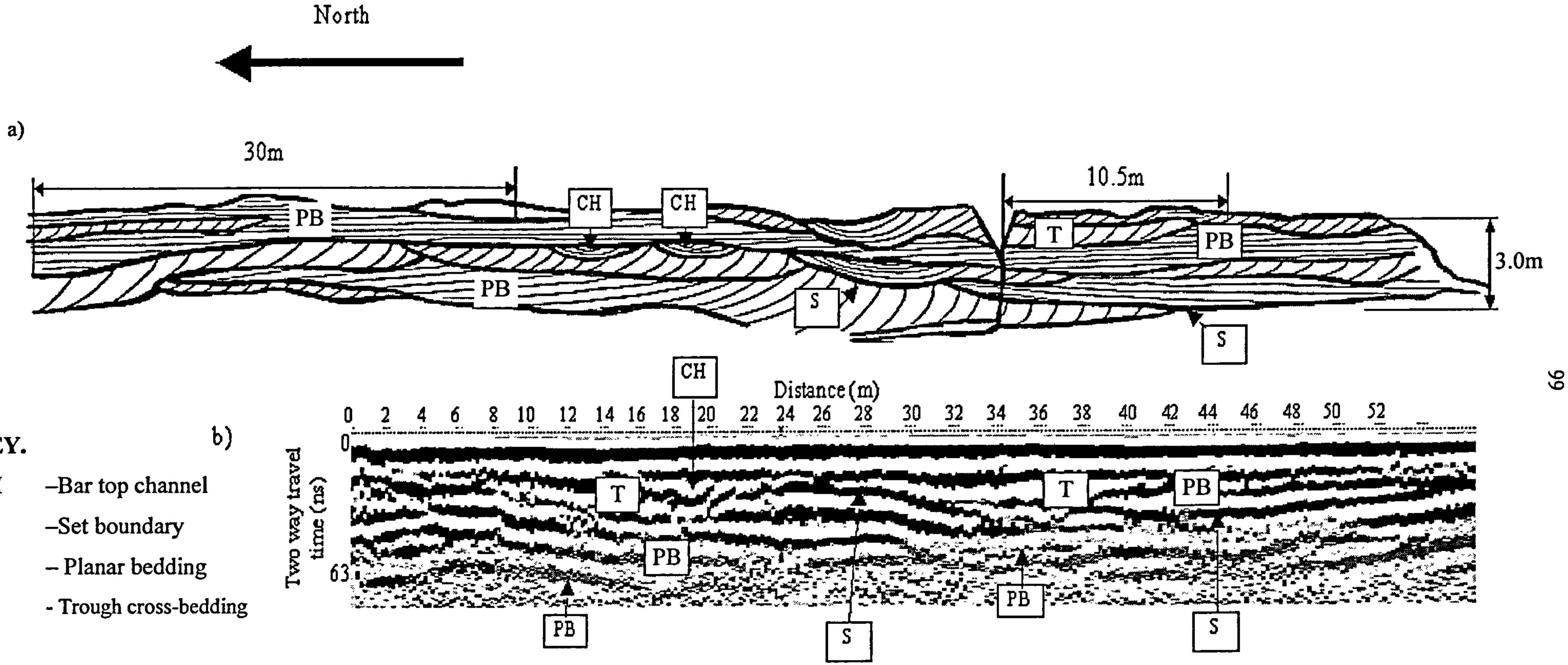

Figure 4.20, Comparison of field sketch and radargram for Great Heck Quarry (SE 588213)
a) Field sketch b) Radargram at 200MHz, at the same scale and positioned directly below (a) enabling correlation between sedimentary and radar features.

The radar image from Great Heck (Figure 4.20b) is effectively a simplified version of the field sketch (Figure 4.20a), where the dominant lithology is trough cross-bedded medium grained sandstone. Comparison with the field sketch shows that coset boundaries (S) and higher order bounding surfaces are visible in the radargram, but individual foresets are not visible. The two adjacent channel/scour features shown on the field sketch are visible on the radar image (CH) as a single large channel/scour feature.

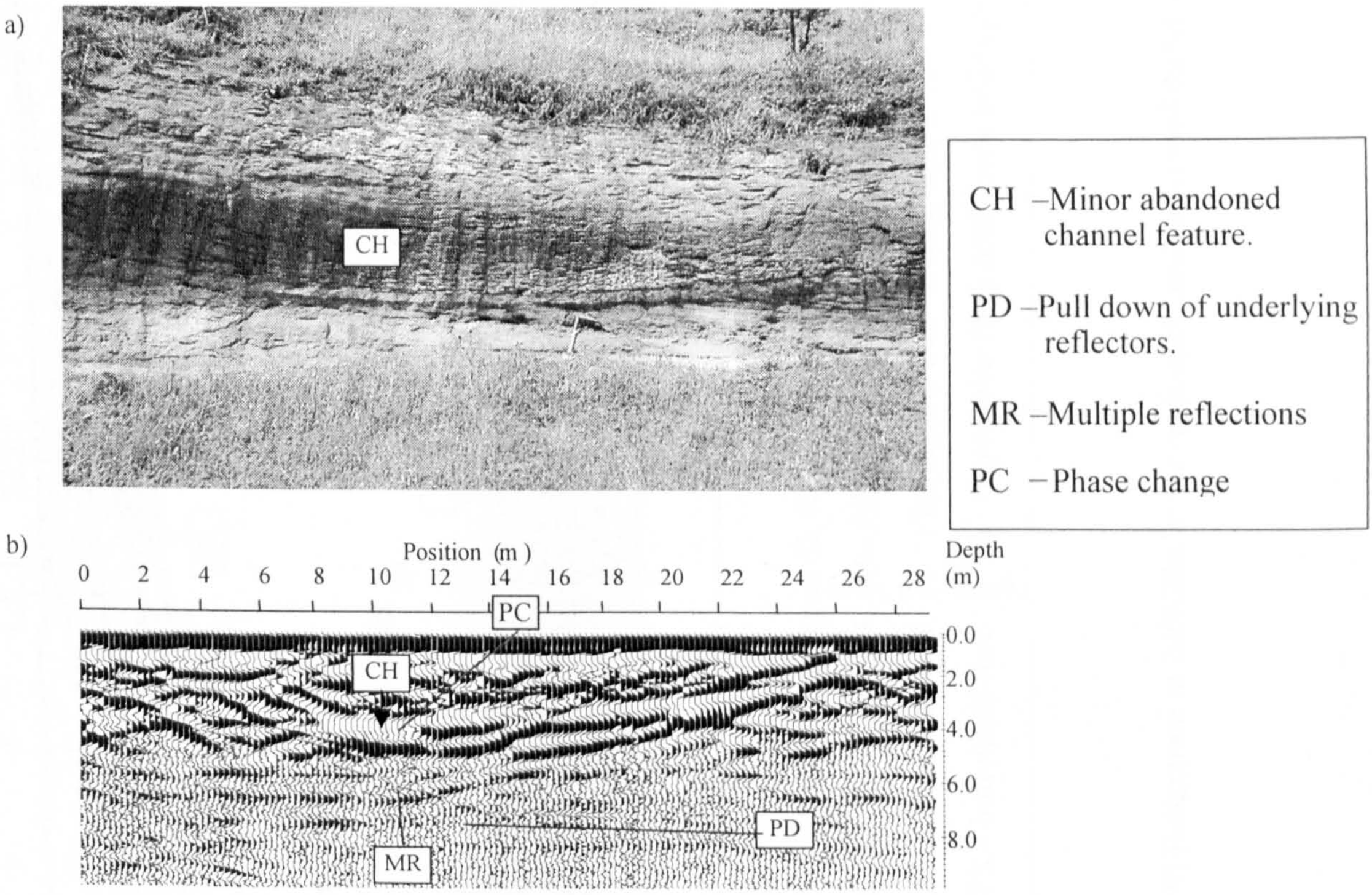

Figure 4.21. Channel at Pollington Quarry (SE 612201) a). Photograph of channel feature. Note hammer for scale. b). Radargram at 200MHz taken parallel to (a) but set 5m behind face.

Figure 4.21a shows a photograph of a larger, although still minor, channel filled with silty, fine grained sandstone and Figure 4.21b shows the corresponding radargram taken 5m back from the cliff edge. The channel feature (CH) is plainly visible in the radargram, as is the 'push-down' of the underlying reflectors (PD), caused by the slowing of the EM waves in the channel fill. The internal structure of the channel is indistinct due to multiple reflections (MR) from within the channel, attenuation, and distortion owing to the 'push-down' effect. There is a phase change (PC) of the returned radar wave, associated with the change from wet to dryer sediments as the radar waves leave the channel. These results appear very similar to the modelling results for channels (see Section 4.4).

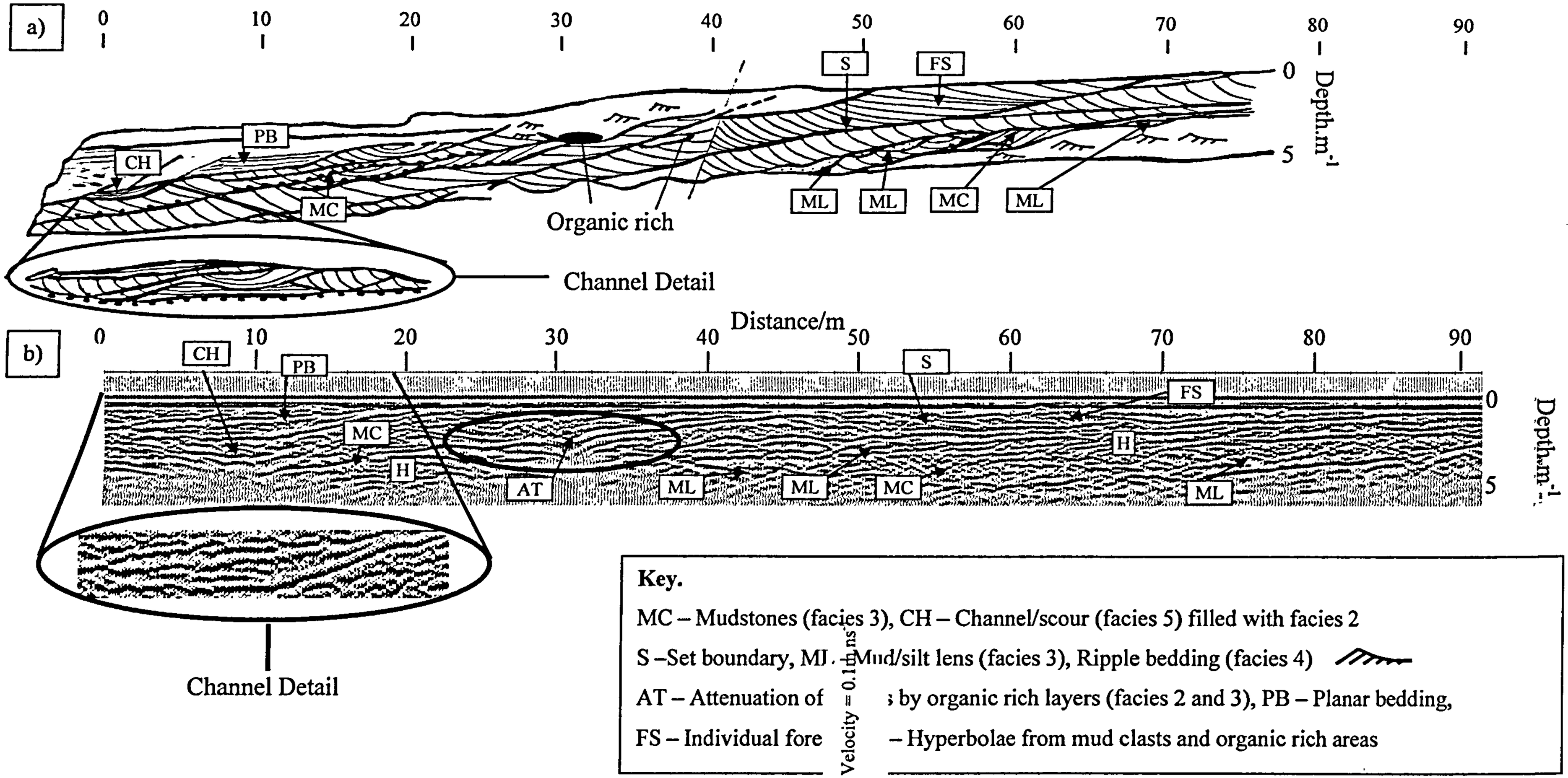

Figure 4.22. Face at Rufford Quarry (SK 596608) a) Field sketch b) Radargram at 200MHz, at the same scale and positioned directly below (a).

The sketch logs from an east facing quarry wall at Rufford quarry (Figures 3.10 and 4.22a) show a variety of features, most of which are visible in the radargram (Figure 4.22b). The channel feature (CH) is filled with clay rich, fine-grained sandstone (facies 2), and is plainly visible, as are many of the set boundaries (S) within facies 1. Two zones with abundant pebbles and mudstone clasts (MC) appear on the radar image as 'rough zones' with many overlapping hyperbolae. The edges of claystone/siltstone lenses consisting predominantly of facies 2 with occasional facies 3 also produce hyperbolae on the radargram (ML), and some of the organic rich layers cause attenuation of the underlying reflectors, as well as velocity push-downs. Ripples (facies 4) are seen on the face log but are not resolved on the radar image. Further features of note on Figure 4.22b are:

1) Individual foresets (FS) are visible. This resolution of features within individual sets is unusual within the study area and denotes an exceptionally clean radar image, with the foresets imaged occurring near the surface, just within the imaged area.
2) Hyperbolae and push-downs from organic rich layers.
3) Hyperbola-rich areas correlating with zones with abundant mud clasts.

4.5.1. GPR Facies.

Interpretation of radar images allows a radar facies scheme to be defined. The facies visible in radar images may then be compared with field sketches and modelling results in order to relate the radar facies with the sedimentary facies, allowing lithology to be directly interpreted from radar images.

GPR Facies 1. The easiest GPR facies to identify is seen on radar images as trough shaped reflections. Principal diagnostic features are the low-angle reflections orientated parallel to palaeocurrent that are laterally continuous over tens of metres, and the trough-shaped reflections orientated perpendicular to palaeocurrent which are usually less than 10 metres across (see Figure 4.18). Figure 4.22 shows foresets (FS) in GPR facies 1, which can be distinguished from sets and cosets by their higher dip and low lateral continuity, however GPR images of individual foresets are rare for the Sherwood Sandstone in the study area. Comparisons between field sketches and the corresponding GPR images shows that radar facies 1 is equivalent to sedimentary facies 1, trough cross-bedded sandstone.

GPR Facies 2. Planar-bedded fine sand/silt layers (PB) are identifiable as extremely strong, laterally continuous over a scale of tens of metres upwards, sub-horizontal radar reflections (Figures 4.20a; 4.20b; 4.22a; 4.22b). These strong reflections often show little visible detail below them, because the radar energy does not penetrate far into these units. Furthermore, facies 2 often shows push down of underlying reflections (Figures 4.21b; 4.22b). GPR facies 2 is equivalent to sedimentary facies 2, fine grained upper-flow deposits.

GPR Facies 3. Clasts and groups of clasts may be identified in radar section by the hyperbolae that they produce at depth (Figure 4.22b). These clasts also produce strong push down effects on the underlying reflections, with marked attenuation of the signal from below and strong multiple reflections (Figures 4.21b; 4.22b). GPR facies 3 is equivalent to the facies 1bobserved at outcrop and may consist of either pebble-rich or mudstone/claystone intraclast-rich layers.

GPR Facies 4. Larger scale claystone/mudstone layers are visible in radar images as strong reflections, often marked by a single hyperbola at each margin, with marked attenuation of underlying reflections (See 'AT', Figure 4.22b)

GPR Facies 5. This facies is identified in radar images as distinctive concave-upwards, incised channel forms, which may be filled with any of the other GPR facies (Symbol CH on Figures 4.20; 4.21; and 4.22). These channels may be recognised by their overall shape, or by the effects of the fill material (increased attenuation, push downs, multiple reflections). GPR facies 5 is equivalent to sedimentary facies 5.

This radar facies scheme and its links to the sedimentary facies for the Sherwood Sandstone in the study area enable individual radargrams to be examined in order to evaluate their subsurface structure where cut faces are not available. This accuracy may be further improved if:

1) Radar lines that were collected perpendicular to each other on the same day are evaluated separately, and the results then compared. Individual imaged sedimentary features should correlate closely between separate lines. However, this technique may cause problems if the lines were collected over a period of time as changes in groundwater conditions will affect the radar images and may potentially create inaccuracy.

2) Lines are collected as a radar grid, and then interpolated to form a block.

4.5.2. Detailed radar log of the subsurface at the Great Heck test site.

Line HEKGD_AA, (Figure 4.23) which was used as the example line for the data processing section (4.3) was collected at the locations of TDR boreholes TDR 1, 2, 3 and 4, which makes understanding of the subsurface at this location very important. The radar images were processed in a standard manner, as described in section 4.3.

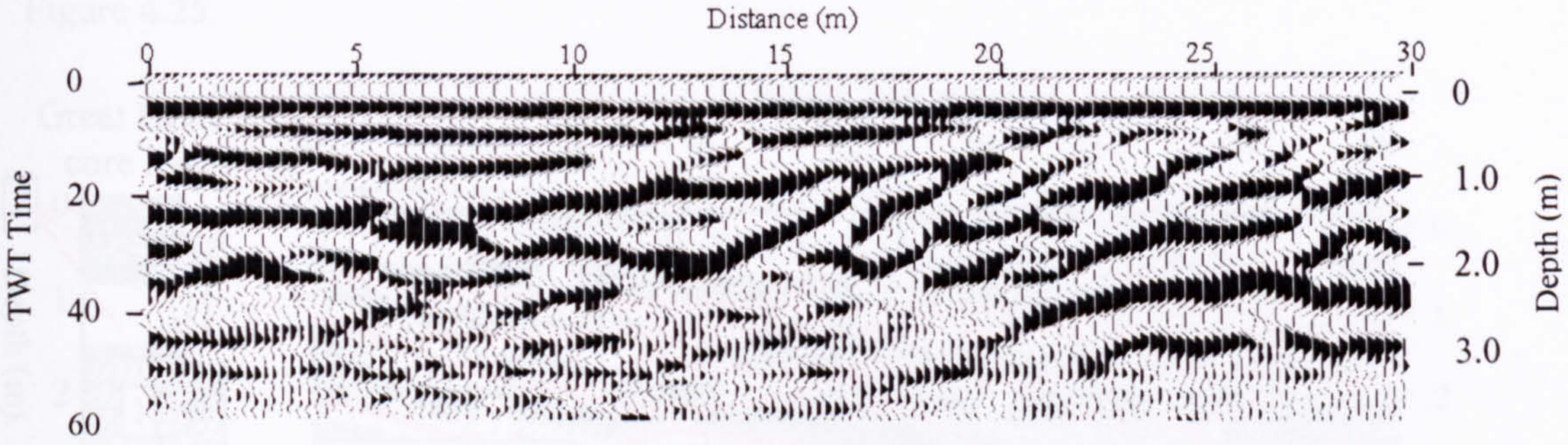

Figure 4.23. Radar line HEKGD_AA, 200MHz, standard processing, parallel to palaeocurrent (right→ left).

The major boundaries (red lines) and areas of increased attenuation (green shading) were manually picked and borehole locations (vertical blue lines) added (Figure 4.24).

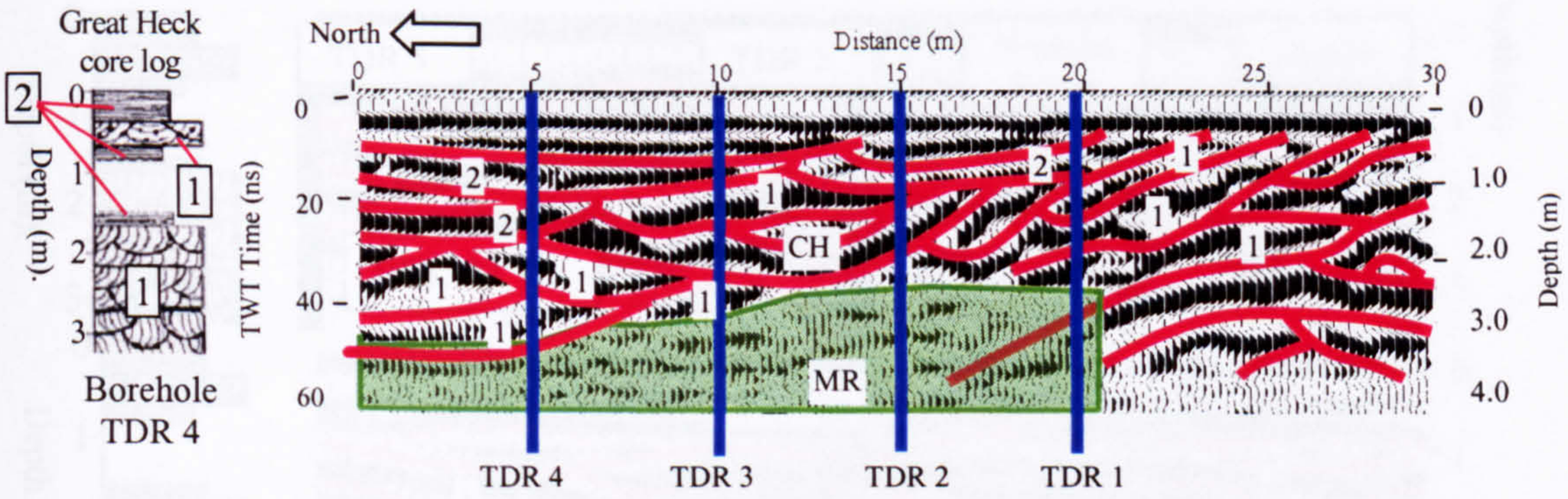

Figure 4.24. Interpretation of radar line HEKGD_AA, with core log taken from borehole TDR4.

The radargrams were interpreted using the radar facies scheme derived above. CH denotes a possible channel feature (radar facies 5) and the presence of increased attenuation and multiple reflections matching the channel (MR) suggests that this channel is filled with wet, fine, silty sandstone. The numbers superimposed on the radargram indicate the interpretation of the pattern of reflectors in terms of facies 1 and 2. Hence, the suspected lithology directly under the Heck test site is a mixture of radar facies 1 and 2, with radar facies 2 being more abundant to the north and in the upper metre of the image.

The radar only provides lithological information at this high (200MHz) frequency down to about 3m depth.

A similar approach may be taken with radar lines HEKG2_A, B, C, and D, which cross Figure 4.24 at the boreholes shown at 90^0. The boreholes are 5m apart and the core log shown was based on the core extracted from borehole TDR 4. These are shown below in Figure 4.25.

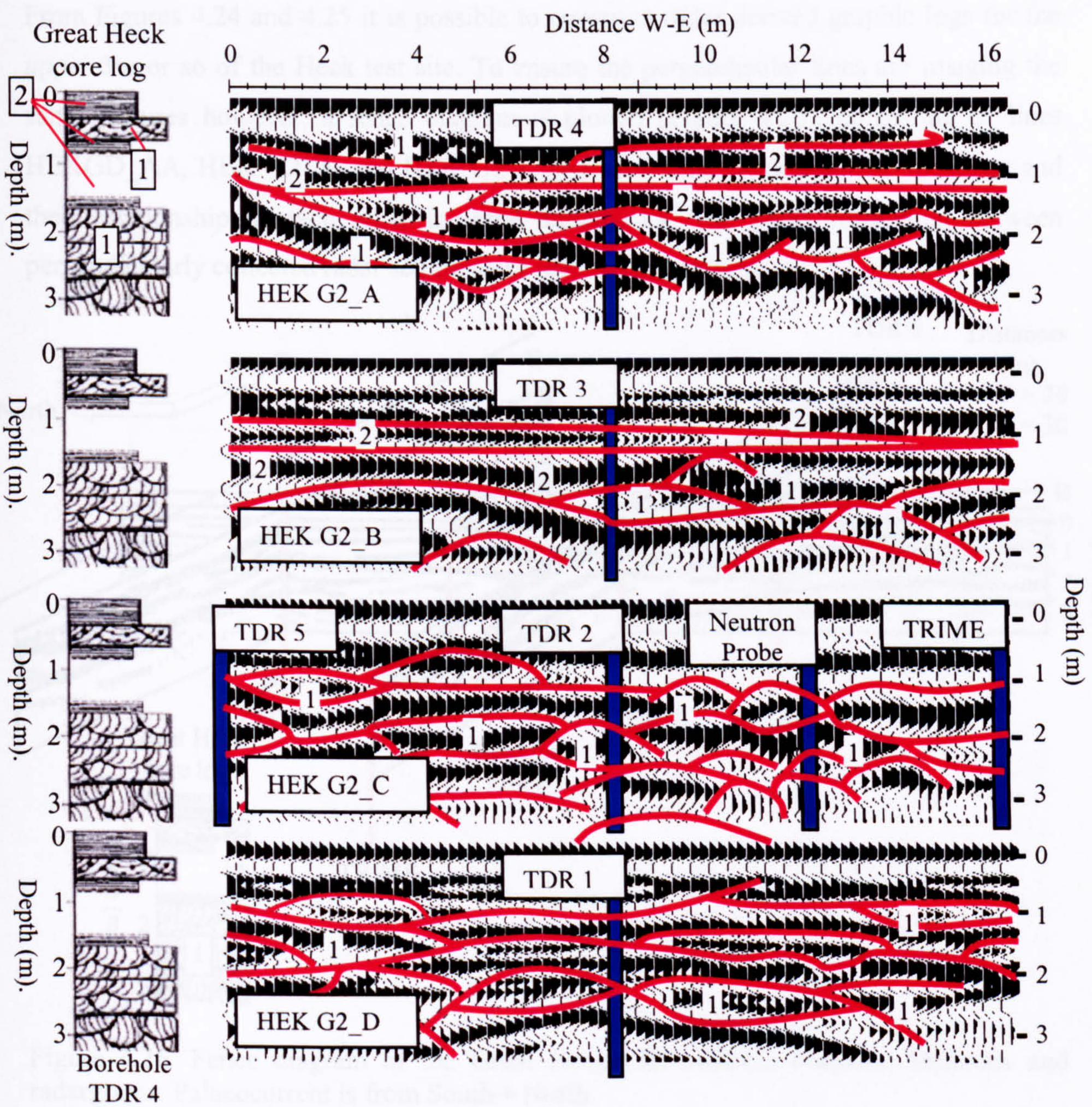

Figure 4.25. Interpreted radar lines HEK G2, A-D collected at 200MHz, in a West→East direction, with standard processing. 1) denotes trough cross bedded units (GPR facies 1), 2) denotes planar bedded units (GPR facies 2).

The various radar lines shown in Figure 4.25. are described in Appendix 1, and are interpreted as:

- G2_A is from the northern end of Figure 4.24, and shows trough cross bedded units at the base, with planar units above.

- G2_B is from 5m south of G2_A, and shows a similar pattern of trough cross beds with overlying planar beds.
- G2_C is from 5m south of G2_B, and shows large quantities of trough cross bedding only.
- G2_D is again from 5m south of G2_C, and shows similar trough cross bedding to G2_C.

From Figures 4.24 and 4.25 it is possible to construct radar derived graphic logs for the upper 3m or so of the Heck test site. To ensure the perpendicular lines are imaging the same features however, a fence diagram is plotted (Figure 4.26), consisting of lines HEKGD_AA, HEK G2_A, and HEK G2_C and shows the Heck borehole locations and their relationship to each other in three dimensions. The good correlation between perpendicularly collected radar sedimentary features is apparent.

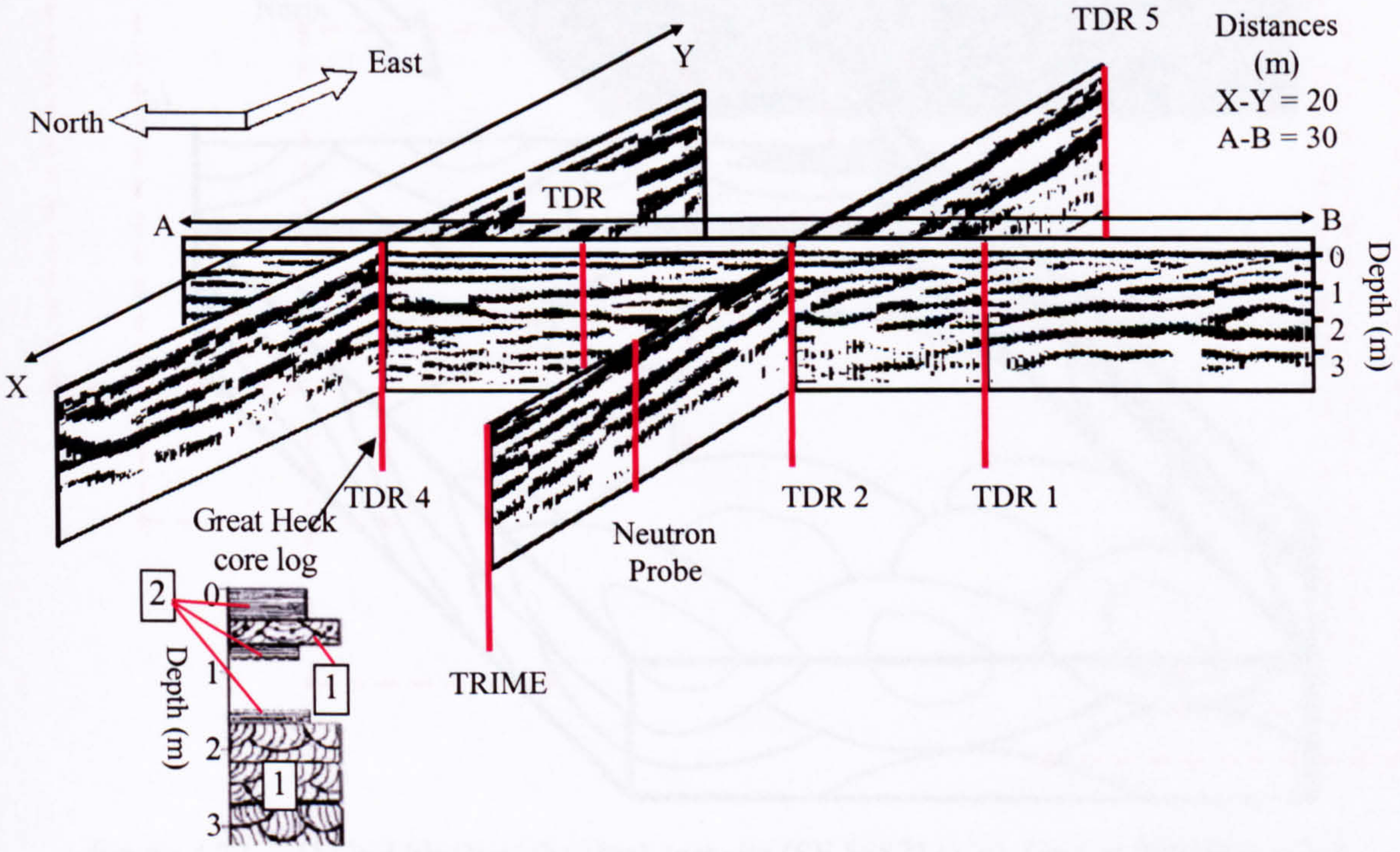

Figure 4.26. Fence diagram of the Great Heck (SE 588213) borehole locations and radargrams. Palaeocurrent is from South→ North.

4.5.3. 3-D sedimentary structure at Heck test site.

From combining 48 radar lines taken at 0.5m spacing, both in N→ S and W→ E directions it was possible to create a 3-D block of the Heck test site which may be sliced or cut to show detail in any direction (e.g. Figure 4.18). Figure 4.27 shows one of these blocks cut

in various ways to show various aspects of the radar derived sedimentary structure of the test site.

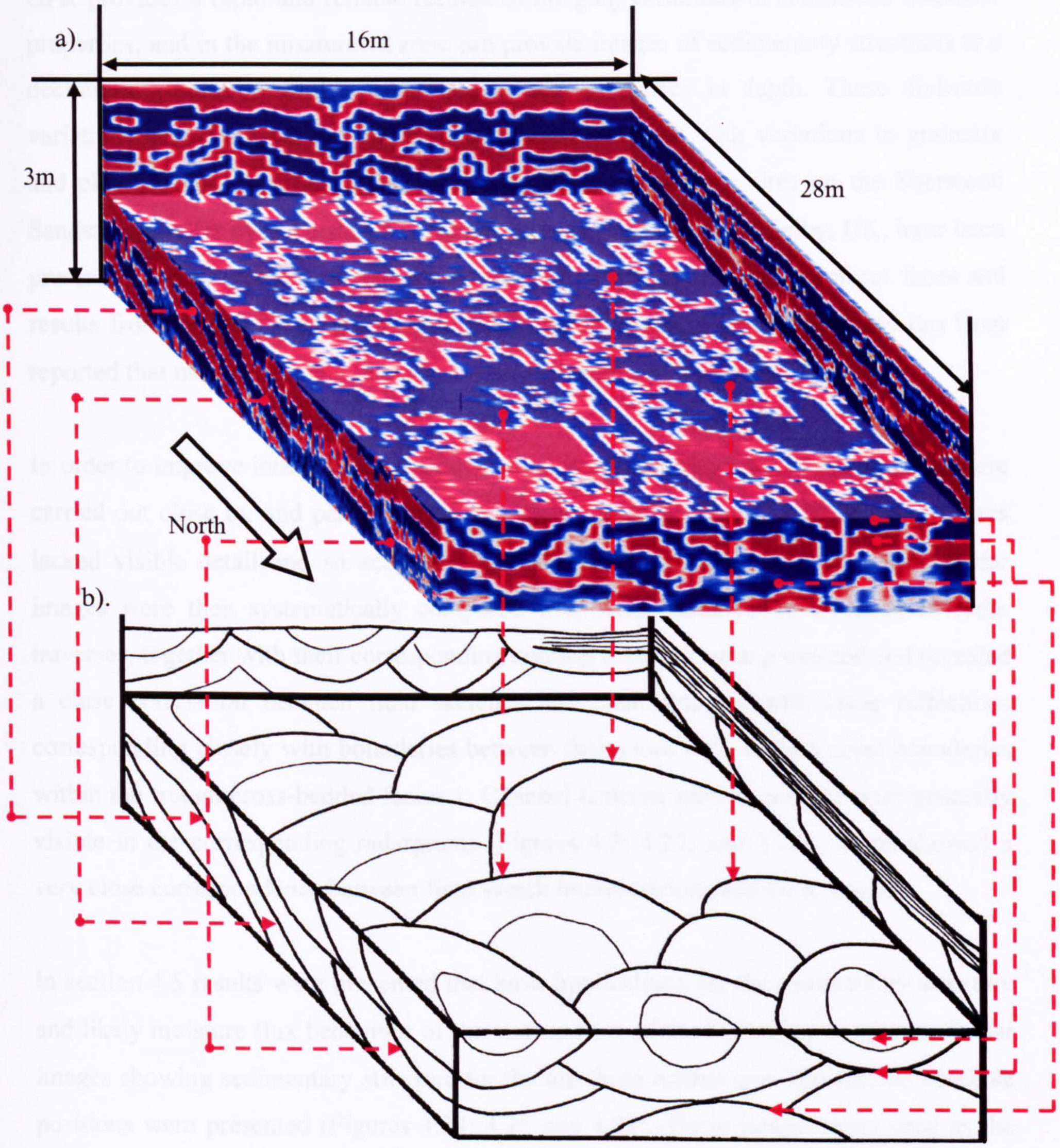

Figure 4.27. 3-D Grid block of the Heck test site (SE 588213). a). Grid at 200MHz, 0.5m spacing between lines, standard processing (see section 4.3). b). Interpretation of a) highlighting the correlation between radar lines in the X, Y and Z directions and showing abundance of trough cross-bedding.

The block shown in Figure 4.27a has been depth sliced to approximately 1.75m and shows the trough cross bedding structures that occur at this depth beneath the entire Heck test site. The blocky nature of the image is due to the limited ability of the interpolation software to smoothly link features between adjacent radar lines. However, the size, orientation and relationship between units can be clearly seen, and this has been interpreted in Figure 4.27b.

4.6 Summary

GPR provides a rapid and reliable method of imaging variations in subsurface dielectric properties, and in the unsaturated zone can provide images of sedimentary structures to a decimetric resolution whilst penetrating to several metres in depth. These dielectric variations arise from varying moisture retention associated with variations in grainsize and clay content. A variety of radar images, taken from three sites on the Sherwood Sandstone aquifer over a distance of 70 km between Mansfield and Selby, UK, have been presented and interpreted, together with field observations from adjacent cut faces and results from an associated grainsize analysis. Additionally, a modelling study has been reported that used ray tracing to assist in survey design and interpretation.

In order to improve interpretation of the features seen in radargrams, radar traverses were carried out close to, and parallel to, accessible rock faces. Photographs of the cut faces lacked visible detail and so accurate field sketching proved the best approach. Radar images were then systematically compared with field sketches. A selection of radar traverses, together with their corresponding outcrop sketches were presented and revealed a close correlation between field sketches and radar images, with radar reflections corresponding closely with boundaries between facies and with set and coset boundaries within the trough cross-bedded facies 1. Channel features seen in outcrop were generally visible in the corresponding radargrams (Figures 4.2; 4.21; and 4.22), which showed a very close correspondence between field sketch interpretations and GPR images.

In section 4.5 results were presented that have implications for the sedimentary structure and likely moisture flux behaviour of the vadose zone of the Sherwood Sandstone. Radar images showing sedimentary structure for the top three metres over the various borehole positions were presented (Figures 4.24; 4.25 and 4.26). These images were used as the source data for grainsize graphic logs in the standard format used previously. Similar to the core (Figure 3.26) and gamma logs (Figure 3.28) presented previously, the radar borehole logs are a representation of the units thought to be present in the subsurface. These logs are presented below in Figure 4.28.

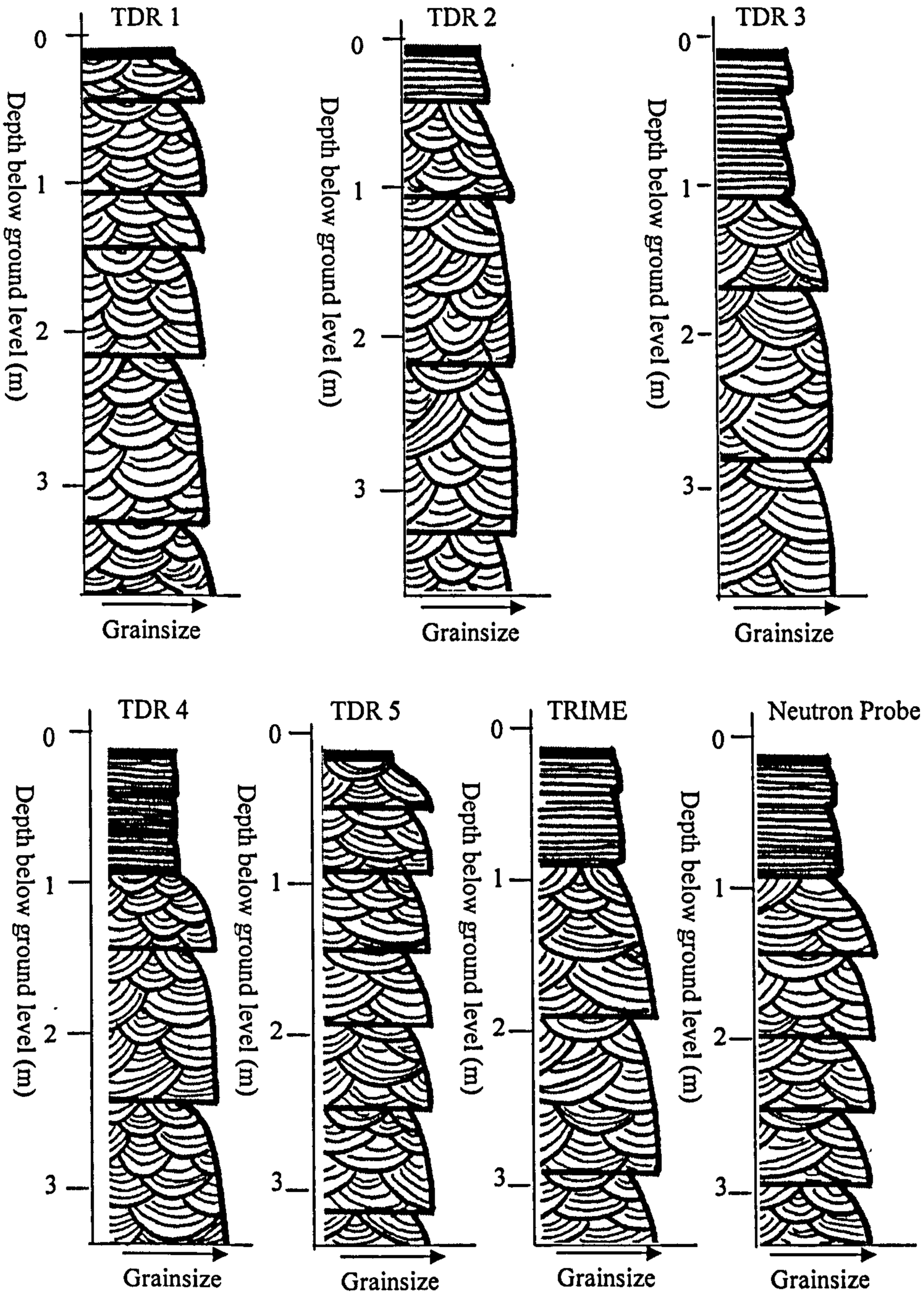

Figure 4.28. Radar derived grainsize logs for Great Heck test site (SE 588213) using stylised fill.

Assumptions made when constructing the radar logs (Figure 4.28), were that trough cross bedded units tend to fine upwards (see sedimentary and core logs in Chapter 3). Individual dune bedforms within a facies unit were split up according to coset locations inferred from the radargram and planar laminated units were assumed to be finer-grained than the trough cross-bedded units (as determined in Chapter 3).

Figure 4.29 shows likely moisture flux pathways within trough cross-bedded units. These pathways may be of great significance with regard to seepage velocity and direction of moisture en route to the water table. It is possible that flow is confined to the coarser grained lag deposits found at the bases of the trough cross-bedding, and may also flow along the tops of finer grained planar units. Hence, once the sedimentary structure from Figure 4.27 is investigated (as in Figure 4.28 below), 3-D blocks allow possible directions in which moisture may move through the sedimentary structure of the test site to be inferred. Radar images show that 'sheets' of planar laminated facies 2 are present under the test site and it is possible that these units will restrict vertical water flow, possibly allowing 'ponding' of water within the overlying layers.

This data is key to the construction of a conceptual model of the nature of moisture migration within the unsaturated zone of the Sherwood Sandstone, which will be discussed in Chapter 5.5.

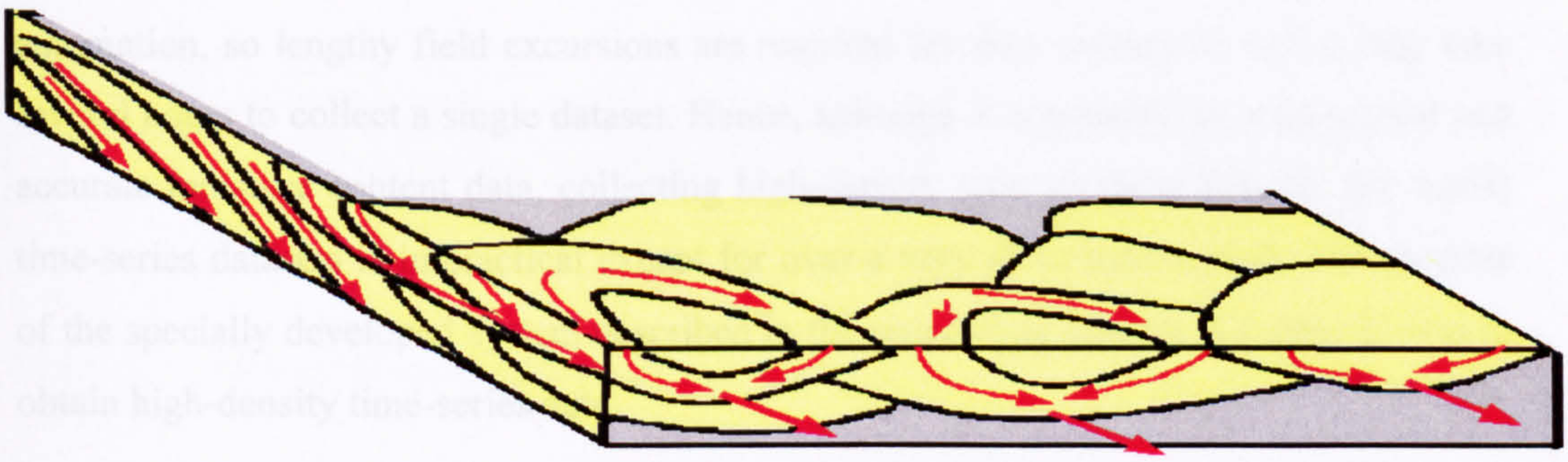

Figure 4.29. Trough cross bedding traced from Figure 4.27. Arrows indicate possible moisture movement directions.

This work shows that interpreting sedimentary structure in the Sherwood Sandstone using GPR is feasible. GPR is ideal for hydrogeological applications as the majority of the features imaged are visible to radar as a result of variations in capillary held moisture, and the amount of capillary retention is controlled by the size of the pore throats in the sediments, which directly influences their permeability properties. Vertical flow (e.g. in the unsaturated zone) may be impeded by the presence of relatively impermeable low-angle cross bedded and planar-bedded fine sandstone units, which correspond to bar top and slack water environments, and occasional mudstone layers representing overbank deposits. The use of GPR has allowed accurate determination of subsurface structure, and provided data that will be linked with other data from Chapters 3 and 5 in Chapter 5.5, for this reason, no further interpretation of the GPR data is considered here.

Chapter 5

MOISTURE CONTENT PROFILING USING THE GRAVIMETRIC, NEUTRON PROBE AND 'TRIME' METHODS

5.1 Introduction

Chapters three and four were primarily concerned with identification of sedimentary structure at a range of scales, from the study area as a whole, through individual outcrops, down to individual boreholes. This chapter is concerned with the production of a hydrological model for the Heck test site, based on time-series moisture content measurements and data from earlier chapters. Time-series moisture content measurements include neutron probe, TRIME and the permanent Time Domain Reflectometry (TDR) probe system developed specifically for this work. The TRIME and neutron probe methods are described in this chapter. Each of these techniques has its own advantages and drawbacks, but one problem common to each of the methods discussed here is the amount of operator input required to collect data. Neither system is amenable to automation, so lengthy field excursions are required for data collection, and it may take several hours to collect a single dataset. Hence, although it is possible to collect good and accurate moisture content data, collecting high-density (one or more datasets per week) time-series datasets is impractical except for over a very short time period. The purpose of the specially developed system described in the succeeding chapter (Chapter 6) was to obtain high-density time-series data.

5.1.1. Rainfall monitoring

Both Chapters 5 and 6 describe vadose zone responses to natural rainfall events from monitoring moisture content profiles within the unsaturated zone of the Triassic Sherwood Sandstone Formation at the Great Heck quarry test site. To allow a comparison to be made between subsurface moisture content fluctuations and infiltration, data regarding rainfall is necessary, together with a method of converting actual rainfall to effective rainfall. Effective rainfall is the quantity of water available for recharge after the effects of evapotranspiration and surface runoff have been taken into account. Evapotranspiration is a combination of two factors, evaporation from the ground surface, and transpiration from vegetation growing on the site, and may be considered as consisting of two parts, actual and potential evapotranspiration. Actual evapotranspiration considers the true quantity of water available, and potential evapotranspiration assumes an unlimited supply of water is available (Dominico and Schwartz, 1997). Hence three situations may occur, and these are summarised in Table 5.1.

1	Precipitation is equal to potential evapotranspiration	No recharge
2	Precipitation is less than potential evapotranspiration	No recharge
3	Precipitation exceeds potential evapotranspiration	Water available for recharge

Table 5.1. Effects of evapotranspiration on recharge (after Dominico and Schwartz, 1997).

Potential evapotranspiration is dependent upon several factors; humidity, the quantity and nature of vegetation cover, the speed at which water is inbibed into the ground and the ambient temperature and wind-speed. Before rainfall data can be compared with vadose zone responses, the effects of evapotranspiration must be taken into account.

MORECS (Meteorological Office Rainfall and Evaporation Calculation System) data is available for the UK. MORECS evapotranspiration data for bare soil (vegetation cover at Great Heck quarry is low) was purchased from the Meteorological Office for square 99, which is the 40x40km grid square within which Great Heck quarry is situated and are presented in Table 5.2. Estimates of daily and weekly evapotranspiration were calculated from the Meteorological Office data and these estimates were used to convert actual rainfall to effective rainfall (for day i) at the Great Heck test site using the equation;

$$P_i = Ea_i + I_i - R_i + B_i + \Delta S_i \qquad \text{Equation 5.1,}$$

where P_i is precipitation (mm), Ea_i is evaporation (mm), R_i is runoff (assumed as zero), I_i is canopy interception loss (assumed as zero mm), B_i is flow bypassing the soil store (assumed as zero mm), and ΔS_i is the storage change in the soil water in mm (Finch, 1998). Using MORECS actual evapotranspiration data for bare soil and soil moisture data from the neutron probe data (see Figure 5.16), Equation 5.1 was used to estimate recharge.

DATE (MONTH ENDING)	PE_BSL_H (mm)	AE_BSL_H (mm)	PE_BSL_M (mm)	AE_BSL_M (mm)	PE_BSL_L	AE_BSL_L
31/12/2002	9.8	9.8	9.4	9.4	9.2	9.2
31/01/2003	17.8	17.8	17.4	17.4	16.7	16.7
28/02/2003	14.5	14.5	12.8	12.8	11.9	11.9
31/03/2003	38.9	37	35.8	33.8	32.8	31.1
30/04/2003	65.8	29.9	60.6	27.4	55.7	25.9
31/05/2003	78.3	76.1	73.6	72.4	69.2	67.9
30/06/2003	105.5	49.4	99	47	92	45.3
31/07/2003	100.1	80.4	93.2	74.7	86.4	69.9
31/08/2003	91.5	19.9	84.5	17	77.6	20.9
30/09/2003	59.8	31.9	55.7	29.7	51.3	30
31/10/2003	35.2	13.8	33.1	12.6	31.5	13.8
30/11/2003	14.9	14.9	14.1	14.1	13.4	13.4

Table 5.2. Meteorological Office evapotranspiration data for square 99. PE = Potential Evaporation, AE = Actual Evaporation, BSL = Bare Soil, H = High available water content, M = Median available water content, L = Low available water content

An automated Campbell Scientific ARG100 tipping bucket raingauge was installed at Great Heck quarry to monitor rainfall events. Due to an equipment malfunction no data were collected until June 2003. Rainfall data for a variety of sites in the Selby area was obtained from the British Atmospheric Data Centre (BADC) and compared with data from the Great Heck rain gauge. The Castleford and South Elmsall weather stations are situated less than 20km from Great Heck quarry and these locations show the closest match to the rainfall events monitored at Great Heck. Hence, an average of the data from these stations was used when no data was available from Great Heck (see Figure 5.1).

Evapotranspiration data were combined with the rainfall data to produce effective rainfall by assuming zero runoff. This was done by calculating average daily actual evapotranspiration values from monthly MORECS data for bare soil (Table 5.2), and subtracting this from the daily rainfall figure, with negative effective rainfall values being treated as zeros. A daily effective rainfall plot (Figure 5.2) and a weekly plot (weekly summation of daily effective rainfall data Figure 5.3) are shown.

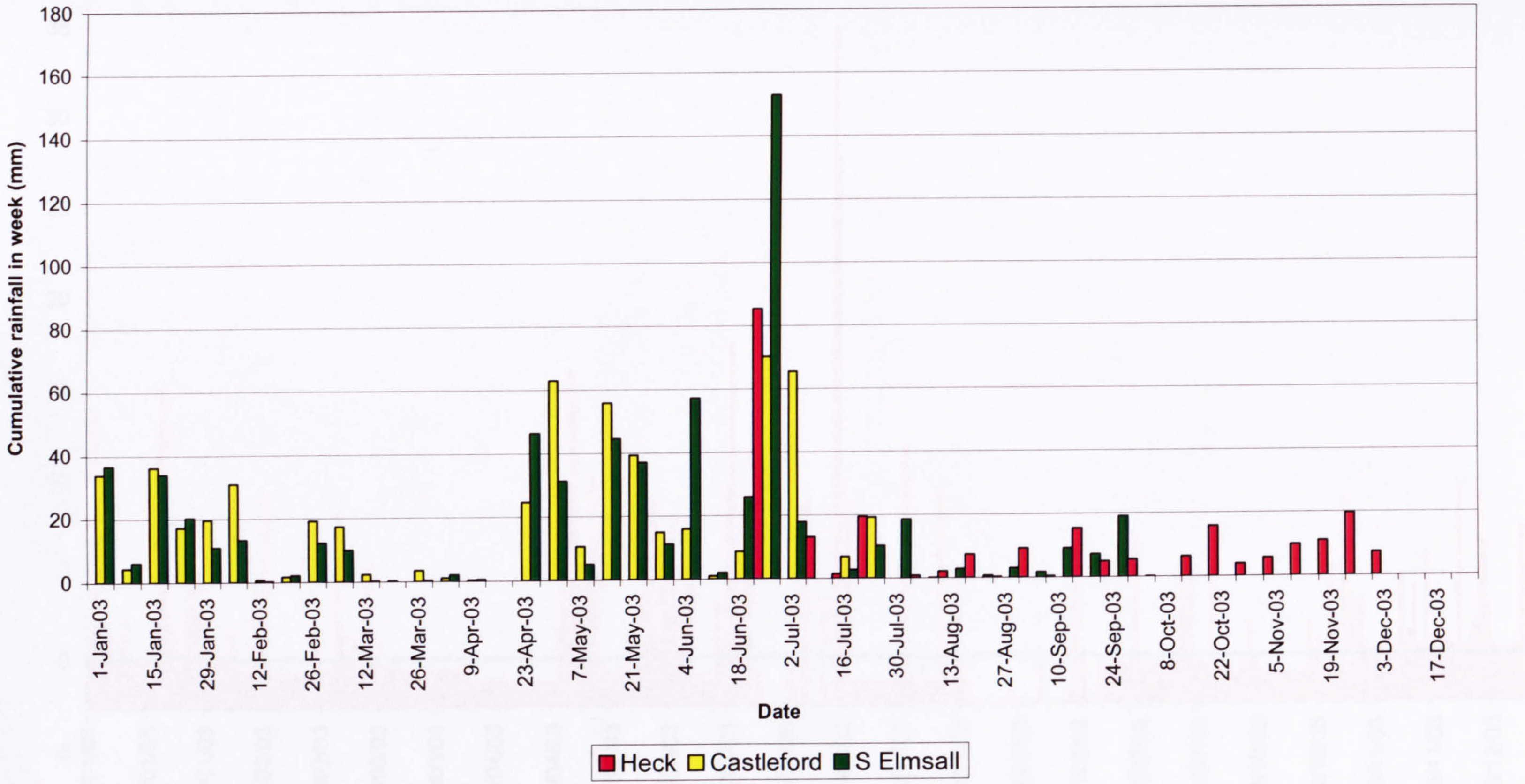

Figure 5.1. Actual weekly rainfall for 3 raingauges in the Great Heck area, 2003.

Figure 5.2. Daily plot of effective rainfall for the Great Heck area, 2003.

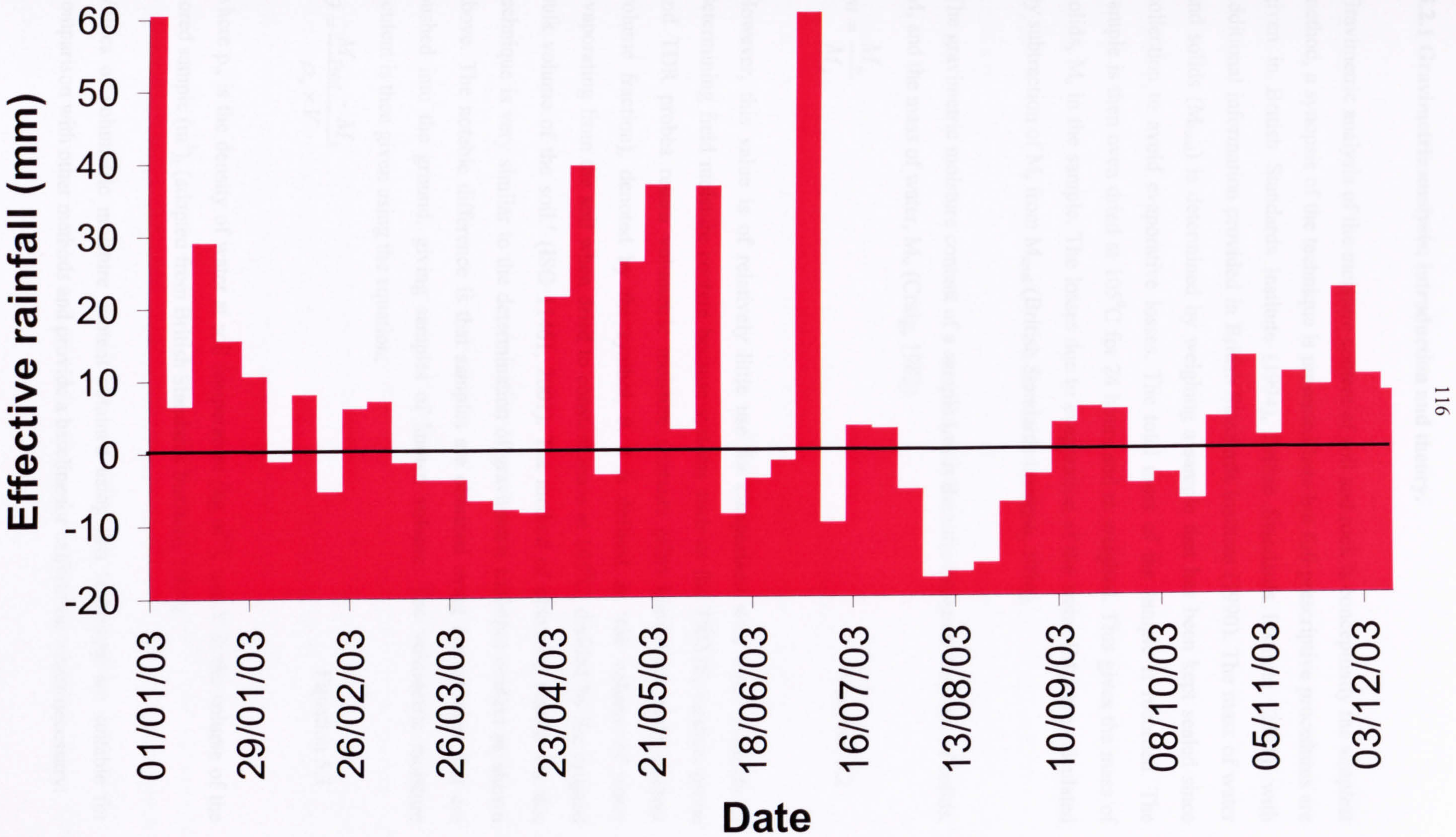

Figure 5.3. Weekly plot of effective rainfall for the Great Heck area, 2003.

5.2.1 Gravimetric analysis; introduction and theory.

Gravimetric analysis of the moisture content of soil and rock is conceptually the simplest method, a synopsis of the technique is presented here but full prescriptive procedures are given in British Standards Institute (1994), British Standards Institute (2001), with additional information provided in British Standards Institute (1990). The mass of water and solids (M_{total}) is determined by weighing a sample that has been kept sealed since collection to avoid evaporative losses. The total mass of the sample is recorded. The sample is then oven dried at 105^{0}C for 24 hours and re weighed. This gives the mass of solids, M_s in the sample. The losses due to evaporation of the water (M_w) are calculated by subtraction of M_s from M_{total} (British Standards Institute, 1994).

The gravimetric moisture content of a sample (m) is the ratio between the mass of solids, M_s and the mass of water, M_w (Craig, 1983).

$$m = \frac{M_w}{M_s} \qquad \text{Equation 5.2}$$

However, this value is of relatively little use for comparison with other methods of determining field moisture content because systems such as the TRIME, neutron probe and TDR probes return volumetric moisture contents (also known as water content volume fraction), denoted by the symbol, θ. θ is defined as 'the volume of water evaporating from the soil when dried to constant mass at 105^{0}C, divided by the original bulk volume of the soil.' (ISO 11461, 2001). The method of obtaining results via this technique is very similar to the determination of gravimetric moisture content m, shown above. The notable difference is that samples are obtained using coring tubes that are pushed into the ground, giving samples of known volume. The volumetric moisture content is then given using the equation;

$$\theta = \frac{M_{Total} - M_s}{\rho_w \times V} \qquad \text{Equation 5.3}$$

where ρ_w is the density of water at soil temperature (kg m^{-3}), and V is the volume of the cored sample (m^3), (adapted from British Standards Institute, 1994).

Values of volumetric moisture content obtained using this technique are suitable for comparison with other methods and provide a baseline for calibration where necessary.

5.2.2 Potential drawbacks of the gravimetric method

The gravimetric method is useful for providing accurate absolute volumetric moisture content values, and is ideal as a baseline for calibrating other techniques. As a means of monitoring moisture flow it does however have very serious drawbacks which severely limit its use. These drawbacks may be grouped into three main categories:

Non-repeatable technique

The gravimetric method relies on the extraction of samples from the rock for laboratory measurement. The act of removing a sample changes the hydraulic properties of the site, and no two samples may be collected from exactly the same location. Hence, accurate and repeatable time-series moisture content monitoring is impossible, and the technique is only useful for determining one-off moisture contents.

Time restraints

To obtain data it is necessary to collect each sample individually, in a manner that preserves the in-situ water content as much as possible. Each sample must then be processed in the laboratory and results calculated. This is necessarily very time consuming, especially if many samples are to be considered, and whilst acceptable for one-off calibration data or taking a moisture content 'snapshot', the time cost means that high time-density monitoring is impractical.

Difficulty of sample collection

British Standards Office (2001) specifies the use of a coring sleeve to extract undisturbed samples of known volume. This is acceptible for most soils, but the Sherwood Sandstone is a rock, albeit a friable rock, and it is extremely difficult to drive any form of sleeve or gouge into it. Some success was achieved using a Cobra percussion drill and gouges, but even using a full percussion system capable of driving its way through rock the Sherwood Sandstone was extremely difficult to core. The samples recovered were frequently shattered on removal, and fine-grained layers were often not recovered at all.

The combination of these drawbacks means that the gravimetric method was not suitable for detailed moisture migration studies and was only used in very limited circumstances. The main practical use of gravimetric data was in checking the accuracy of the TRIME unit in the Sherwood Sandstone, but no long term monitoring was conducted using this method.

5.2.3. Gravimetric Results

Sandstone cores were taken from various locations within Hatfield quarry. Four boreholes were drilled using a Cobra percussion drill, and five samples collected for gravimetric analysis of their moisture content (*m*) and volumetric moisture content (θ). Jared West and Kirk Handley of the School of Earth Sciences, University of Leeds collected the samples, and the gravimetric analysis was carried out by Kirk Handley. The purpose of the sampling was to validate the calibration of the TRIME unit (see section 5.3). As discussed previously (Chapter 5.2.2), there are considerable problems associated with recovery of samples suitable for volumetric moisture content analysis from the Sherwood Sandstone, and extraction of core as per ISO 11461, 2001 was not practical. To enable gravimetric analysis, an in-situ dry density of the rock of 1.81kg m^{-3} was assumed for all samples, following the findings of Pokar (2002), who was able to calculate the bulk density of cores from the Sherwood Sandstone at the Hatfield field site, from mercury intrusion porosimetry tests. By multiplying the moisture content (*m*) by the dry density of the rock, it was possible to convert mass fraction moisture contents into volumetric moisture contents.

Borehole	Moisture content, *m* (%)	Volumetric moisture content, θ (%)
HQ1	5.91	10.70
HQ1	6.56	11.87
HQ2	4.90	8.87
HQ3	18.69	33.83
HQ4	9.81	17.76

Table 5.2. Results of gravimetric analysis conducted by West and Handley on the Sherwood Sandstone at Hatfield Quarry (West, *pers. comm.*, 2001).

Gravimetric analysis was the reference method used by West *et. al.* (2003) to determine the relationship between volumetric moisture content and permittivity that was appropriate to the Sherwood Sandstone in the study area.

5.3.1 The TRIME system, introduction and theory

The TDR with intelligent micromodule elements, or TRIME system is a commercially available volumetric moisture content measuring system based on TDR principles (Stacheder *et. al.*, 2000). Manufactured by IMKO, Germany, and distributed worldwide, this system has been applied to detecting moisture content in soils, civil engineering materials, foodstuffs and a wide variety of porous media. The TRIME system is highly portable, being self-contained and extremely lightweight and is capable of delivering rapid and accurate moisture content readings over a range of saturations.

Various probes are available for the TRIME system, including two and three electrode probes, surface probes and several other permutations of probe design. The system may also be linked to a computer to gain data regarding bulk electrical conductivity of the medium surrounding the probe, battery capacity and status information (Stacheder *et al.*, 2000). Details of the various probes (apart from the borehole packer) and computer-derived data will not be discussed here as these were not used. This section introduces the theory of the TRIME unit, but only where it differs from conventional TDR, describes the various components of the borehole packer system and briefly discusses the field data collection methodology.

The TRIME unit utilises the same basic physical properties of electromagnetic wave propagation as conventional TDR (discussed in Chapter 6.1), with similar probe designs, but with two important differences. The first difference is the way the probes are interrogated. A voltage pulse is sent down to the probe in a similar manner to conventional TDR. However, the reflected voltage is sampled using an algorithm that times the arrival of specific voltage levels. The second difference is that the probes themselves use a PVC (Polyvinylchloride) sheath around the electrodes. This sheath would reduce the sensitivity of conventional TDR systems, but the TRIME algorithm depends on its presence (Stacheder *et al.*, 1994; 2000). The packer-mounted probe used here utilises a two-electrode configuration (See Chapter 6.1, and 6.2), with the electrodes made from lead foil. These electrodes are mounted to the inside of an inflatable packer, which is lowered into the borehole and then inflated to push the electrodes close to the soil (or in this case rock). The manner of packer operation is analogous to the permanent installations described in Chapter 6 except that after a reading is taken, the packer is deflated and moved to a new location.

The TRIME system depends on complex electronic hardware, both in the probes and control unit, consisting of various microprocessors and application specific integrated circuits (ASICs) which provide the necessary computing power (Stacheder *et. al.*, 2000). An example of a TRIME pulse is shown in Figure 5.4.

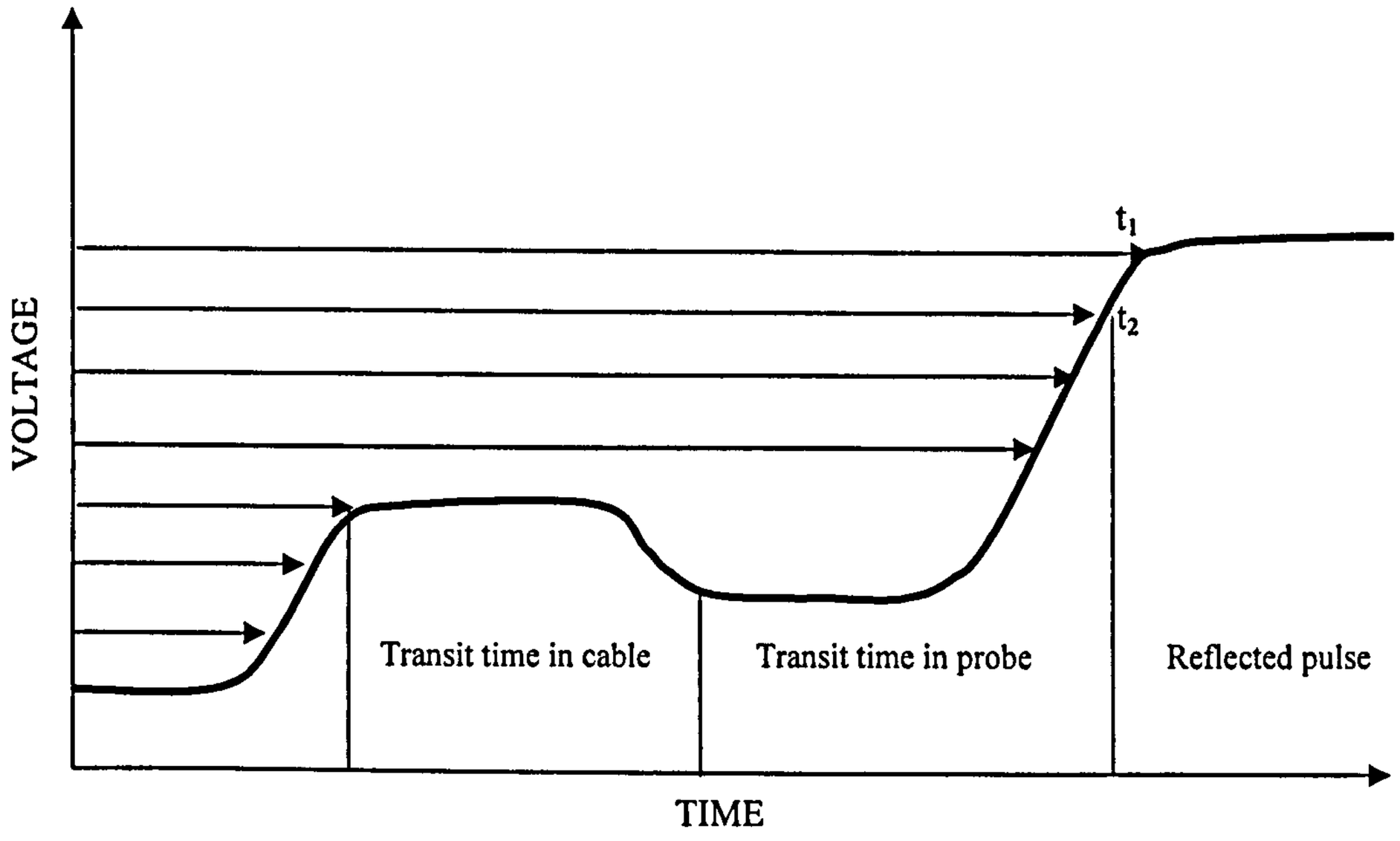

Figure 5.4. TRIME trace and evaluation method (from Stacheder *et al.*, 1994).

For the TRIME system to function correctly, the returned voltage amplitude must be greater than the transmitted pulse, as can be seen in figure 5.4. Otherwise the system would not be able to 'see' the probe electrodes. This high amplitude return signal is obtained by reducing attenuation to a minimum. All parts of the system (cables, pulse generator and probe) are all impedance matched with no balun in the system. The 0.5-1mm thick PVC sheath is necessary for reducing attenuation, by acting like a high-pass filter, it removes low frequency and DC noise from the system and although reducing system sensitivity was found to improve measurement accuracy (Stacheder *et. al.*, 1994). The designers of the TRIME system claim a temporal measurement accuracy of 3 picoseconds as a result of these accuracy improvements.

Because the transmitted voltages are lower than the reflected ones, the TRIME unit cannot measure the transmitted pulse. To allow for this, the packer-mounted probe contains a memory chip containing calibration data specific to that type of probe (cable length, electrode length, coating thickness; Stacheder *et. al.*, 1994). Hence the system sends a voltage pulse down the cable, and then samples at regular intervals and records the time at which higher voltage reflections arrive back from the probe. Data from the probe memory chip is then used to give the necessary calibration and the system is able to

estimate moisture content via the relationship derived by Topp *et al.* (1980). In order to attain the required accuracy, two million measurements are averaged for each moisture content reading, which is normally delivered in under 20 seconds after the button on the control box has been pressed.

In use, the system is extremely simple (Figure 5.5), consisting of a small box, with one button, a digital display and three connector jacks- one for the charging unit, one for connecting the system to a computer and one for connecting to the probe. Taking readings is also simple, the packer-mounted probe is connected to the charged control unit, the packer is lowered into an uncased borehole, inflated using a car foot pump and the button pressed. A few seconds later the volumetric moisture content θ is displayed on the LCD screen to two decimal places. The packer is then deflated and moved to a new depth and the process is repeated as often as is required.

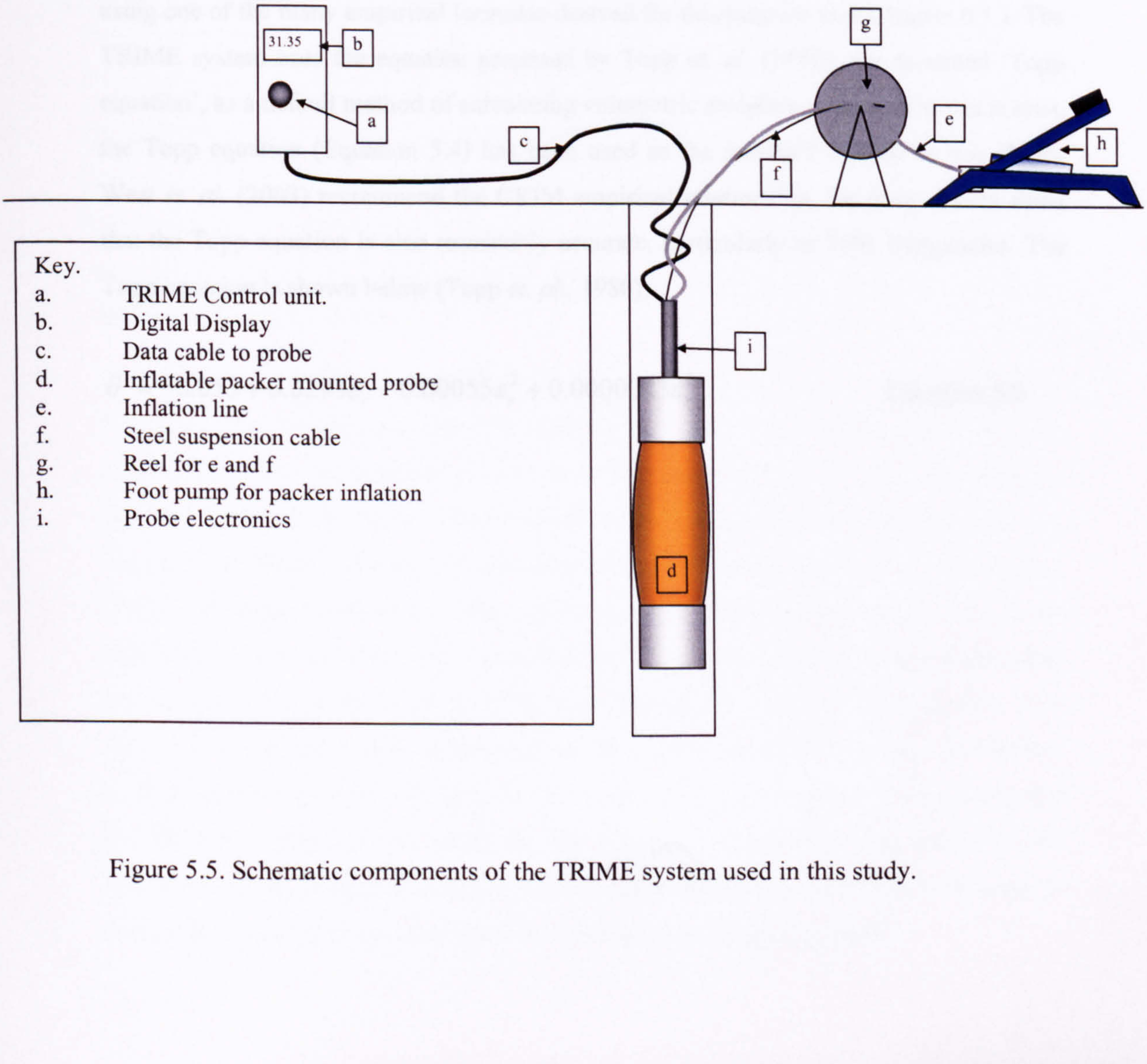

Figure 5.5. Schematic components of the TRIME system used in this study.

The TRIME system is able to calculate volumetric moisture content from the timed reflection of pulses from the probe electrodes in the same manner as conventional TDR systems. The one-way EM pulse travel time within the electrodes is multiplied by the velocity of an EM wave in a vacuum ($3x10^8 ms^{-1}$) to give an apparent electrode length (L_a). This is then divided by the true length of the electrodes (L), which is either input into the software for conventional TDR or recorded on the probe EEPROM chip for the TRIME, to give a value of L_a/L. The L_a/L value may be converted to a relative permittivity value ε_r, averaged along the probe length, using the relationship (Topp *et. al.*, 1980);

$$\sqrt{\varepsilon_r} = \frac{L_a}{L} \qquad \text{Equation 5.4}$$

A correction factor is then applied to remove the dielectric contribution of the packer itself (see Chapter 6 for a detailed review of a correction factor for conventional TDR packers). The corrected permittivity may be converted into a volumetric moisture content using one of the many empirical formulae derived for this purpose (see Chapter 6.1.). The TRIME system uses the equation proposed by Topp *et. al.* (1980), the so-called 'Topp equation', as a default method of calculating volumetric moisture content. For this reason, the Topp equation (Equation 5.4) has been used as the standard method in this thesis. West *et. al.* (2003) recommend the CRIM empirical relationship, but their results show that the Topp equation is also reasonably accurate, particularly at TDR frequencies. The Topp equation is shown below (Topp *et. al.*, 1980);

$$\theta = -0.053 + 0.0293\varepsilon_r - 0.00055\varepsilon_r^2 + 0.0000043\varepsilon_r^3 \qquad \text{Equation 5.5}$$

5.3.2. Trime calibration.

The TRIME unit is described as being accurate in sandy, clay poor soils. Stacheder *et al.*, (2000) demonstrated that the TRIME calibration is comparable with other empirical calibrations. Before relying on TRIME data, it was decided to validate the manufacturers calibration for the unit in the Sherwood Sandstone at Hatfield Quarry by comparing gravimetrically determined volumetric moisture content with TRIME data. Jared West and Kirk Handley of the Department of Earth Sciences, University of Leeds conducted this calibration, and the gravimetric analysis was described in Chapter 5.2.3.

Samples were taken from boreholes for gravimetric analysis and the TRIME packer was lowered into the freshly drilled borehole, and volumetric moisture content readings taken. These values are compared in Table 5.4 and Figure 5.6 below.

Borehole	Gravimetric Volumetric moisture content, θ (%)	TRIME Volumetric moisture content, θ (%)
HQ1	10.70	13
HQ1	11.87	12.7
HQ2	8.87	7.9
HQ3	33.83	43.8
HQ4	17.76	18.5

Table 5.4. Comparison of gravimetric and TRIME volumetric moisture content for Hatfield Quarry (SE 653075).

It can be seen that there is some variation between the TRIME and gravimetric data, particularly at high saturation levels such as in Borehole HQ3, which was well within the capillary fringe as the packer was observed to be floating prior to inflation. This is a feature of the TRIME system, and Stacheder *et. al.* (2000) note that this effect may occur at high moisture content and/or high pore-water conductivity values. Hence excessively high TRIME derived values, over the known mean porosity of the Sherwood Sandstone in the study area (approximately 30-35%), were assumed to indicate full saturation (θ = 35%). However, other data points derived from plotting TRIME against gravimetric moisture contents plotted very close to the 1:1 line plotted on Figure 5.6, suggesting that the TRIME calibration was valid for the Sherwood Sandstone. The scatter in the datapoints below 20 percent moisture content was probably due to the effects of using an average bulk density of the rock when calculating values of gravimetric θ.

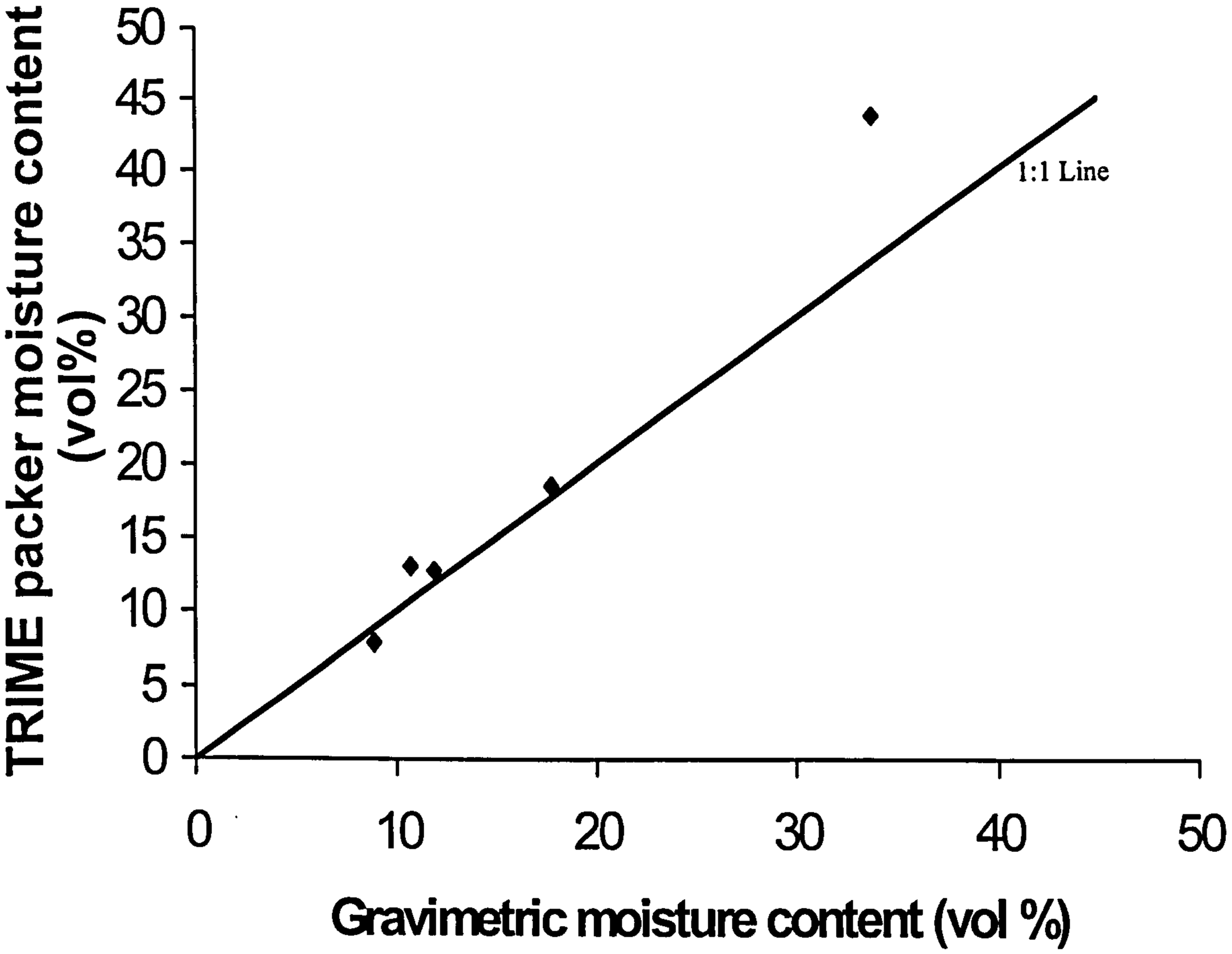

Figure 5.6. Validation plot for the TRIME unit in Hatfield Quarry (SE 653075). Solid line is a 1:1 plot.

The TRIME system was used for regular collection of volumetric moisture content profiles in an uncased borehole at the Great Heck test site.

5.3.3. Potential drawbacks with the TRIME system.

The TRIME system is a proven and efficient way of collecting moisture content information in a relatively repeatable manner. However, several factors potentially limit the usefulness of the system, as used in this study, for long term monitoring of moisture migration and these factors are described below.

The TRIME packer system relies on measuring the moisture content of exposed walls in uncased boreholes. At the Great Heck test site, the upper metre of the borehole was cased and capped, thus preventing the ingress of any standing water that may pool on the site during rainfall events. However, an open borehole is still present on the test site, and this may act as a conduit, allowing water to bypass the rock matrix of the site and short circuit the hydrogeological system. This would be a serious bypass conduit within the phreatic zone with water freely being exchanged through the rock pore – borehole void interface.

Capillary forces in the vadose zone resist free-flow of water under normal rainfall conditions. Capillary suction tends to hold moisture within the rock matrix, and significant pressure heads are necessary to drive water out of the rock and into the borehole void (Domenico and Schwartz, 1997). Hence, except after extreme rainfall events, moisture running down the borehole walls is expected to be minimal. Water vapour is not subject to the same capillary forces and may be transmitted freely by open boreholes in the vadose zone but this was not thought to be significant compared with the quantity of water flowing through the rock matrix particularly as subsurface tempratures remain cool, at about 10^0C all year round. Wealthall *et al.*, (2001) concluded from their study of fractures in the unsaturated Triassic sandstones in Cheshire that open conduits were unlikely to influence vadose zone flow except for rare occasions where the system was overloaded and contained large pressure heads.

Uncased boreholes may suffer caving and collapse if left open for long periods of time. Hence it is possible that voids may appear and / or the borehole may become blocked with fallen debris preventing the packer being lowered. The TRIME borehole at Great Heck was drilled to 14m, but became blocked at 11.5m due to a local constriction of the borehole walls. The packer-mounted probe is lowered down the borehole on a cable marked at 50cm intervals so there is no control on the direction the probe is facing within the borehole at depth. Errors may also occur in lowering the probe to exactly the same level and orientation each time it is used. To determine if this was likely to be a significant problem the packer was lowered to a series of depths, inflated at each depth and a moisture content reading taken. The packer was then withdrawn to the surface and re-lowered into the hole and efforts were made to rotate the

packer to a different orientation as the readings were repeated. This procedure was repeated twice and results showed a maximum of 0.8% variation (Table 5.5).

Packer depth (m)	Reading 1 (%)	Reading 2 (%)	Reading 3 (%)	Reading 4 (%)
6.5	14.4	14.6	15.1	15.2
8.25	20.8	20.8	20.7	20.8
8.75	28.0	28.1	28.2	28.3

Table 5.5. Effects of packer position upon recorded volumetric moisture contents. Data collected on March 26th 2003.

TDR based systems are extremely sensitive to air gaps between the electrodes and the rock (see Chapter 6). Increases in inflation pressure may force the electrodes into better contact, and improve the reliability of recorded moisture contents. To evaluate the minimum pressure needed for accurate moisture content determination, the packer was lowered into the borehole and a series of moisture content readings taken at different numbers of strokes on the pump. The results of this are shown in Figure 5.7 which shows that errors are mostly associated with lower inflation pressures. A standard practice of inflating the packer to 1.5bar was therefore introduced, which gave good results without running the risk of packer over-inflation.

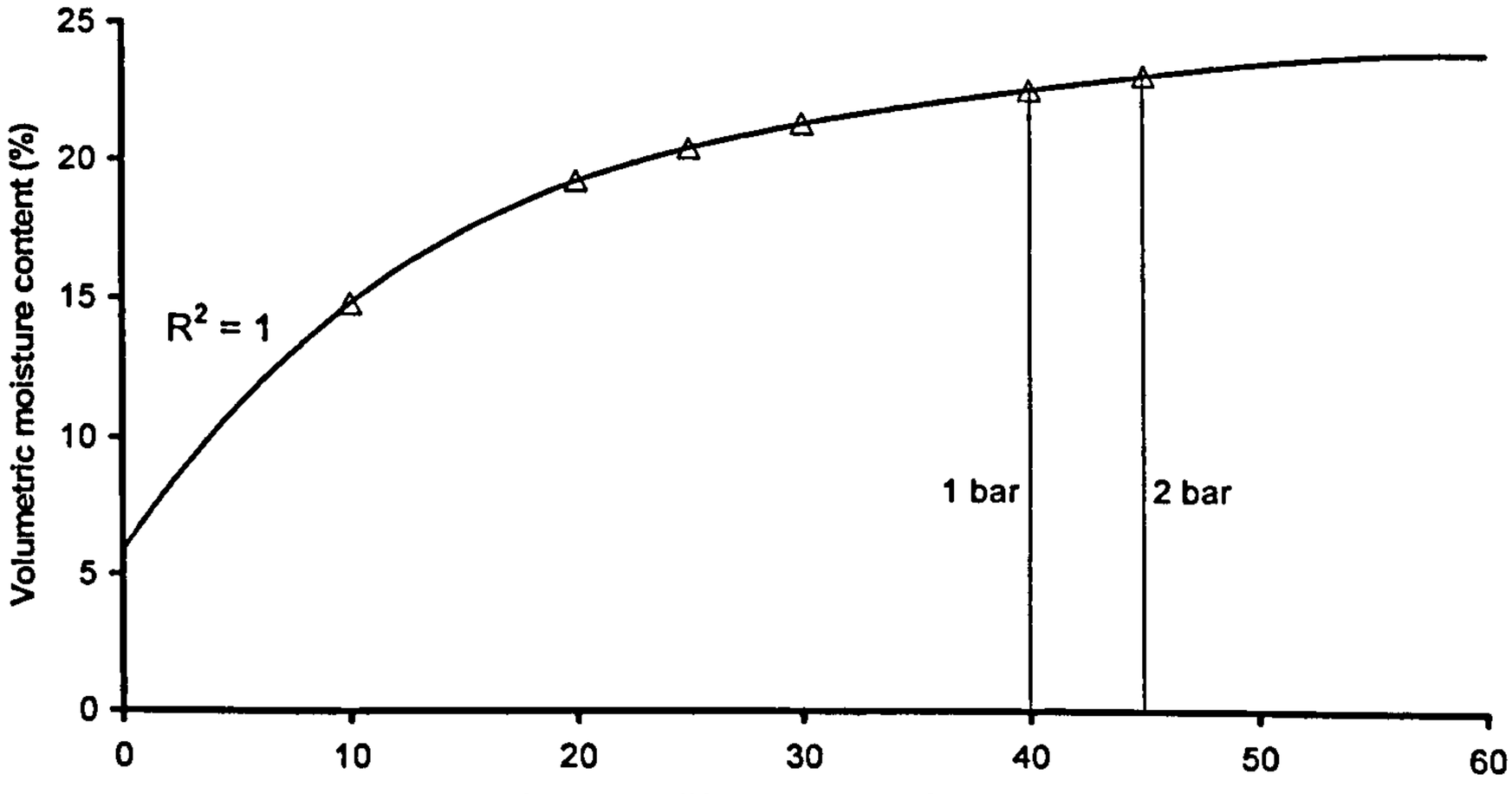

Figure 5.7. Results of pressure determination for TRIME packer. 40 strokes = 1bar pressure, 45 strokes = 2bar pressure.

Taking an individual reading using the TRIME is easy and quick. However, between readings the packer has to be deflated, moved and then re-inflated. This is a slow process and typically it took between two and three hours to collect a dataset from the Great Heck borehole. The TRIME system was used for collection of periodic (approximately monthly) moisture profiles.

5.3.4. TRIME results

Eleven moisture content profiles were collected for the uncased TRIME borehole at Great Heck test site between December 2002 and December 2003. Figure 5.8 is a frequency distribution. The population of data above 33% was considered to be unrepresentative as results indicate saturation levels greater than the rock porosity, as described in section 5.3.2.

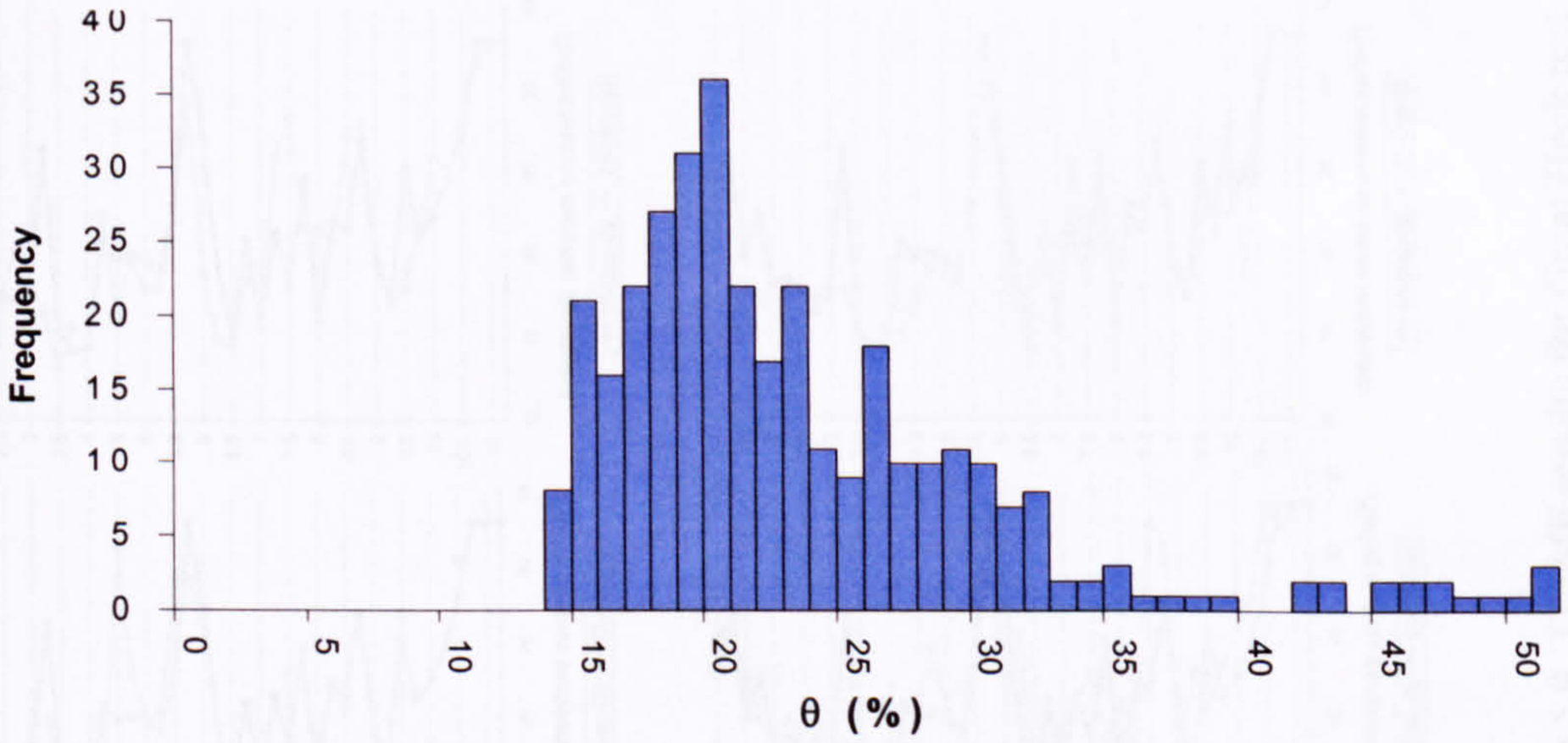

Figure 5.8. Frequency histogram of TRIME moisture content data.

Figure 5.9 presents these data as a series of moisture content depth profiles, together with a plot showing effective rainfall for 2003 (see Chapter 5.1.1). Each depth profile is plotted alongside the initial depth profile collected on the 18th December 2002. Data presented in Figure 5.9. shows that there was a wide range of volumetric moisture contents present in the unsaturated zone throughout the year, with values ranging from free-drained, at about 14%, to fully saturated at 33%.

The effective rainfall plot shows that between the end of April and the end of June 2003 there was regular rainfall, with a significant rainfall event occurring at the beginning of July. This may be seen in the moisture content depth profiles for March, May June and July as a steady increase in moisture content in the upper 2.75m of the plots, with the July plot showing increases down to 3m. Below these levels variation in moisture content may be observed, but the behaviour of the system is more complex, with most depths showing low levels of moisture fluctuation and low moisture content (e.g. 3.5m depth). However, some layers show large moisture content fluctuations (e.g. 4.5m and 8.5m depth), some depths remain consistently wet throughout the year (e.g. 5.75m depth). Moisture content generally increases towards the base of the profile as the rock becomes saturated as a result of the ≈10.5m semi-permanent perched water table (see below). Plotting the

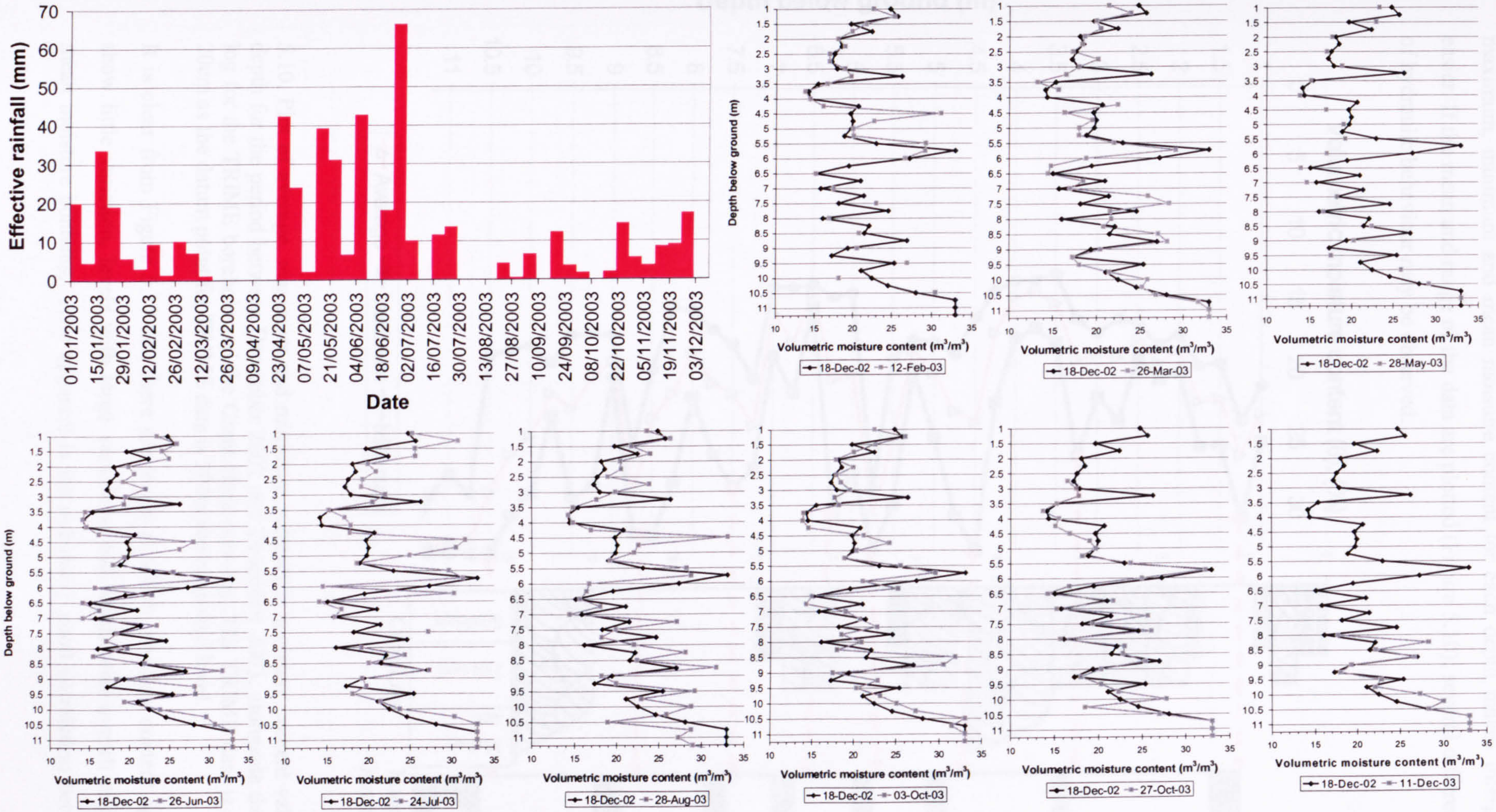

Figure 5.9. TRIME results for Great Heck test site(SE 588213), 2002-2003.

maximum, minimum and mean moisture content for each depth makes interpretation easier. If the mean and range of the data are plotted (Figure 5.10), several different styles of hydraulic behaviour may be observed.

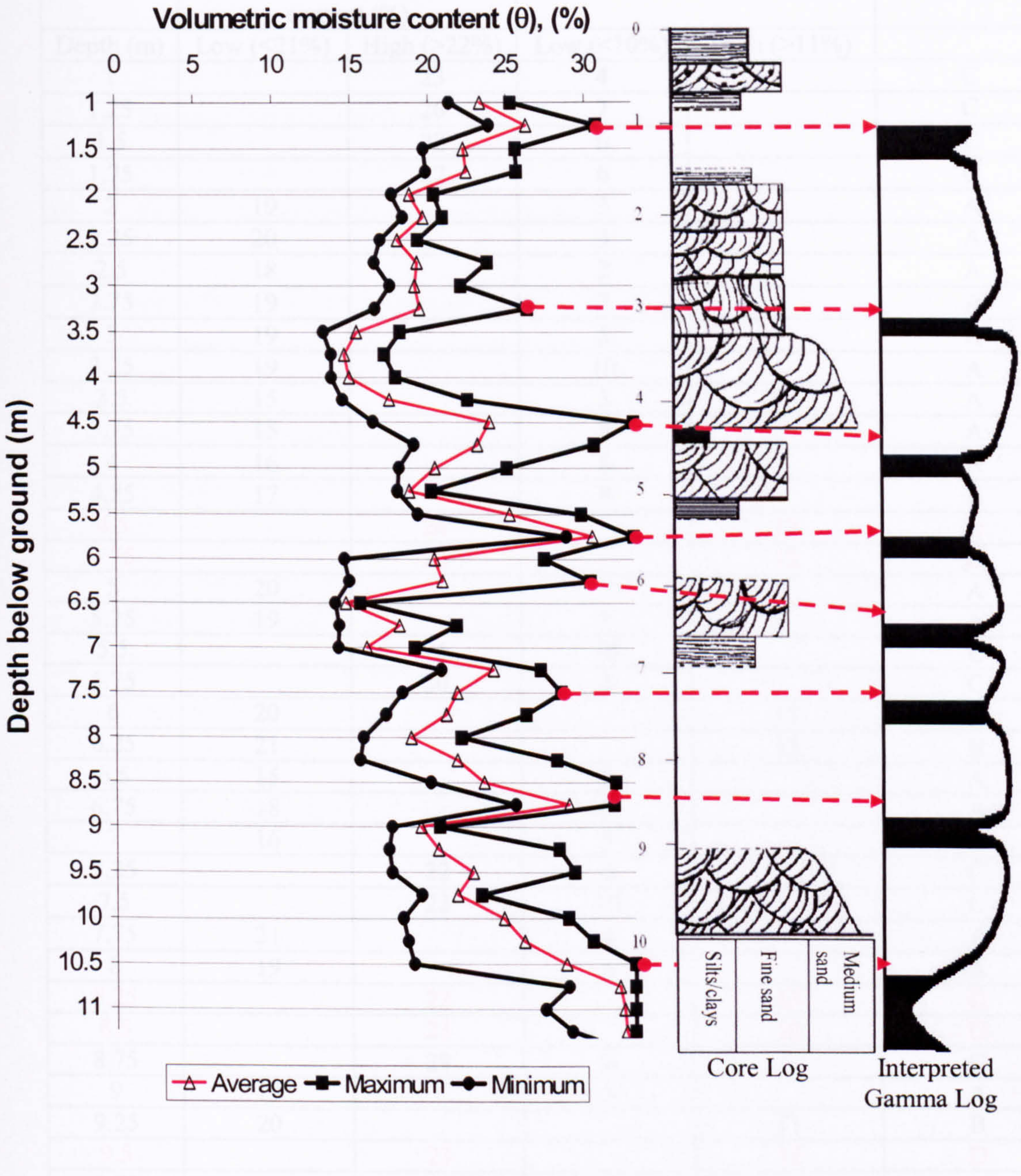

5.10. Plot of average, maximum and minimum volumetric moisture content values with depth for the period between December 2002 and December 2003, alongside the gamma log for the TRIME borehole and the Great Heck core log. The TRIME data is offset by 20cm as the datum point for TRIME data is 20cm above ground level.

It is clear from Figure 5.10 that there are levels at which moisture content appears to show little variation, levels with large variations, and levels with overall high or low mean moisture contents. Also apparent is the extremely good correlation between the

moisture content peaks and the bases of coarse-grained layers immediately above fine-grained layers shown in the gamma log.

	Mean volumetric moisture content (%)		Data range (%)		Population
Depth (m)	Low (<21%)	High (>22%)	Low (<10%)	High (>11%)	
1		23	4		C
1.25		26	7		C
1.5		22	6		C
1.75		22	6		C
2	19		3		A
2.25	20		3		A
2.5	18		2		A
2.75	19		7		A
3	19		5		A
3.25	19		10		A
3.5	15		5		A
3.75	15		3		A
4	16		4		A
4.25	17		8		A
4.5		24		17	D
4.75		23		12	D
5	20		7		A
5.25	19		2		A
5.5		25	10		C
5.75		30	4		C
6	20			13	B
6.25	21			15	B
6.5	15		2		A
6.75	18		8		A
7	16		5		A
7.25		22	6		C
7.5		22	10		C
7.75	21		4		A
8	19		6		A
8.25		22		13	D
8.5		23		12	D
8.75		29	6		C
9	19		3		A
9.25	20			11	B
9.5		23		12	D
9.75		22	4		C
10		25		11	D
10.25		26		12	D
10.5		29		14	D
10.75		32	4		C
11		32	6		C
11.25		32	4		C

Table 5.6. Summary of TRIME data range and mean moisture content at different depths.

The data for each level are divided into four populations according to the mean moisture content and range of moisture content over the year (Table 5.6). The values of 21.5% and 10.5% which were used to divide the data are the median values of the populations of means and ranges respectively. Each level was classified into one of the categories below:

a) Zones of low mean moisture content and low range (population A).
b) Zones of low mean moisture content and high range (population B).
c) Zones of high mean moisture content and low range (population C).
d) Zones of high mean moisture content and high range (population D).

These populations give an indication of the relative positions of layers which show specific moisture content behaviour at Great Heck test site.

The interpretation of the hydraulic behaviour classification derived above is considered further in sections 5.3.5 and 5.5.

Having identified units with four differing styles of moisture content behaviour it was possible to produce time-series plots (moisture content variation against time) for each hydraulic population. These plots (Figure 5.11) show how the system was reacting to rainfall events. Time series are shown for 3.0, 3.75, 5.25, and 7.00m depth (population A), 6.0 and 9.25m depth (population B), 1.5, 5.75, 8.75 and 10.75m depth (population C), and 1.25, 3.25, 4.5, 7.5 and 8.5m depth (population D).

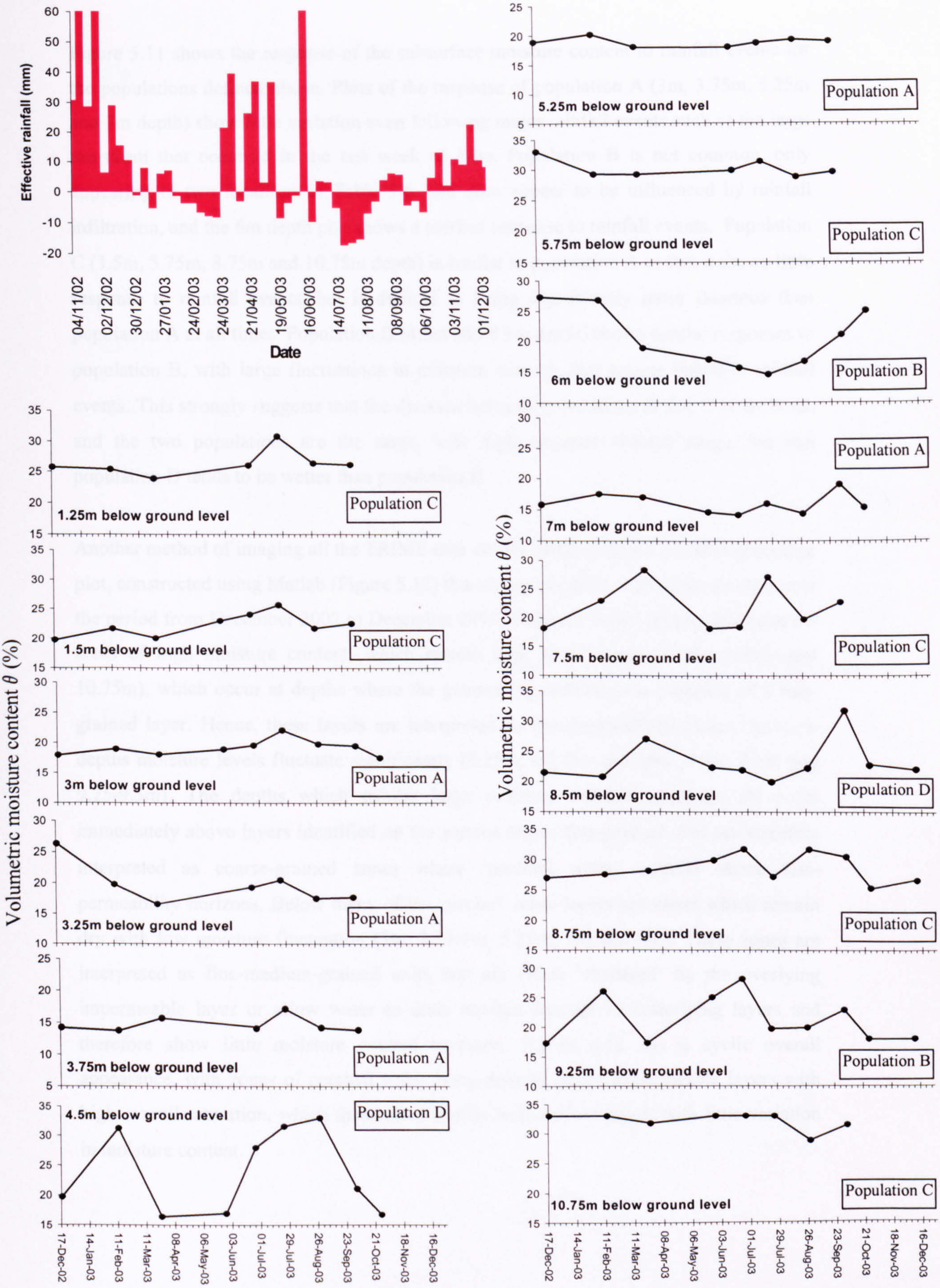

Figure 5.11. Time series TRIME moisture contents.

Figure 5.11 shows the response of the subsurface moisture content to rainfall events for the populations defined above. Plots of the response of population A (3m, 3.75m, 5.25m and 7m depth) show little variation even following major rainfall events such as the large rainstorm that occurred in the last week of June. Population B is not common, only appearing in two locations in Table 5.6, and does appear to be influenced by rainfall infiltration, and the 6m depth plot shows a marked response to rainfall events. Population C (1.5m, 5.75m, 8.75m and 10.75m depth) is similar to population A in that it shows little response to rainfall events, but is defined as being significantly more saturated than population A at all times. Population D (4.5m and 8.5m depth) shows similar responses to population B, with large fluctuations in moisture content, that appear linked to rainfall events. This strongly suggests that the division between populations B and D is artificial, and the two populations are the same, with high moisture content range, but that population D tends to be wetter than population B.

Another method of imaging all the TRIME data on one image is to use a coloured contour plot, constructed using Matlab (Figure 5.12) that shows variation in moisture content over the period from December 2002 to December 2003. This plot shows clearly that there are areas of high moisture content, which remain high at all times (5.75m 8.75m and 10.75m), which occur at depths where the gamma log indicates the presence of a fine-grained layer. Hence, these layers are interpreted as low permeability layers. At some depths moisture levels fluctuate significantly (1.25m, 4.5-5m, 6-6.25m, 7.5m, 8.5m and 9.25-9.5m). The depths which exhibit large moisture content variations all occur immediately above layers identified on the gamma log as fine-grained, and are therefore interpreted as coarse-grained zones where 'perched water' collects above low-permeability horizons. Below many of the perched water layers are zones which remain dry with low moisture fluctuation (3m, 3.75-4m, 5.25m, 7m and 9m). These zones are interpreted as fine-medium-grained units that are either 'sheltered' by the overlying impermeable layer or allow water to drain straight through to underlying layers and therefore show little moisture content variation. Figure 5.12 has a cyclic overall appearance, with zones of perched water lying directly above impermeable layers with high overall saturation, which themselves overlie well-drained layers with little variation in moisture content.

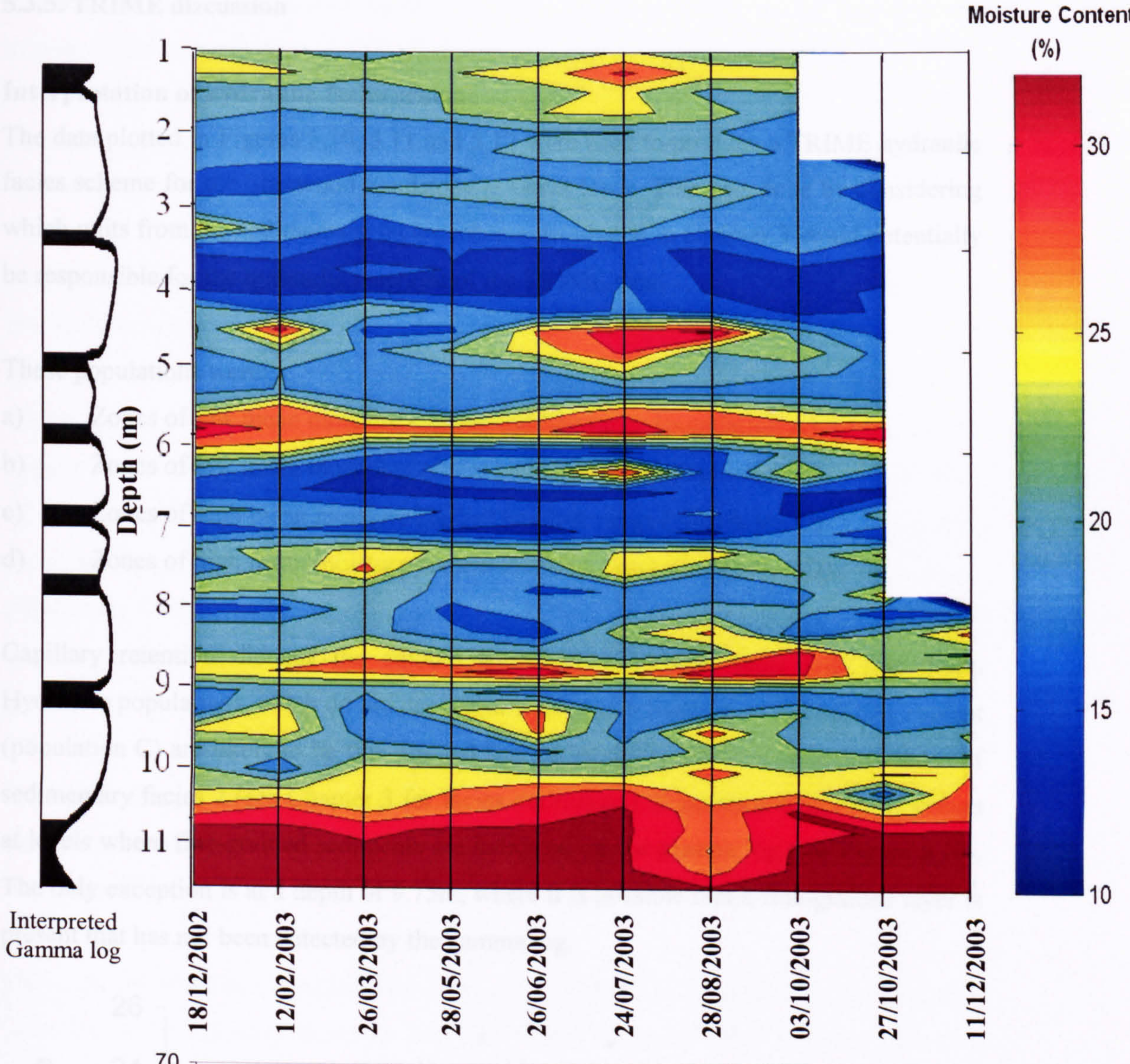

Figure 5.12. Contour plot of TRIME moisture contents, Dec 2002 to Dec 2003.

5.3.5. TRIME discussion

Interpretation of hydraulic facies scheme

The data plotted in Figures 5.10, 5.11 and 5.12 were used to produce a TRIME hydraulic facies scheme for the Sherwood Sandstone at Great Heck. This was done by considering which units from the sedimentary facies scheme developed in Chapter 3 could potentially be responsible for the hydraulic response of the TRIME data.

These populations were:

a) Zones of low mean moisture content and low range (population A).

b) Zones of low mean moisture content and high range (population B).

c) Zones of high mean moisture content and low range (population C).

d) Zones of high mean moisture content and high range (population D).

Capillary retention dictates the amount by which individual units will free drain. Hydraulic populations which do not dry out or show much fluctuation in moisture content (population C) are likely to be fine-grained low permeability sandstones such as those of sedimentary facies 2 (see Chapter 3 for facies definitions). Population C normally occurs at levels where fine-grained sediments are indicated on the gamma log (see Figure 5.10). The only exception is at a depth of 9.75m, where it is possible that a fine-grained layer is present that has not been detected by the gamma log.

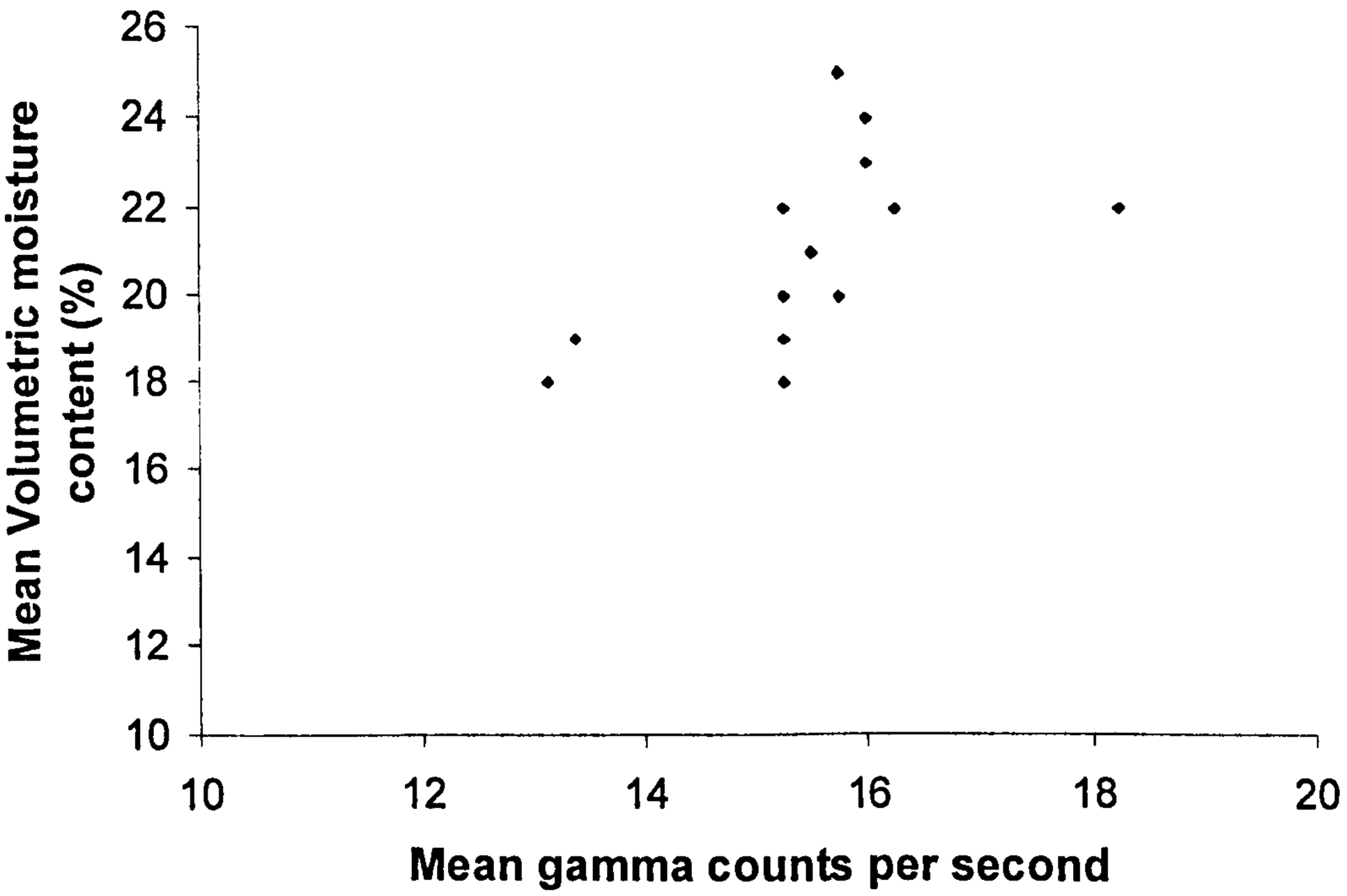

Figure 5.12a Crossplot of gamma results with mean volumetric moisture content results from TRIME data

Populations with low moisture content and low scatter are likely to be free draining, coarser sediments which are either bypassed by flow in preferential pathways, or the water may move through them with a high seepage velocity, and no data showing this rapid transit has been collected. This tends to suggest that population A represents coarser-grained sandstones, i.e. sedimentary facies 1.

Any hydraulic population that demonstrates either high moisture content fluctuations or low moisture content is likely to be relatively coarse-grained, as capillary tension restricts drainage in fine sediment. This suggests that populations B and D are coarse-grained layers, again probably sedimentary facies 1. However, their high levels of scatter tend to suggest that water is actively moving through these populations. A possible explanation of the moisture content behaviour is that population D represents perched water as discussed in Chapter 3. Population D often occurs (see Table 5.6) directly above population C, fine-grained low permeability layers. Hence, it is likely that water is 'ponding' above these finer grained layers, which only drain at low moisture flow conditions.

Population B only occurs at two depths, 9.25-9.5m and 6-6.5m (see Table 5.6). At both depths, examination of Figures 5.11 and 5.12 suggest this layer should be re-classified as population D.

Using this information, together with data from Chapter 3 it is possible to link hydraulic behaviour to sedimentary facies for the Sherwood Sandstone at the Heck test site. This linkage is summarised in Table 5.7.

Hydraulic population	Description	Sedimentary facies
A	Free-drained, permeable layers	1
C	Fine-grained low-permeability layers	2
D	Permeable trough cross-bedded units associated with locally saturated conditions immediately above facies B.	1

Table 5.7. Hydraulic facies scheme for the Sherwood Sandstone based on TRIME data.

5.4.1 Neutron probe introduction and theory

Neutron probes have become an established method of investigating water content to any desired depth. They offer rapid, non-destructive estimation of subsurface moisture content and are capable of delivering accurate moisture content profiles with reasonable ease (Williams et al, 1981). Thus the neutron method provides an ideal yardstick to evaluate the performance of the TDR system and to help characterise the hydraulic properties of the Heck test site.

The neutron probe was first developed in the 1950's to monitor soil moisture content (Greacen, 1981), and the physics behind the neutron probe concept is extremely elegant, relying on the conservation of momentum of subatomic particles following inter-particle collisions. This physics is discussed by Bell (1987). At its most basic, the system consists of a fast neutron source, a slow neutron detector and a counter to sum up the number of slow neutrons detected over a set period of time. The method of operation is also extremely simple and is summarised in Figure 5.13. below.

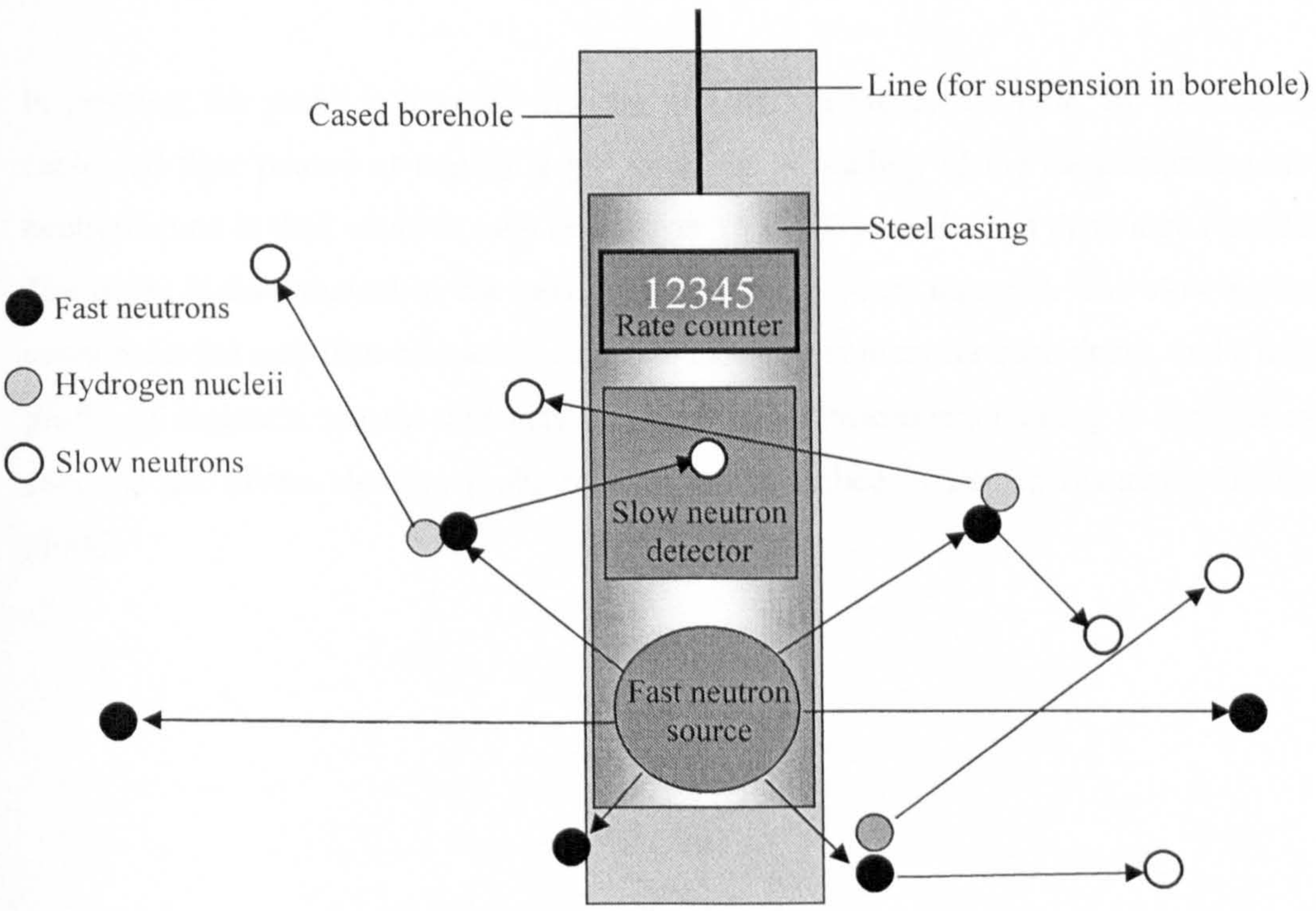

Figure 5.13. Basic schematic diagram of neutron probe.

The fast neutron emitter sends out a large number of high velocity neutrons through interatomic space. These neutrons continue away from the source unless they collide with other subatomic particles in the soil. Normally these other particles will have masses that

are very different to the incoming neutrons, if they are less massive (electrons) they will have little/no effect on the fast neutron, which will continue on its path. If the particles are much more massive (most atomic nucleii) then the neutron will bounce off, its direction will change but its velocity will remain very close to its pre-impact velocity. However, if the neutrons impact with objects of similar mass, then both the neutron and the impacted object will bounce off each other in random directions at velocities approximately half that of the incoming neutron. These slowed particles may then continue on to impact other, similarly sized particles, causing further scattering and slowing. In this way, provided sufficient subatomic particles of correct mass are present in the rock or soil, a cloud of randomly moving slow neutrons will be initiated in the area around the fast neutron source. The slow neutron detector may then record the number of these slow neutrons detected by the rate counter, and the degree of back scattering of neutrons over time is then determined. The important factor as regards moisture content is that the particles with the most appropriate mass to cause this back-scattering effect are hydrogen nuclei (a single proton). Hydrogen nuclei are most common, in the ground environment as the major constituent of water (H_2O), and so the rate of scatter may be used to determine the amount of water in the ground.

In practice, the probe is lowered into the ground, via the access tube, by its electrical cable and then paused at regular depth intervals. A reading of the back-scattered slow neutron count is then taken at each depth over 16 or 64 seconds, and this value recorded. The probe is then moved to the next depth and the process repeated. The slow neutron count recorded may then be used to calculate moisture content for each depth, and a depth profile of moisture content thus may be constructed. Procedures relating to the safe and accurate use of the Neutron probe method are described in British Standards Institute (1996).

5.4.2 Potential drawbacks

Neutron probes have become an established method of investigating water content to any desired depth. However as a practical field tool they do present some problems. The neutron probe contains a sealed radioactive source, therefore training in radiological procedures is necessary for operators, dosimeter badges are required and special precautions have to be taken when storing and handling the probe (Selker *et al.*, 1993, Evett and Steiner, 1995). Furthermore they require a permanently open (although cased) access hole which may provide a pathway for moisture migration even when covered with a sealed access lid. Care must also be taken to install the access tube correctly, without air gaps or voids, in order for the system to yield good data.

The measurement volume is also variable, ranging from 15 to 60cm depending on moisture content of the rock (Ferre *et al.*, 1998b), and the system is not amenable to automation making regular time series data difficult to obtain. As the sampled volume may be quite large the neutron method will tend to smear out rapid and abrupt changes in moisture content into more gradual features (Williams et al, 1981). Hence the resolution of this method is not sufficient for use at depth intervals of less than 100mm. The depth interval used in the sampling of the Sherwood Sandstone was 100mm so smearing effects should be limited to acceptable levels. All the other methods of determining moisture content used (TRIME, TDR) also average results down the electrode lengths so smearing effects in the neutron probe are slightly less than for the TDR based methods.

Problems may also be incurred by variations in temperature or soil composition, the system is susceptible to thermal drift (Bell, 1987) and so large variations in probe temperature (particularly seasonal variation) may limit the effectiveness of the neutron probe method. This should not be a significant problem at the Heck test site as generally subsurface temperatures below a metre depth or so are fairly stable.

Soil composition may also have an effect on the stability of the slow neutron cloud discussed in the previous section. All elements possess nuclei that are capable of scattering fast neutrons, and if enough collisions occur, the neutrons will eventually slow to the point where they are visible to the slow neutron detector. However, the ability of most elements to scatter fast neutrons is rather limited and so, although scatter by elements other than hydrogen will occur, this phenomenon is merely a background effect and can be easily calibrated out. A more significant problem is the ability of certain elements to 'capture' slow neutrons and thus prevent their detection by the system.

Cadmium, boron, iron and chlorine have the ability to capture such neutrons (Bell, 1987), (although iron has less ability to capture neutrons than the others), and so reduce the amount of slow neutrons detected. Again this is a matter of correct calibration and using the probe in environments where such elements are limited. Fortunately, the Sherwood Sandstone contains little iron (only thin haematite grain staining) and little of the other elements so a generic sand calibration was used.

The neutron probe also responds to the total hydrogen content of its surroundings (Bell, 1981, Greacen, 1981), not just the porewater hydrogen content. This is not a problem in relatively clay free rock, but in areas with high clay content, or well-developed soil horizons with significant clay horizons, great care must be taken with this system.

However, despite these drawbacks, as a moisture monitoring method the neutron probe is capable of delivering accurate moisture content profiles with reasonable ease and provides an ideal yardstick to evaluate the performance of the TDR system and to help characterise the hydraulic properties of the Heck test site.

5.4.3. Neutron probe calibration.

The neutron probe records a count rate (number of scattered neutrons.time^{-1}), which is converted into an estimate of volumetric moisture content using a calibration curve. The calibration function used here is;

$$\theta = 1.0509\left(\frac{C}{C_w}\right) - 0.0251 \qquad \text{Equation 5.6}$$

where C is the neutron count rate (output data from the neutron probe), and C_w is the counts per second in a large drum of water. C_w was established experimentally as approximately 900, within a sealed length of the plastic access tube used at the Great Heck test site in a 45-gallon drum of water.

5.4.4. Neutron probe results

The neutron probe results are plotted as depth profiles in Figure 5.14. The results nearest to the surface (at 0, 0.1, 0.2 and 0.3m) may be discarded as the access tube protruded 0.1m above ground level, and the probe records abnormal measurements when influenced by surface effects. Below 0.3m (0.2m below ground) the results are consistent with the corresponding TRIME data. The neutron probe data are compared with the TRIME data in Figure 5.15.

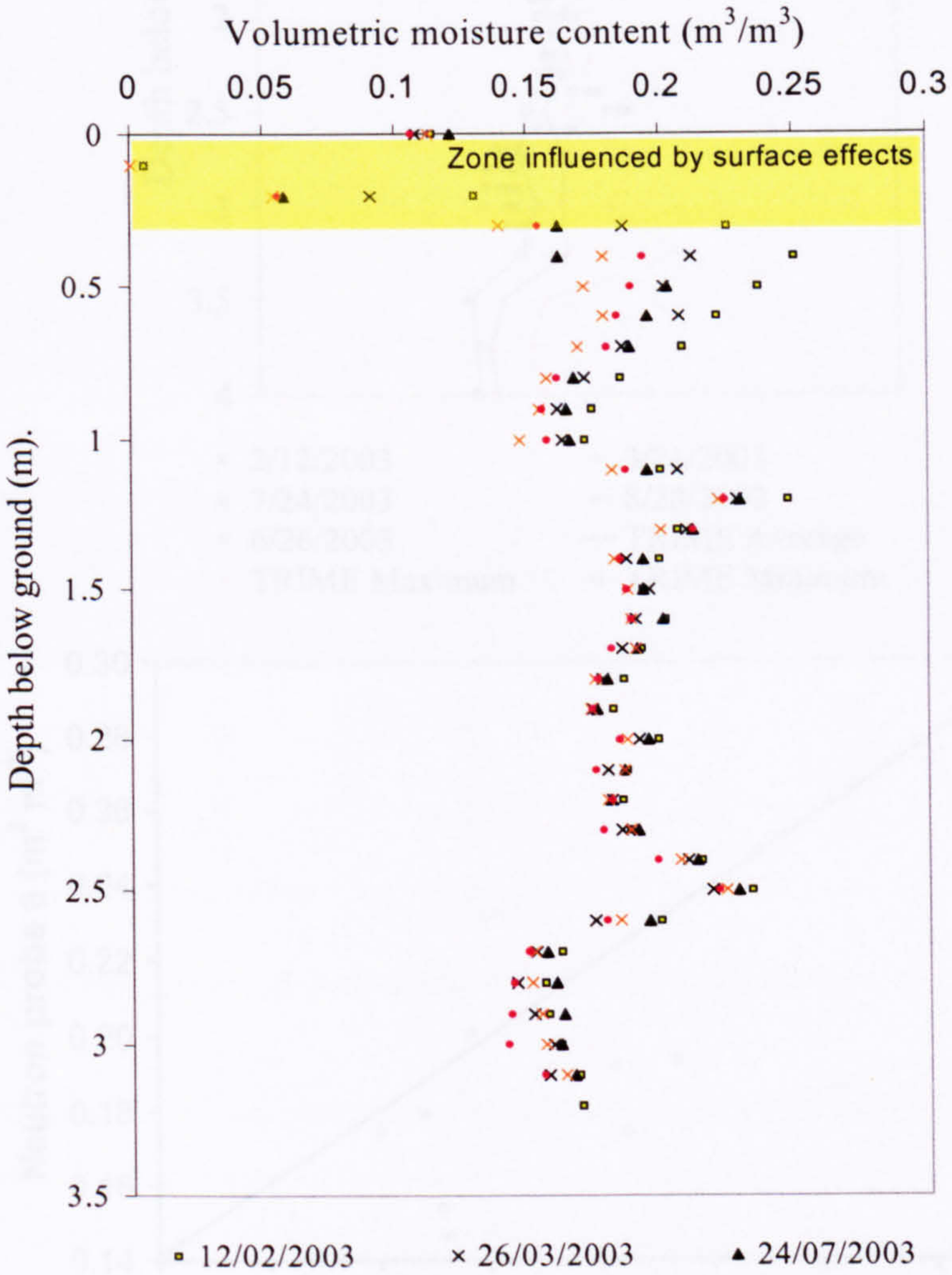

Figure 5.14. Scatter plot of Neutron probe results from Great Heck test site (SE 588213 February-November 2003).

Results from Figure 5.14 show a range of saturations from ≈4 to 25 percent. When plotted with the TRIME results (Figure 5.15.) the moisture contents from the neutron probe are consistently about 5% lower than the corresponding TRIME data. Either lateral variation between the TRIME and neutron probe boreholes (5m apart), or a small air gap around the neutron probe access tube is likely to be responsible for this discrepancy.

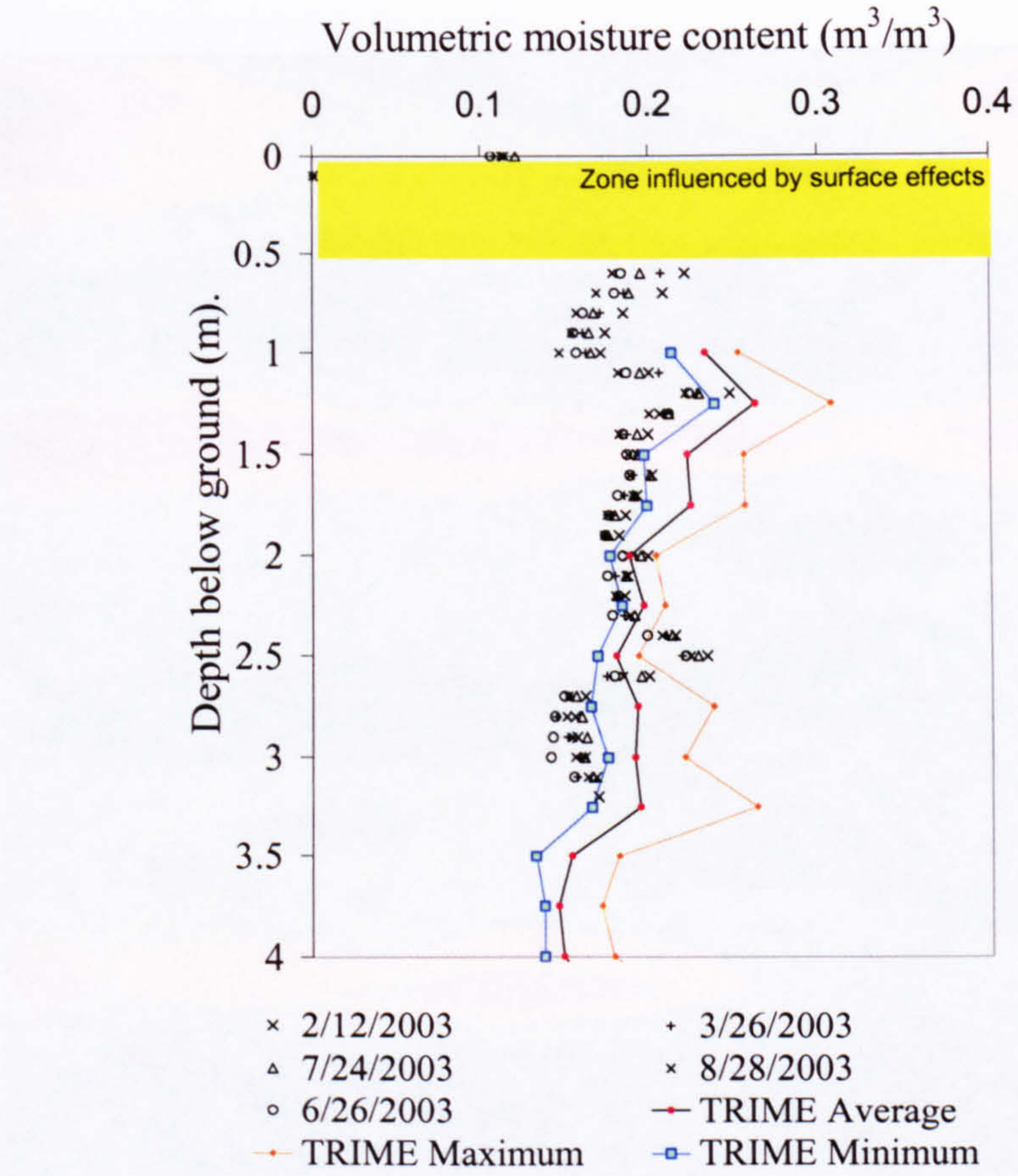

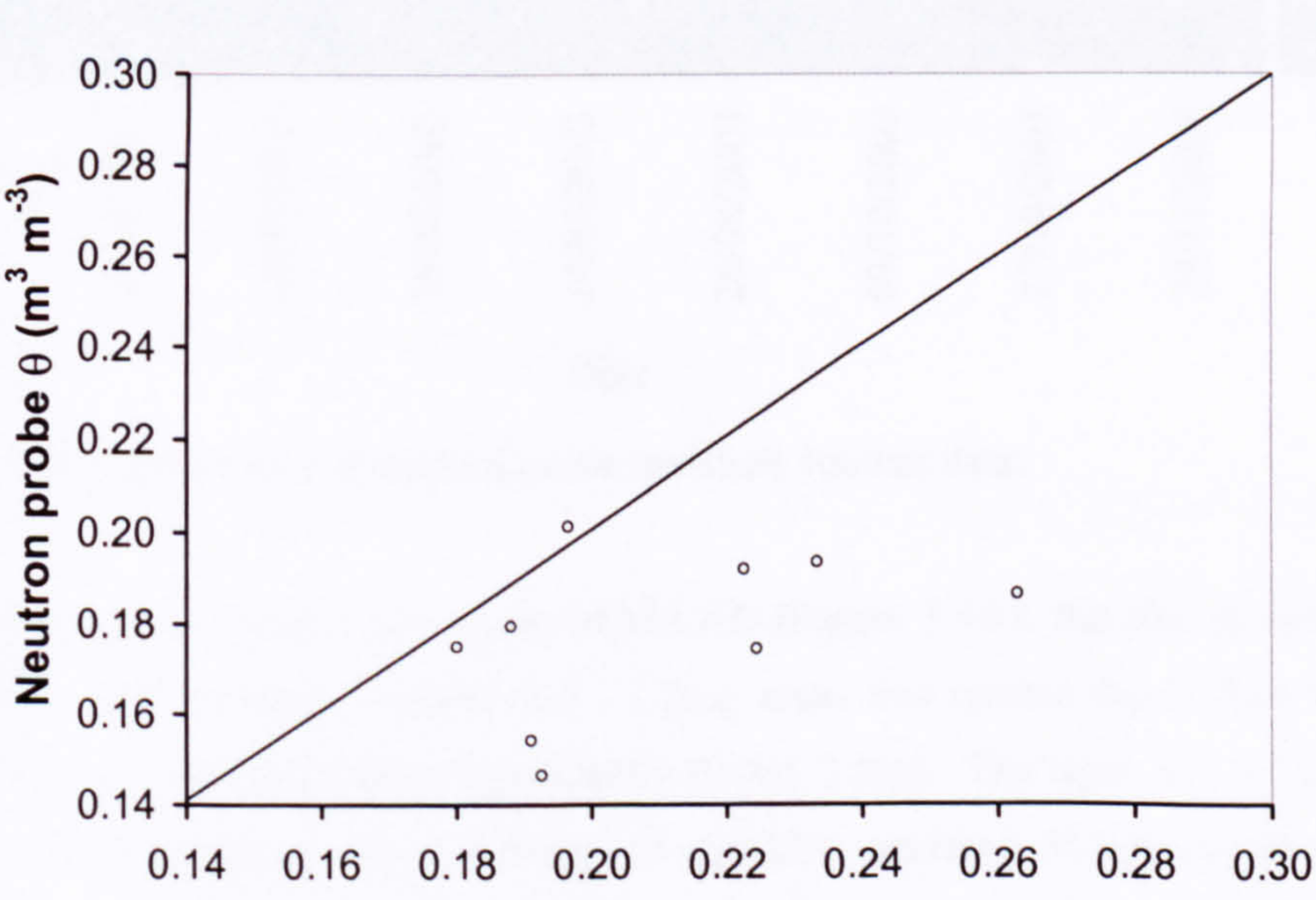

Figure 5.15. a) comparison between Neutron Probe and TRIME results, b) Neutron probe/TRIME crossplot for top 3.2m, black line represents a 1:1 plot.

The neutron probe results show large variation above about 0.7m below ground, where evapotranspiration effects operate. The range of moisture contents below this is typically about 5% which is less than the corresponding results from the TRIME, and is probably due to the larger volume sampled by the neutron probe method.

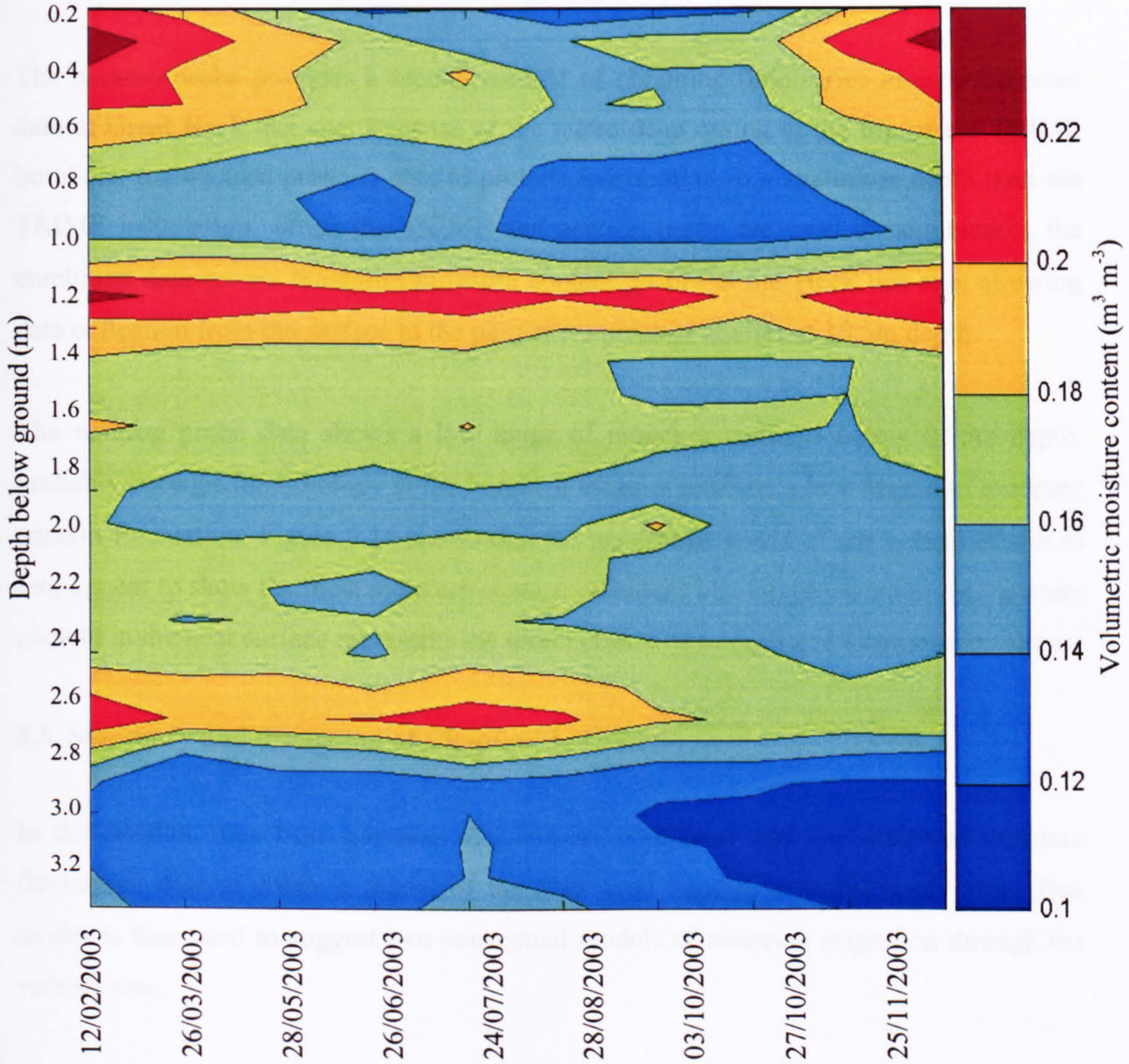

Figure 5.16.Contour plot of neutron probe moisture content data.

When plotted as a contour plot using MATLAB (Figure 5.16.), the plot shows areas of consistently high moisture content (1.0 - 1.2m), areas that remain dry (1.8m), and areas where moisture levels fluctuate significantly (0.4m, 2.5m). The layer at 1.0-1.2m below ground stays consistently wet at between 18 and 22% saturated all year round and this is interpreted as a shallow fine-grained layer that retains water even under high levels of evapotranspiration. The layers above (0.2-0.9m) show significant variation and saturation data from these levels give an indication of effective rainfall (see Section 5.1.1).

The neutron probe provides a moisture content dataset that is independent to the TRIME and TDR systems as it does not rely on dielectric properties of the rock, and allows the moisture content profile of the Great Heck test site to be extended to just under half a metre from the ground surface.

5.4.5. Discussion of neutron probe results

The neutron probe provides a second method of obtaining time-series moisture content data at Great Heck test site. Because of the metre deep casing at the top of the TRIME borehole, the neutron probe is able to provide information to a shallower depth than the TRIME installation. When the TRIME and neutron probe are used in conjunction, the combined data covers the entire moisture content profile at the Heck test site, allowing data collection from the surface to the permanent perched aquifer at 10.5m depth.

The neutron probe data shows a low range of moisture contents below 0.75m depth, probably because the lithology at the borehole location exhibits a low degree of moisture content fluctuation. Figure 5.14 shows that the uppermost levels of the system (down to 1m) appear to show the most moisture content variation. The larger variations in moisture content in the near surface represents the direct effects of rainfall and evapotranspiration.

5.5. Summary and discussion of Chapters 3, 4 and 5

In this section, data from previous chapters are combined with the observed moisture fluctuation data to create a model of the Sherwood Sandstone in the study area. This model is then used to suggest two conceptual models of moisture migration through the vadose zone.

Lithological structure of the Great Heck test site

The quantification of sedimentary features presented in Chapter 3 suggests that the Great Heck test site is representative of the Sherwood Sandstone in the Northeast of England. Observational and geophysical evidence presented in Chapters 3, 4 and 5, lead to a series of synthetic and actual sedimentary logs that are reproduced in Figure 5.17. The purpose of this is to produce an outline three-dimensional view beneath the Great Heck test site, so that potential preferential pathways or conduits between boreholes can be located. The coloured sections joining features between the boreholes in Figure 5.17 represent an interpretation of the lateral continuity of sedimentary units. The yellow shaded areas represent trough cross-bedded units, and the grey shaded areas represent planar laminated units. Many of the logs used in the construction of Figure 5.17 were derived from GPR data, which has resulted in truncated logs for all boreholes except the TRIME and TDR 4 boreholes. This has therefore limited the depth to which features may be laterally

interpreted but face logs (see Chapter 3) show that the units remain laterally persistent over distances of tens of metres.

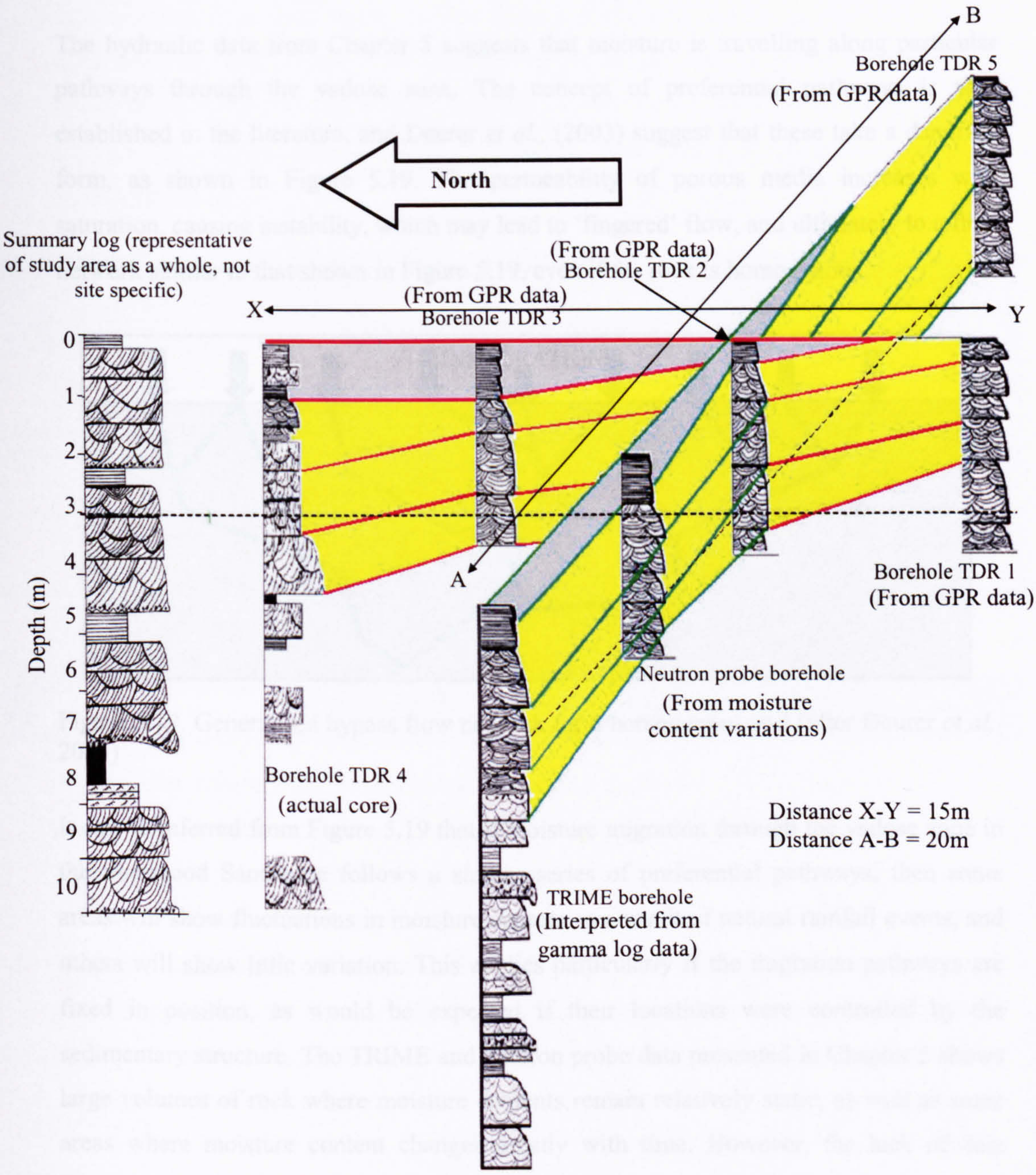

Figure 5.17. Linked boreholes at Great Heck test site (SE 588213). Depth scale as per summary log on far left of figure.

Hydraulic data from the TRIME and Neutron probe discussed in Chapter 5 suggests that water is ponding at certain depths. Planar laminated units may act as barriers to vertical flow, causing perched water tables at times of increased hydraulic loading, providing hydraulic heads that may drive lateral moisture migration. The geological model shown in Figure 5.17 was used to provide lithological constraints on the interpretation of results obtained from the packer mounted TDR system (See Chapter 6).

5.6. Conceptual vadose zone flow models

The hydraulic data from Chapter 5 suggests that moisture is travelling along particular pathways through the vadose zone. The concept of preferential pathways is well established in the literature, and Deurer *et al.,* (2003) suggest that these take a dendritic form, as shown in Figure 5.19. The permeability of porous media increases with saturation, causing instability, which may lead to 'fingered' flow, and ultimately to a flow network similar to that shown in Figure 5.19, even if the rock is homogenous.

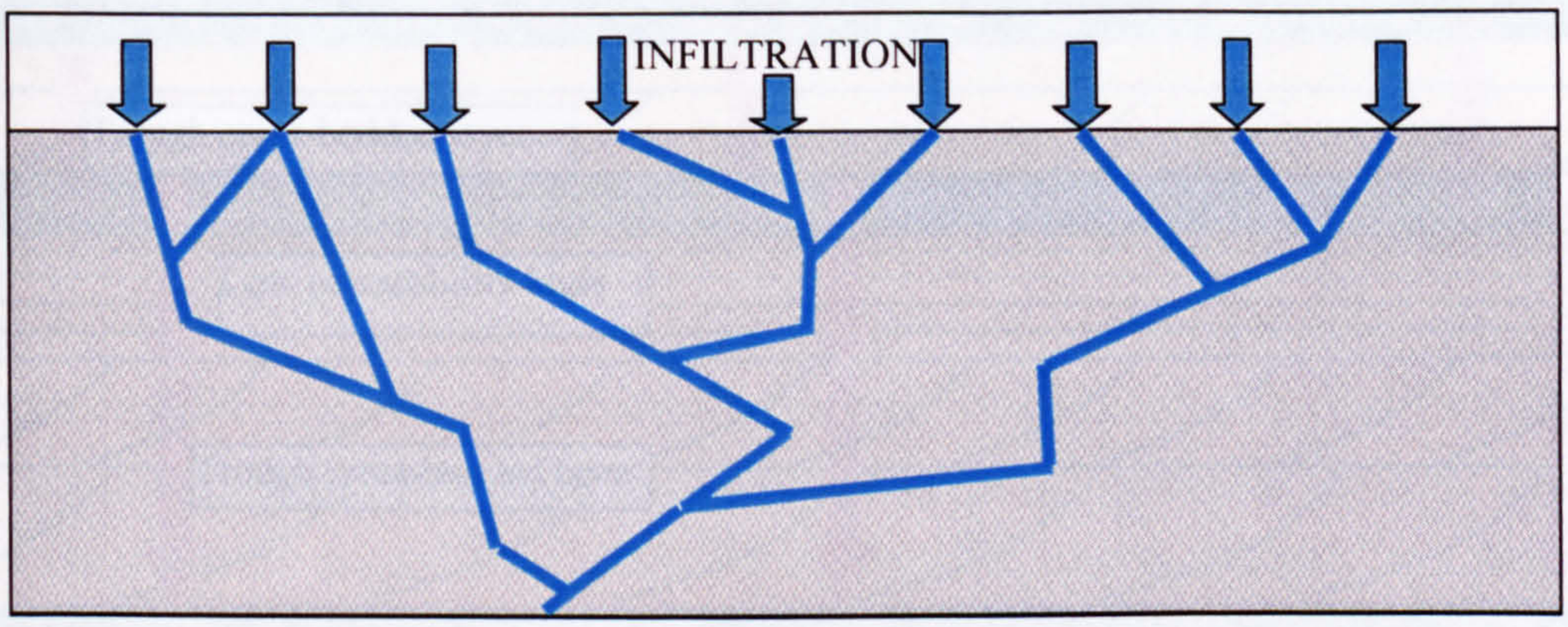

Figure 5.19. Generalised bypass flow network for a homogenous soil (after Deurer *et al.,* 2003)

It can be inferred from Figure 5.19 that if moisture migration through the vadose zone in the Sherwood Sandstone follows a similar series of preferential pathways, then some areas will show fluctuations in moisture content as a result of natural rainfall events, and others will show little variation. This applies particularly if the migration pathways are fixed in position, as would be expected if their locations were controlled by the sedimentary structure. The TRIME and neutron probe data presented in Chapter 5 shows large volumes of rock where moisture contents remain relatively static, as well as some areas where moisture content changes greatly with time. However, the lack of data density in the time domain means that the possibility that the majority of the water is migrating in a vertical direction cannot be dismissed (see Chapter 6 for examples of vertical flow models that do not show wetting fronts). Steady-state flow, where the moisture content remains the same, but water is continually migrating through the rock is also possible.

Data presented in chapters three to six may therefore be used to constrain a series of conceptual models for moisture migration in the vadose zone of the Sherwood Sandstone.

Model 1. Vertical flow

This model is essentially the plug-flow model described in Chapter 2. Infiltrated moisture moves solely in a downward direction (Figure 5.20). Horizontal permeability is not considered by this model, and seepage velocities are purely dictated by vertical permeability and are constrained by capillary tension. Hence, water is only able to cross between lithologies with different pore throat sizes when propelled by sufficient hydrostatic head.

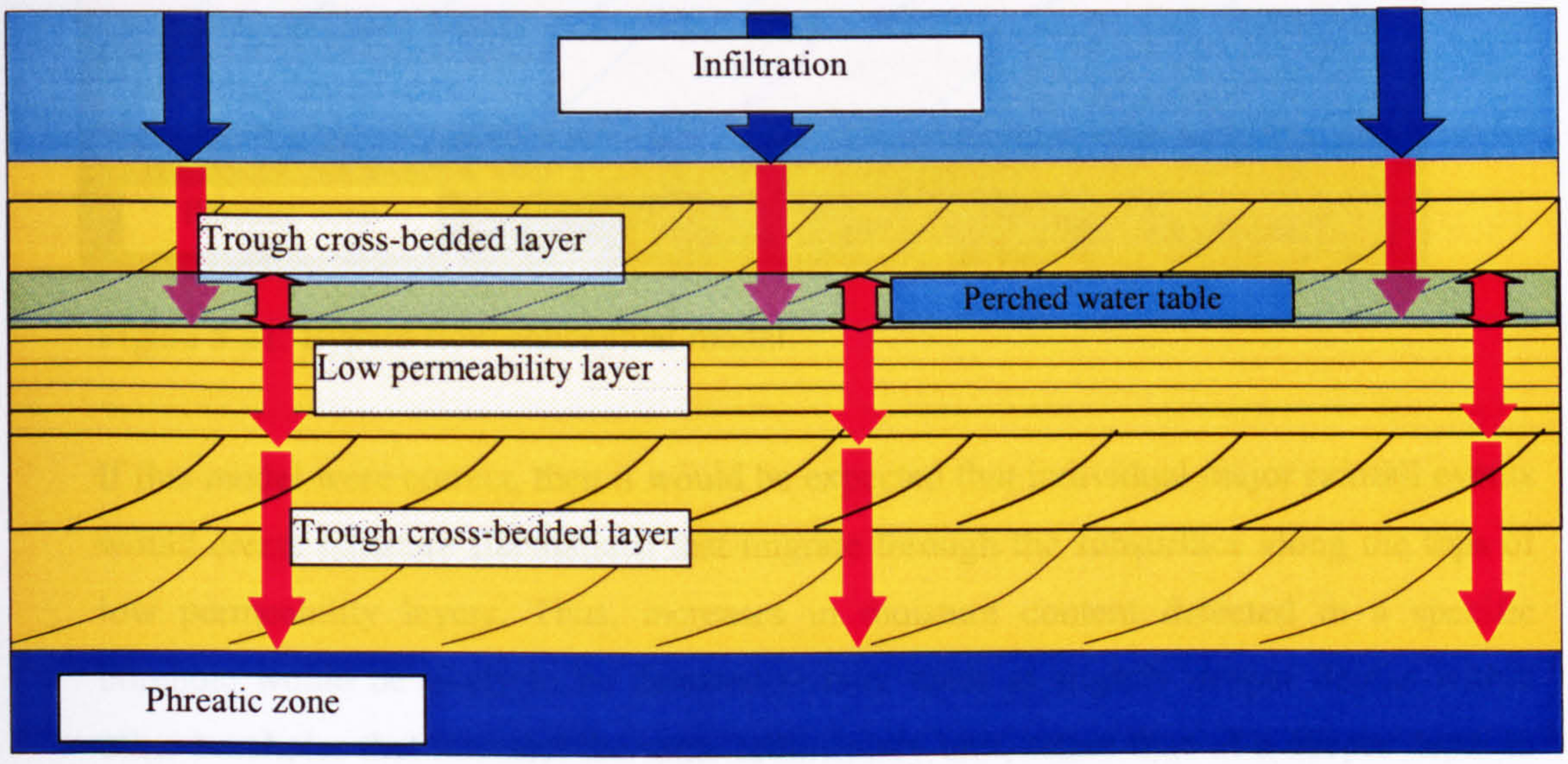

Figure 5.20. Pure vertical flow conceptual model.

If this model is correct, then it would be expected that individual major rainfall events could be monitored by mass balance methods as they move towards the water table. Moisture would tend to form perched aquifers upon low permeability units, with water migrating through the low permeability units once sufficient hydrostatic head had been built up. Hence the permeability of such a system would be controlled by the permeability of the least permeable unit.

Model 2 Bypass flow

Here, infiltrated moisture moves in a direction controlled by the local permeability field (Figure 5.21). Both horizontal and vertical permeabilities are considered by this model, seepage velocities are controlled by the vectors of hydraulic gradient and highest permeability. Once in coarser-grained units, the water will tend to flow horizontally until it finds an easy path downwards.

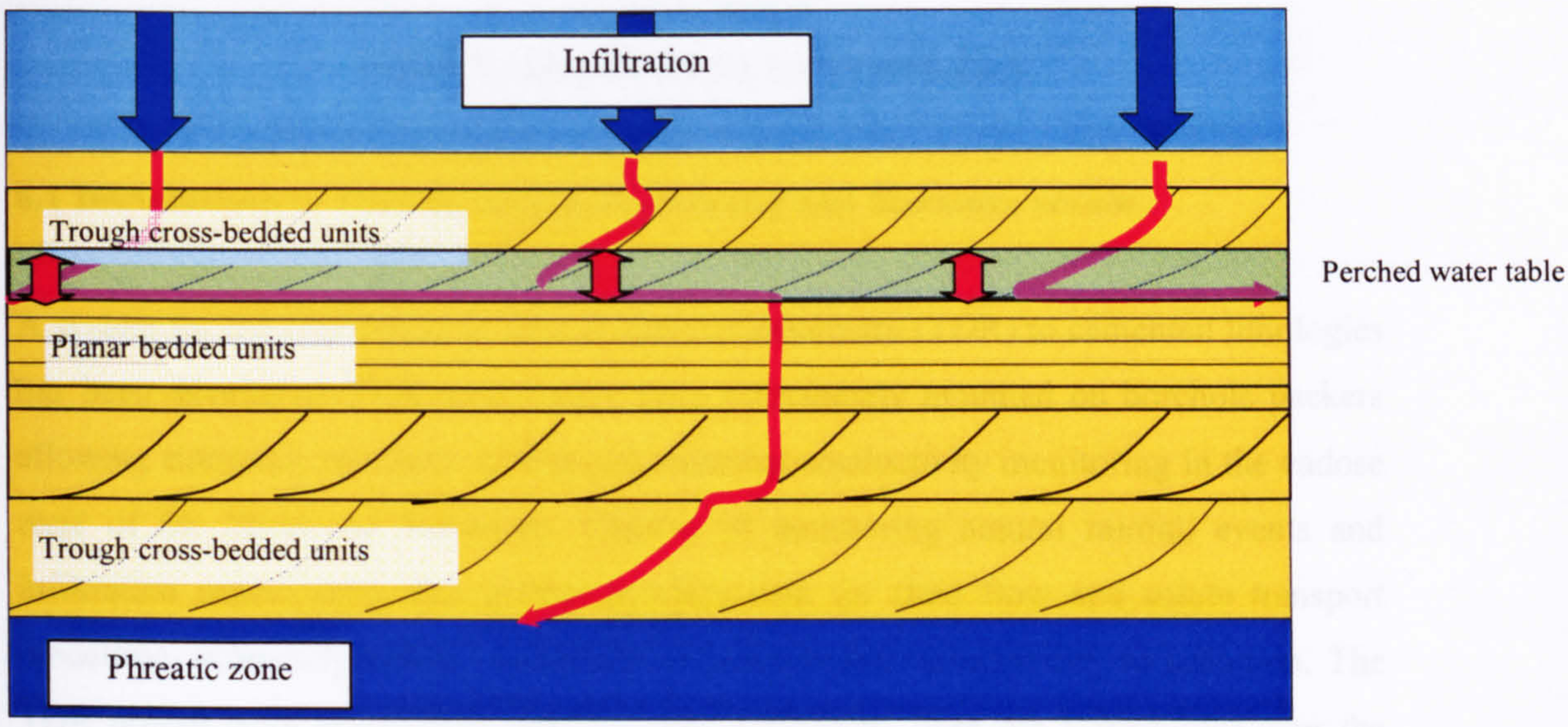

Figure 5.21. Bypass flow conceptual model.

If this model were correct, then it would be expected that individual major rainfall events would create moisture fluctuations that migrate through the subsurface along the tops of low permeability layers. Thus, increases in moisture content detected in a specific borehole would be likely to be detected at later dates at slightly deeper depths within other boreholes that intersect the same sedimentary unit, rather than at a deeper depth in the same borehole. Flow would be via a series of conduits or perched water tables, each flowing in a direction and velocity dependent upon the vector product of horizontal/vertical permeability and hydraulic gradient. Hence, the permeability of such a system at a particular level would be strongly influenced by the permeability, continuity and topography of the most permeable unit. If this model is correct, the moisture content of an individual column through the vadose zone will not remain constant, i.e. mass will not be conserved within vertical columns due to lateral flow. Absolute proof of bypass flow would be if a response to an identifiable rainfall event was seen in a deep layer within a borehole, and subsequently the same rainfall event was detected in the same borehole at a shallower depth.

It is probable that both the models described here play a role in describing how moisture migrates through the vadose zone. However, one mechanism will probably be dominant, although this dominance may vary according to seasonal rainfall loading. Subsequent chapters will present data that has a high temporal frequency (daily) and a mass balance model that clarifies which mechanisms control vertical moisture migration.

CHAPTER 6
TIME DOMAIN REFLECTOMETRY.

6.1 Introduction to Time Domain Reflectometry and literature review.

A system for the application of time domain reflectometry (TDR) to cemented lithologies has been developed. TDR probes have been permanently mounted on borehole packers allowing automatic moisture content and electrical conductivity monitoring in the vadose zone of the Sherwood Sandstone. Capable of monitoring natural rainfall events and infiltration experiments, this system provides data for fluid flow and solute transport modelling, ultimately aiding assessment of groundwater vulnerability to pollution. The TDR probes were designed to produce good reflections from the waveguides over the range of dielectric constants seen in the field, thus allowing accurate determination of moisture content, with maximum sensitivity to the dielectric constant of the rock. Comparative results show that the TDR system provides results consistent with other techniques such as the neutron probe and TRIME systems.

Over the previous two decades the technique of time domain reflectometry has been developed as a highly accurate method for measuring moisture content in soils to an accuracy within 1-2 percent of the true volumetric water content (Topp *et al.*, 1980, Jones *et al.*, 2002). TDR hardware is relatively inexpensive and may easily be automated (Huang & Dowding, 1994) and so it has gained wide acceptance as a useful technique for monitoring electrical conductivity and moisture flux in unconsolidated sediments, particularly by soil scientists (Wraith & Das, 1998, Jones *et al.*, 2002. Ferré & Rudolph, 1998; Al Hagrey & Michaelson, 1999; Robinson *et al.*, 1999). Many systems and probe designs are now commercially available for use in soils. However, its application for monitoring moisture content in rocks is less well developed, mainly because of the difficulty in inserting the TDR probes without air gaps (Hokett *et al.*, 1992; Sakaki *et al.*, 1998).

Previous attempts to solve this problem using borehole packers have focussed on the use of short packers with TDR waveguides embedded in their walls that are inserted in uncased boreholes on a temporary basis, such as the TRIME system (Stacheder *et al.*, 1994, 2000). However, such systems may produce errors when used to collect time-series moisture content data, due to the repeated repositioning of the TDR waveguides between subsequent readings and difficulties in maintaining a consistent probe orientation. Tests

reported in Chapter 5 however, indicated that this did not cause significant inaccuracies with data collected at the Great Heck test site. Open boreholes may also act as preferential flow paths for water in extreme rainfall conditions (although data reported in Chapter 5 suggests that this was not common during the monitoring period). The main drawback with systems such as the TRIME and neutron probe is that these systems require manual data collection, which limits their applicability for frequent collection of moisture content profiles.

A borehole packer system is reported here, in which packers with multiple TDR waveguides were permanently installed in boreholes by filling with grout. The aim was to provide time series moisture content data at a range of depths, to track lateral and vertical water and pollutant movements within the vadose zone. TDR data therefore complement those obtained in previous chapters and also other studies that have used cross-borehole radar to inform groundwater vulnerability assessment (Binley *et al.* 2001a&b; 2002). Such data may ultimately aid the development of stochastic models of vadose zone flow. The principal advantages of TDR over techniques such as cross-borehole radar for determination of moisture flux are improved accuracy and the ease with which a TDR installation may be fully automated (Huang & Dowding, 1994, Jones *et al.*, 2002). Such a system may collect regular datasets without supervision (beyond monthly visits for data downloads and battery changing). This level of automation enabled the collection of moisture content profiles on a daily schedule, allowing monitoring of seasonal moisture variation with a data density high enough to image individual rainfall events.

<u>Summary of TDR advantages over other methods.</u>

- The system, once installed, could be easily automated so frequent readings were taken without the necessity of constant site visits.
- The technique provided demonstrably accurate moisture content readings.
- The technique can accurately measure conductivity, so saline intrusion tests were possible.
- The technique is largely independent of variations in lithology (West *et al.*, 2003).
- Sealed boreholes should not act as a preferential pathway to water movement.
- The field electrodes were simple and cheap to construct.

Hence a TDR system was an obvious method for monitoring seasonal change in vadose zone moisture contents, and Chapter 6 describes the development and use of a system designed to be permanently installed in rock.

TDR Theory, basic introduction.

The velocity with which a voltage step travels through a wire is determined by the dielectric properties of the material surrounding that wire (Topp, 1980). The relationship between velocity and dielectric properties is the same as described in Chapter 4, Equation 4.4. In the case of TDR, the a voltage pulse is sent through an open circuited coaxial line where the inner and outer coaxial conductors are not in electrical continuity. Part of the transmitted voltage is reflected every time the impedance of the wire changes. Commercially available systems have been developed based on these reflected pulses, which calculate the velocity of a voltage pulse through a probe, and hence determine the relative dielectric permittivity (ε_r) of the medium (soil or rock) surrounding the electrodes.

Generally ε_r values are given by,

$$\varepsilon_r = \left(\frac{c\Delta t_s}{2L}\right)^2 \qquad \text{Equation 6.1}$$

where c is the velocity of an electromagnetic wave in a vacuum ($3x10^8 ms^{-1}$), Δt_s is the travel time of the TDR signal within the TDR probe (s) and L is the length of the TDR probe (m) (Huisman *et al.*, 2002).

The TDR pulse generator (in this study a Campbell Scientific TDR 100 unit) transmits a short rise time voltage step through coaxial cables to a TDR probe mounted in or against the material under investigation. Part of this voltage step is reflected each time the step meets an impedance change and this reflected signal travels back to the TDR device which detects it as a change in voltage. Provided coaxial cable and connectors all have equal impedence (usually 50Ω), and the TDR has impedance usually around 250-300Ω, the first voltage rise (1) in Figure 6.1 detected at the TDR unit represents the reflection from the top of the probe. The second voltage rise (2) results from the reflection at the abrupt impedance change at the open ends of the TDR probe. The time difference (Δt_s) between the two voltage steps represents the time taken for the voltage step to travel down and back up the probe (2L). Hence, by knowing the true length of the TDR probe the permittivity (K_a) of the material around the probe may be calculated using equation 6.1.

In practice, the TDR hardware usually records a trace or plot of reflection coefficient (see Equations 6.2 and 6.3 for definition) against apparent distance (which equals $\Delta t_s.L$) (Figure 6. 1). The timing circuit times variations in the voltage detected at the TDR unit. This data may then be exported to either a PC or a datalogger where it is interpreted by software. The user specifies the true length of the electrodes (L), and roughly at what apparent cable length (pulse velocity in cable x true cable length) voltage steps 1 and 2 will be received at the TDR unit. Software packages are available that detect the voltage rises that occur as the reflections arrive back at the unit, and can accurately determine the time difference between them.

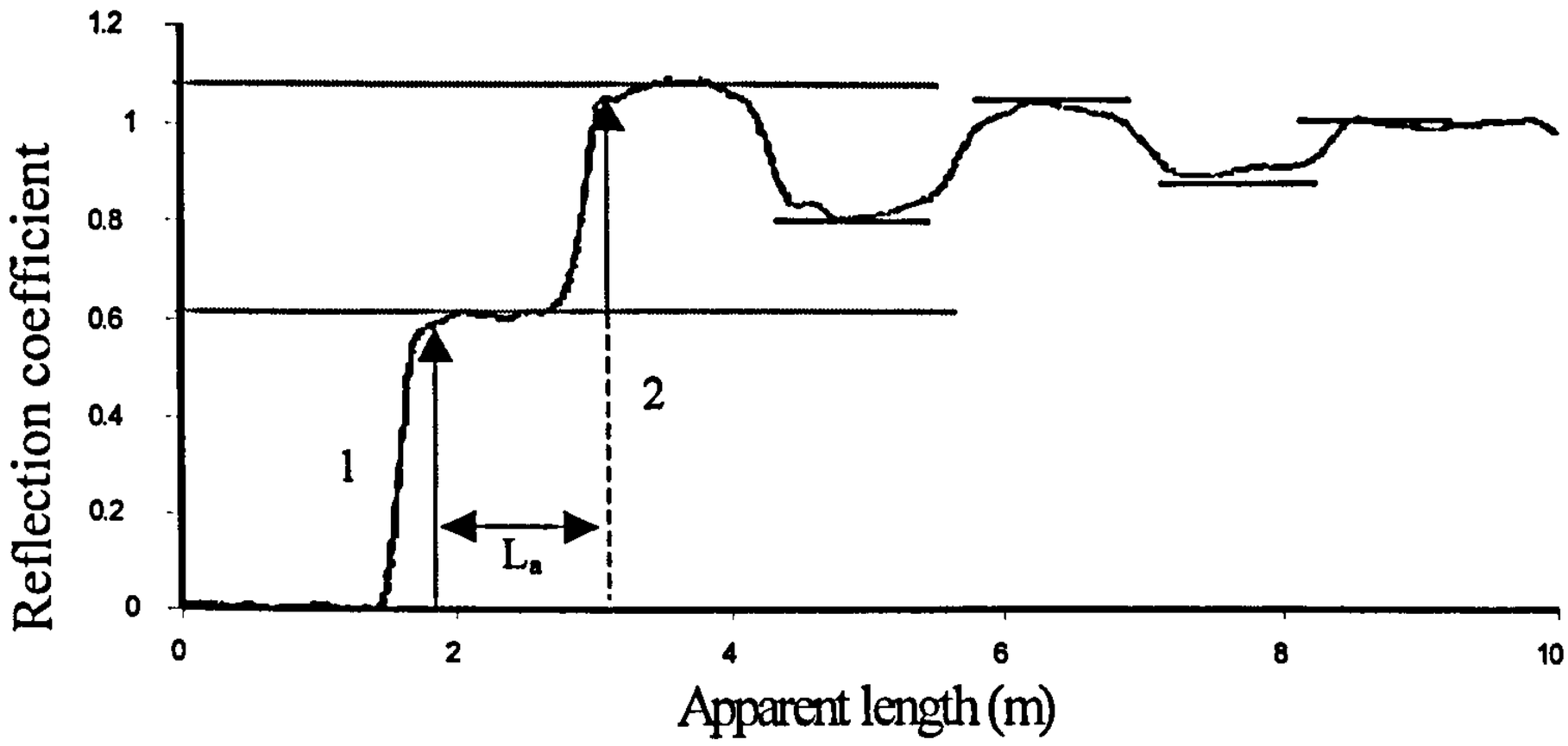

Figure 6.1. A typical TDR trace

The time difference (Δt_s) represents the time taken for the pulse to travel down and back up the length of the electrodes. The velocity of light in a vacuum ($C = 3x10^8 ms^{-1}$) is used to calculate an apparent length for the electrodes (L_a) using the equation, $2L_a=(\Delta t_s.C)$. The ratio L_a/L is then calculated, and some programs output this value (Campbell Scientific CS208) while others (Campbell Scientific PC TDR) calculate the moisture content directly. They are able to do this because the ratio, L_a/L equals the square root of the relative permittivity (ε_r) of the material around the electrodes.

Water has a much higher dielectric constant than air or mineral solids. Hence it is possible to use the permittivity obtained from the TDR system for determining moisture content using one of the many equations designed for this purpose. The most commonly used equation is that proposed by Topp (1980). However there are many other empirical calibration equations in the literature, designed for various soil types, and a few of these are listed in table 6.1. Work done by West *et al.* (2003) suggests that the CRIM method, using a mineral dielectric permittivity of 5 is ideal for the Sherwood Sandstone. However,

the majority of the software packages used in this study calculate moisture content via the Topp equation. This calibration has been shown to work well in clay-poor sandy environments (West *et al.*, 2003), so to avoid introducing inconsistencies into the data TDR moisture contents reported in this thesis have been calculated after Topp (1980).

Reference	Equation
Topp *et al.* (1980)	$\theta_v = -0.053 + 0.0293\varepsilon_r - 0.00055\varepsilon_r^2 + 0.0000043\varepsilon_r^3$
Baran, (1994)	$\theta_v = -0.062164 + 0.023831\varepsilon_r - 0.000598\varepsilon_r^2 + 0.000006\varepsilon_r^3$
Ledieu *et al.* (1986)	$\theta_v = 5.688T_c - 3.38\rho - 15.29$
Malicki *et al.* (1996)	$\theta_v = \frac{\sqrt{K_a} - 0.819 - 0.168\rho 0.159\rho^2}{7.17 + 1.18\rho}$

Table 6.1. Moisture content calibration equations (abridged from Wright *et al.*, 2001) where ρ is dry soil bulk density in g cm^{-3}.

6.2 TDR probe design.

To obtain time-series data from a TDR system in rock it was decided to mount the probes on inflatable packers that could be permanently grouted into uncased boreholes. Initially two field sites were selected, adjacent to Hatfield Quarry and in Great Heck Quarry. TDR packers were subsequently designed and emplaced at these locations, with the Hatfield installation (three TDR packers) preceding the Heck installation (four packers) by over twelve months. However the Hatfield installation failed because of the bursting of the single skinned packers that were used, and difficulties due to the roughness and caving of the borehole walls prior to installation. However, as a result of lessons learned at the Hatfield test site, the packer design was modified and four TDR packers were successfully installed at Great Heck test site.

Operating in the range 500-1000MHz, TDR penetrates much less into the rock than GPR and thus has a much smaller sampling volume (West *et al.*, 2003). This means that it is absolutely vital that TDR electrodes are positioned so that they have minimum air gap between the electrode and the rock. The packer system described here was designed to achieve this with a permanent installation. Laboratory tests carried out by Persson and Berndtsson (1998) and Selker *et al.* (1993) showed that surface (or borehole) mounted TDR probes were feasible, and would provide accurate ε_r values for the rock medium

provided correctly calibrated. Hence TDR probes optimised for use in such an environment were designed and constructed for field use.

The probe optimisation was conducted by Yi Huang and Mansor Nakhkash at the Department of Electrical and Electronic Engineering, University of Liverpool, UK., and the remainder of this section is a description of their work. Probe impedance needs to be optimised so that both the first and second reflections can be distinguished clearly over the range of moisture contents expected in field conditions, thus facilitating the determination of the two-way travel time for the signal within the waveguides. Assuming the transmission line formed by the waveguides has zero loss, changes in impedance happen abruptly where the coaxial cable is joined to the waveguides, and the coaxial cable has 50Ω impedance, an expression for the reflection co-efficient for the first reflection, R, (see Figure 6.2) may be derived. The reflection coefficient is represented by the symbol Γ (see Chapter 4), the transmission line impedance by R and Z is the impedance of the waveguides.

$$\Gamma = \frac{Z - R}{Z + R} \quad \text{(Rizzi, 1988)} \qquad \text{Equation 6.2.}$$

Substituting known values for Z, the first reflection, Γ_R is given by:

$$\Gamma_R = \frac{Z - 50}{Z + 50} \qquad \text{Equation 6.3}$$

The second reflection co-efficient (Γ_T), which is a result of two transmissions (cable ⇒ waveguides and waveguides ⇒ cable) plus the reflection from the waveguide tips is given by:

$$\Gamma_T = \frac{200Z}{(Z + 50)^2} \qquad \text{Equation 6.4}$$

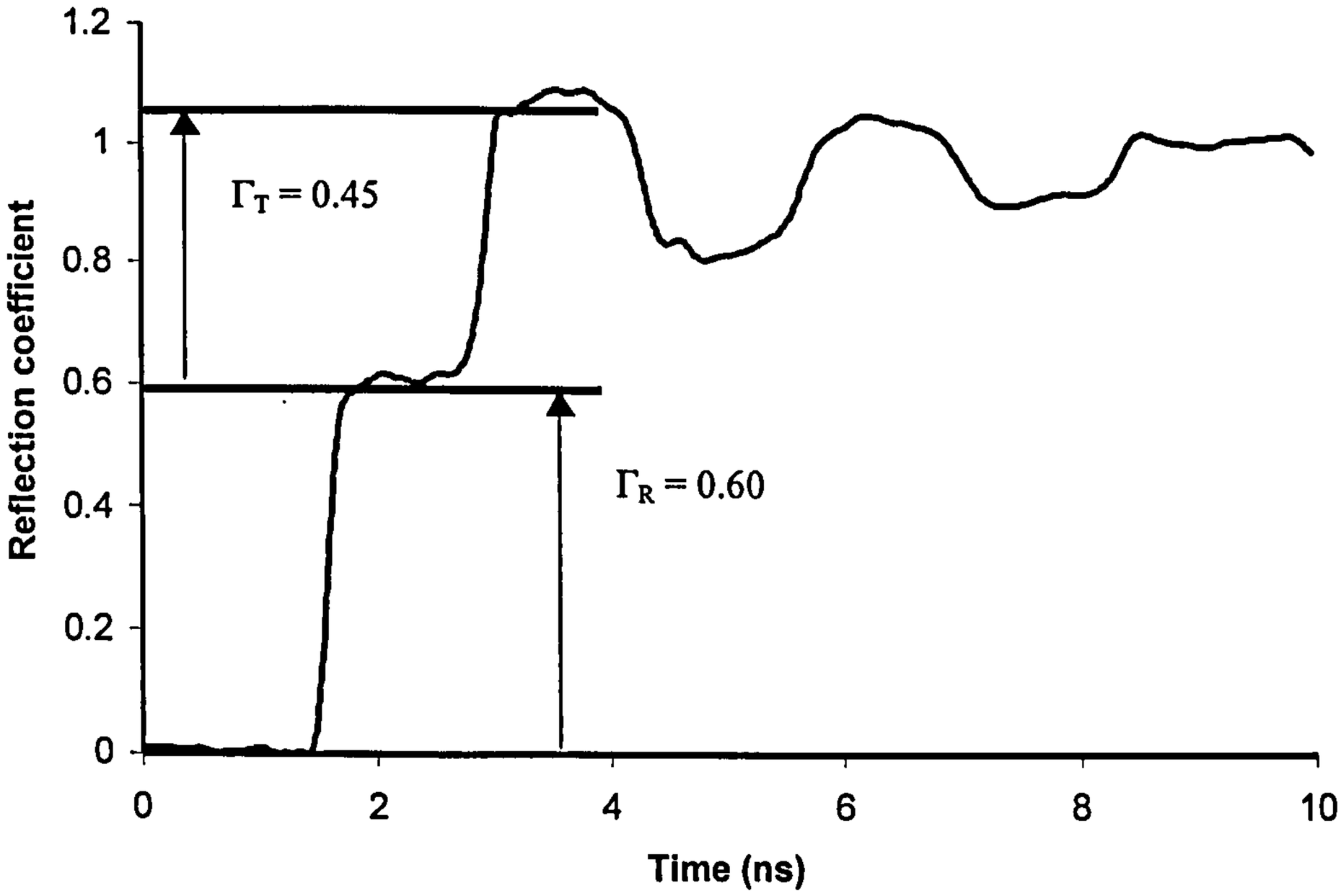

Figure 6.2. TDR trace for prototype probe

The dependence of Γ_R and Γ_T on Z is illustrated in Figure 6.3, which shows that as Γ_R increases, Γ_T decreases. As Z nears 50Ω the first reflection becomes small, hence the TDR waveguides need to have a characteristic impedance greater than 50Ω. The intersection where both jumps are equal can be found by equating (1) with (2) giving a result Z of 211.8Ω. Hence, the optimum probe impedance is 211.8Ω. However, probe impedance depends on the dielectric properties of the medium as well as probe geometry, with increasing dielectric constant leading to reduced probe impedance. Hence in practice a range of probe impedances will occur, according to the dielectric constant of the rock. In order to investigate this, impedances for various probe geometries were modelled by Mansor Nakhkash and Yi Huang at the University of Liverpool Dept. of Electrical and Electronic Engineering, using Concerto (Vector Fields, Oxford, UK) and Cray LC (Cray Research, Seattle, USA) finite-difference time-domain (FDTD) method software for electromagnetic simulation, programs that are particularly suited for TDR and GPR applications.

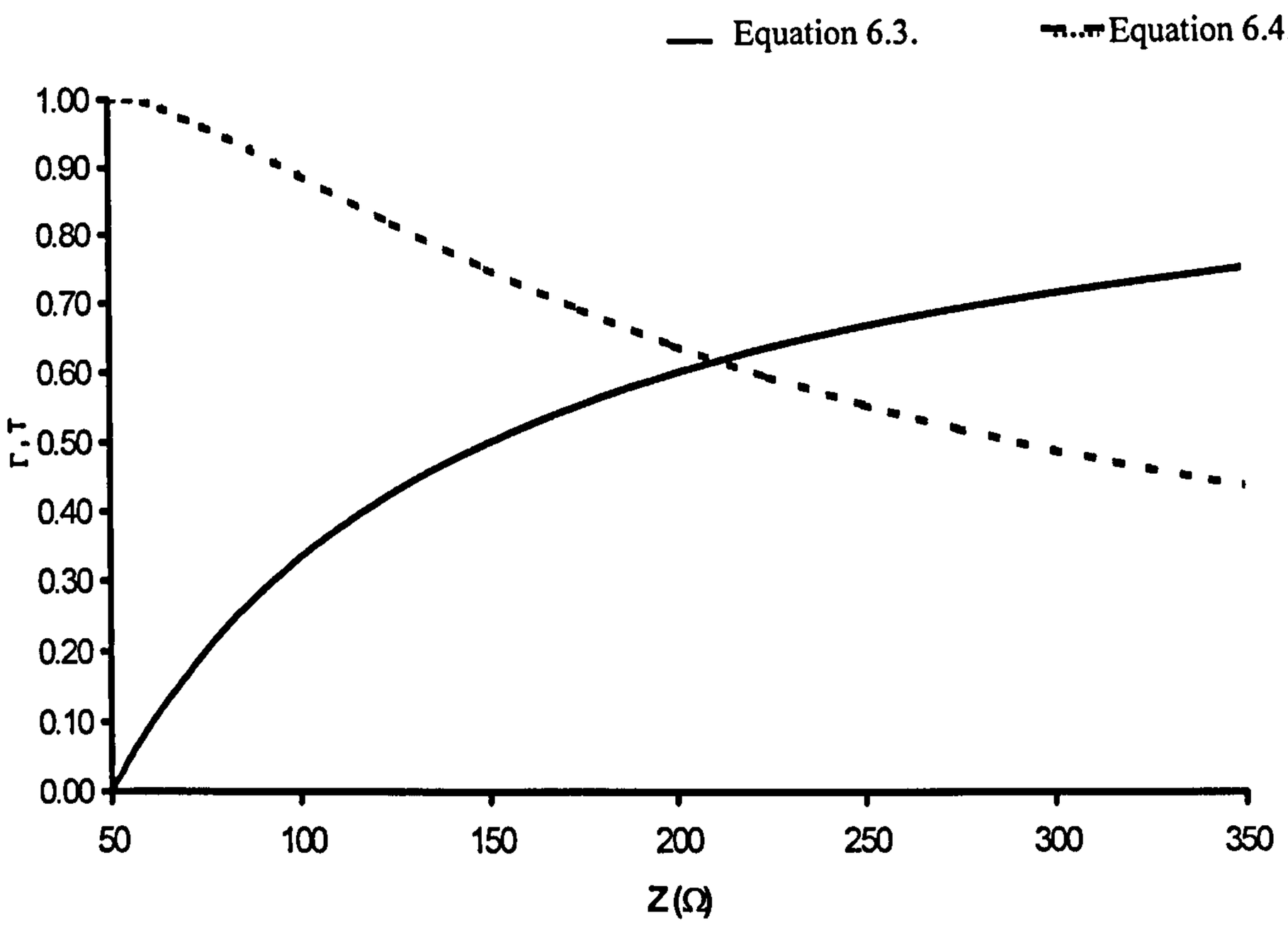

Figure 6.3. Dependence of reflection co-efficient on probe impedance

The results of this modelling showed that in order to provide detectable first and second reflections over the range of dielectric constants expected in the field (3 for dry rock to 37 for saturated rock), the impedance of the packer-mounted probe in air needs to be greater than 250Ω. This ensures the impedance of the probe remains above 50Ω, and the first reflection, remains detectable even in saturated rock conditions. However the Z value in air should not be too large so as to reduce the second reflection to small values. As a compromise impedance of 275Ω in air was selected.

Kraus (1984) proposed an equation to determine approximate probe impedance. Where s is electrode separation and d is electrode radius, probe impedance is given by:

$$Z = \left(\frac{120}{\sqrt{K}}\right) \times \ln\left(\frac{s}{d}\right) \qquad \text{Equation 6.5}$$

Using equation 6.5 with Z of 275Ω and K_{air} of 1 the ratio of probe spacing to probe diameter of 9.89:1 may be determined

The next step in waveguide design was to identify a waveguide geometry that would produce characteristic impedance of 275Ω in air, when placed on an appropriate backing

material. Further simulation with LC software showed that for thin waveguides mounted on thick plastic backing, an impedance of 275Ω in air was attainable when the ratio of waveguide separation to waveguide width was equal to 10, regardless of the actual dimensions of the waveguides. This agrees strongly with the calculated value from equation 6.5 above and other researchers (Knight, 1992).

As equations 6.2 and 6.3 do not account for losses in the coaxial cable or the BNC connector, it was considered necessary to measure the impedance of a probe constructed to the above specifications, as a check. A prototype probe was constructed from aluminium of thickness 0.5mm, consisting of 250mm long waveguides, 3mm in width, separated by a 3cm gap, and attached to 6mm thick neoprene backing material with adhesive. A typical TDR trace obtained using the Campbell Scientific TDR 100 unit for this probe arrangement in air is shown in Figure 6.2. Assuming no loss in the probe itself (essentially correct for the air/backing material combination), the impedance is:

$$Z = 50\,\frac{2+\sqrt{4+\beta^2}}{\beta} \qquad \text{Where } \beta = T/R \qquad \text{Equation 6.6.}$$

From Figure 6.2, the first reflection co-efficient R is 0.60 and the second T is 0.45, so β is 0.78, and Z is 276Ω. This is very close to the theoretical value predicted from the LC software (275Ω). Probe orientation was optimised by testing of six waveguide assemblies with flat electrodes suitable for packer mounting (with three different waveguide widths and spacings all obeying the 1:10 ratio). A bonded neoprene backing material was used and this method of construction allowed each assembly to be used either circumferentially or vertically (figure 6.2.3).

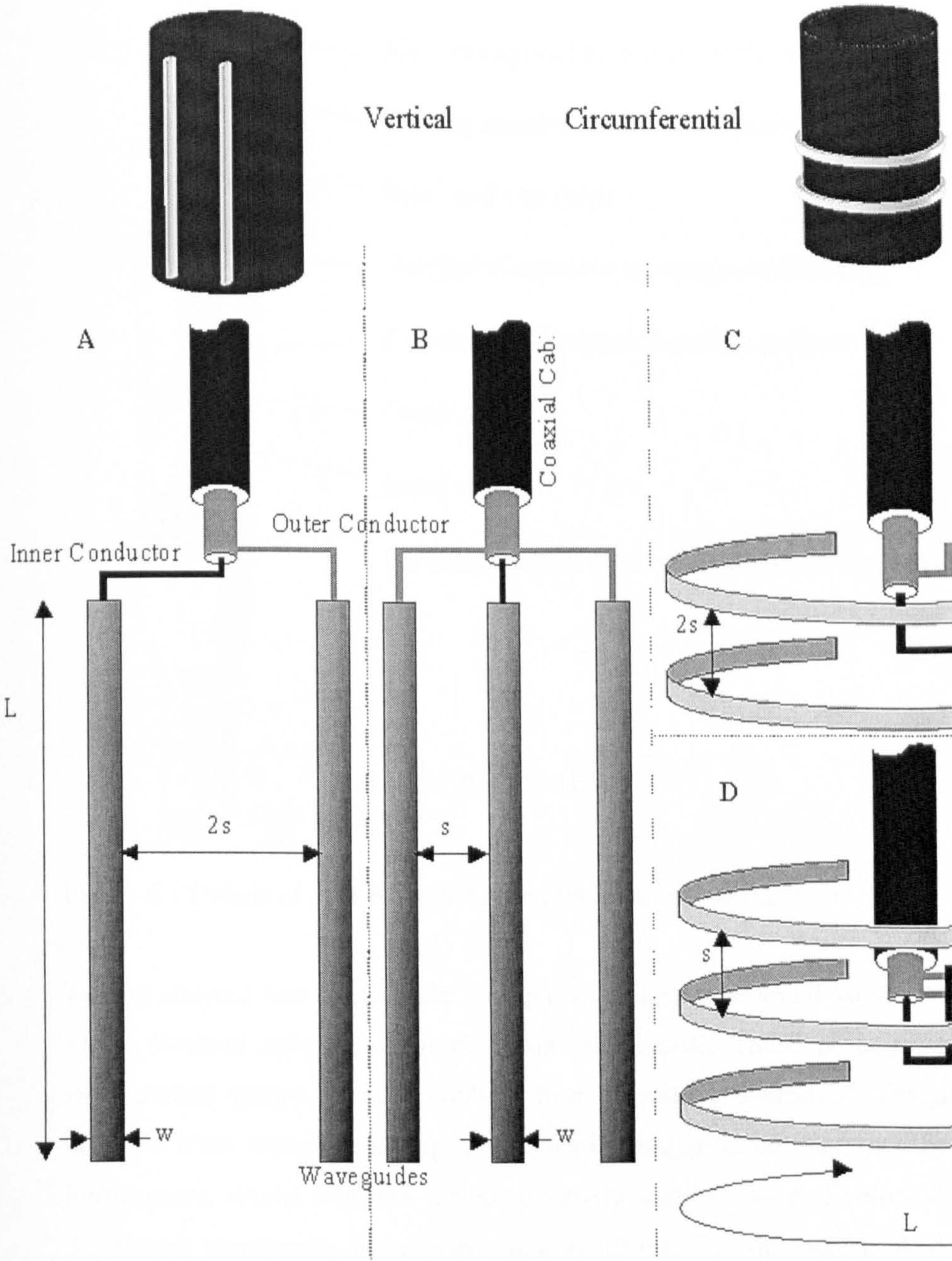

Figure 6.4, Waveguide orientation.

Figure 6.4 above shows vertical and circumferential 2 and 3 probe electrode configurations. The four variations (A, B, C and D) were constructed in 2, 3 and 5mm electrode widths. The 2mm electrode designs proved difficult to construct, with problems in cutting the electrodes accurately and delamination of the waveguides from the neoprene backing and so the 2mm design was abandoned. Figure 6.5 below shows the two potential probe orientations mounted upon an inflatable packer.

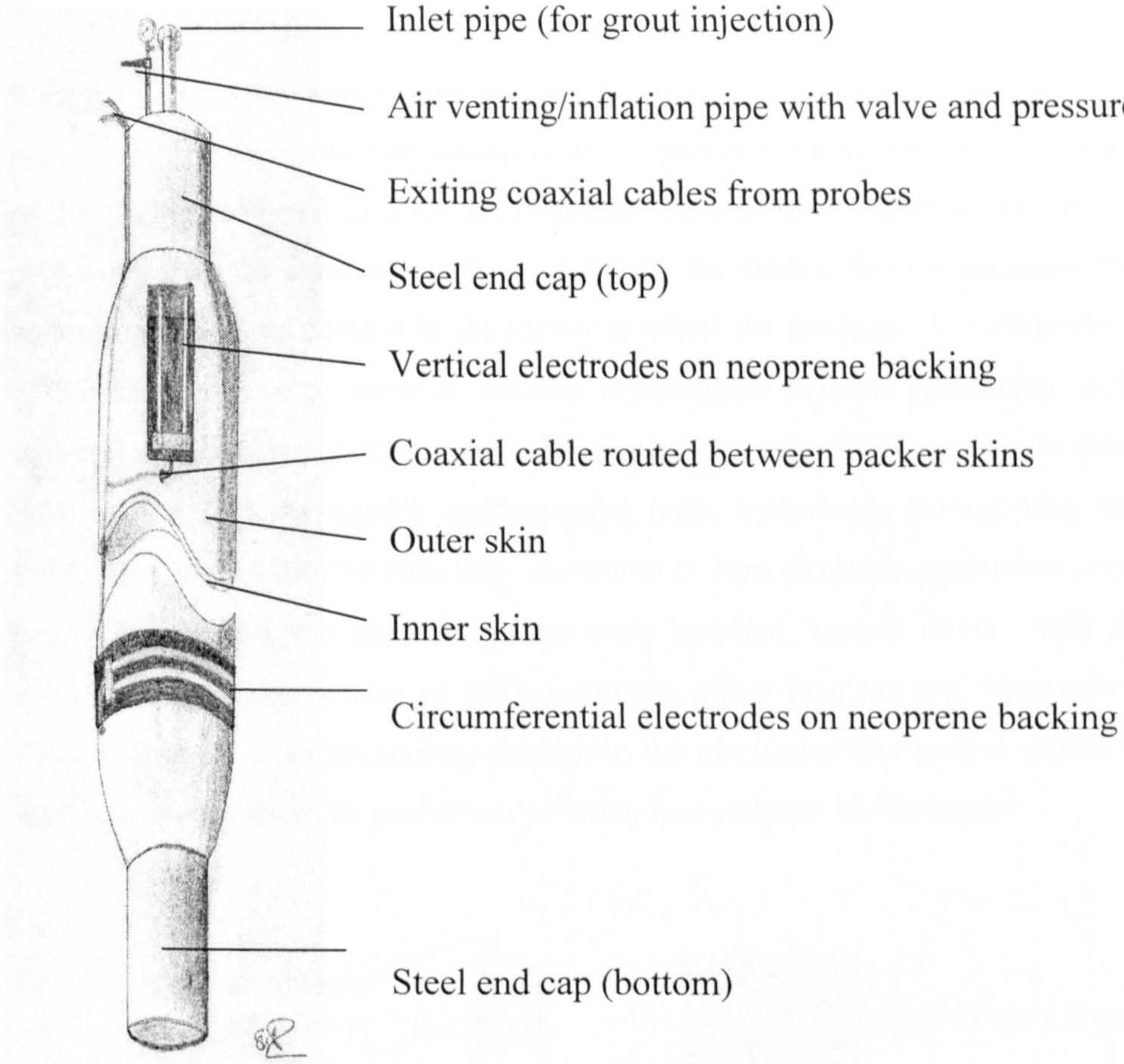

Figure 6.5 Details of packer showing possible electrode orientations.

Testing showed that 2-electrode waveguide designs performed well. Moisture content values obtained using a 3-electrode Campbell Scientific CS605 probe produced 1:1 lines when plotted against moisture contents from the various 2-electrode designs constructed in house when tested at varying saturations in disaggregated Sherwood Sandstone sand. Furthermore, results from the spatial sensitivity analysis reported below showed that the 2-electrode waveguides had greater spatial sensitivity than the 3-electrode designs.

The circumferential waveguide configuration was difficult to construct, problems were encountered attempting to bond thin, flexible and non-elastic waveguide assemblies satisfactorily to an expanding packer. Waveguide length was limited to the circumference of the packer and the circumferential arrangement reduced the system sensitivity to the dielectric constant of the rock (compared with that of the system using vertically mounted waveguides). The better sensitivity of the vertical arrangement is the result of the electrical field lines in the circumferential arrangement penetrating further into the packer (Jones *et al.*, 2002) and therefore being more influenced by the materials used in packer construction. Hence, waveguides mounted circumferentially were not developed further.

With the vertical waveguide arrangement, larger waveguide separations provide improved penetration. However the curved nature of the packer surface, also led to greater influence of the packer materials at greater waveguide separations. In practice, this is not a major problem unless the penetration of the packer by the electric field is sufficient to allow the water content of the cement in the packer to affect the readings. A waveguide separation of 50mm was decided upon as the best compromise between sensitivity to the packer material and adequate penetration into the rock. Hence the TDR waveguide design (figure 6.6), uses a 10:1 waveguide width:spacing ratio, 2-electrode waveguides, with 30 cm long, 5mm wide stainless steel strip electrodes at 5cm electrode separation (centre line to centre line). Note that the waveguides were installed 'upside down', with the coaxial cable exiting at the bottom of the waveguides rather than the top. This was to prevent delamination or possible serious damage to the electrodes and packer should the probes start to separate from the packer whilst being lowered into the borehole.

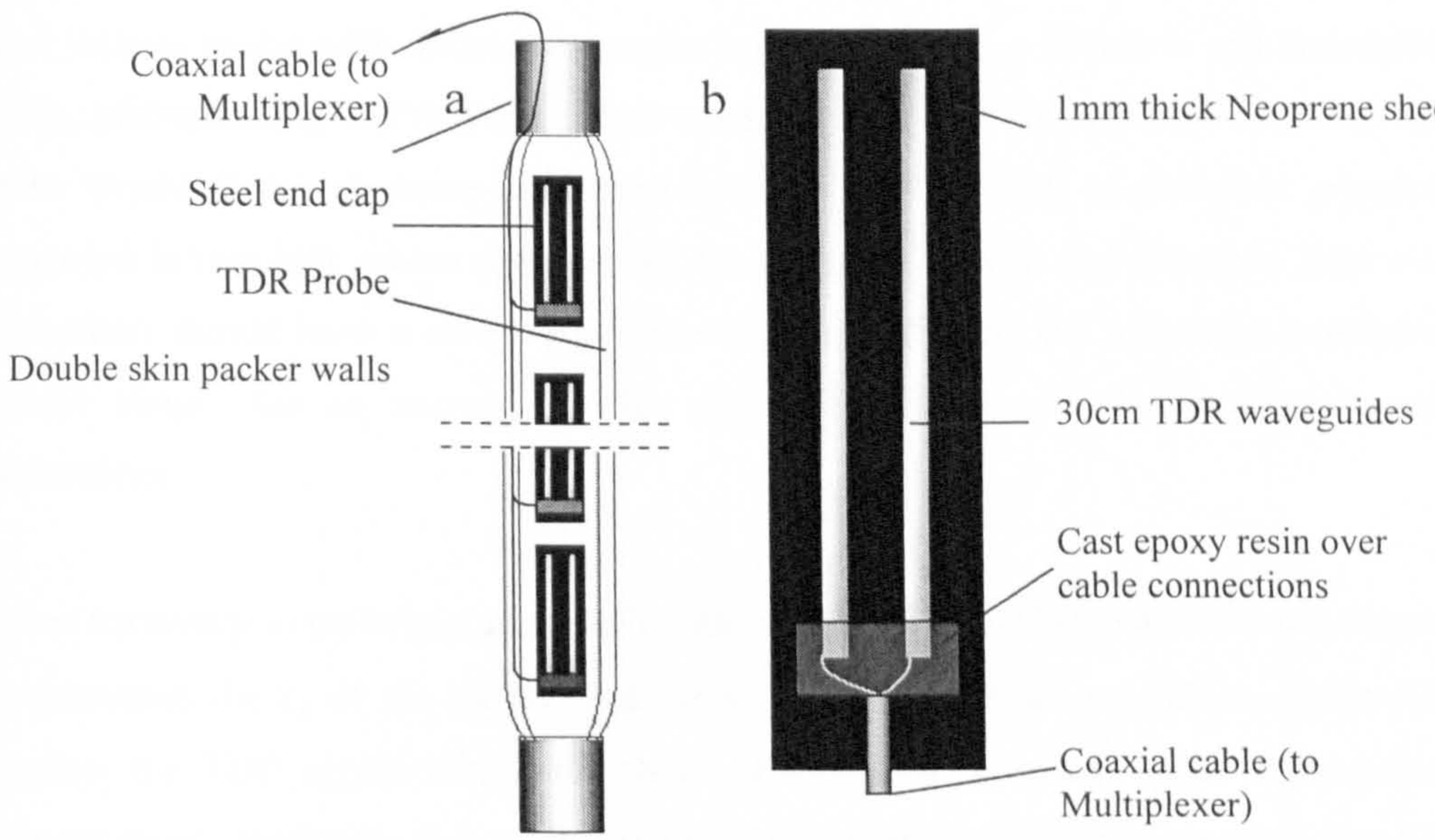

Figure 6.6. (a) packer design, (b) waveguide assembly design.

6.3.1. TDR calibration using standard fluids

It has been shown (Persson and Berndtsson, 1988, Selker et al, 1993, Marheshwarla et al.,1995) that TDR probes do not need to be inserted into the matrix under investigation. Although insertion is the normal method of emplacement into soils, this poses severe problems when the material under investigation is a rock, even one as friable as the Sherwood Sandstone in the study area. Provided account is taken of the dielectric properties of the backing medium behind the TDR probes, it is possible to place the probes in contact with the medium under investigation and still get good moisture content results. For a non-curvilinear contact point the distribution of apparent dielectric constant is governed by,

$$\varepsilon_{eff} = \left(\frac{(\varepsilon_{a1} + \varepsilon_{a2})}{2} \right) \qquad \text{Equation 6.7}$$

where ε_{eff} is measured effective dielectric constant of a TDR probe placed between two semi infinite media with dielectric constant values ε_{a1} and ε_{a2}. (Persson and Berndtsson, 1988., Maheshwarla, 1995). From this it would be expected that a packer mounted TDR probe would give a response equivalent to averaging two sets of dielectric properties measured in two half spaces representing the backing material and the rock. Hence any calibration should have a weighting factor close to 50% and the measured permittivity should simply be an average of the rock permittivity and the backing material permittivity.

It was necessary to undertake probe calibration using liquids of known dielectric constant to determine the ε_a of the packer and probe backing material, as well as determining whether the TDR signal within the rock corresponded to a half space measurement. Cement grout identical to that used in the field (see section 6.4.1.) was cast into a suitable container, with a field probe assembly on its 1mm thick neoprene backing bonded to the surface of the cement using epoxy resin to seal the concrete and to simulate a packer-mounted array (Figure 6.7)

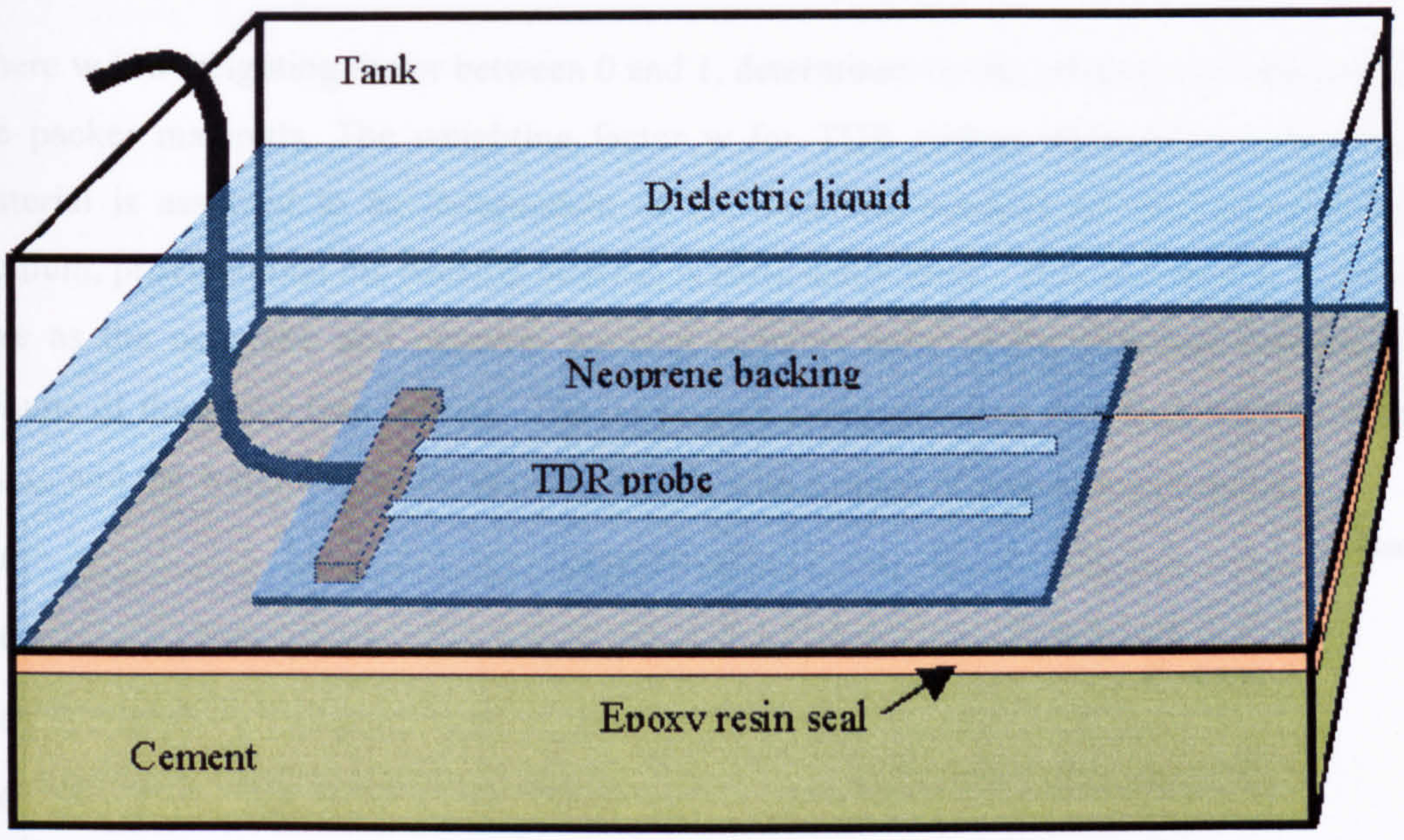

Figure 6.7. TDR calibration cell.

The container was filled with liquids of known permittivity (see Table 6.3.3.1.) and TDR traces and apparent moisture content recorded for each fluid. All calibration tests were carried out at 20°C using a Campbell Scientific TDR 100 unit, using Campbell Scientific PC TDR 2.0 software. These moisture content values were converted to apparent dielectric constant ε_{eff} by the inverse of the Topp equation (Topp, 1980)

Material	Relative dielectric constant
Acetone	(20^0C) 21
Methanol	(25^0C) 32.6
Cyclohexane	(20^0C) 2
Water	(20^0C) 80.4
Air	1

Table 6.2. Dielectric properties of standard liquids

As the waveguides are mounted on the packer assembly, measured dielectric constant will depend partially on the dielectric properties of the neoprene/cement behind the waveguides and partially on the dielectric properties of the measurement medium. The measured relative dielectric constant ε_{eff} will thus be given by

$$\varepsilon_{eff} = \varepsilon_{medium}(1-w) + \varepsilon_{packer}.w \qquad \text{Equation 6.8}$$

where w is a weighting factor between 0 and 1, determined by the relative contribution of the packer materials. The weighting factor w for TDR probes attached to a backing material is assumed to be independent of the dielectric constant of the measurement medium, provided that the backing material is sufficiently thick. This assumption is valid here as the neoprene and concrete backing contains most of the rearward sensitivity volume of the probe (see below). The purpose of calibration was thus to determine both K_{packer} and the weighting factor w using liquids with a range of dielectric constants.

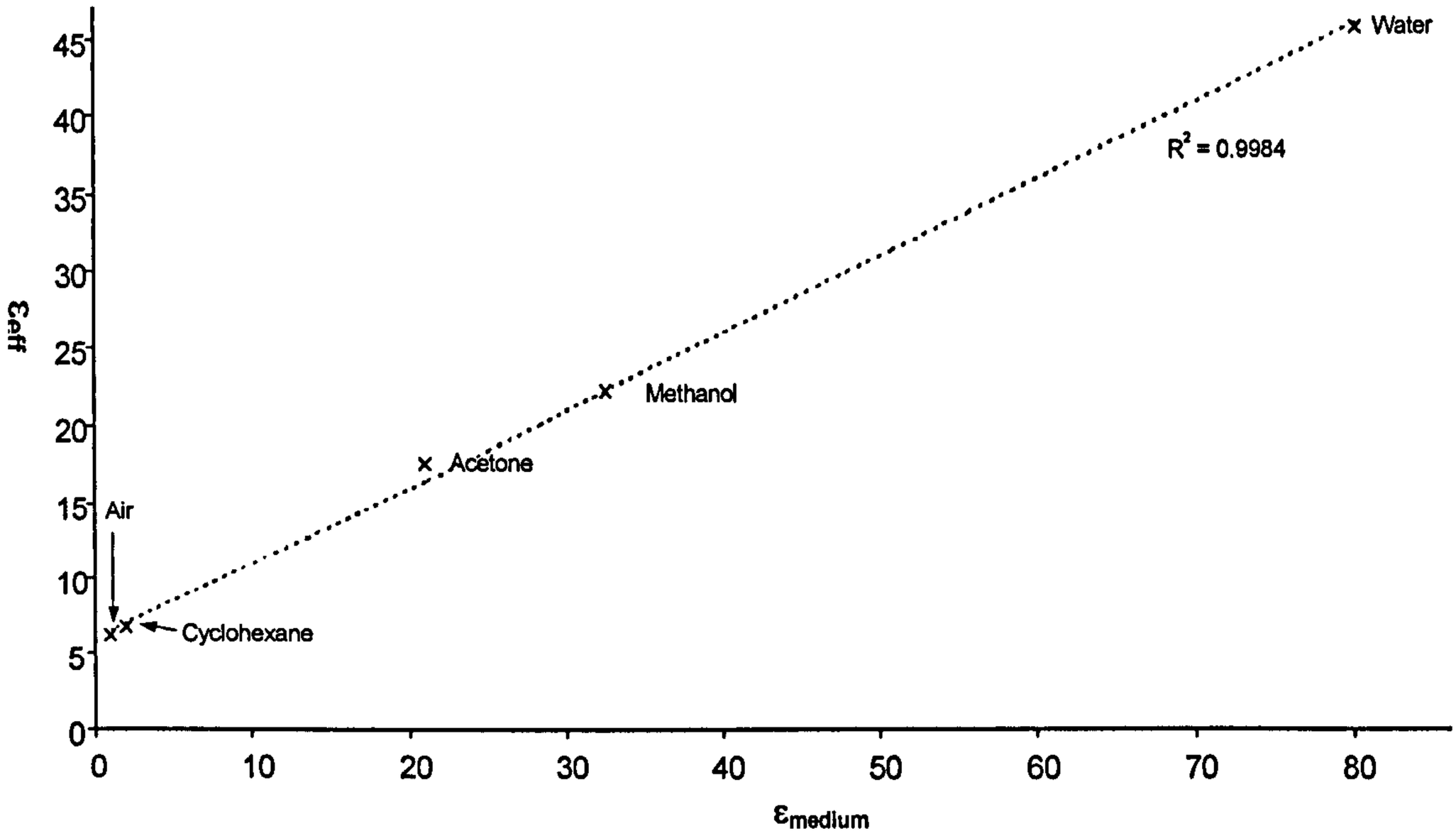

Figure 6.8. Packer mounted waveguide calibration using liquids of known dielectric constant.

Figure 6.8 shows a plot of the relative dielectric constants of the standard liquids against the relative dielectric constants measured by the packer assembly immersed in these liquids. Also shown is a plot of equation 6.8 with the parameters ε_{packer} and w optimised for best fit to the data. The calibrated values of w and ε_{packer} for this range are 0.5 and 12.0 respectively. The weighting factor of 0.5 matches that expected from equation 6.8, further increasing confidence in the calibration.

Hence, to provide a calibration for the field probes equation 6.8. needs to be solved for ε_{medium} in order that the field data may be corrected to true values.

$$\varepsilon_{medium} = \frac{\varepsilon_{eff} - (\varepsilon_{packer} . w)}{(1 - w)} \qquad \text{Equation 6.9}$$

6.3.2 Spatial sensitivity.

Knight (1992) investigated the dependence of the spatial sensitivity of TDR probes on waveguide geometry. For typical waveguide geometries with waveguide separation ratios of around 10, sensitivity is focussed in the immediate proximity to the waveguides, but with some sensitivity in an ellipse perpendicular to the waveguides. A variation on the method described by Baker and Lascano (1989) was used to investigate the sensitivity of the packer-mounted electrodes. A test waveguide assembly was immersed in a water bath that allowed accurate and controlled movement of a bar (1cm^2 in cross section) of low permittivity plastic across the face of the electrode array. This was moved laterally past the waveguides, with the apparent moisture content being measured for each position. The bar was then shimmed away from the waveguides using 1mm thick strips of neoprene (checked by micrometer) and the procedure repeated until a three-dimensional picture of spatial sensitivity had been completed. The apparatus used is shown in figure 6.9.

This water bath technique was used to conduct a spatial sensitivity analysis of the 4 main electrode designs 3mm width (2 and 3 electrode) and 5mm width (2 and 3 electrode). The electrode seperation was always ten times the electrode width. In practice, the 5mm electrodes were the easiest to construct and attach to the neoprene.

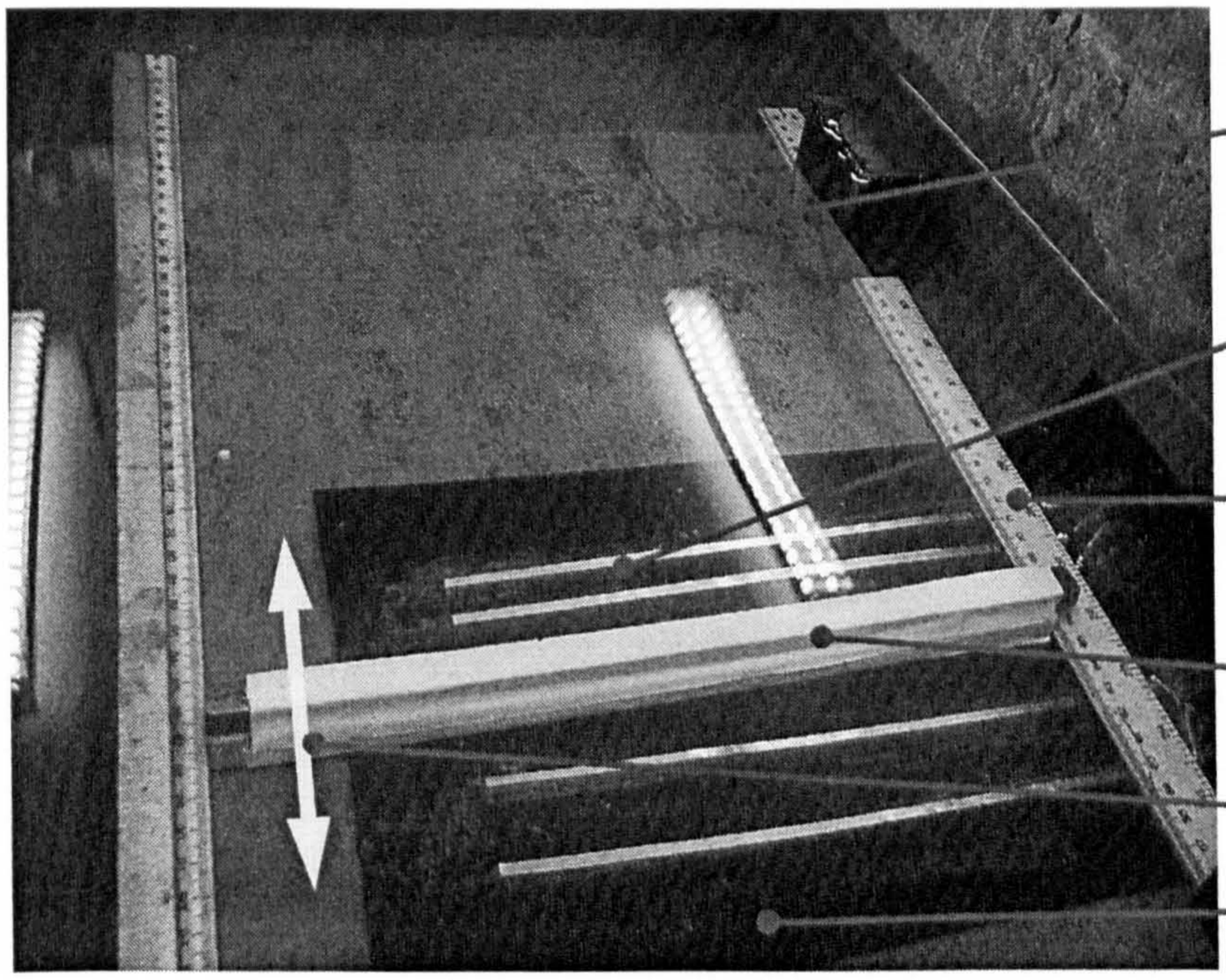

Figure 6.9, Spatial sensitivity analysis apparatus.

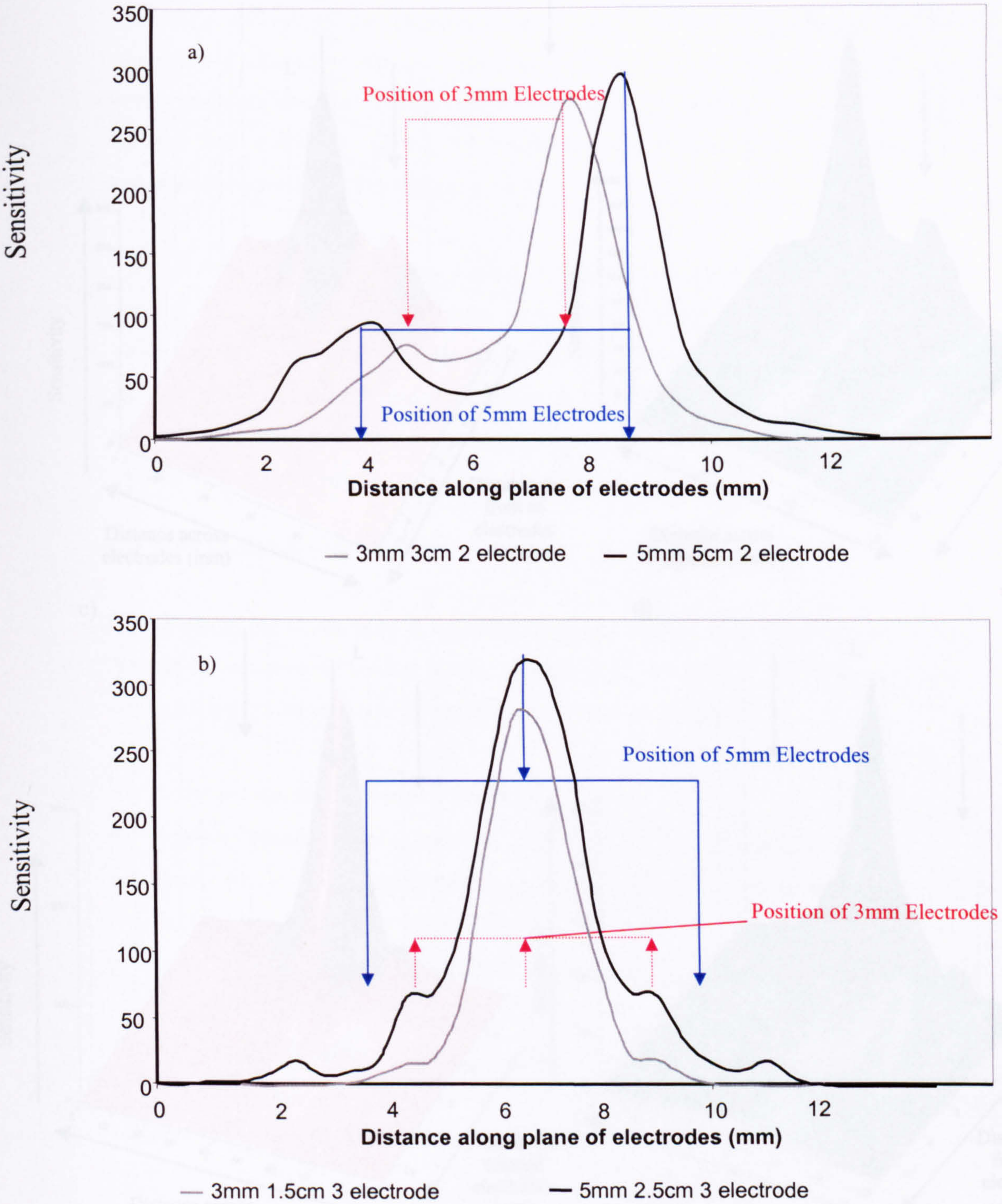

Figure 6.10. Spatial sensitivity in water results (single pass across electrodes) a) two electrode and b) three electrode probes.

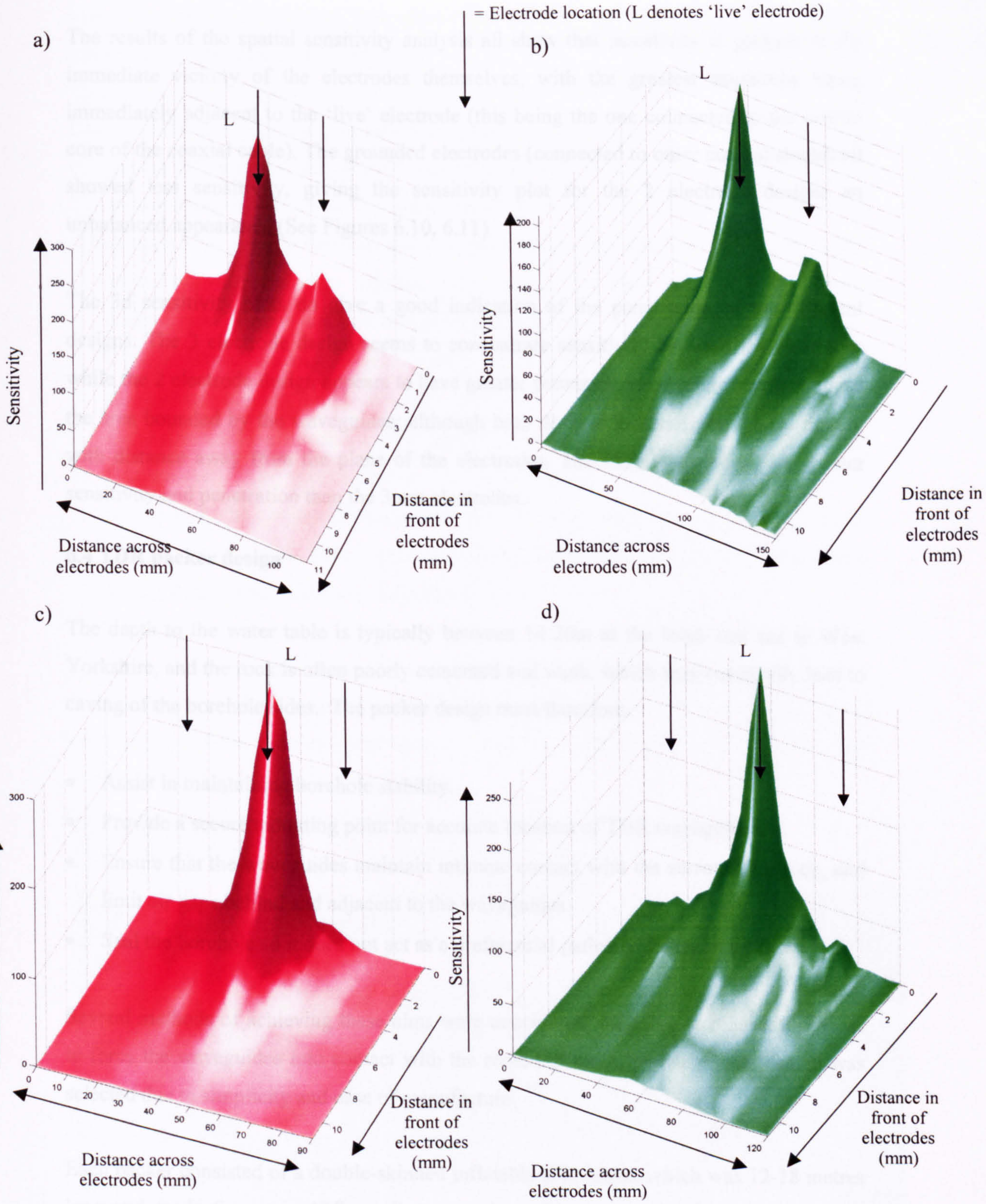

Figure 6.11, Spatial sensitivity in water (multiple passes across electrodes) a) 2 electrode, width 3mm, spacing 30mm. b) 2 electrode, width 5mm, spacing 50mm. c) 3 electrode, width 3mm, spacing 30mm. d) 3 electrode, width 5mm, spacing 50mm. All electrodes 300mm long.

The results of the spatial sensitivity analysis all show that sensitivity is greatest in the immediate vicinity of the electrodes themselves, with the greatest sensitivity being immediately adjacent to the 'live' electrode (this being the one connected to the central core of the coaxial cable). The grounded electrodes (connected to outer coaxial shield) all showed less sensitivity, giving the sensitivity plot for the 2 electrode designs an unbalanced appearance (See Figures 6.10, 6.11)

The 3d sensitivity plots do give a good indication of the penetration of the different designs. The 3 electrode design seems to concentrate sensitivity between the electrodes while the 2 electrode design appears to have greater penetration and return results outside the area bounded by the waveguides; although both designs lose sensitivity very rapidly with distance away from the plane of the electrodes. The 5mm electrodes give greater sensitivity and penetration than the 3mm electrodes.

6.4 TDR packer design

The depth to the water table is typically between 14-20m at the Heck test site in West Yorkshire, and the rock is often poorly cemented and weak, which may eventually lead to caving of the borehole sides. The packer design must therefore:

- Assist in maintaining borehole stability.
- Provide a secure mounting point for accurate location of TDR waveguides.
- Ensure that the waveguides maintain intimate contact with the surrounding rock, and limit air gaps behind and adjacent to the waveguides.
- Seal the borehole so it does not act as a preferential pathway for moisture flow.

Several methods of achieving these aims were considered, including mechanical devices to force the waveguides into contact with the rock, but the inflatable packer design was selected due to simplicity and ease of manufacture.

Each packer consisted of a double-skinned inflatable membrane, which was 12-18 metres long and made from two 125mm diameter tubes of impermeable, flexible and elastic material (Chlorino material DP205, manufactured by Chlorino Ltd, Italy). These membranes were sealed at both ends with metal caps, with the upper cap drilled and tapped to allow grout injection and pressurisation. Each packer was fitted with up to sixteen TDR waveguide assemblies before being lowered into the borehole where they

were pressurised to force the waveguides into contact with the rock and filled with cement grout (See Figures 6.5 and 6.6).

Use of large (10m+) inflating packers did present some problems:

- During inflation packers expand vertically as well as laterally. Any waveguides mounted directly to the packer would potentially have been subjected to tension and damage. The spacing between the waveguides could also increase, altering the probe impedance characteristics. Hence, TDR waveguides were mounted on neoprene backing rather than directly on the packers themselves.
- Cement shrinks upon curing, typically by approximately 0.7%. To prevent the waveguides moving away from the borehole wall and introducing air gaps, a shrinkage reducing agent (Eclipse manufactured by W.R. Grace & Co. Cambridge, Connecticut, USA) was added to the grout mixture. The use of compressible neoprene in the waveguide assemblies also allowed some cement shrinkage to be accommodated, while allowing the waveguides to maintain contact with (and mould to) any minor irregularities in the borehole wall.

Figure 6.12 shows several packers, some completed and some in the process of construction in the field at both test sites. Note the Hatfield packer (Figure 6.12A) has an extra series of electrodes mounted upon it. These are resistivity electrodes, which were not successful and are not discussed further.

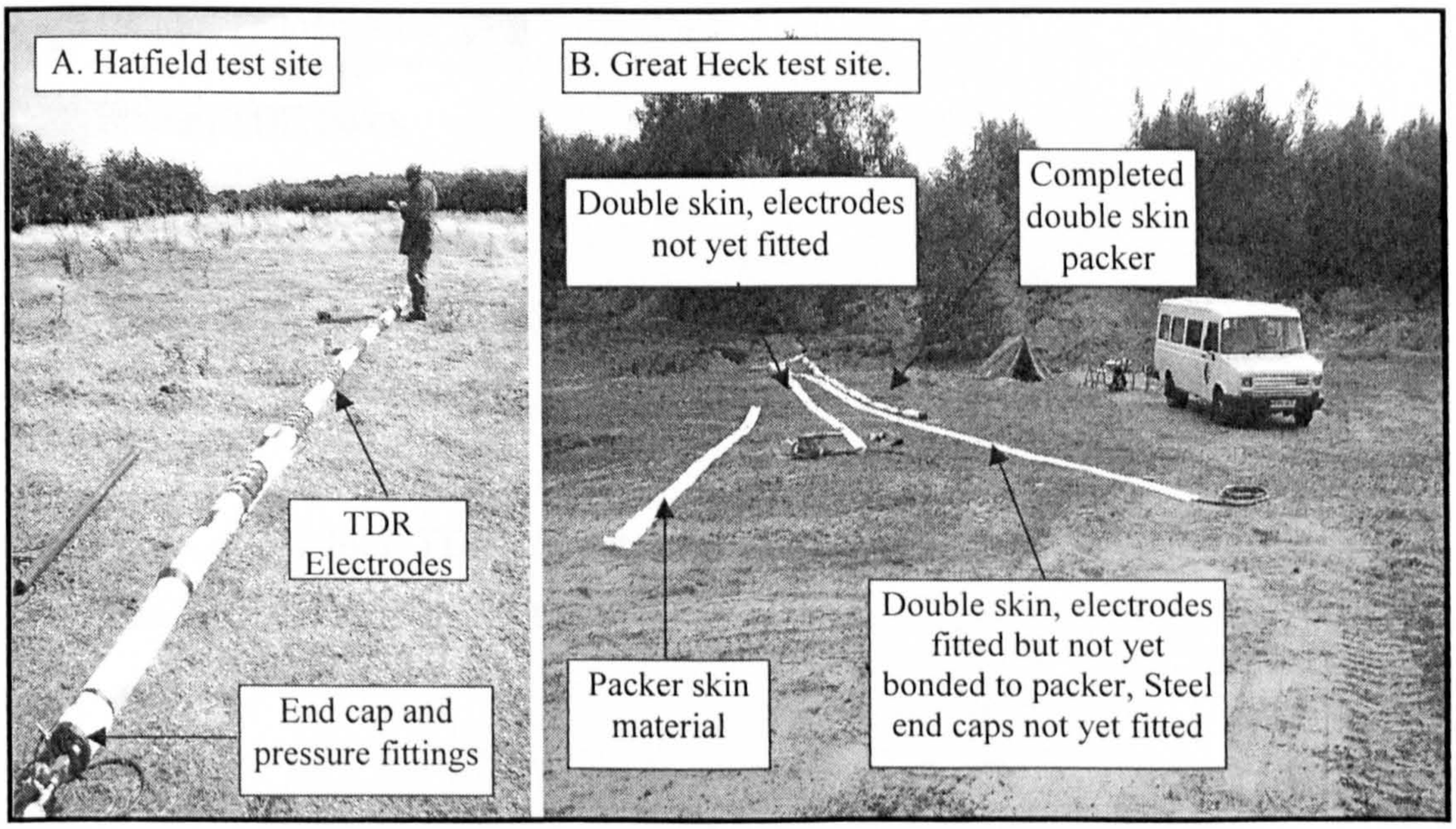

Figure 6.12. TDR packers in the field, prior to installation.

6.4.1 Installation at Heck.

The drilling at Heck was carried out by Drilcorp (Durham) between the 7th and 10th October 2002. A pattern of six boreholes was drilled in a cruciform pattern with the long axis oriented North>South (palaeoflow direction was South→North). Double skinned TDR packers were installed into four of these boreholes between 8th and 23rd October 2002.

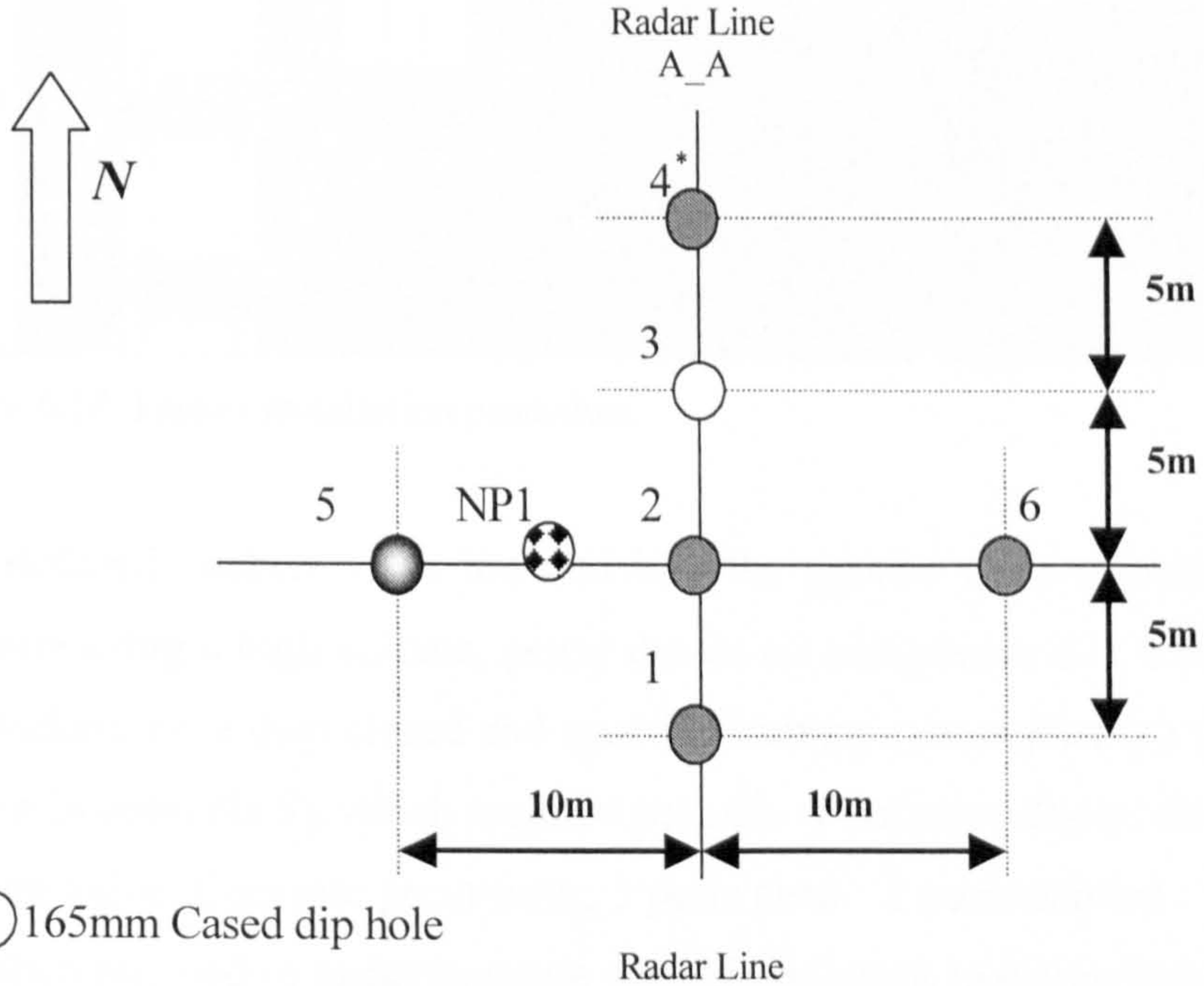

Figure 6.13 Heck (SE 588213) borehole layout.

Installation of all four TDR packers was completed successfully following the procedure outlined in Figure 6.14.

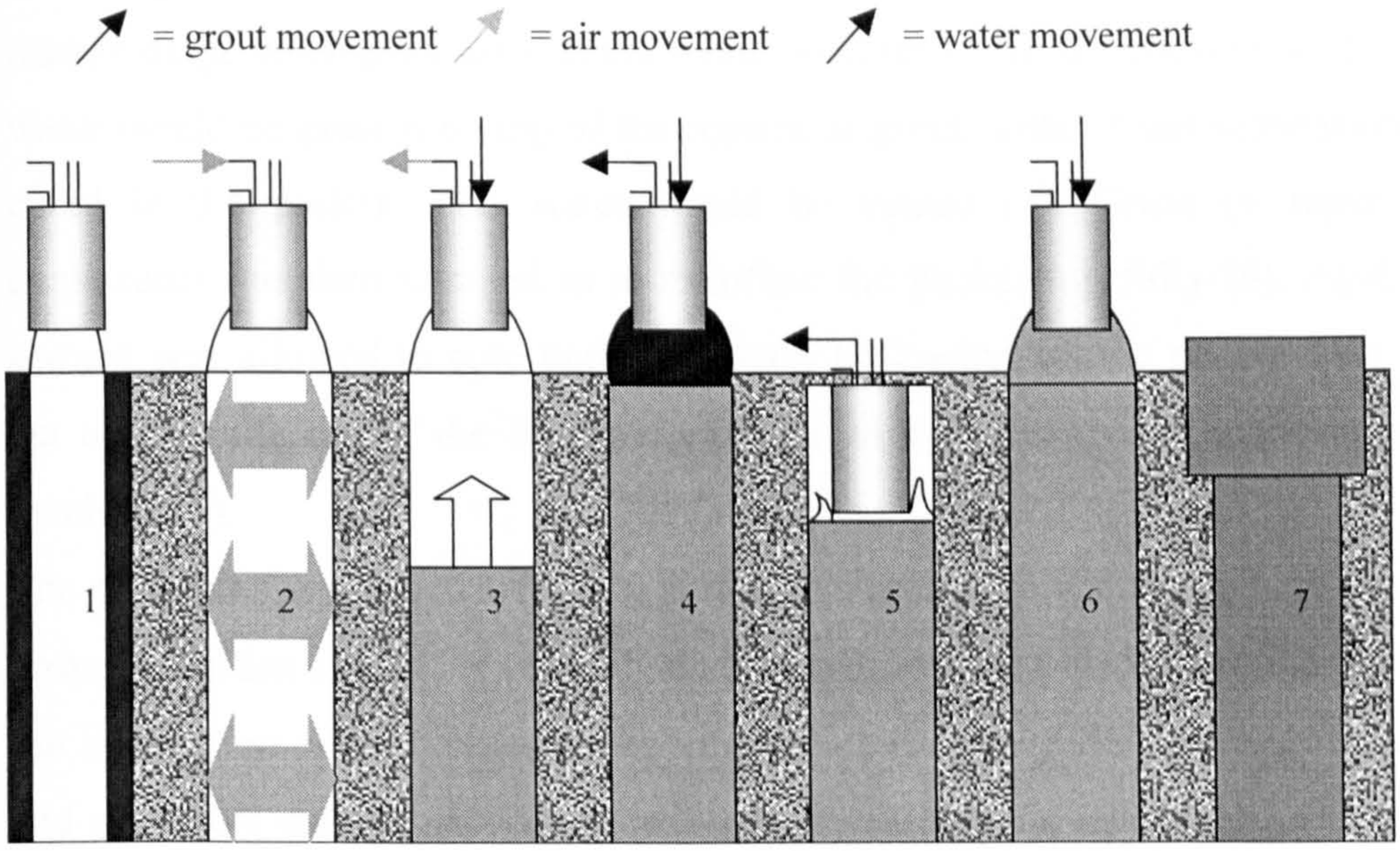

Figure 6.14. Packer installation procedure.

The deflated packers were lowered into the ground (1) and inflated to ≈1Bar pressure using a high volume, petrol driven air compressor (2). The air valves on the packers were then closed and used for venting excess pressure (except for the packer in borehole 5), which required periodic re-inflation due to air leakage at the surface valve. Concrete grout (mix; 3 parts sand : 2 parts cement : 4 parts water) was then pumped in under pressure through the grout injection hole using a cadet 250 hand operated grout pump (3). Air was vented periodically to maintain constant pressure as grout was injected. Grace Advil plasticiser and Grace Eclipse shrinkage reducer were also added according to the manufacturers instructions. As the packers became close to full with grout, great care was taken to vent air regularly in order to prevent them bursting. When the packers were very close to full, water (on top of the grout) would be vented instead of air (4). This was the most critical moment in packer installation, where the packers were most vulnerable to bursting. Finally, when grout could be seen in the top 10cm of the packer (through the inflated packer skin), the concrete taps were closed and the concrete allowed to harden with the packer still pressurised. It was noted during the previous installation at Hatfield Quarry that the concrete took too long to achieve a reasonable set in the confines of the packer so Febspeed (manufactured by Degussa Construction Chemicals) rapid cure admixture was added to the final ½ m of grout injected. Pressure was maintained by using the air compressor as

necessary, until the concrete grout had hardened sufficiently to maintain the packer shape when pressure was removed (8-12 hrs). At this point up to 1.5m of water would be present on top of the cement as grout settled from suspension and cured in the packer. This water would be vented (5). Grout (+ rapid cure admixture) was then pumped in to re-inflate the packer top fully (6). Again the cement was allowed to cure under pressure. Following set the packer tops were cut off and the top of the borehole plugged with a cement cap and / or access manhole (7).

The boreholes were then left for a period of one month for the cement grout to properly harden and moisture contents in the surrounding rock to stabilise before the installation was automated using a series of Campbell Scientific multiplexers and a CR10X datalogger. This allows ongoing automatic interrogation of all the TDR probes at regular time intervals and stores the data for periodic collection.

Borehole No.	Depth after backfilling (m)	Diameter (mm)	Depth to water table (m).	Instrumentation	No electrodes	Comments
1	11.6	165	Dry	TDR	16	High density TDR hole
2	17+	165	14.3	TDR	14	
3	20	165	14.6			Dipmeter hole
4	17m	165	14.6	TDR	14	Hole cored at 100mm but core proved unrecoverable below 10m, so hole re-drilled to 20m at 165mm diameter.
5	12m	165	Dry	TDR	8	
6		100	Dry	TRIME		Hole left open and uncased for TRIME use.

Table 6.3. Great Heck test site (SE 588213) boreholes.

Installation of all four TDR packers was completed successfully. The depths to the various probes are shown in figure 6.15 below.

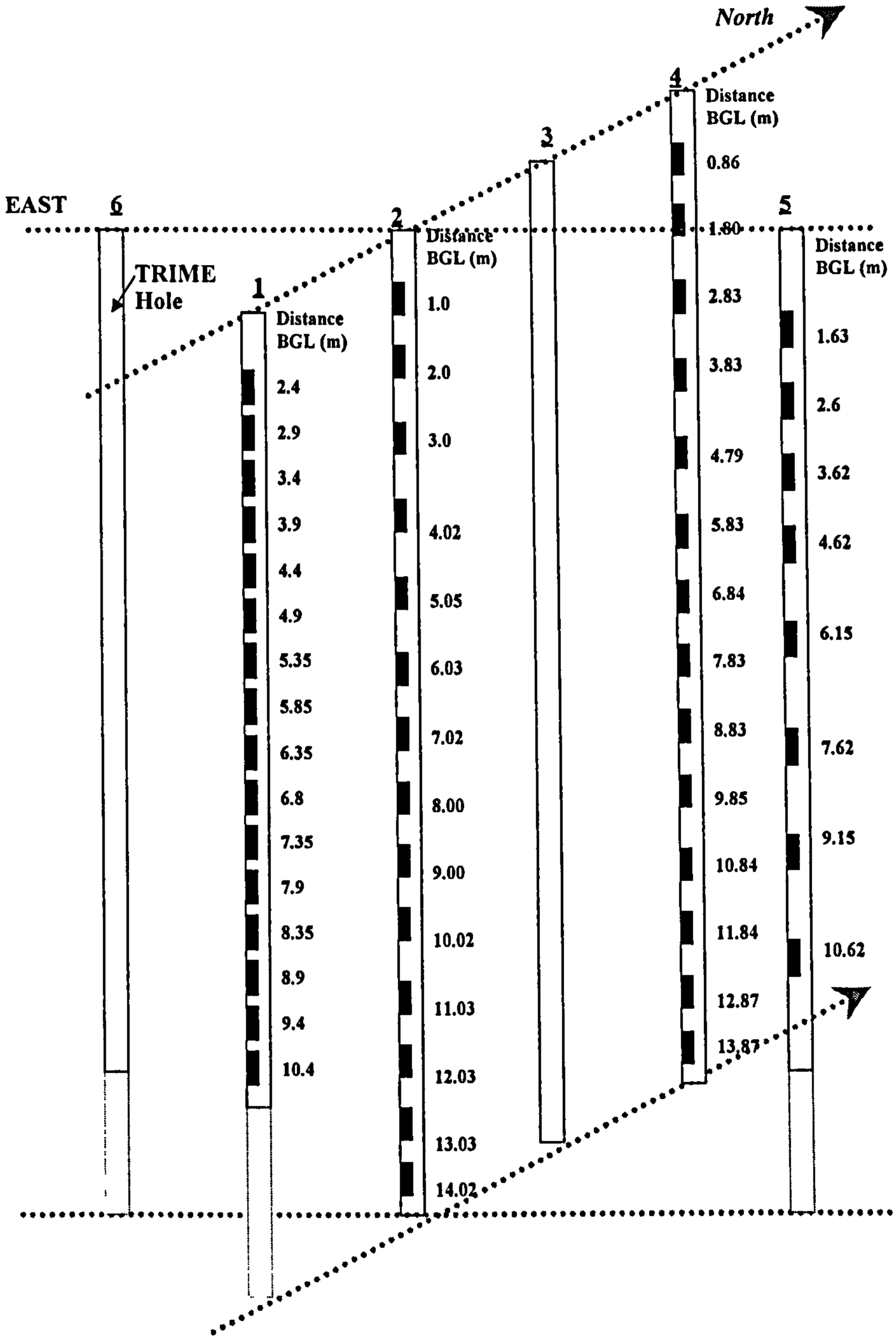

Figure 6.15. Installed TDR probes at Heck (SE 588213). Depths given are to the tops of the probes. For lateral spacings see Figure 6.13.

6.4.2. Multiplexing and datalogging.

The Great Heck TDR array was automated using a system consisting of 52 TDR probes, connected to eight, second level Campbell Scientific SDMX 50 8 channel 50Ω multiplexers using 50Ω low-loss coaxial cable. These multiplexers were then linked back to a first level SDMX 50 multiplexer, connected to a Campbell Scientific TDR 100 unit, with the system as a whole being controlled by a Campbell Scientific CR10X datalogger. The system was constructed in a similar manner to that anticipated by Huang and Dowding (1994). The multiplexing of the various TDR probes back to one central controlling TDR unit and datalogger results in some coaxial cable lengths of up to 35m running between the TDR unit and some of the TDR probes. Thomsen et al (2000), demonstrate that although the longer cables do impact upon the TDR traces inasmuch as they increase the voltage rise time and smooth the traces, they do not adversely affect the moisture content values returned by the system. Using low loss coaxial cable they report being able to easily analyse TDR traces with cable lengths of over 50m, nearly double the maximum cable length used in the Great Heck installation.

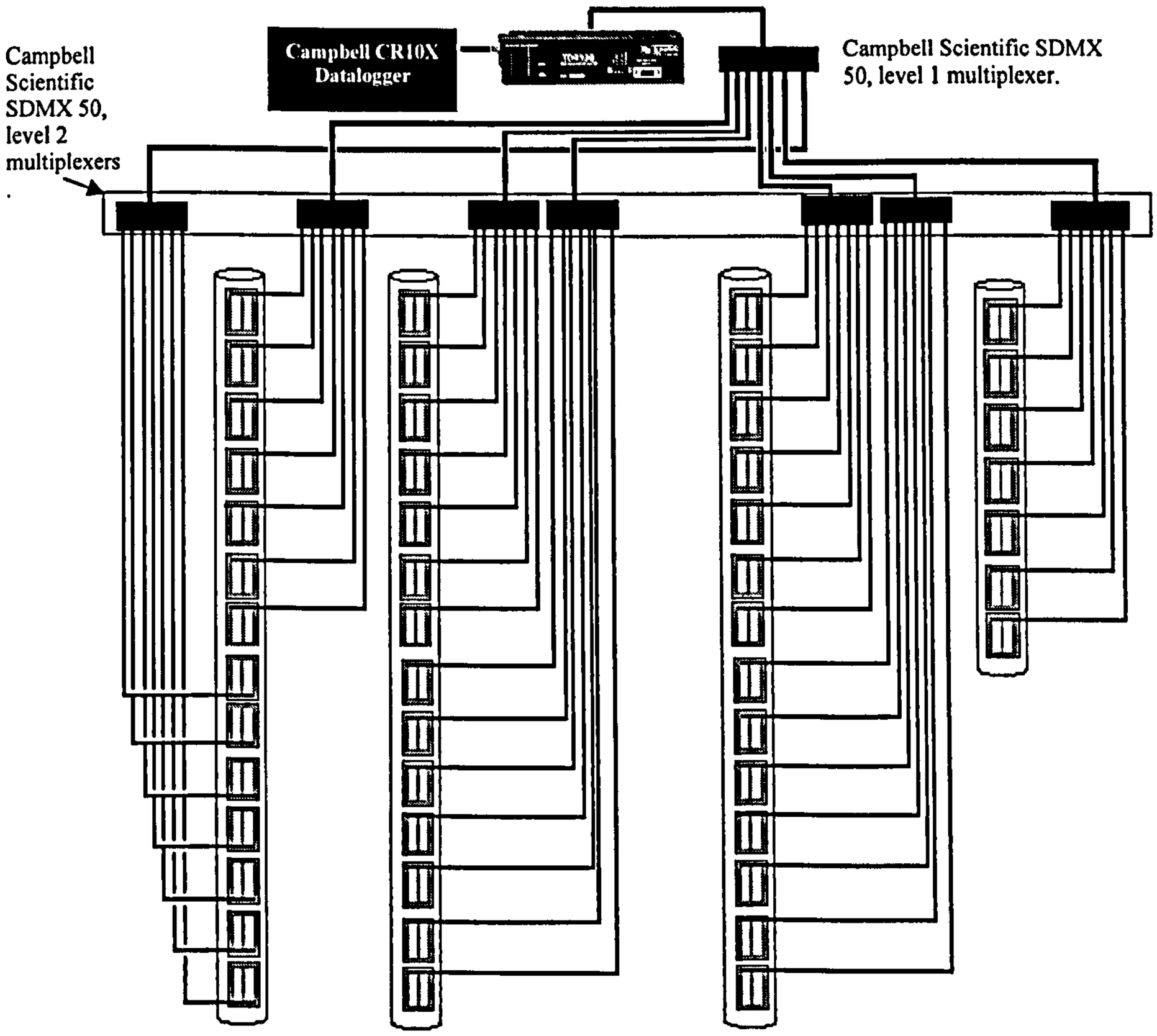

Figure 6.16. Schematic of Great Heck Quarry test site (SE 588213) TDR installation.

The programming commands for the multiplexed system were written in Campbell Scientific PC208W programming language based on a program originally written by Peter Winship at Leeds University. The text of this program is presented in appendix 3.

The system was set to record daily TDR trace waveforms and L_a/L values at 00.01hrs GMT, and was capable of recording for periods of over 28 days without user intervention. Data downloads were usually conducted along with battery changes at monthly intervals. One period of data loss was suffered in February 2003 which was caused by a period of extremely cold weather, which prematurely discharged the system battery, preventing readings being taken. The system is capable of recording data over much shorter time intervals (from approximately 5-10 minutes upwards) but every 24hrs provided a good compromise between memory (and battery) usage and temporal resolution.

The multiplexed system as described proved to be robust and reliable, if fitted with solar panels and a telephone link the TDR array could have been fully automated so no site visits would have been necessary. This would have been more expensive, would have left above-ground equipment visible to passers by (the automated system was buried with an access cover for data collection). It was not necessary here as monthly visits to the Great Heck test site were required for TRIME and neutron probe data collection.

6.5.1. Sources of error in TDR results.

Examination of the moisture content data returned by the TDR probes show that:

1) some TDR probes deliver unrealistically high moisture content values,
2) some TDR probes deliver unrealistically low moisture content values,
3) time-series data for some TDR probes shows relatively high scatter, whereas other probes show much more systematic variation with low scatter.

Unrealistic moisture contents (some probes).

Between December 2002 and December 2003 over 17,000 volumetric moisture content values were collected from 52 packer-mounted TDR probes installed at the Great Heck test site. These data were converted to moisture content using the calibration determined in section 5.3.2, and a frequency distribution histogram for moisture content was plotted (Figure 6.17). The moisture content measurements were divided into four groups as indicated by the red lines on Figure 6.17, based on the positions of troughs in the distribution.

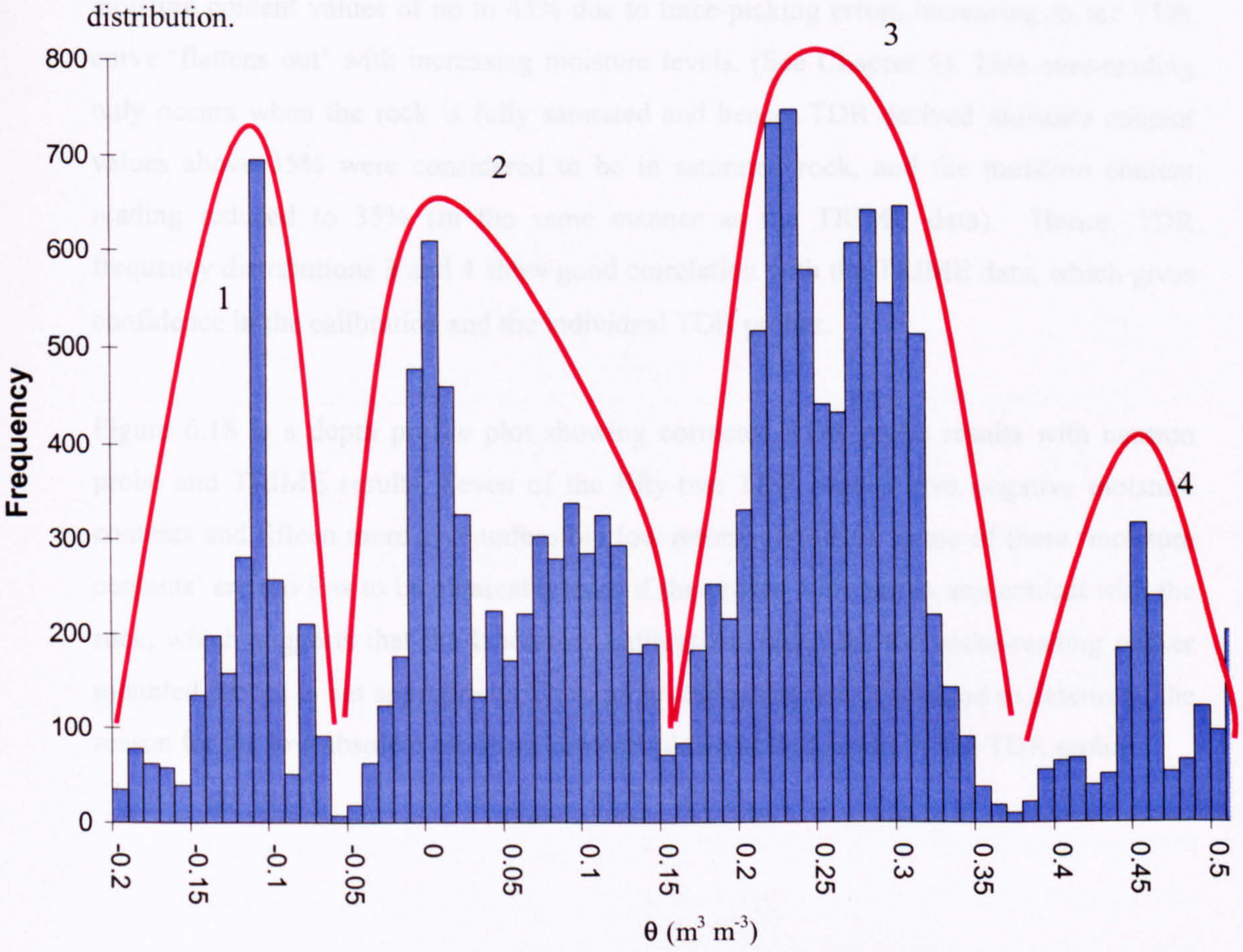

Figure 6.17. Frequency distribution for all 17,000 corrected TDR moisture content values.

TDR frequency distributions 3 and 4 are similar to the TRIME distribution described in section 5.3.4, but distributions 1 and 2 represent moisture content values that are unrealistically low (<14%). Time-series data from probes showing unrealistically low moisture content values showed moisture content variations comparable with those from the 'good' probes (see next section). This suggests that these probes were sensitive to the moisture content of the rock but incorrectly calibrated. Probes recording moisture contents of less than 14% (the minimum moisture content returned by the TRIME) were considered to be malfunctioning, and these probes are investigated further below.

Frequency distributions 3 and 4, on Figure 6.17, are comparable with the bimodal TRIME frequency distribution described in section 5.3.4. Both the TRIME and TDR frequency distribution 3 shows a peak frequency at 20-25% moisture content, with a second peak at 27-35%, and a smaller third peak (TDR distribution 4) at around 45-50%. The peak at 45-50% is larger on the TDR plot than on the TRIME plot, and this is probably due to the fact that there are a number of deep TDR probes, down to 14m below ground, which are in saturated rock. The porosity of the Sherwood Sandstone in the test area is approximately 35%, but at high saturation levels the TDR technique frequently produces moisture content values of up to 45% due to trace-picking errors increasing as the TDR curve 'flattens out' with increasing moisture levels. (See Chapter 5). This over-reading only occurs when the rock is fully saturated and hence, TDR derived moisture content values above 35% were considered to be in saturated rock, and the moisture content reading reduced to 35% (in the same manner as the TRIME data). Hence, TDR frequency distributions 3 and 4 show good correlation with the TRIME data, which gives confidence in the calibration and the individual TDR probes.

Figure 6.18 is a depth profile plot showing corrected TDR probe results with neutron probe and TRIME results. Seven of the fifty-two TDR probes give negative moisture contents and fifteen more give unfeasibly low returns (θ<14%). Some of these 'moisture contents' are too low to be obtainable even if the probes were not in any contact with the rock, which suggests that the laboratory calibration model for the under-reading packer mounted probes is not appropriate. Thus, an investigation was conducted to determine the reason for the low absolute moisture contents obtained from some of the TDR probes.

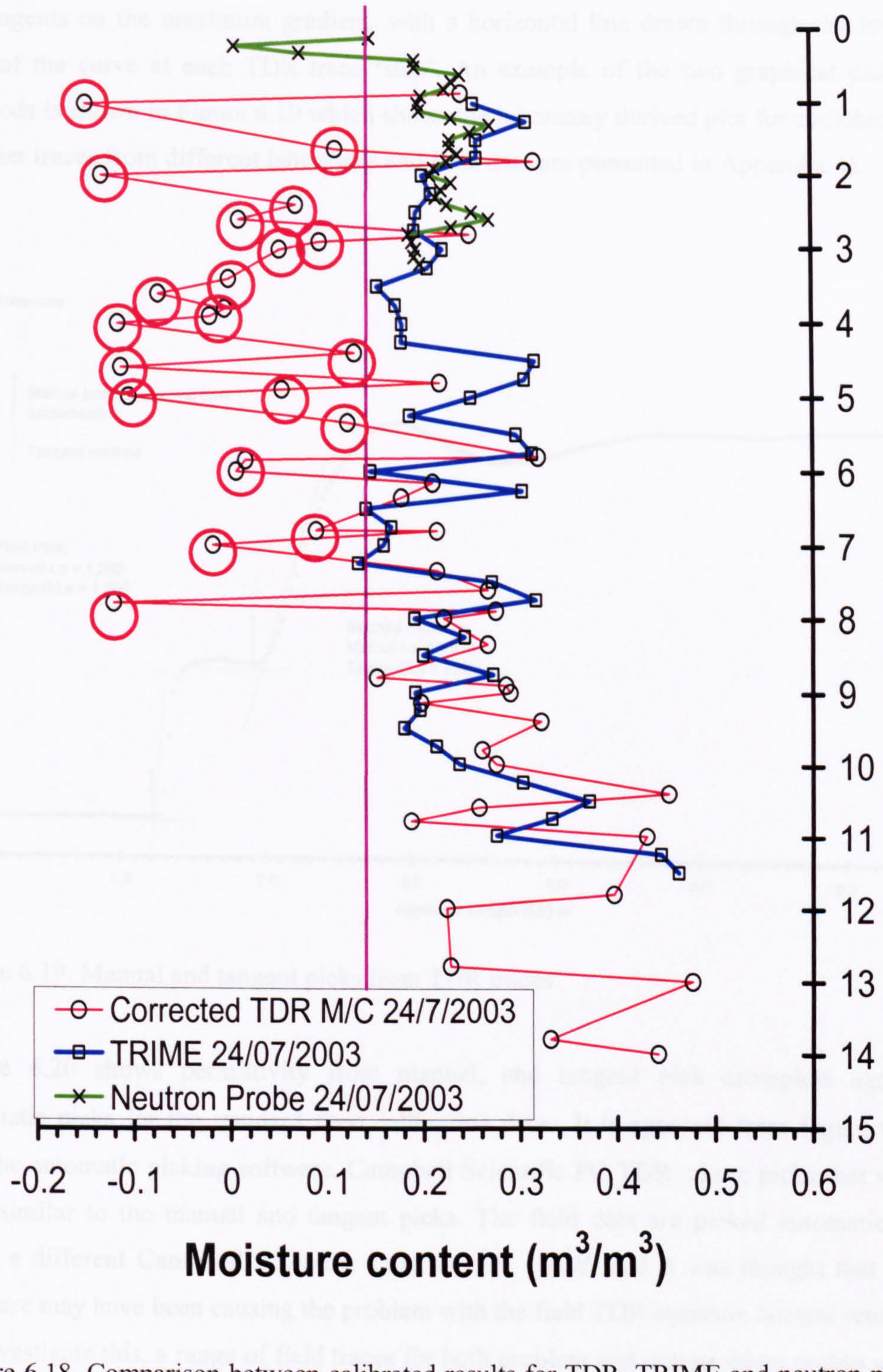

Figure 6.18. Comparison between calibrated results for TDR, TRIME and neutron probe on 24th July, 2003, ringed points indicate 'problem' probes.

Firstly, further investigation of TDR trace shape and picking was conducted. One possibility was that the Campbell Scientific PC208W software had been mispicking some of the apparent probe length (L_a) values from the TDR traces. To investigate this, all the traces from the standard fluid calibration tests and a selection of field traces were plotted and graphically picked. Two manual methods of graphical picking were used, following

the approach of Huismann *et al.*, (2002); i) picks of curve inflexion points (ii) intersection of tangents on the maximum gradient, with a horizontal line drawn through the lowest part of the curve at each TDR trace 'step'. An example of the two graphical picking methods is shown in Figure 6.19 which shows the laboratory derived plot for cyclohexane (further traces from different laboratory and field data are presented in Appendix 4).

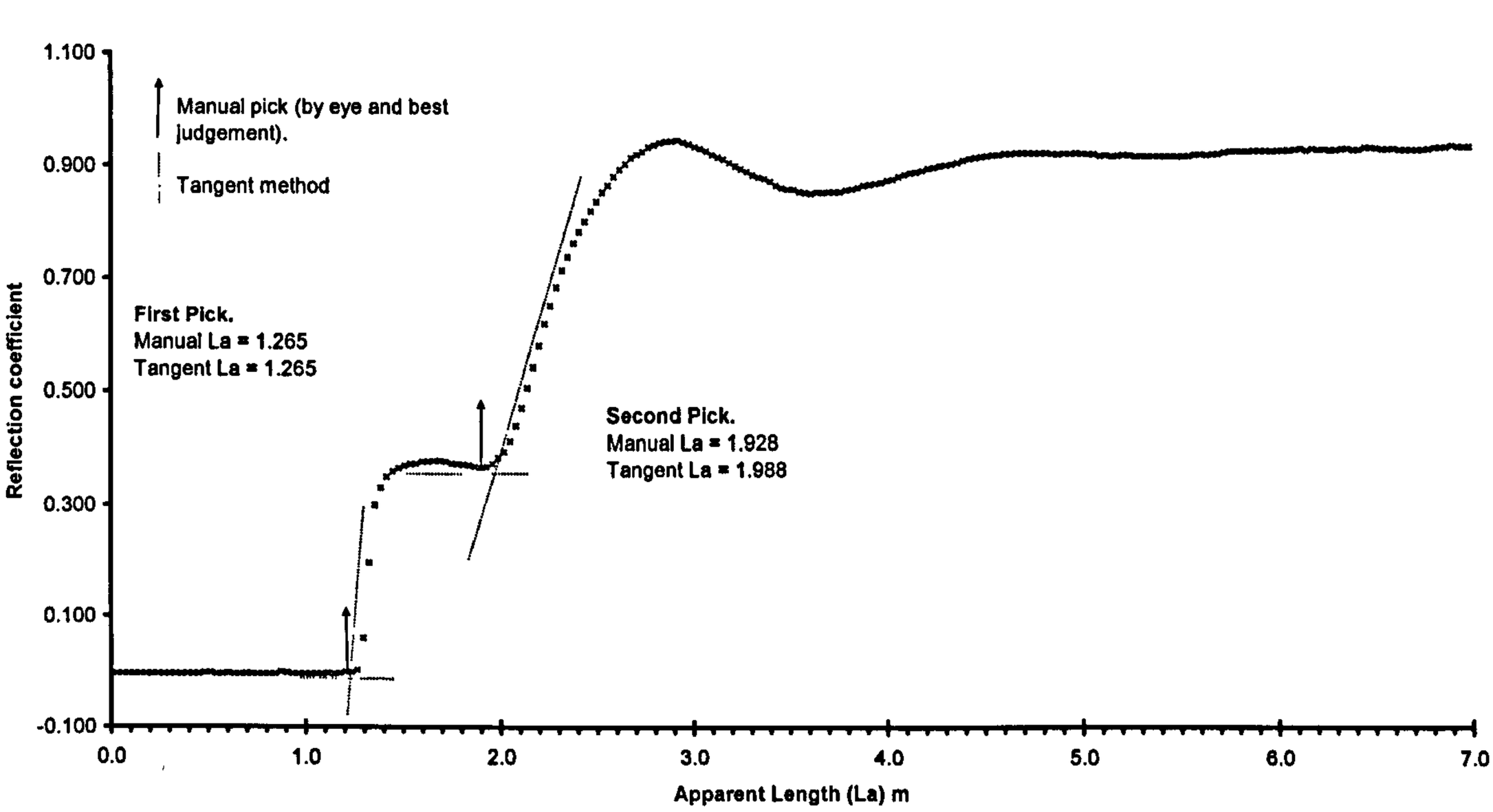

Figure 6.19. Manual and tangent picks from TDR traces

Figure 6.20 shows permittivity from manual, and tangent pick crossplots against automatic picks for the standard fluid calibration data. It is apparent from Figure 6.20 that the automatic picking software, Campbell Scientific PC TDR, chose picks that were very similar to the manual and tangent picks. The field data are picked automatically using a different Campbell Scientific program, PC 208W, and it was thought that this software may have been causing the problem with the field TDR moisture content returns. To investigate this, a range of field traces for both problem and non-problem probes were picked using the manual method and then the calculated L_a/L values plotted against the values returned by the Campbell Scientific PC208W automatic picking software. These data are shown below in Figure 6.21.

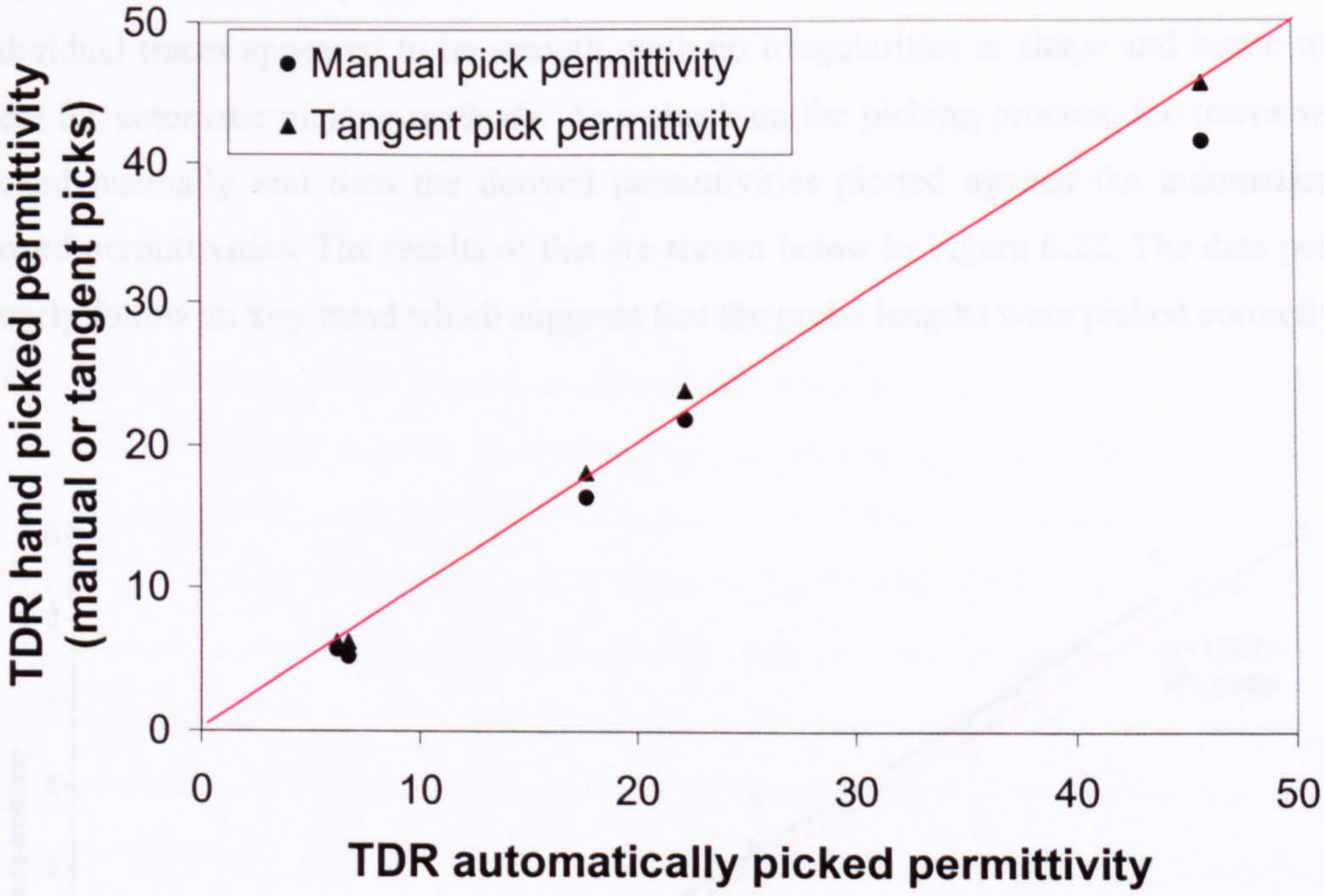

Figure 6.20. Comparison of picking methods for calibration cell. Red line is an x=y plot.

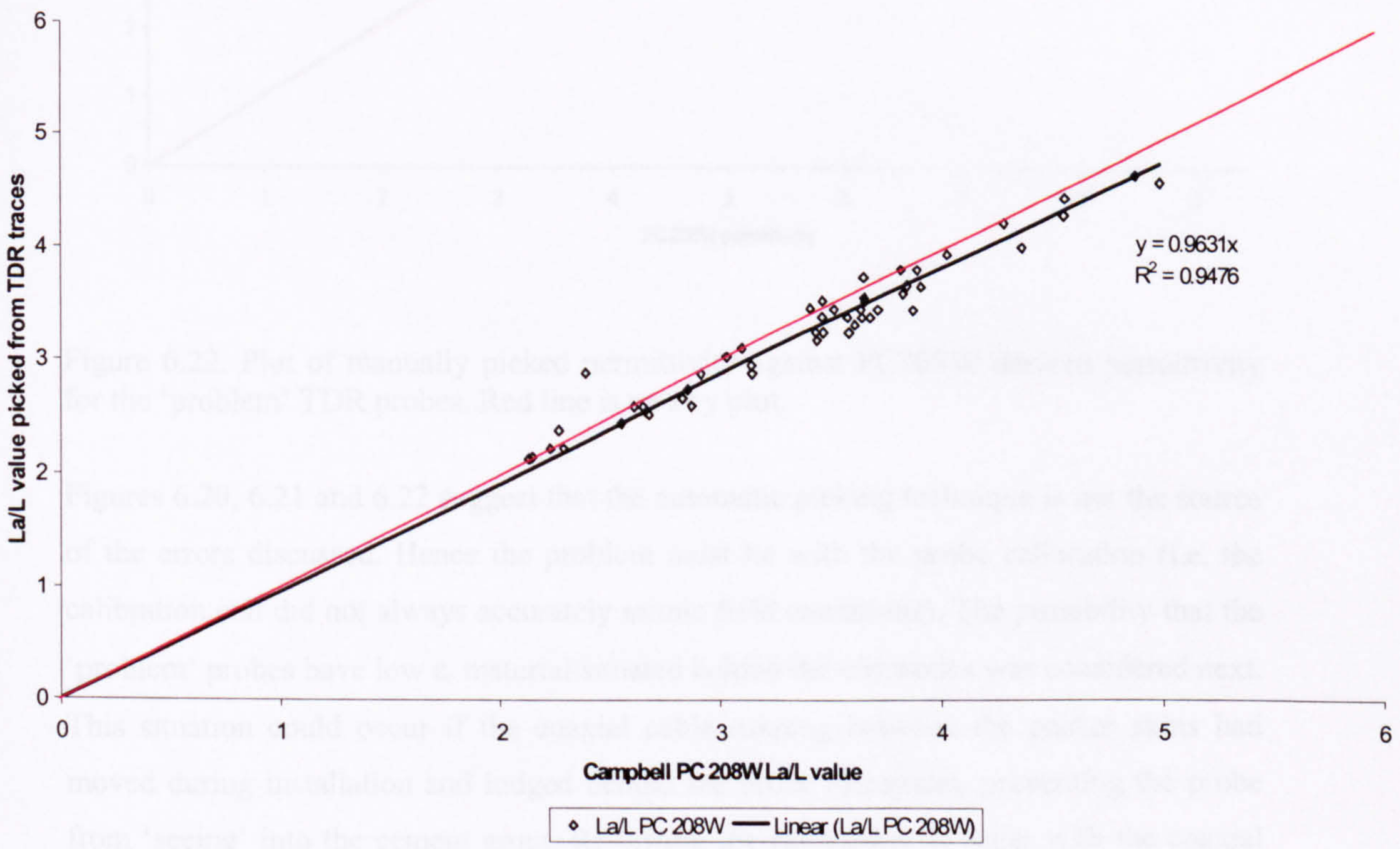

Figure 6.21. Comparison between PC208W and manual picks for a range of field TDR traces. Red line is an x=y plot.

Figure 6.21 showed that there was little error in the picking of the PC 208W apparent probe lengths. The probes that are recording erroneously low moisture content values are

emplaced at various depths. Careful examination of the traces showed nothing unusual, individual traces appeared to be smooth, with no irregularities in shape and hence were ideal for automatic picking methods. As a check on the picking process, the traces were picked manually and then the derived permittivities plotted against the automatically picked permittivities. The results of this are shown below in Figure 6.22. The data points closely follow an x=y trend which suggests that the probe lengths were picked correctly.

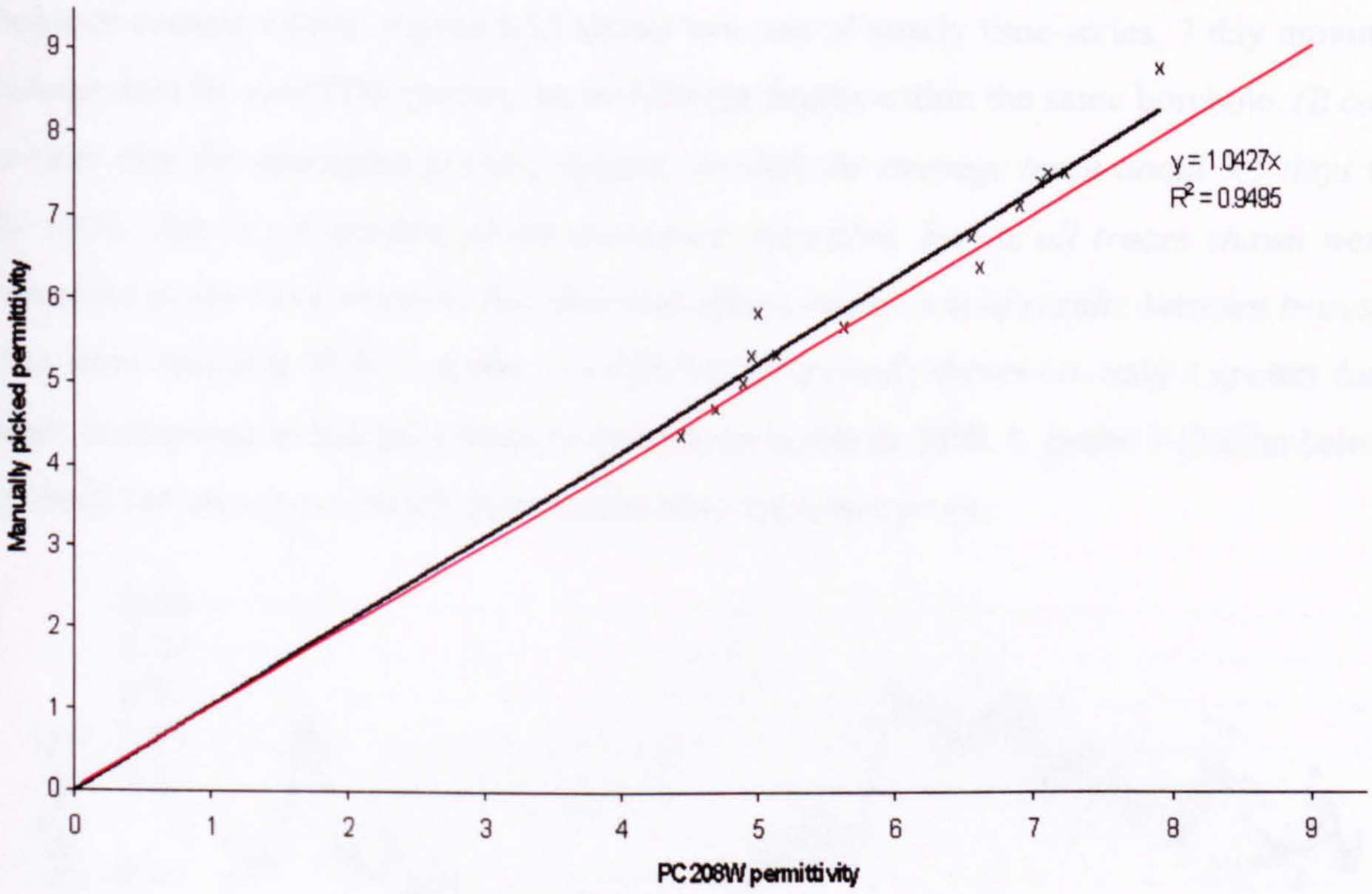

Figure 6.22. Plot of manually picked permittivity against PC208W derived permittivity for the 'problem' TDR probes. Red line is an x=y plot.

Figures 6.20, 6.21 and 6.22 suggest that the automatic picking technique is not the source of the errors discussed. Hence the problem must lie with the probe calibration (i.e. the calibration cell did not always accurately mimic field conditions). The possibility that the 'problem' probes have low ε_r material situated behind the electrodes was considered next. This situation could occur if the coaxial cable running between the packer skins had moved during installation and lodged behind the probe electrodes, preventing the probe from 'seeing' into the cement grout. Re-testing the calibration in water with the coaxial cable in various locations behind the probe showed that the calibration variables (w and K_{packer}) could change markedly, leading to low readings like those seen in some field probes. The data returned from the TDR system indicate an air gap behind the electrodes rather than the front. This is because the 'problem' electrodes showed similar moisture content variation responses to the good probes. If air gaps were present between the

electrodes and the rock a different, probably flat response would be expected. Hence, it can be concluded that the under-reading electrodes (those that returned low θ values <14%) give an accurate indication of fluctuation in moisture content over time, although they cannot provide accurate absolute moisture content data.

High data scatter (some probes)

Some probes showed high degrees of data scatter when presented as time series, and the probes showing high degrees of scatter were not necessarily the probes recording low moisture content values. Figure 6.23 shows two sets of yearly time-series, 7 day moving average data for two TDR probes, set in different depths within the same borehole. *(It can be seen that the averaging process appears to shift the average trace about 3.5 days to the right. This is an artefact of the averaging algorithm, but as all traces shown were processed in the same manner, this does not affect comparison of results between traces).* Data from borehole TDR 5, probe 1 (1.63m below ground) shows not only a greater data range in response to rainfall events to those from borehole TDR 5, probe 3 (3.62m below ground), but also shows much more scatter than the lower probe.

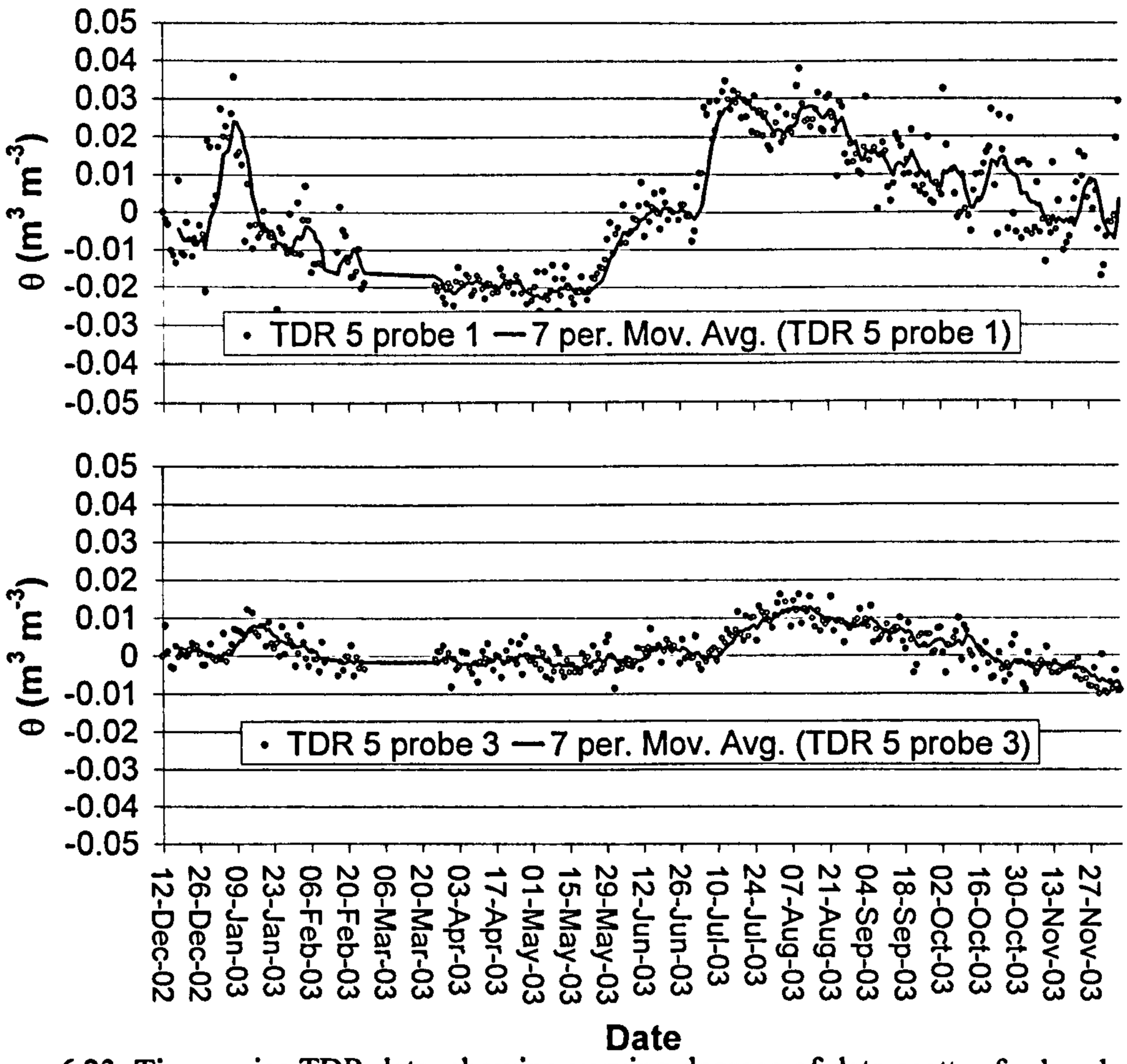

Figure 6.23. Time series TDR data, showing varying degrees of data scatter for borehole TDR 5, probes 1 and 3.

Histograms showing the relative frequencies of reflection coefficients were plotted for both high-scatter and low-scatter TDR probes and these are shown in Figure 6.24 below. Plotting as a histogram allows comparison between hundreds of reflection coefficient values, rather than the averaging values from a few traces. Between the Γ_T and Γ_R peaks there are a range of reflection coefficients that could be from either reflection.

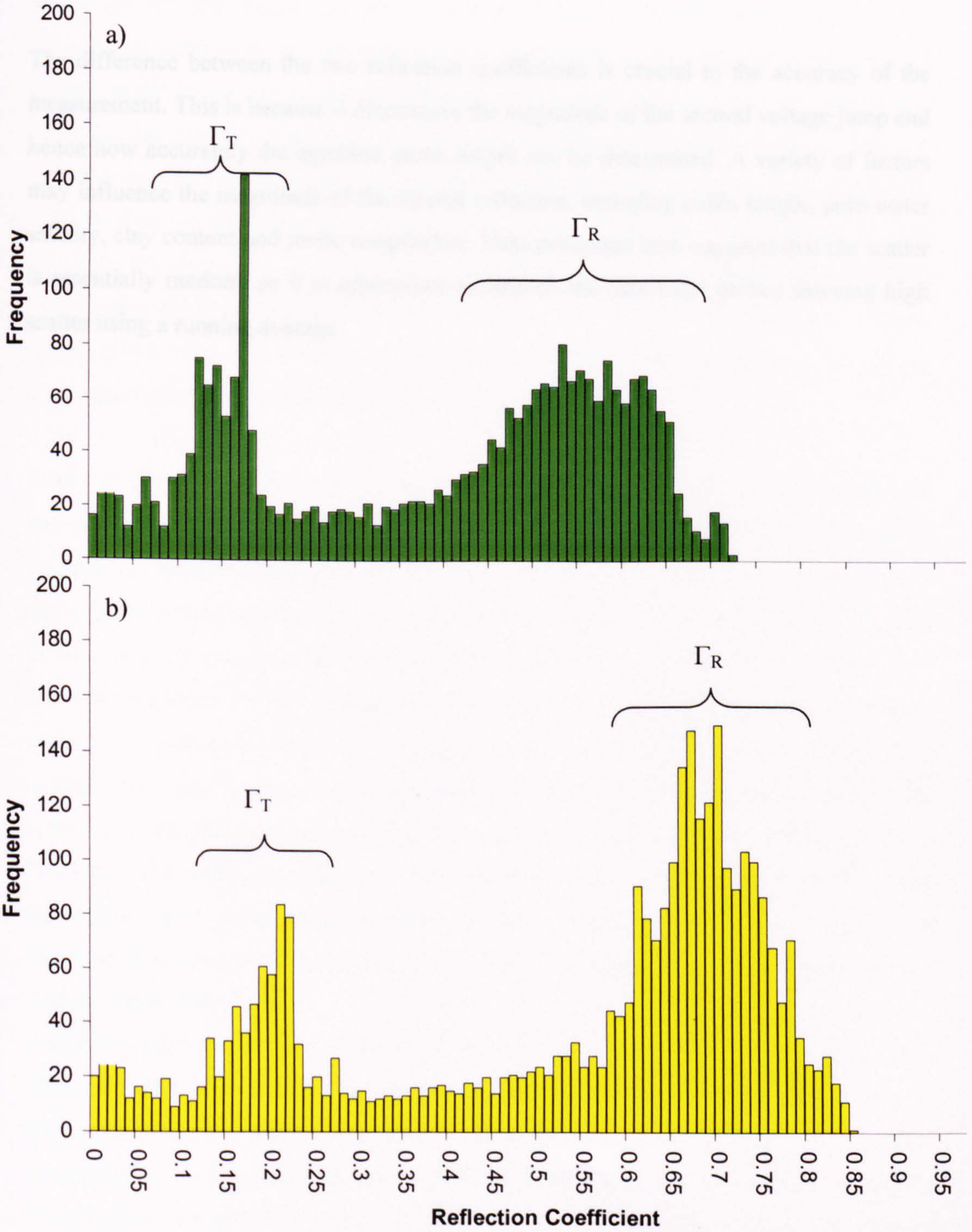

Figure 6.24. Frequency distribution histograms for a) high-scatter and b) low-scatter TDR probes.

Both high and low-scatter TDR probes show similar reflection coefficients for the returned reflection from the start of the probes (Γ_R). The low-scatter probes (Figure 6.24b) generally show higher values for reflection coefficient for the reflections from the ends of the probes (Γ_T) than the high-scatter probes, which means that the apparent probe length can be determined more accurately.

The difference between the two reflection coefficients is crucial to the accuracy of the measurement. This is because it determines the magnitude of the second voltage jump and hence how accurately the apparent probe length can be determined. A variety of factors may influence the magnitude of the second reflection, including cable length, pore-water salinity, clay content and probe temperature. Data presented here suggests that the scatter is essentially random, so it is appropriate to smooth the data from probes showing high scatter using a running average.

6.5.2 TDR results

Absolute moisture content data; borehole TDR 4.

Full results for all TDR probes installed at the Great Heck test site on permanent packers are presented here. Absolute values of time-series moisture content data from borehole TDR 4 (which was the cored hole) are compared with the core log and TRIME moisture content data, and time-series moisture content variations are compared between boreholes across the test site. Figure 6.25 shows absolute moisture content values from borehole TDR 4 compared with the borehole log from the same hole. As stated in Chapter 6.5.1 it is appropriate to smooth scattered TDR data using a 7 day running average (shown as a solid line on plots) and it is this line that is described and interpreted. Also shown is effective rainfall over the 2002/2003 period. The TDR data shows more detail than the TRIME data, as the time-series data density is much greater. However, within each borehole, the vertical resolution of the TDR data is less than the TRIME data (0.5-1.5m compared with 25cm for the TRIME). The permanent packer TDR electrodes are also longer (29cm) than the TRIME packer (25cm) electrodes. The results from the packer permanently installed in borehole TDR 4 are presented first.

Probe 1, sited 0.86m below ground showed strong correlation between moisture content and effective rainfall. The ground was initially wet in December 2002, and steadily became less saturated, changing from $\theta = 26\%$ in December 2002 to $\theta = 21\%$ by May 2003, when saturation levels started to climb as a response to April rainfall events. The moisture content continued to rise until July 2003 as a response to the spring rainfall, until the rock was again at 25% saturation. Following this the rock became less saturated as water either drained to lower levels or was removed by evapotranspiration, and moisture content levels only began to climb as a result of autumn rainfall in November 2003. This response is similar to that determined from the near-surface TRIME data (See Figure 5.11) at 1.25m below ground level, with a similar range of values ($\theta = 20$-25%) and appears to show about 1 month delay between rainfall event and moisture content response. It is likely that the TDR probe is recording moisture moving through coarse-medium grained sandstone.

Probe 2, 1.80m below ground shows some relationship between moisture content and effective seasonal rainfall, but not the close correlation observed at some other depths. In December 2002, the ground was initially fully saturated, with a volumetric moisture content value of 35%, which dropped rapidly to 30% moisture content by February 2003. The moisture content then remained fairly constant through the summer, but started falling in October, dropping to 26% moisture content by the end of 2003. Probe 2 shows

limited response to some rainfall inputs (e.g. that seen in late July 2003). Some moisture content fluctuation is a response to rainfall, with rainfall events appearing as minor moisture fluctuations with approximately one-month delay from rainfall time-series. The high overall moisture content suggests that the rock at this level is fine-grained.

Probe 3, 2.83m below ground, again shows good correlation between moisture content and rainfall data. In December 2002, the ground at this depth was initially fairly dry ($\theta \approx$ 20%), and became wetter up to θ = 24% as a response to December 2002 rainfall. By February 2003 the rock at this level was wet (θ = 24%), and rapidly drained down to θ = 20% by March 2003, remaining constant until June 2003, when saturation started to climb as a response to mid-April rainfall events. The moisture content continued to rise until mid-September 2003 as a response to the spring/early summer rainfall, when the rock was again at 25% saturation. From mid-September onwards the rock slowly drained, with some small increases in moisture content, but little autumn 2003 rainfall had reached this depth during the monitoring period. The core log indicates that the probe is in medium-grained sandstone.

Probe 5, 4.79m below ground shows $\approx$ 5% variation in volumetric moisture content throughout the year with the ground becoming steadily drier over the winter and spring of 2002-2003, following an initially high moisture content value (27%) in December 2002. Probe 5 reached its driest reading in mid-July 2003 and moisture content levels increased steadily until late August 2003 as a response to early summer (May-July) rainfall. From August to December 2003, moisture levels remained relatively constant. The core log indicates that the probe is in medium-grained sandstone.

Probe 6, 5.83m below ground shows 5-6% variation in volumetric moisture content throughout the year and became drier over the winter of 2002-2003, following initially high moisture content values in December 2002, when the ground was fully saturated, with a volumetric moisture content value of 35%. The moisture content dropped rapidly to 30% by February 2003, before remaining fairly constant through to early summer. Moisture content levels then rose steadily from May 2003 until November 2003 as a response to the summer rainfall. From November 2003, moisture levels show a sharp decline. The overall moisture content is higher for probe 6 than the surrounding probes, so it is likely that probe 6 is sited either in a fine-grained layer, or a perched water table. If the inflexion points, where the spring drying is replaced by the summer wetting are examined, Probe 6 also responds in a different manner to probe 5, appearing to react significantly faster to rainfall. Probe 6 responds to the summer rainfall by mid-May, some 6 weeks before probe 5 located above (see black arrows on Figure 6.26). Also shown are vertical/near vertical link arrows (dashed red arrows) linking moisture peaks in probe 3 with probe 6 with close to zero time delay. The fact that probe 6 responds extremely

rapidly to rainfall patterns seen in shallower boreholes suggests that it may possibly be experiencing some degree of bypass flow, thus reducing response delay times.

Probe 7, 6.84m below ground shows approximately 5% variation in volumetric moisture content throughout the year and became drier over the winter of 2002-2003, following initially high moisture content values (θ =24%) from December 2002. Probe 7 achieved its driest in mid-July 2003 but moisture content levels remained fairly constant until the end of 2003. The core log indicates that the probe is below a fine-grained sandstone layer.

Probes 8 and 9 are omitted as they did not produce absolute moisture content data.

Probe 10 (9.85m). Here, the response is virtually flat, there appears to be little moisture content variation throughout the year although some drying of the system appears to have occurred between December 2002 and February 2003. Moisture content is consistently around 25% and so it is likely that this layer is shielded by an overlying fine-grained sandstone layer.

Probe 12 (10.84m). This probe returned saturated moisture contents throughout the year. This depth corresponding with the permanent perched water table at 10.75m encountered within the TRIME borehole.

Probe 13. (12.87m) This probe returns similar data to probes 7 and 5. The moisture content fell slowly until March 2003, where moisture levels remained constant, with possibly a slow increase from about August onwards. The response to seasonal rainfall appears very damped and moisture contents vary by under 5% throughout the year. However, the fact that this layer is not saturated proves that probe 12 is situated within a perched water table and not the true saturated zone.

Probe 14 (13.87m). This probe is in the capillary fringe, close to the true water table, which is normally at 14-14.5m depth. The steady increase in moisture content is most likely due to water table rise caused by variations in the pumping regime from the water abstraction well adjacent to the Great Heck sand quarry.

Other TDR borehole absolute moisture content results

Figures 6.26 to 6.28 present the absolute moisture content values for boreholes TDR 01, TDR 02 and TDR 05 respectively. Unlike borehole TDR 04, reliable absolute moisture content values are generally available for the deeper probes only, and the trends seen in Figures 6.26 to 6.28 are described in Table 6.4. (the column headed 'group' is explained below).

Borehole	Probe	Depth (m)	Min θ (%)	Max θ (%)	Group	Comments
TDR 01	9	6.35	16	19	3	Moisture levels increased during Jan 2003, and then gradually decreased until late May 2003. Early summer rain induced gradual wetting from late May – mid Aug 2003, followed by steady drying until Dec 2003.
TDR 01	11	7.35	19	23	3	Gentle decrease in moisture content from Dec 2002 to mid May 2003 followed by steady wetting until Dec 2003.
TDR 01	12	7.9	27	32	3	Rapid draining from 30% moisture content in Dec 2002 to 27% by late Jan 2003. Moisture contents then remained steady until mid May 2003 when steady wetting commenced until Dec 2003.
TDR 01	13	8.35	26	29	1c	Moisture contents remained steady at about 26-27% until the start of June 2003 before increasing gently to 28-29% by the end of Dec 2003.
TDR 01	14	8.9	27	29	3	Moisture contents remained steady at about 26-27% until the start of June 2003 before increasing gently to 28-29% by the end of Dec 2003.
TDR 01	15	9.4	29	33	1a	Moisture contents remained steady throughout the year at approximately 30% except for rapid responses to rainfall events in July and Dec 2003 where moisture contents rose rapidly to 33% (fully saturated). This probe is probably responding to perched water above a fine-grained layer (see probe 16).
TDR 01	16	10.4	33	33	1b	Saturated throughout the year, even though true water table is at >14m. Probe probably sited within fine-grained aquitard layer.
TDR 02	8	8.0	23	25	2	Gentle decrease in moisture content from Dec 2002 to Aug 2003 followed by steady wetting until Dec 2003.
TDR 02	9	9.0	29	32	1c	Very gentle decrease in moisture content from Dec 2002 to mid May 2003, followed by slow but steady wetting until Dec 2003. Probe probably sited within a fine grained layer which drains slowly and shows little variation in moisture content.
TDR 02	10	10.02	27	30	3	Moisture content remained steady at approximately 30% until Feb 2003, then decreased gently to 27% by the end of June 2003, followed by gradually increasing moisture content levels until Dec 2003.
TDR 02	11	11.03	33	33	1b	Saturated throughout the year, even though true water table is at >14m. Probe probably sited within fine-grained aquitard layer.
TDR 02	12	12.03	21	25	1a	Rapid reduction in moisture content from Dec 2002 to Jan 2003 followed by increasing moisture content until end Oct 2003, after which moisture contents reduced over Nov and Dec 2003.
TDR 02	13	13.03	33	33	1b	Saturated throughout the year, even though true water table is at >14m. Probe probably sited within fine-grained aquitard layer.
TDR 02	14	14.02	33	33	1b	Saturated throughout the year, probably responding to true water table at >14m.
TDR 05	5	6.15	20	23	2	Slow reduction in moisture content from Dec 2002 to June 2003 followed by slow wetting until Dec 2003
TDR 05	6	7.62	26	27	2	Little overall change in moisture content, which remained approximately 27%
TDR 05	7	9.15	17	23	2	High scatter data showing little overall change in moisture content apart from gradual increase from May-Dec 2003.
TDR 05	8	10.62	24	27	1c	Little overall change in moisture content apart from gradual increase over year, but much less scatter than probe above.

Table 6.4. Absolute TDR moisture contents from boreholes TDR 01, 02 and 05.

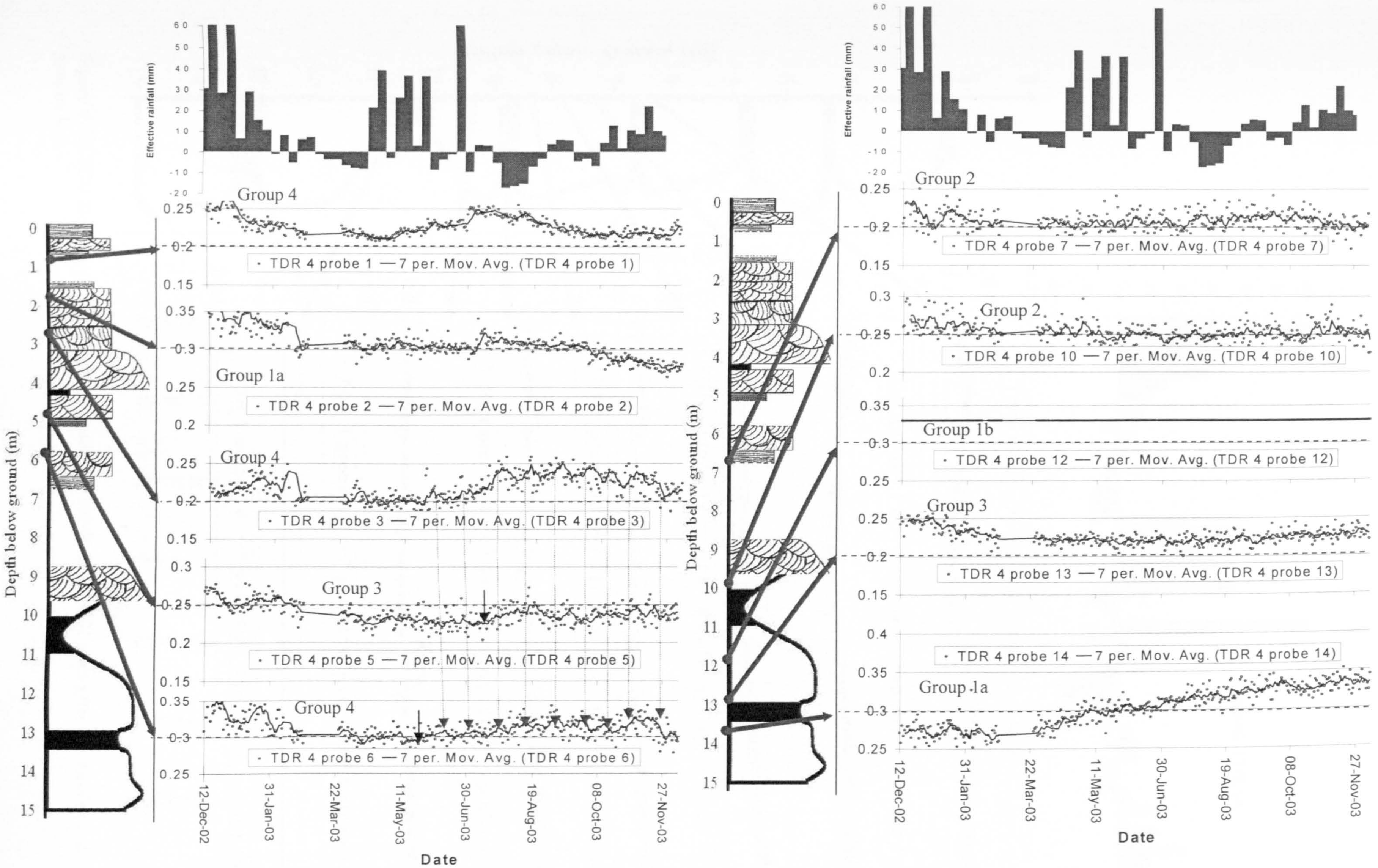

Figure 6.25. TDR absolute moisture content results for borehole TDR 04, showing group (see below) with effective rainfall and core/gamma logs (Solid lines represent running averages over 7 data points).

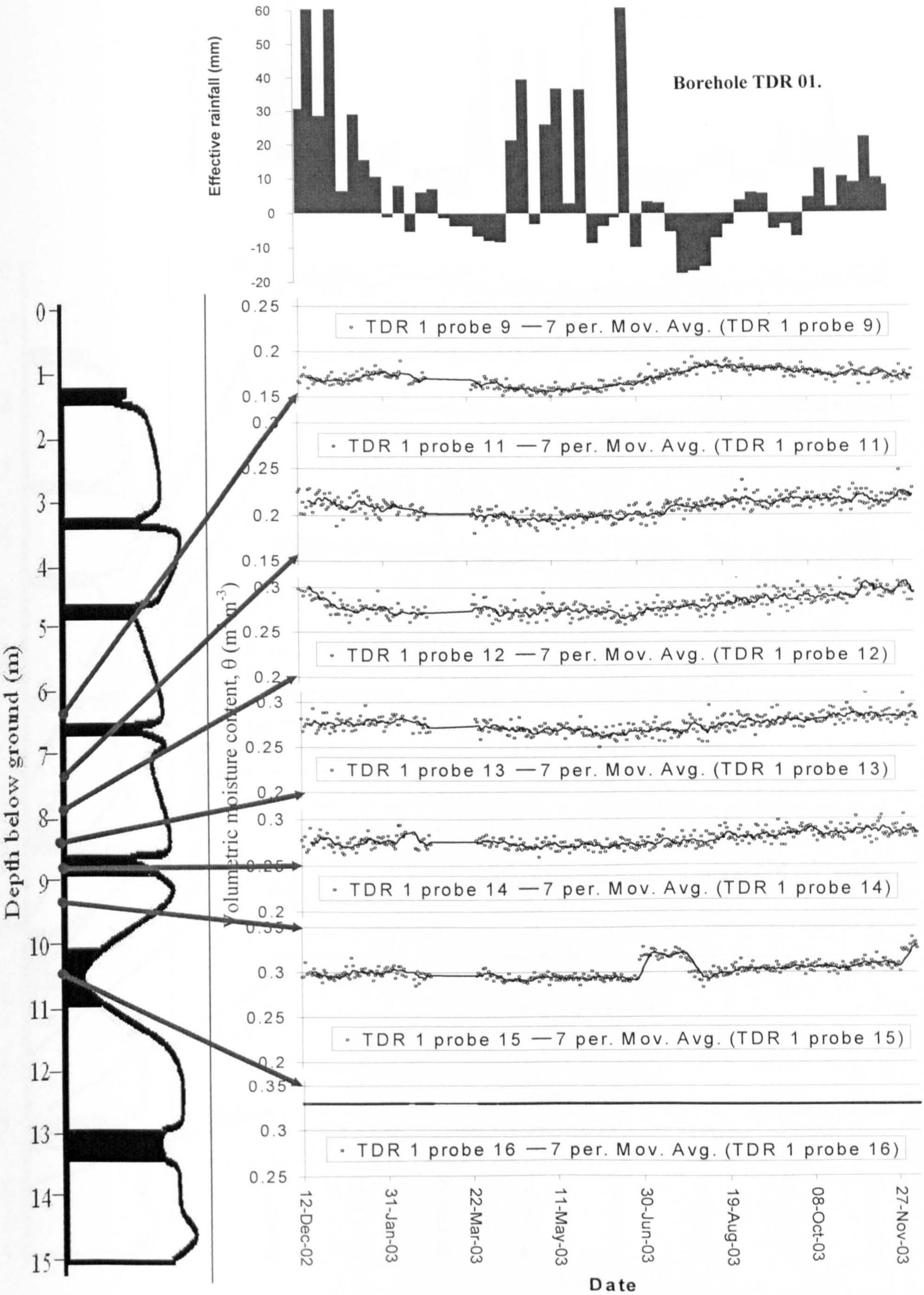

Figure 6.26. TDR absolute moisture content results for borehole TDR 01 with effective rainfall and gamma log.

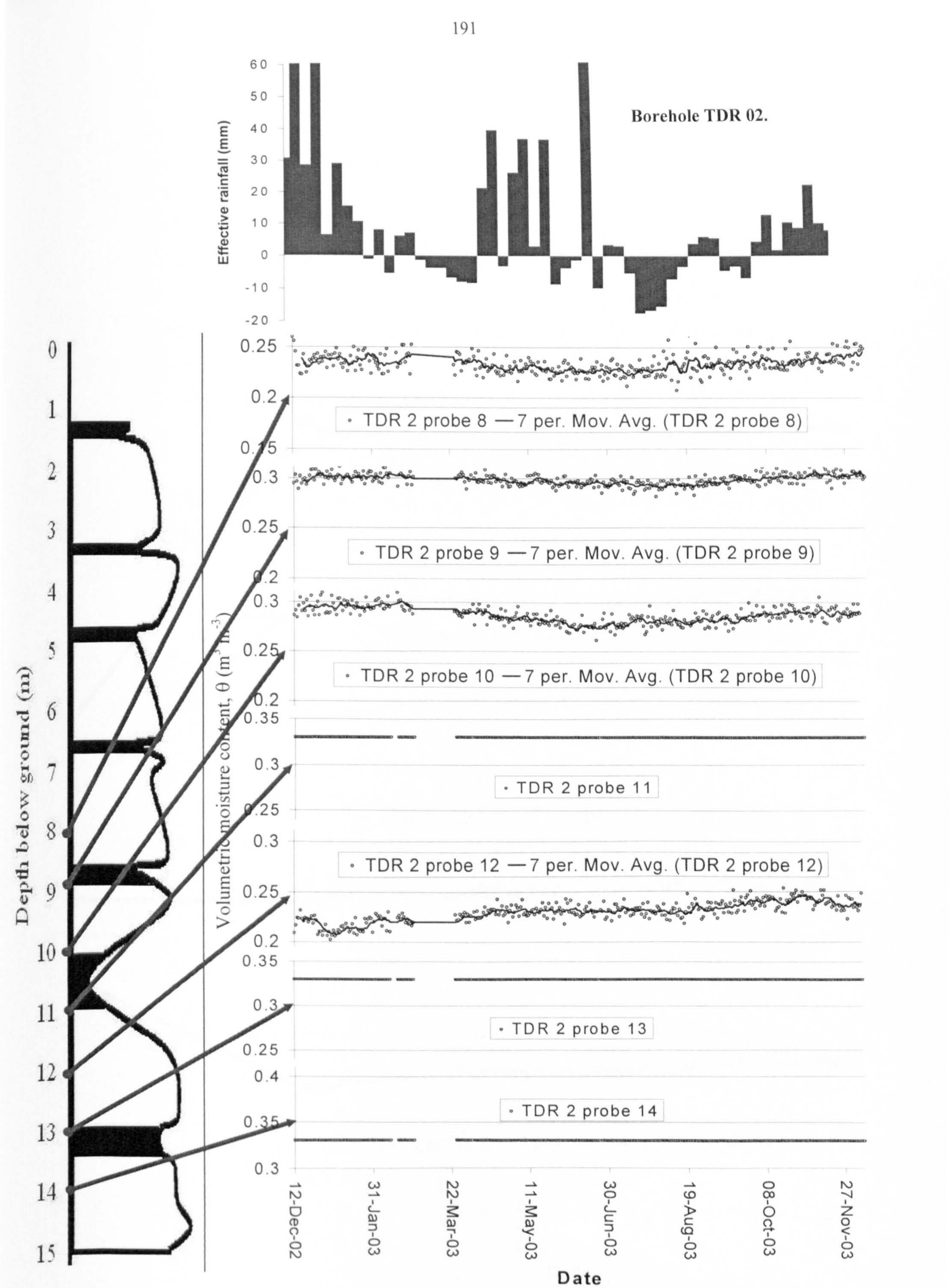

Figure 6.27. TDR absolute moisture content results for borehole TDR 02 with effective rainfall and gamma log.

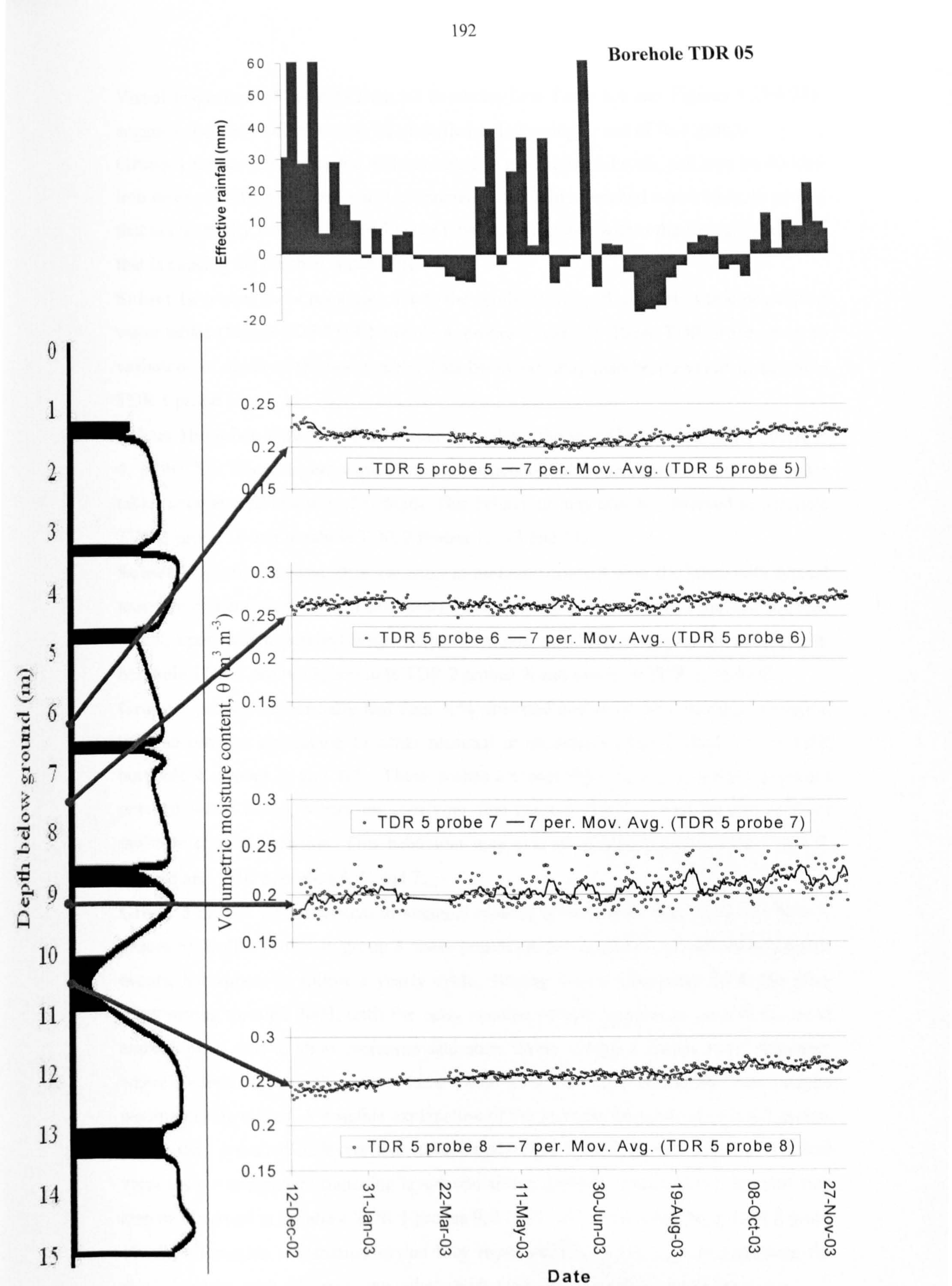

Figure 6.28. TDR absolute moisture content results for borehole TDR 05 with effective rainfall and gamma log.

Visual inspection of the data from all boreholes (see Table 6.4 and Figures 6.25-6.28), suggests that the TDR plots may be classified as belonging to one of four groups.

Group 1 probes are associated with saturated or near saturated rock, and may be divided into three subsets; a) probes which are sometimes within a perched water table; b) probes that are normally within a perched water table and c) probes within the fine-grained layer that is causing the perched water table.

Subset 1a probes show responses due to the capillary fringe that overlies true or perched water tables (Figure 6.25 TDR borehole 4, probes 2 and 14). These TDR probes react to variations in depth of the water table. This behaviour may also be observed in borehole TDR 1 probe 15.

Subset 1b probes showed full saturation throughout the year (Figure 6.25 TDR borehole 4, probe 12). These layers were normally associated with the persistent perched water tables encountered below 10.5m depth. This behaviour may also be observed in borehole TDR 1 probe 16 and borehole TDR 2 Probes 11, 13 and 14.

Subset 1c probes showed little variation in moisture content over the year, with typical moisture contents over 25%. These probes are probably sited in the fine-grained aquitard layers, upon which perched water tables form and this behaviour may be observed in borehole TDR 1 probe 13, borehole TDR 2 probes 9, and borehole TDR 5, probe 8.

Group 2 probes are normally less than 30% saturated and show little moisture variation with no obvious correlation to either seasonal or short-term rainfall (Figure 6.25 TDR borehole 4, probes 7, and 10). These probes are probably situated directly underneath perched water zones, where an overlying fine-grained layer is restricting significant moisture content variation. This behaviour may also be observed in boreholes TDR 2, probe 8 and TDR 5, probes 5, 6, and 7.

Group 3 probes are responsive to seasonal rainfall input (Figure 6.25 TDR borehole 4, probes 5). Unlike probes in group 4, these probes are not responsive to individual rainfall events, but appear to follow a yearly cycle. Starting wet in December 2002, the plots show drying through 2003, until the early summer rainfall appears to reverse the trend and the plots start to show increased saturation levels. Group 3 probes show responses where individual rainfall pulses have been smoothed and attenuated into annual wetting/drying cycles. A possible explanation of the seasonal response of Group 3 probes is that they are sited in layers that have largely been bypassed, with only the residual vertical-flow component transiting layers containing group 3 probes. This behaviour may also be observed in borehole TDR 1 probes 9, 11, 12, and 14, and borehole TDR 2 probe 10. An alternative explanation is that they represent a series of signals containing the rainfall events, with different time delays, added together to produce a smooth curve.

Group 4 probes show a clear response to short-term (weekly-monthly) rainfall input (Figure 6.25 TDR borehole 4, probes 1, 3, and 6). The heavy rainfall event that occurred in the first week in July is often visible as a significant moisture content 'step'. This behaviour is not seen in Figures 6.26-6.28 because the probes shown are sited at much greater depths than Figure 6.25, with the shallowest probe that returned reliable absolute moisture contents being at a depth of over 6m.

Moisture content variation

Absolute values of moisture content were used to describe the different probe responses, but for many probes the only reliable results were moisture content variation data. These data are mainly from the shallower levels where probes recording accurate absolute moisture content values were sparse. They allow further conclusions to be drawn about moisture movement within the Great Heck test site.

Figure 6.29 shows time-series variations in moisture content from 12th Dec 2002 values, for all the TDR probes in borehole TDR 04. This plot shows essentially the same features discussed in relation to Figure 6.36, except that the absolute moisture contents are not apparent and probes which do not give absolute moisture contents are included. The plots show a more complex picture of the extent of moisture content variations and correlations with effective rainfall. Full time-series moisture content variation data for the other TDR boreholes, together with arrowed (approximate) inflexion point locations are shown in Figures 6.30 to 6.32.

Table 6.5 is a summary of the time-series TDR results, with each probe classified into the most appropriate response group and comments on the timing of probe response and degree of scatter. Responsiveness to rainfall events was determined according to whether the December 2002-January 2003 rainfall was resolvable into two or more separate events on the plot.

Table 6.6 shows the time delay at the moisture content inflexion caused by the probe response to the onset of effective rainfall in spring 2003 at various probes, together with the probe depth. Where possible, the time delay was calculated by determining the inflexion point in the 7 day averaged response corresponding to the first significant rise in moisture content seen in the spring/summer of 2003 for each plot. The date of inflexion was given as the date of the nearest data point, as determined the data spreadsheet. This inflexion point was assumed to represent the response to the onset of spring/summer effective rainfall (21 April) at the probe.

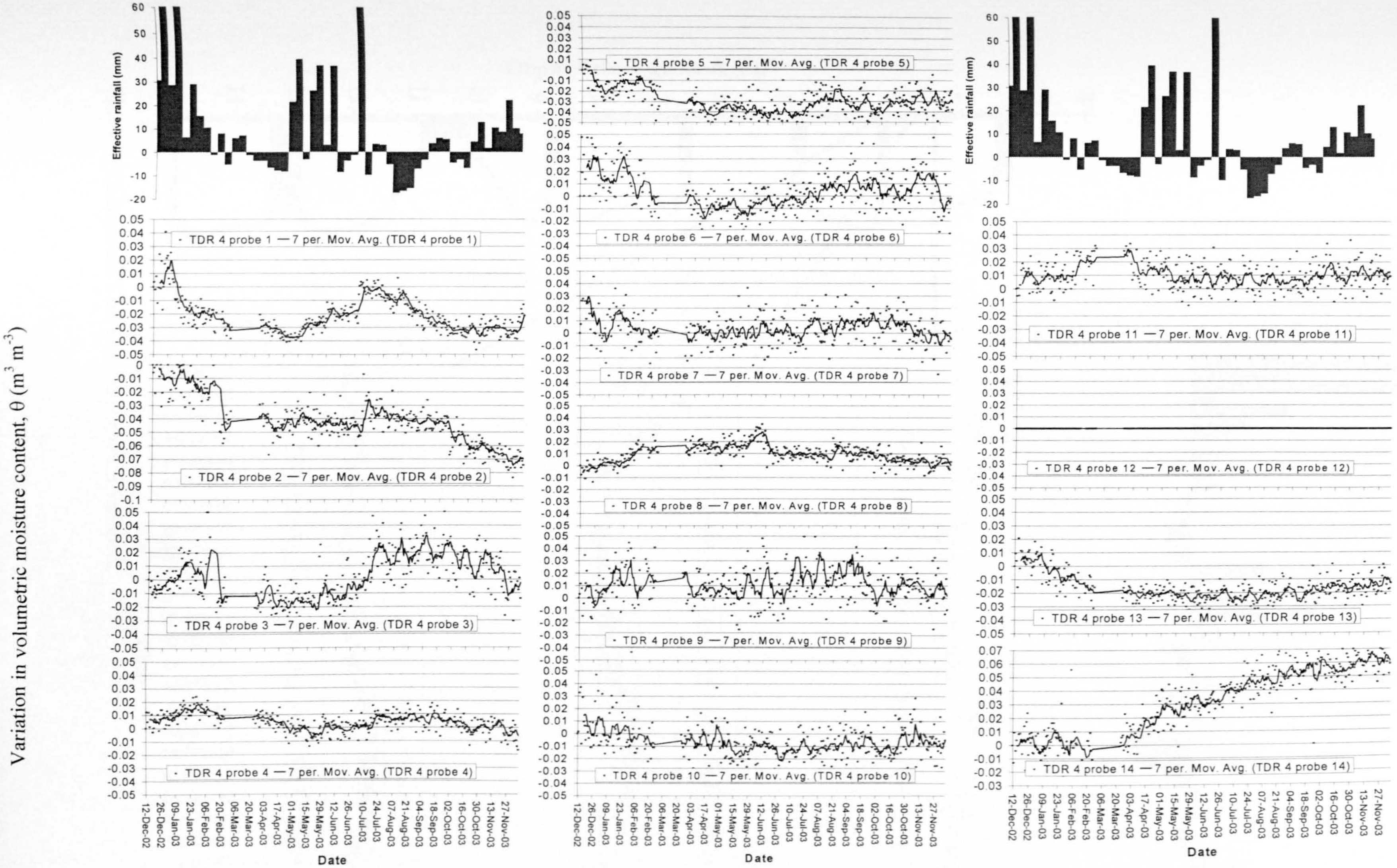

Figure 6.29. Time-series moisture content variation data for borehole TDR 04.

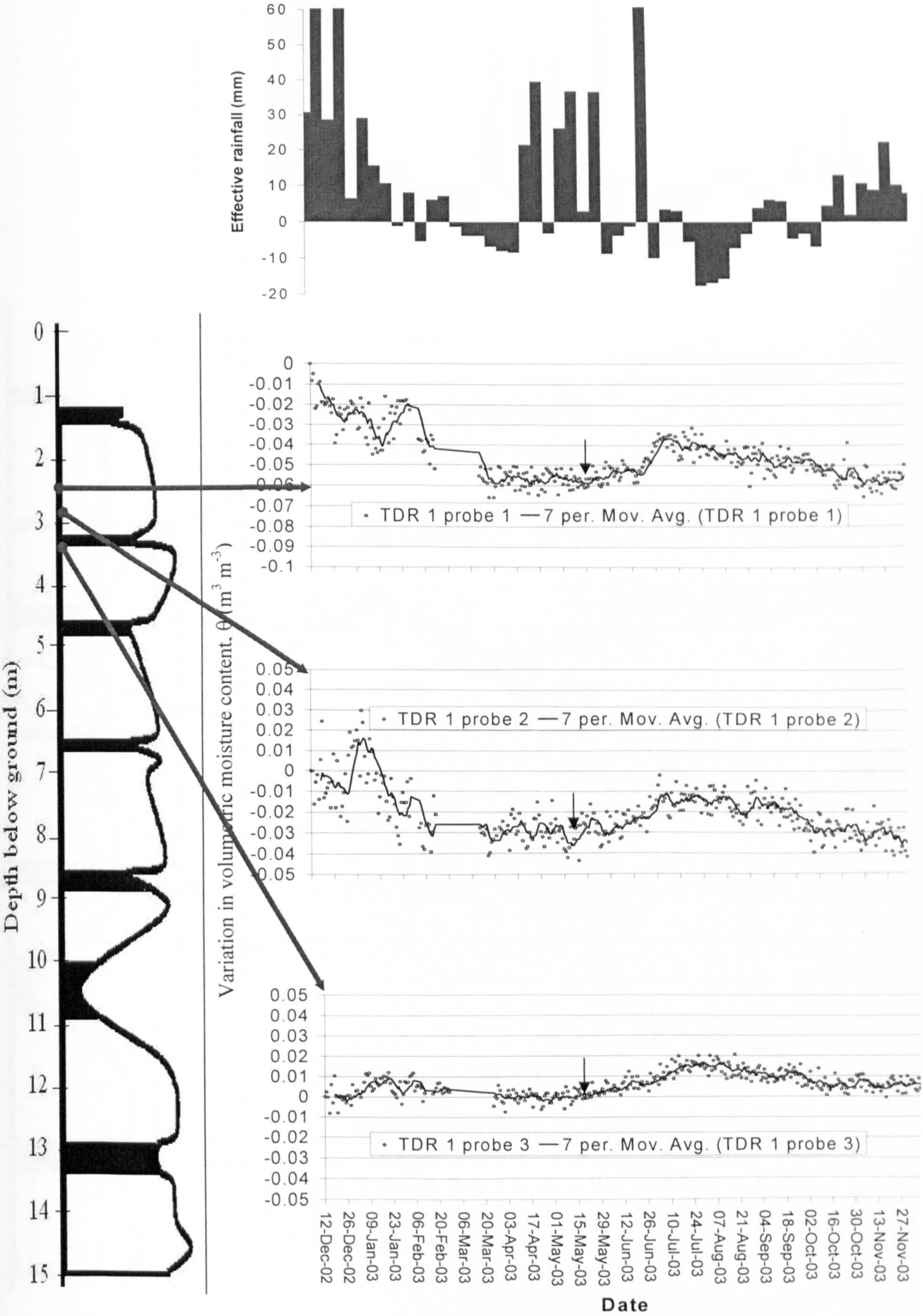

Figure 6.30a Borehole TDR 1 moisture content variation.

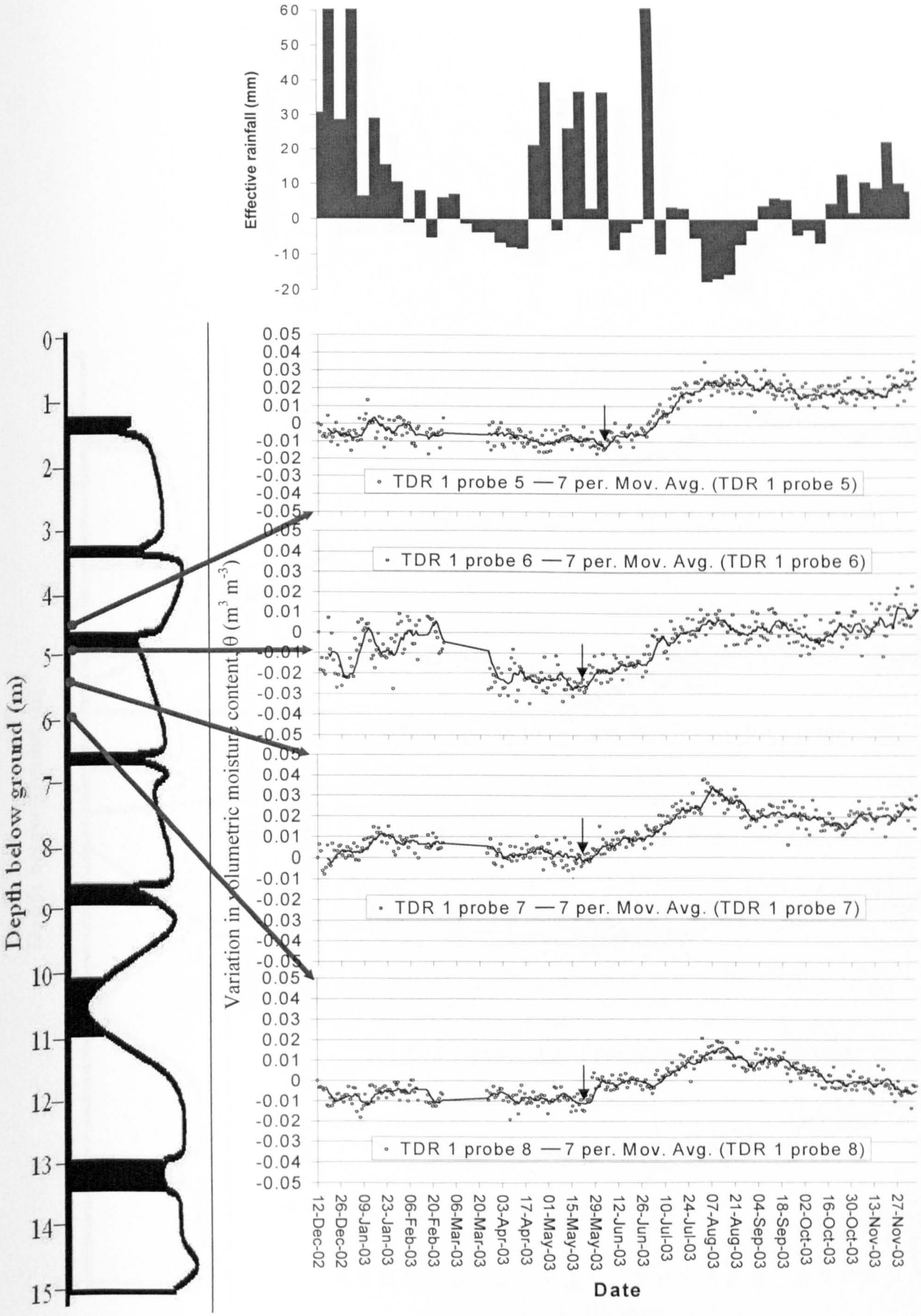

Figure 6.30b Borehole TDR 1 moisture content variation.

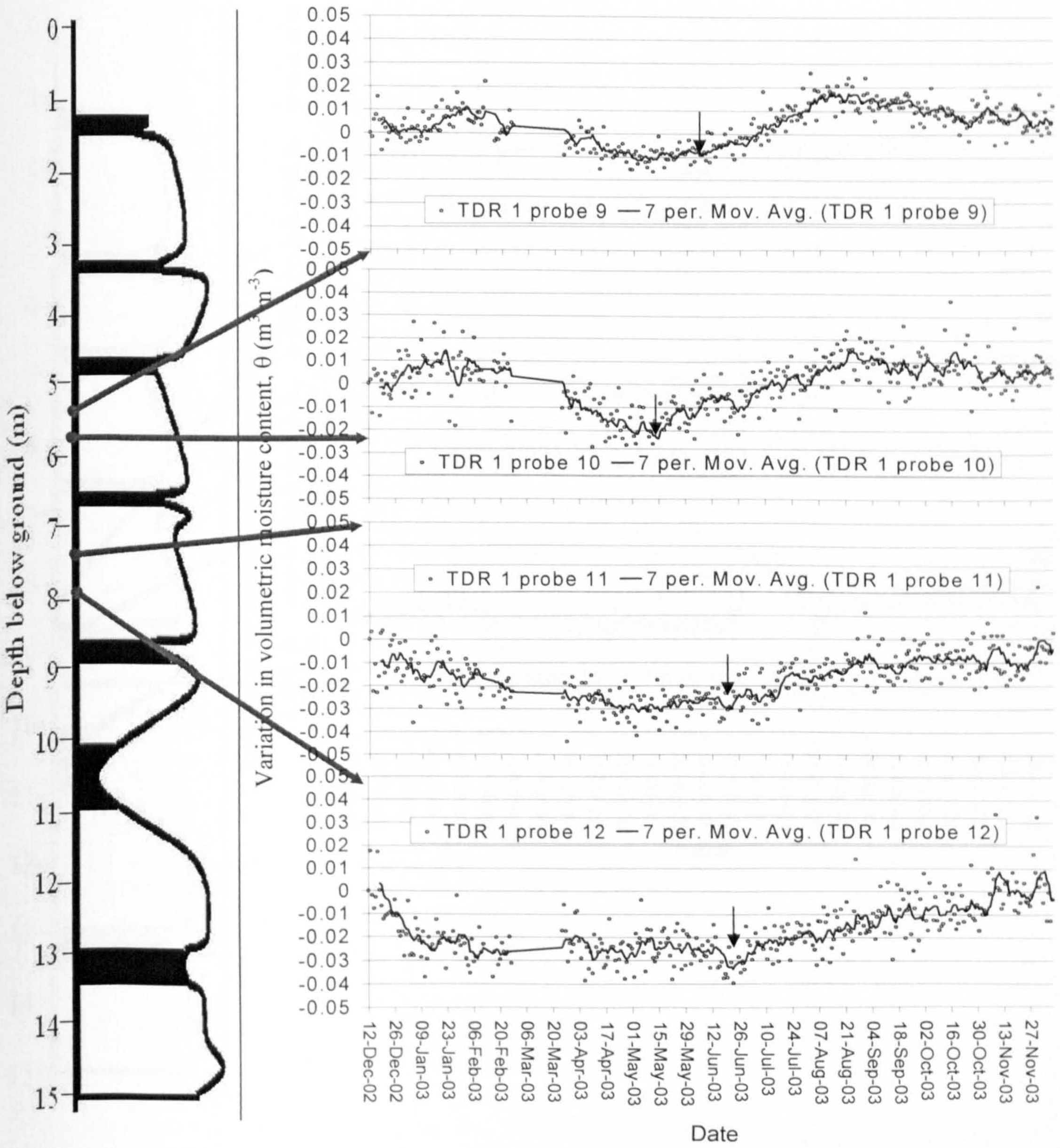

Figure 6.30c Borehole TDR 1 moisture content variation.

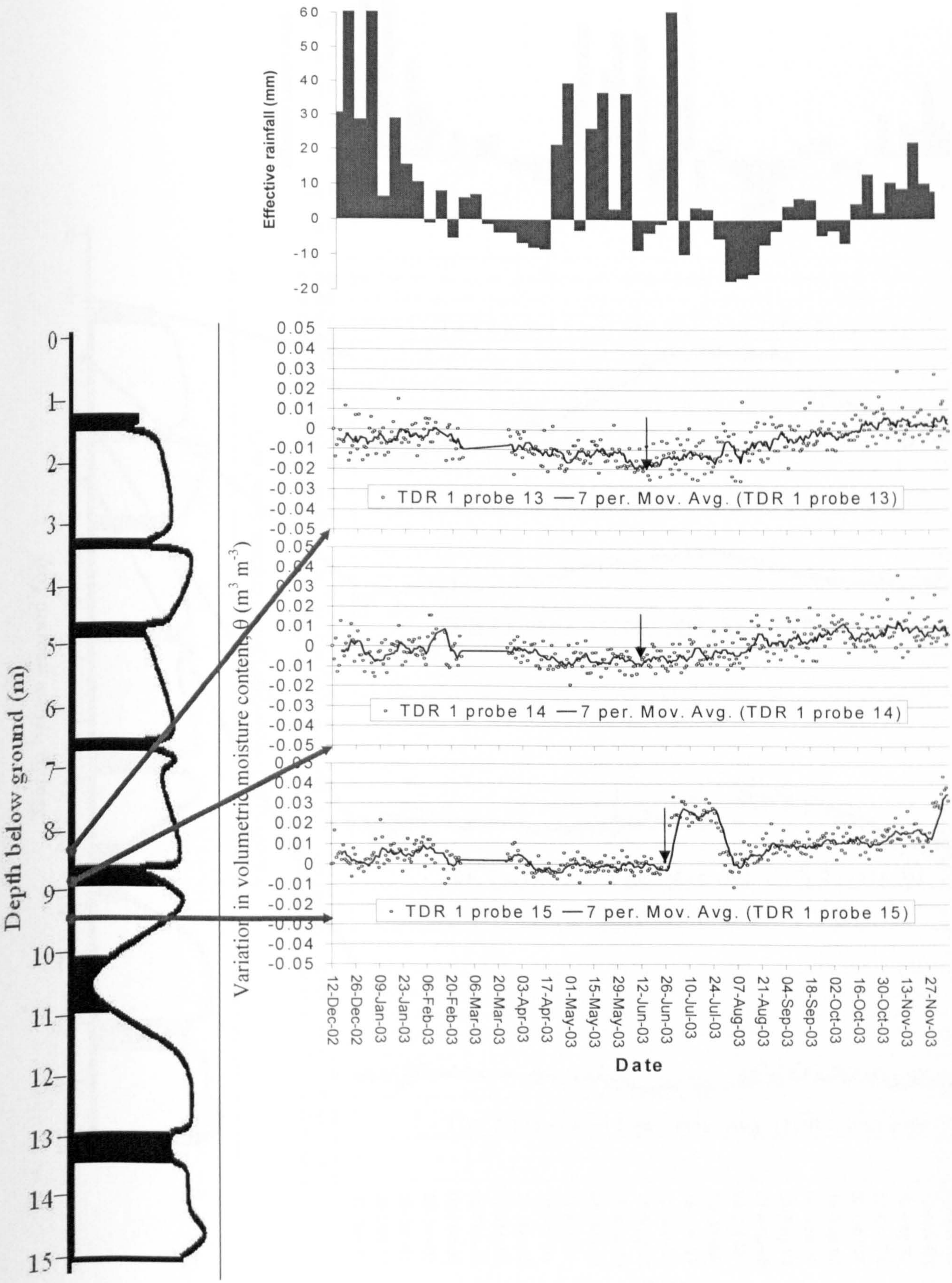

Figure 6.30d Borehole TDR 1 moisture content variation.

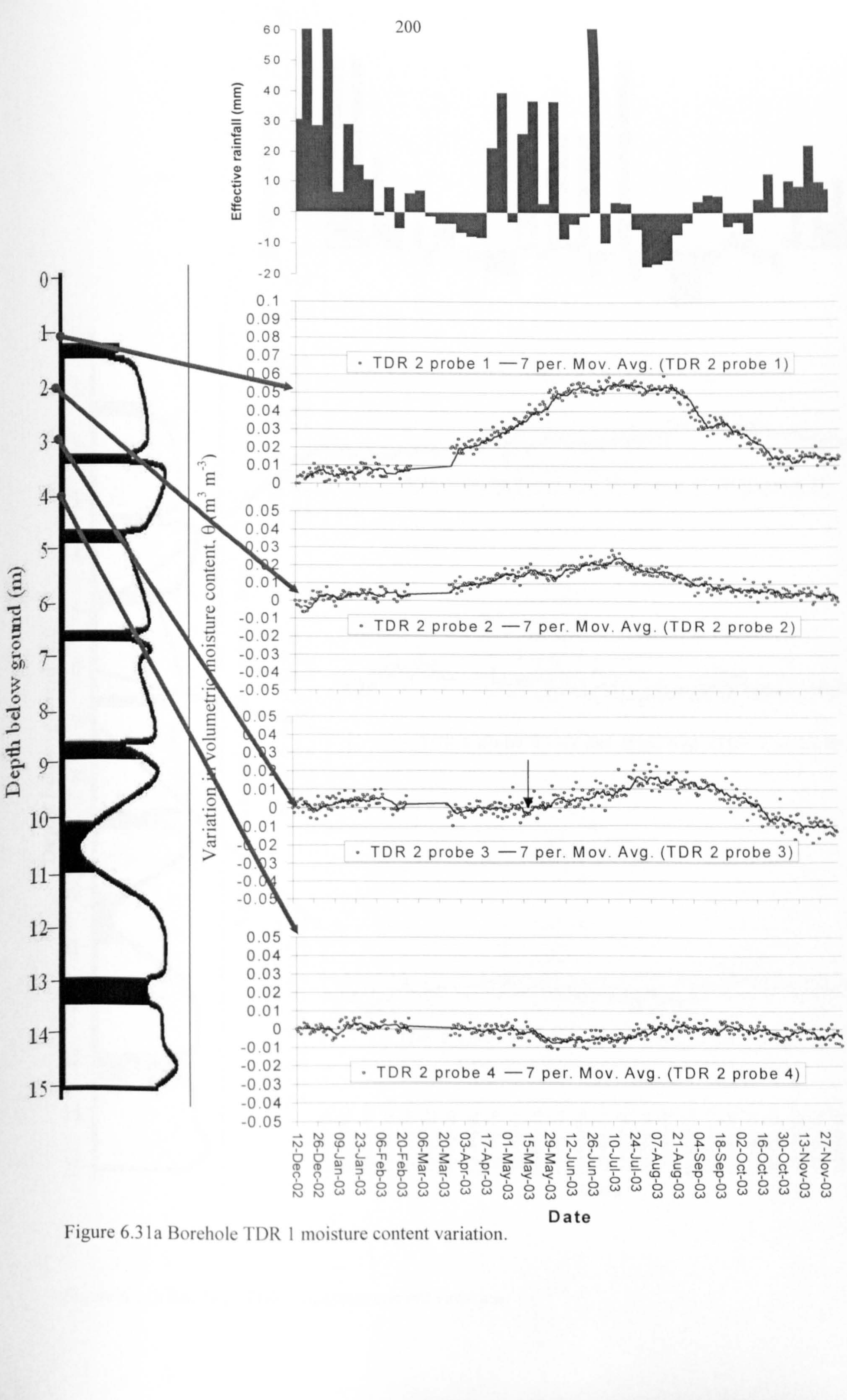

Figure 6.31a Borehole TDR 1 moisture content variation.

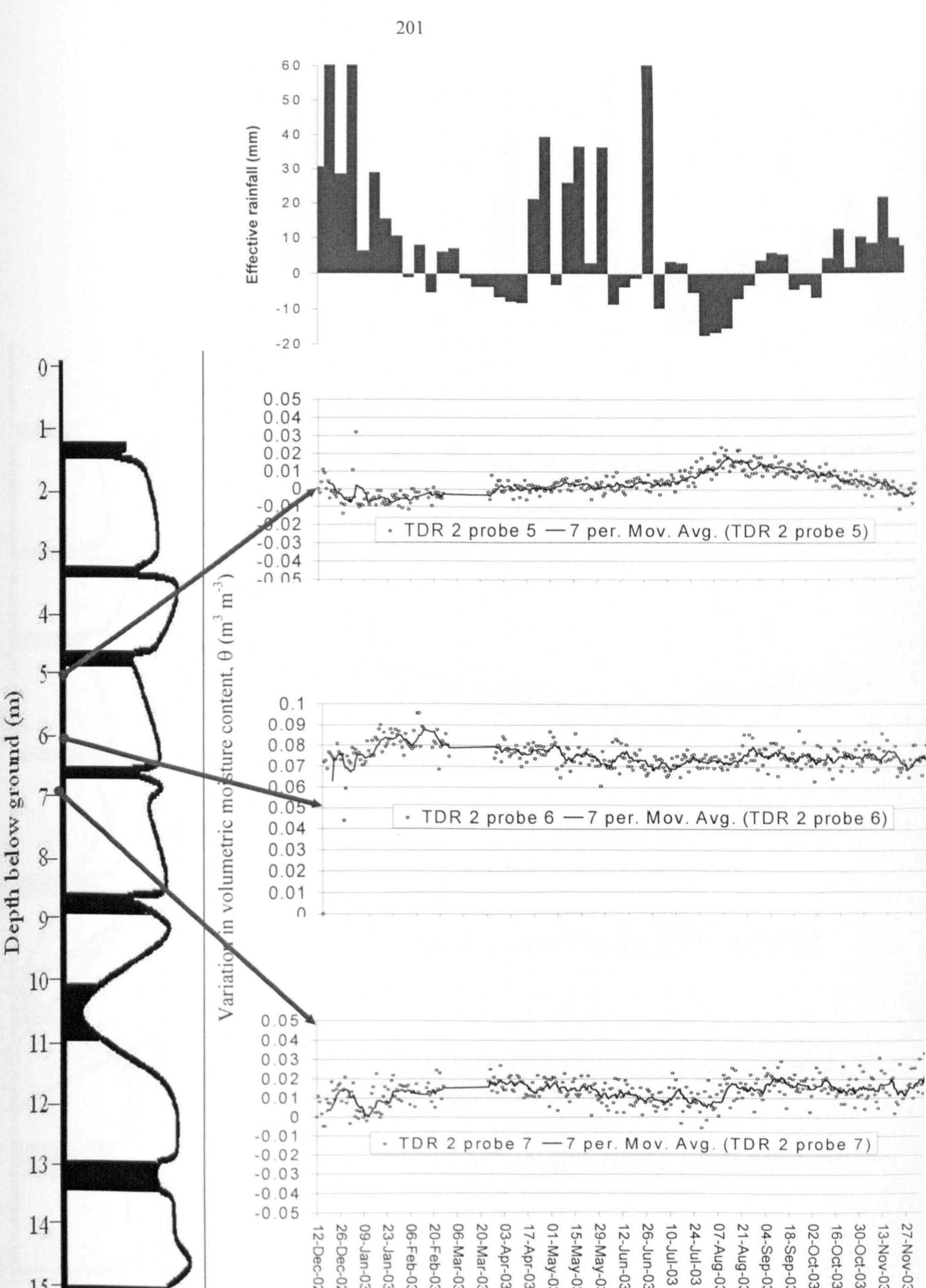

Figure 6.31b Borehole TDR 2 moisture content variation.

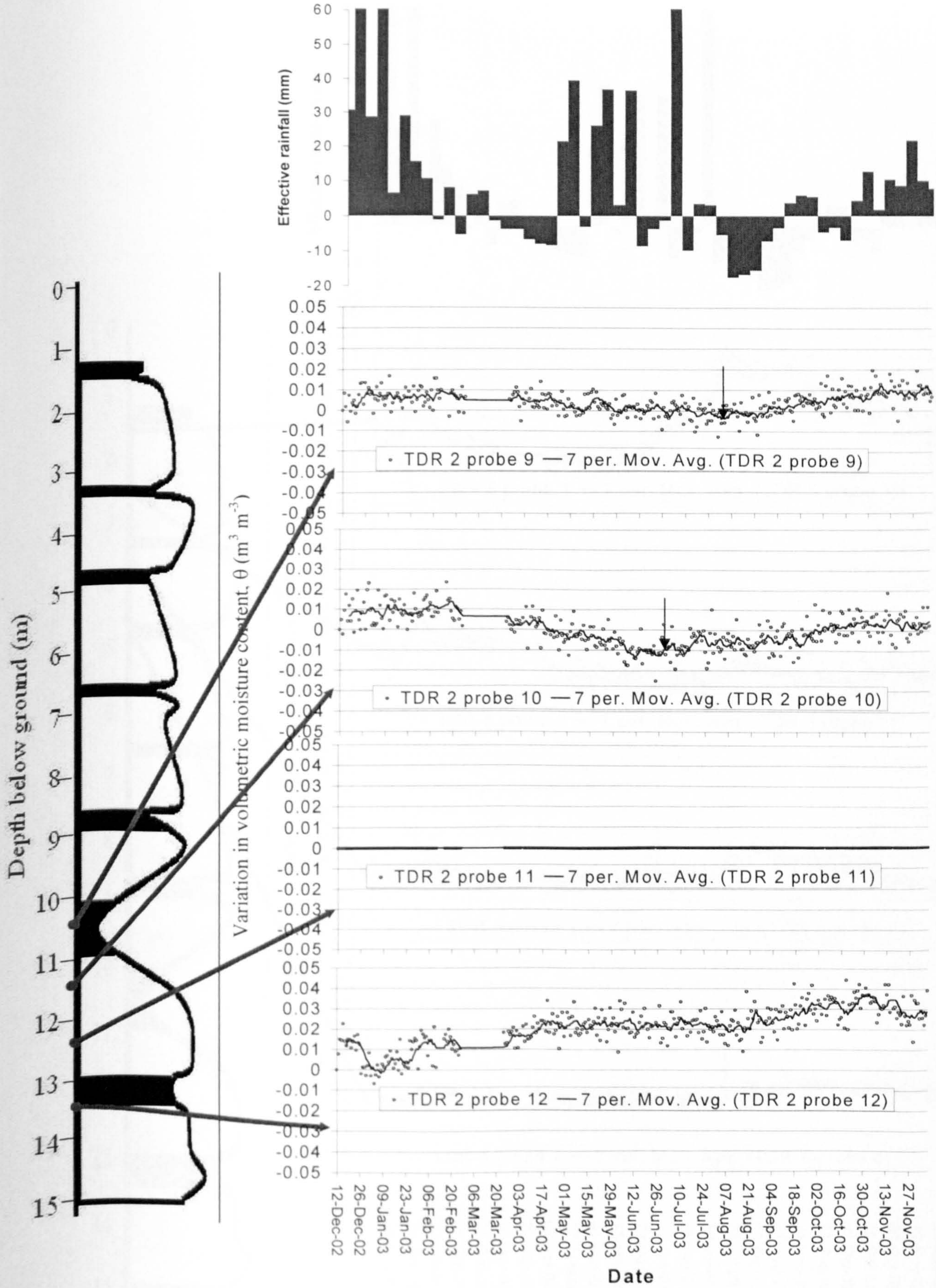

Figure 6.31c Borehole TDR 2 moisture content variation. Rock fully saturated at 13 and 14m so results not shown.

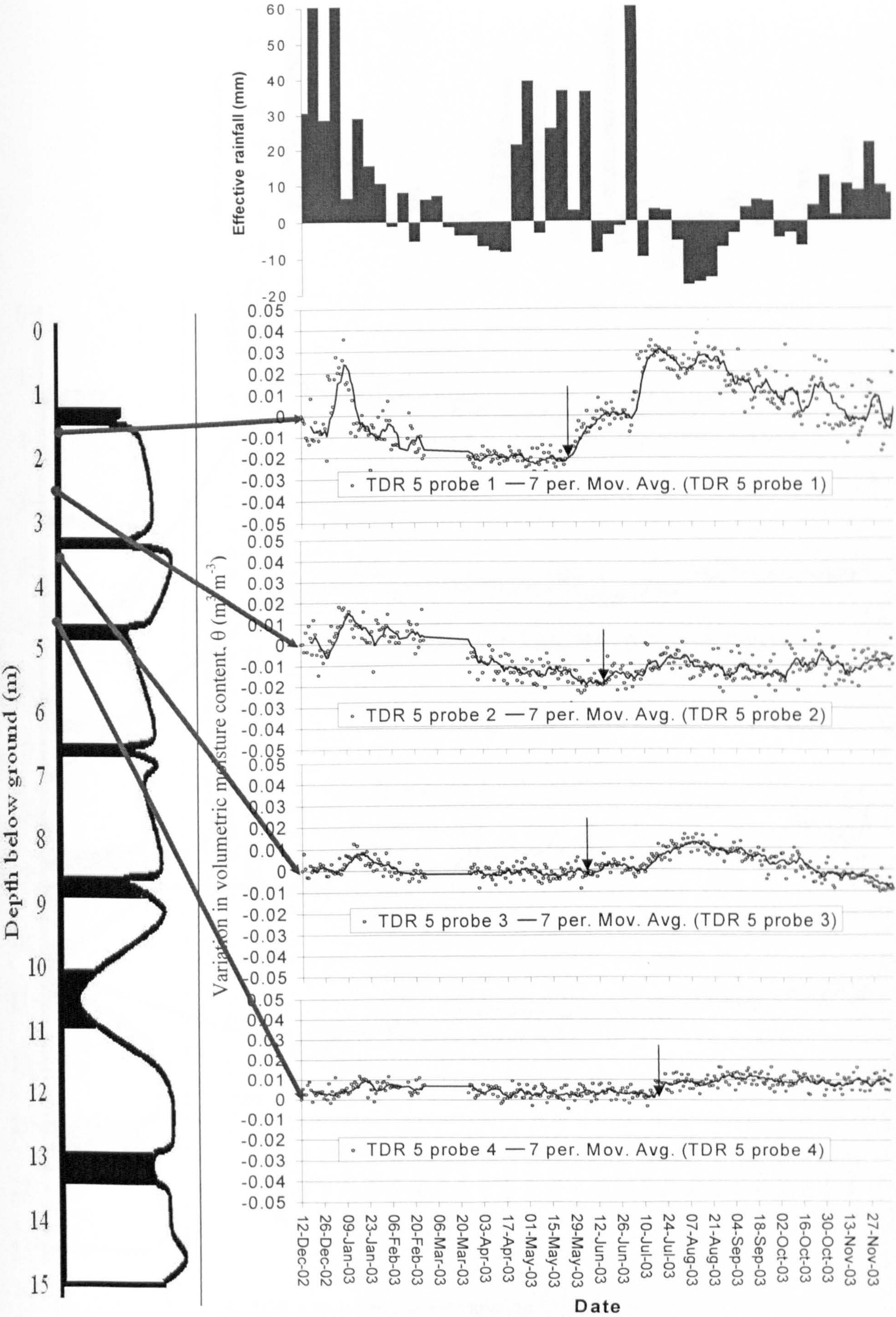

Figure 6.32a Borehole TDR 5 moisture content variation.

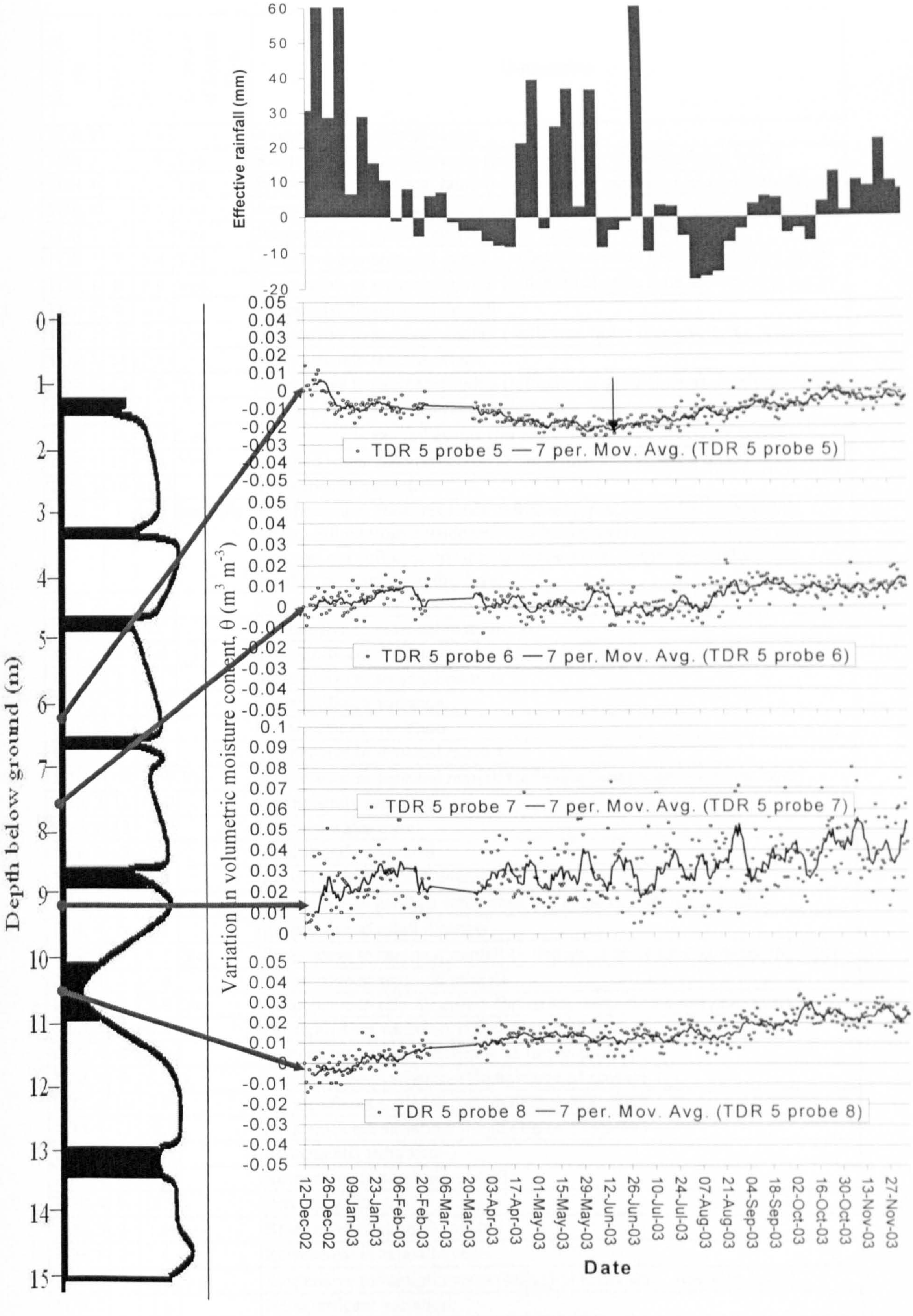

Figure 6.32b Borehole TDR 5 moisture content variation.

Borehole No.	Probe No.	Depth (m)	Evidence of Bypass Flow	Explanation
TDR 1	1	2.4		Responsive to rainfall events
TDR 1	2	2.9	Yes	Responsive to rainfall events (inflexion faster than overlying layer)
TDR 1	3	3.4	Yes	Responsive to seasonal rainfall (inflexion at same time as overlying layer)
TDR 1	5	4.4	Yes	Responsive to seasonal rainfall (inflexion at same time as overlying layer)
TDR 1	6	4.9	Yes	Responsive to rainfall events (faster than overlying layer)
TDR 1	7	5.4	Yes	Responsive to seasonal rainfall (inflexion at same time as overlying layer)
TDR 1	8	5.9	Yes	Responsive to seasonal rainfall (inflexion at same time as overlying layer)
TDR 1	9	6.4		Responsive to seasonal rainfall
TDR 1	10	6.8	Yes	Responsive to seasonal rainfall (inflexion faster than overlying layer)
TDR 1	11	7.4		Responsive to rainfall events
TDR 1	12	7.9	Yes	Responsive to seasonal rainfall (inflexion at same time as overlying layer)
TDR 1	13	8.4	Yes	Responsive to seasonal rainfall (inflexion faster than overlying layer)
TDR 1	14	8.9	Yes	Responsive to rainfall events (inflexion faster than overlying layer)
TDR 1	15	9.4	Yes	Perched water zone (inflexion at same time as overlying layer)
TDR 1	16	10.4		Permanently saturated
TDR 2	1	1.0	Possibly	Perched water zone, responds before major April rainfall so possible lateral inflow from outside test area has occurred, or the moisture deficit in soil was not sufficient to stop the earliest true (rather than effective) rainfall penetrating to this level.
TDR 2	2	2.0		Shielded layer under perched water zone
TDR 2	3	3.0		Responsive to seasonal rainfall
TDR 2	4	4.0		No significant variation.
TDR 2	5	5.1		Responsive to seasonal rainfall
TDR 2	6	6.0		No significant variation.
TDR 2	7	7.0		No significant variation.
TDR 2	9	9.0		Responsive to seasonal rainfall
TDR 2	10	10.0	Yes	Responsive to seasonal rainfall (inflexion faster than overlying layer)
TDR 2	11	11.0		Permanently saturated
TDR 2	12	12.0		Perched water zone
TDR 2	13	13.0		Permanently saturated
TDR 4	1	0.9		Responsive to rainfall events
TDR 4	2	1.8		Controlled by perched water zone but some rainfall input evident.
TDR 4	3	2.8		Responsive to rainfall events
TDR 4	4	3.8	Yes	Responsive to seasonal rainfall (inflexion at same time as overlying layer)
TDR 4	5	4.8		Responsive to seasonal rainfall
TDR 4	6	5.8	Yes	Responsive to rainfall events (inflexion faster than overlying layer)
TDR 4	7	6.8		No significant variation. (High degree of scatter)
TDR 4	8	7.8		Perched water zone (inflexion as fast as probe 6)
TDR 4	9	8.8		No significant variation. (High degree of scatter)
TDR 4	10	9.9		No significant variation. (High degree of scatter)
TDR 4	11	10.8		No significant variation. (High degree of scatter)
TDR 4	12	11.8		Permanently saturated
TDR 4	13	12.9		Responsive to seasonal rainfall
TDR 4	14	13.9		Perched water zone
TDR 5	1	1.6		Responsive to rainfall events
TDR 5	2	2.6		Responsive to rainfall events
TDR 5	3	3.6	Yes	Responsive to rainfall events (inflexion faster than overlying layer)
TDR 5	4	4.6		No significant variation
TDR 5	5	6.2		Responsive to seasonal rainfall
TDR 5	6	7.6		Responsive to seasonal rainfall
TDR 5	7	9.2		No significant variation. (High degree of scatter)
TDR 5	8	10.6		Perched water zone

Table 6.5. Summary of time-series TDR results.

Borehole	Probe No.	Depth (m)	Time of Spring/ Summer rainfall response	Delay to Spring / Summer rain (days)
TDR 1	1	2.4	1/6/2003	41
TDR 1	2	2.9	21/5/2003	30
TDR 1	3	3.4	22/5/2003	31
TDR 1	5	4.4	6/6/2003	46
TDR 1	6	4.9	23/5/2003	32
TDR 1	7	5.4	23/5/2003	32
TDR 1	8	5.9	24/5/2003	33
TDR 1	9	6.4	4/6/2003	44
TDR 1	10	6.8	16/5/2003	25
TDR 1	11	7.4	21/6/2003	61
TDR 1	12	7.9	24/6/2003	64
TDR 1	13	8.4	9/6/2003	49
TDR 1	14	8.9	12/6/2003	52
TDR 1	15	9.4	Perched water table 29/6/2003	69
TDR 1	16	10.4	Permanent perched water table, no response visible	
TDR 2	1	1.0	Perched water table, appears insensitive to evapotranspiration, possibly fed by lateral flow from outside test area.	
TDR 2	2	2.0	Sheltered zone below perched aquifer, no response visible.	
TDR 2	3	3.0	19/5/2003	28
TDR 2	4	4.0	No significant variation	
TDR 2	5	5.1	Flat response, unable to resolve inflexion.	
TDR 2	6	6.0	No significant variation	
TDR 2	7	7.0	No significant variation	
TDR 2	9	9.0	3/8/2003	104
TDR 2	10	10.0	7/7/2003	77
TDR 2	11	11.0	Permanent perched water table, no response visible	
TDR 2	12	12.0	Perched water table, probably fed by lateral flow	
TDR 2	13	13.0	Permanent perched water table, no response visible	
TDR 4	1	0.9	1/5/2003	10
TDR 4	2	1.8	Response dominated by perched water table.	
TDR 4	3	2.8	25/5/2003	34
TDR 4	4	3.8	31/5/2003	40
TDR 4	5	4.8	7/7/2003	77
TDR 4	6	5.8	25/5/2003	34
TDR 4	7	6.8	No significant variation	
TDR 4	8	7.8	Perched water table. Responds by 15/5/2003	24
TDR 4	9	8.8	No significant variation; high scatter	
TDR 4	10	9.9	No significant variation; high scatter	
TDR 4	11	10.8	No significant variation; high scatter	
TDR 4	12	11.8	Permanent perched water table, no response visible	
TDR 4	13	12.9	Flat response, unable to resolve inflexion.	
TDR 4	14	13.9	Response dominated by perched water table.	
TDR 5	1	1.6	22/5/2003	31
TDR 5	2	2.6	13/6/2003	53
TDR 5	3	3.6	7/6/2003	47
TDR 5	4	4.6	15/7/2003	85
TDR 5	5	6.2	18/6/2003	58
TDR 5	6	7.6	7/7/2003	77
TDR 5	7	9.2	No significant variation; high scatter	
TDR 5	8	10.6	14/7/2003	84

Table 6.6. Time delays from TDR moisture content variation data.

Tables 6.5 and 6.6 show that the TDR probes situated in several layers react to rainfall events either simultaneously with, or significantly before some overlying layers. This can

only realistically be explained by moisture migrating via lateral flow which bypasses some overlying layers, allowing moisture to migrate more rapidly than by vertical flow alone.

The pressure pulse resulting from early summer rainfall appears to advance at a rate ranging from approximately 0.05m day^{-1} to nearly 0.3 m day^{-1}, however the rate of movement of the individual water molecules will be considerably less. The velocity was obtained by dividing the probe depth by the time delay, giving an average velocity from the surface. This means that at best case scenario, with the pressure pulse requiring 1000 days to penetrate a 10m thick vadose zone, any entrained pollutants would take even longer, and so the aquifer could be considered safe from most pollutants. The worst case scenario, which is more likely as it takes account of bypass flow, requires a pressure pulse travel time of only 33 days.

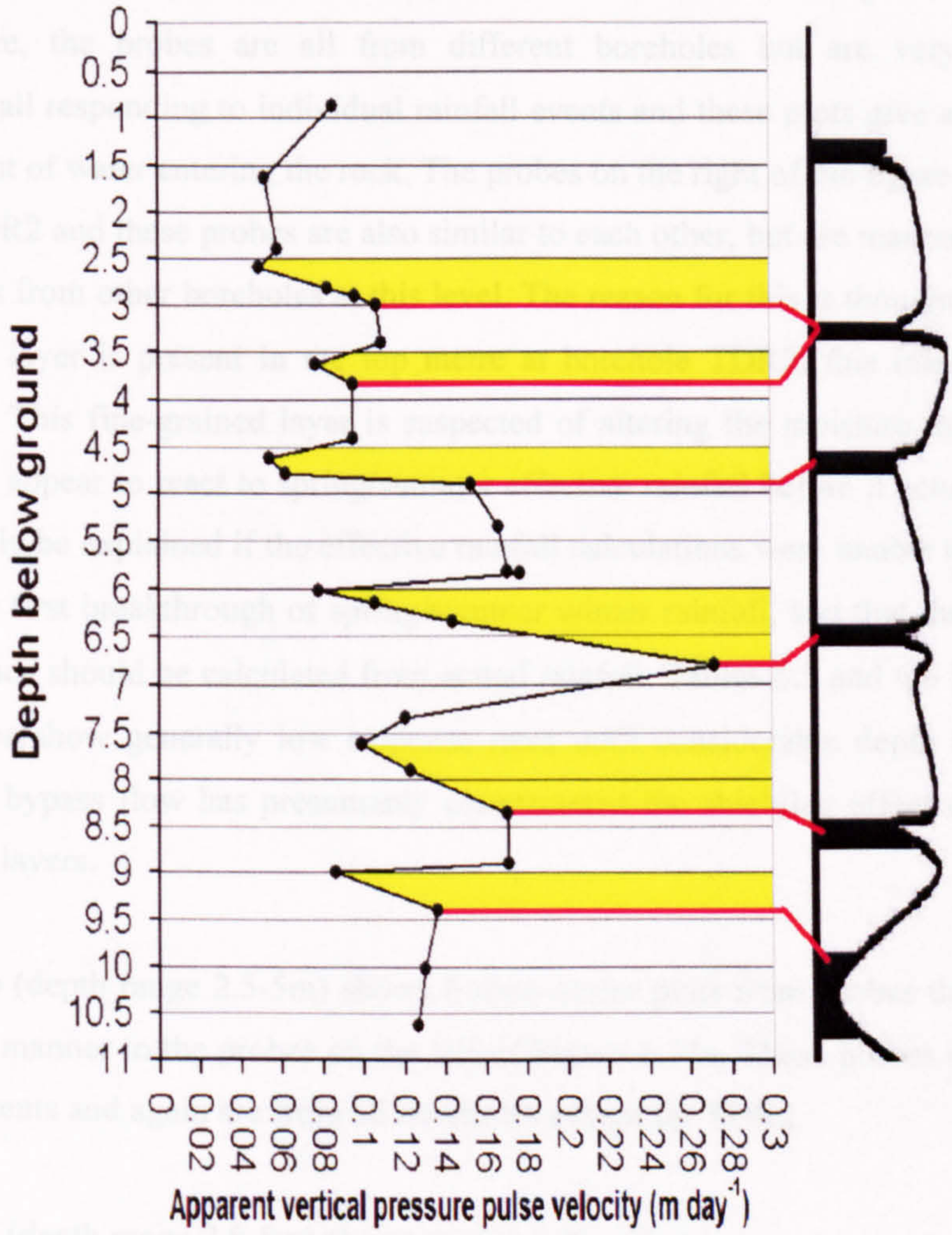

Figure 6.33. Plot of apparent pressure pulse velocity with probe depth for all TDR holes.

Figure 6.33 shows a plot of probe depth against pressure pulse advance for all probes and a pattern of increased pulse advance rates at various depths is shown by the yellow highlighted areas. These yellow zones represent depths within the rock volume where either bypass or lateral flow is most likely to be occurring. Significant lateral/bypass flow layers are seen at 2.5 - 3.0m, 4.5 - 5.0m, 6.0 - 6.75m, 7.5 - 8.5m and at 9.0 - 9.5m. Also shown is the interpreted gamma log from the TRIME hole which shows the presence of fine grained layers close to the bypass zones, each one being within 0.5m which shows good correlation between the various boreholes. Figure 6.33 shows that the lateral/bypass flow network is continuous across the test site, and suggests that time-series moisture content data should correlate between boreholes at similar depths.

Figure 6.34 groups the TDR probes by their emplacement depth.

Figure 6.34a (depth range <2.5m) shows probes that fall into two categories. On the left of the figure, the probes are all from different boreholes but are very similar in appearance, all responding to individual rainfall events and these plots give an indication of the amount of water entering the rock. The probes on the right of the figure are all from borehole TDR2 and these probes are also similar to each other, but are markedly different to the probes from other boreholes at this level. The reason for this is thought to be that a fine-grained layer is present in the top metre at borehole TDR2; this may be seen in Figure 4.25. This fine-grained layer is suspected of altering the moisture inflow, as the TDR probes appear to react to spring/summer effective rainfall before it actually occurs! This may only be explained if the effective rainfall calculations were unable to accurately calculate the first breakthrough of spring/summer winter rainfall, and that the time delay in this instance should be calculated from actual rainfall. Tables 6.5 and 6.6 indicate that TDR2 probes show generally low response rates until considerable depth (>7.5m), by which point bypass flow has presumably counteracted the shielding effect of the upper fine-grained layers.

Figure 6.34b (depth range 2.5-5m) shows 6 time–series plots from probes that react in a very similar manner to the probes on the left of Figure 6.34a. These probes react rapidly to rainfall events and again are from all boreholes except for TDR2.

Figure 6.34c (depth range 2.5-5m) shows probes with either low response or only a muted seasonal response. These probes must all be shielded by an overlying lithology, which is reducing the quantities of water intersecting the probes.

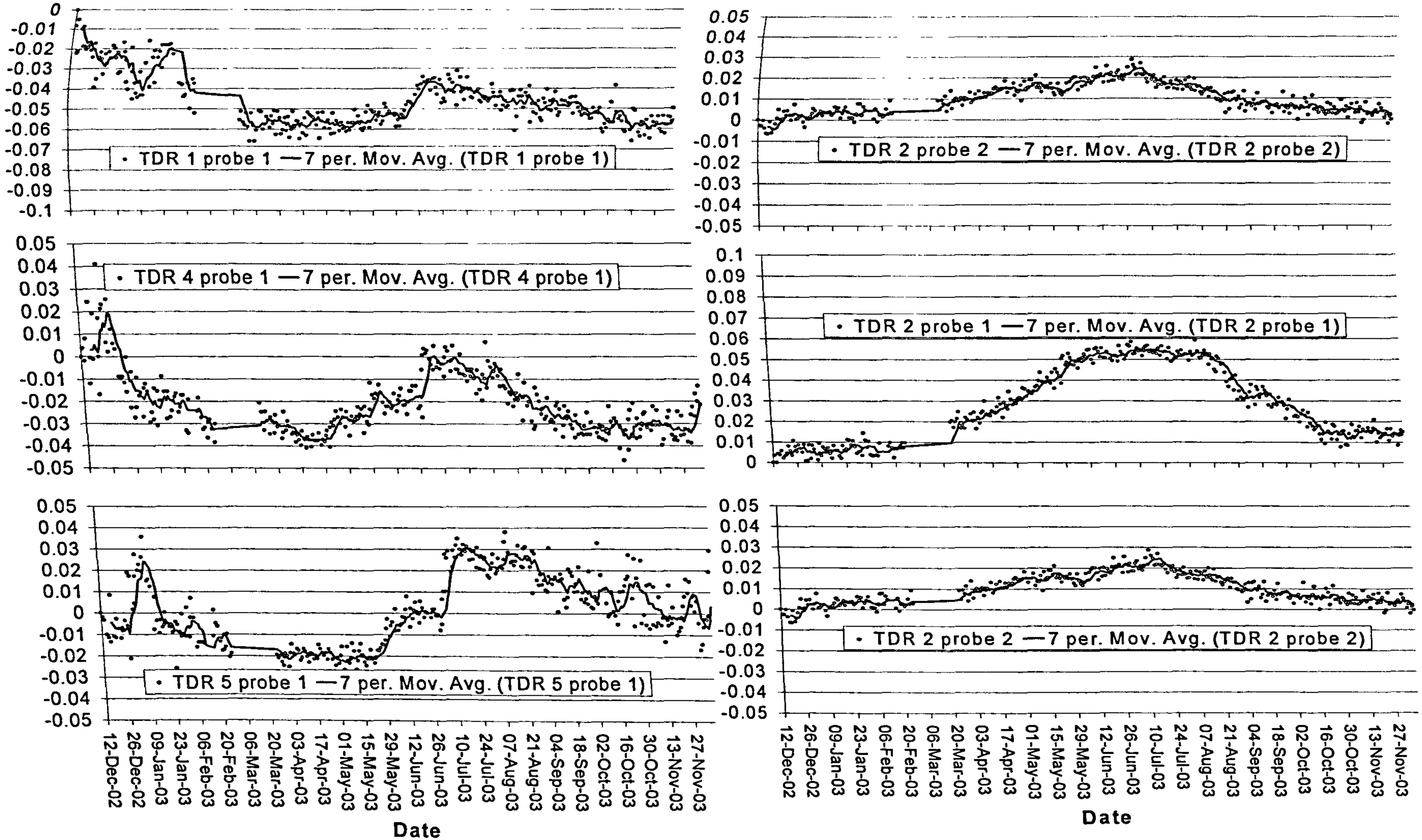

Figure 6.34a Shallow TDR probe time series moisture contents < 2.5m depth.

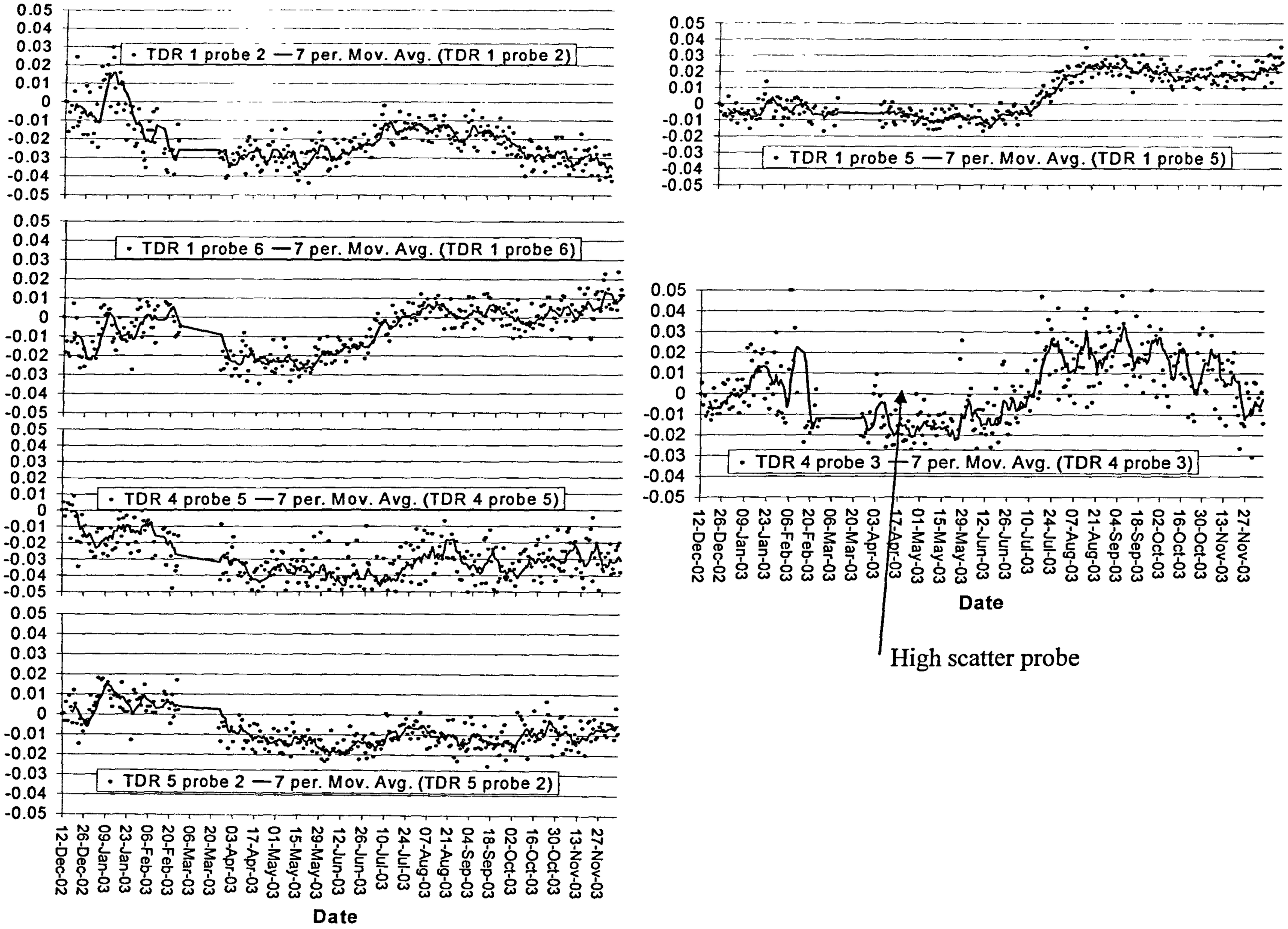

Figure 6.34b TDR probe time series moisture contents for probes that react to individual rainfall events 2.5-5m depth.

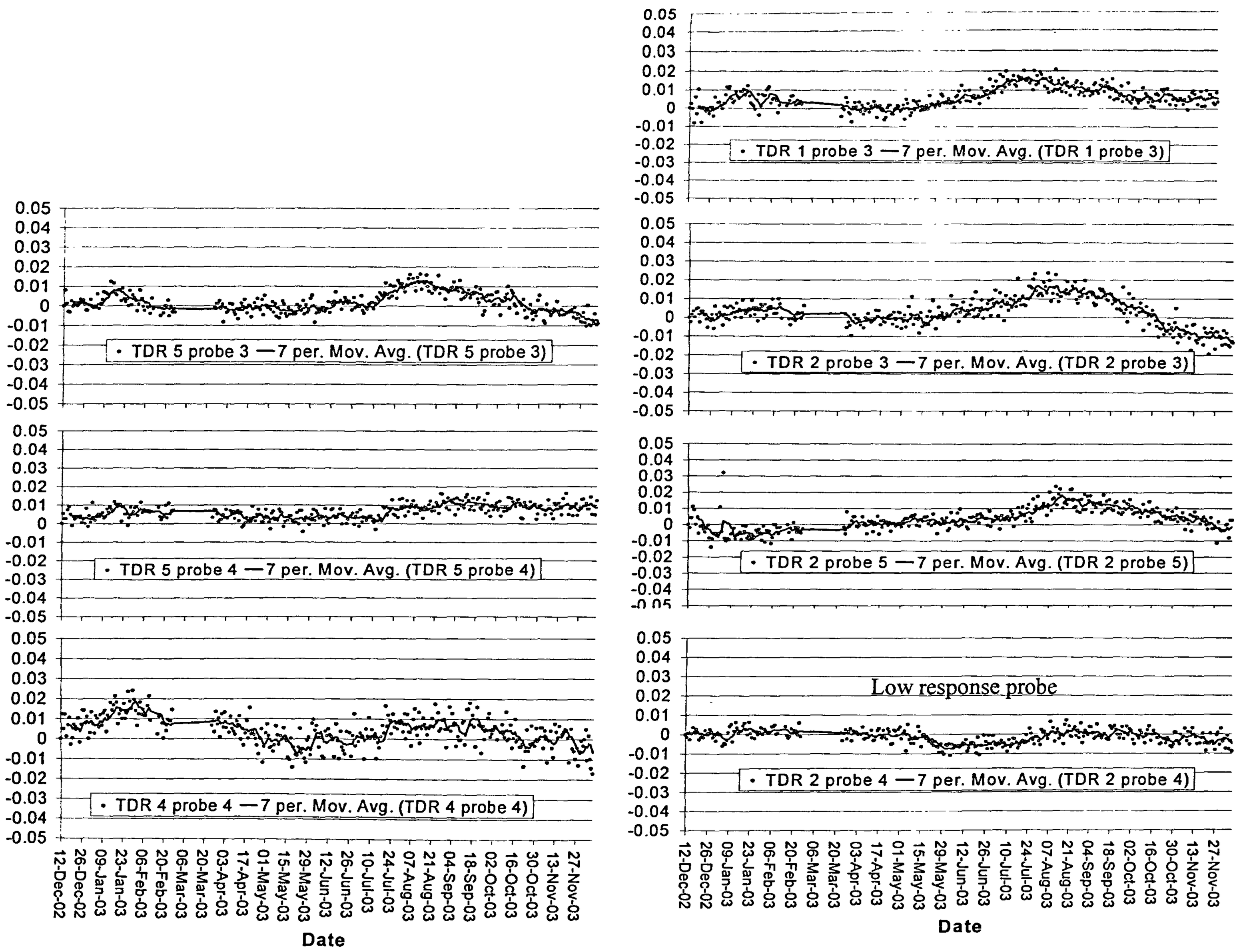

Figure 6.34c TDR probe time series moisture contents for probes that react to seasonal rainfall, 2.5-5m depth.

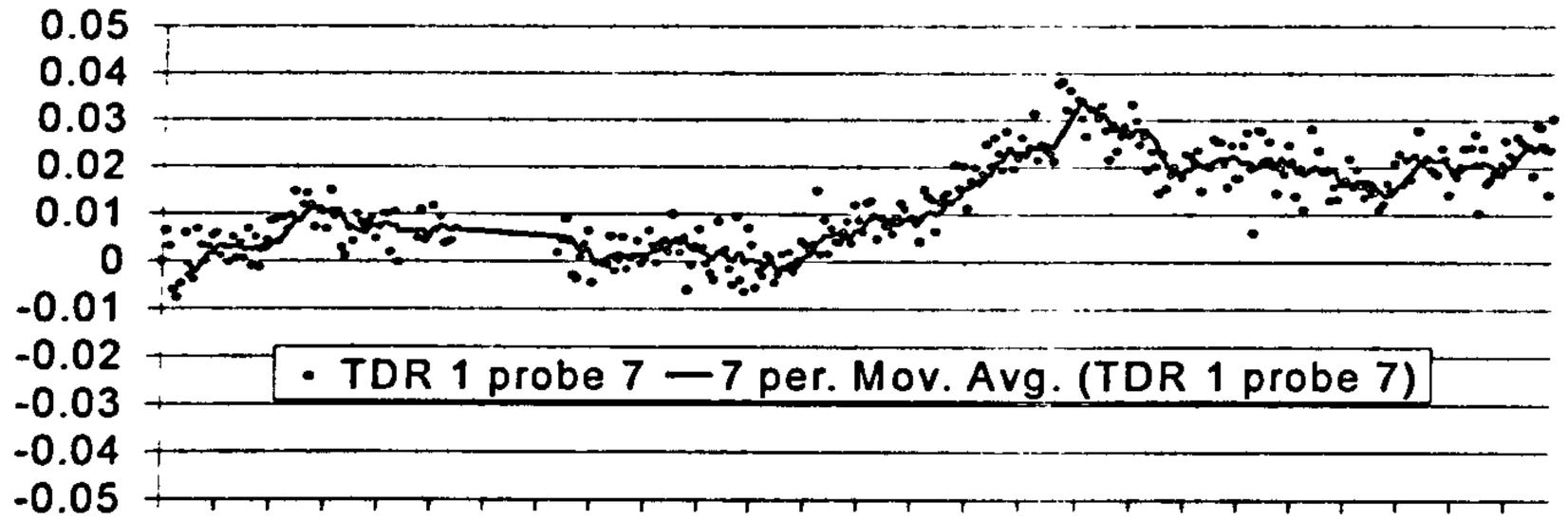

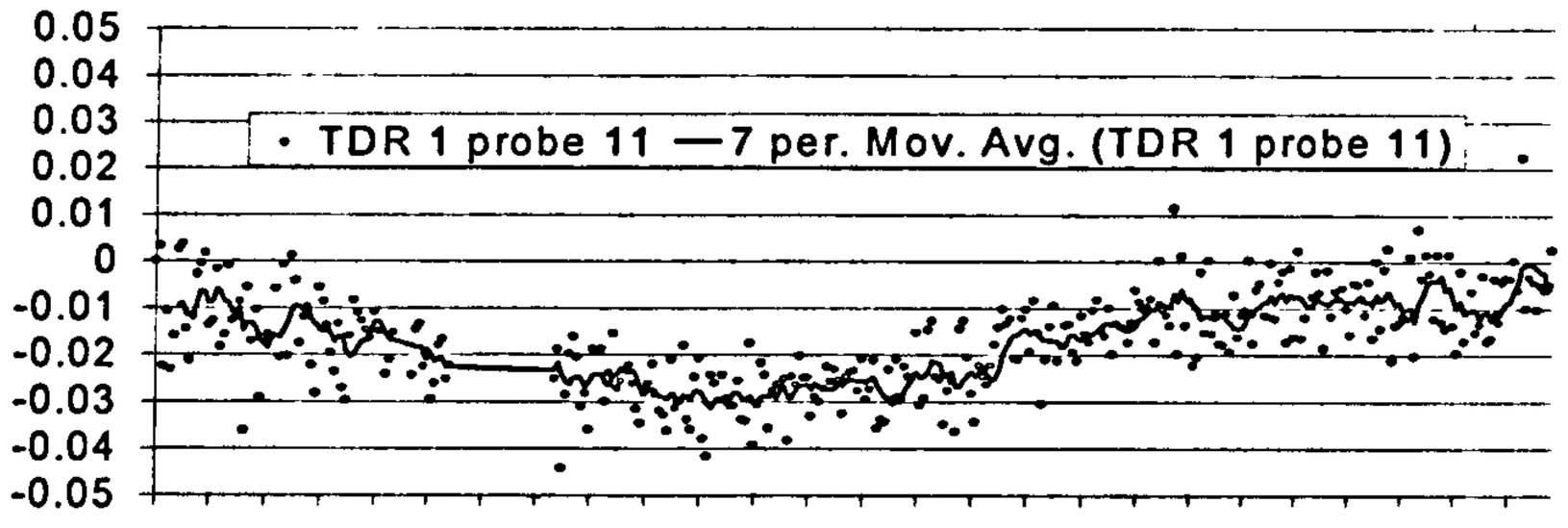

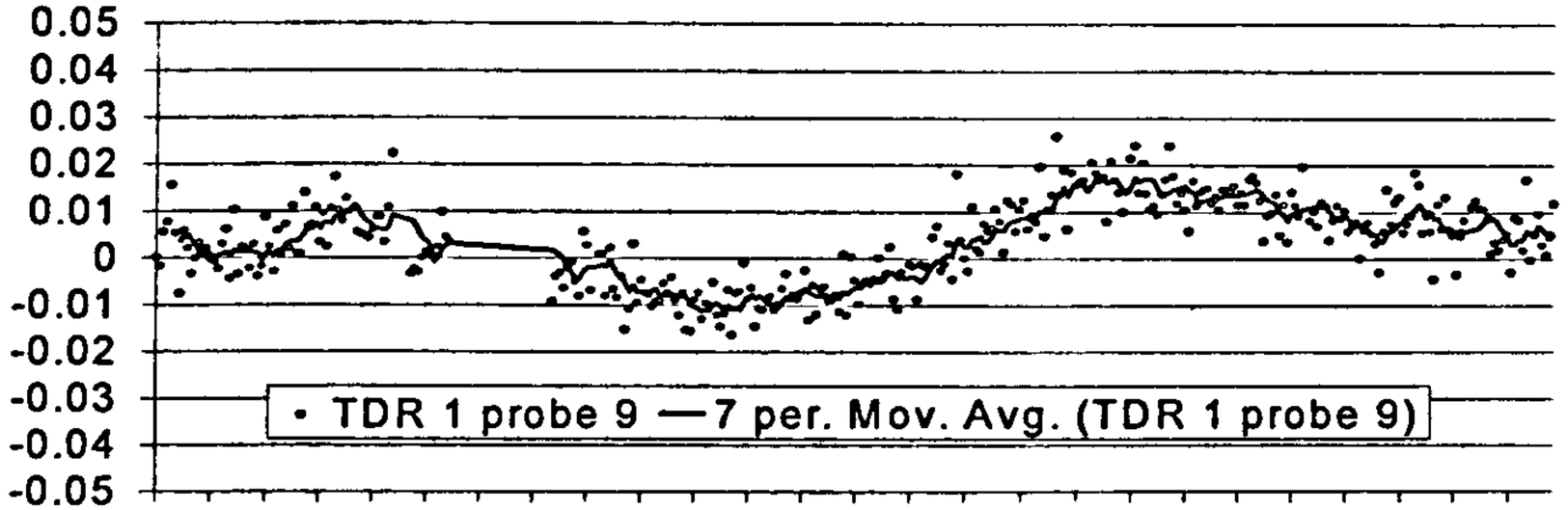

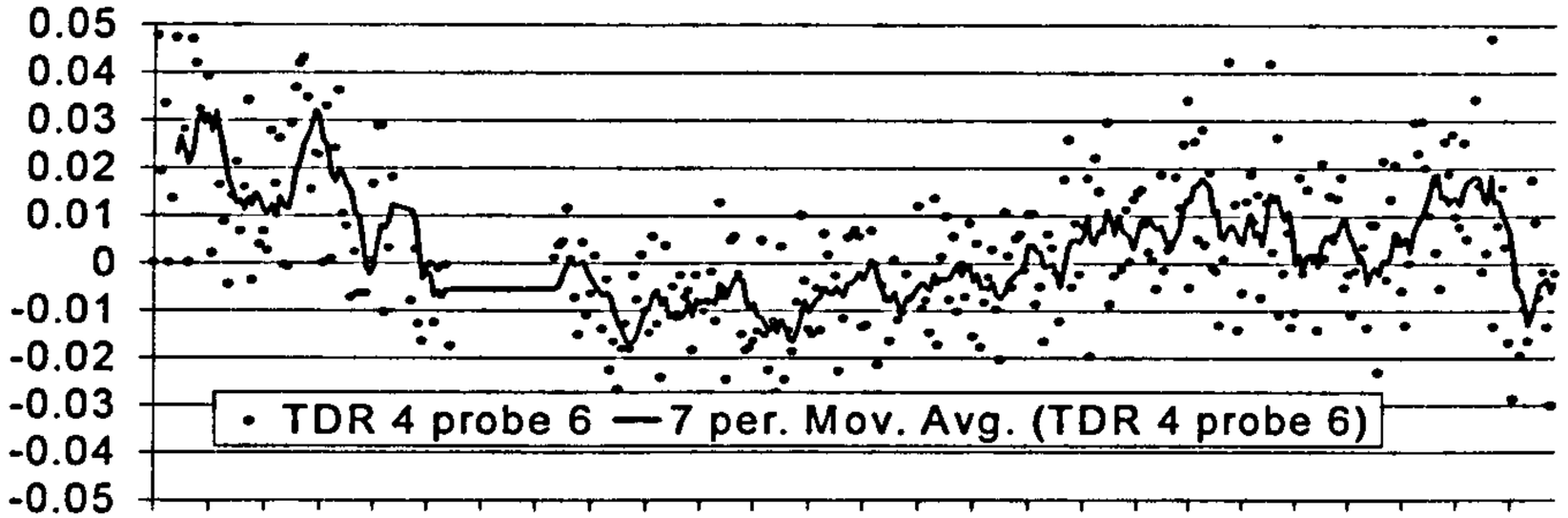

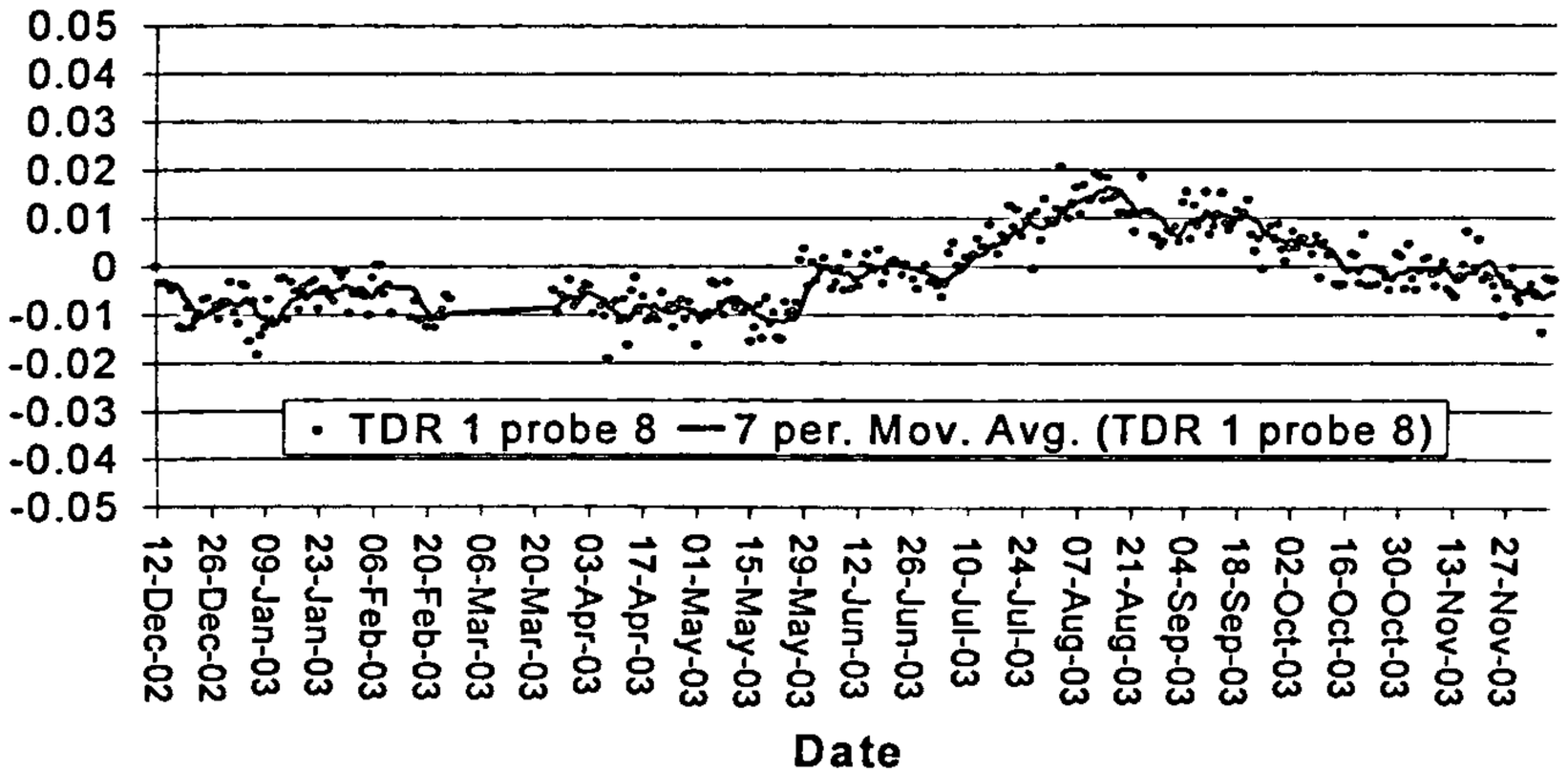

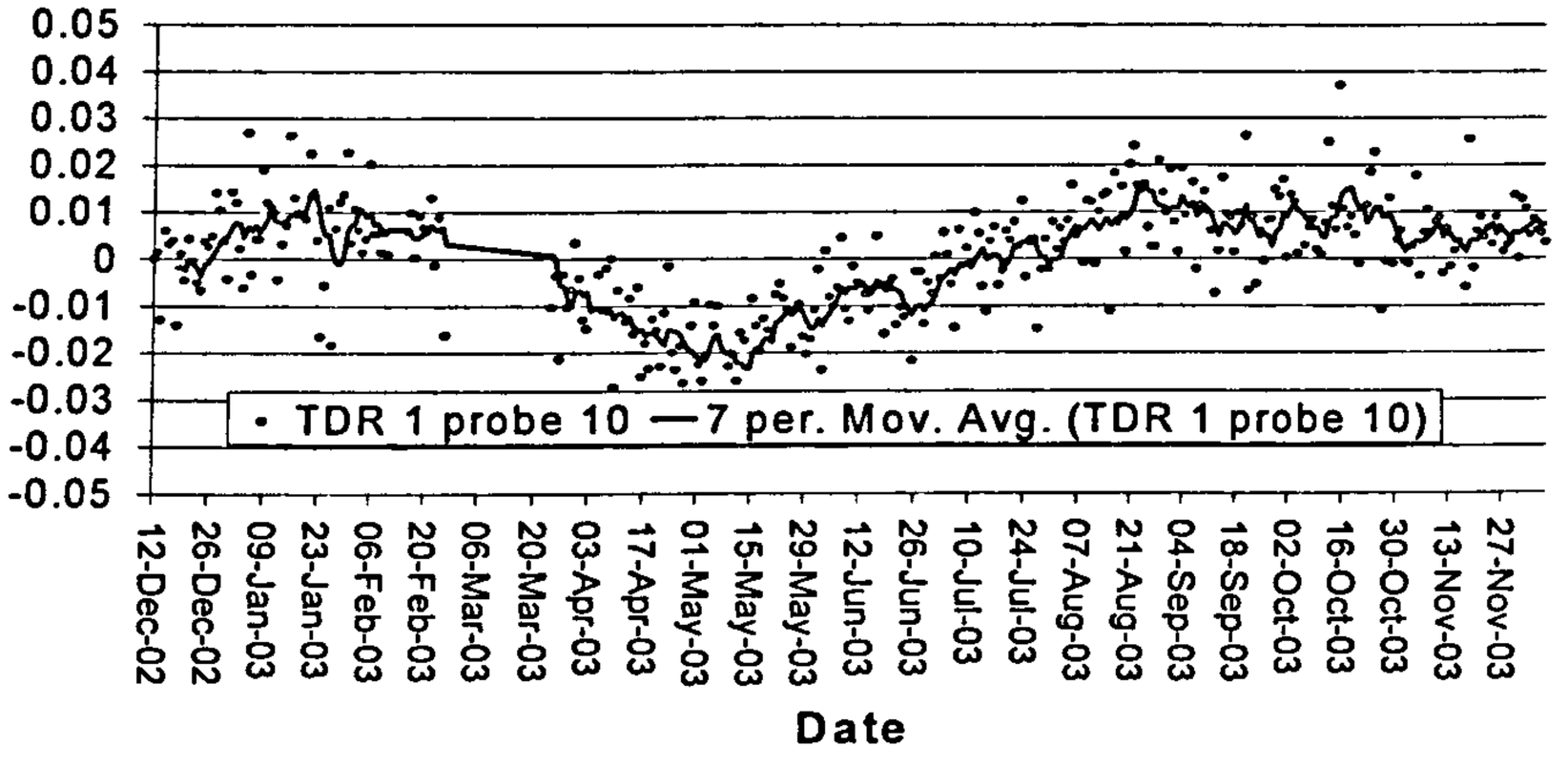

Figure 6.34d TDR probe time series moisture contents for probes that react significantly to rainfall, 5-7.5m depth.

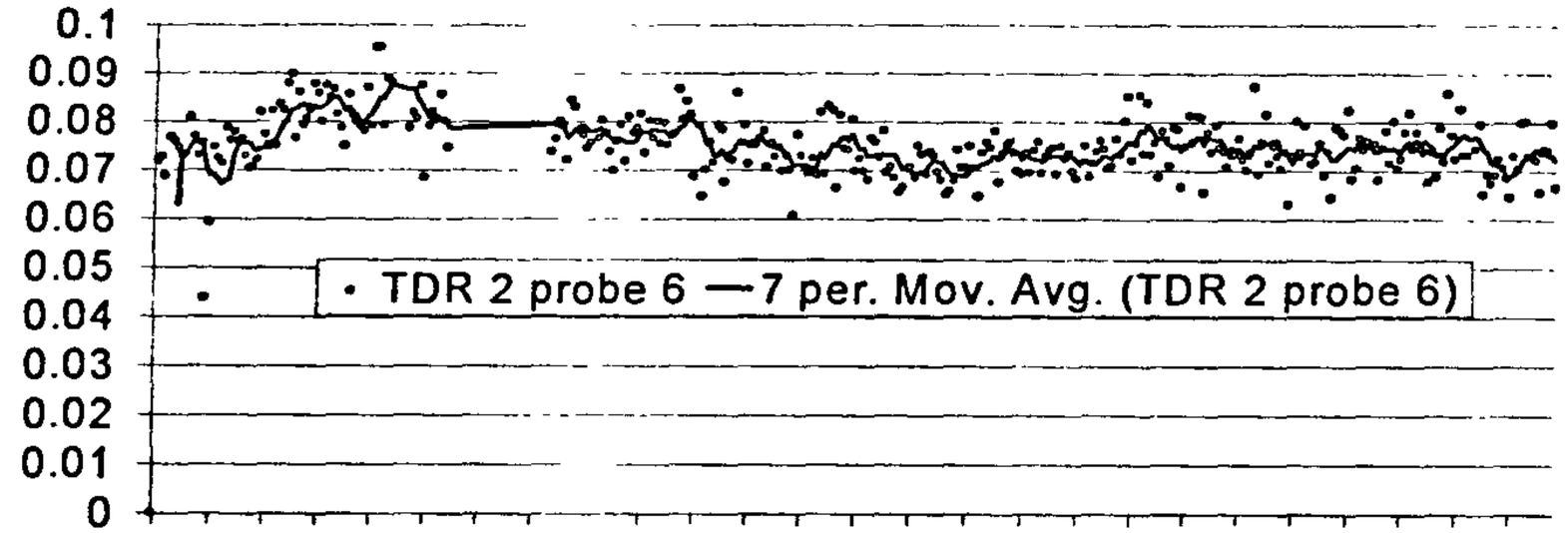

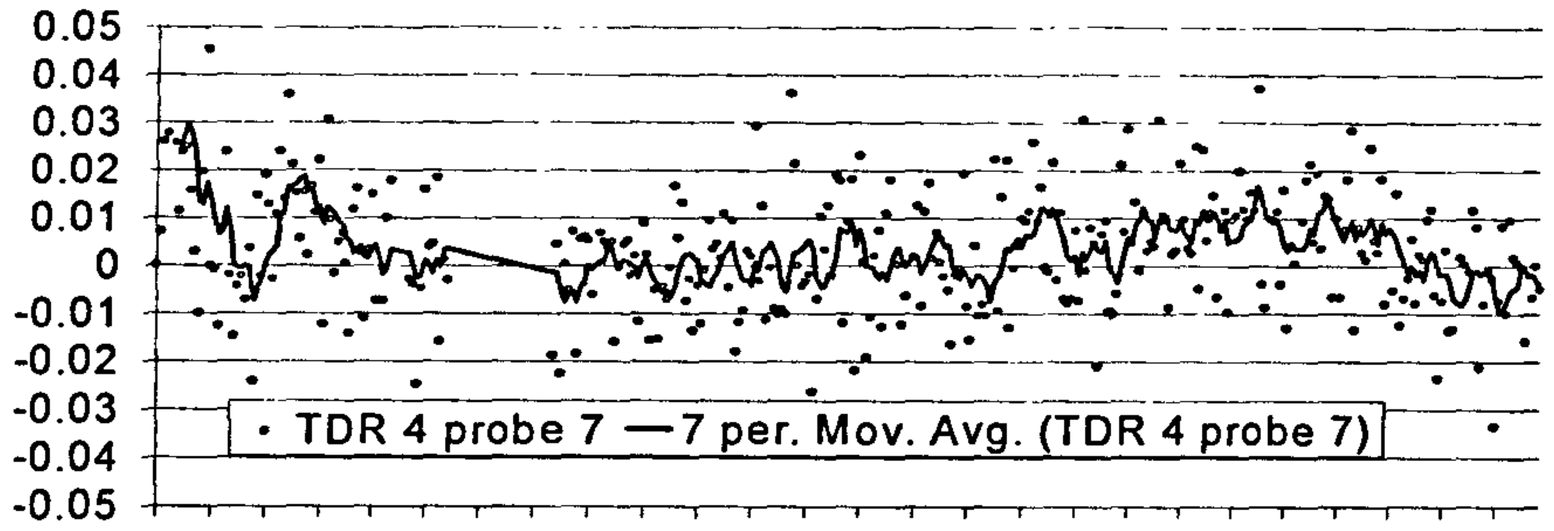

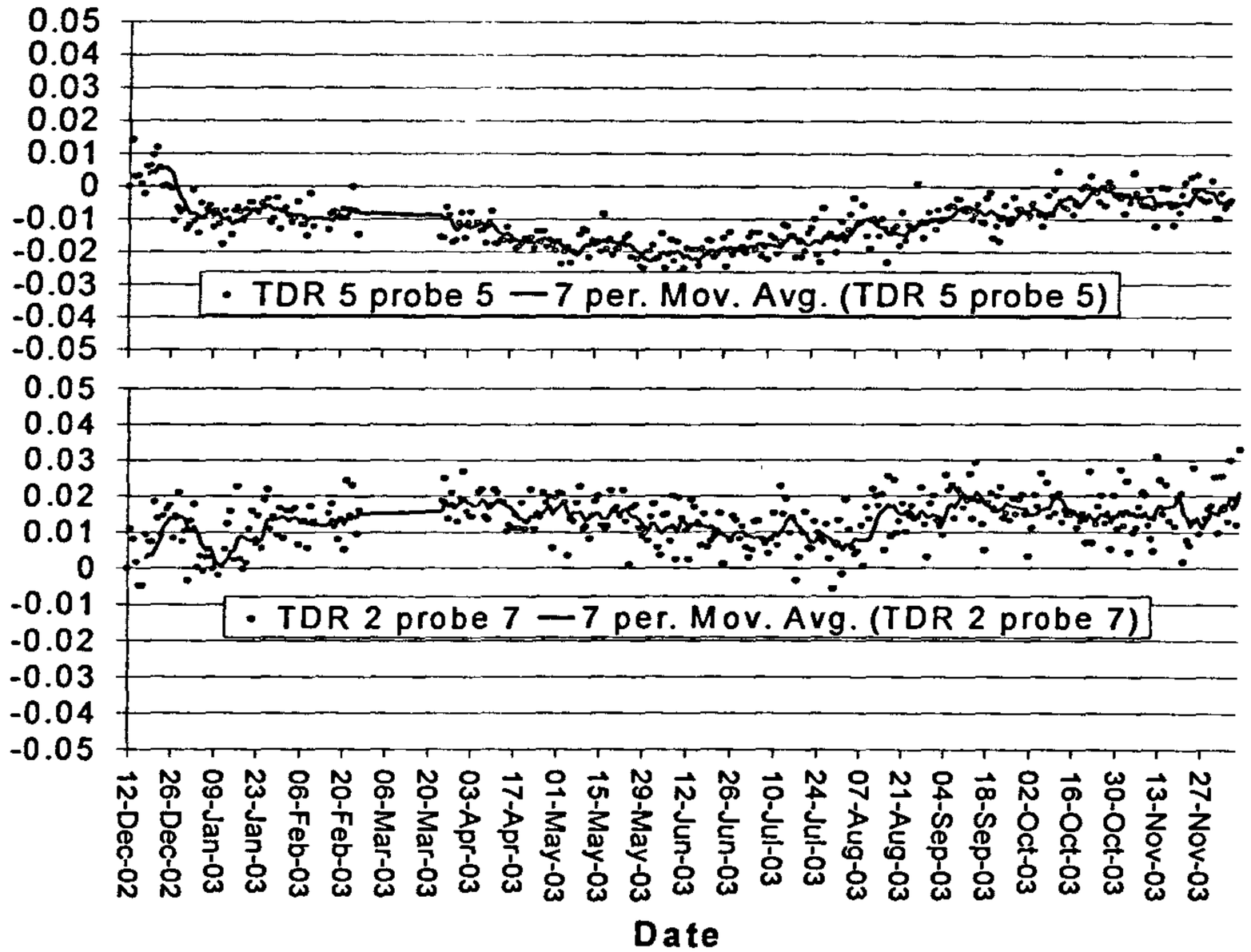

Figure 6.34e TDR probe time series moisture contents for low response or high scatter probes 5-7.5m depth.

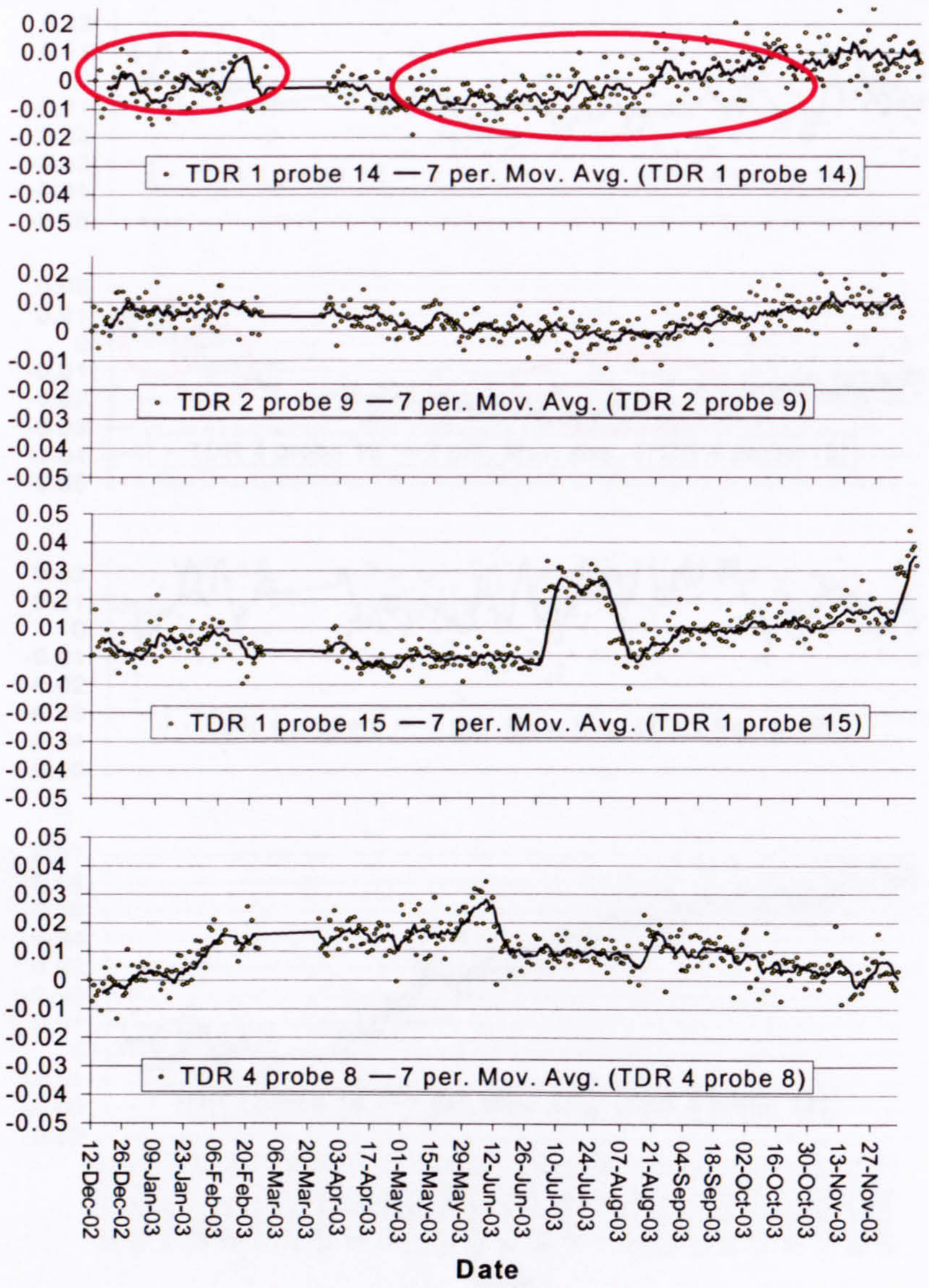

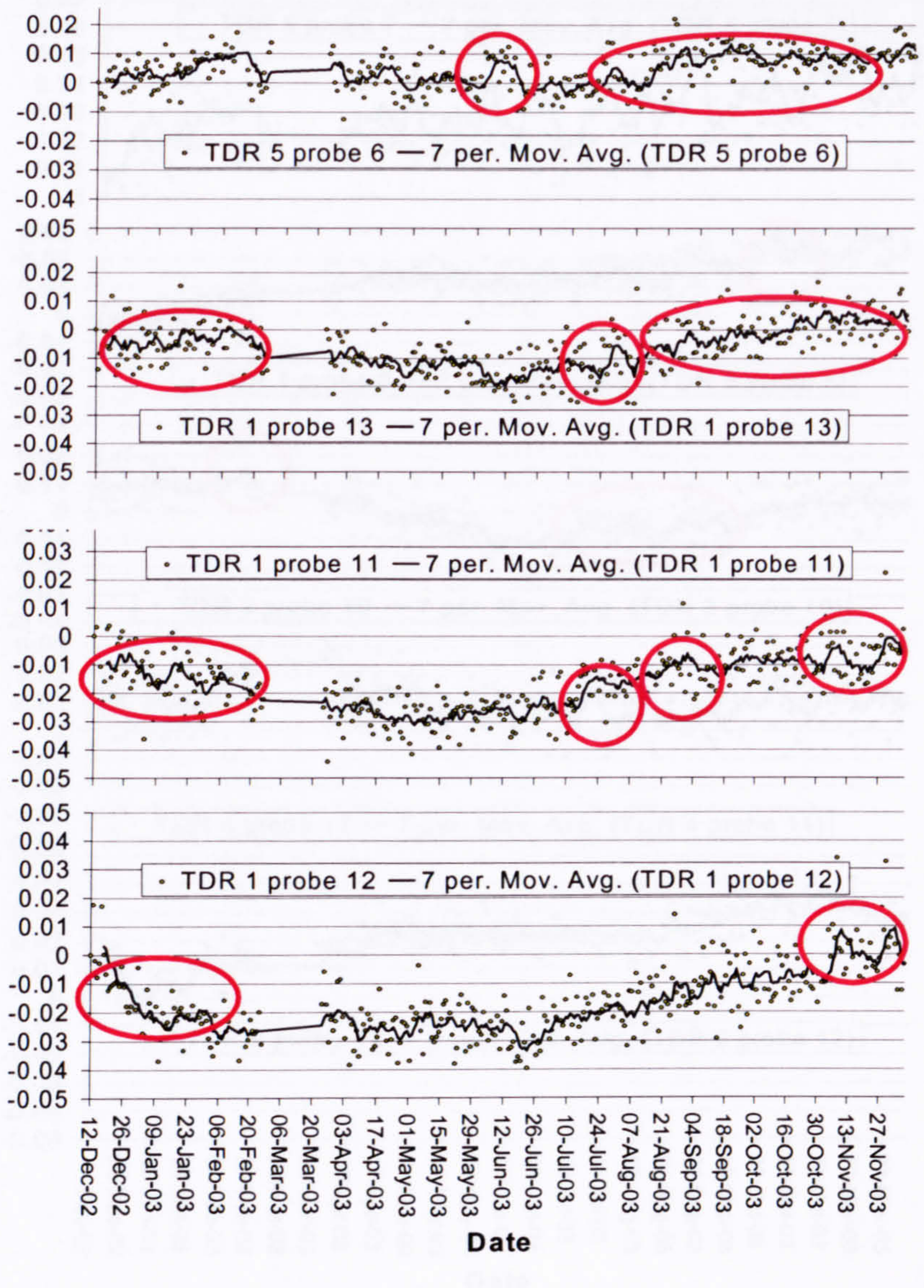

Figure 6.34f TDR probe time series moisture contents for probes over 7.5m depth (part 1),

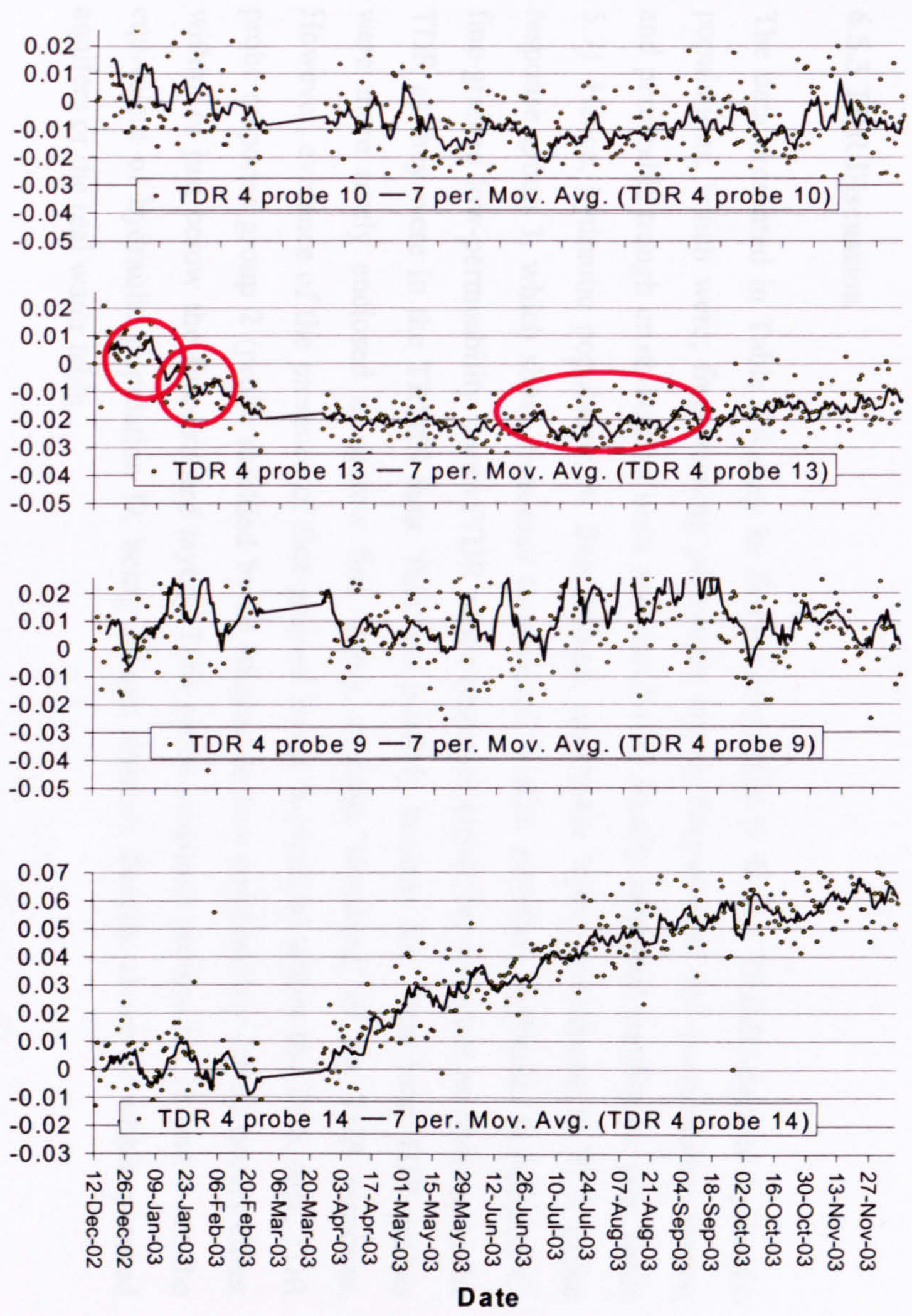

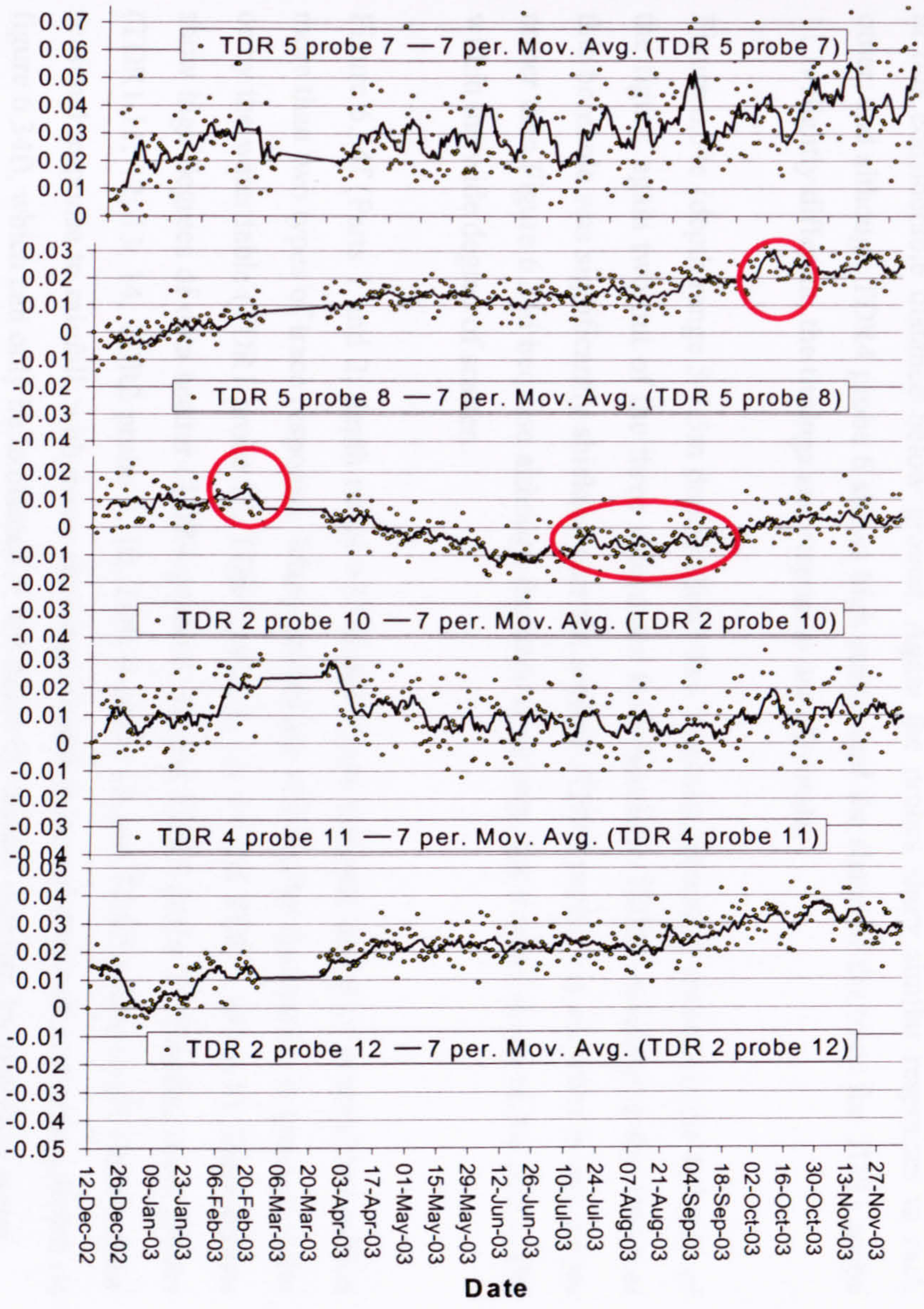

Figure 6.34f TDR probe time series moisture contents for probes over 7.5m depth (part 2),

Figure 6.34d (depth range 5-7.5m depth) shows probes which react significantly to rainfall, even at this considerable distance below ground. Again the probes show similar responses to each other, and although TDR4 probe 6 shows high scatter and the shape of the trace for TDR1 probe 11 is slightly different, the timings and responses are all similar.

Figure 6.34e (depth range 5-7.5m depth) shows low response, shielded probes on the left side of the figure, again two out of the three shown are from borehole TDR2, reinforcing the idea that this borehole was significantly shielded near the surface. TDR4 probe 7 is included in this figure rather than Figure 6.34d because although the trace does vary, the overall shape of the plot is flat within the wide degree of scatter.

Figure 6.34f (Parts 1 and 2; depth range >7.5m depth) are the only group of probes that exhibit more than two types of trace response. Many probes are affected by fluctuation in perched water or by the water table (TDR1 probe 15, TDR4 probe 8; 11; 14 and TDR 5 probe 8). Some probes show high degrees of data scatter (TDR4 probe 9; 10 and TDR5 probe 7). Finally, some probes (TDR1 11; 12; 13; 14, TDR2 probe 9; 10, TDR 4 probe 13 and TDR5 probe 6) all clearly show seasonal response to rainfall, with many showing distinct pulses of moisture recharge (circled on figure 6.34f), which can only be explained at this depth by rapidly moving, bypass-flow water.

6.5.3 TDR Discussion

The data presented in Table 6.4 may be further simplified to fit the TRIME-derived hydraulic populations, which were; free-draining permeable layers; fine-grained low-permeability layers; and permeable trough cross-bedded units associated with locally saturated conditions. (see Table 5.7). Hence, hydraulic population A, free-drained, permeable layers correspond to TDR probe response group 3, which show responses to seasonal rainfall patterns. Hydraulic population C, fine-grained low-permeability layers (TDR probe response group 1c) were not as obvious in the TDR as they were in the TRIME data. This was possibly because the 30cm long TDR probes were more rarely enclosed in narrow fine layers, causing 'smearing' of the TDR response. However, evidence of the presence of fine-grained layers is plentiful within the TDR data, TDR probe response group 2 (probe shielded by or situated in low permeability layer) occurs either within, or just below the fine-grained layers. TDR probe response groups 1a, 1b and 4 are the equivalent of hydraulic population D, being always situated directly above or within perched aquifers or the real water table.

Shallow group 4 TDR probes record fluctuations in moisture content caused by downwards percolating water. However, TRIME, neutron probe (see Chapter 5), and modelling data (presented below-this chapter) show that attenuation and smearing of the responses to individual rainfall events occur below even thin fine-grained layers. Hence, deeper group 4 probes must be in layers where travel time from the surface is sufficiently fast to allow rainfall events to be reflected in the recorded data. Comparing the delay between rainfall event and TDR response (See Table 6.5) shows that group 4 often respond to rain inputs very quickly, even at depth, and frequently possess shorter time-delays than group 3 probes at shallower depths. This result means that bypass flow must be occurring, and that deep group 4 probes are situated within coarse-grained layers, fed by bypass flow mechanisms.

Overall, the TDR data shows that different responses to rainfall events at different depths are seen within the boreholes, which indicates that lateral heterogeneities are important with regard to vadose zone water movement and that bypass flow is important. Figure 6.31 shows that response times of various layers vary widely as a result of bypass flow, with pressure pulse transit times for a 10m thick vadose zone varying from 3 years to 1 month. However, this is almost certainly displaced water rather than the actual rainfall that has penetrated at this rate.

6.6. Modelling hydraulic behaviour

Mass balance modelling. The aim of modelling flow in the unsaturated zone of the Sherwood Sandstone was to identify patterns of moisture content variation arising from various moisture flow mechanisms. Data provided by modelling could then be compared with TRIME, neutron probe and TDR results, and used to assist in the interpretation of flow mechanisms using field data. Free water is likely to migrate through the vadose zone by one of three mechanisms, vertical flow, sub-horizontal (bypass) flow or a mixture of vertical and bypass flow. The TDR data showed that bypass flow occurs, (some layers responded to rainfall faster than those higher up the profile) so the model described here allowed different levels of vertical bypass flow across two low-permeability units. Vertical flow was modelled for an isolated rock column, with effective rainfall entering at the ground surface, and the equivalent recharge volume eventually exiting the base of the column. To simulate bypass flow, a user-defined percentage of the water ponding upon low-permeability layers was allowed to bypass these layers, although all water so removed was re-introduced to the column at greater depth.

Flow model. The model simulates the behaviour of a 10.8m tall column with a $1m^2$ plan area. The column was comprised mainly of homogenous sandstone (sedimentary facies 1). The free-drained saturation of this unit is assumed to be 0.15 $m^3.m^{-3}$ based on neutron probe and TRIME data. Also modelled are two finer-grained sandstone layers (sedimentary facies 2), both assumed to be 0.5m thick (based on the Great Heck core log –see Chapter 3), at 3.5 to 4 and 7.5 to 8m depth respectively. The fine-grained units were assumed to be saturated at all times. Porosity of all units was assumed to be 0.35 $m^3\ m^{-3}$. The vertical hydraulic conductivity of the fine sandstone layers could be varied by the user during calibration.

Model assumptions and functions. This model depends upon some basic assumptions. The moisture retained in all of the units at zero time represented residual water content and was assumed static. This replicated the capillary retention of moisture within the vadose zone, where the downward force exerted by gravity is balanced by an upward forces arising from variations in capillary suction (ψ). The residual water content in the coarse-grained sandstone (0.15 $m^3.m^{-3}$) was assumed to be immobile under all conditions. However, the residual water within the fine-grained layers (i.e. occupying 100% of the void space) is assumed to move under the hydraulic surcharge occurring from perched water tables that form on top of such layers.

Within the coarse layers, water in excess of the residual water content was assumed to be transmitted downwards at a permeability specified by the user. Upon reaching a fine-grained layer, downward migrating water was assumed to collect to form a perched water table. The depth of the perched water table (m) was calculated from the volume of water present (m^3) the plan area of the column ($1m^2$) and the volume of available voids. The depth of the resulting perched water table was corrected for the presence of residual water (i.e. porosity minus the coarse-grained residual saturation). The resulting volume of water in the cell representing the perched water table was found by mass balance, i.e., the quantity of water in the cell during the previous timestep, plus any additional water reaching the perched water table from above, minus losses due to infiltration and bypass flow through the underlying fine-grained layer. A percentage of the volume of ponded water at a perched aquifer level was allowed to migrate instantaneously downwards to specified deeper levels to simulate lateral flow utilising a bypass flowpath around the impermeable layer and this percentage could be varied by the user. The amount of infiltration through the fine-grained unit was found using Darcy's Law. Because the fine-grained layers were assumed saturated, water entering the unit top displaced the equivalent volume of water from the base of the unit. This process was assumed to be instantaneous, irrespective of the fine-grained layers' thickness.

The perched water tables were assumed to produce a hydraulic gradient, driving infiltration through the fine-grained layers. This gradient was a function of the depth of the perched water table and the thickness of the fine-grained layer. It was assumed that at low perched water table depths, the hydraulic gradient (i_{low}) may be calculated by; $i_{low} = \Delta h/\Delta y$, where Δh was the depth of ponded water and Δy the fine-grained unit thickness. At higher ponded head values, the expression for i was assumed to become $i_{high} = (\Delta h+\Delta y)/\Delta y$; which assumes that the difference in elevation across the fine-grained layer was fully effective in driving flow. A transition zone between these two relationships was assumed between depths of 5cm and 50cm as shown in Figure 6.35. (one tenth and equal to the value of fine-grained thickness Δy used respectively).

An expression for vertical hydraulic gradient in the fine sandstone layers was derived by plotting both of the equations described above against perched aquifer depth, assuming a fine-grained layer thickness of 0.5m. It was then possible to define a further function ($i_{combined}$), describing the hydraulic gradient for all ponded depths (see Figure 6.35). The expression (Equation 6.10) has an R^2 confidence value greater than 0.99, and was used to convert ponded depth Δh to vertical hydraulic gradient ($i_{combined}$) within 0.5m thick fine-grained layers:

$$i_{combined} = 2.937\Delta h^6 - 18.1\Delta h^5 + 41.858\Delta h^4 - 43.867\Delta h^3 + 18.65\Delta h^2 + 1.4789\Delta h$$

Equation 6.10.

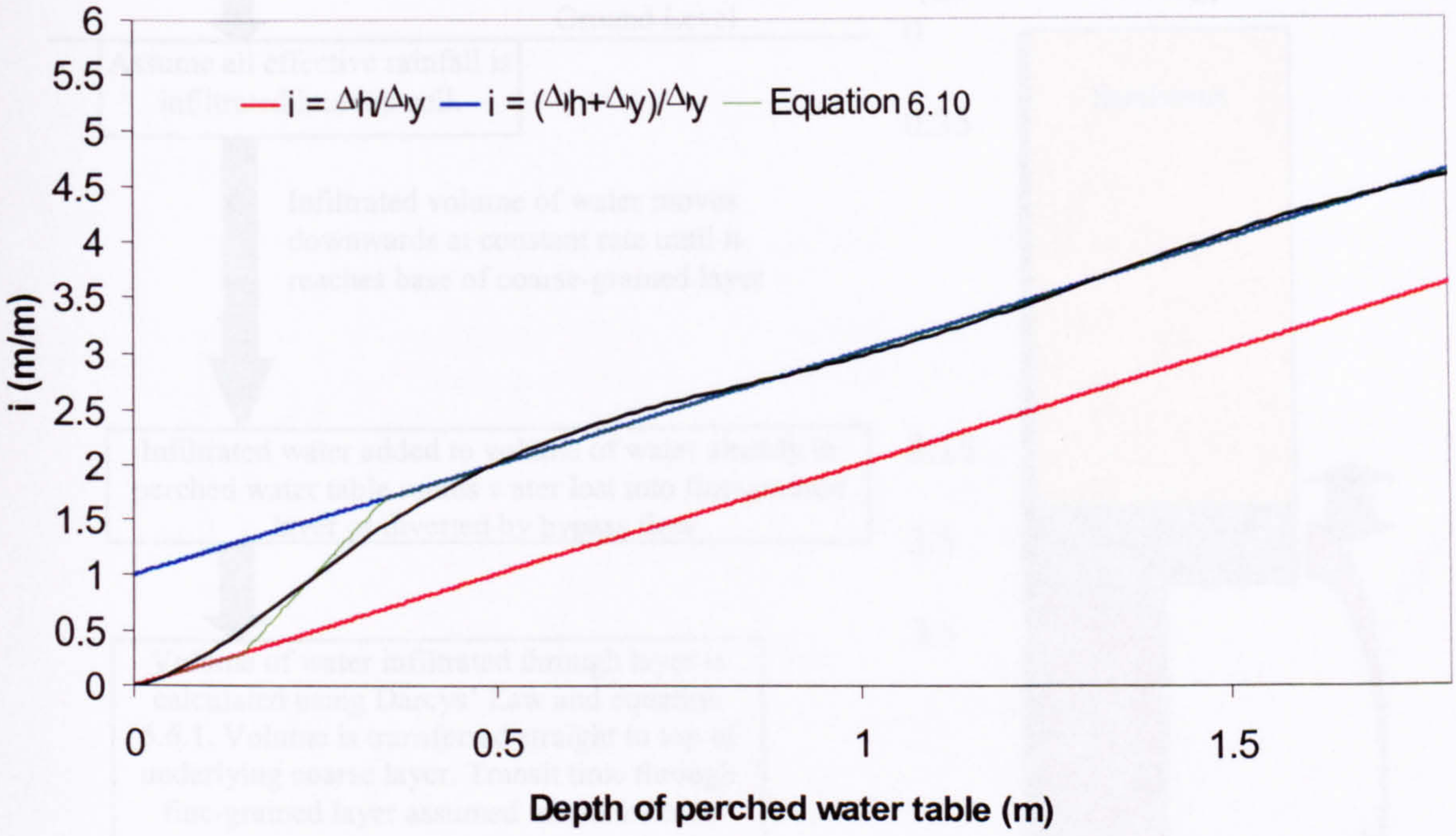

Figure 6.35. Plot of perched water table depth with hydraulic gradient in the fine layers. Black line is a regression on line $I_{combined}$.

Darcy's Law, q = k.A.i, was used to calculate the flow through the fine-grained layers, where, q was the flow in $m^3.day^{-1}$, k was the hydraulic conductivity ($m.day^{-1}$), A was the plan area of the column ($1m^2$), and i was the $i_{combined}$ value from Equation 6.10 ($m\ m^{-1}$), derived from the depth of the perched water table. The net result of the 'ramped' hydraulic gradient determined by Equation 6.10 was to allow initiation of ponding in response to water reaching the fine grained layers from above. The volume of water admitted into the top of the fine-grained unit was assumed to displace the equivalent volume of water from the base of the unit. The model therefore transfers the water moving into the top of the fine-grained layer directly through to the top of the underlying coarse-grained layer for further migration. A schematic diagram describing the modelling processes used is shown below (Figure 6.36).

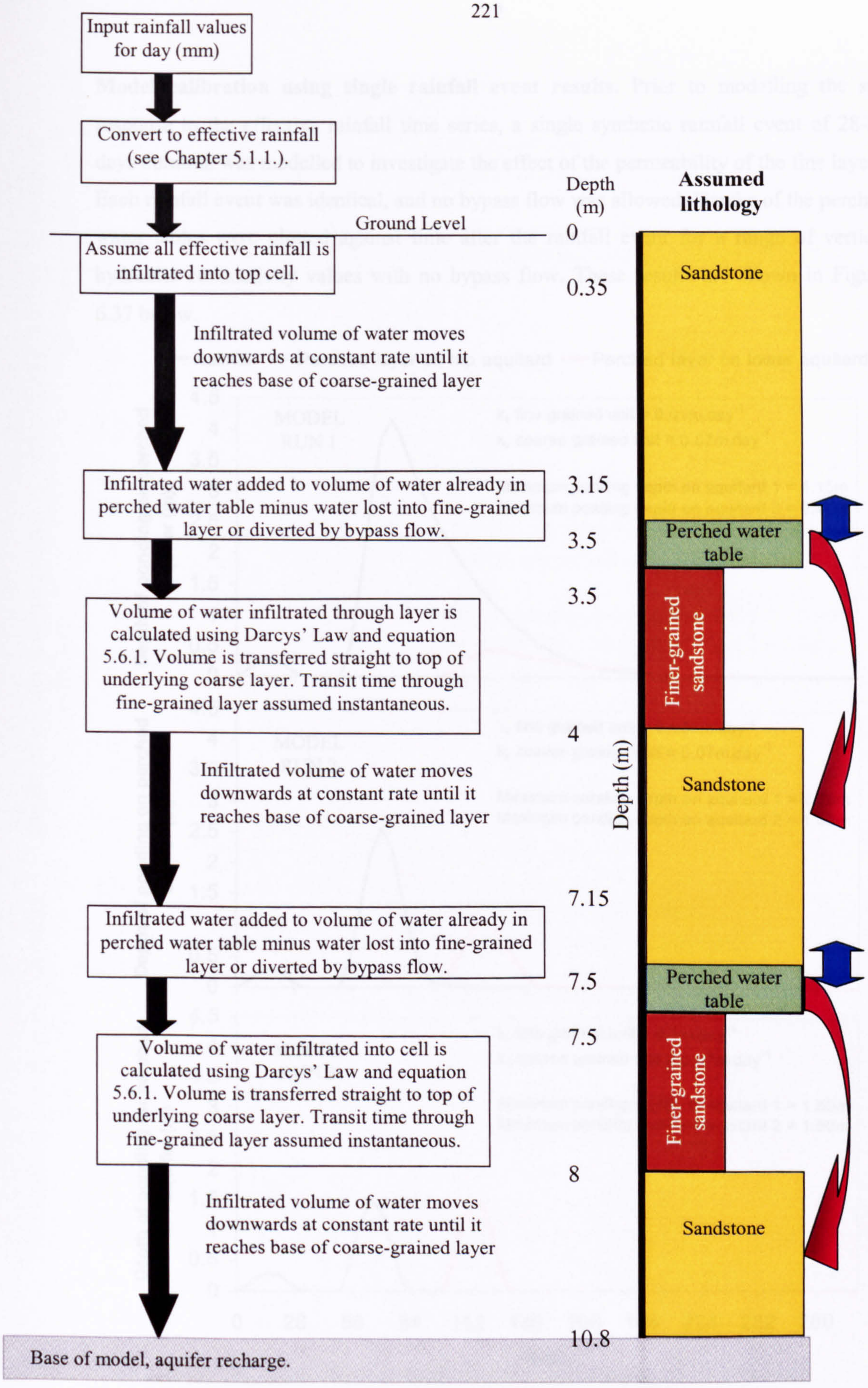

Figure 6.36. Vertical flow model flowchart. Red arrows indicate bypass flow.

Model calibration using single rainfall event results. Prior to modelling the site response to the effective rainfall time series, a single synthetic rainfall event of 28-30 days duration was modelled to investigate the effect of the permeability of the fine layers. Each rainfall event was identical, and no bypass flow was allowed. Depths of the perched water tables were plotted against time after the rainfall event for a range of vertical hydraulic conductivity values with no bypass flow. These results are shown in Figure 6.37 below.

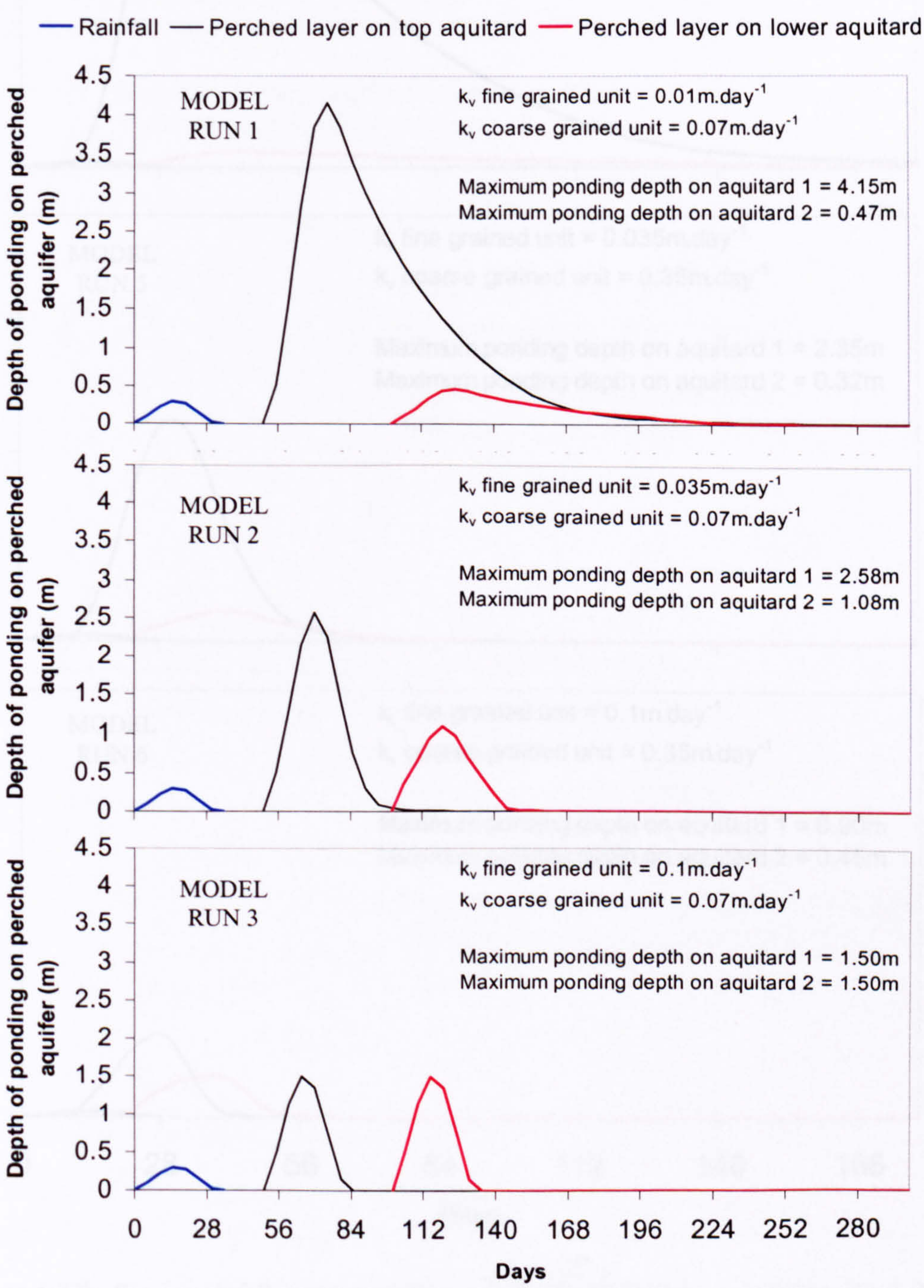

Figure 6.37a. Single rainfall event modelling results for vertical k_{coarse} = 0.07m.day^{-1}. No bypass flow allowed.

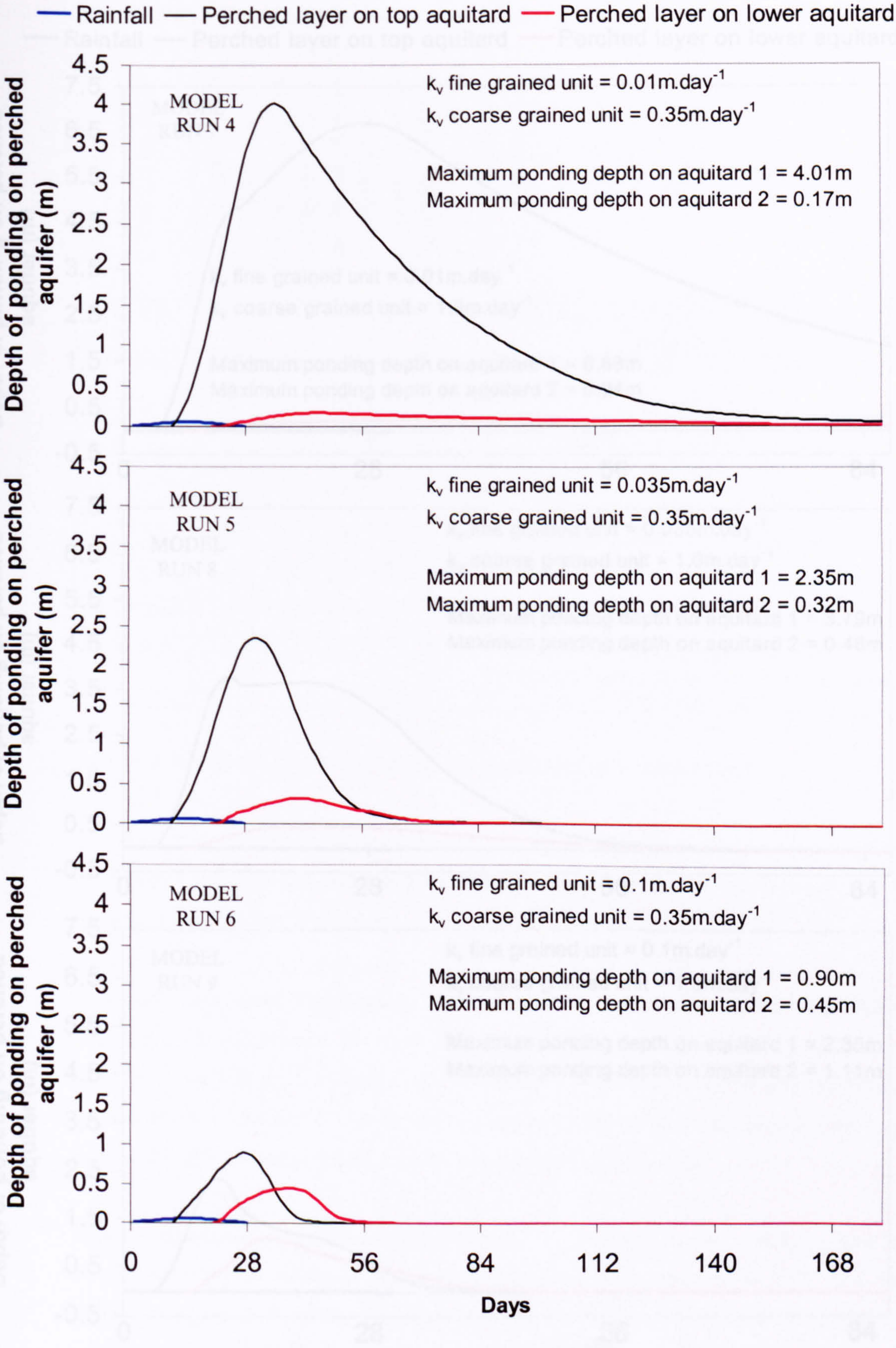

Figure 6.37b. Single rainfall event modelling results for vertical k_{coarse} = 0.35m.day^{-1}. No bypass flow allowed.

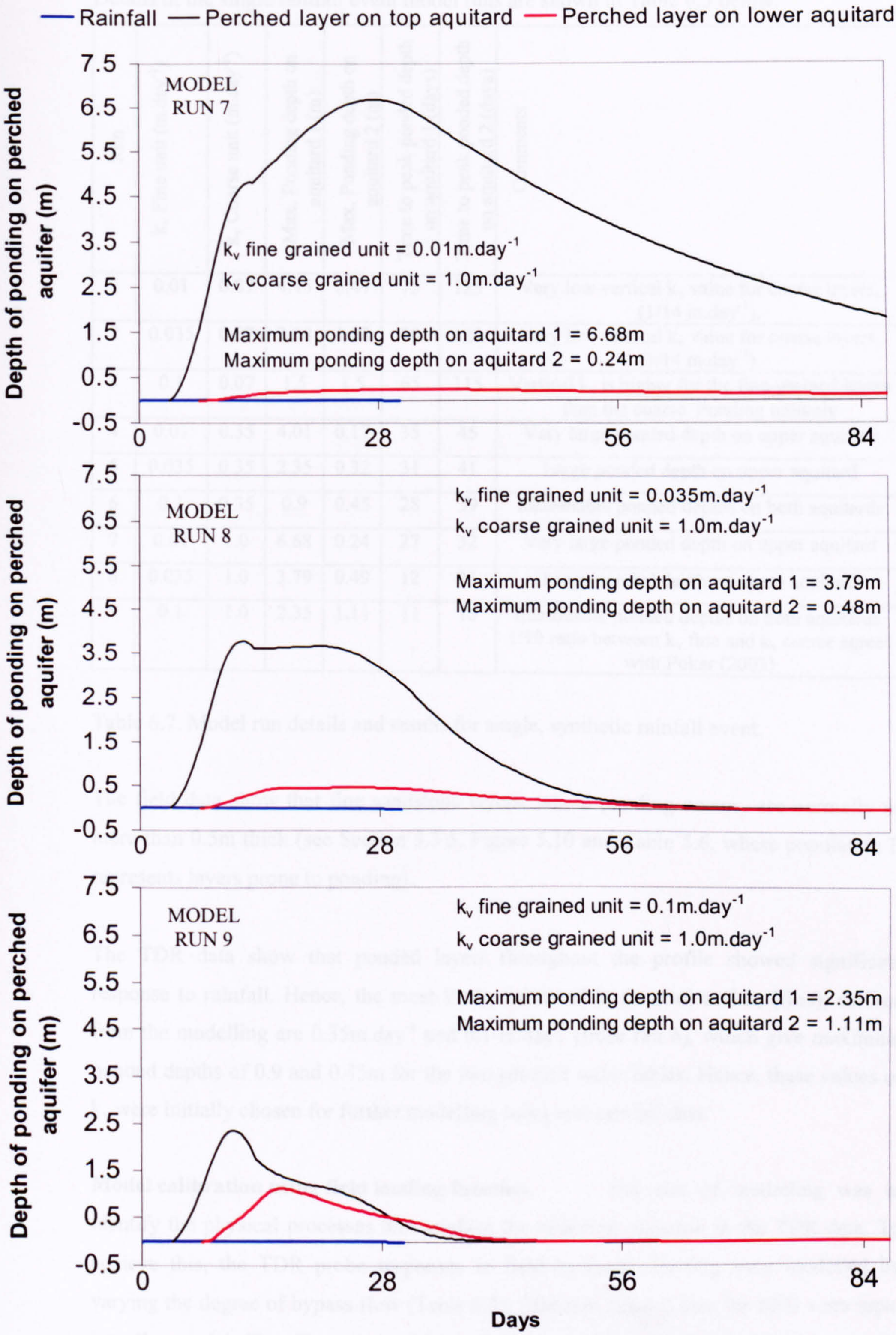

Figure 6.37c. Single rainfall event modelling results for vertical k_{coarse} = 1m.day^{-1}. No bypass flow allowed.

Details of the single rainfall event model runs are shown in Table 6.5 below.

Run	k_v Fine unit ($m.day^{-1}$)	k_v Coarse unit ($m.day^{-1}$)	Max. Ponding depth on aquitard 1 (m)	Max. Ponding depth on aquitard 2 (m)	Time to peak ponded depth on aquitard 1 (days)	Time to peak ponded depth on aquitard 2 (days)	Comments
1	0.01	0.07	4.15	0.47	75	125	Very low vertical k_v value for coarse layers, ($1/14$ $m.day^{-1}$).
2	0.035	0.07	2.58	1.08	70	120	Very low vertical k_v value for coarse layers, ($1/14$ $m.day^{-1}$).
3	0.1	0.07	1.5	1.5	65	115	Vertical k_v is higher for the fine-grained layers than the coarse. Ponding unlikely
4	0.01	0.35	4.01	0.17	35	45	Very large ponded depth on upper aquitard
5	0.035	0.35	2.35	0.32	31	41	Large ponded depth on upper aquitard
6	0.1	0.35	0.9	0.45	28	39	Reasonable ponded depths on both aquitards
7	0.01	1.0	6.68	0.24	27	32	Very large ponded depth on upper aquitard
8	0.035	1.0	3.79	0.49	12	23	Large ponded depth on upper aquitard
9	0.1	1.0	2.35	1.11	11	16	Reasonable ponded depths on both aquitards. 1:10 ratio between k_v fine and k_v coarse agrees with Pokar (2002)

Table 6.7. Model run details and results for single, synthetic rainfall event.

The field data show that fine sandstone layers, where ponding occurs, are normally no more than 0.5m thick (see Section 5.3.5, Figure 5.10 and Table 5.6, where population D represents layers prone to ponding).

The TDR data show that ponded layers throughout the profile showed significant response to rainfall. Hence, the most likely values of k_v (coarse) and k_v (fine), derived from the modelling are $0.35 m.day^{-1}$ and 0.1 $m.day^{-1}$ (from run 6), which give maximum ponded depths of 0.9 and 0.45m for the two perched water tables. Hence, these values of k_v were initially chosen for further modelling using real rainfall data.

Model calibration using field loading function. The aim of modelling was to identify the physical processes that produce the observed response in the TDR data. To achieve this, the TDR probe responses to field hydraulic loading were modelled by varying the degree of bypass flow (Table 6.8). Effective rainfall data for 2003 were input into the model (See Chapter 5). Figure 6.38 shows the responses of the two model perched water tables to real rainfall loading with varying degrees of bypass flow, with K_v (coarse) = $0.35 m.day^{-1}$ and K_v (fine) = $0.1 m.day^{-1}$.

Run	k_v Fine unit ($m.day^{-1}$)	k_v Coarse unit ($m.day^{-1}$)	Percentage of bypass flow allowed per day (% day^{-1}).	Max. Ponding depth on aquitard 1 (m)	Max. Ponding depth on aquitard 2 (m)	Comments
10	0.1	0.35	10	0.102	0.056	Time lag between 2 ponded layers = 10 days
11	0.1	0.35	20	0.092	0.052	
12	0.1	0.35	30	0.082	0.048	
13	0.1	0.35	40	0.075	0.058	
14	0.1	0.35	50	0.066	0.065	Time lag between ponded layers = 0 days
15	0.1	0.35	25	0.087	0.048	25% per day bypass flow selected for further modelling

Table 6.8. Model run details for site effective rainfall data with varying bypass flow.

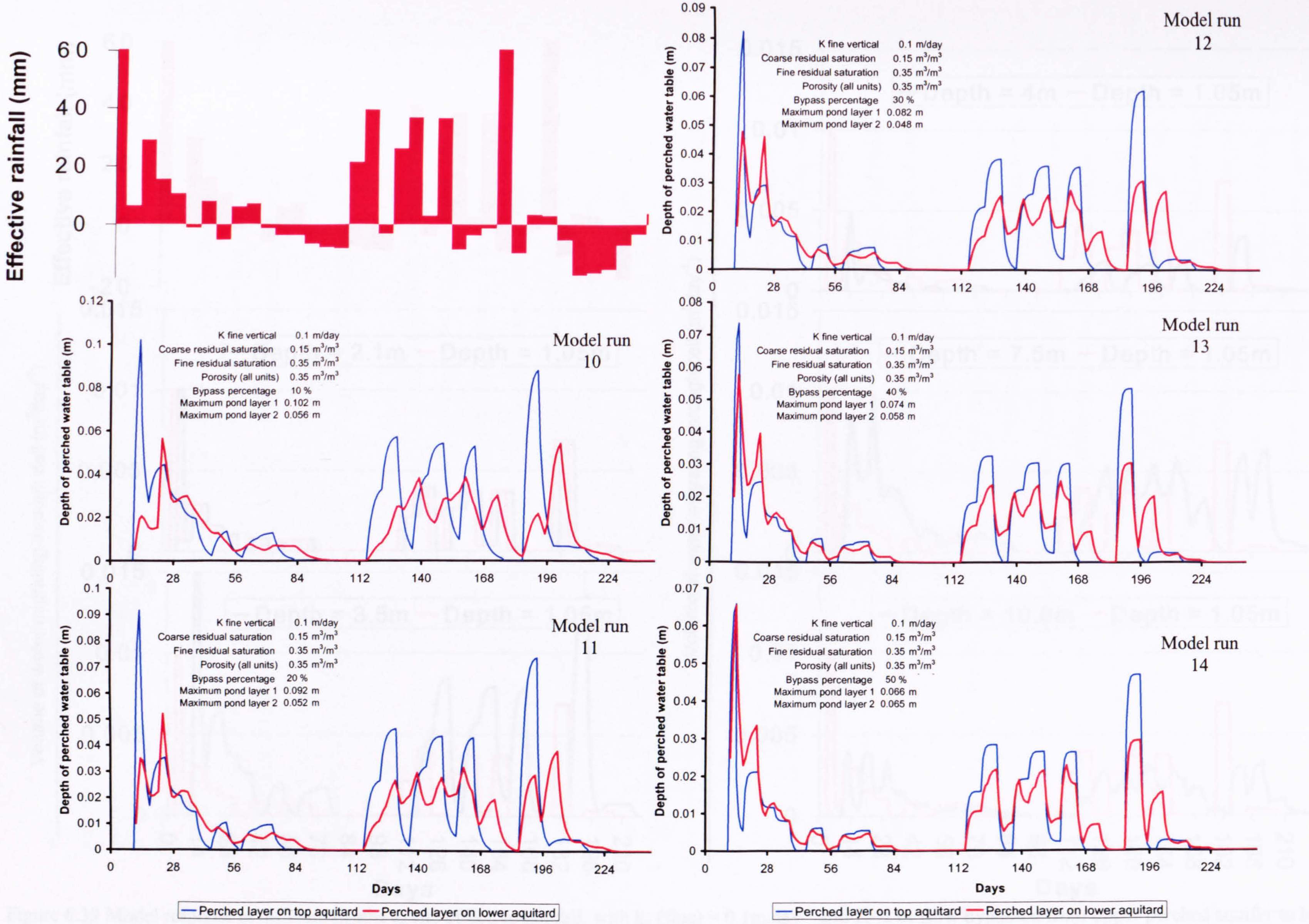

Figure 6.38. Model response to site effective rainfall and the effects of varying bypass flow from day 0 (12/Dec/2002) to day 225 (12/Aug/2003).

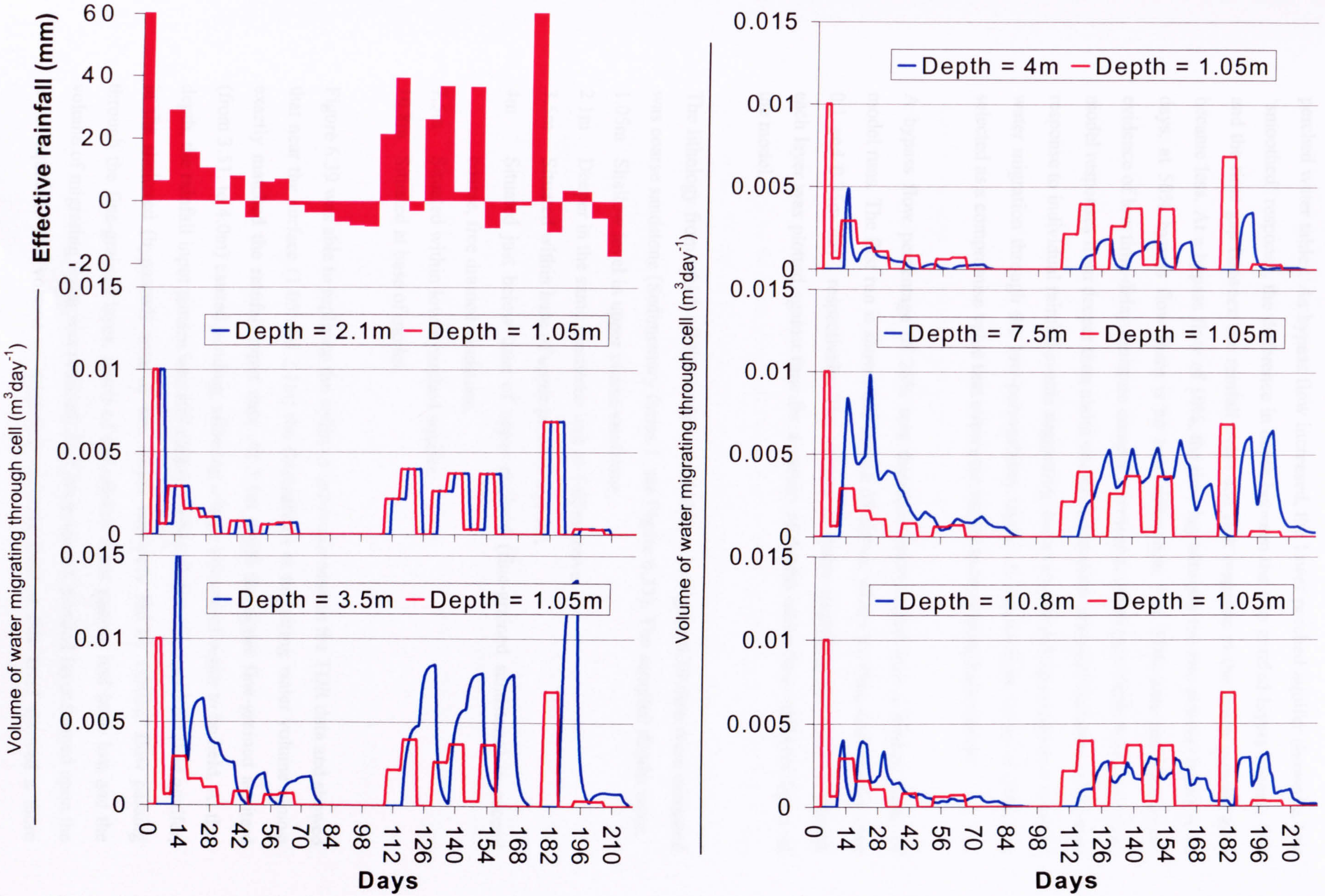

Figure 6.39 Model response at different depths to site effective rainfall, with k_v (fine) = 0.1m.day^{-1} and 25% of flow bypassed from upper perched aquifer to lower perched aquifer.

Figure 6.38 shows that varying the levels of bypass flow had three main effects on the perched water tables. As bypass flow increased, the lower perched aquifer showed a less 'smoothed' response, the difference in depth between the two ponded layers became less and the time gap between the rainfall event and first response at the lower ponded level became less. At a bypass flow of 10%, the time lag between the two ponded layers is 10 days, at 50% bypass flow there is no time difference. The TDR data provides ample evidence of low time-delay moisture content increases at depth (see Table 6.4). However, model responses from deeper than about 6m tended to show seasonal variation rather than response to individual rainfall events suggesting that some smoothing occurs as a result of water migration through the low-permeability layers. A bypass flow value of 25% was selected as a compromise value that allows the model to reproduce both effects.

A bypass flow percentage of 25% was therefore incorporated into a further series of model runs. The first run is shown in Figure 6.39 above, where K_v (fine and coarse) were 0.1 and 0.35m day^{-1} respectively. The volume of water migrating downwards through each layer was plotted against time for a variety of depths taken from different layers of the model.

The lithology from which all the model values shown in Figure 6.39 data were extracted was coarse sandstone (Sedimentary facies 1, see Figure 6.33). The sampled depths were;

1.05m Shallow level in upper coarse sandstone,

2.1m Deeper in the same sandstone unit as 1.05m above,

3.5m Situated within base of upper perched aquifer,

4m Situated just below base of upper aquitard (fine-grained sandstone) in second coarse, free drained sandstone,

7.5m Situated within lower perched aquifer.

10.8m Situated at base of model.

Figure 6.39 was able to replicate the styles of behaviour seen in the TDR data and showed that near the surface (1.05 and 2.1m) the fluctuations in migrating water volume almost exactly matched the rainfall input data. At 3.5m depth the upper fine-grained aquitard (from 3.51. to 4.0m) caused ponding, allowing a large volume of water to be held. At this depth, the rainfall input pattern was still clearly visible. Below the upper perched aquifer, in the sheltered (bypassed) zone at 4m, which was only fed by vertical flow passing through the fine-grained layer, much of the rainfall input pattern had been lost and the volume of migrating water was reduced. At 7.5m a second, ponded layer formed upon the lower aquitard. The volume of migrating moisture held at this level showed a more

complicated pattern which appeared to be influenced by rainfall patterns but with extra 'peaks' because of the patterns of bypass and vertical flow from the upper layers. At 10.8m, at the base of the model, all the rainfall input into the model was present, i.e. the mass balance calculation was correct as all the bypass flow is included. The pattern of the 10.8m deep plot showed no obvious relationship to rainfall events, and produced a plot that was very similar to the group 3 TDR probe plots. The model also predicted that some deep layers would show responses before some of the shallower layers, as shown in the TDR field data. An increasing time delay may be seen between the first arrival times of individual rainfall events seen at 1.05m, 2.1m, 3.5m and 4m. The bypass-fed perched layer seen at 7.5m however, reacts to rainfall events at a similar time delay to the upper perched layer at 3.5m depth, and reacts before the layer at 4m depth. The response at 10.8m is a mixture of two sets of bypass flow and vertical flow components and thus only reflects seasonal patterns rather than individual events.

Hence, this model was able to produce plots with a similar form to almost all of the yearly TDR data plots. To facilitate comparison between field and synthetic data, the thickness of the perched water tables shown in Figure 6.38 were converted into moisture contents at 0.15m above the top of the uppermost fine-grained unit using the equation proposed by van Genuchten (1980),

$$\theta = \theta_r + \frac{\theta_s - \theta_r}{\left(1 + |\alpha\psi|^n\right)^m} \qquad \text{Equation 6.10}$$

Average values for van Genuchten parameters for sands were confirmed to be accurate for the Sherwood Sandstone by Yoshida (2000). The values used were m = 0.63, n =2.68 and α = 0.145, with values of θ_r (residual volumetric moisture content) and θ_s (saturated volumetric moisture content) of 0.15 and 0.35 respectively (from model input parameters).

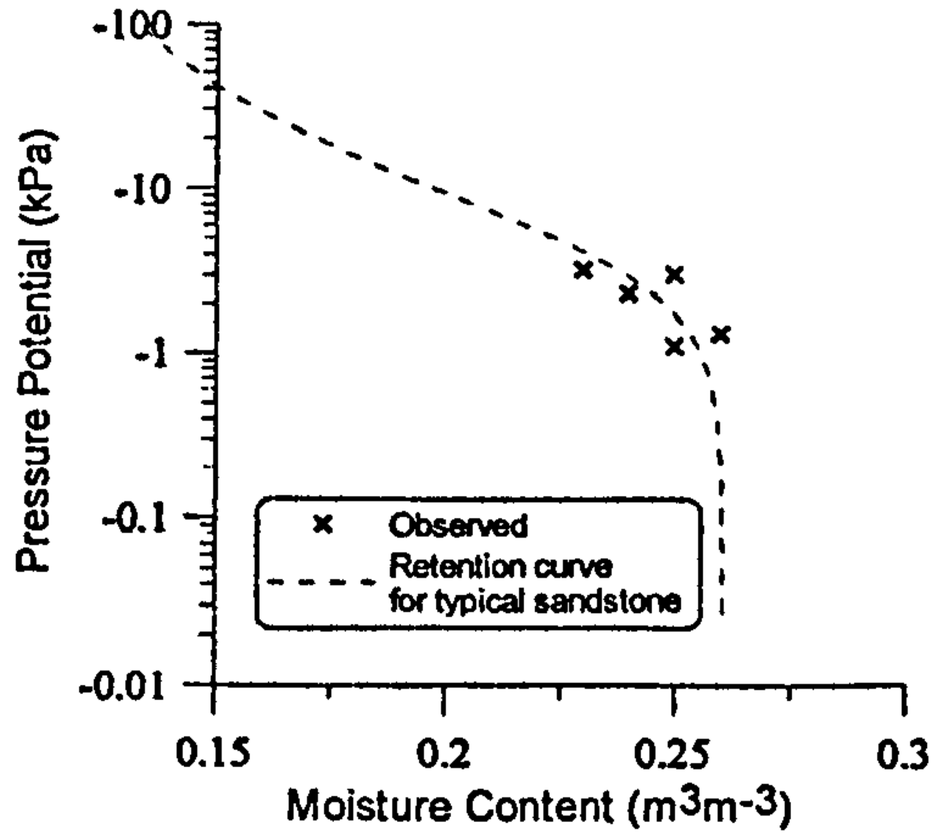

Figure 6.40. Soil water retention data for sandstone and typical sandstone retention curve (Yoshida, 2000).

The moisture content time-series derived using the van Genuchten equation is shown below. The vertical hydraulic conductivity of the fine sandstone layers, k_v (fine) was kept at 0.1m.day^{-1}. This gave moisture content fluctuations of similar size to field results for the upper perched water table, however the time-delay is shorter in the field data .

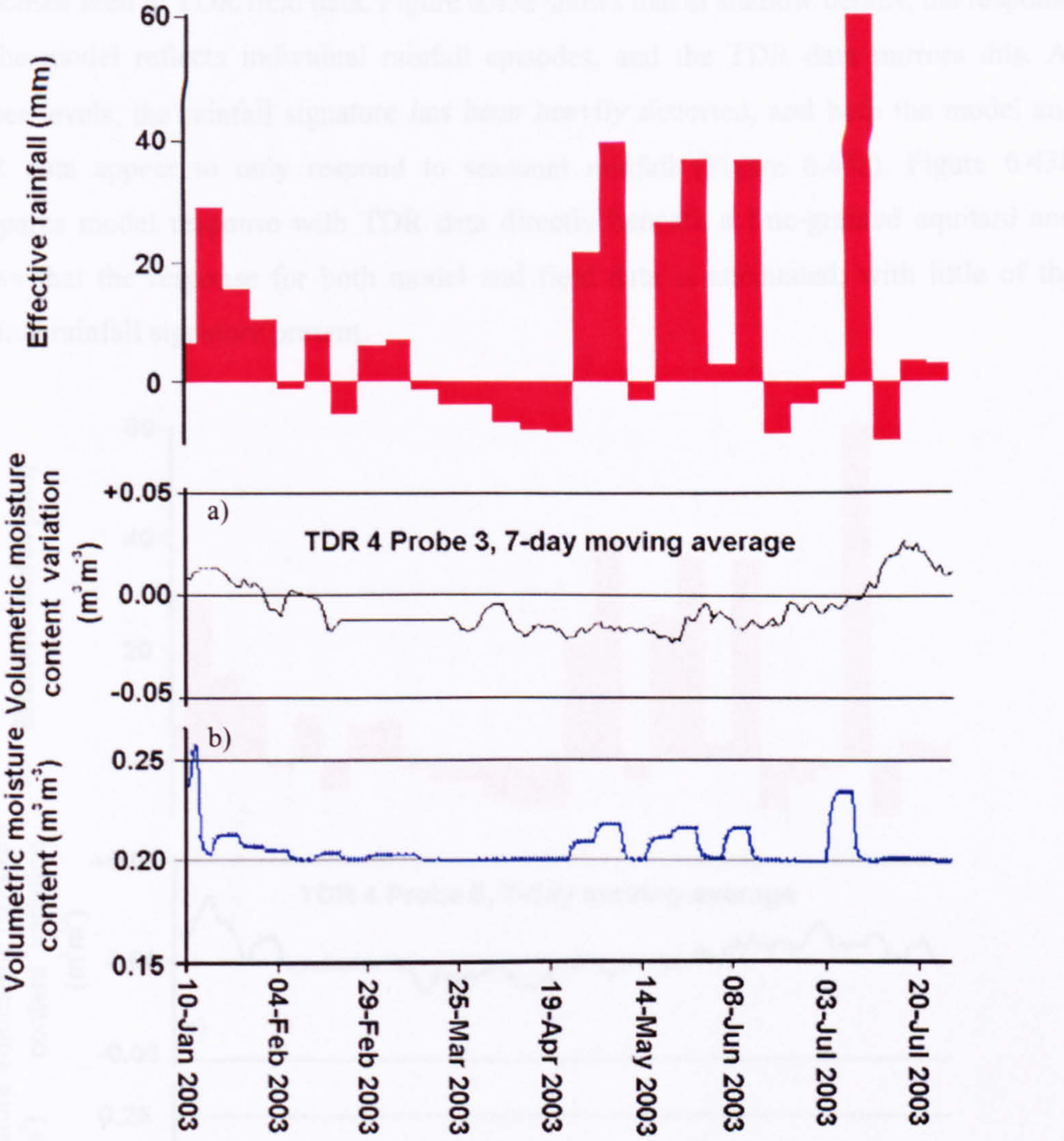

Figure 6.41. a) Field probe TDR 3, Borehole TDR 4 (just above perched aquifer layer) moisture fluctuation data. b) Modelled time-series fluctuation in moisture content using the van Genuchten (1980) equation. (4.5m depth. 25% bypass flow).

The same approach as Figure 6.41 was taken for the lower modelled ponded layer, and results for this model run are shown in Figure 6.42. Again, the model appeared to closely match the pattern of the field data, although again the time lag from effective rainfallof the model response was shorter than that shown by the TDR results. This was probably due to the model assuming bypass flow as instantaneous. The model assumed this because bypass flow is likely to be much faster than vertical flow through fine-grained

layers. Obviously, flow cannot be truly instant, but each bypass pathway will allow transport at a different velocity so this simplification avoided introducing too many unknown factors

Figure 6.43 indicates that the response of the model at other depths is very similar to responses seen in TDR field data. Figure 6.43a shows that at shallow depths, the response of the model reflects individual rainfall episodes, and the TDR data mirrors this. At deeper levels, the rainfall signature has been heavily distorted, and both the model and TDR data appear to only respond to seasonal rainfall (Figure 6.43c). Figure 6.43b compares model response with TDR data directly beneath a fine-grained aquitard and shows that the response for both model and field data is attenuated, with little of the original rainfall signature present.

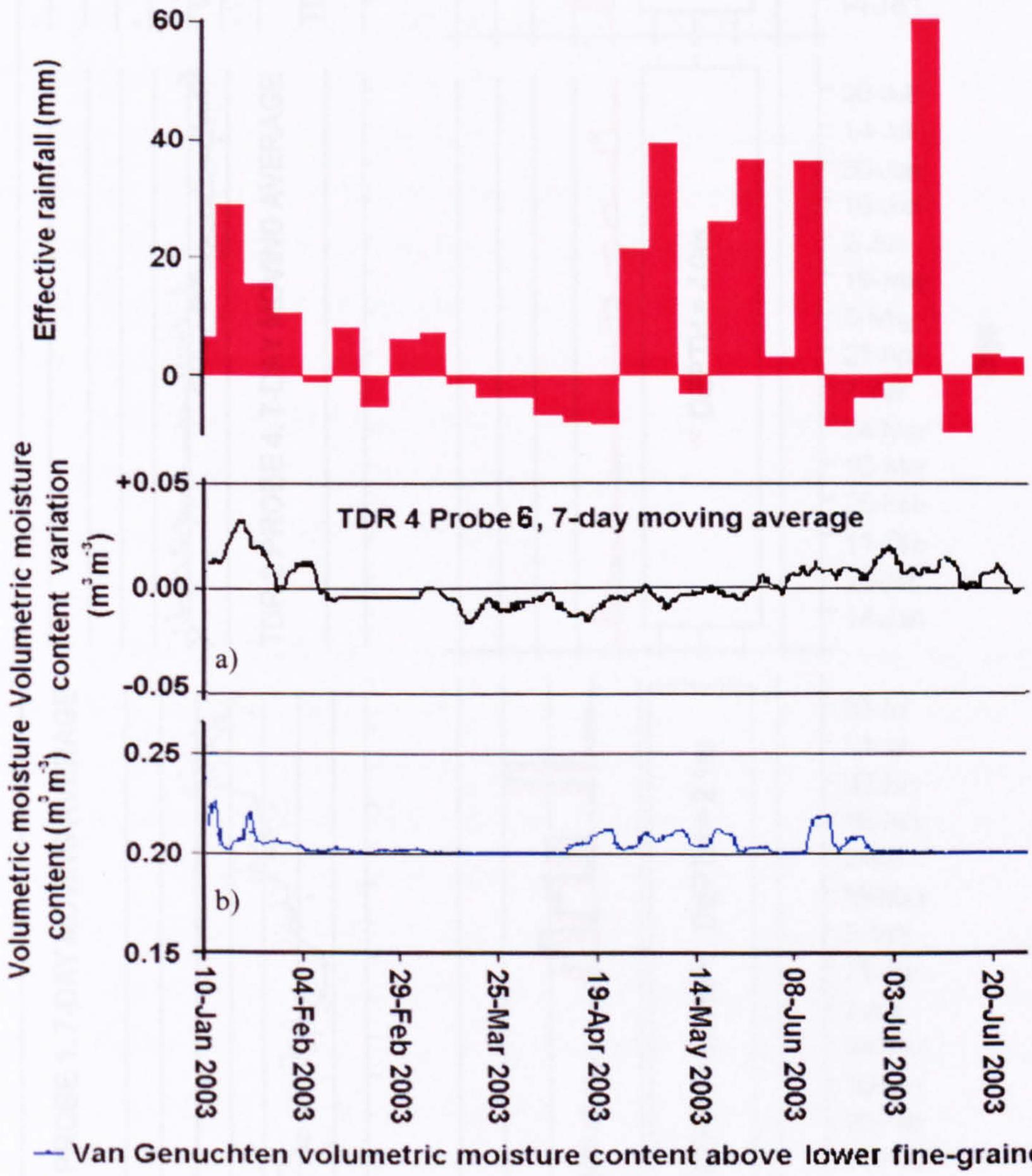

Figure 6.42. a) Field TDR probe 6, Borehole TDR 4 moisture fluctuation data. b) Modelled time-series fluctuation in moisture content using the van Genuchten (1980) equation. (7.5m depth. 25% bypass flow).

a)

b)

c)

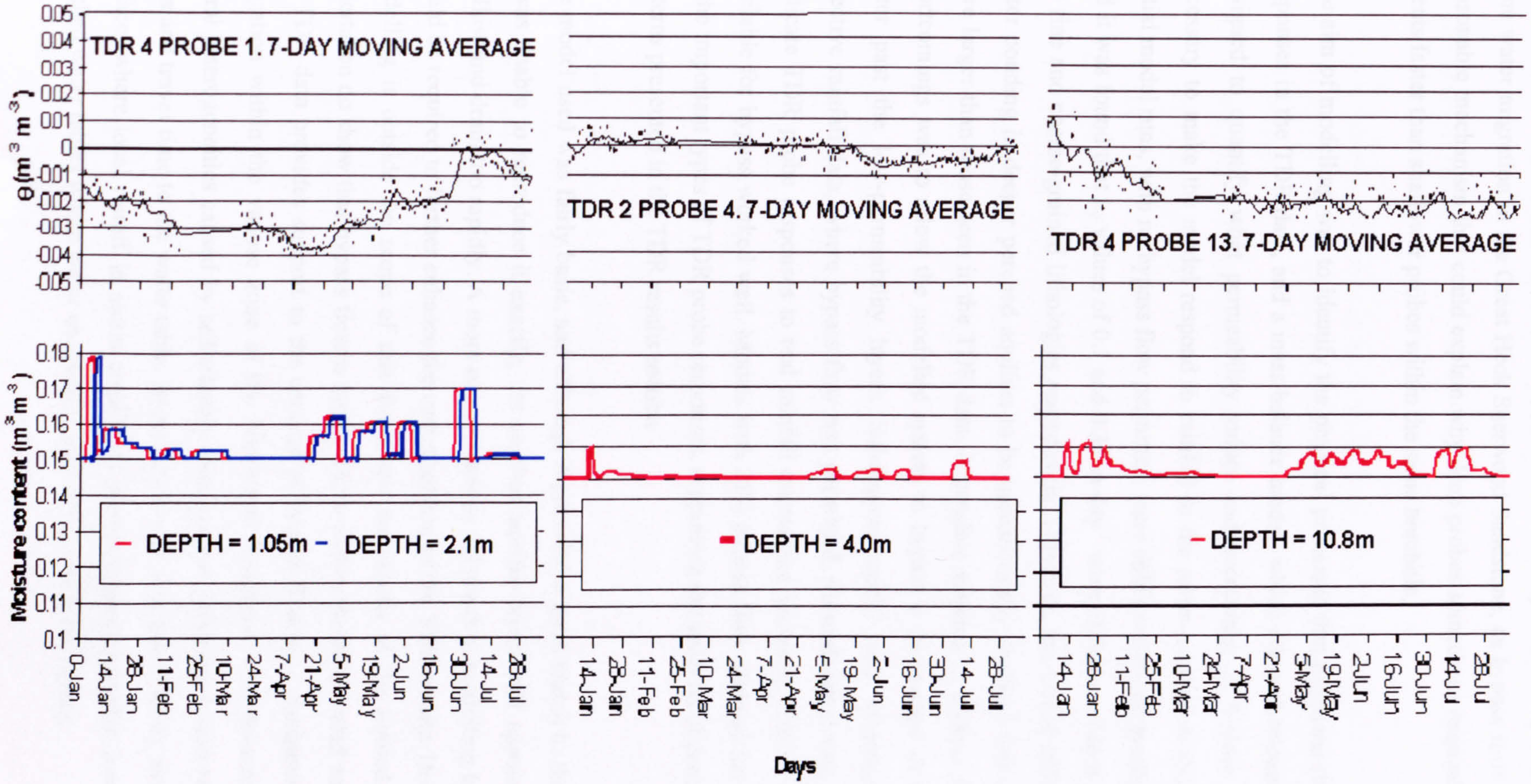

Figure 6.43. A comparison of modelled moisture content with field TDR data a) 2.1m depth; b) 4.0m depth; c) 10.8m depth.

6.6.1 Modelling summary

Results from the TDR data suggest that bypass flow is an important component of vadose zone water migration in the Great Heck Sherwood Sandstone, as bypass flow is the only reasonable mechanism that could explain why deep probes sometimes respond to rainfall events faster than shallower probes within the same borehole.

The aim of modelling was to identify the physical processes that produced the observed responses in the TDR data, and a mass-balance model, which allowed bypass flow, was designed to quantify what permeability values and percentage of bypass flow were necessary to make the model respond to rainfall in the same manner as the field data. Initial model runs, with no bypass flow permitted, were able to replicate perched aquifers, and it was found that k_v values of 0.1 and 0.35 m day^{-1} were optimum values to replicate the fine and coarse-grained lithologies respectively. However, the model still caused the water ponding in deeper perched aquifers to be unrealistically shallow, and time delays were larger than those seen in the TDR data. A possible solution to address the model's shortcomings was to allow the modelled system to bypass a percentage of the ponded water past the low-permeability layers. Subsequent model runs incorporating field effective rainfall data, where bypass flow was permitted, showed that it was possible to replicate TDR probe responses to real rainfall events and allowing 25% of flow to be available for bypass worked well. Models with 25% bypass flow allowed the replication of the important types of TDR probe responses, supporting the analysis of probe response patterns presented in the TDR results section.

The model used was fairly basic, and although it provided a good match to the field data it was unable to reproduce it exactly, the perched aquifer layers still appear to be too shallow and drain too rapidly. A more comprehensive approach to modelling bypass flow would be required to further enhance the understanding of the TDR results. However, this modelling is outside the scope of this thesis and the results of the limited modelling undertaken do show that bypass flow is highly likely within the unsaturated zone. Hence, the TDR data provides support to the concept of bypass flow as a mechanism of flow migration within the vadose zone of the Sherwood Sandstone, and demonstrates that lateral heterogeneities caused by sedimentary structure can influence moisture migration rates and travel time to the water table. Bypass flow may originate directly from the near surface, where local runoff in storm conditions is routed to topographic lows, or from perched water tables where water encounters gaps in the overlying layers.

CHAPTER 7
SUMMARY OF RESULTS, CONCLUSIONS AND POTENTIAL FOR FUTURE RESEARCH

7.1 Summary of results.

The original research objectives at the start of the study reported in this thesis were;

a. To design and test a new method of applying the TDR technique within a rock environment.
b. To quantify and characterise the Sherwood Sandstone in the study area and to understand its origins;
c. To identify and characterise heterogeneities influencing groundwater flow and specifically vadose zone flow;
d. To propose conceptual models of vadose zone flow and to test these against evidence from field moisture measurements;
e. To estimate water travel times through the vadose zone;

The literature indicates that the present structure of the Sherwood Sandstone aquifer is a result of the Triassic depositional environment modified by subsequent diagenetic processes. Investigation of outcrop and cut faces showed that the combination of depositional and diagenetic processes have resulted in a highly porous, friable and permeable rock ($\phi \approx 33$-35%). The Sherwood Sandstone in the Northeast of England was deposited distally in a braided river environment and is texturally and mineralogically mature, being comprised of poorly cemented, haematite-stained, fine-medium quartz grains with some mud and silt clasts and lenses. Five principal sedimentary facies were determined for the study area (see Table 3.1):

1) Fine-Medium-grained trough cross-bedded sandstones deposited in major river channels, which form approximately 70% of the bulk rock and may be laterally continuous over tens of metres.

2) Fine-grained clay/silt-rich, low-angle laminated sandstones that represent deposition outside major channels. Forming a further 25% of the bulk rock, facies 2 deposits are often laterally continuous on a scale of tens to hundreds of metres.

3) Rare claystone layers (slack water/overbank deposits), which are usually less than ten metres in length and form at most 1% of the rock.

4) Small scale, shallow water, ripple cross-stratification (further 1%).

5) Infilled minor channels/scours (4% of the rock) that are usually less than 10 metres wide.

Ground penetrating radar surveys have shown that GPR facies 1 (trough cross-bedded sandstone) produces reflections representing set/coset boundaries between individual dunes rather than avalanche foreset surfaces, since the latter were often below the spatial resolution of GPR. GPR facies 2 (laterally extensive sheets of very fine-grained sandstone up to a metre thick) were visible on radar images as particularly strong radar reflections often with hyperbolae visible at their margins. Clay rich, slack water/overbank deposits (GPR facies 4) were not common although clay clasts derived from these deposits produced strong hyperbolic reflectors (GPR facies 3). Forward modelling of the radar response and field verification has shown that fine sandstone and claystone units attenuated the radar reflections markedly, and were likely to produce a single strong reflector of limited extent. Smaller clay/silt-rich clasts and groups of clasts were generally marked by hyperbolae. Abandoned minor channel infills (GPR facies 5) were also seen in radar images from the concave shape of the underlying reflectors. Ripple beds (sedimentary facies 4) were below the resolution of the radar system.

The subsurface architecture of a test site at Great Heck Quarry (SE 588 213) was characterised using a combination of surface radar profiles, gamma and core logs. The sedimentary structure beneath the Great Heck test site was found to principally consist of trough cross-beds, interspersed with sub-horizontal, very fine/fine-grained, planar-laminated layers. Geophysical data were used to extrapolate the layers corresponding to sedimentary and GPR facies 2 within the bulk of the (facies 1) sandstone rock from core data. Permeability studies conducted in the Sherwood Sandstone, particularly the work of Pokar (2002) suggested that facies 2 was significantly less permeable than facies 1. Outcrop observations following heavy rainfall in Late 2000/early 2001 indicated that the permeability contrast between layers was causing perched aquifers to form above finer-grained layers, which caused water to flow laterally out of rock faces.

Data from a neutron probe and an off-the-shelf device for measuring moisture content based on the principles of TDR (TRIME packer) were used to monitor the hydraulic response in the vadose zone at the Great Heck test site at monthly intervals under natural rainfall loading. TRIME and neutron probe time-series and depth profile data showed that perched aquifers periodically form above low permeability horizons. This allowed the construction of two opposing conceptual models of vadose zone moisture flow behaviour. A series of packer mounted TDR sensors were designed, calibrated and installed at the Great Heck test site and logged automatically at daily intervals. The high temporal

resolution of the TDR data was used to provide further detail on the behaviour of water migrating through the various layers. Evidence confirming the existence of bypass flow past fine-grained layers, and estimates of response time to natural rainfall events at different depths were presented. A simplified model of the vadose zone, consisting of hydraulically resistive layers with varying proportions of bypass flow was constructed and calibrated to produce model responses to real rainfall events that corresponded with the equivalent TDR responses.

7.2 Conclusions

a. The permanently installed TDR packer system is ideal for long-term monitoring and is capable of providing automated moisture content measurements with very high temporal resolution. Provided care is taken with routing of coaxial cables, the system reported here can produce accurate absolute moisture content values at high temporal density.
b. The Sherwood Sandstone in the study area is comprised of five facies, with trough cross-stratification and planar-laminated layers being dominant.
c. Aquifer heterogeneity influences moisture flow patterns under natural rainfall loadings in the vadose zone of the Sherwood Sandstone and is likely to be important for saturated zone flow. The overall distribution of sedimentary facies within the area investigated suggests that horizontal flow within the saturated zone of the Sherwood Sandstone aquifer will occur dominantly through the trough cross-bedded, fine-medium grained sandstone (facies 1), focussed in the basal sections of fining upwards units, which represent a low proportion of the overall porosity. This is likely to lead to relatively rapid contaminant transport compared with that expected for more pervasive flow and also may explain why permeabilities estimated from pumping tests in the study area are greater than most core based measurements.
d. Muddy facies representing bar-top, slack water, and occasional overbank deposits are likely to locally inhibit vertical flow. This restriction of vertical migration causes both temporary and permanent perched aquifers to form, which may provide sufficient hydrostatic head to force moisture to migrate laterally until a preferential flowpath is encountered.
e. Estimates of pressure pulse arrival times derived from moisture content data following rainfall events, range between 3 years and 1 month at a depth of 10m, and the mean response time is 90 days for a 10m thick vadose zone. This suggests that in areas where bypass flow dominates, groundwater may be at greater risk

than suggested by conventional 'plug flow' models, and that vulnerability is dictated by the amount of bypass flow. However, one year of data collection is insufficient to resolve pressure front migration velocity to a high degree of accuracy and further monitoring using the TDR system is necessary.

f. Modelling results showed that synthetic moisture fluctuations could be generated using real effective rainfall data. These synthetic responses corresponded with real moisture content data if 25% of flow was available for bypass flow, with k_v values of 0.1 and 0.35 m day^{-1} for facies 1 and 2 respectively. The model was able to replicate all of the important types of TDR probe responses.

7.3 Implications for further work

The TDR system at Great Heck is still functioning and presents an ideal opportunity for a longer-term study of moisture flux over several years. The data presented here, together with any data from long term monitoring would be ideal input data for stochastic modelling using more advanced modelling methods than the simple mass-balance models presented in this thesis. More advanced models should be able to provide more detail on the mechanisms by which fluids migrate across the vadose zone with the aim of developing more accurate methods of predicting groundwater vulnerability than are used at present.

The possibility also exists for monitoring the response of the vadose zone when stressed by a large scale water injection, preferably following a prolonged drought for maximum contrast. It is hoped that a test of this type will be conducted in the future, before the system is eventually quarried out. An injection test would provide 'worst case' information on pulse travel times, with the rock being nearer saturation than from rainfall events only, which should allow significant perched water tables to form very quickly. A single large pulse would be easy to separate from background rainfall events due to its limited timespan and large volume of water injected and so clearer response time data would be available than from natural events alone.

The TDR technique has been shown to work in a borehole environment and the packer design reported in this thesis could be adapted to monitoring moisture flux for wider geological applications. In this thesis, the spatial sensitivity of two and three electrode probes was investigated, further work on probe design which would allow greater penetration into the rock could greatly increase the usefulness of TDR as a tool for moisture flux monitoring.

The GPR technique may also be useful in monitoring vadose zone moisture migration. At present the detection of migrating water is complicated by out of plane reflections and diffractions, but new techniques in high-resolution/high-speed 3D data collection and true 3D processing and migration are starting to become available (Anderson et al, 1999) which may allow 3D moisture content fluctuation data to be acquired at sufficient resolution to image moisture flux.

References

Aigner,T., Schauer,M., Junghans,W.-D. and Reinhardt. 1995
Outcrop gamma ray logging and its applications:examples from the German Triassic. *Sedimentary Geology*. Vol. 100 pp. 47-61.

al Hagrey,S.A., Michaelsen,J. 1999.
Resistivity and percolation study of preferential flow in vadose zone at Bokhorst, Germany. *Geophysics*, 64, 746-753#

Allaby,A., and Allaby,M., 1990.
Oxford concise dictionary of Earth sciences. Oxford University Press.

Allen, D.J., Brewerton, L.J., Coleby, L.M., Gibbs, B.R., Lewis,M.A., MacDonald, A.M., Wagstaff, S.J. and Williams, A.T., 1997.
The physical properties of major aquifers in England and Wales. British Geological Survey, technical report WD/97/34, pp.157 – 287.

Anderson,M.P., Aiken,J.S.,Webb,E.K.,Mickelson,D.M. , 1999.
Sedimentology and hydrogeology of two braided stream deposits. *Sedimentary Geology 129* (1999) pp 187-100 Elsevier Science BV.

Annan, A.P., Waller, W.M., Strangway, D.W., Rossiter, J.R., Redman, J.D., and Watts. R.D. 1975.
The electromagnetic response of a low-loss, two layer, dielectric earth for horizontal dipole excitation. *Geophysics*, Vol. 40. No. 2. pp. 285-298.

Arche,A. and Lopez-Gomez,J., 1999.
Tectonic and geomorphic controls on the fluvial styles of the Eslida Formation, Middle Triassic, Eastern Spain. *Tectonophysics 315* (1999) pp. 187 – 207 Elsevier BV.

Ashworth, P.J., Best,J,L., Roden,J.E., Bristow,C.S., and Klassens,G.J. 2000.
Morphological evolution and dynamics of a large, sand braid bar, Jamuna River, Bangladesh. *Sedimentology.* Vol. 47, pp. 533-555

Aspiron, U., and Aigner, T. 1997.
Aquifer architecture analysis using ground penetrating radar; Triassic and Quaternary examples (S. Germany). *Environmental Geology*, Vol. 31. No. 1-2. pp. 66-75.

Aspiron, U., and Aigner, T. 1999.
Towards realistic aquifer models: three-dimensional georadar surveys of Quaternary gravel deltas (Singen Basin, SW Germany). *Sedimentary geology*, Vol. 129. pp. 281-297.

Baker,J.M, Lascano,R.J. 1989.
The spatial sensitivity of time-domain reflectometry.
Soil Science, 147(5), 378-384

Barker,R.D. and Worthington,P.F. 1973.
Some Hydrogeological Properties of the Bunter Sandstone of Northwest England. *Geoexploration*, 11, 151-170 Elsevier Scientific Publishing Company, Amsterdam.

Bell,J.P. 1987.
Neutron probe practice. Institute of Hydrology Report 19, third edition.

Best,J.L., Ashworth,P.J., Bristow,C.S., and Rodin,J. 2003.
Three-dimensional architecture of a large, mid-channel sand braid bar, Jamuna River, Bangladesh. *Journal of Sedimentary Research.* Vol. 73 No. 4., pp. 516-530.

Bloomfield,J.P., Gooddy,D.C., Bright,M.I., and Williams,P.J. 2001.
Pore throat size distributions in Permo-Triassic sandstones from the United Kingdom and some implications for contaminant hydrology. *Hydrogeology Journal.* Vol. 9 219-230

Binley,A.M, Winship, P., Middleton, R, Pokar, M and West, L.J. 2002.
High resolution characterisation of vadose zone dynamics in the Sherwood Sandstone using cross-borehole radar. *Water Resources. Research.* Vol. 37. No. 11. pp. 2639-2652.

Binley,A.M., Middleton,R., Pokar,M. and West,L.J. 2001a.
Observations of Seasonal Dynamics in the Vadose Zone using Borehole Radar and Resistivity. In: Proc. Symp. *Applications of Geophysics to Engineering and Environmental Problems (SAGEEP2001)*, Environmental and Engineering Geophysical Society, Denver, CO. (VZC-3).

Binley,A.M., Winship,P and Pokar,M. 2001b.
Cross borehole radar and resistivity tomography: a comparison of techniques in unsaturated sandstone.'
In: Proc. Symp. *Applications of Geophysics to Engineering and Environmental Problems (SAGEEP2001)*, Environmental and Engineering Geophysical Society, Denver, CO. (VZC-1).

Brereton,N.R., Evans,C.J. & Kingdon,A. 1998.
Hydrogeological and geotechnical rock property characterization from geophysics. *Proceedings of the Yorkshire Geological Society*. Vol. 52, Part 2, pp. 199-213.

Bridge, J.S. 1993.
The interaction between channel geometry, water flow, sediment transport and deposition in braided rivers. From Best, J.L., and Bristow, C.S., (eds), *Braided Rivers*, Geological Society Special Publication no. 75, pp. 13-71,

Bridge, J.S., 2003.
Rivers and Floodplains: Forms, Processes and Sedimentary Record. Blackwell Science (UK). ISBN: 0632064897

Bridge, J.S. and Lunt, I, A., 2003.
Depositional models for braided rivers. (In Review), In; *Braided Rivers* (Eds. Sambrook Smith, G., Best, J.L. Bristow, C.S., Gurnell, A. and Petts, G.), Spec. Publication, Int. Ass. Sedimentologists.

Bridge, J S. and Tye, R. S. 2000.
Interpreting the dimensions of ancient fluvial channel bars, channels, and channel belts from wireline-logs and cores. *AAPG Bulletin.* vol.84. no.8. pp.1205-1228.

Bristow, C.S. 1987. *Sedimentology of large braided rivers, ancient and modern.* Unpublished PhD thesis, University of Leeds.

Bristow, C.S. 1993.
Sedimentary structures exposed in bar tops in the Brahmaputra River, Bangladesh. In *Braided Rivers (Eds. Best,J.L., and Bristow,C.S.).* Geological Society Special Publication No. 75., Geological Society, London. Pp. 277-289.

Bristow, C.S., and Best, J.L. 1993.
Braided rivers: perspectives and problems. In *Braided Rivers (Eds. Best,J.L., and Bristow,C.S.).* Geological Society Special Publication No. 75., Geological Society, London. Pp. 1-11.

Bristow, C.S., Skelly, R.L., and Ethridge, F.G. 1999.
Crevasse splays from the rapidly aggrading, sand bed, braided Niobrara River, Nebraska: effect of base level rise. *Sedimentology.* Vol. 46. 1029-1047.

Bristow. C.S., Bailey, S.D., and Lancaster, N. 2000.
The sedimentary structure of linear sand dunes. *Nature*. Vol. 406 (6791) 56-59

British Standard 1377-1. 1990.
Methods of test for Soils for civil engineering purposes. Part 1: General requirements and sample preparation. British Standards Institution (BSI). London.

British Standard 7755-3.1. 1994.
Soil Quality, Part 3: Chemical methods- Section 3.1. Determination of dry matter and water content on a mass basis by a gravimetric method. British Standards Institution (BSI). London.

British Standard 7755-5.2. 1996.
Soil Quality, Part 5: Physical methods- Section 5.2.. Determination of water content in the unsaturated zone- Neutron depth probe method. British Standards Institution (BSI). London.

British Standard BS ISO 11461. 2001..
Soil quality- . Determination of water content as a volume fraction using coring sleeves- gravimetric method. British Standards Institution (BSI). London.

Brown, S., Sellwood, B.W., & Wright, V.P. 1996.
Basin Analysis Techniques, S338 Sedimentary Processes and Basin Analysis. Revised edition, 1996 The Open University, Milton Keynes. ISBN 0 7492 8180 4

Bryant, I. & Burley, S, 1989.
Permo-Triassic fluvial sediments of the Sherwood Sandstone Group in the Bawtry-Selby area of South Yorkshire and Nottinghamshire. 28th Annual General Meeting of the British Sedimentological Research Group BSRG, Leeds, 1989 Field Excursion Guide. ISBN 0 9515439 1 1

Buist, D.S., and Thompson, D.B. 1982.
Sedimentology, engineering properties and exploitation of the pebble beds in the Sherwood Sandstone Group (?Lower Trias) of North Staffordshire with particular reference to highway schemes. *The Mercian Geologist.* Vol. 8, No.4 241-268

Burley, S.D. 1984.
Patterns of Diagenesis in the Sherwood Sandstone Group (Triassic), United Kingdom. *Clay Minerals* 19, 403-440.

Cant, D.J. 1978.
Bedforms and bar types in the South Saskatchewan River. *Journal of Sedimentary Petrology*, Vol. 48, No. 4, pp. 1321-1330

Cant, D.J., and Walker R.G., 1978.
Fluvial processes and facies sequences in the sandy braided South Saskatchewan River, Canada. *Sedimentology*, vol.25, no.5, pp.625-646.

Cardimona,S.J., Clement,W.P., Kadinsky-Cade,K. 1998.
Seismic reflection and ground penetrating radar imaging of a shallow aquifer. *Geophysics* Vol. 63, Issue 4, 1310-1317.

Chadwick,R.A., 1985.
Seismic reflection in investigations into the stratigraphy and structural evolution of the Worcester Basin. *Journal of the Geological Society, London.* Vol. 142, pp. 187-202

Conyers,L.B. & Goodman,D. 1997.
Ground penetrating radar, an introduction for archeologists. Altimira Press, Walnut Creek, CA. ISBN 0-7619-8928-5

Corbeanau,R.M., Soegaard,K., Szerbiak,R.B., Thurmond, J.B., McMechan,G.A., Wang. D., Snelgrove, S., Forster, C.B., and Menitove, A. 2001.
Detailed internal architecture of a fluvial channed sandstone determined from outcrop, cores, and 3-D ground penetrating radar: Example from the Cretaceous Ferron Sandstone member, east central Utah. *AAPG Bulletin* Vol. 85, No. 9 1583-1608

Corbeanau,R.M., McMechan,G.A., Szerbiak,R.B., and Soegaard,K. 2002.
Prediction of 3D fluid permeability and mudstone distributions from ground penetrating radar (GPR) attributes: Example from the Cretaceous Ferron Sandstone member, east central Utah. *Geophysics* Vol. 67, No. 5 1495-1504

Craig, R.F. 1983.
Chapter 1.5 Phase relationships. In *Soil Mechanics. 4th edition.* Van Nostrand Reinhold (UK). Pp. 22-27.

Dade,W.B. 2000.
Grain size, sediment transport and alluvial channel pattern. *Geomorphology* 35 (2000) pp. 199-126 Elsevier Science BV.

Davis,J.L., and Annan,A.P. 1989.
Ground penetrating radar for high resolution mapping of soil and rock stratigraphy. *Geophysical Prospecting.* Vol.37, 531-551

DeVos,W, Verniers,J., Herbosch,A., Vanguestaine, M. 1993.
A new geological map of the Brabant Massif, Belgium. *Geology Magazine.* 130 (5), 1993 pp. 605-611 Cambridge University Press.

Dominico,P.A. & Schwartz,F.W. 1997.
Physical and chemical hydrogeology. 2nd Ed. John Wiley & Sons New York, NY.

ISBN 0-471-59762-7

Downing, R.A., 1998.
Groundwater, our hidden asset, Natural Environment Resource Council.

Deurer, M., Green, S.R., Clothier, B.E., Böttcher, J., Duijnisveld, W.H.M. 2003.
Drainage networks in soils. A concept to describe bypass-flow pathways. *Journal of Hydrology*. Vo. 272. pp. 148-162.

Edmunds,W.M. & Smedley,P.L. 1992.
The East Midlands Triassic Aquifer: hydrogeochemical evolution 1975-1992
British Geological Survey Technical Report WD/92/23R Hydrogeology Series.

Environment Agency. 1998.
The Environment of England and Wales, a Snapshot. Environment Agency, Bristol.

Evans,D.J., Rees,J.G. and Holloway,S. 1993.
The Permian to Jurassic stratigraphy and structural evolution of the central Cheshire Basin. Journal of the Geological Society of London. Vol. 150. Part 5. Pp.857-870.

Evett, S.R., and Steiner, J.L. 1995.
Precision of neutron scattering and capacitance type soil water gauges from field calibration. *Soil Science of America Journal*. Vol.59 No.4, 961-968

Ferré, P.A., Rudolph, D.L., 1998.
The use of time domain reflectometry for vertically profiling the water content through the unsaturated zone. In: *Proc. Symp. Applications of Geophysics to Engineering and Environmental Problems (SAGEEP1998),*
Environmental and Engineering Geophysical Society, Denver, CO.

Ferré, P.A., Rudolph, D.L., and Kachanoiski, R.G. 1998.
Water content response of a profiling time domain reflectometry probe. *Journal of the Soil Science Society of America*, Vol 62:865-873.

Finch, J.W. 1998.
Estimating direct groundwater recharge using a simple water balance model - sensitivity to land surface parameters. *Journal of Hydrology*, Vol. 211. pp112-125.

Ford, M. & Tellam, J.H. 1994.
Source, Type and Extent of inorganic contamination within the Birmingham urban aquifer system, UK. *Journal of Hydrology* Vol. 156. pp. 101-135
Elsevier Science B.V.

Freeze, R.A., and Cherry, J.A. 1979. *Groundwater*. Prentice Hall

Gaunt, G.D. 1994.
Geology of the country around Goole, Doncaster and the Isle of Axholme. Memoir for one-inch sheets 79 and 88 (England and Wales).
British Geological Survey
HMSO, London.

Geological Survey of Canada. 2003.
Natural gamma logging. *In Website of the Geological Survey of Canada.* http://borehole.gsc.nrcan.gc.ca/gamma_e.html. – accessed 19/10/2003

Glennie, K.W. 1998.
Petroleum Geology of the North Sea, 4th Edition. Blackwell Science Ltd, Oxford. ISBN 0 632 03845 4

Gloaguen, E., Choteau, M., Marcotte, D., and Chapuis, R. 2001.
Estimation of hydraulic conductivity of an unconfined aquifer using cokriging of GPR and hydrostratigraphic data. *Applied Geophysics.* Vol. 47. pp. 135-152.

Goodman D. 1994.
Ground-penetrating radar simulation in engineering and archaeology *Geophysics,* vol 59-2, p224-232

Greacen,E.L. 1981 .
Introduction *in* Greacen, E.L. (Editor). *Soil water assessment by the neutron method.* CSIRO., 1-2

Hammon,W.S.III., Zeng,X.,Corbeanu,R.M., and McMechan. 2002
Estimation of the spatial distribution of fluid permeability from surface and tomographic GPR data and core, with a 2D example from the Ferron Sandstone, Utah. *Geophysics.* Vol 67, No. 5 1505-1515.

Harris,R.C., and Lowe,D.R. 1984.
Changes in the organic fraction of leachate from two domestic refuse sites on the Sherwood Sandstone, Nottinghamshire. *Quarterly Journal of Engineering Geology.* Vol 17. pp, 57-69

Hawkins, T.R.W. and Chadha, D.S. 1990.
Locating the Sherwood Sandstone Aquifer with the aid of resistivity surveying in the Vale of York. *Quarterly Journal of Engineering Geology.* Vol 23. pp, 229-241

Hokett,S.L., Chapman,J.B., and Russell,C.E. 1992.
Potential use of time domain reflectometry for measuring water content in rock. *Journal of Hydrology,* 138, 89-96.

Huang,F., Dowding,C.H. 1994.
Telemetric and multiplexing enhancement of TDR measurements. In: *Proc. Symp. International Symposium and Workshop on Time Domain Reflectometry for Innovative Geotechnical Applications (TDR 1994),* Infrastructure Technology Institute, Evanston, Il.

Huisman,J.A., Weerts,A.H., Heimovaara,T.J., and Bouten,W., 2002.
Comparison of travel time analysis and inverse modelling for soil water content determination with time domain reflectometry. *Water Resources Research,* Vol 38, No 6, 10.1029/2001WR000259

Huggenberger,P., and Aigner,T. 1999.
Introduction to the special issue on aquifer sedimentology: problems, perspectives and modern approaches. *Sedimentary Geology.* Vol. 129, pp. 179-186.

Huggenberger, P., 1993.
Radar facies: recognition of facies patterns and heterogeneities within Pleistocene Rhine Gravels, NE Switzerland. In: Best, J.L., and Bristow, C.S., (eds), *Braided Rivers, Geological Society Special Publication no. 75,* pp 13-71.

Interpex. 1997.
Gradix V1 Manual. Ground penetrating radar processing and interpretation., Interpex Limited, Golden, Colorado.

Jackson, D. I., and Mulholland, P. 1993.
Tectonic and stratigraphic aspects of the East Irish Sea Basin and adjacent areas: contrasts in their post-Carboniferous structural styles. *In* Parker, J. R. (Ed.) *Petroleum Geology of North West Europe, Proceedings of the 4th Conference.* Geological Society, London, pp 791-808.

Jol.H.M. 1995.
Ground penetrating antennae frequencies and transmission powers compared for penetration depth, resolution and reflection continuity. *Geophysical Prospecting.* Vol.43, No. 5, 693-709

Jol, H.M., Lawton, D.C., and Smith, D.G. 2002.
Ground penetrating radar: 2-D and 3-D subsurface imaging of a coastal barrier spit, Long Beach, WA, USA. *Geomorphology.* Vol. 53. pp. 165-181

Jones,S.B., Wraith,J.M., Or,D. 2002.
Time domain reflectometry measurement principles and applications. *Hydrol. Process*. 16, 141-153.

Keary, P. and Brooks, M., 1991.
An Introduction to Geophysical Exploration, Blackwell Science.

Kimblin,R.T. 1995.
The chemistry and origin of groundwater in Triassic sandstone and Quaternary deposits, northwest England and some UK comparisons. *Journal of Hydrology* 172 (1995) 293-311 Elsevier Science B.V..

Knight,J.H. 1992.
Sensitivity of time domain reflectometry measurements to lateral variations in soil water content. *Water Resour. Res*. 28, 2345-2352

Koukis, G. 1974.
Physical, mechanical and chemical properties of the Triassic Sandstone Aquifer of the Vale of York. Unpublished PhD thesis, University of Leeds.

Kraus,J.D.,1984.
Electromagnetics. 3rd ed. McGraw Hill. New York.

Lake,R.D. 1999.
The Wakefield District- a concise account of the geology. Memoir of the British Geological Survey, Sheet 78 (England and Wales). The Stationery Office, London. ISBN 0 11 884554 3

Larossa Rodriguez,C.G., da Cunha Neto,J.A.B., and Prata,A.T. 1999.
Using time domain reflectometry to measure moisture content discontinuity of an artificial soil. *Journal of Experimental Thermal and Fluid Scie*nce. Vol 20., 25-33

Leddy,J.O., Ashworth,P.J., and Best,J.L. 1993.
Mechanisms of anabranch avulsion within gravel bed braided rivers: observations from a scaled physical model. In *Braided Rivers (Eds. Best,J.L., and Bristow,C.S.).* Geological Society Special Publication No. 75., Geological Society, London pp119-127.

Ledieu, J., De Ridder, P., De Clerck, P., and Dautrebande, S. 1986.
A method of measuring soil moisture by time-domain reflectometry. *Journal of Hydrology.* Vol.88. pp. 319-328.

Lewin. K, Young.C, Sims.P,Blakey,N. Oakes,D. Reynolds,P. & Bradshaw,K. 1996
Long-term monitoring of non-contained landfills: Burntstump and Gorsethorpe on the Sherwood Sandstone. Final Report to the Department of the Environment. Report No: DoE 4130/1 DoE Report No. CWM 138/96. Department of the Environment.

Malicki, M.A., Plagge, R and Roth, C. H. 1996.
Improving the calibration of dielectric TDR soil moisture determination taking into account the solid soil. *European Journal of Soil Science.* Vol. 47. pp357-366.

Marheshwarla, S.V., Venkatasubramanian,R., Boehm.R.F. 1995.
Comparison of time domain reflectometry performance factors for several dielectric geometries: Theory and experiments. *Water Resources Research.* Vol 31 No.8., pp1927-1933

Marshall, J.D. 2000.
Sedimentology of a Devonian fault-bounded braidplain and lacustrine fill in the lower part of the Skrinkle Sandstones, Dyfed, Wales. *Sedimentology,* Vol. 47. 325-342.

Moreton,D.J., Ashworth,P.J., and Best,L.J. 2002.
The physical scale modelling of braided alluvial architecture and estimation of subsurface permeability. *Basin Research.* Vol. 14, pp. 265-285.

Morozova,G.S., & Smith,N.D. 2000.
Holocene avulsion styles and sedimentation patterns of the Saskatchewan River, Cumberland Marshes, Canada. *Sedimentary Geology* 130 (2000) pp.81-105 Elsevier Science.

Murray, T., Gooch, D. L., and Stuart, G. W. 1997.
Structures within the surge front at Bakaninbreen, Svalbard, using Ground – penetrating radar. *Annals of Glaciology,* Vol. 24. International Glaciological Society.

Nirex Report SA/97/023, 1997.
Sellafield Geological and Hydrogeological Investigations. Sedimentology and sedimentary architecture of the St Bees Sandstone Formation in West Cumbria. United Kingdom Nirex Limited.

Nissen,H.H., Moldrup,P., de Jonge,W., and Jacobsen,O.H. 1999.
Time domain reflectometry coil probe measurements of water content during fingered flow. *Soil Sci. Soc. Am. J.* 63:493-500

Page,K.J., Nanson,G.C., and Frazier,P.S. 2003
Floodplain formation and sediment stratigraphy resulting from oblique accretion on the Murrumbidgee River, Australia. *J. Sedimentary Research* Vol. 73 No. 1, pp 5-14

Pay, M.D., Astin,T.R., and Parker,A. 2000.
Clay mineral distribution in the Devonian-Carboniferous sandstones of the Clair Field, west of Shetland, and its significance for reservoir quality. *Clay Minerals.* Vol. 35, pp. 151-162.

Persson,M., and Berndtsson,R., 1988.
Noninvasive water content and electrical conductivity laboratory measurements using time domain reflectometry. *Soil Science Journal of America.* Vol.62:1471-1476.

Persson,M., and Berndtsson,R. 1997.
Estimating transport parameters in an undisturbed soil column using time domain reflectometry and transfer function theory. *Journal of Hydrology* Vol.205, 232-247

Pettijohn,F.J. 1957.
Sedimentary Rocks. Second edition. Harper & Row, New York.

Pharaoh,T.C., Molyneux,S.G., Merriman,R.J., Lee,M.K., Verniers,J. 1993.
The Caledonides of the Anglo-Brabant Massif reviewed. Geology Magazine. 130 (5), 1993 pp. 561-562 Cambridge University Press.

Pokar, M. 2002.
Investigation of the unsaturated zone in the Sherwood Sandstone using petrophysical and geophysical monitoring methods. Unpublished PhD thesis, University of Leeds.

Pokar, M., West, L.J., Odling, N.E. 2003.
Petrophysical characterisation of the Sherwood Sandstone from East Yorkshire. In: *The Permo-Triassic Sandstones* (Eds. R.Barker and J. Tellam), Special Publication of the Geological Society of London.

Ramingwong, T., 1974.
Hydrogeology of the Keuper sandstone in the Droitwich syncline area – Worcestershire. Unpublished PhD thesis, University of Birmingham.

Reynolds,J.M. 1997.
An introduction to applied and environmental geophysics John Wiley & Sons Chichester, W. Sussex ISBN 0-471-95555-8

Rizzi,P.A. 1988.
Microwave Engineering Passive Circuits. Chapter 3 Transmission Line Theory. Prentice Hall International.

Robinson,D.A., Gardner,C.M.K., Cooper,J.D. 1999.
Measurement of relative permittivity in sandy soils using TDR, capacitance and theta probes, comparison, including the effects of bulk soil electrical conductivity. *Journal of Hydrology* 223, 198-211

Roth, K., Schulin,R., Fluehler, H., Attinger, W. 1990.
Calibration of time domain reflectometry for water content measurement using a composite dielectric approach. *Water Resources Research.* Vol.26, no.10, pp.2267-2273.

Ruffell,A.U., Shelton,R. 1999.
The control of sedimentary facies by climate during phases of crustal extension: examples from the Triassic of onshore and offshore England and Ireland. *Journal of the Geological Society*. Vol.156, No.Pt4, pp.779-789. IS: 0016-7649

Sakaki,T., Sugihara,K., Adachi,T, Nishida,K and Lin,W. 1998.
Application of time domain reflectometry to determination of volumetric water content in rock. *Water Resources Research,* 34, 2623-2631.

Sandberg, S.K., Slater, L.D., and Versteeg. R. 2002.
An integrated geophysical investigation into the hydrogeology of an anisotropic unconfined aquifer. *Journal of Hydrology*. Vol. 267. Pp. 227-243.

Schmidt.V., and McDonald,D.A., 1979a.
The role of secondary porosity in sandstones. In, Scholle,P.A., and Schluger,P.R. (eds.) *Aspects of Diagenesis*. SEPM Special Publication 26 pp. 209-225.

Schmidt.V., and McDonald,D.A., 1979b.
Texture and recognition of secondary porosity in sandstones. In, Scholle,P.A., and Schluger,P.R. (eds.) *Aspects of Diagenesis*. SEPM Special Publication 26 pp. 209-225.

Selker, J.S., Graff,L., and Steenhuis,T. 1993.
Noninvasive time domain reflectometry moisture measurement probe. *Soil Sci. Soc. Am. J.* 57:934-936

Skelly, R.A., Bristow, C.S., and Ethridge, F.G. 2003.
Architecture of channel belt deposits in an aggrading shallow sandbed braided river: the lower Niobrara River, northeast Nebraska. *Sedimentary Geology*. Vol. 158. Pp249-270.

Stacheder, M., Fundinger, R., Koehler,K. 1994.
A new Time Domain Reflectometry System (TRIME) to measure soil moisture and electrical conductivity. In: *Symposium and workshop on Time domain reflectometry in environmental, infrastructure, and mining applications.* Special Publication - United States. Bureau of Mines, Report: SP 19-94, pp.56-65.

Stacheder, M., Koehler, K. and Fundinger, R., 2000
New Time Domain Reflectometry sensors for water content determination in porous media. In: (Editors) Baltes, H., Göpel, W and Hesse, J. *Sensors update Vol. 7, Special topics, RF and microwave sensing of moist materials, food and other dielectrics.* Wiley-VCH Verlag GmbH, Weinheim.

Szerbiak, R.B., McMechan, G.A., Corbeanu, R., Forster,C., and Snelgrove, S.H. 2002.
3-D characterization of a clastic reservoir analog: From 3-D GPR data to a 3-D fluid permeability model. *Geophysics*, Vol. 66 No. 4. pp. 1026-1037.

The Open University. 1995.

S236 Geology Block 6, Historical Geology Revised edition, 1995 The Open University, Milton Keynes. ISBN 0 7492 5198 0

Thorne, C.R., Russell, A.P.G., and Alam,M.K. 1993.
Planform pattern and channel evolution of the Bramaputra River, Bangladesh. In *Braided Rivers (Eds. Best,J.L., and Bristow,C.S.).* Geological Society Special Publication No. 75., Geological Society, London. pp. 257-276.

Topp,G.C., J.L.Davis and Annan,A.P. 1980.
Electromagnetic determination of soil water content: Measurement in coaxial transmission lines. *Water Resour. Res.* 16(3), 574-582.

Truss,S.W., West,L.J., Winship,P., Nakhkash,M., Huang,Y. 2001.
A time domain reflectometry packer for use in rock. in Proc. *The second international symposium and workshop on Time Domain Reflectometry for geotechnical applications.* Infrastructure Research Institute Evanston, Il.
ISBN 0-9712631-0-8

Tucker,M.E. 1991.
Sedimentary Petrology, an introduction to the origin of sedimentary rocks Second edition Blackwell Science, Oxford. ISBN 0 632 02961 7

United Nations, 2003.
Agenda 21, Chapter 18, Protection of the quality and supply of freshwater resources: Application of integrated approaches to the development, management and use of water resources. Johannesburg Earth Summit, United Nations.

Van Dam,R.L., and Schlager,W. 2000.
Identifying causes of ground penetrating radar reflections using time domain reflectometry and sedimentological analyses. *Sedimentology*, Vol. 47, 435-449.

van Genuchten, M.T., 1980, A closed-form equation for predicting the hydraulic conductivity of unsaturated soils, Soil Science Society of America Journal, Volume 44: Madison, Soil Science Society of America, p. 892-898.

van Overmeeren, R.A. 1998.
Radar facies of unconsolidated sediments in the Netherlands: A radar stratigraphy interpretation method for hydrogeology. *J. Applied Geophysics*, 40 1-18.

Van Overmeeren, R.A., Gehrels, J.C., and Sariowan, S.V. 1997
Ground penetrating radar for determining volumetric soil water content: Results of comparative measurements at two test sites. *J. Hydrology*. Vol. 197. pp.316-338

Vercoutere,C and Van Den Haute,P. 1993.
Post Palaeozoic cooling and uplift of the Brabant Massif as revealed by apatite fission track analysis. *Geology Magazine*. 130 (5), 1993, pp.639-646
Cambridge University Press.

Walker R.G. 1992.
Facies, facies models and modern stratigraphic concepts. *In.* Walker, R.G and James,N.P (eds.), *Facies Models, response to sea level change.* Geological Association of Canada.

Walker,T.R.,Waugh,B., and Crone,A.J. 1978.
Diagenesis in first cycle desert alluvium of Cenozoic age, southwestern United States and northwestern Mexico. *Geological Society of America Bulletin* v.89, p. 19-32, Doc. No. 80102, January 1978.

Waugh,B., and McD.Whitaker, J.H., 1982.
Sandstone Diagenesis. *Joint Association for Petroleum Exploration Courses (UK) (JAPEC). Course Notes No.10., University of Leicester, 5-7 July, 1982.*

Wealthall,G.P., Steele,A., Bloomfield,J.P., Moss,R.H., and Lerner,D.N. 2001
Sediment filled fractures in the Permo-Triassic sandstones of the Cheshire Basin: observations and implications for pollutant transport. *Journal of Contaminant Hydrology* Vol.50, 41-51

West,L.J., Huang, Y. and Handley, K. 2001.
Dependence of sandstone dielectric behaviour on moisture content and lithology. In: *Proc. Symp. Applications of Geophysics to Engineering and Environmental Problems (SAGEEP2001)* Environmental and Engineering Geophysical Society Denver, CO. (GTD-5).

West,L.J., Handley, K., Huang, Y., and Pokar, M. 2003.
Radar frequency dielectric dispersion in sandstone: Implications for determination of moisture and clay content. *Water Resources Research*, Vol 39, No.2, 1026, doi:10.1029/2001WR000923.

Whittaker,A. 1985.
Atlas of onshore sedimentary basins in England and Wales. Blackie, Glasgow and London.

Williams,J., Holmes,J.W., Williams,B.G., and Winkworth,R.E. 1981.
Application in agriculture, forestry and environmental science *in* Greacen, E.L. (Editor). *Soil water assessment by the neutron method.* CSIRO., 3-15

Willis,B.J., and White,C.D. 2000
Quantitative outcrop data for flow simulation. *Journal of Sedimentary Research.* Vol. 70 No. 4 pp.788-802

Woodward, J., Ashworth, P.J., Best, J.L., Sambrook Smith, G.H., and Simpson, C.J. 2003.
The use and application of ground penetrating radar in sandy fluvial environments: methodological considerations, *in* Bristow, C.S., and Jol, H., eds, *Ground Penetrating Radar in Sediments*: Geological Society of London, Special Publication 211.

Wraith,J.M., Das,B.S. 1998.
Monitoring soil water and ionic solute distributions using time-domain reflectometry. *Soil & Tillage Research* 47, 145-150

Yates,P.G.J. 1992.
The material strength of sandstones of the Sherwood Sandstone Group of North Staffordshire with reference to microfabric. *The Quarterly Journal of Engineering Geology.* Vol.25. No. 2 pp. 107-113.

Yoshida, K. 2000. *Groundwater vulnerability of the Triassic Sandstone Aquifer in the Selby area, North Yorkshire*, Unpublished PhD thesis, University of Leeds.

Yoshida, K., West, L.J., and Bottrell, S.H. 2003.
Groundwater flow modelling of the Selby area of the Triassic Sandstone Aquifer, Yorkshire, UK. In: *The Permo-Triassic Sandstones* (Eds. R.Barker and J. Tellam), Special Publication of the Geological Society. London.

Young,R.A. & Sun,J., 1999.
Revealing stratigraphy in ground penetrating radar using domain filtering. *Geophysics*, Vol 64, No 2 (March-April,) pp435-442.

Appendix 1. Details of radar lines.

NAME	BEARING	FREQUENCY (MHZ)	ANTENNA SEPARATION (M)	STEP (M)	COMMENTS
HECK01(+1A)	214	50	1	0.5	COLLECTED ACROSS GRASSY TEST AREA.
HECK02	214	200	1	0.1	AS HECK01 BUT FREQUENCY CHANGED TO 200MHZ
HECK 02A	214	200	1	0.1	HECK 02 STOPPED AT 20M, CONTINUED AS HECK02A
HECK200C	214	200	CMP	0.2	CMP ON LINE HECK 01
HECK03	S>N	200	1	0.1	CROSSES LINES 01& 02 AT 20M MARK
HEC 227A	N>S	100	1	0.2	
HEC 227B	S>N	100	2	0.2	
HEC227CP	CMP	100	CMP	0.2	CMP ALONG LINE 227A & 227B
HEC227C	E>W	100	1	0.2	
HEC227D	N>S	100	1	0.2	BEARING 200 DEGREES.
HEC237A	N>S	100	1	0.2	BEARING 204DEGREES, LONG QUARRY LINE.
HEC237B	N>S	100	1	0.2	MISSING SECTION FROM HEC 237A
VELOCITY PROFILING (ANTENNAE DOWN CLIFF FACE).					
HECV1	VERTICAL	200	N/A	0.1	XMTR ON QRY TOP, RCVR DOWN FACE
HECV2	VERTICAL	200	N/A	0.1	XMTR ON QRY TOP, RCVR DOWN FACE
HECV3	VERTICAL	200	N/A	0.1	XMTR ON QRY TOP, RCVR DOWN FACE
HECV4	VERTICAL	200	N/A	0.1	XMTR ON QRY TOP, RCVR DOWN FACE
RADAR GRID					1/2M BETWEEN LINES.
HEKGD_V	N>S	200	1	0.2	FURTHEST EAST LINE
HEKGD_U	N>S	200	1	0.2	0.5M WEST OF LINE ABOVE
HEKGD_T	N>S	200	1	0.2	
HEKGD_S	N>S	200	1	0.2	
HEKGD_R	N>S	200	1	0.2	
HEKGD_Q	N>S	200	1	0.2	REDONE, XMTR BAT FLAT
HEKGD_P	N>S	200	1	0.2	
HEKGD_O	N>S	200	1	0.2	VAN MOVED AWAY
HEKGD_N	N>S	200	1	0.2	BOX+VAN MOVED. HYPERBOLA @ 16M=VAN
HEKGD_M	N>S	200	1	0.2	
HEKGD_L	N>S	200	1	0.2	
HEKGD_K	N>S	200	1	0.2	
HEKGD_J	N>S	200	1	0.2	
HEKGD_I	N>S	200	1	0.2	

HEKGD_H	N>S	200	1	0.2	
HEKGD_G	N>S	200	1	0.2	
HEKGD_F	N>S	200	1	0.2	
HEKGD_E	N>S	200	1	0.2	
HEKGD_D	N>S	200	1	0.2	
HEKGD_C	N>S	200	1	0.2	
HEKGD_B	N>S	200	1	0.2	
HEKGD_A	N>S	200	1	0.2	
HEKGD_AA	N>S	200	1	0.2	LINE OF BOREHOLES
HEKGD_1	N>S	200	1	0.2	
HEKGD_2	N>S	200	1	0.2	
HEKGD_3	N>S	200	1	0.2	
HEKGD_4	N>S	200	1	0.2	
HEKGD_5	N>S	200	1	0.2	
HEKGD_6	N>S	200	1	0.2	
HEKGD_7	N>S	200	1	0.2	
HEKGD_8	N>S	200	1	0.2	
HEKGD_9	N>S	200	1	0.2	
HEKGD_10	N>S	200	1	0.2	
HEKGD_11	N>S	200	1	0.2	
HEKGD_12	N>S	200	1	0.2	
HEKGD_13	N>S	200	1	0.2	
HEKGD_14	N>S	200	1	0.2	
HEKGD_15	N>S	200	1	0.2	
HEKGD_16	N>S	200	1	0.2	
HEKGD_17	N>S	200	1	0.2	
HEKGD_18	N>S	200	1	0.2	
HEKGD_19	N>S	200	1	0.2	
HEKGD_20	N>S	200	1	0.2	
HEKGD_21	N>S	200	1	0.2	
HEKGD_22	N>S	200	1	0.2	
WEST>EAST GRID (OVER BOREHOLE LOCATIONS)					
HEKG2_A	W>E	200	1	0.2	CROSSES B/H 4 RUNS 5.5M FROM N>S GRID START
HEKG2_B	W>E	200	1	0.2	CROSSES B/H 3 RUNS 10.5M FROM N>S GRID START
HEKG2_C	W>E	200	1	0.2	CROSSES B/H 2,5,6 RUNS 15.5M FROM N>S GRID START
HECG2_D	W>E	200	1	0.2	CROSSES B/H 1 RUNS 20.5M FROM N>S GRID START
RADAR LINE ON TEMP BENCH					
HEK3009A	N>S	200	1	0.1	LINE 2-3M IN FROM FACE
RADAR LINE ABOVE HECK SEDIMENTARY LOGS					
HEC 12902	N>S	200	1	0.2	LINE 1-3M IN FROM FACE
HEC1292B	N>S	200	1	0.2	LINE 1-3M IN FROM FACE

Appendix 1 Table 1. Great Heck radar lines.

NAME	BEARING	FREQUENCY (MHZ)	ANTENNA SEPARATION (M)	STEP (M)	COMMENTS
RADAR GRID 2					
HAT 0406A	S>N	50	2	0.2	1M SPACING BETWEEN LINES
HAT 0406B	S>N	50	2	0.2	1M TO EAST OF LINE ABOVE
HAT 0406C	S>N	50	2	0.2	1M TO EAST OF LINE ABOVE
HAT 0406D	S>N	50	2	0.2	1M TO EAST OF LINE ABOVE
HAT 0406E	S>N	50	2	0.2	1M TO EAST OF LINE ABOVE
HAT 0406F	S>N	50	2	0.2	1M TO EAST OF LINE ABOVE
HAT 0406G	S>N	50	2	0.2	1M TO EAST OF LINE ABOVE
HAT 0406H	S>N	50	2	0.2	1M TO EAST OF LINE ABOVE
HAT 0406I	S>N	50	2	0.2	1M TO EAST OF LINE ABOVE
HAT 0406J	S>N	50	2	0.2	1M TO EAST OF LINE ABOVE
HAT 0406K	S>N	50	2	0.2	1M TO EAST OF LINE ABOVE
HAT 04061	W>E	50	2	0.2	1M SPACING BETWEEN LINES
HAT 04062	W>E	50	2	0.2	1M TO NORTH OF LINE ABOVE
HAT 04053	W>E	50	2	0.2	1M TO NORTH OF LINE ABOVE
HAT 04064	W>E	50	2	0.2	1M TO NORTH OF LINE ABOVE
HAT 04065	W>E	50	2	0.2	1M TO NORTH OF LINE ABOVE
HAT 04066	W>E	50	2	0.2	1M TO NORTH OF LINE ABOVE
HAT 04067	W>E	50	2	0.2	1M TO NORTH OF LINE ABOVE
HAT 0306A	W>E	50	2	0.5	QUARRY LONG LINE 2 PARALLEL TO Q201
HAT 0306B	S>N	200	1	0.2	BOTTOM OF QUARRY BENCH NEAR GRID 2
HAT 0306C					
HAT 0306D					
HATFLD01		50			LINE USELESS DUE TO SCATTERING
HATFLD02		50			LINE USELESS DUE TO SCATTERING
HATFLD03		50			LINE USELESS DUE TO SCATTERING
HATGDA01	E>W	50	1	0.5	HATFIELD SITE GRID NORTHERNMOST LINE
HATGDA02	E>W	50	1	0.5	2M SOUTH OF LINE ABOVE. LINE USELESS DUE TO SCATTERING
HATGDA03	E>W	50	1	0.5	AS ABOVE
HATGDA04	E>W	50	1	0.5	AS ABOVE
HATGDA05	E>W	50	1	0.5	AS ABOVE
HATGDA06	E>W	50	1	0.5	AS ABOVE
HATGRA07	E>W	50	1	0.5	AS ABOVE
HATGDA08	E>W	50	1	0.5	AS ABOVE
HATGDA09	E>W	50	1	0.5	AS ABOVE
HATGRA10	E>W	50	1	0.5	AS ABOVE
HATGDA11	E>W	50	1	0.5	AS ABOVE
HATLN04		200			HAT SITE LINES
HATLN05		200			LINE USELESS DUE TO SCATTERING

HATLN06		50			LINE USELESS DUE TO SCATTERING
HATFIELD QUARRY GRID 1. 1M SEPARATION BETWEEN LINES, GRID ORDER N>S					
HATQ001	W>E	100	1	0.1	NORTHERNMOST LINE
HATQ102	W>E	100	1	0.1	1M SOUTH OF LINE ABOVE
HATQ103	W>E	100	1	0.1	1M SOUTH OF LINE ABOVE
HATQ104	W>E	100	1	0.1	1M SOUTH OF LINE ABOVE
HATQ105	W>E	100	1	0.1	1M SOUTH OF LINE ABOVE
HATQ106	W>E	100	1	0.1	1M SOUTH OF LINE ABOVE
HATQ107	W>E	100	1	0.1	1M SOUTH OF LINE ABOVE
HATQ108	W>E	100	1	0.1	1M SOUTH OF LINE ABOVE
HATQ109	W>E	100	1	0.1	1M SOUTH OF LINE ABOVE
HATQ110	W>E	100	1	0.1	1M SOUTH OF LINE ABOVE
HATQ111	W>E	100	1	0.1	1M SOUTH OF LINE ABOVE
HATQ112	W>E	100	1	0.1	1M SOUTH OF LINE ABOVE
HATQ113	W>E	100	1	0.1	1M SOUTH OF LINE ABOVE
HATQ114	W>E	100	1	0.1	1M SOUTH OF LINE ABOVE
HATQ115	W>E	100	1	0.1	1M SOUTH OF LINE ABOVE
HATQ116	W>E	100	1	0.1	1M SOUTH OF LINE ABOVE
HATQ201	W>E	50	1	0.5	HATFIELD LONG LINE BEHIND FACE

Appendix 1 Table 2, Hatfield radar lines.

NAME	BEARING	FREQUENCY (MHZ)	ANTENNA SEPARATION (M)	STEP (M)	COMMENTS
POLLINGTON, ALL LINES PARALLEL TO FACE					
POLL01	E-W	200	0.5	0.1	1.5-2M BEHIND FACE (ON CLIFF)
POLL02	E-W	200	0.5	0.1	1M BEHIND FACE (ON CLIFF)
POLL03A	E-W	100	1.0	0.2	15M BEHIND FACE
POLL03B	E-W	200	CMP	0.2	15M BEHIND FACE
RUFFORD, ALL LINES PARALLEL TO FACE					
RUFF01A	210^0	200	1.0	0.2	3M BEHIND FACE
RUFF02A	30^0	200	1.0	0.2	28M BEHIND FACE
RUFFCMP	30^0	200	CMP	0.2	ALONG LINE RUFF 02A

Appendix 1 Table 3. Pollington and Rufford radar lines.

Appendix 2. TDR reflection theory.

The physics behind why TDR reflections occur is fairly basic, being governed mainly by Ohm's Law. This physics is discussed by Rizzi (1988). In its simplest terms, if a voltage pulse such as that generated by the TDR unit is applied to an open circuit in a wire with resistance (impedance) R, the voltage pulse travelling down the wire will obey Ohm's Law, where V= voltage, I= amperage and R= resistance.

$V=IR$

Hence a reduced voltage pulse with an attendant current will travel down the wire (or TDR probe). When it gets to the end of the probe this pulse cannot go anywhere, the circuit is open so no current flow is possible and there is an unbalanced voltage present in the system. To satisfy Ohm's Law and balance the unbalanced voltage the wave is reflected and flows back up the wire, with an amperage identical to but exactly opposite to the initial input amperage. Hence a steady state is reached. with the sum of the reduced voltages equalling the input voltage, and the amps cancelling out to zero.

This may best be explained by examining a theoretical example (after Rizzi, 1988).

Using Ohm's Law and assuming that a 12V Battery with internal resistance R_G= 70Ω has been connected to an open circuited transmission line, with electrodes 30cm in length (L). The surge impedance of the transmission line (Z_0) (i.e. impedance when the pulse is initially sent down the circuit) is assumed to be 50Ω and the velocity of the voltage pulse is assumed to be $2x10^8 ms^{-1}$.

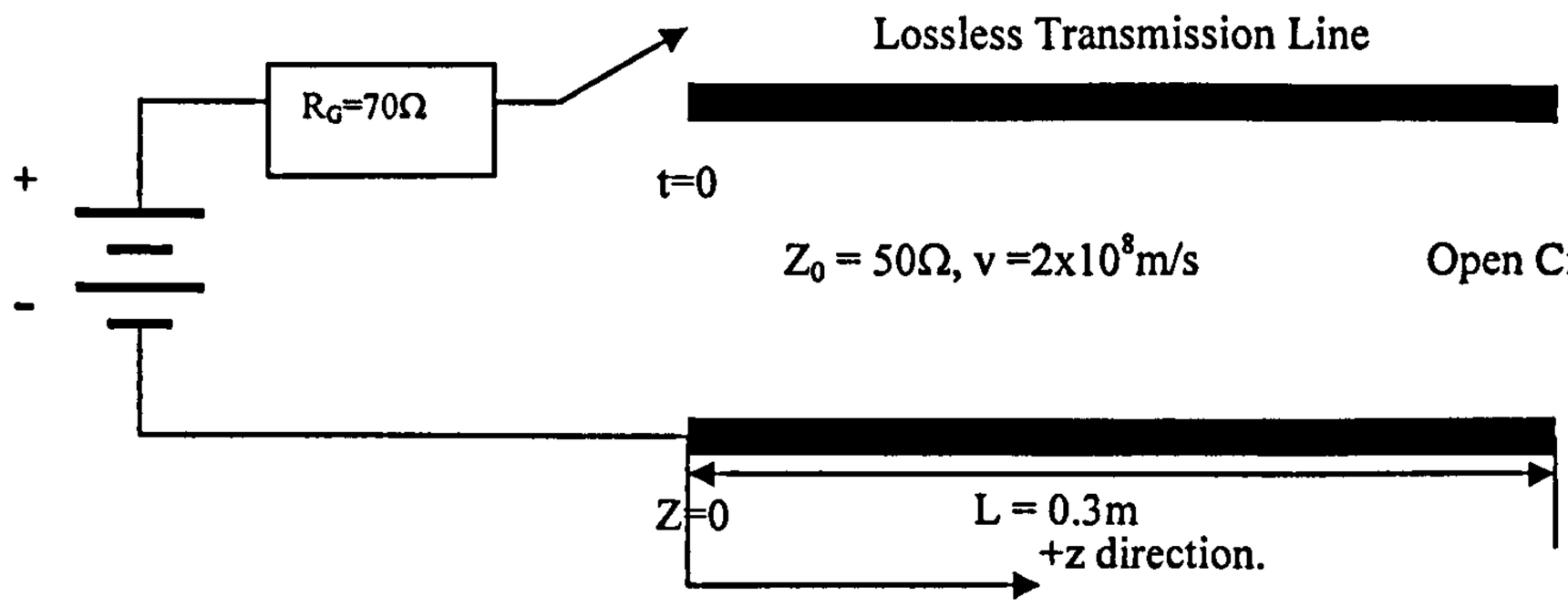

Figure A2.1, Summary of TDR circuit for calculation of theoretical reflection coefficient.

At a time immediately after the voltage pulse is released (t = 0+), the battery outputs a voltage of 12V, which is transmitted to the open circuit, but there is an impedance of 120Ω present in the system (from $R_g + Z_0$). Hence, according to Ohm's Law,

$I = V/R$, so $I = 12/120$ $(V/(Z_0 + R_g))$, hence **$I = 0.1A$**

But $V = I \times Z_0$, so $V = 50 \times 0.1$ **$V = 5V$**

So a pulse, with voltage 5V and current 0.1A travels down the open circuit at a velocity of $2x10^8 ms^{-1}$. But, when the wave reaches the open end of the circuit, two contradictory requirements exist,

1). V/I must be equal to Z_0, so 5V/0.1A must equal 50Ω, which it does.

2). As the circuit is open, impedance is essentially infinite so to obey Ohm's Law, the current must be 0.

So $I = V/R = 10/\infty = \mathbf{0A}$

The easiest way to reconcile this problem of the current and voltage being simultaneously 0.1A at 5V and 0A at 0V is to introduce a reflected wave, which travels in the opposite direction to the initial wave. This allows the imbalance to cancel out such that at z = 0.3m (open end of circuit),

$$V_{total} = V^+ + V^- \text{ and } I_{total} = I^+ - I^- = 0.$$

+ and - indicate the forward and reverse waves. Equation 6.1.3 proves that to satisfy Ohm's Law, the voltage pulse **must** be reflected from the open end of the circuit.

The reflected values of V and I may be calculated.

$I_{total} = I^+ - I^- = 0$ so $I^+ = 0.1A$ and $I^- = \mathbf{0.1A}$

$V^+ = I^+ Z^0 = 0.1 \times 50\Omega = \mathbf{5V}.$

If the reflection coefficient back at the load is defined as Γ_L,

$$\text{Then } \Gamma_L \equiv V^-/V^+ = I^-/I^+, \text{ So } \Gamma_L \textbf{ must} = +1$$

Hence, assuming infinite resistance at the electrode open tips, a reverse wave identical to the out wave reflects back up the circuit.

Multiple reflections.

In practice the system is a little more complicated. Fig 6.1.1 shows an actual TDR trace, taken in air. A reflection occurs every time the impedance of the system changes abruptly. This first jump (1) is the reflection as the pulse reaches the waveguide electrodes. The second jump (2) is the reflection from the ends of the electrodes and the time between the two jumps is used to calculate the permittivity of the surrounding material. There is a finite resistance across the ends of the electrodes because in real conditions, the electrode waveguides are in limited electrical contact. This finite resistance is a function of the material separating the electrodes and gives rise to reflection coefficients that do not equal 1. Because of this, some proportion of the TDR pulse is reflected back and forth within the TDR waveguides. Hence TDR traces exhibit multiple reflections that can be seen in Figure 6.1.1. The attenuation rate of these multiple reflections is determined by the conductivity of the soil, hence salinity of the pore-waters may also be determined using TDR.

The most important property of the reflected voltage pulse as regards moisture content determination is that the speed of the voltage pulse through the TDR probe electrodes varies with the dielectric constant of the material surrounding the probe. High dielectric constants mean slower speeds and by knowing the length of the electrodes (L) and by timing the gap between the reflected pulses from the start and end of the electrodes, the dielectric constant may be determined.

Appendix 3. Campbell Scientific CR10X program for TDR data collection at Great Heck Quarry.

```
;{CR10X}
*Table 1 Program
  01: 60.0000   Execution Interval (seconds)

1: If time is (P92)
 1: 0       Minutes (Seconds --) into a
 2: 1440      Interval (same units as
above)
 3: 30      Then Do

   2: Z=F (P30)
    1: 7      F
    2: 0      Exponent of 10
    3: 1      Z Loc [ _____ ]

   3: Do (P86)
    1: 10       Set Output Flag High
(Flag 0)

   4: Sample (P70)
    1: 1      Reps
    2: 1      Loc [ _____ ]

   5: Real Time (P77)
    1: 220          Day,Hour/Minute
(midnight = 2400)

   6: Do (P86)
    1: 10       Set Output Flag High
(Flag 0)

   7: Set Active Storage Area (P80)
    1: 1      Final Storage Area 1
    2: 1      Array ID

   8: TDR100 Measurement (P119)
    1: 0      SDM Address
    2: 1      Waveform
    3: 1101     MMMP Mux & Probe
Selection
    4: 20     Waveform Averaging
    5: 1      Vp
    6: 240     Points
    7: 22     Cable Length (meters)
    8: 5      Window Length (meters)
    9: .29    Probe Length (meters)
   10: 0      Probe Offset (meters)
   11: 3      Loc [ _____ ]
   12: 1      Mult
   13: 0      Offset

   9: TDR100 Measurement (P119)
    1: 0      SDM Address
    2: 0      La/L for Water Content
    3: 1101     MMMP Mux & Probe
Selection
    4: 20     Waveform Averaging
    5: 1      Vp
    6: 240     Points
    7: 22     Cable Length (meters)
    8: 5      Window Length (meters)
    9: .29    Probe Length (meters)
   10: 0      Probe Offset (meters)
   11: 2      Loc [ _____ ]
   12: 1      Mult
   13: 0      Offset

   10: Sample (P70)
    1: 251     Reps
    2: 1      Loc [ _____ ]

   11: Do (P86)
    1: 10       Set Output Flag High
(Flag 0)

   12: Set Active Storage Area (P80)
    1: 1      Final Storage Area 1
    2: 2      Array ID

   13: TDR100 Measurement (P119)
    1: 0      SDM Address
    2: 1      Waveform
    3: 1201     MMMP Mux & Probe
Selection
    4: 20     Waveform Averaging
    5: 1      Vp
    6: 240     Points
    7: 23     Cable Length (meters)
    8: 5      Window Length (meters)
    9: .29    Probe Length (meters)
   10: 0      Probe Offset (meters)
   11: 3      Loc [ _____ ]
   12: 1      Mult
   13: 0      Offset

   14: TDR100 Measurement (P119)
    1: 0      SDM Address
    2: 0      La/L for Water Content
    3: 1201     MMMP Mux & Probe
Selection
    4: 20     Waveform Averaging
    5: 1      Vp
    6: 240     Points
    7: 23     Cable Length (meters)
    8: 5      Window Length (meters)
    9: .29    Probe Length (meters)
   10: 0      Probe Offset (meters)
   11: 2      Loc [ _____ ]
   12: 1      Mult
   13: 0      Offset

   15: Sample (P70)
    1: 251     Reps
    2: 1      Loc [ _____ ]

   16: Do (P86)
    1: 10       Set Output Flag High
(Flag 0)

   17: Set Active Storage Area (P80)
    1: 1      Final Storage Area 1
    2: 3      Array ID

   18: TDR100 Measurement (P119)
    1: 0      SDM Address
    2: 1      Waveform
    3: 1301     MMMP Mux & Probe
Selection
    4: 20     Waveform Averaging
    5: 1      Vp
    6: 240     Points
    7: 23.5    Cable Length (meters)
    8: 5      Window Length (meters)
    9: .29    Probe Length (meters)
   10: 0      Probe Offset (meters)
   11: 3      Loc [ _____ ]
   12: 1      Mult
   13: 0      Offset

   19: TDR100 Measurement (P119)
    1: 0      SDM Address
    2: 0      La/L for Water Content
    3: 1301     MMMP Mux & Probe
Selection
    4: 20     Waveform Averaging
    5: 1      Vp
    6: 240     Points
    7: 23.5    Cable Length (meters)
    8: 5      Window Length (meters)
    9: .29    Probe Length (meters)
   10: 0      Probe Offset (meters)
   11: 2      Loc [ _____ ]
   12: 1      Mult
   13: 0      Offset

   20: Sample (P70)
    1: 251     Reps
    2: 1      Loc [ _____ ]

   21: Do (P86)
    1: 10       Set Output Flag High
(Flag 0)

   22: Set Active Storage Area (P80)
    1: 1      Final Storage Area 1
    2: 4      Array ID

   23: TDR100 Measurement (P119)
    1: 0      SDM Address
    2: 1      Waveform
    3: 1401     MMMP Mux & Probe
Selection
    4: 20     Waveform Averaging
    5: 1      Vp
    6: 240     Points
    7: 23     Cable Length (meters)
    8: 5      Window Length (meters)
    9: .29    Probe Length (meters)
   10: 0      Probe Offset (meters)
   11: 3      Loc [ _____ ]
   12: 1      Mult
   13: 0      Offset

   24: TDR100 Measurement (P119)
    1: 0      SDM Address
    2: 0      La/L for Water Content
    3: 1401     MMMP Mux & Probe
Selection
    4: 20     Waveform Averaging
    5: 1      Vp
    6: 240     Points
    7: 23     Cable Length (meters)
    8: 5      Window Length (meters)
    9: .29    Probe Length (meters)
   10: 0      Probe Offset (meters)
   11: 2      Loc [ _____ ]
   12: 1      Mult
   13: 0      Offset

   25: Sample (P70)
    1: 251     Reps
    2: 1      Loc [ _____ ]

   26: Do (P86)
```

1: 10 Set Output Flag High (Flag 0)

27: Set Active Storage Area (P80)
1: 1 Final Storage Area 1
2: 5 Array ID

28: TDR100 Measurement (P119)
1: 0 SDM Address
2: 1 Waveform
3: 1501 MMMP Mux & Probe Selection
4: 20 Waveform Averaging
5: 1 Vp
6: 240 Points
7: 25 Cable Length (meters)
8: 5 Window Length (meters)
9: .29 Probe Length (meters)
10: 0 Probe Offset (meters)
11: 3 Loc [_____]
12: 1 Mult
13: 0 Offset

29: TDR100 Measurement (P119)
1: 0 SDM Address
2: 0 La/L for Water Content
3: 1501 MMMP Mux & Probe Selection
4: 20 Waveform Averaging
5: 1 Vp
6: 240 Points
7: 25 Cable Length (meters)
8: 5 Window Length (meters)
9: .29 Probe Length (meters)
10: 0 Probe Offset (meters)
11: 2 Loc [_____]
12: 1 Mult
13: 0 Offset

30: Sample (P70)
1: 251 Reps
2: 1 Loc [_____]

31: Do (P86)
1: 10 Set Output Flag High (Flag 0)

32: Set Active Storage Area (P80)
1: 1 Final Storage Area 1
2: 6 Array ID

33: TDR100 Measurement (P119)
1: 0 SDM Address
2: 1 Waveform
3: 1601 MMMP Mux & Probe Selection
4: 20 Waveform Averaging
5: 1 Vp
6: 240 Points
7: 26 Cable Length (meters)
8: 5 Window Length (meters)
9: .29 Probe Length (meters)
10: 0 Probe Offset (meters)
11: 3 Loc [_____]
12: 1 Mult
13: 0 Offset

34: TDR100 Measurement (P119)
1: 0 SDM Address
2: 0 La/L for Water Content
3: 1601 MMMP Mux & Probe Selection
4: 20 Waveform Averaging
5: 1 Vp
6: 240 Points
7: 26 Cable Length (meters)
8: 5 Window Length (meters)
9: .29 Probe Length (meters)
10: 0 Probe Offset (meters)
11: 2 Loc [_____]
12: 1 Mult
13: 0 Offset

35: Sample (P70)
1: 251 Reps
2: 1 Loc [_____]

36: Do (P86)
1: 10 Set Output Flag High (Flag 0)

37: Set Active Storage Area (P80)
1: 1 Final Storage Area 1
2: 7 Array ID

38: TDR100 Measurement (P119)
1: 0 SDM Address
2: 1 Waveform
3: 1701 MMMP Mux & Probe Selection
4: 20 Waveform Averaging
5: 1 Vp
6: 240 Points
7: 26 Cable Length (meters)
8: 5 Window Length (meters)
9: .29 Probe Length (meters)
10: 0 Probe Offset (meters)
11: 3 Loc [_____]
12: 1 Mult
13: 0 Offset

39: TDR100 Measurement (P119)
1: 0 SDM Address
2: 0 La/L for Water Content
3: 1701 MMMP Mux & Probe Selection
4: 20 Waveform Averaging
5: 1 Vp
6: 240 Points
7: 26 Cable Length (meters)
8: 5 Window Length (meters)
9: .29 Probe Length (meters)
10: 0 Probe Offset (meters)
11: 2 Loc [_____]
12: 1 Mult
13: 0 Offset

40: Sample (P70)
1: 251 Reps
2: 1 Loc [_____]

41: Do (P86)
1: 10 Set Output Flag High (Flag 0)

42: Set Active Storage Area (P80)
1: 1 Final Storage Area 1
2: 8 Array ID

43: TDR100 Measurement (P119)
1: 0 SDM Address
2: 1 Waveform
3: 1801 MMMP Mux & Probe Selection
4: 20 Waveform Averaging
5: 1 Vp
6: 240 Points
7: 27 Cable Length (meters)
8: 5 Window Length (meters)
9: .29 Probe Length (meters)
10: 0 Probe Offset (meters)
11: 3 Loc [_____]
12: 1 Mult
13: 0 Offset

44: TDR100 Measurement (P119)
1: 0 SDM Address
2: 0 La/L for Water Content
3: 1801 MMMP Mux & Probe Selection
4: 20 Waveform Averaging
5: 1 Vp
6: 240 Points
7: 27 Cable Length (meters)
8: 5 Window Length (meters)
9: .29 Probe Length (meters)
10: 0 Probe Offset (meters)
11: 2 Loc [_____]
12: 1 Mult
13: 0 Offset

45: Sample (P70)
1: 251 Reps
2: 1 Loc [_____]

46: Do (P86)
1: 10 Set Output Flag High (Flag 0)

47: Set Active Storage Area (P80)
1: 1 Final Storage Area 1
2: 9 Array ID

48: TDR100 Measurement (P119)
1: 0 SDM Address
2: 1 Waveform
3: 2101 MMMP Mux & Probe Selection
4: 20 Waveform Averaging
5: 1 Vp
6: 240 Points
7: 27 Cable Length (meters)
8: 5 Window Length (meters)
9: .29 Probe Length (meters)
10: 0 Probe Offset (meters)
11: 3 Loc [_____]
12: 1 Mult
13: 0 Offset

49: TDR100 Measurement (P119)
1: 0 SDM Address
2: 0 La/L for Water Content
3: 2101 MMMP Mux & Probe Selection
4: 20 Waveform Averaging
5: 1 Vp
6: 240 Points
7: 27 Cable Length (meters)
8: 5 Window Length (meters)
9: .29 Probe Length (meters)
10: 0 Probe Offset (meters)
11: 2 Loc [_____]
12: 1 Mult
13: 0 Offset

50: Sample (P70)
1: 251 Reps
2: 1 Loc [_____]

51: Do (P86)
1: 10 Set Output Flag High (Flag 0)

52: Set Active Storage Area (P80)
1: 1 Final Storage Area 1

```
   2: 10      Array ID

   53: TDR100 Measurement (P119)
    1: 0      SDM Address
    2: 1      Waveform
    3: 2201      MMMP Mux & Probe
Selection
    4: 20     Waveform Averaging
    5: 1      Vp
    6: 240     Points
    7: 28     Cable Length (meters)
    8: 5      Window Length (meters)
    9: .29    Probe Length (meters)
   10: 0      Probe Offset (meters)
   11: 3      Loc [ _____ ]
   12: 1      Mult
   13: 0      Offset

   54: TDR100 Measurement (P119)
    1: 0      SDM Address
    2: 0      La/L for Water Content
    3: 2201      MMMP Mux & Probe
Selection
    4: 20     Waveform Averaging
    5: 1      Vp
    6: 240     Points
    7: 28     Cable Length (meters)
    8: 5      Window Length (meters)
    9: .29    Probe Length (meters)
   10: 0      Probe Offset (meters)
   11: 2      Loc [ _____ ]
   12: 1      Mult
   13: 0      Offset

   55: Sample (P70)
    1: 251     Reps
    2: 1       Loc [ _____ ]

   56: Do (P86)
    1: 10         Set Output Flag High
(Flag 0)

   57: Set Active Storage Area (P80)
    1: 1       Final Storage Area 1
    2: 11      Array ID

   58: TDR100 Measurement (P119)
    1: 0      SDM Address
    2: 1      Waveform
    3: 2301      MMMP Mux & Probe
Selection
    4: 20     Waveform Averaging
    5: 1      Vp
    6: 240     Points
    7: 29     Cable Length (meters)
    8: 5      Window Length (meters)
    9: .29    Probe Length (meters)
   10: 0      Probe Offset (meters)
   11: 3      Loc [ _____ ]
   12: 1      Mult
   13: 0      Offset

   59: TDR100 Measurement (P119)
    1: 0      SDM Address
    2: 0      La/L for Water Content
    3: 2301      MMMP Mux & Probe
Selection
    4: 20     Waveform Averaging
    5: 1      Vp
    6: 240     Points
    7: 29     Cable Length (meters)
    8: 5      Window Length (meters)
    9: .29    Probe Length (meters)
   10: 0      Probe Offset (meters)
   11: 2      Loc [ _____ ]
   12: 1      Mult
   13: 0      Offset

   60: Sample (P70)
    1: 251     Reps
    2: 1       Loc [ _____ ]

   61: Do (P86)
    1: 10         Set Output Flag High
(Flag 0)

   62: Set Active Storage Area (P80)
    1: 1       Final Storage Area 1
    2: 12      Array ID

   63: TDR100 Measurement (P119)
    1: 0      SDM Address
    2: 1      Waveform
    3: 2401      MMMP Mux & Probe
Selection
    4: 20     Waveform Averaging
    5: 1      Vp
    6: 240     Points
    7: 30     Cable Length (meters)
    8: 5      Window Length (meters)
    9: .29    Probe Length (meters)
   10: 0      Probe Offset (meters)
   11: 3      Loc [ _____ ]
   12: 1      Mult
   13: 0      Offset

   64: TDR100 Measurement (P119)
    1: 0      SDM Address
    2: 0      La/L for Water Content
    3: 2401      MMMP Mux & Probe
Selection
    4: 20     Waveform Averaging
    5: 1      Vp
    6: 240     Points
    7: 30     Cable Length (meters)
    8: 5      Window Length (meters)
    9: .29    Probe Length (meters)
   10: 0      Probe Offset (meters)
   11: 2      Loc [ _____ ]
   12: 1      Mult
   13: 0      Offset

   65: Sample (P70)
    1: 251     Reps
    2: 1       Loc [ _____ ]

   66: Do (P86)
    1: 10         Set Output Flag High
(Flag 0)

   67: Set Active Storage Area (P80)
    1: 1       Final Storage Area 1
    2: 13      Array ID

   68: TDR100 Measurement (P119)
    1: 0      SDM Address
    2: 1      Waveform
    3: 2501      MMMP Mux & Probe
Selection
    4: 20     Waveform Averaging
    5: 1      Vp
    6: 240     Points
    7: 31     Cable Length (meters)
    8: 5      Window Length (meters)
    9: .29    Probe Length (meters)
   10: 0      Probe Offset (meters)
   11: 3      Loc [ _____ ]
   12: 1      Mult
   13: 0      Offset

   69: TDR100 Measurement (P119)
    1: 0      SDM Address
    2: 0      La/L for Water Content
    3: 2501      MMMP Mux & Probe
Selection
    4: 20     Waveform Averaging
    5: 1      Vp
    6: 240     Points
    7: 31     Cable Length (meters)
    8: 5      Window Length (meters)
    9: .29    Probe Length (meters)
   10: 0      Probe Offset (meters)
   11: 2      Loc [ _____ ]
   12: 1      Mult
   13: 0      Offset

   70: Sample (P70)
    1: 251     Reps
    2: 1       Loc [ _____ ]

   71: Do (P86)
    1: 10         Set Output Flag High
(Flag 0)

   72: Set Active Storage Area (P80)
    1: 1       Final Storage Area 1
    2: 14      Array ID

   73: TDR100 Measurement (P119)
    1: 0      SDM Address
    2: 1      Waveform
    3: 2601      MMMP Mux & Probe
Selection
    4: 20     Waveform Averaging
    5: 1      Vp
    6: 240     Points
    7: 31     Cable Length (meters)
    8: 5      Window Length (meters)
    9: .29    Probe Length (meters)
   10: 0      Probe Offset (meters)
   11: 3      Loc [ _____ ]
   12: 1      Mult
   13: 0      Offset

   74: TDR100 Measurement (P119)
    1: 0      SDM Address
    2: 0      La/L for Water Content
    3: 2601      MMMP Mux & Probe
Selection
    4: 20     Waveform Averaging
    5: 1      Vp
    6: 240     Points
    7: 31     Cable Length (meters)
    8: 5      Window Length (meters)
    9: .29    Probe Length (meters)
   10: 0      Probe Offset (meters)
   11: 2      Loc [ _____ ]
   12: 1      Mult
   13: 0      Offset

   75: Sample (P70)
    1: 251     Reps
    2: 1       Loc [ _____ ]

   76: Do (P86)
    1: 10         Set Output Flag High
(Flag 0)

   77: Set Active Storage Area (P80)
    1: 1       Final Storage Area 1
    2: 15      Array ID

   78: TDR100 Measurement (P119)
    1: 0      SDM Address
    2: 1      Waveform
```

3: 2701 MMMP Mux & Probe Selection
4: 20 Waveform Averaging
5: 1 Vp
6: 240 Points
7: 32 Cable Length (meters)
8: 5 Window Length (meters)
9: .29 Probe Length (meters)
10: 0 Probe Offset (meters)
11: 3 Loc [_____]
12: 1 Mult
13: 0 Offset

79: TDR100 Measurement (P119)
1: 0 SDM Address
2: 0 La/L for Water Content
3: 2701 MMMP Mux & Probe Selection
4: 20 Waveform Averaging
5: 1 Vp
6: 240 Points
7: 32 Cable Length (meters)
8: 5 Window Length (meters)
9: .29 Probe Length (meters)
10: 0 Probe Offset (meters)
11: 2 Loc [_____]
12: 1 Mult
13: 0 Offset

80: Sample (P70)
1: 251 Reps
2: 1 Loc [_____]

81: Do (P86)
1: 10 Set Output Flag High (Flag 0)

82: Set Active Storage Area (P80)
1: 1 Final Storage Area 1
2: 16 Array ID

83: TDR100 Measurement (P119)
1: 0 SDM Address
2: 1 Waveform
3: 2801 MMMP Mux & Probe Selection
4: 20 Waveform Averaging
5: 1 Vp
6: 240 Points
7: 0 Cable Length (meters)
8: 5 Window Length (meters)
9: .29 Probe Length (meters)
10: 0 Probe Offset (meters)
11: 3 Loc [_____]
12: 1 Mult
13: 0 Offset

84: TDR100 Measurement (P119)
1: 0 SDM Address
2: 0 La/L for Water Content
3: 2801 MMMP Mux & Probe Selection
4: 20 Waveform Averaging
5: 1 Vp
6: 240 Points
7: 0 Cable Length (meters)
8: 5 Window Length (meters)
9: .29 Probe Length (meters)
10: 0 Probe Offset (meters)
11: 2 Loc [_____]
12: 1 Mult
13: 0 Offset

85: Sample (P70)
1: 251 Reps
2: 1 Loc [_____]

86: Do (P86)
1: 10 Set Output Flag High (Flag 0)

87: Set Active Storage Area (P80)
1: 1 Final Storage Area 1
2: 17 Array ID

88: TDR100 Measurement (P119)
1: 0 SDM Address
2: 1 Waveform
3: 3101 MMMP Mux & Probe Selection
4: 20 Waveform Averaging
5: 1 Vp
6: 240 Points
7: 27 Cable Length (meters)
8: 5 Window Length (meters)
9: .29 Probe Length (meters)
10: 0 Probe Offset (meters)
11: 3 Loc [_____]
12: 1 Mult
13: 0 Offset

89: TDR100 Measurement (P119)
1: 0 SDM Address
2: 0 La/L for Water Content
3: 3101 MMMP Mux & Probe Selection
4: 20 Waveform Averaging
5: 1 Vp
6: 240 Points
7: 27 Cable Length (meters)
8: 5 Window Length (meters)
9: .29 Probe Length (meters)
10: 0 Probe Offset (meters)
11: 2 Loc [_____]
12: 1 Mult
13: 0 Offset

90: Sample (P70)
1: 251 Reps
2: 1 Loc [_____]

91: Do (P86)
1: 10 Set Output Flag High (Flag 0)

92: Set Active Storage Area (P80)
1: 1 Final Storage Area 1
2: 18 Array ID

93: TDR100 Measurement (P119)
1: 0 SDM Address
2: 1 Waveform
3: 3201 MMMP Mux & Probe Selection
4: 20 Waveform Averaging
5: 1 Vp
6: 240 Points
7: 28 Cable Length (meters)
8: 5 Window Length (meters)
9: .29 Probe Length (meters)
10: 0 Probe Offset (meters)
11: 3 Loc [_____]
12: 1 Mult
13: 0 Offset

94: TDR100 Measurement (P119)
1: 0 SDM Address
2: 0 La/L for Water Content
3: 3201 MMMP Mux & Probe Selection
4: 20 Waveform Averaging
5: 1 Vp
6: 240 Points
7: 28 Cable Length (meters)
8: 5 Window Length (meters)
9: .29 Probe Length (meters)
10: 0 Probe Offset (meters)
11: 2 Loc [_____]
12: 1 Mult
13: 0 Offset

95: Sample (P70)
1: 251 Reps
2: 1 Loc [_____]

96: Do (P86)
1: 10 Set Output Flag High (Flag 0)

97: Set Active Storage Area (P80)
1: 1 Final Storage Area 1
2: 19 Array ID

98: TDR100 Measurement (P119)
1: 0 SDM Address
2: 1 Waveform
3: 3301 MMMP Mux & Probe Selection
4: 20 Waveform Averaging
5: 1 Vp
6: 240 Points
7: 30 Cable Length (meters)
8: 5 Window Length (meters)
9: .29 Probe Length (meters)
10: 0 Probe Offset (meters)
11: 3 Loc [_____]
12: 1 Mult
13: 0 Offset

99: TDR100 Measurement (P119)
1: 0 SDM Address
2: 0 La/L for Water Content
3: 3301 MMMP Mux & Probe Selection
4: 20 Waveform Averaging
5: 1 Vp
6: 240 Points
7: 30 Cable Length (meters)
8: 5 Window Length (meters)
9: .29 Probe Length (meters)
10: 0 Probe Offset (meters)
11: 2 Loc [_____]
12: 1 Mult
13: 0 Offset

100: Sample (P70)
1: 251 Reps
2: 1 Loc [_____]

101: Do (P86)
1: 10 Set Output Flag High (Flag 0)

102: Set Active Storage Area (P80)
1: 1 Final Storage Area 1
2: 20 Array ID

103: TDR100 Measurement (P119)
1: 0 SDM Address
2: 1 Waveform
3: 3401 MMMP Mux & Probe Selection
4: 20 Waveform Averaging

```
   5: 1      Vp
   6: 240    Points
   7: 32     Cable Length (meters)
   8: 5      Window Length (meters)
   9: .29    Probe Length (meters)
  10: 0      Probe Offset (meters)
  11: 3      Loc [ _____ ]
  12: 1      Mult
  13: 0      Offset

  104:       TDR100    Measurement
(P119)
   1: 0      SDM Address
   2: 0      La/L for Water Content
   3: 3401     MMMP Mux & Probe
Selection
   4: 20     Waveform Averaging
   5: 1      Vp
   6: 240    Points
   7: 32     Cable Length (meters)
   8: 5      Window Length (meters)
   9: .29    Probe Length (meters)
  10: 0      Probe Offset (meters)
  11: 2      Loc [ _____ ]
  12: 1      Mult
  13: 0      Offset

  105: Sample (P70)
   1: 251    Reps
   2: 1      Loc [ _____ ]

  106: Do (P86)
   1: 10       Set Output Flag High
(Flag 0)

  107:    Set Active Storage Area
(P80)
   1: 1      Final Storage Area 1
   2: 21     Array ID

  108:       TDR100    Measurement
(P119)
   1: 0      SDM Address
   2: 1      Waveform
   3: 3501     MMMP Mux & Probe
Selection
   4: 20     Waveform Averaging
   5: 1      Vp
   6: 240    Points
   7: 33     Cable Length (meters)
   8: 5      Window Length (meters)
   9: .29    Probe Length (meters)
  10: 0      Probe Offset (meters)
  11: 3      Loc [ _____ ]
  12: 1      Mult
  13: 0      Offset

  109:       TDR100    Measurement
(P119)
   1: 0      SDM Address
   2: 0      La/L for Water Content
   3: 3501     MMMP Mux & Probe
Selection
   4: 20     Waveform Averaging
   5: 1      Vp
   6: 240    Points
   7: 33     Cable Length (meters)
   8: 5      Window Length (meters)
   9: .29    Probe Length (meters)
  10: 0      Probe Offset (meters)
  11: 2      Loc [ _____ ]
  12: 1      Mult
  13: 0      Offset

  110: Sample (P70)
   1: 251    Reps
   2: 1      Loc [ _____ ]

  111: Do (P86)
   1: 10       Set Output Flag High
(Flag 0)

  112:    Set Active Storage Area
(P80)
   1: 1      Final Storage Area 1
   2: 22     Array ID

  113:       TDR100    Measurement
(P119)
   1: 0      SDM Address
   2: 1      Waveform
   3: 3601     MMMP Mux & Probe
Selection
   4: 20     Waveform Averaging
   5: 1      Vp
   6: 240    Points
   7: 35     Cable Length (meters)
   8: 5      Window Length (meters)
   9: .29    Probe Length (meters)
  10: 0      Probe Offset (meters)
  11: 3      Loc [ _____ ]
  12: 1      Mult
  13: 0      Offset

  114:       TDR100    Measurement
(P119)
   1: 0      SDM Address
   2: 0      La/L for Water Content
   3: 3601     MMMP Mux & Probe
Selection
   4: 20     Waveform Averaging
   5: 1      Vp
   6: 240    Points
   7: 35     Cable Length (meters)
   8: 5      Window Length (meters)
   9: .29    Probe Length (meters)
  10: 0      Probe Offset (meters)
  11: 2      Loc [ _____ ]
  12: 1      Mult
  13: 0      Offset

  115: Sample (P70)
   1: 251    Reps
   2: 1      Loc [ _____ ]

  116: Do (P86)
   1: 10       Set Output Flag High
(Flag 0)

  117:    Set Active Storage Area
(P80)
   1: 1      Final Storage Area 1
   2: 23     Array ID

  118:       TDR100    Measurement
(P119)
   1: 0      SDM Address
   2: 1      Waveform
   3: 3701     MMMP Mux & Probe
Selection
   4: 20     Waveform Averaging
   5: 1      Vp
   6: 240    Points
   7: 36     Cable Length (meters)
   8: 5      Window Length (meters)
   9: .29    Probe Length (meters)
  10: 0      Probe Offset (meters)
  11: 3      Loc [ _____ ]
  12: 1      Mult
  13: 0      Offset

  119:       TDR100    Measurement
(P119)
   1: 0      SDM Address
   2: 0      La/L for Water Content
   3: 3701     MMMP Mux & Probe
Selection
   4: 20     Waveform Averaging
   5: 1      Vp
   6: 240    Points
   7: 36     Cable Length (meters)
   8: 5      Window Length (meters)
   9: .29    Probe Length (meters)
  10: 0      Probe Offset (meters)
  11: 2      Loc [ _____ ]
  12: 1      Mult
  13: 0      Offset

  120: Sample (P70)
   1: 251    Reps
   2: 1      Loc [ _____ ]

  121: Do (P86)
   1: 10       Set Output Flag High
(Flag 0)

  122:    Set Active Storage Area
(P80)
   1: 1      Final Storage Area 1
   2: 24     Array ID

  123:       TDR100    Measurement
(P119)
   1: 0      SDM Address
   2: 1      Waveform
   3: 3801     MMMP Mux & Probe
Selection
   4: 20     Waveform Averaging
   5: 1      Vp
   6: 240    Points
   7: 38     Cable Length (meters)
   8: 5      Window Length (meters)
   9: .29    Probe Length (meters)
  10: 0      Probe Offset (meters)
  11: 3      Loc [ _____ ]
  12: 1      Mult
  13: 0      Offset

  124:       TDR100    Measurement
(P119)
   1: 0      SDM Address
   2: 0      La/L for Water Content
   3: 3801     MMMP Mux & Probe
Selection
   4: 20     Waveform Averaging
   5: 1      Vp
   6: 240    Points
   7: 38     Cable Length (meters)
   8: 5      Window Length (meters)
   9: .29    Probe Length (meters)
  10: 0      Probe Offset (meters)
  11: 2      Loc [ _____ ]
  12: 1      Mult
  13: 0      Offset

  125: Sample (P70)
   1: 251    Reps
   2: 1      Loc [ _____ ]

  126: Do (P86)
   1: 10       Set Output Flag High
(Flag 0)

  127:    Set Active Storage Area
(P80)
```

```
   1: 1      Final Storage Area 1
   2: 25     Array ID

 128:        TDR100    Measurement
(P119)
   1: 0      SDM Address
   2: 1      Waveform
   3: 4101     MMMP Mux & Probe
Selection
   4: 20     Waveform Averaging
   5: 1      Vp
   6: 240    Points
   7: 39     Cable Length (meters)
   8: 5      Window Length (meters)
   9: .29    Probe Length (meters)
  10: 0      Probe Offset (meters)
  11: 3      Loc [ _________ ]
  12: 1      Mult
  13: 0      Offset

 129:        TDR100    Measurement
(P119)
   1: 0      SDM Address
   2: 0      La/L for Water Content
   3: 4101     MMMP Mux & Probe
Selection
   4: 20     Waveform Averaging
   5: 1      Vp
   6: 240    Points
   7: 39     Cable Length (meters)
   8: 5      Window Length (meters)
   9: .29    Probe Length (meters)
  10: 0      Probe Offset (meters)
  11: 2      Loc [ _________ ]
  12: 1      Mult
  13: 0      Offset

 130: Sample (P70)
   1: 251    Reps
   2: 1      Loc [ _________ ]

 131: Do (P86)
   1: 10       Set Output Flag High
(Flag 0)

 132:  Set Active Storage Area
(P80)
   1: 1      Final Storage Area 1
   2: 26     Array ID

 133:        TDR100    Measurement
(P119)
   1: 0      SDM Address
   2: 1      Waveform
   3: 4201     MMMP Mux & Probe
Selection
   4: 20     Waveform Averaging
   5: 1      Vp
   6: 240    Points
   7: 40     Cable Length (meters)
   8: 5      Window Length (meters)
   9: .29    Probe Length (meters)
  10: 0      Probe Offset (meters)
  11: 3      Loc [ _________ ]
  12: 1      Mult
  13: 0      Offset

 134:        TDR100    Measurement
(P119)
   1: 0      SDM Address
   2: 0      La/L for Water Content
   3: 4201     MMMP Mux & Probe
Selection
   4: 20     Waveform Averaging
   5: 1      Vp
   6: 240    Points
   7: 40     Cable Length (meters)
   8: 5      Window Length (meters)
   9: .29    Probe Length (meters)
  10: 0      Probe Offset (meters)
  11: 2      Loc [ _________ ]
  12: 1      Mult
  13: 0      Offset

 135: Sample (P70)
   1: 251    Reps
   2: 1      Loc [ _________ ]

 136: Do (P86)
   1: 10       Set Output Flag High
(Flag 0)

 137:  Set Active Storage Area
(P80)
   1: 1      Final Storage Area 1
   2: 27     Array ID

 138:        TDR100    Measurement
(P119)
   1: 0      SDM Address
   2: 1      Waveform
   3: 4301     MMMP Mux & Probe
Selection
   4: 20     Waveform Averaging
   5: 1      Vp
   6: 240    Points
   7: 42     Cable Length (meters)
   8: 5      Window Length (meters)
   9: .29    Probe Length (meters)
  10: 0      Probe Offset (meters)
  11: 3      Loc [ _________ ]
  12: 1      Mult
  13: 0      Offset

 139:        TDR100    Measurement
(P119)
   1: 0      SDM Address
   2: 0      La/L for Water Content
   3: 4301     MMMP Mux & Probe
Selection
   4: 20     Waveform Averaging
   5: 1      Vp
   6: 240    Points
   7: 42     Cable Length (meters)
   8: 5      Window Length (meters)
   9: .29    Probe Length (meters)
  10: 0      Probe Offset (meters)
  11: 2      Loc [ _________ ]
  12: 1      Mult
  13: 0      Offset

 140: Sample (P70)
   1: 251    Reps
   2: 1      Loc [ _________ ]

 141: Do (P86)
   1: 10       Set Output Flag High
(Flag 0)

 142:  Set Active Storage Area
(P80)
   1: 1      Final Storage Area 1
   2: 28     Array ID

 143:        TDR100    Measurement
(P119)
   1: 0      SDM Address
   2: 1      Waveform
   3: 4401     MMMP Mux & Probe
Selection
   4: 20     Waveform Averaging
   5: 1      Vp
   6: 240    Points
   7: 43     Cable Length (meters)
   8: 5      Window Length (meters)
   9: .29    Probe Length (meters)
  10: 0      Probe Offset (meters)
  11: 3      Loc [ _________ ]
  12: 1      Mult
  13: 0      Offset

 144:        TDR100    Measurement
(P119)
   1: 0      SDM Address
   2: 0      La/L for Water Content
   3: 4401     MMMP Mux & Probe
Selection
   4: 20     Waveform Averaging
   5: 1      Vp
   6: 240    Points
   7: 43     Cable Length (meters)
   8: 5      Window Length (meters)
   9: .29    Probe Length (meters)
  10: 0      Probe Offset (meters)
  11: 2      Loc [ _________ ]
  12: 1      Mult
  13: 0      Offset

 145: Sample (P70)
   1: 251    Reps
   2: 1      Loc [ _________ ]

 146: Do (P86)
   1: 10       Set Output Flag High
(Flag 0)

 147:  Set Active Storage Area
(P80)
   1: 1      Final Storage Area 1
   2: 29     Array ID

 148:        TDR100    Measurement
(P119)
   1: 0      SDM Address
   2: 1      Waveform
   3: 4501     MMMP Mux & Probe
Selection
   4: 20     Waveform Averaging
   5: 1      Vp
   6: 240    Points
   7: 45     Cable Length (meters)
   8: 5      Window Length (meters)
   9: .29    Probe Length (meters)
  10: 0      Probe Offset (meters)
  11: 3      Loc [ _________ ]
  12: 1      Mult
  13: 0      Offset

 149:        TDR100    Measurement
(P119)
   1: 0      SDM Address
   2: 0      La/L for Water Content
   3: 4501     MMMP Mux & Probe
Selection
   4: 20     Waveform Averaging
   5: 1      Vp
   6: 240    Points
   7: 45     Cable Length (meters)
   8: 5      Window Length (meters)
   9: .29    Probe Length (meters)
  10: 0      Probe Offset (meters)
  11: 2      Loc [ _________ ]
  12: 1      Mult
  13: 0      Offset
```

150: Sample (P70)
1: 251 Reps
2: 1 Loc [_____]

151: Do (P86)
1: 10 Set Output Flag High (Flag 0)

152: Set Active Storage Area (P80)
1: 1 Final Storage Area 1
2: 30 Array ID

153: TDR100 Measurement (P119)
1: 0 SDM Address
2: 1 Waveform
3: 4601 MMMP Mux & Probe Selection
4: 20 Waveform Averaging
5: 1 Vp
6: 240 Points
7: 0 Cable Length (meters)
8: 5 Window Length (meters)
9: .29 Probe Length (meters)
10: 0 Probe Offset (meters)
11: 3 Loc [_____]
12: 1 Mult
13: 0 Offset

154: TDR100 Measurement (P119)
1: 0 SDM Address
2: 0 La/L for Water Content
3: 4601 MMMP Mux & Probe Selection
4: 20 Waveform Averaging
5: 1 Vp
6: 240 Points
7: 0 Cable Length (meters)
8: 5 Window Length (meters)
9: .29 Probe Length (meters)
10: 0 Probe Offset (meters)
11: 2 Loc [_____]
12: 1 Mult
13: 0 Offset

155: Sample (P70)
1: 251 Reps
2: 1 Loc [_____]

156: Do (P86)
1: 10 Set Output Flag High (Flag 0)

157: Set Active Storage Area (P80)
1: 1 Final Storage Area 1
2: 31 Array ID

158: TDR100 Measurement (P119)
1: 0 SDM Address
2: 1 Waveform
3: 5101 MMMP Mux & Probe Selection
4: 20 Waveform Averaging
5: 1 Vp
6: 240 Points
7: 34 Cable Length (meters)
8: 5 Window Length (meters)
9: .29 Probe Length (meters)
10: 0 Probe Offset (meters)
11: 3 Loc [_____]
12: 1 Mult
13: 0 Offset

159: TDR100 Measurement (P119)
1: 0 SDM Address
2: 0 La/L for Water Content
3: 5101 MMMP Mux & Probe Selection
4: 20 Waveform Averaging
5: 1 Vp
6: 240 Points
7: 34 Cable Length (meters)
8: 5 Window Length (meters)
9: .29 Probe Length (meters)
10: 0 Probe Offset (meters)
11: 2 Loc [_____]
12: 1 Mult
13: 0 Offset

160: Sample (P70)
1: 251 Reps
2: 1 Loc [_____]

161: Do (P86)
1: 10 Set Output Flag High (Flag 0)

162: Set Active Storage Area (P80)
1: 1 Final Storage Area 1
2: 32 Array ID

163: TDR100 Measurement (P119)
1: 0 SDM Address
2: 1 Waveform
3: 5201 MMMP Mux & Probe Selection
4: 20 Waveform Averaging
5: 1 Vp
6: 240 Points
7: 35 Cable Length (meters)
8: 5 Window Length (meters)
9: .29 Probe Length (meters)
10: 0 Probe Offset (meters)
11: 3 Loc [_____]
12: 1 Mult
13: 0 Offset

164: TDR100 Measurement (P119)
1: 0 SDM Address
2: 0 La/L for Water Content
3: 5201 MMMP Mux & Probe Selection
4: 20 Waveform Averaging
5: 1 Vp
6: 240 Points
7: 35 Cable Length (meters)
8: 5 Window Length (meters)
9: .29 Probe Length (meters)
10: 0 Probe Offset (meters)
11: 2 Loc [_____]
12: 1 Mult
13: 0 Offset

165: Sample (P70)
1: 251 Reps
2: 1 Loc [_____]

166: Do (P86)
1: 10 Set Output Flag High (Flag 0)

167: Set Active Storage Area (P80)
1: 1 Final Storage Area 1
2: 33 Array ID

168: TDR100 Measurement (P119)
1: 0 SDM Address
2: 1 Waveform
3: 5301 MMMP Mux & Probe Selection
4: 20 Waveform Averaging
5: 1 Vp
6: 240 Points
7: 37 Cable Length (meters)
8: 5 Window Length (meters)
9: .29 Probe Length (meters)
10: 0 Probe Offset (meters)
11: 3 Loc [_____]
12: 1 Mult
13: 0 Offset

169: TDR100 Measurement (P119)
1: 0 SDM Address
2: 0 La/L for Water Content
3: 5301 MMMP Mux & Probe Selection
4: 20 Waveform Averaging
5: 1 Vp
6: 240 Points
7: 37 Cable Length (meters)
8: 5 Window Length (meters)
9: .29 Probe Length (meters)
10: 0 Probe Offset (meters)
11: 2 Loc [_____]
12: 1 Mult
13: 0 Offset

170: Sample (P70)
1: 251 Reps
2: 1 Loc [_____]

171: Do (P86)
1: 10 Set Output Flag High (Flag 0)

172: Set Active Storage Area (P80)
1: 1 Final Storage Area 1
2: 34 Array ID

173: TDR100 Measurement (P119)
1: 0 SDM Address
2: 1 Waveform
3: 5401 MMMP Mux & Probe Selection
4: 20 Waveform Averaging
5: 1 Vp
6: 240 Points
7: 37 Cable Length (meters)
8: 5 Window Length (meters)
9: .29 Probe Length (meters)
10: 0 Probe Offset (meters)
11: 3 Loc [_____]
12: 1 Mult
13: 0 Offset

174: TDR100 Measurement (P119)
1: 0 SDM Address
2: 0 La/L for Water Content
3: 5401 MMMP Mux & Probe Selection

4: 20 Waveform Averaging
5: 1 Vp
6: 240 Points
7: 37 Cable Length (meters)
8: 5 Window Length (meters)
9: .29 Probe Length (meters)
10: 0 Probe Offset (meters)
11: 2 Loc [_____]
12: 1 Mult
13: 0 Offset

175: Sample (P70)
1: 251 Reps
2: 1 Loc [_____]

176: Do (P86)
1: 10 Set Output Flag High (Flag 0)

177: Set Active Storage Area (P80)
1: 1 Final Storage Area 1
2: 35 Array ID

178: TDR100 Measurement (P119)
1: 0 SDM Address
2: 1 Waveform
3: 5501 MMMP Mux & Probe Selection
4: 20 Waveform Averaging
5: 1 Vp
6: 240 Points
7: 40 Cable Length (meters)
8: 5 Window Length (meters)
9: .29 Probe Length (meters)
10: 0 Probe Offset (meters)
11: 3 Loc [_____]
12: 1 Mult
13: 0 Offset

179: TDR100 Measurement (P119)
1: 0 SDM Address
2: 0 La/L for Water Content
3: 5501 MMMP Mux & Probe Selection
4: 20 Waveform Averaging
5: 1 Vp
6: 240 Points
7: 40 Cable Length (meters)
8: 5 Window Length (meters)
9: .29 Probe Length (meters)
10: 0 Probe Offset (meters)
11: 2 Loc [_____]
12: 1 Mult
13: 0 Offset

180: Sample (P70)
1: 251 Reps
2: 1 Loc [_____]

181: Do (P86)
1: 10 Set Output Flag High (Flag 0)

182: Set Active Storage Area (P80)
1: 1 Final Storage Area 1
2: 36 Array ID

183: TDR100 Measurement (P119)
1: 0 SDM Address
2: 1 Waveform
3: 5601 MMMP Mux & Probe Selection
4: 20 Waveform Averaging
5: 1 Vp
6: 240 Points
7: 42 Cable Length (meters)
8: 5 Window Length (meters)
9: .29 Probe Length (meters)
10: 0 Probe Offset (meters)
11: 3 Loc [_____]
12: 1 Mult
13: 0 Offset

184: TDR100 Measurement (P119)
1: 0 SDM Address
2: 0 La/L for Water Content
3: 5601 MMMP Mux & Probe Selection
4: 20 Waveform Averaging
5: 1 Vp
6: 240 Points
7: 42 Cable Length (meters)
8: 5 Window Length (meters)
9: .29 Probe Length (meters)
10: 0 Probe Offset (meters)
11: 2 Loc [_____]
12: 1 Mult
13: 0 Offset

185: Sample (P70)
1: 251 Reps
2: 1 Loc [_____]

186: Do (P86)
1: 10 Set Output Flag High (Flag 0)

187: Set Active Storage Area (P80)
1: 1 Final Storage Area 1
2: 37 Array ID

188: TDR100 Measurement (P119)
1: 0 SDM Address
2: 1 Waveform
3: 5701 MMMP Mux & Probe Selection
4: 20 Waveform Averaging
5: 1 Vp
6: 240 Points
7: 42 Cable Length (meters)
8: 5 Window Length (meters)
9: .29 Probe Length (meters)
10: 0 Probe Offset (meters)
11: 3 Loc [_____]
12: 1 Mult
13: 0 Offset

189: TDR100 Measurement (P119)
1: 0 SDM Address
2: 0 La/L for Water Content
3: 5701 MMMP Mux & Probe Selection
4: 20 Waveform Averaging
5: 1 Vp
6: 240 Points
7: 42 Cable Length (meters)
8: 5 Window Length (meters)
9: .29 Probe Length (meters)
10: 0 Probe Offset (meters)
11: 2 Loc [_____]
12: 1 Mult
13: 0 Offset

190: Sample (P70)
1: 251 Reps
2: 1 Loc [_____]

191: Do (P86)
1: 10 Set Output Flag High (Flag 0)

192: Set Active Storage Area (P80)
1: 1 Final Storage Area 1
2: 38 Array ID

193: TDR100 Measurement (P119)
1: 0 SDM Address
2: 1 Waveform
3: 5801 MMMP Mux & Probe Selection
4: 20 Waveform Averaging
5: 1 Vp
6: 240 Points
7: 44 Cable Length (meters)
8: 5 Window Length (meters)
9: .29 Probe Length (meters)
10: 0 Probe Offset (meters)
11: 3 Loc [_____]
12: 1 Mult
13: 0 Offset

194: TDR100 Measurement (P119)
1: 0 SDM Address
2: 0 La/L for Water Content
3: 5801 MMMP Mux & Probe Selection
4: 20 Waveform Averaging
5: 1 Vp
6: 240 Points
7: 44 Cable Length (meters)
8: 5 Window Length (meters)
9: .29 Probe Length (meters)
10: 0 Probe Offset (meters)
11: 2 Loc [_____]
12: 1 Mult
13: 0 Offset

195: Sample (P70)
1: 251 Reps
2: 1 Loc [_____]

196: Do (P86)
1: 10 Set Output Flag High (Flag 0)

197: Set Active Storage Area (P80)
1: 1 Final Storage Area 1
2: 39 Array ID

198: TDR100 Measurement (P119)
1: 0 SDM Address
2: 1 Waveform
3: 6101 MMMP Mux & Probe Selection
4: 20 Waveform Averaging
5: 1 Vp
6: 240 Points
7: 46 Cable Length (meters)
8: 5 Window Length (meters)
9: .29 Probe Length (meters)
10: 0 Probe Offset (meters)

11: 3 Loc [_____]
12: 1 Mult
13: 0 Offset

199: TDR100 Measurement (P119)
1: 0 SDM Address
2: 0 La/L for Water Content
3: 6101 MMMP Mux & Probe Selection
4: 20 Waveform Averaging
5: 1 Vp
6: 240 Points
7: 46 Cable Length (meters)
8: 5 Window Length (meters)
9: .29 Probe Length (meters)
10: 0 Probe Offset (meters)
11: 2 Loc [_____]
12: 1 Mult
13: 0 Offset

200: Sample (P70)
1: 251 Reps
2: 1 Loc [_____]

201: Do (P86)
1: 10 Set Output Flag High (Flag 0)

202: Set Active Storage Area (P80)
1: 1 Final Storage Area 1
2: 40 Array ID

203: TDR100 Measurement (P119)
1: 0 SDM Address
2: 1 Waveform
3: 6201 MMMP Mux & Probe Selection
4: 20 Waveform Averaging
5: 1 Vp
6: 240 Points
7: 47 Cable Length (meters)
8: 5 Window Length (meters)
9: .29 Probe Length (meters)
10: 0 Probe Offset (meters)
11: 3 Loc [_____]
12: 1 Mult
13: 0 Offset

204: TDR100 Measurement (P119)
1: 0 SDM Address
2: 0 La/L for Water Content
3: 6201 MMMP Mux & Probe Selection
4: 20 Waveform Averaging
5: 1 Vp
6: 240 Points
7: 47 Cable Length (meters)
8: 5 Window Length (meters)
9: .29 Probe Length (meters)
10: 0 Probe Offset (meters)
11: 2 Loc [_____]
12: 1 Mult
13: 0 Offset

205: Sample (P70)
1: 251 Reps
2: 1 Loc [_____]

206: Do (P86)
1: 10 Set Output Flag High (Flag 0)

207: Set Active Storage Area (P80)
1: 1 Final Storage Area 1
2: 41 Array ID

208: TDR100 Measurement (P119)
1: 0 SDM Address
2: 1 Waveform
3: 6301 MMMP Mux & Probe Selection
4: 20 Waveform Averaging
5: 1 Vp
6: 240 Points
7: 49 Cable Length (meters)
8: 5 Window Length (meters)
9: .29 Probe Length (meters)
10: 0 Probe Offset (meters)
11: 3 Loc [_____]
12: 1 Mult
13: 0 Offset

209: TDR100 Measurement (P119)
1: 0 SDM Address
2: 0 La/L for Water Content
3: 6301 MMMP Mux & Probe Selection
4: 20 Waveform Averaging
5: 1 Vp
6: 240 Points
7: 49 Cable Length (meters)
8: 5 Window Length (meters)
9: .29 Probe Length (meters)
10: 0 Probe Offset (meters)
11: 2 Loc [_____]
12: 1 Mult
13: 0 Offset

210: Sample (P70)
1: 251 Reps
2: 1 Loc [_____]

211: Do (P86)
1: 10 Set Output Flag High (Flag 0)

212: Set Active Storage Area (P80)
1: 1 Final Storage Area 1
2: 42 Array ID

213: TDR100 Measurement (P119)
1: 0 SDM Address
2: 1 Waveform
3: 6401 MMMP Mux & Probe Selection
4: 20 Waveform Averaging
5: 1 Vp
6: 240 Points
7: 50 Cable Length (meters)
8: 5 Window Length (meters)
9: .29 Probe Length (meters)
10: 0 Probe Offset (meters)
11: 3 Loc [_____]
12: 1 Mult
13: 0 Offset

214: TDR100 Measurement (P119)
1: 0 SDM Address
2: 0 La/L for Water Content
3: 6401 MMMP Mux & Probe Selection
4: 20 Waveform Averaging
5: 1 Vp
6: 240 Points
7: 50 Cable Length (meters)
8: 5 Window Length (meters)
9: .29 Probe Length (meters)
10: 0 Probe Offset (meters)
11: 2 Loc [_____]
12: 1 Mult
13: 0 Offset

215: Sample (P70)
1: 251 Reps
2: 1 Loc [_____]

216: Do (P86)
1: 10 Set Output Flag High (Flag 0)

217: Set Active Storage Area (P80)
1: 1 Final Storage Area 1
2: 43 Array ID

218: TDR100 Measurement (P119)
1: 0 SDM Address
2: 1 Waveform
3: 6501 MMMP Mux & Probe Selection
4: 20 Waveform Averaging
5: 1 Vp
6: 240 Points
7: 51 Cable Length (meters)
8: 5 Window Length (meters)
9: .29 Probe Length (meters)
10: 0 Probe Offset (meters)
11: 3 Loc [_____]
12: 1 Mult
13: 0 Offset

219: TDR100 Measurement (P119)
1: 0 SDM Address
2: 0 La/L for Water Content
3: 6501 MMMP Mux & Probe Selection
4: 20 Waveform Averaging
5: 1 Vp
6: 240 Points
7: 51 Cable Length (meters)
8: 5 Window Length (meters)
9: .29 Probe Length (meters)
10: 0 Probe Offset (meters)
11: 2 Loc [_____]
12: 1 Mult
13: 0 Offset

220: Sample (P70)
1: 251 Reps
2: 1 Loc [_____]

221: Do (P86)
1: 10 Set Output Flag High (Flag 0)

222: Set Active Storage Area (P80)
1: 1 Final Storage Area 1
2: 44 Array ID

223: TDR100 Measurement (P119)

```
   1: 0      SDM Address
   2: 1      Waveform
   3: 6601     MMMP Mux & Probe
Selection
   4: 20     Waveform Averaging
   5: 1      Vp
   6: 240     Points
   7: 54     Cable Length (meters)
   8: 5      Window Length (meters)
   9: .29    Probe Length (meters)
  10: 0      Probe Offset (meters)
  11: 3      Loc [ _____ ]
  12: 1      Mult
  13: 0      Offset

  224:       TDR100    Measurement
(P119)
   1: 0      SDM Address
   2: 0      La/L for Water Content
   3: 6601     MMMP Mux & Probe
Selection
   4: 20     Waveform Averaging
   5: 1      Vp
   6: 240     Points
   7: 54     Cable Length (meters)
   8: 5      Window Length (meters)
   9: .29    Probe Length (meters)
  10: 0      Probe Offset (meters)
  11: 2      Loc [ _____ ]
  12: 1      Mult
  13: 0      Offset

  225: Sample (P70)
   1: 251     Reps
   2: 1      Loc [ _____ ]

  226: Do (P86)
   1: 10       Set Output Flag High
(Flag 0)

  227:    Set Active Storage Area
(P80)
   1: 1      Final Storage Area 1
   2: 45     Array ID

  228:       TDR100    Measurement
(P119)
   1: 0      SDM Address
   2: 1      Waveform
   3: 7101     MMMP Mux & Probe
Selection
   4: 20     Waveform Averaging
   5: 1      Vp
   6: 240     Points
   7: 24     Cable Length (meters)
   8: 5      Window Length (meters)
   9: .29    Probe Length (meters)
  10: 0      Probe Offset (meters)
  11: 3      Loc [ _____ ]
  12: 1      Mult
  13: 0      Offset

  229:       TDR100    Measurement
(P119)
   1: 0      SDM Address
   2: 0      La/L for Water Content
   3: 7101     MMMP Mux & Probe
Selection
   4: 20     Waveform Averaging
   5: 1      Vp
   6: 240     Points
   7: 24     Cable Length (meters)
   8: 5      Window Length (meters)
   9: .29    Probe Length (meters)
  10: 0      Probe Offset (meters)
  11: 2      Loc [ _____ ]
  12: 1      Mult
  13: 0      Offset

  230: Sample (P70)
   1: 251     Reps
   2: 1      Loc [ _____ ]

  231: Do (P86)
   1: 10       Set Output Flag High
(Flag 0)

  232:    Set Active Storage Area
(P80)
   1: 1      Final Storage Area 1
   2: 46     Array ID

  233:       TDR100    Measurement
(P119)
   1: 0      SDM Address
   2: 1      Waveform
   3: 7201     MMMP Mux & Probe
Selection
   4: 20     Waveform Averaging
   5: 1      Vp
   6: 240     Points
   7: 25.7    Cable Length (meters)
   8: 5      Window Length (meters)
   9: .29    Probe Length (meters)
  10: 0      Probe Offset (meters)
  11: 3      Loc [ _____ ]
  12: 1      Mult
  13: 0      Offset

  234:       TDR100    Measurement
(P119)
   1: 0      SDM Address
   2: 0      La/L for Water Content
   3: 7201     MMMP Mux & Probe
Selection
   4: 20     Waveform Averaging
   5: 1      Vp
   6: 240     Points
   7: 25.7    Cable Length (meters)
   8: 5      Window Length (meters)
   9: .29    Probe Length (meters)
  10: 0      Probe Offset (meters)
  11: 2      Loc [ _____ ]
  12: 1      Mult
  13: 0      Offset

  235: Sample (P70)
   1: 251     Reps
   2: 1      Loc [ _____ ]

  236: Do (P86)
   1: 10       Set Output Flag High
(Flag 0)

  237:    Set Active Storage Area
(P80)
   1: 1      Final Storage Area 1
   2: 47     Array ID

  238:       TDR100    Measurement
(P119)
   1: 0      SDM Address
   2: 1      Waveform
   3: 7301     MMMP Mux & Probe
Selection
   4: 20     Waveform Averaging
   5: 1      Vp
   6: 240     Points
   7: 27     Cable Length (meters)
   8: 5      Window Length (meters)
   9: .29    Probe Length (meters)
  10: 0      Probe Offset (meters)
  11: 3      Loc [ _____ ]
  12: 1      Mult
  13: 0      Offset

  239:       TDR100    Measurement
(P119)
   1: 0      SDM Address
   2: 0      La/L for Water Content
   3: 7301     MMMP Mux & Probe
Selection
   4: 20     Waveform Averaging
   5: 1      Vp
   6: 240     Points
   7: 27     Cable Length (meters)
   8: 5      Window Length (meters)
   9: .29    Probe Length (meters)
  10: 0      Probe Offset (meters)
  11: 2      Loc [ _____ ]
  12: 1      Mult
  13: 0      Offset

  240: Sample (P70)
   1: 251     Reps
   2: 1      Loc [ _____ ]

  241: Do (P86)
   1: 10       Set Output Flag High
(Flag 0)

  242:    Set Active Storage Area
(P80)
   1: 1      Final Storage Area 1
   2: 48     Array ID

  243:       TDR100    Measurement
(P119)
   1: 0      SDM Address
   2: 1      Waveform
   3: 7401     MMMP Mux & Probe
Selection
   4: 20     Waveform Averaging
   5: 1      Vp
   6: 240     Points
   7: 28     Cable Length (meters)
   8: 5      Window Length (meters)
   9: .29    Probe Length (meters)
  10: 0      Probe Offset (meters)
  11: 3      Loc [ _____ ]
  12: 1      Mult
  13: 0      Offset

  244:       TDR100    Measurement
(P119)
   1: 0      SDM Address
   2: 0      La/L for Water Content
   3: 7401     MMMP Mux & Probe
Selection
   4: 20     Waveform Averaging
   5: 1      Vp
   6: 240     Points
   7: 28     Cable Length (meters)
   8: 5      Window Length (meters)
   9: .29    Probe Length (meters)
  10: 0      Probe Offset (meters)
  11: 2      Loc [ _____ ]
  12: 1      Mult
  13: 0      Offset

  245: Sample (P70)
   1: 251     Reps
   2: 1      Loc [ _____ ]

  246: Do (P86)
```

```
   1: 10       Set Output Flag High
(Flag 0)

  247:  Set  Active  Storage  Area
(P80)
   1: 1      Final Storage Area 1
   2: 49     Array ID

  248:      TDR100    Measurement
(P119)
   1: 0      SDM Address
   2: 1      Waveform
   3: 7501     MMMP Mux & Probe
Selection
   4: 20     Waveform Averaging
   5: 1      Vp
   6: 240    Points
   7: 31     Cable Length (meters)
   8: 5      Window Length (meters)
   9: .29    Probe Length (meters)
  10: 0      Probe Offset (meters)
  11: 3      Loc [ _________ ]
  12: 1      Mult
  13: 0      Offset

  249:      TDR100    Measurement
(P119)
   1: 0      SDM Address
   2: 0      La/L for Water Content
   3: 7501     MMMP Mux & Probe
Selection
   4: 20     Waveform Averaging
   5: 1      Vp
   6: 240    Points
   7: 31     Cable Length (meters)
   8: 5      Window Length (meters)
   9: .29    Probe Length (meters)
  10: 0      Probe Offset (meters)
  11: 2      Loc [ _________ ]
  12: 1      Mult
  13: 0      Offset

  250: Sample (P70)
   1: 251    Reps
   2: 1      Loc [ _________ ]

  251: Do (P86)
   1: 10       Set Output Flag High
(Flag 0)

  252:  Set  Active  Storage  Area
(P80)
   1: 1      Final Storage Area 1
   2: 50     Array ID

  253:      TDR100    Measurement
(P119)
   1: 0      SDM Address
   2: 1      Waveform
   3: 7601     MMMP Mux & Probe
Selection
   4: 20     Waveform Averaging
   5: 1      Vp
   6: 240    Points
   7: 33     Cable Length (meters)
   8: 5      Window Length (meters)
   9: .29    Probe Length (meters)
  10: 0      Probe Offset (meters)
  11: 3      Loc [ _________ ]
  12: 1      Mult
  13: 0      Offset

  254:      TDR100    Measurement
(P119)
   1: 0      SDM Address
   2: 0      La/L for Water Content
   3: 7601     MMMP Mux & Probe
Selection
   4: 20     Waveform Averaging
   5: 1      Vp
   6: 240    Points
   7: 33     Cable Length (meters)
   8: 5      Window Length (meters)
   9: .29    Probe Length (meters)
  10: 0      Probe Offset (meters)
  11: 2      Loc [ _________ ]
  12: 1      Mult
  13: 0      Offset

  255: Sample (P70)
   1: 251    Reps
   2: 1      Loc [ _________ ]

  256: Do (P86)
   1: 10       Set Output Flag High
(Flag 0)

  257:  Set  Active  Storage  Area
(P80)
   1: 1      Final Storage Area 1
   2: 51     Array ID

  258:      TDR100    Measurement
(P119)
   1: 0      SDM Address
   2: 1      Waveform
   3: 7701     MMMP Mux & Probe
Selection
   4: 20     Waveform Averaging
   5: 1      Vp
   6: 240    Points
   7: 35     Cable Length (meters)
   8: 5      Window Length (meters)
   9: .29    Probe Length (meters)
  10: 0      Probe Offset (meters)
  11: 3      Loc [ _________ ]
  12: 1      Mult
  13: 0      Offset

  259:      TDR100    Measurement
(P119)
   1: 0      SDM Address
   2: 0      La/L for Water Content
   3: 7701     MMMP Mux & Probe
Selection
   4: 20     Waveform Averaging
   5: 1      Vp
   6: 240    Points
   7: 35     Cable Length (meters)
   8: 5      Window Length (meters)
   9: .29    Probe Length (meters)
  10: 0      Probe Offset (meters)
  11: 2      Loc [ _________ ]
  12: 1      Mult
  13: 0      Offset

  260: Sample (P70)
   1: 251    Reps
   2: 1      Loc [ _________ ]

  261: Do (P86)
   1: 10       Set Output Flag High
(Flag 0)

  262:  Set  Active  Storage  Area
(P80)
   1: 1      Final Storage Area 1
   2: 52     Array ID

  263:      TDR100    Measurement
(P119)
   1: 0      SDM Address
   2: 1      Waveform
   3: 7801     MMMP Mux & Probe
Selection
   4: 20     Waveform Averaging
   5: 1      Vp
   6: 240    Points
   7: 38     Cable Length (meters)
   8: 5      Window Length (meters)
   9: .29    Probe Length (meters)
  10: 0      Probe Offset (meters)
  11: 3      Loc [ _________ ]
  12: 1      Mult
  13: 0      Offset

  264:      TDR100    Measurement
(P119)
   1: 0      SDM Address
   2: 0      La/L for Water Content
   3: 7801     MMMP Mux & Probe
Selection
   4: 20     Waveform Averaging
   5: 1      Vp
   6: 240    Points
   7: 38     Cable Length (meters)
   8: 5      Window Length (meters)
   9: .29    Probe Length (meters)
  10: 0      Probe Offset (meters)
  11: 2      Loc [ _________ ]
  12: 1      Mult
  13: 0      Offset

  265: Sample (P70)
   1: 251    Reps
   2: 1      Loc [ _________ ]

266: End (P95)

267: Serial Out (P96)
   1: 71     Storage Module

*Table 2 Program
  01: 0.0000     Execution Interval
(seconds)

*Table 3 Subroutines

End Program
```

Appendix 4. Radar line locations.

Great Heck SE 588 213 Unscaled sketch map

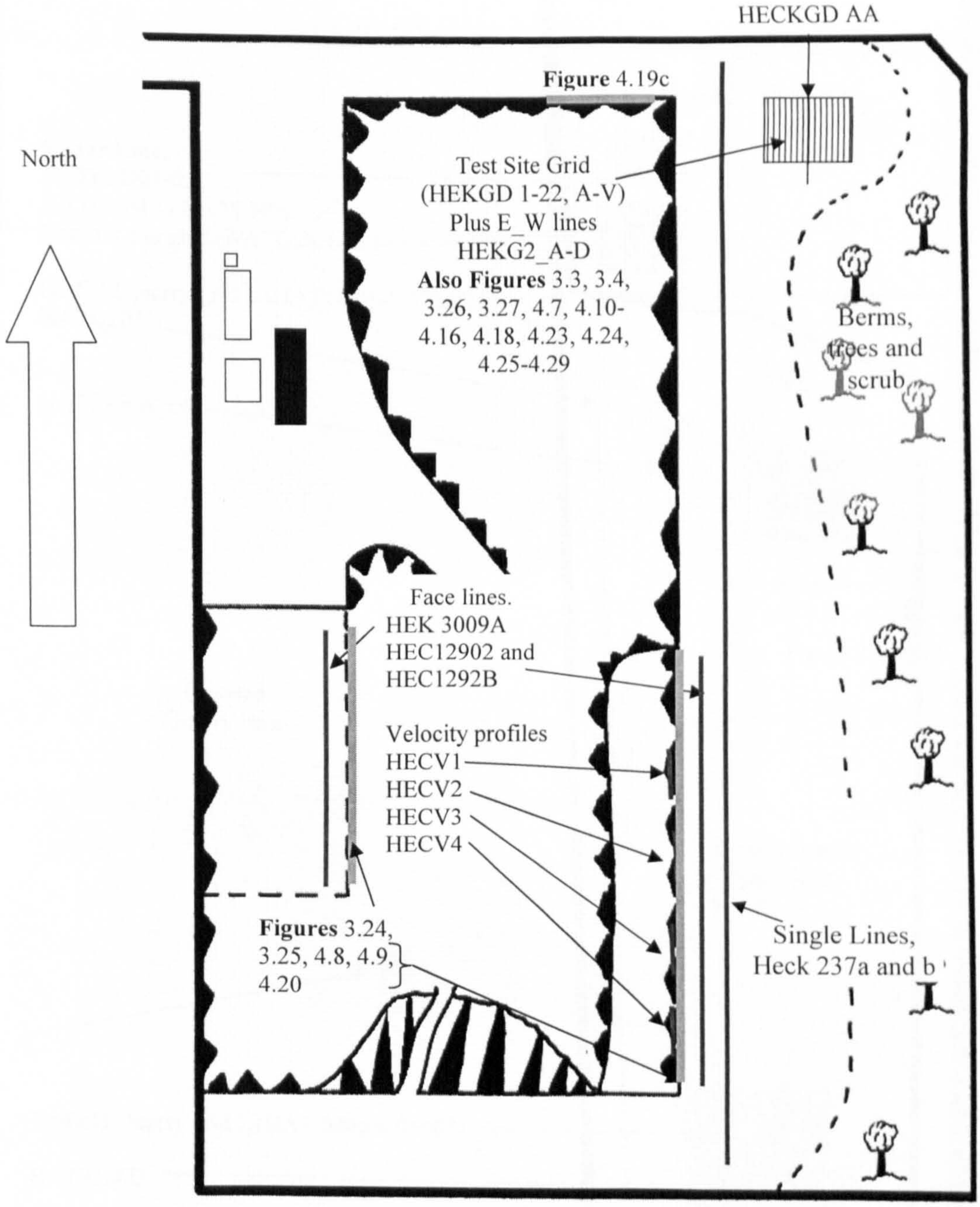

Hatfield Quarry SE 653 075 Unscaled sketch map.

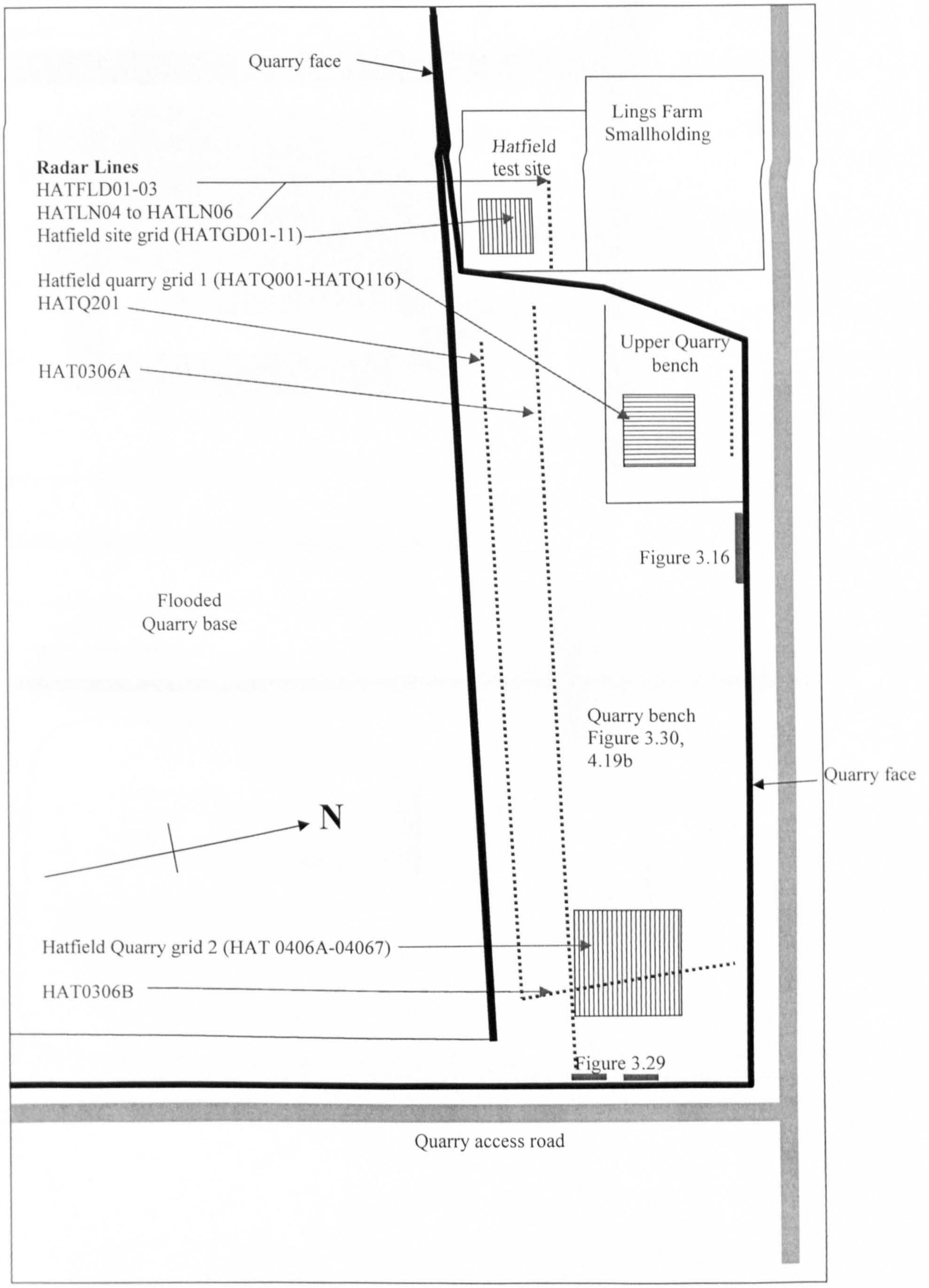

Pollington Quarry SE 612 201 Unscaled sketch map.

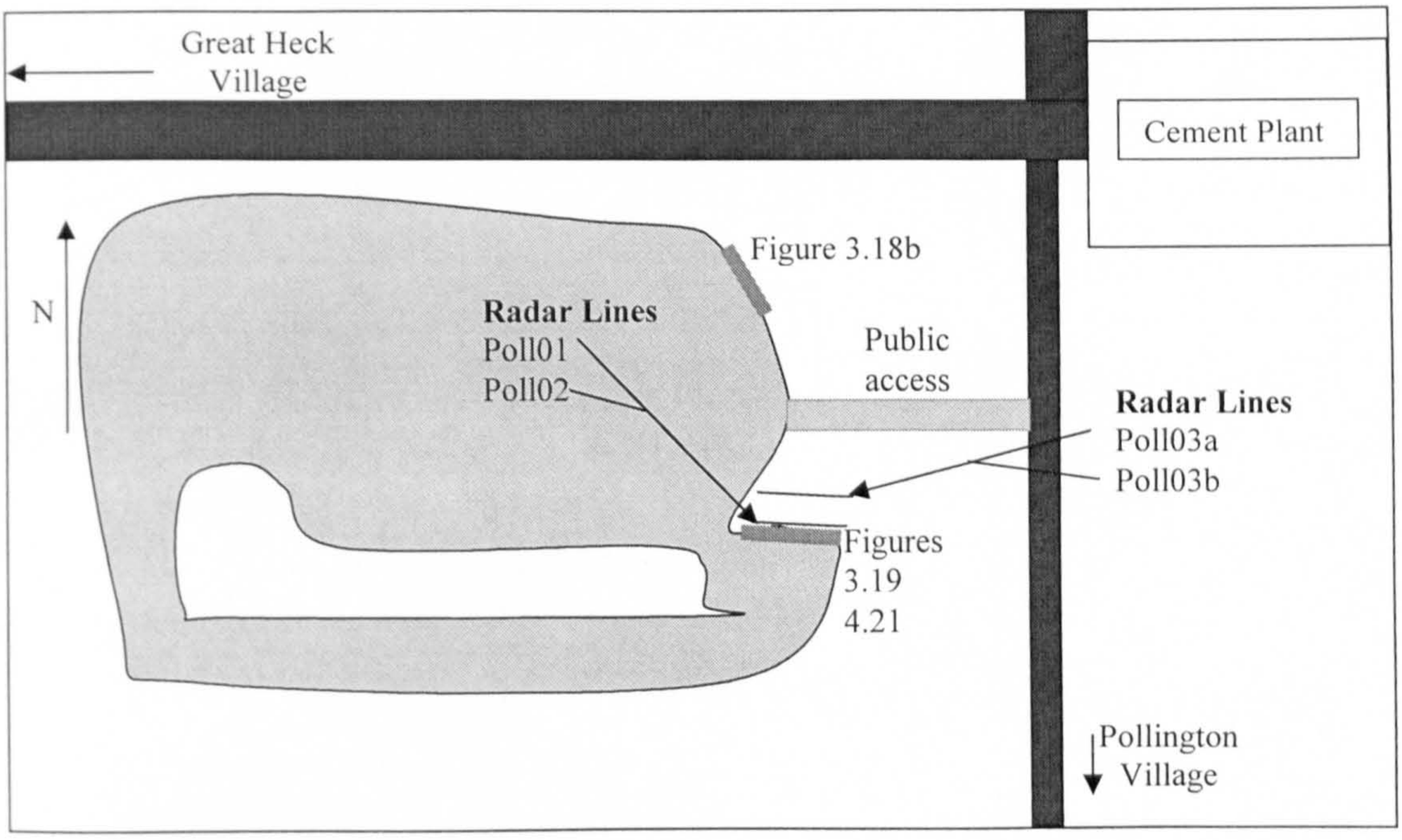

Rufford Quarry SK 596 608 Unscaled sketch map